

# Rare Earth and Transition Metal Doping of Semiconductor Materials: Synthesis, Magnetic Properties and Room Temperature Spintronics

Edited by V. Dierolf, I. T. Ferguson and J. M. Zavada

# **Rare Earth and Transition Metal Doping of Semiconductor Materials**

**Related titles**

*Nanostructured Semiconductor Oxides for the Next Generation of Electronics and Functional Devices: Properties and Applications*

(ISBN 978-1-78242-220-4)

*Graphene: Properties, Preparation, Characterisation and Devices*

(ISBN 978-0-85709-508-4)

*Silicon-On-Insulator (SOI) Technology*

(ISBN 978-0-85709-526-8)

Woodhead Publishing Series in Electronic and  
Optical Materials: Number 87

# Rare Earth and Transition Metal Doping of Semiconductor Materials

Synthesis, Magnetic Properties and  
Room Temperature Spintronics

*Edited by*

*V. Dierolf, I.T. Ferguson, J.M. Zavada*



ELSEVIER

AMSTERDAM • BOSTON • CAMBRIDGE • HEIDELBERG  
LONDON • NEW YORK • OXFORD • PARIS • SAN DIEGO  
SAN FRANCISCO • SINGAPORE • SYDNEY • TOKYO

Woodhead Publishing is an imprint of Elsevier





Woodhead Publishing is an imprint of Elsevier  
The Officers' Mess Business Centre, Royston Road, Duxford, CB22 4QH, UK  
50 Hampshire Street, 5th Floor, Cambridge, MA 02139, USA  
Langford Lane, Kidlington, OX5 1GB, UK

Copyright © 2016 Elsevier Ltd. All rights reserved.

No part of this publication may be reproduced or transmitted in any form or by any means, electronic or mechanical, including photocopying, recording, or any information storage and retrieval system, without permission in writing from the publisher. Details on how to seek permission, further information about the Publisher's permissions policies and our arrangements with organizations such as the Copyright Clearance Center and the Copyright Licensing Agency, can be found at our website: [www.elsevier.com/permissions](http://www.elsevier.com/permissions).

This book and the individual contributions contained in it are protected under copyright by the Publisher (other than as may be noted herein).

### Notices

Knowledge and best practice in this field are constantly changing. As new research and experience broaden our understanding, changes in research methods, professional practices, or medical treatment may become necessary.

Practitioners and researchers must always rely on their own experience and knowledge in evaluating and using any information, methods, compounds, or experiments described herein. In using such information or methods they should be mindful of their own safety and the safety of others, including parties for whom they have a professional responsibility.

To the fullest extent of the law, neither the Publisher nor the authors, contributors, or editors, assume any liability for any injury and/or damage to persons or property as a matter of products liability, negligence or otherwise, or from any use or operation of any methods, products, instructions, or ideas contained in the material herein.

ISBN: 978-0-08-100041-0 (print)

ISBN: 978-0-08-100060-1 (online)

### British Library Cataloguing-in-Publication Data

A catalogue record for this book is available from the British Library

### Library of Congress Cataloguing-in-Publication Data

A catalog record for this book is available from the Library of Congress

For information on all Woodhead Publishing publications  
visit our website at <http://store.elsevier.com/>



Working together  
to grow libraries in  
developing countries

[www.elsevier.com](http://www.elsevier.com) • [www.bookaid.org](http://www.bookaid.org)

# Contents

List of contributors	ix
Woodhead Publishing Series in Electronic and Optical Materials	xi
<b>Part One Theory of magnetism in III-V semiconductors</b>	<b>1</b>
<b>1 Computational nanomaterials design for nanospintronics: room-temperature spintronics applications</b>	<b>3</b>
<i>H. Katayama-Yoshida, K. Sato, T. Fukushima, A. Masago, M. Seike</i>	
1.1 Introduction	3
1.2 Disordered dilute magnetic semiconductors	8
1.3 Spinodal nanodecomposition and high blocking temperature	15
1.4 Rare-earth impurities in gallium nitride	25
1.5 MgO-based high- $T_C$ nanospintronics	31
References	37
<b>2 Electronic structure of magnetic impurities and defects in semiconductors: a guide to the theoretical models</b>	<b>43</b>
<i>W.R.L. Lambrecht</i>	
2.1 Introduction	43
2.2 Electronic structure of transition-metal and rare-earth elements in semiconductors	45
2.3 Computational methods dealing with strongly correlated electrons	50
2.4 Magnetism	60
2.5 Case study: Gd in GaN	71
Acknowledgments	91
References	92
<b>3 Energetics, atomic structure, and magnetism of rare earth-doped GaN bulk and nanoparticles</b>	<b>103</b>
<i>V. Kumar, J.M. Zavada</i>	
3.1 Introduction	103
3.2 Methods of calculation	109
3.3 Doping of bulk GaN with Eu and codoping with Si	111
3.4 Doping of rare earths in GaN nanoparticles	115
3.5 Conclusions	121
Acknowledgments	123
References	123

<b>Part Two</b>	<b>Magnetic semiconductors based on rare earth/transition metals</b>	<b>127</b>
<b>4</b>	<b>Prospects for rare-earth-based dilute magnetic semiconductor alloys and hybrid magnetic rare-earth/semiconductor heterostructures</b>	<b>129</b>
	<i>S. Dong, J.K. Furdyna, X. Liu</i>	
4.1	Introduction	129
4.2	Single-phase magnetic semiconductor alloys based on rare earths	133
4.3	Inhomogeneous and mixed-phase magnetic rare-earth systems	142
4.4	Heterostructures of semiconductor and magnetic rare-earth compounds	146
4.5	Rare-earth-based layered chalcogenides and pnictides, including mixed anion systems	151
4.6	Spintronic possibilities with antiferromagnetic rare-earth compounds	156
4.7	Conclusions	158
	References	159
<b>5</b>	<b>Electron spin resonance studies of GaAs:Er,O</b>	<b>169</b>
	<i>H. Ohta, S. Okubo, Y. Fujiwara</i>	
5.1	Introduction and previous studies	169
5.2	Sample preparations	172
5.3	Electron spin resonance results in Kobe	175
5.4	Discussion and proposed models	188
5.5	Summary	192
	References	193
<b>6</b>	<b>Gadolinium-doped gallium-nitride: synthesis routes, structure, and magnetism</b>	<b>195</b>
	<i>A. Ney</i>	
6.1	Introduction	195
6.2	General considerations and experimental methods	197
6.3	GaN:Gd samples with colossal magnetic moments	203
6.4	Gd ion implantation into various GaN samples	207
6.5	Synchrotron-based investigations on molecular beam epitaxy grown GaN:Gd	213
6.6	Summary of magnetic properties of GaN:Gd	220
	References	221
<b>7</b>	<b>MOCVD growth of Er-doped III-N and optical-magnetic characterization</b>	<b>225</b>
	<i>N. Nepal, H.X. Jiang, J.Y. Lin, B. Mitchell, V. Dierolf, J.M. Zavada</i>	
7.1	Introduction	225
7.2	MOCVD growth of Er-doped III-N films	226
7.3	Optical properties	234

7.4	Magnetic properties of III-N:Er thin films	240
7.5	Summary	254
	Acknowledgments	254
	References	255
<b>8</b>	<b>Growth of Eu-doped GaN and its magneto-optical properties</b>	<b>259</b>
	<i>A. Koizumi, B. Mitchell, V. Dierolf, Y. Fujiwara</i>	
8.1	Introduction	259
8.2	Growth of Eu-doped GaN by OMVPE	261
8.3	Nature of Eu incorporation into GaN: structural, optical, and magneto-optical properties	268
8.4	Summary and conclusions	278
	Acknowledgments	279
	References	279
<b>9</b>	<b>Optical and magnetic characterization of III-N:Nd grown by molecular beam epitaxy</b>	<b>281</b>
	<i>G.D. Metcalfe, E.D. Readinger, N. Woodward, V. Dierolf, N. Nepal, J.M. Zavada</i>	
9.1	Introduction	281
9.2	Molecular beam epitaxy growth	282
9.3	Optical characterization	287
9.4	Magnetic properties	298
9.5	Applications to quantum sciences	309
9.6	Conclusions	310
	References	310
<b>Part Three Properties of magnetic semiconductors for spintronics</b>		<b>313</b>
<b>10</b>	<b>Transition metal and rare earth doping in GaN</b>	<b>315</b>
	<i>M.H. Kane, S. Gupta, I.T. Ferguson</i>	
10.1	Introduction	315
10.2	Classic exchange mechanisms	318
10.3	MOCVD growth of $\text{Ga}_{1-x}\text{TM}_x\text{N}$ and $\text{Ga}_{1-x}\text{RE}_x\text{N}$	331
10.4	Experimental studies for $\text{Ga}_{1-x}\text{Cr}_x\text{N}$	343
10.5	LEDs containing nitride dilute magnetic semiconductors	358
10.6	Conclusions	363
	References	364
<b>11</b>	<b>Gadolinium-doped III-nitride diluted magnetic semiconductors for spintronics applications</b>	<b>371</b>
	<i>H. Asahi, Y.K. Zhou, S. Emura, S. Hasegawa</i>	
11.1	Introduction	371
11.2	Growth and structural properties of Gd-doped III-nitride semiconductors	372

11.3	Properties of Gd-doped III-nitride semiconductors	374
11.4	Properties of Dy-doped GaN	385
11.5	Spintronic device application	389
11.6	Summary	392
	References	393
<b>12</b>	<b>Ferromagnetic behavior in transition metal-doped III-N semiconductors</b>	<b>395</b>
	<i>N.A. El-Masry, J.M. Zavada, N. Nepal, S.M. Bedair</i>	
12.1	Introduction	395
12.2	Transition metal-doping of III-V nitride films by diffusion	398
12.3	Mn doping of GaN films by MOCVD	414
12.4	Fermi level engineering of magnetic behavior of GaMnN	421
12.5	Room-temperature spintronic device based on GaMnN	427
12.6	Summary and concluding remarks	431
	Acknowledgments	432
	References	432
<b>13</b>	<b>Bipolar magnetic junction transistors for logic applications</b>	<b>435</b>
	<i>B.W. Wessels</i>	
13.1	Introduction	435
13.2	Spin diodes	435
13.3	Bipolar magnetic junction transistor	438
13.4	Applications	443
	Acknowledgments	444
	References	444
	<b>Index</b>	<b>447</b>

# List of contributors

- H. Asahi** Osaka University, Osaka, Japan
- S.M. Bedair** North Carolina State University, Raleigh, NC, United States
- V. Dierolf** Lehigh University, Bethlehem, PA, United States
- S. Dong** University of Notre Dame, Notre Dame, IN, United States
- N.A. El-Masry** North Carolina State University, Raleigh, NC, United States
- S. Emura** Osaka University, Osaka, Japan
- I.T. Ferguson** Missouri University of Science and Technology, Rolla, MO, United States
- Y. Fujiwara** Osaka University, Suita, Osaka, Japan
- T. Fukushima** Osaka University, Osaka, Japan
- J.K. Furdyna** University of Notre Dame, Notre Dame, IN, United States
- S. Gupta** Georgia Institute of Technology, Atlanta, GA, United States
- S. Hasegawa** Osaka University, Osaka, Japan
- H.X. Jiang** Texas Tech University, Lubbock, TX, United States
- M.H. Kane** Texas A&M University, Galveston, TX, United States
- H. Katayama-Yoshida** Osaka University, Osaka, Japan
- A. Koizumi** Osaka University, Suita, Osaka, Japan
- V. Kumar** Dr. Vijay Kumar Foundation, Gurgaon, Haryana, India; Shiv Nadar University, Uttar Pradesh, India
- W.R.L. Lambrecht** Department of Physics, Case Western Reserve University, Cleveland, OH, United States
- J.Y. Lin** Texas Tech University, Lubbock, TX, United States
- X. Liu** University of Notre Dame, Notre Dame, IN, United States
- A. Masago** Osaka University, Osaka, Japan

- G.D. Metcalfe** U.S. Army Research Laboratory, Sensors and Electron Devices Directorate, Adelphi, MD, United States
- B. Mitchell** University of Mount Union, Alliance, OH, United States
- N. Nepal** U.S. Naval Research Laboratory, Washington, DC, United States
- A. Ney** Johannes Kepler University, Linz, Austria
- H. Ohta** Kobe University, Kobe, Japan
- S. Okubo** Kobe University, Kobe, Japan
- E.D. Readinger** International Rectifier Corp., St. Paul, MN, United States
- K. Sato** Osaka University, Osaka, Japan
- M. Seike** Osaka University, Osaka, Japan
- B.W. Wessels** Northwestern University, Evanston, IL, United States
- N. Woodward** Lehigh University, Bethlehem, PA, United States
- J.M. Zavada** NYU Tandon School of Engineering, Brooklyn, NY, United States
- Y.K. Zhou** Osaka University, Osaka, Japan

# Woodhead Publishing Series in Electronic and Optical Materials

- 1 **Circuit analysis**  
*J. E. Whitehouse*
- 2 **Signal processing in electronic communications: For engineers and mathematicians**  
*M. J. Chapman, D. P. Goodall and N. C. Steele*
- 3 **Pattern recognition and image processing**  
*D. Luo*
- 4 **Digital filters and signal processing in electronic engineering: Theory, applications, architecture, code**  
*S. M. Bozic and R. J. Chance*
- 5 **Cable engineering for local area networks**  
*B. J. Elliott*
- 6 **Designing a structured cabling system to ISO 11801: Cross-referenced to European CENELEC and American Standards**  
**Second edition**  
*B. J. Elliott*
- 7 **Microscopy techniques for materials science**  
*A. Clarke and C. Eberhardt*
- 8 **Materials for energy conversion devices**  
*Edited by C. C. Sorrell, J. Nowotny and S. Sugihara*
- 9 **Digital image processing: Mathematical and computational methods**  
**Second edition**  
*J. M. Blackledge*
- 10 **Nanolithography and patterning techniques in microelectronics**  
*Edited by D. Bucknall*
- 11 **Digital signal processing: Mathematical and computational methods, software development and applications**  
**Second edition**  
*J. M. Blackledge*
- 12 **Handbook of advanced dielectric, piezoelectric and ferroelectric materials: Synthesis, properties and applications**  
*Edited by Z.-G. Ye*
- 13 **Materials for fuel cells**  
*Edited by M. Gasik*
- 14 **Solid-state hydrogen storage: Materials and chemistry**  
*Edited by G. Walker*
- 15 **Laser cooling of solids**  
*S. V. Petrushkin and V. V. Samartsev*



- 16 **Polymer electrolytes: Fundamentals and applications**  
*Edited by C. A. C. Sequeira and D. A. F. Santos*
- 17 **Advanced piezoelectric materials: Science and technology**  
*Edited by K. Uchino*
- 18 **Optical switches: Materials and design**  
*Edited by S. J. Chua and B. Li*
- 19 **Advanced adhesives in electronics: Materials, properties and applications**  
*Edited by M. O. Alam and C. Bailey*
- 20 **Thin film growth: Physics, materials science and applications**  
*Edited by Z. Cao*
- 21 **Electromigration in thin films and electronic devices: Materials and reliability**  
*Edited by C.-U. Kim*
- 22 **In situ characterization of thin film growth**  
*Edited by G. Koster and G. Rijnders*
- 23 **Silicon-germanium (SiGe) nanostructures: Production, properties and applications in electronics**  
*Edited by Y. Shiraki and N. Usami*
- 24 **High-temperature superconductors**  
*Edited by X. G. Qiu*
- 25 **Introduction to the physics of nanoelectronics**  
*S. G. Tan and M. B. A. Jalil*
- 26 **Printed films: Materials science and applications in sensors, electronics and photonics**  
*Edited by M. Prudenziati and J. Hormadaly*
- 27 **Laser growth and processing of photonic devices**  
*Edited by N. A. Vainos*
- 28 **Quantum optics with semiconductor nanostructures**  
*Edited by F. Jahnke*
- 29 **Ultrasonic transducers: Materials and design for sensors, actuators and medical applications**  
*Edited by K. Nakamura*
- 30 **Waste electrical and electronic equipment (WEEE) handbook**  
*Edited by V. Goodship and A. Stevels*
- 31 **Applications of ATILA FEM software to smart materials: Case studies in designing devices**  
*Edited by K. Uchino and J.-C. Debus*
- 32 **MEMS for automotive and aerospace applications**  
*Edited by M. Kraft and N. M. White*
- 33 **Semiconductor lasers: Fundamentals and applications**  
*Edited by A. Baranov and E. Tournie*
- 34 **Handbook of terahertz technology for imaging, sensing and communications**  
*Edited by D. Saeedkia*
- 35 **Handbook of solid-state lasers: Materials, systems and applications**  
*Edited by B. Denker and E. Shklovsky*
- 36 **Organic light-emitting diodes (OLEDs): Materials, devices and applications**  
*Edited by A. Buckley*
- 37 **Lasers for medical applications: Diagnostics, therapy and surgery**  
*Edited by H. Jelínková*

- 
- 38 **Semiconductor gas sensors**  
*Edited by R. Jaaniso and O. K. Tan*
- 39 **Handbook of organic materials for optical and (opto)electronic devices: Properties and applications**  
*Edited by O. Ostroverkhova*
- 40 **Metallic films for electronic, optical and magnetic applications: Structure, processing and properties**  
*Edited by K. Barmak and K. Coffey*
- 41 **Handbook of laser welding technologies**  
*Edited by S. Katayama*
- 42 **Nanolithography: The art of fabricating nanoelectronic and nanophotonic devices and systems**  
*Edited by M. Feldman*
- 43 **Laser spectroscopy for sensing: Fundamentals, techniques and applications**  
*Edited by M. Baudelet*
- 44 **Chalcogenide glasses: Preparation, properties and applications**  
*Edited by J.-L. Adam and X. Zhang*
- 45 **Handbook of MEMS for wireless and mobile applications**  
*Edited by D. Uttamchandani*
- 46 **Subsea optics and imaging**  
*Edited by J. Watson and O. Zielinski*
- 47 **Carbon nanotubes and graphene for photonic applications**  
*Edited by S. Yamashita, Y. Saito and J. H. Choi*
- 48 **Optical biomimetics: Materials and applications**  
*Edited by M. Large*
- 49 **Optical thin films and coatings**  
*Edited by A. Piegari and F. Flory*
- 50 **Computer design of diffractive optics**  
*Edited by V. A. Soifer*
- 51 **Smart sensors and MEMS: Intelligent devices and microsystems for industrial applications**  
*Edited by S. Nihitanov and A. Luque*
- 52 **Fundamentals of femtosecond optics**  
*S. A. Kozlov and V. V. Samartsev*
- 53 **Nanostructured semiconductor oxides for the next generation of electronics and functional devices: Properties and applications**  
*S. Zhuiykov*
- 54 **Nitride semiconductor light-emitting diodes (LEDs): Materials, technologies and applications**  
*Edited by J. J. Huang, H. C. Kuo and S. C. Shen*
- 55 **Sensor technologies for civil infrastructures**  
**Volume 1: Sensing hardware and data collection methods for performance assessment**  
*Edited by M. Wang, J. Lynch and H. Sohn*
- 56 **Sensor technologies for civil infrastructures**  
**Volume 2: Applications in structural health monitoring**  
*Edited by M. Wang, J. Lynch and H. Sohn*
- 57 **Graphene: Properties, preparation, characterisation and devices**  
*Edited by V. Skákalová and A. B. Kaiser*

- 
- 58 **Silicon-on-insulator (SOI) technology**  
*Edited by O. Kononchuk and B.-Y. Nguyen*
- 59 **Biological identification: DNA amplification and sequencing, optical sensing, lab-on-chip and portable systems**  
*Edited by R. P. Schaudies*
- 60 **High performance silicon imaging: Fundamentals and applications of CMOS and CCD sensors**  
*Edited by D. Durini*
- 61 **Nanosensors for chemical and biological applications: Sensing with nanotubes, nanowires and nanoparticles**  
*Edited by K. C. Honeychurch*
- 62 **Composite magnetoelectrics: Materials, structures, and applications**  
*G. Srinivasan, S. Priya and N. Sun*
- 63 **Quantum information processing with diamond: Principles and applications**  
*Edited by S. Praver and I. Aharonovich*
- 64 **Advances in non-volatile memory and storage technology**  
*Edited by Y. Nishi*
- 65 **Laser surface engineering: Processes and applications**  
*Edited by J. Lawrence, C. Dowding, D. Waugh and J. Griffiths*
- 66 **Power ultrasonics: Applications of high-intensity ultrasound**  
*Edited by J. A. Gallego-Juárez and K. F. Graff*
- 67 **Advances in delay-tolerant networks (DTNs): Architectures, routing and challenges**  
*Edited by J. J. P. C. Rodrigues*
- 68 **Handbook of flexible organic electronics: Materials, manufacturing and applications**  
*Edited by S. Logothetidis*
- 69 **Machine-to-machine (M2M) communications: Architecture, performance and applications**  
*Edited by C. Anton-Haro and M. Dohler*
- 70 **Ecological design of smart home networks: Technologies, social impact and sustainability**  
*Edited by N. Saito and D. Menga*
- 71 **Industrial tomography: Systems and applications**  
*Edited by M. Wang*
- 72 **Vehicular communications and networks: Architectures, protocols, operation and deployment**  
*Edited by W. Chen*
- 73 **Modeling, characterization and production of nanomaterials: Electronics, photonics and energy applications**  
*Edited by V. Tewary and Y. Zhang*
- 74 **Reliability characterisation of electrical and electronic systems**  
*Edited by J. Swingler*
- 75 **Industrial wireless sensor networks: Monitoring, control and automation**  
*Edited by R. Budampati and S. Kolavennu*
- 76 **Epitaxial growth of complex metal oxides**  
*Edited by G. Koster, M. Huijben and G. Rijnders*
- 77 **Semiconductor nanowires: Materials, synthesis, characterization and applications**  
*Edited by J. Arbiol and Q. Xiong*

- 
- 78 **Superconductors in the power grid**  
*Edited by C. Rey*
- 79 **Optofluidics, sensors and actuators in microstructured optical fibres**  
*Edited by S. Pissadakis*
- 80 **Magnetic nano- and microwires: Design, synthesis, properties and applications**  
*Edited by M. Vázquez*
- 81 **Robust design of microelectronic assemblies against mechanical shock, temperature and moisture**  
*E.-H. Wong and Y.-W. Mai*
- 82 **Biomimetic technologies: Principles and applications**  
*Edited by T. D. Ngo*
- 83 **Directed self-assembly of block co-polymers for nano-manufacturing**  
*Edited by R. Gronheid and P. Nealey*
- 84 **Photodetectors**  
*Edited by B. Nabet*
- 85 **Fundamentals and applications of nanophotonics**  
*Edited by J. Haus*
- 86 **Advances in chemical mechanical planarization (CMP)**  
*Edited by S. Babu*
- 87 **Rare earth and transition metal doping of semiconductor materials: Synthesis, magnetic properties and room temperature spintronics**  
*Edited by V. Dierolf, I. T. Ferguson and J. M. Zavada*

This page intentionally left blank

## Part One

# Theory of magnetism in III-V semiconductors

This page intentionally left blank

# Computational nanomaterials design for nanospintronics: room-temperature spintronics applications

1

H. Katayama-Yoshida, K. Sato, T. Fukushima, A. Masago, M. Seike  
Osaka University, Osaka, Japan

## 1.1 Introduction

Electrons are always carrying the charge ( $e^-$ ), electron mass ( $m_e$ ), and spin ( $S = 1/2$ ) that are caused by the relativistic quantum mechanics. The  $e^-$  of electron can carry the charge current (electric and magnetic fields), the  $m_e$  of electron can carry the heat (kinetic energy), and the  $S$  can carry the spin current (angular momentum) in the condensed matter (see Fig. 1.1). Today's consumer electronics strongly depends on the achievements in silicon-based microelectronics that enable a high degree of system integration based on Si-CMOS technology. However, this technology will reach its limits in terms of energy consumption and system integration by around 2020. To go beyond these limitations, we need to develop, for instance, more energy-efficient (nonvolatile), high-speed (THz), and higher-density (Tbit/Inch<sup>2</sup>) nanoscale-size system-integrated devices that utilize the spin property of the charged carriers (spintronics), as schematically depicted in Fig. 1.1. Other technologies that have been proposed to overcome the limitation of Si-CMOS technology are moltronics (molecular-electronics), quantronics (quantum-electronics), and atomtronics (atom-switching electronics) [1–4].

In parallel to the to these new classes of electronics, we also need to develop bottom-up nanotechnology to fabricate the functional nanosuperstructures, including self-organized nanocrystal growth methods as alternatives to the top-down nanotechnology such as Si-CMOS-based nanolithography. In this chapter, we propose the self-organized nanosuperstructure fabrication method based on the spinodal nanotechnology by controlling the dimensionality (2D or 3D) of the crystal growth. We discuss the design and realization of *Konbu* phase by 2D crystal growth and *Dairiseki* phase by 3D crystal growth conditions, combined with the shape controlled by vapor pressure modulation.

The most probable candidate for the new class of electronics to go beyond the limitation of Si-CMOS technology is semiconductor nanospintronics, by combining the spin- and charge-degree of freedoms based on the already exciting semiconductor nanotechnology. This was developed during the last half-century and is now very sophisticated, where we can control the spin–spin interaction by electric-field gating



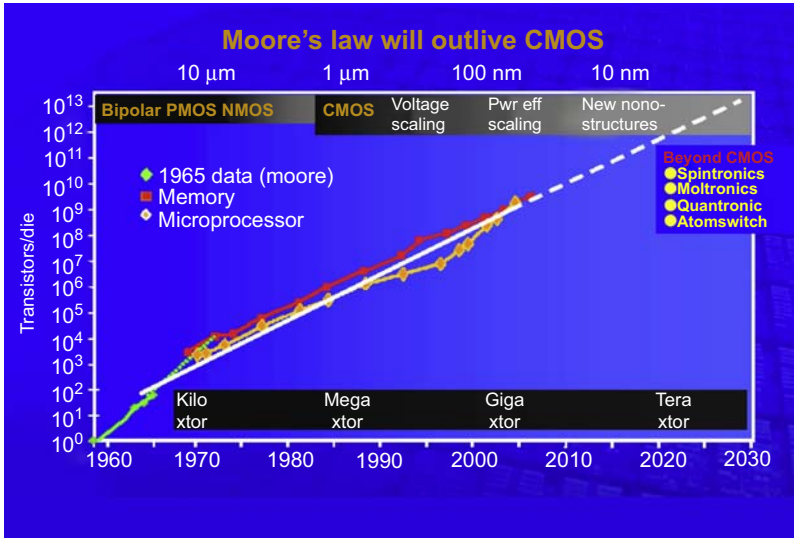


**Figure 1.1** Illustration of Gordon Moore's law for Si-CMOS-based semiconductor memory and microprocessor. Past progress of memory and microprocessor is based on this law. Around 2020, Si-CMOS technology is reaching the dead-end and physical fabrication limits on energy consumption and the size effect in the electric-field gating. The candidate to go beyond the Si-CMOS technology may be spintronics, moltronics, quantronics, or atomtronics.

combined with the fabrication method of Si-CMOS technology and spin-degree of freedom. However, we need the realistic semiconductor nanospintronics materials for devices that should have the super-high Curie temperature ( $T_C$ )  $>$  1000 K in order to avoid the spin fluctuation and the instability of the magnetization caused by the weak magneto-crystal anisotropy or shape anisotropy at the room temperature ( $T = 300$  K) for the realization of realistic semiconductor nanospintronics for industrial applications. For the realization of semiconductor nanospintronics, we should design and realize (1) the super-high-  $T_C$  ferromagnetic semiconductors ( $T_C >$  1000 K) in which we can control the spin-spin interaction from ferromagnetic to antiferromagnetic (or paramagnetic) by the electric-field gating, or (2) the superparamagnetic nanostructure materials with super-high blocking temperature ( $T_B >$  1000 K) caused by the magneto-crystal anisotropy or shape anisotropy in which we can control the magnetic spin-spin interaction from ferromagnetic to paramagnetic in the nanosuperstructures of magnetic semiconductors by the electric-field gating (see Fig. 1.2).

To design and realize these nanospintronics materials based on ab initio electronic structure calculation and multiscale simulation for the design and fabrication of self-organized nanosuperstructures, semiconductor nanospintronics materials, and also nanospintronics devices, we have developed the Computational Nano-Materials Design (CMD<sup>®</sup>) system as shown in Fig. 1.3.

Historically, the progress of the industrial society is based on the basic research on the materials (Materials); we develop the devices based on research and development

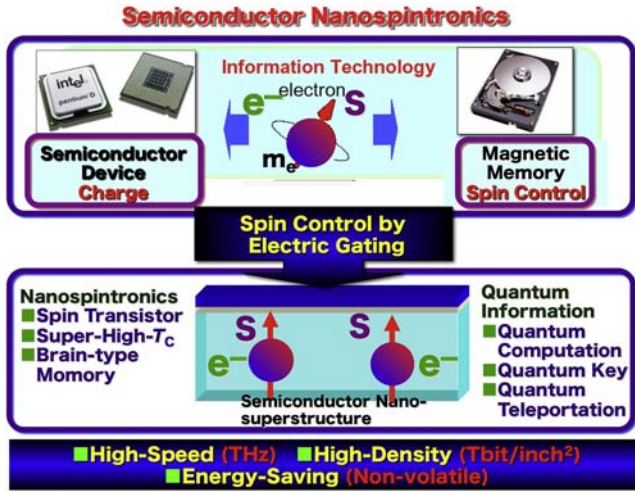


**Figure 1.2** Schematic explanation of semiconductor nanospintronics [1,3,5]. By controlling the magnetic spin–spin interaction by the electric-field gating in the nanoscale size, we can fabricate the semiconductor nanospintronics devices by controlling the spin current (angular momentum), charge (electric-field), and atomic-mass current (kinetic energy or heat) of the electrons.

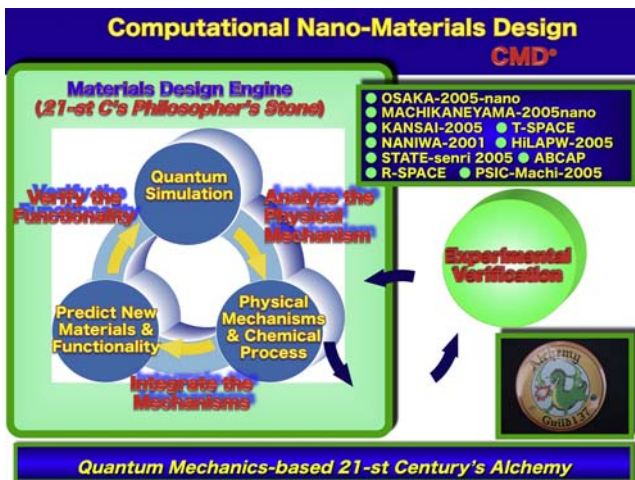


**Figure 1.3** Computational Nano-Materials Design (CMD<sup>®</sup>) System, which was developed in Osaka University [1,3,5]. Based on the ab initio electronic structure calculations and multiscale simulations, we can analyze the physical mechanism and chemical fabrication process. Then based on the physical and chemical process mechanisms, we can predict the new functionalities and new materials. Finally, using the quantum simulations, we can verify the functionality and device applicability. Combining CMD<sup>®</sup> with the experimental verification, we can design and realize the new functional materials and devices.

(R&D), where a large gap called “Death Valley” always exists between the basic research (Materials) and R&D (Devices) (see Fig. 1.4). Then, based on R&D, we can industrialize the system and software by developing the system integration, where a large gap called “Darwin’s Sea” always exists between R&D and the industrialization. In “Darwin’s Sea,” a strong competition between the developing company exists and as natural selection always occurs, finally only one profitable company can survive through in the competitive market.

In general, it takes more than half a century, even in the case of successful Si-CMOS technology, to reach from the basic research to industrialization by the bottom-up development through the three hierarchal industrial structures of Materials, Devices, and System and Software (see Fig. 1.4). In order to accelerate the development from the bottom up through the hierarchy structures, we have developed the CMD<sup>®</sup> system, where we start from the prediction and design of the likely future society, and propose the suitable system and software necessary to solve future problems related to energy, environment, social security, and an aging society. Then, in order to realize the system and software to solve our future problems, we can design the devices based on the R&D. Therefore, we can design the new materials and functionalities that we need for the development of the functional devices in R&D. In the CMD<sup>®</sup> system, we can follow the top-down methodology in order to shorten the development time based on the CMD<sup>®</sup> and Experimental Verifications.

In this section, first of all, we discuss the ferromagnetic mechanism in disordered dilute magnetic semiconductors and reliable evaluation method of  $T_C$  comparing

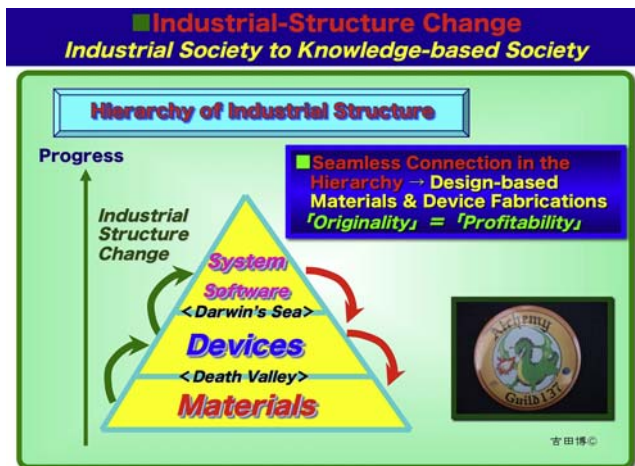


**Figure 1.4** Hierarchy of industrial structure of Materials (basic research), Devices (R&D), and System and Software (industrialization) [1,3,5]. Our society changes from an industrial society to a knowledge-based society. At the interface between the different hierarchal structures, large gaps exist, such as “Death Valley” and “Darwin’s Sea.” To make a seamless connection between the gaps, we need design-based materials and device fabrication. Here, the originality in the materials design is the origin of the profitability in the market.

with the available experimental data. Then, we discuss how to increase the  $T_C$  by codoping in order to increase the solubility of magnetic impurities in semiconductors, superparamagnetic phenomena to increase the blocking temperature by spinodal nanodecomposition using the low solubility of the magnetic impurities in semiconductors. We also discuss the shape control of nanomagnets by controlling the spinodal nanodecomposition and dimensionality of the crystal growth (2D or 3D). In order to combine the high solubility by codoping, high-efficiency light emission by codoping, and magnetic interactions such as p-f exchange mechanism, we discuss the new functionality of rare-earth impurity-doped wide bandgap semiconductors, including the circularly polarized light emission. Finally, based on these results, we discuss the design of  $d^0$  ferromagnetism without 3d transition metal (TM) impurities and without rare-earth impurities in conventional oxides such as MgO, where using the spinodal nanodecomposition caused by the low solubility of defects and impurities by controlling the high blocking temperature of superparamagnetism.

In the CMD<sup>®</sup> System (see Fig. 1.3), first we propose the physical mechanism and chemical-reaction mechanism for the fabrication of new functional materials based on the analysis of the mechanisms by quantum simulations using the developed applications for the quantum simulations and multiscale simulations. Second, after we understand the physical mechanism and chemical processes, we can design and predict the new functional materials and process methods based on the quantum simulations and multiscale simulations. Third, then we can check the new functionality based on the quantum simulations. By iterating these three steps, we can design and realize the new functional materials based on the quantum simulations and multiscale simulations (see Fig. 1.3).

In Section 1.2, we discuss the electronic structure of disordered dilute magnetic semiconductors, the mechanism of ferromagnetic interaction caused by long-ranged Zener's p-d exchange interaction, and the short-ranged Zener's double exchange interaction; the calculation of  $T_C$  by Monte Carlo simulation (MCS); and the codoping method in order to increase the solubility of magnetic impurities to increase the percolations of short-ranged magnetic interactions [2]. In Section 1.3, we discuss the spinodal nanodecomposition and high blocking temperature of superparamagnetism based on the multiscale simulation of the spinodal nanodecomposition based on the ab initio calculation and MCS of the crystal growth by controlling the crystal growth dimensionality (2D and 3D) in the thermal nonequilibrium crystal growth condition and dynamically created new phases such as *Dairiseki* phase (quantum dot) and *Konbu* phase (nanowire), where  $T_B$  becomes dominant showing hysteresis caused by the large magneto-crystal anisotropy and shape anisotropy in the superparamagnetism [6]. In Section 1.4, we discuss the electronic structure of rare-earth impurities in GaN, computational design of materials for high-efficiency light emission, high-density doping of rare-earth impurities to realize the magnetism, and circular-polarized light emitting diodes (LEDs) based on ab initio electronic structure calculations. Finally, in Section 1.5, we discuss the electronic structure of MgO-based high- $T_C$  nanospintronics materials with  $d^0$  ferromagnetism, including the electronic structure, the  $d^0$  ferromagnetism without magnetic TM impurities with very high  $T_B$  in *Konbu* and *Dairiseki* phases caused by the 2D and 3D spinodal nanodecomposition.

## 1.2 Disordered dilute magnetic semiconductors

The discovery of the carrier-induced ferromagnetism in dilute magnetic semiconductors (DMSs) such as (Ga, Mn)As and (In, Mn)As was followed by vast series of experimental and theoretical investigations concerning the fundamental mechanism of the ferromagnetism and its application to the semiconductor spintronics [7–14]. So far, on the ferromagnetism in DMS, two important mechanisms are proposed theoretically. One is the p-d exchange mechanism [15,16] and the other is the double exchange mechanism [17]. Owing to the recent accurate transport measurements and detailed spectroscopic analysis, discussion on the dominant mechanism has been reconsidered carefully [18–20]. However, there seems a consensus that the two mechanisms play the most important role to describe the magnetism of DMS. Therefore, in this section, first we give a brief discussion on the p-d and the double exchange mechanisms based on the first-principles calculations, and then describe how accurately we can predict  $T_C$  of DMS from first principles [12]. Finally, three strategies to realize room-temperature ferromagnetism are proposed.

### 1.2.1 p-d exchange and double exchange mechanisms

Most of the DMS systems are synthesized by doping magnetic impurities (usually 3d TMs such as Mn and Cr), in compound semiconductors such as GaAs, InAs, and ZnTe. Since the valence band of the host semiconductor is constructed from p-states of anion, the key factor in determining the electronic structure and magnetic state is the relative position between d-states of the TM ion and p-states of the anion [12,21].

When TM impurities are introduced in the host semiconductors, d-states of TM hybridize with p-states of host anion. If the d-states of TM are higher in energy than p-states of anion, normally TM d-states appear in the bandgap and form impurity bands. When the induced impurity bands are partially occupied, the band energy of the system is lowered due to the broadening of the impurity bands. Since the band broadening effectively occurs in the ferromagnetic configuration of magnetic moments of TM impurities compared to antiferromagnetic configuration, the ferromagnetic state is stabilized. This situation is schematically shown in Fig. 1.5(a). This mechanism is called double exchange [17] and is important typically in wide bandgap semiconductor-based DMS such as (Ga, Mn)N and (Ga, Cr)N, Cr-doped DMS (Zn, Cr)Te, and so on. Since overlapping wave functions cause band broadening, the interaction range of the double exchange is usually short due to the exponential decay of the wave function of the impurity states that are usually located in the middle of the bandgap.

On the other hand, when the d-states of TM are lower in energy than the p-states of anion, TM d-bands appear at the lower part of the valence bands. Due to the hybridization between TM d-bands and the valence bands, the valence bands are shifted up in energy. If the magnetic moments of TM impurities align ferromagnetically, the valence bands show net spin splitting. Therefore, hole doping in this system induces magnetic polarization in the valence bands and the system gains magnetic energy. Since this energy gain is not achieved when the direction of the magnetic moments

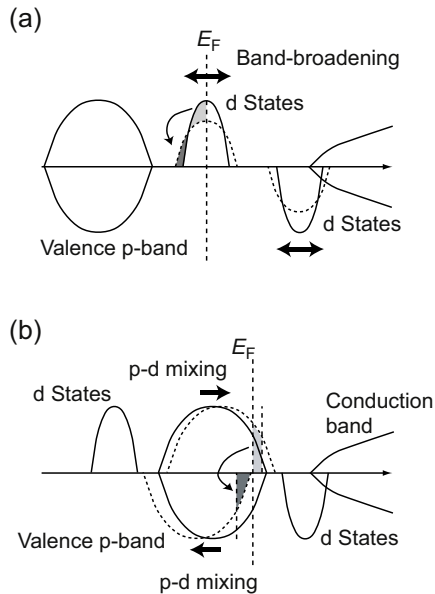


**Figure 1.5** Schematic picture of the density of states of (a) double exchange system and (b) p-d exchange system.

From Belhadji B, et al. *J Phys: Condens Matter* 2007;19:436227.

are antiferromagnetic (therefore, no magnetic polarization of the valence bands), the ferromagnetic state becomes stable. This situation is illustrated in Fig. 1.5(b). This mechanism is called p-d exchange [15,16] and is important typically in Mn-doped narrow gap DMS systems. In the p-d exchange systems, magnetic polarization of valence bands mediates ferromagnetic interaction, therefore, the interaction range is intrinsically long.

The electronic structure of typical III-V DMS systems was calculated by using the Korringa-Kohn-Rostoker coherent potential approximation (KKR-CPA) within the local density approximation (LDA). Calculated density of states (DOS) of (Ga, Mn)N, (Ga, Mn)P, (Ga, Mn)As, and (Ga, Mn)Sb is shown in Fig. 1.6 [12]. We can recognize transition from a typical double exchange system (Ga, Mn)N (Fig. 1.6(a)) to the p-d exchange system (Ga, Mn)Sb (Fig. 1.6(d)). (Ga, Mn)P (Fig. 1.6(b)) and (Ga, Mn)As (Fig. 1.6(c)) are in between [12,21,22].

Typical TM concentration in DMS is 10–20%. In this concentration range, it is crucial for accurate  $T_C$  prediction to take the interaction range into account. This is easily understood by the analogy to the site percolation problem. For example, when the magnetic interaction is extremely short and only the nearest neighbor interaction is important, under the percolation threshold the ferromagnetic network cannot spread over the crystal to make the whole system ferromagnetic. Even above the threshold, if the concentration is not high enough  $T_C$  might be suppressed very much. We call this the magnetic percolation effect, and this effect is not correctly considered in the  $T_C$  calculation by the mean field approximation (MFA), because



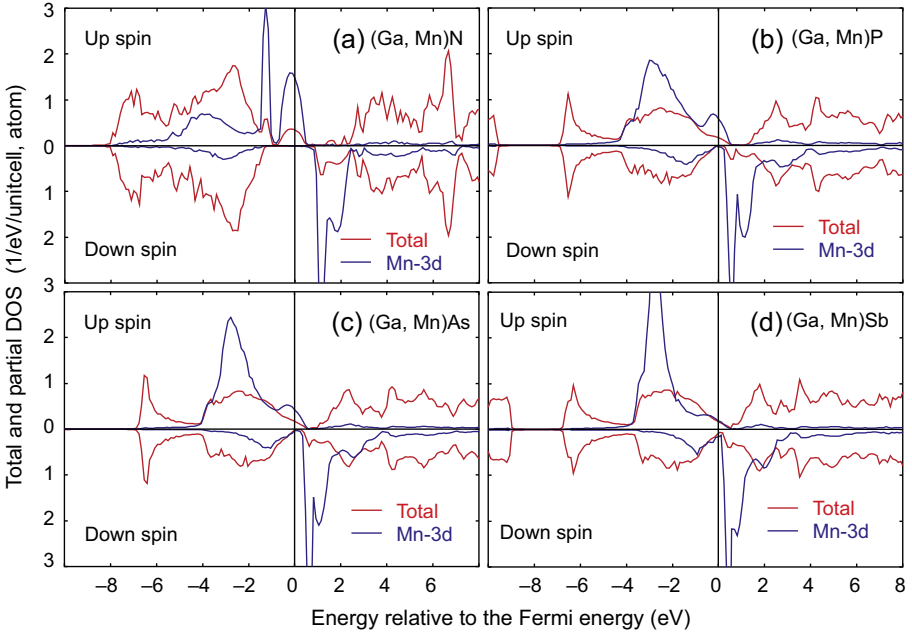


**Figure 1.6** Calculated DOS of (a) (Ga, Mn)N, (b) (Ga, Mn)P, (c) (Ga, Mn)As, and (d) (Ga, Mn)Sb by using the KKR-CPA-LDA. Total DOS and partial density of d-states at Mn site are plotted.

From Sato K, Bergqvist L, Kudrnovsky J, Dederichs PH, Eriksson O, Turek I, et al. Rev Mod Phys 2010;82:1633.

random distribution of TM impurities in the crystal is averaged out in the MFA. For the calculation of  $T_C$  beyond the MFA we have to perform MCS. The importance of the magnetic percolation effect depends on the interaction range. For example, if the interaction range is infinitely long, the MFA becomes accurate. As explained, the interaction range depends on the mechanism that mediates the ferromagnetic interactions, and the mechanism reflects the electronic structure of DMS. Therefore, in order to calculate  $T_C$  of DMS accurately with full account of the chemical trend, we need to calculate effective exchange interactions between TM impurities as a function of distance, and the calculated exchange interactions should be used in the MCS [12,23]. This point is discussed in the next subsection.

### 1.2.2 Reliable calculation of $T_C$

The effective exchange interactions between TM impurities can be calculated from first-principles by using the mapping on the classic Heisenberg model. In the classic Heisenberg model, the magnetic state of the system is described by the Hamiltonian:

$$H = - \sum_{i \neq j} J_{ij} \vec{e}_i \cdot \vec{e}_j, \quad [1.1]$$

where  $\vec{e}_i$  denotes the unit vector along the direction of magnetic moment at site  $i$  and  $J_{ij}$  is the effective exchange interaction between site  $i$  and  $j$ . According to the Liechtenstein et al.,  $J_{ij}$  can be estimated by using the multiple scattering theory as:

$$J_{ij} = -\Im \frac{1}{\pi} \int_{-\infty}^{\epsilon_F} \delta t_i \tau_{ij} \delta t_j \tau_{ji} d\epsilon, \quad [1.2]$$

where  $\delta t_i = t_i^\uparrow - t_i^\downarrow$  ( $t_i^\uparrow$  is atomic  $t$ -matrix at site  $i$  for spin-up state),  $\tau_{ij}$  is the scattering path operator connecting sites  $i$  and  $j$ ,  $\epsilon$  is the energy, and  $\epsilon_F$  is the Fermi energy [24]. This expression can be easily evaluated in the framework of the KKR-CPA method to describe the substitutional disorder.

Calculated  $J_{ij}$  shows a clear chemical trend as shown in Fig. 1.7 [22]. In (Ga, Mn)N, the interaction range is quite short, reflecting the double exchange nature of the exchange interactions in wide bandgap semiconductors. In (Ga, Cr)N, the calculated  $J_{ij}$  is also very short range. Since the nearest neighbor interaction is very large,  $T_C$  by the MFA becomes very high even for low concentration. However, this high  $T_C$  is the artifact of the MFA and realistic estimation of  $T_C$  by the MCS gives a very

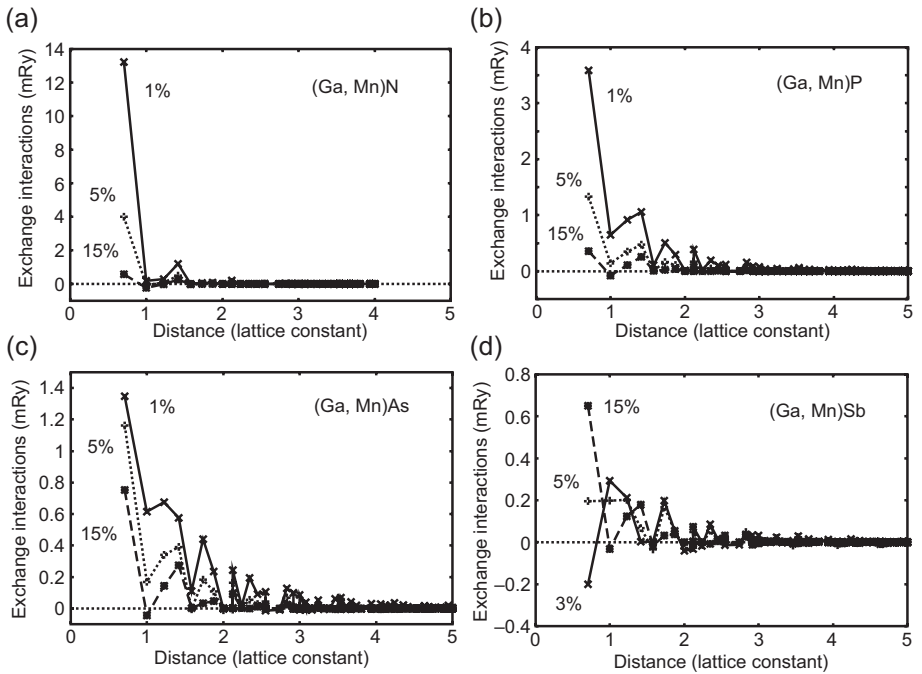


**Figure 1.7** Calculated exchange interactions between Mn impurities in (a) (Ga, Mn)N, (b) (Ga, Mn)P, (c) (Ga, Mn)As, and (d) (Ga, Mn)Sb as a function of distance.

From Dederichs PH, Sato K, Katayama-Yoshida H. Phase Transitions 2005;78:851.



low value. Therefore, the double exchange system is realistic as high- $T_C$  DMS only when high concentration doping is possible.

On the other hand in (Ga, Mn)Sb and (Ga, Mn)As (Fig. 1.7(d) and (c)), the interaction range is relatively long due to the p-d exchange nature of the exchange interactions. In the p-d exchange systems, the interactions are generally weak compared to the double exchange systems; however, due to the long range nature of the interactions the p-d exchange has an advantage over the double exchange for low concentration to realize the ferromagnetism. Actually, so far the best investigated DMSs are (Ga, Mn)As and (In, Mn)As.

(Zn, Cr)Te and (Ga, Mn)P are in between the double exchange and the p-d exchange. As explained in the previous subsection, the relative importance of the two mechanisms depends on the relative location of TM d-states compared to the host valence bands, therefore real systems are distributed between two extreme cases, namely the double and the p-d exchange, showing wide variety and the complexity of real materials.

Typical results of the MCS for  $T_C$  of (Ga, Mn)N, (Ga, Mn)P, (Ga, Mn)As, (Ga, Mn)Sb, (Zn, Cr)Te, and (Ga, Cr)N are shown in Fig. 1.8 [12,23,25]. For (Ga, Mn)P, (Ga, Mn)As, and (Zn, Cr)Te, the MCS results reproduce experimental results very well. The overestimation of  $T_C$  by MFA and RPA is clearly seen in the figure for all systems, but the degree of the overestimation depends on the interaction range. According to the MCS of  $T_C$  it is well understood that high concentration doping of TM impurities is necessary for realizing high  $T_C$ . Based on this guideline toward high  $T_C$ , high concentration doping has been attempted experimentally for various systems. However, it has been revealed that homogeneous high concentration doping is quite difficult to realize even with nonequilibrium crystal growth technique [26]. In the next subsection, we propose three strategies for overcoming this difficulty.

### 1.2.3 Toward high $T_C$

According to the first-principles predictions, generally high concentration doping is needed for rising  $T_C$ , therefore, low solubility of TM impurities in DMS prevents us from realizing high  $T_C$ . This is the intrinsic nature of DMS and in the previous experimental fabrication of DMS materials this difficulty has been partly overcome by using nonequilibrium crystal growth techniques. However, the theoretically required concentration to reach room-temperature ferromagnetism is too high to realize and we need a new approach. So far, we have proposed some material designs along the following three directions.

- Codoping method

One of the indications of the tendency for phase separation appears in the calculated mixing energy. The mixing energy  $\Delta E$  of (Ga, Mn)As is calculated as:

$$\Delta E(x) = E(Ga_{1-x}Mn_xAs) - (1-x)E(GaAs) - xE(MnAs), \quad [1.3]$$

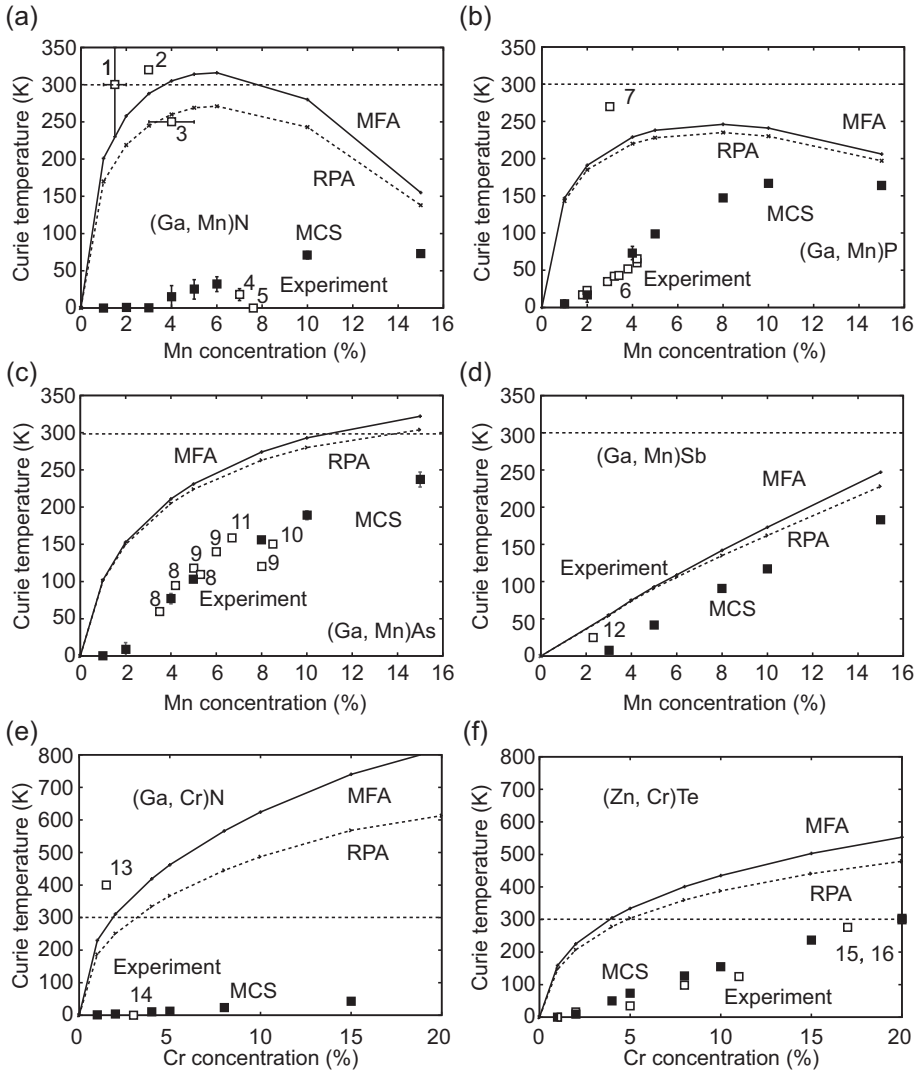


**Figure 1.8** Calculated Curie temperature of (a) (Ga, Mn)N, (b) (Ga, Mn)P (c) (Ga, Mn)As, (d) (Ga, Mn)Sb, (e) (Ga, Cr)N, and (f) (Zn, Cr)Te. Curie temperature is calculated as a function of TM concentration. MFA, random phase approximation (RPA), and MCS were used for the calculations. The numbers are references for the experimental results.

From Sato K, Fukushima T, Katayama-Yoshida H. *J Phys: Condens Matter* 2007;19:365212.

where  $x$  is the concentration of Mn and  $E(x)$  is the energy of compound X, respectively. By definition, positive  $\Delta E$  indicates that (Ga, Mn)As favors phase separation to GaAs and MnAs. Reflecting the experimental low solubility of Mn in GaAs, the mixing energy of (Ga, Mn)As is calculated to be positive. Positive mixing energy is also calculated for

the other DMS systems, such as (Ga, Mn)N, (Ga, Cr)N, (Zn, Cr)Te, and so on, and corresponds reasonably to the experimental observation of phase separation in these DMS.

In the codoping method, in addition to TM impurities, carrier dopants are introduced simultaneously. The additional carrier dopants should be chosen so that they compensate carriers originating from TM impurities. Since the TM impurity normally behaves as an acceptor, in the codoping for DMS we should choose donor impurities. Due to the introduction of codopants, the mixing energy of TM impurities is lowered and phase separation is suppressed, leading to high solubility [27]. This is an advantage of the codoping, but it has a disadvantage too. Because of the compensation of hole carriers, the ferromagnetism is weakened due to the codoping. Therefore, after the crystal growth by using the codoping method, the codopants should be removed from the crystal to recover the ferromagnetism. From this point of view, mobile interstitial donor impurities are proposed as good codopants for DMS. It has been shown that Li interstitial works ideally as the codopant for (Ga, Mn)As [28,29]. As another possibility of codoping, rare-earth impurity and N-vacancy codoping in GaN will be proposed in Section 1.4.

- Superparamagnetic blocking phenomena

So far, we have focused on the homogeneous DMS systems. The homogeneous DMS might be easy to handle when we consider the fabrication of spintronics devices with high reproducibility. If we are only interested in ferromagnetic behavior of DMS, we can make use of inhomogeneous (namely phase separated) DMS. The inhomogeneous DMS can be considered a hybrid material, where for example in (Ga, Mn)As case, nanomagnets of MnAs (or (Ga, Mn)As with high concentration of Mn) are embedded in the host semiconductor GaAs. These nanomagnets are expected to have high  $T_C$ , but due to the absence of magnetic exchange interaction between nanomagnets the system becomes superparamagnetic. If the size of the nanomagnets is small enough to be single magnetic domain and the magnetic anisotropy is important, the direction of magnetization of the nanomagnet is fixed along the magnetic easy axis. Since the magnetization reversal is blocked below the blocking temperature ( $T_B$ ), the system looks like ferromagnets for  $T < T_B$ . Since we can control the size of the nanomagnets by tuning crystal growth condition, materials design for high- $T_B$  inhomogeneous DMS is possible [30]. An example of materials design along this idea will be described in Section 1.3.

- Search for new materials

Forgetting about the advantage of usual III-V semiconductors that have compatibility with the present electronics and extending host materials to other than III-V semiconductors, we can choose exotic semiconductors as host semiconductors for new DMS. For example, IV-VI semiconductor such as GeTe is known to show high solubility of TM impurities and materials design of GeTe-based DMS was proposed [31,32]. The theoretical prediction was partly supported by experimental results. We can choose even oxides as host materials. Due to the strongly correlated nature of oxides, there is a possibility to realize ferromagnetism without any TM impurities. This is called  $d^0$ -magnetism [33–36] and is discussed in detail in Section 1.5 together with self-organization of nanostructures in oxides.

In this section, we have discussed the origin of the ferromagnetism and first-principles method for calculating  $T_C$  of DMS. It is emphasized that the magnetic percolation is important to understand and design the magnetic properties of DMS. Based on this knowledge, we have discussed three possible directions toward high- $T_C$  DMS materials. Some of them will be discussed further in the next sections.

## 1.3 Spinodal nanodecomposition and high blocking temperature

As discussed in Section 1.2.3, the inhomogeneity in DMS systems has attracted a lot of attention, because this feature could open the way to new and novel spintronic devices by utilizing  $T_B$ . Such a movement started with the inconsistency between the theory and experiment; that is, in the experiments [26,37,38], room-temperature ferromagnetism was observed for low concentration of the magnetic impurities, whereas the theory predicted very low  $T_C$  for low concentration of the magnetic impurities due to the missing magnetic percolation [12]. In 2006, Sato and Katayama-Yoshida [39] proposed that spinodal nanodecomposition (spinodal decomposition in nanoscale size) is an important role for the inhomogeneity in DMS, based on ab initio calculations. Since their work, many people have been interested in the inhomogeneity of the magnetic impurities in DMS, and then the spinodal nanodecomposition has been actually observed in the experiments [40,41], as shown in Fig. 1.9. In this section, we will present the theoretical investigations of the inhomogeneity in DMS systems by ab initio calculations, and also demonstrate the simulation of the 2D (*Konbu*-phase) and 3D (*Dairiseki* phase) spinodal nanodecompositions by the Monte Carlo method.

### 1.3.1 Mixing energy

We begin by discussing mixing energy in DMS systems. Fig. 1.10 shows the mixing energies of (a) (Ga, Mn)N, (b) (Ga, Cr)N, (c) (Ga, Mn)As, and (d) (Zn, Cr)Te by the red lines as a function of the TM impurity concentration [12,42]. All these DMS systems have convex concentration dependencies of the mixing energy with the positive values, leading to the phase separation; these four systems have the miscibility gaps. In the calculations of Fig. 1.10, the crystal structure is assumed to be zinc blende structure. Therefore, these DMS systems undergo the phase separation coherently with keeping the zinc blende structure; for example, for the case of (Ga, Mn)N, the zinc blende GaN and MnN are generated in the crystal. In particular, (Ga, Mn)N and (Ga, Cr)N with their wide bandgaps have the larger mixing energies, compared to the cases of (Ga, Mn)As and (Zn, Cr)Te. In this sense, it is considered that the fabrication of homogeneous nitride DMSs are very difficult by experiment. We note that since the calculations in Fig. 1.10 are performed by the KKR-CPA method, the structural optimization, which causes the reduction of the mixing energy, is not taken into account. We can see the effect of structural optimization for mixing energy by the supercell calculation and cluster expansion method in [43]. In Fig. 1.10, the mixing energies calculated by the codoping method are also shown. By introducing additional codopants, such as O, N, and I atoms, into DMS, we can drastically reduce the mixing energy, so that the solubility of the TM impurities increases [28,29]. This is due to the energy gain by the self-compensation between the TM impurities (acceptor) and codopant (donor). The previous discussion focused on the phase stability of DMS

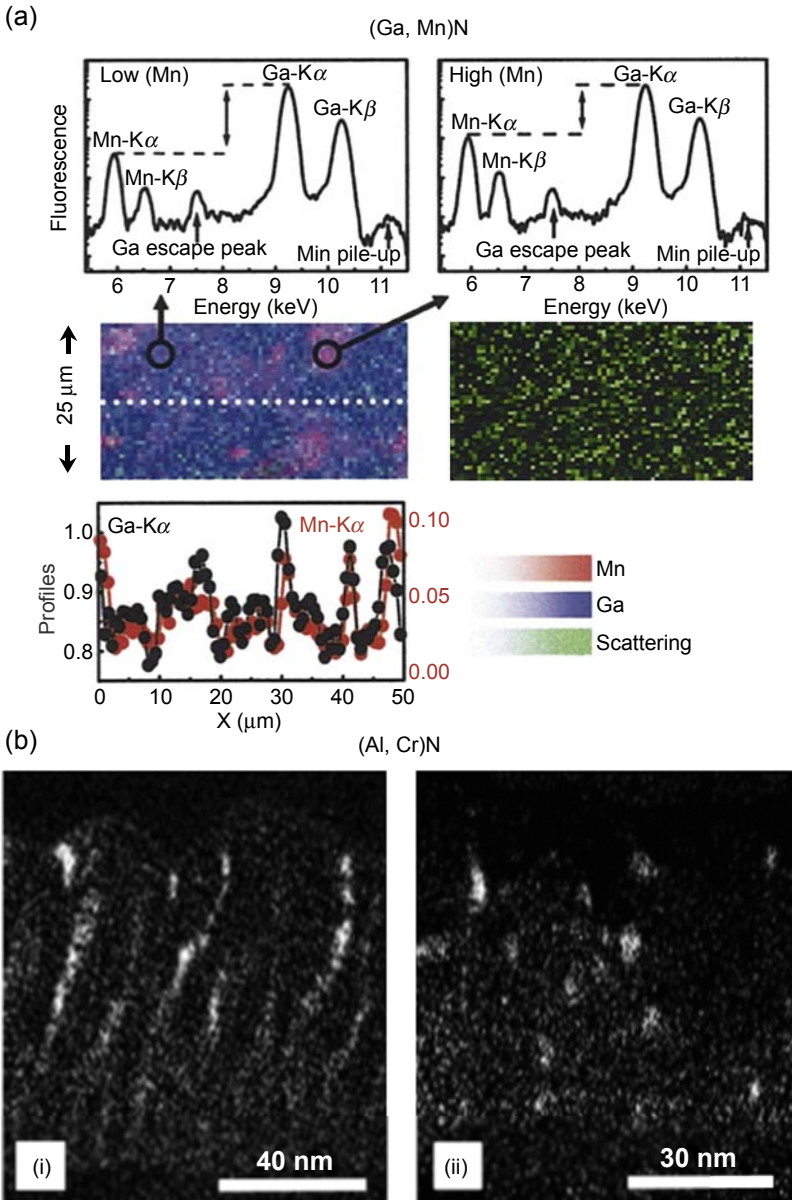


**Figure 1.9** (a) Color map of the highest doped (Ga, Mn)N sample (Mn = 11%). Red, blue, and green correspond to the Mn-K $\alpha$ , Ga-K $\alpha$  fluorescence line, and inelastic (Compton) scattering signal, respectively. Ga (in black) and Mn (in red) profiles along the white scan line are shown in the lower part. (From Martínez-Criado G, Somogyi A, Ramos S, Campo J, Tucoulou R, Salome M, et al. *Appl Phys Lett* 2005;86:131927.) (b) Energy-filtered electron micrographs showing Cr distribution for 4% Cr-doped AlN grown at different substrate temperatures: (i) 700°C; (ii) 800°C. (From Gu L, Wu SY, Liu HX, Singh RK, Newman N, Smith DJ. *J Magn Mater* 2005;290–291:1395.)

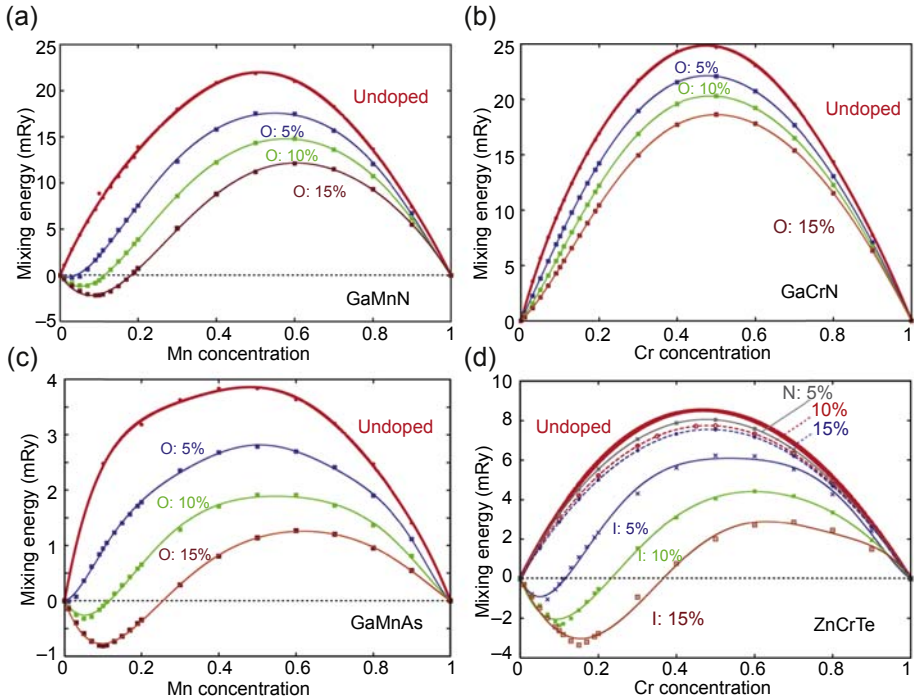


**Figure 1.10** Calculated mixing energies of (a) Mn in GaN, (b) Cr in GaN, (c) Mn in GaAs, and (d) Cr in ZnTe.

From Sato K, Bergqvist L, Kudrnovsky J, Dederichs PH, Eriksson O, Turek I, et al. *Rev Mod Phys* 2010;82:1633; Sato K, Fukushima T, Katayama-Yoshida H. *Jpn J Appl Phys* 2007; 46:L1120.

systems at zero temperature. For finite temperature, we need to calculate the mixing free energy:

$$F_M(c) = E_M(c) - TS, \quad [1.4]$$

where  $T$  is temperature and  $S$  is mixing entropy. From the behavior of the mixing free energy, the phase diagrams of the spinodal decomposition and binodal decompositions can be easily described.

### 1.3.2 Chemical pair interaction

As in the previous discussion, the general DMS systems undergo the spinodal nanodecomposition, so that the distribution of the magnetic impurities in DMS is no longer homogeneous. In order to closely investigate the configuration of the magnetic impurities under the spinodal nanodecomposition and how the inhomogeneity of the

magnetic impurities affects the magnetism in DMS, we calculate the chemical pair interaction. For a binary alloy  $A_{1-c}B_c$ , the chemical pair interaction between sites  $i$  and  $j$ ,  $V_{ij}$ , is defined by:

$$V_{ij} = V_{ij}^{AA} + V_{ij}^{BB} - 2V_{ij}^{AB}, \quad [1.5]$$

where  $V_{ij}^{AB}$  is potential energy when the A and B atoms occupy the  $i$  and  $j$  sites, respectively. As understood from the definition, the negative  $V_{ij}$  means attractive interaction, whereas the positive one leads to repulsive interaction. Ducastelle and Gautier [44] proposed a prescription to calculate the effective pair interaction, now called generalized perturbation method (GPM). The development of GPM for KKR-CPA formalism was done by Turchi [45]. In GPM, the chemical pair interaction can be calculated by

$$V_{ij} = -\frac{1}{\pi} \int \text{ImTr}_L \{ \Delta T^{ij} \Delta T^{ji} \} d\varepsilon, \quad \Delta = t_A^{-1}(\varepsilon) - t_B^{-1}(\varepsilon). \quad [1.6]$$

Here,  $t_{A(B)}$  is the single site  $t$ -matrix of the atom A (B) and  $T^{ij}$  is the scattering path operator. Fig. 1.11 shows the chemical pair interaction in (a) (Ga, Mn)N, (b) (Ga, Cr)N, (c) (Ga, Mn)As, and (d) (Zn, Cr)Te as a function of the distance between the two magnetic impurities. As shown in Fig. 1.11, most chemical pair interactions of these systems have the negative values, leading to attractive interaction, and the first nearest neighbor interactions are considerably strong compared to the other pairs. Therefore, (Ga, Mn)N, (Ga, Cr)N, (Ga, Mn)As, and (Zn, Cr)Te undergo phase separation due to the attractive pair interactions; the spinodal nanodecomposition can occur during the crystal growth. Such tendency of the chemical pair interactions is consistent with the calculated convex positive mixing energy in Fig. 1.10.

### 1.3.3 Simulation of the spinodal nanodecomposition: Dairiseki phase versus Konbu phase

Based on the chemical pair interaction calculated by the GPM, we can simulate the spinodal nanodecomposition in DMS by using the Monte Carlo method. The spinodal nanodecomposition is a kind of phase separation in alloys. For cases of phase separations in alloys, the ordinary Ising model, where the order parameter is not conserved, is not appropriate. Therefore, a correct model to describe phase separations of alloys is the conserved order parameter Ising model:

$$H = -\frac{1}{2} \sum_{i \neq j} V_{ij} \sigma_i \cdot \sigma_j, \quad [1.7]$$

where  $V_{ij}$  is the chemical pair interaction.  $\sigma_i$  is the occupation number of an impurity atom at site  $i$ ; that is,  $\sigma_i = 1$  if site  $i$  is occupied by a TM impurity,



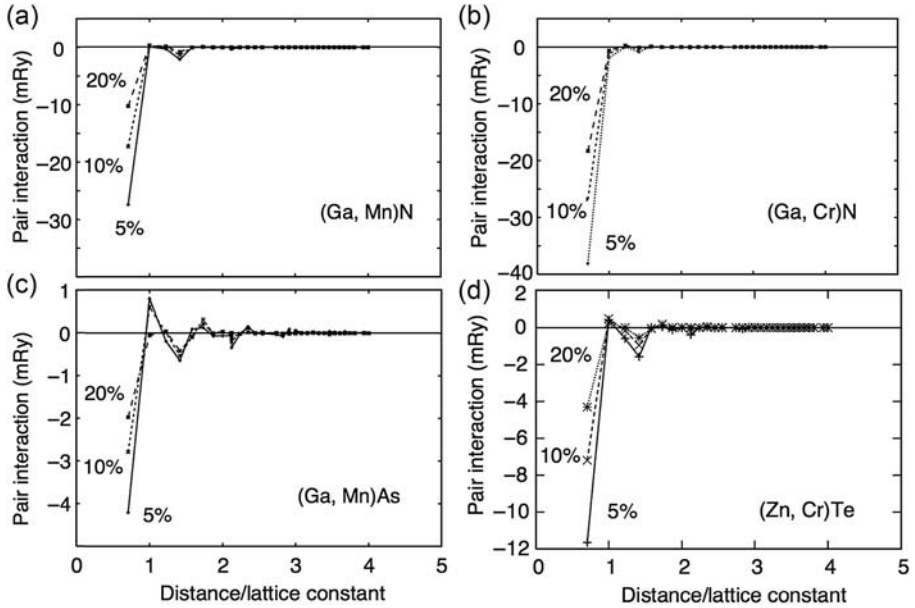


**Figure 1.11** Chemical pair interactions between (a) Mn in GaN, (b) Cr in GaN, (c) Mn in GaAs, and (d) Cr in ZnTe as function of distance normalized to the lattice constant. Negative interactions indicate that the pair interactions are attractive.

From Sato K, Bergqvist L, Kudrnovsky J, Dederichs PH, Eriksson O, Turek I, et al. Rev Mod Phys 2010;82:1633; Fukushima T, Sato K, Katayama-Yoshida H, Dederichs PH. Jpn J Appl Phys 2006;45:L416.

whereas  $\sigma_i = 0$  if site  $i$  is occupied by a host atom. Here, we apply Kawasaki algorithm [47] for the conserved order parameter Ising model.

### 1.3.3.1 Dairiseki phase

First, the simulations of spinodal nanodecomposition for 3D crystal growth are considered. In this case, a large face-centered cubic (FCC) supercell is prepared, and then the TM impurities in DMS are randomly distributed as an initial configuration. Starting from the random distribution of the impurities, we choose one impurity site and try to move the impurity to a site that is chosen from the unoccupied nearest neighbor sites by obeying the Monte Carlo criterion. The trial site can be any one of the nearest neighbor sites, (ie, one of the 12 sites in FCC case). Fig. 1.12(a) and (c) show the simulation results of the 3D spinodal nanodecomposition for (Zn, Cr)Te and (Ga, Mn)N, respectively. These figures are the snapshots of TM impurity distribution after 100 Monte Carlo steps per the magnetic site. Only Cr and Mn impurities are indicated by the red points and the nearest neighbor bonds are combined by the white bars. The impurity concentration is fixed to 5% for all cases and we take  $17 \times 17 \times 17$  conventional FCC cells as a simulation box. The simulations are performed at scaled temperature of  $k_B T/V_{01} = 0.5$  for each case. This corresponds to 916 and 2164 K for



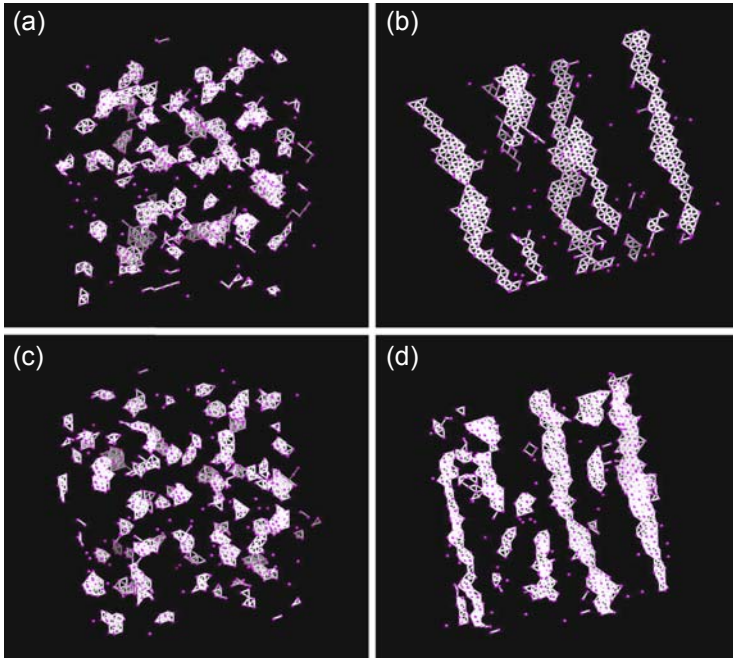


**Figure 1.12** Simulated spinodal nanodecomposition phases in the bulk (a) (Zn, Cr)Te and (c) (Ga, Mn)N, and in (b) (Zn, Cr)Te and (d) (Ga, Mn)N under the layer-by-layer growth condition. In the figures, only magnetic sites are indicated by the *red points*. The concentration of magnetic impurities is 5% for each case.

From Sato K, Bergqvist L, Kudrnovsky J, Dederichs PH, Eriksson O, Turek I, et al. *Rev Mod Phys* 2010;82:1633; Fukushima T, Sato K, Katayama-Yoshida H, Dederichs PH. *Jpn J Appl Phys* 2006;45:L416.

(Zn, Cr)Te and (Ga, Mn)N, respectively. These systems are quenched from  $T = \infty$  to  $T = 0.5k_B|V_{01}|$  at the 0 Monte Carlo step. As shown in [Fig. 1.12\(a\) and \(c\)](#), the magnetic impurities form more isolated cluster with increasing the Monte Carlo steps, compared to the initial random configuration, so that the systems become superparamagnetic. We call such spinodal phase “three-dimensional *Dairiseki* phase,” where *Dairiseki* means the marble in Japanese. Actually, the three-dimensional *Dairiseki* phase was experimentally observed in (Ga, Mn)N, (Ga, Cr)N, (Al, Cr)N, and (Zn, Cr)Te [[26,41,48,49](#)]. It is easily speculated that these complicated configurations of the magnetic impurities strongly affect the magnetism in DMS systems. The  $T_C$  values of (a) (Ga, Mn)N, (b) (Ga, Cr)N, (c) (Ga, Mn)As, and (d) (Zn, Cr)Te with the *Dairiseki* phase calculated by RPA are presented in [Fig. 1.13](#). The horizontal axis is the Monte Carlo step corresponding to the annealing time in a crystal growth experiment. The RPA method can exactly take the magnetic percolation effect into consideration, and provide the realistic estimation of  $T_C$ . Since the calculated results depend on the initial configuration of the magnetic impurities in the simulation box, we simulate the 30 different spinodal nanodecomposition phases to take configuration

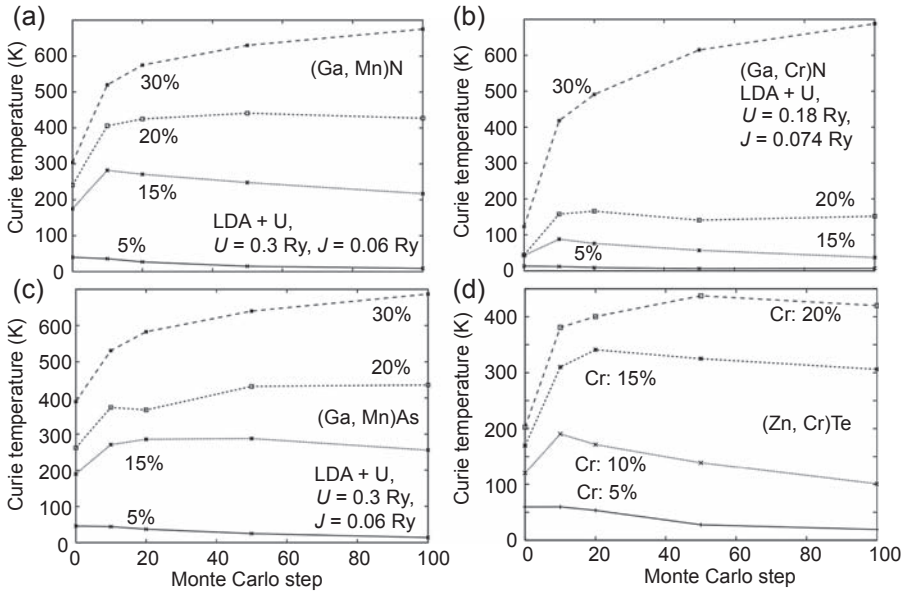


**Figure 1.13**  $T_C^{\text{RPA}}$  of (a) (Ga, Mn)N, (b) (Ga, Cr)N, (c) (Ga, Mn)As, and (d) (Zn, Cr)Te as a function of the number of Monte Carlo steps per impurity. As increasing the Monte Carlo steps, the phase separation develops. For higher concentrations,  $T_C$  increases due to the increased percolation path by clustering. On the other hand, for lower concentrations,  $T_C$  decreases and the system becomes superparamagnetic.

From Sato K, Bergqvist L, Kudrnovsky J, Dederichs PH, Eriksson O, Turek I, et al. *Rev Mod Phys* 2010;82:1633; Sato K, Katayama-Yoshida H, Dederichs PH. *Jpn J Appl Phys* 2005;44:L948.

average. As shown in Fig. 1.13, in the case of the low magnetic impurity concentrations, the  $T_C$  values decrease with the Monte Carlo step. Such a tendency can be understood from the fact that the ferromagnetic interactions work only in the small clusters, however cannot spread over the entire crystal (ie, the superparamagnetism is stable in the case of the low TM impurity concentration). On the other hand, the calculated  $T_C$  values increase with the Monte Carlo step in the high concentration region above the percolation threshold. This is because the magnetic impurities can establish the magnetic percolating paths with forming the large clusters. Therefore, the strong ferromagnetic interactions, originating from the first nearest neighbor atoms, can contribute the high  $T_C$ .

### 1.3.3.2 Konbu phase

Next, the nonequilibrium layer-by-layer crystal growth simulations with the 2D spinodal nanodecomposition are introduced [46]. In this simulation, the atomic diffusion is restricted only on the surface, and only the nearest neighbor sites on the same surface can be candidates for a trial site in the layer-by-layer simulation (one of the four sites in

FCC (100) plane). Moreover, the ideal layer-by-layer growth is assumed; after annealing process of the first layer, the resulting configuration of the first layer is fixed. Then, we deposit the second layer and start the annealing only for the second layer. Repeating this process for the required number of layers, we can obtain the spinodal nanodecomposition phase under the layer-by-layer growth condition. Fig. 1.12(b) and (d) show the simulation results of the layer-by-layer simulation with the 2D spinodal nanodecomposition for (Zn, Cr)Te and (Ga, Mn)N, respectively. In contrast to the 3D spinodal nanodecomposition cases, the quasi-1D structures appear when the layer-by-layer growth is assumed. Due to the attractive interactions the magnetic impurities favor to gather each other. By the layer-by-layer condition, the magnetic impurities cannot move out from the initial planes, so that the shape of the cluster is spontaneously controlled resulting in the quasi-1D shape. We call this quasi-1D phase the “one-dimensional *Konbu* phase,” where *Konbu* means seaweed in Japanese. Actually, the *Konbu* phase was observed experimentally in (Al, Cr)N and GeMn systems [41,50]. Note that the *Konbu* phase has very low  $T_C$ , because the ferromagnetic interaction does not work between the quasi-1D clusters. However, if the volumes of the clusters are large enough, the system shows hysteretic behavior even at high temperature because of the superparamagnetic blocking phenomena. This point will be discussed in the next section.

### 1.3.4 Superparamagnetic blocking phenomena

If the clusters by the *Dairiseki* and *Konbu* phases are large enough, superparamagnetic blocking phenomenon becomes important and affects the magnetization process. The rotation of the magnetic moment of one cluster does not occur freely and is blocked by the energy barrier due to the magneto-crystalline and shape anisotropy energies. It can be assumed that the average time to flip the magnetization obeys relaxation time:

$$\frac{1}{\tau} \propto e^{-\left(\frac{KV}{k_B T}\right)}, \quad [1.8]$$

where  $K$ ,  $V$ ,  $T$ , and  $k_B$  are anisotropy constant, volume of the system, temperature, and Boltzmann constant, respectively. Since the anisotropy energy is proportional to the volume of the cluster, if the cluster is large enough, the relaxation time to flip the magnetization becomes quite long; the  $T_B$  of such *Dairiseki* and *Konbu* phases could be high [51]. As a result, depending on the observation time, a hysteresis loop appears in the magnetization curve, even if there is no correlation between the magnetic clusters and  $T_C$  of the system is very low. In the last of this section, the simulations of the magnetic hysteresis curve due to the blocking phenomena in DMS are introduced by the Monte Carlo method. Here, the classic Heisenberg model with a magnetic anisotropy term is assumed:

$$H = - \sum_{i \neq j} J_{ij} \mathbf{e}_i \cdot \mathbf{e}_j - \sum_i A (\mathbf{e}_i^z)^2 + \mu B_z \sum_i \mathbf{e}_i^z, \quad [1.9]$$

where  $J_{ij}$  is the exchange interaction between the sites  $i$  and  $j$  calculated by the Liechtenstein formula,  $\mathbf{e}_i$  is the unit vector parallel to the magnetization at site  $i$ ,  $B_z$  is the external field, and  $\mu$  is the absolute value of the magnetic moment. When the relaxation process like the blocking phenomena is simulated, the anisotropy term becomes very important. In present simulation, the experimental anisotropy constant is employed. Additionally, we need to develop the general Monte Carlo method because the usual Monte Carlo method simulates the thermal equilibrium state of a system and cannot describe meta-stable state, which is responsible for the magnetic hysteresis. In order to describe the relaxation process by the Monte Carlo method, we employ the local algorithm developed by Dimitrov [52]. In the local algorithm, a trial state is chosen from one of the states near the current position in the phase space, in contrast to the Metropolis algorithm, where a trial state is picked up randomly. According to this algorithm, the maximum angle between the original direction and trial direction of the sampled magnetic moment is limited within a certain degree in our simulation. As a result, the effect of the energy barrier between the stable and *meta*-stable states is properly reflected in the relaxation process of the MCS.

Fig. 1.14 shows the simulation results of the blocking phenomena obtained by the local algorithm for  $(\text{Ga}_{0.95}, \text{Mn}_{0.05})\text{N}$  with the homogeneous *Dairiseki* and *Konbu* phases [12,53]. The magnetization curves are shown as a function of temperature in upper panels (a)–(c) and of external field in lower panels (d)–(f). The insets in (d), (e), and (f) are the snapshots of the Mn distributions, where the cluster size of the *Konbu* phase (f) is larger than that of *Dairiseki* phase (e), and there are only small clusters in the homogeneous phase (d). The temperature dependence of the magnetization is calculated by increasing temperature under a small external magnetic field for the two initial magnetization directions: one is parallel to the external field, and another is antiparallel. Above  $T_B$ , the two magnetization curves show the same temperature dependence. As shown in Fig. 1.14(f), the formation of the larger clusters in the *Konbu* phase results in the higher  $T_B$  than in the case of the *Dairiseki* phase.  $T_C$  of  $(\text{Ga}_{0.95}, \text{Mn}_{0.05})\text{N}$  with the homogeneous phase is also indicated by the arrow in Fig. 1.14(a). The magnetic hysteresis curves are simulated for  $T = 0.5T_C$ ,  $T_C$ , and  $2T_C$ . The horizontal axis is the external field, which is scaled by the nearest neighbor interaction  $|J_{01}|$ , and the magnetization is normalized so as to become 1.0 when all magnetic moments are parallel. As shown in Fig. 1.14(e) and (f), the homogeneous system does not show the hysteresis loop above  $T_C$ . On the other hand, even if  $T = 2T_C$ , the hysteresis loop can be observed in the *Dairiseki* and *Konbu* phases. Thus, the magnetic hysteresis of DMS is appreciably affected by the inhomogeneity of the magnetic impurities. In the experiment, circumventing the spinodal nanodecomposition is very difficult under the thermal nonequilibrium crystal growth. Therefore, the cluster size and its distribution depend on the crystal growth conditions. In other words, the magnetic properties of DMS strongly depend on the details of the experimental conditions. This is why the  $T_C$  values observed by experiments are scattered in DMS, such as  $(\text{Ga}, \text{Mn})\text{N}$  [37,54–58].

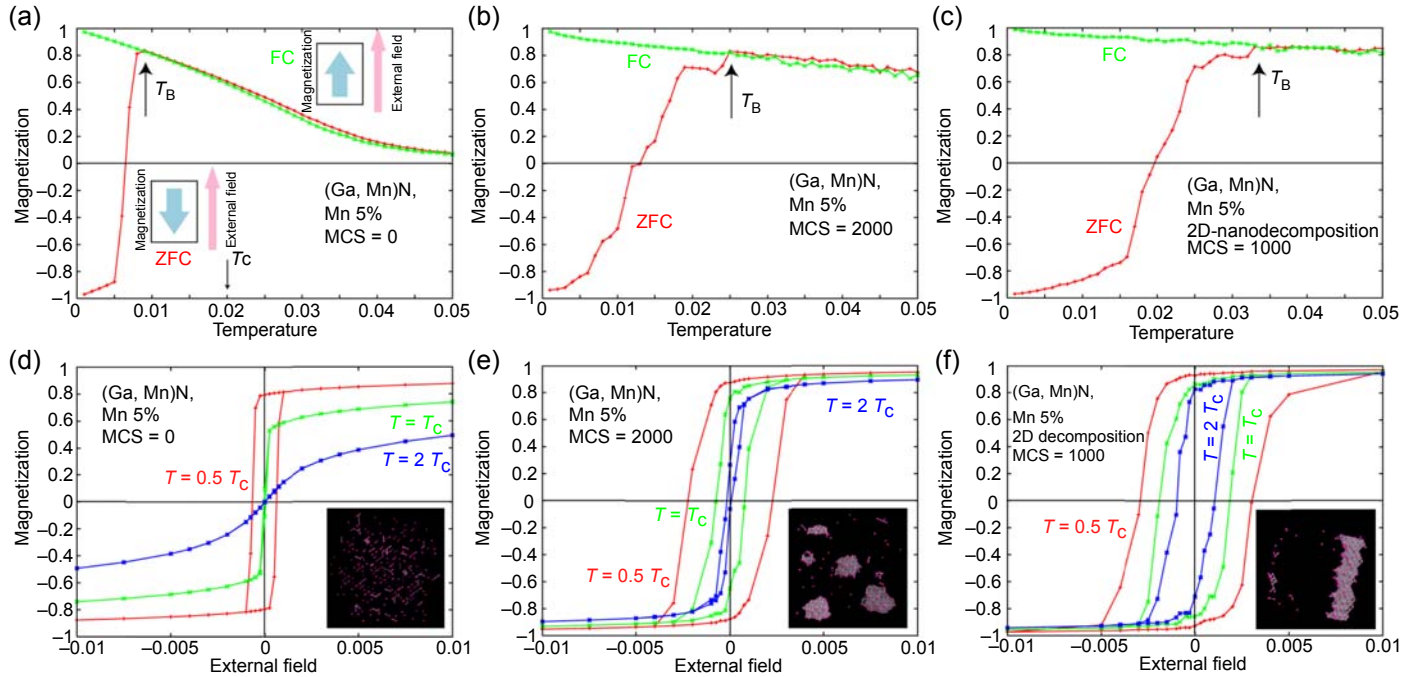


**Figure 1.14** Simulated results of the superparamagnetic blocking phenomenon in (Ga, Mn)N. Upper panels: Magnetization as function of temperature starting from parallel or antiparallel configurations of initial magnetization to the external field. Lower panels: Magnetization as a function of external field. The simulations are performed for homogeneous Mn distribution ((a) and (d)), *Dairiseki* phase ((b) and (e)), and *Konbu* phase ((c) and (f)). The insets in the lower panels show snapshots of Mn distribution in (Ga, Mn)N for the respective phases. Temperature ( $k_B T$ ) and external field are scaled by the strength of the nearest neighbor interaction  $|J_{01}|$ .

From Sato K, Bergqvist L, Kudrnovsky J, Dederichs PH, Eriksson O, Turek I, et al. Rev Mod Phys 2010;82:1633; Sato K, T. Fukushima, H. Katayama-Yoshida, Jpn J Appl Phys 2007;46:L682.

## 1.4 Rare-earth impurities in gallium nitride

Rare-earth-doped gallium nitride (GaN) epilayers are commonly used in blue and green LEDs [59–63]. Though GaN-based red LEDs are still in the research phase, these materials enable fabrication of GaN-based monolithic full-color LEDs, which work on a seamless condition for operating bias voltage, electrodes, substrates, and so on. Therefore, it gives us the prospect of not only a simple LED but also multifunctional activity in these materials. In this section, we discuss the spintronics potential in the luminescent materials toward the production of novel abilities to show the multifunctional activity. In the first subsection, we describe a computational material design of a high-efficient luminescent material for the red LEDs based on Eu-doped GaN. In the second subsection, we demonstrate that the codoping is high-density doping. In the third subsection, we explain the magnetic properties of the luminescent center. In the fourth subsection, we mention the circularly polarized luminescence. Finally we discuss the spintronics potential in the summary.

### 1.4.1 High-efficiency light emission

Nishikawa et al. reported the first GaN-based red LED, Eu-doped GaN [64]. Thereby, the monolithic full-color LEDs became an exactly true story. However, the current Eu-doped GaN does not have enough luminescent intensity to be made available in the market. Therefore, we have reports about enhancement of the intensity. For example, Wang et al. reported the enhancement by codoping Si along with Eu into GaN [66]. Moreover, Nishikawa et al. reported the enhancement by codoping Mg [65]. Furthermore, Mitchell et al. also reported about the codoping method using Mg and Eu, and discussed the atomic configurations of the luminescent centers [67,68]. In this study, we examine the computational material design toward the high-efficiency red light emission based on the Eu-doped GaN [69,70].

So far, we have found clues—O makes a donor level strongly localized in GaN [71–74], and Mg doping usually induces a shallow acceptor level in GaN [72–75]. If impurities form a cluster when Mg and O atoms are codoped along with Eu into GaN, we must obtain a special electronic state, which is illustrated in Fig. 1.15. This figure illustrates that the donor and acceptor levels form an energy path of excitons, holes, and/or electrons from the host bands to the luminescent centers, namely the f-states of Eu atoms. This locally narrow bandgap generates a spatial dependence on the energy gradient of the valence and the conduction bands. Therefore, the complexes attract excitons, holes, and electrons that occur and/or float in the host material by the energy gradient.

In the first step, we estimate the total energies of various modifications that mimicked (Eu, Mg, O)-doped GaN, where these impurities occupy atomic positions different from each other. Herein, we used Vienna Ab-initio Simulation Package (VASP) throughout this section [76]. As a result, we obtained characteristic atomic configurations as stable structures. These structures are chain-like ones such as Eu-O-Mg-N-Eu. The result suggests that the phase separation occurs in this material. Each phase has an energy gap that differs from the other phase. That is, the bandgap is

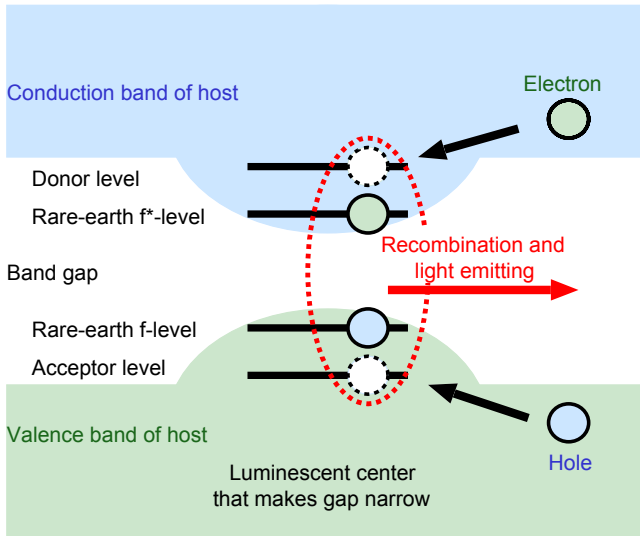


**Figure 1.15** Plot of the material design toward a good luminescence LED. This figure illustrates that a complex of impurities makes the band gap generated by the host elements narrow; thereby, it attracts the excitons that are around itself, and traps. Finally the excitons recombine and convert to light efficiently.

1.42 eV around the chain complex, whereas it is 1.80 eV at a position distant from the complex. Herein, usual density functional method calculation commonly underestimates bandgaps; for example, the experimental value 3.4 eV in the pure crystal GaN. Anyway, the bandgap decreases around the impurity complex.

In the second step, we see the partial DOS (pDOS) of the most stable modification. Fig. 1.16(a)–(c) show pDOS of Eu, Mg, and O atoms. Moreover, Fig. 1.16(d) and (e) indicate pDOS of N atoms near the impurities and distant from them, respectively. In this figure, we can easily recognize that the Eu f-states show the large exchange splitting. Moreover, we can see another exchange splitting in the p-states of O and N atoms near the impurities, where the splitting makes an opposite shift to the Eu splitting. On the other hand, Mg shows very small splitting, and N atoms distant from them exhibit no exchange splitting. This is that a cluster with magnetic moment is generated in the nonmagnetic host material. Because the cluster has a bandgap narrower than that of the host, excitons are attracted and trapped by the complex, and it finally must be converted to light efficiently.

### 1.4.2 High-density doping

The solubility is usually very low, when the rare-earth is doped into semiconducting materials [64,77]. For example, Sanna et al. reported that the formation energy of Er into GaN crystal is about 10.0 eV, which is one of the highest formation energies of doped elements into semiconducting materials [78–80]. However, they proposed



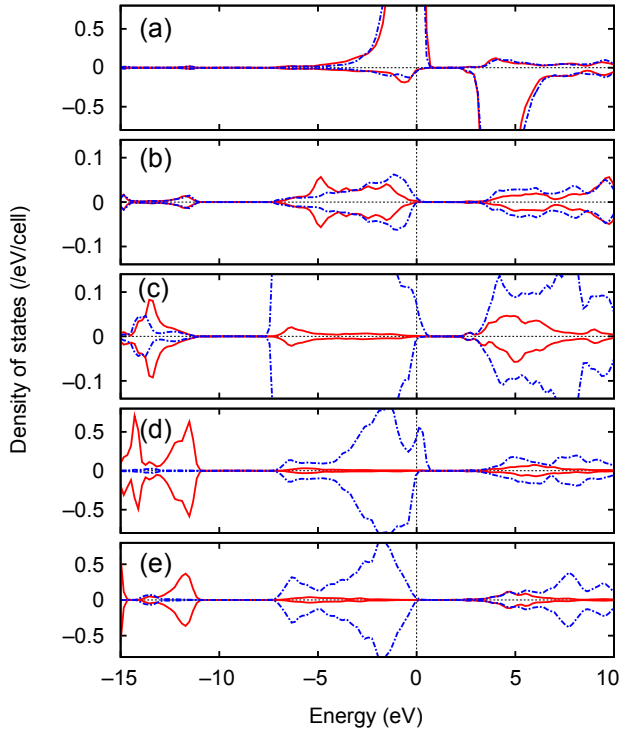


**Figure 1.16** pDOS of impurities in (Eu, Mg, O)-doped GaN. (a)–(c) show f-states of the two Eu atoms, s-states (red solid lines) and p-states (blue dashed lines) of Mg, s-states and p-states of O. (d) and (e) show s-states (red solid) and p-states (blue dashed) of N atoms near the impurities and distant from them, respectively.

that the formation energy becomes lower due to the vacancy doping along with Er. This subsection describes such examples; that is, high-density doping becomes possible by doping the rare-earth along with specific elements.

Fig. 1.17(a) and (b) show various formation energies in the atmospheric limitation of Ga-rich and Ga-poor, respectively. In Fig. 1.17(a), we can see the formation energy in Ga-rich for single doping of Eu, which is from 5.0 to 10.0 eV within Fermi energy displacements from the valence band maximum (VBM) 0.0 eV to the conduction band minimum (CBM) 1.8 eV. It does not change when Eu is doped along with Mg into GaN. However, we can reduce the formation energy down to 1.0 to 5.0 eV by codoping O along with Eu and Mg by decreasing the partial pressure of Ga. In Fig. 1.17(b), we can see it is Ga-poor for single doping of Eu. The formation energy is from 2.0 to 5.0 eV within the Fermi energy displacements. When doping Eu along with Mg, we can reduce it slightly. However, we can considerably reduce the formation energy by doping O along with Eu and Mg. The formation energy is negative, that is from  $-4.0$  to  $0.0$  eV within these displacements. We can explain that a compensation induces the behavior. This is mainly because of ionic radii of Eu, Mg, and O atoms;



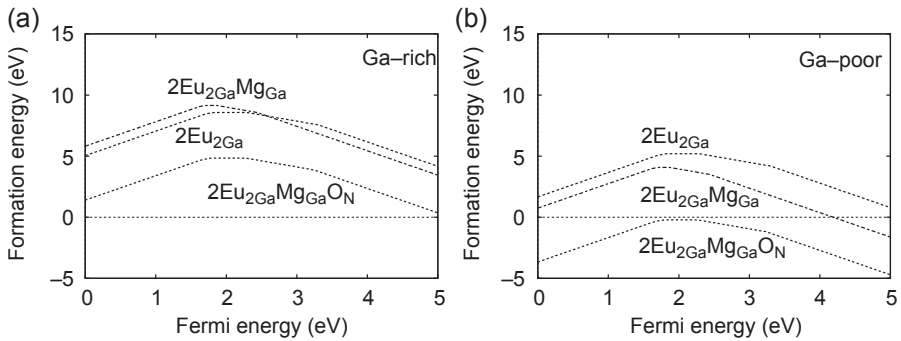


**Figure 1.17** Formation energies of GaN:(2Eu), GaN:(2Eu, Mg), and GaN:(2Eu, Mg, O) as functions of Fermi energy, where the crystal growth conditions are Ga-rich (a) and Ga-poor (b). We can change the Fermi energy from the VBM 0 eV to the CBM 1.8 eV.

that is, these impurity atoms exist under the spatial compensations. Moreover, the reduction of the Madelung energy by forming the metal-oxygen complexes also induces the Eu-O and Mg-O clusterization. This clusterization induction works as a charge compensation when we dope a pair of acceptor and donor elements simultaneously, where Mg works as an acceptor and O works as a donor. We call the codoping method a codoping method by a compensated atomic pair.

Fig. 1.18 shows the binding energies for the chain-like complex and Eu-Mg that were estimated from the formation energies. The binding energy exhibits a negative value of  $-1.23$  eV with any Fermi level displacements. On the other hand, the binding energy of Eu-Mg shows a negative value of  $-0.13$  eV only near VBM. Therefore, the clusterization easily occurs with codoping of Eu, Mg, and O more than codoping of Eu and Mg. The codoping is realized by thermal nonequilibrium crystal growth methods such as molecular beam epitaxy (MBE) or metal-organic chemical vapor deposition [74,81–83].

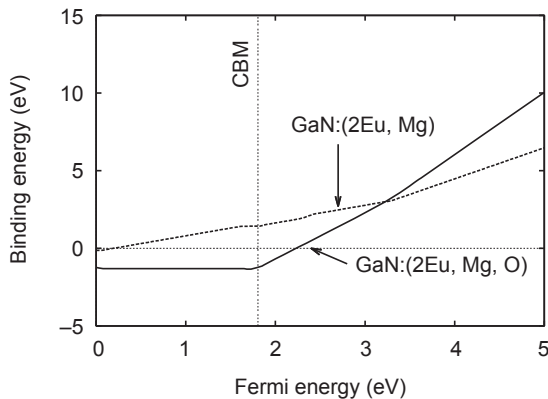


**Figure 1.18** Binding energy of GaN:(2Eu, Mg, O) and GaN:(2Eu, Mg) as functions of Fermi energy. A vertical dashed line denotes the conduction band minimum.

### 1.4.3 Zener's $p$ - $f$ exchange interaction

As described earlier, the impurities form the chain-like cluster in this crystal. Because Eu atoms originally have a magnetic moment, (Eu, Mg, O)-doped GaN also has a magnetic property. In this subsection, we describe the magnetic property. We have already researched the electronic structure with pDOS of this material in the previous subsection, shown in Fig. 1.16. Therein, we saw the large exchange splitting about the Eu atoms, and the atoms near the Eu atoms showed small exchange splitting which is opposite shift to the Eu atoms. It is actually similar to Zener's  $p$ - $d$  exchange interaction—we call it the  $p$ - $f$  exchange interaction [12,84,85]. And moreover, we can notice the existence of the double exchange interaction between Eu atoms from the position of the  $f$ -states of Eu relative to Fermi level. The two types of the interactions promote stabilization of the system into the ferromagnetic states.

Fig. 1.19 shows the  $z$ -component of the spin-polarized charge density. These charge maps were plotted on the 2D plane passing through three atomic positions of the two Eu and one Mg atoms [85]. In this figure, we can easily notice two kinds of areas: the red areas denote the positive spin-polarized charge density, and the blue areas indicate the negative one. The red and blue areas correspond to the majority and the minority spin states, respectively. The majority spin density areas lie on the Eu atom sites. On the other hand, the minority spin density areas are located around the N(O) atom sites. However, these are the nearest neighbors of the Eu atoms and the other atoms have spin densities too small to show in this figure. In particular, the spin density around N(O) clearly shows the polarization orientation opposite to that around Eu. This is quite characteristic of Zener's  $p$ - $f$  exchange interaction. Considering a fact that the spin injection from the half-metallic into a semiconductor induces the

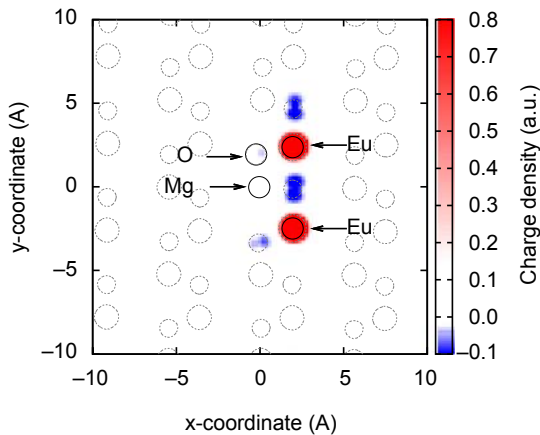


**Figure 1.19** Spin-polarized charge density map of the  $z$ -components of the most stable modification. The map is plotted on the 2D plane passing three atomic positions of Mg and two Eu atoms. Herein the *black solid circles* are impurity atoms, which are labeled by the corresponding symbols, and *large and small gray circles* denote Ga and N atoms near the plane, respectively.

circular polarization, we can expect that the electronic states generated by the p-f exchange interaction are suitable for the circularly polarized luminescence.

#### 1.4.4 Circularly polarized luminescence

The circularly polarized luminescence is used not only in scientific observations but also in entertainment and medical tools such as 3D displays [86–88]. Moreover, it is expected to be applied in quantum computing, spintronics, biological probe, and so on [89–91]. It is becoming increasingly important. However, the current sources of the circularly polarized light need large, complex, or extra constructions like crystal retarders, the spin-injection method, and inorganic LEDs [92–94]. If we replace those sources with inorganic LEDs, we can construct such devices in a simpler manner. Though, very recently, few examples have been reported by Zhang et al. about  $\text{WSe}_2$  and by Sircar et al. about Si-Ge/Si quantum dots, the other inorganic materials basically have never been observed in visible rays [95,96].

In this subsection, we theoretically predict that this material possesses an ability to emit the circularly polarized light when it has the electronic structure as described earlier. As described earlier, the cluster has a half-metallic electronic structure. Therefore, we can expect circularly polarized luminescence, but the transitions in which the spin direction changes are formally forbidden. However, it is partly allowed in general when the spin–orbit interaction works well. We can see the intensity of the spin–orbit interaction in the pDOS onto the noncollinear components, which is shown in Fig. 1.20. In this figure, we can see the  $(\uparrow\downarrow)$  and  $(\downarrow\uparrow)$  components of the f-states as the red and blue lines, respectively. Moreover, the majority spin, namely  $(\uparrow\uparrow)$ , and the minority spin  $(\downarrow\downarrow)$  components are represented by the gray lines along the positive and negative vertical axes, respectively. In this figure, we can see most volumes of the noncollinear components in an energy range around  $-1.0$  eV, around which both  $(\uparrow\uparrow)$  and  $(\downarrow\downarrow)$  components have the largest volumes. Therefore, the transitions can be allowed.

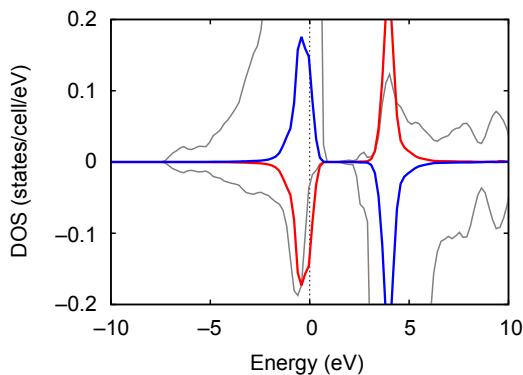


**Figure 1.20** pDOS of the noncollinear spin components. Red and blue lines are noncollinear spin components. Gray lines denote the majority and minority spin components of the f-states of Eu.

However, the circularly polarized luminescence has never been reported in experimental procedures. We think that it is caused because the ferromagnetic states are not stable at room temperature, because the total energy difference  $\Delta E$  between the ferromagnetic states and the antiferromagnetic states is very small, about 1.0–4.0 meV in our calculations. The energy difference causes very small transition temperature  $T_c$  from the ferromagnetic to the antiferromagnetic states in accordance with the mean field theory relation  $k_B T_c = 2\Delta E/3c$ , where  $c$  is a concentration of Eu [23]. Even if the stable state in room temperature is the antiferromagnetic state, the transition must occur with spin inversion as long as it is an intraatomic transition. However, the transition may occur without spin inversion, when we regard the antiferromagnetic states as a paramagnetic ones approximately. Otherwise, a lowering of the system symmetry and a large effective coulombic interaction, which is so-called *plus U*, work; hence, the f-states of Eu would be divided into a couple of levels. The transition may occur between the levels with the same spin moments actually.

### 1.4.5 Summary

In this section, we have discussed the electronic structures suitable for the high-efficient luminescence and the spintronics in the Eu-doped GaN systems. Codoping the rare-earth Eu into GaN provides with the red light emitting, but it is slightly poor as commercial productions. Therefore, we have proposed a novel luminescent center from a standpoint of the computational materials design. Codoping Eu along with a compensated pair of Mg and O, which work an acceptor and a donor in this crystal, make assembly of these impurities in this crystal. The assemblage has a low formation and binding energies; hence, we can obtain the atomic configurations spontaneously, namely, through the spinodal decompositions. Moreover, the cluster has a characteristic magnetic property, which is Zener's p-f exchange interaction, but no magnetic moment outside the cluster. This electronic structure induces the half-metallic, and then it is suitable for the circularly polarized luminescence. Based upon these factors, we believe that the electronic and magnetic properties may give us the multifunctional activity, and be useful to prolong or control the lifetime, color, and intensity of the LEDs.

## 1.5 MgO-based high- $T_c$ nanospintronics

$d^0$  ferromagnetism refers to a unique class of magnetism wherein the ferromagnets contain no magnetic elements. In the discovery of  $d^0$  ferromagnets, a series of computational materials design (CMD) has played an essential role [97]. In 2004, we initially and theoretically demonstrated the existence of p-bands in  $K_2(S, Si)$  and  $K_2(S, Ge)$  in which deep impurity bands consisting of 3p orbitals were introduced in the bandgap with partially filled 3p shells stabilizing a ferromagnetic state [98]. This principle was applied to 2p orbitals in  $Ca(O, C)$ ,  $Ca(O, N)$  [99],  $Mg(O, C)$ ,  $Mg(O, N)$ ,  $Sr(O, C)$ ,  $Sr(O, N)$ ,  $Ba(O, C)$ , and  $Ba(O, N)$  [100]. Further, many DMSs containing no

magnetic elements, such as alkaline-chalcogenide- [101], alkaline-earth-chalcogenide- [101–103],  $\text{SiO}^{2-}$ - [104], and diamond-based [105]  $d^0$  ferromagnets, were similarly designed. After our aforementioned series of CMD of  $d^0$  ferromagnets, many experimental works also reported the existence of ferromagnetism in materials such as N-doped MgO [106], C- or N-doped ZnO [107,108], pristine (undoped)  $\text{HfO}_2$  [109],  $\text{TiO}_2$  [110],  $\text{In}_2\text{O}_3$  [110], ZnO [110],  $\text{SnO}_2$  [111], and MgO [112,113]. These  $d^0$  ferromagnets can be classified into two groups of anion-substituted and cation-substituted. The first group involves anions of semiconductors or insulators being substituted by impurities of smaller valency. The second group involves cations being substituted by vacancies (or impurities of smaller valency). In this section, based upon ab initio electronic structure calculation and multiscale simulation, we discuss the origin of  $d^0$  ferromagnetism and magnetic properties of dynamically created nanostructures (spinodal nanodecomposition) in MgO-based  $d^0$  ferromagnets with N atoms or Mg vacancies ( $V_{\text{Mg}}$ ) as representative examples.

In order to understand the origin of the  $d^0$  ferromagnetism, their electronic structures in the ferromagnetic states are calculated by KKR-CPA within the pseudo-self-interaction-corrected LDA (PSIC-LDA) (Fig. 1.21). In the  $\text{Mg}(\text{O}, \text{N})$ , spin-polarized impurity 2p bands are introduced into the bandgap, and the impurity bands are partially filled by electrons. In  $(\text{Mg}, V_{\text{Mg}})\text{O}$ , the valence bands mainly consist of O 2p-orbitals that exhibit spin-polarization. The origin of  $d^0$  ferromagnetism in the present systems can be understood as follows: local magnetic moments in the materials are spontaneously formed by highly correlated narrow oxygen-2p bands ( $U > W$ ,  $U$ : Correlation energy,  $W$ : band width) and the ferromagnetic states are stabilized due to the kinetic energy gain from itinerant spin-polarized electrons, which result from the partial occupation of the narrow oxygen-2p bands.

Next, magnetic effective exchange interactions and  $T_C$  are calculated to evaluate the stability of magnetic state. In the present systems, the interactions using

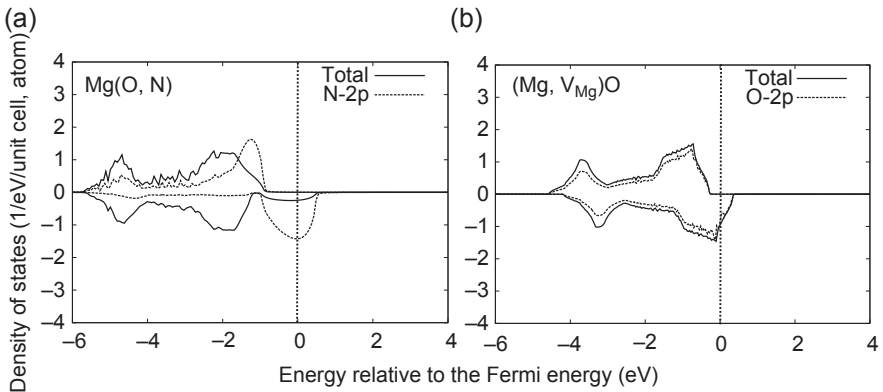


**Figure 1.21** The total and partial DOS of (a)  $\text{Mg}(\text{O}, \text{N})$  and (b)  $(\text{Mg}, V_{\text{Mg}})\text{O}$  with 10% doping concentration calculated by KKR-CPA-PSIC. The *solid lines* and *dotted lines* represent the total DOS and N-2p partial DOS, respectively. The positive and negative values of the DOS represent the values for the up and down spins, respectively [114,115].

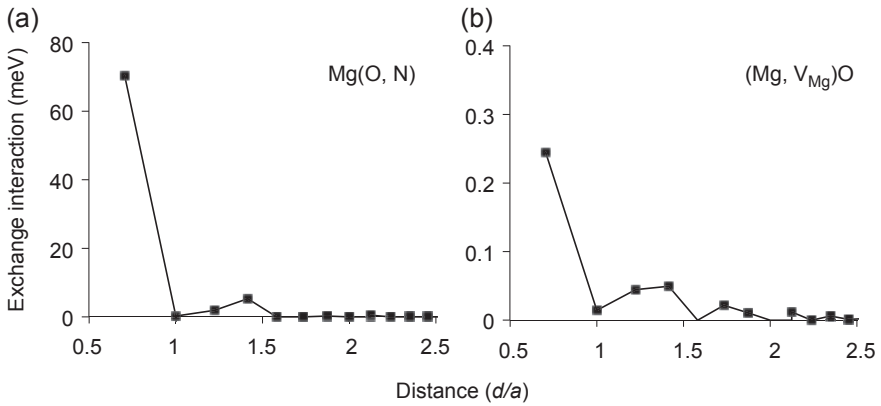


**Figure 1.22** Distance dependence of the effective exchange interaction between O atoms in (a) Mg(O, N) and (b) (Mg, V<sub>Mg</sub>)O with 10% doping concentration calculated by Liechtenstein's formula within the PSIC-LDA [115,120].

Liechtenstein's formula [116] are short-ranged and dominant only for the first few neighbors (Fig. 1.22). Recent studies reveal that the MFA greatly overestimates  $T_C$  for such materials where the exchange interactions are short-ranged and the concentration of magnetic sites is smaller than the magnetic percolation threshold. This percolation threshold is 20% for the FCC structure of MgO when we focus only on the nearest neighbor interactions [117]. The reason for this overestimation is that the approximation counts all the exchange interactions as significant interactions, regardless of whether they are sufficiently strong to contribute to the  $T_C$  under thermal fluctuations. For proper  $T_C$  estimation in such case, beyond-MFA approach using MCS is known to be effective. This approach takes more calculation cost compared to the MFA but has obtained good agreement between theory and experiments in many homogeneous DMSs, such as (Ga, Mn)As [117–119]. For this reason, the MCS is performed [117] for Mg(O, N) to avoid the overestimation of  $T_C$  by accounting for the magnetic percolation effect and the MFA is used and for (Mg, V<sub>Mg</sub>)O. In (Mg, V<sub>Mg</sub>)O, the local magnetic moments originate not from the dopants but from the O-2p orbitals of the host material. Therefore, due to the high O concentration, the magnetic correlation in the present system should be long range. This long-range correlation ensures the validity of the MFA for the calculation  $T_C$  of (Mg, V<sub>Mg</sub>)O. The present simulations show that the  $T_C$  increased linearly as a function of the doping concentrations and could reach room temperature at sufficient doping concentrations of 15% for (Mg, V<sub>Mg</sub>)O and 20% for Mg(O, N) (Fig. 1.23).

Thus far, we have discussed the magnetic properties assuming that the dopants are homogeneously distributed at assigned sites. Hereafter, a favored configuration of dopant distribution is investigated. The present calculation procedure consists of two steps. The first step is the calculation of the chemical pair interactions between the two dopants embedded in a supercell. The second step is the simulation of the

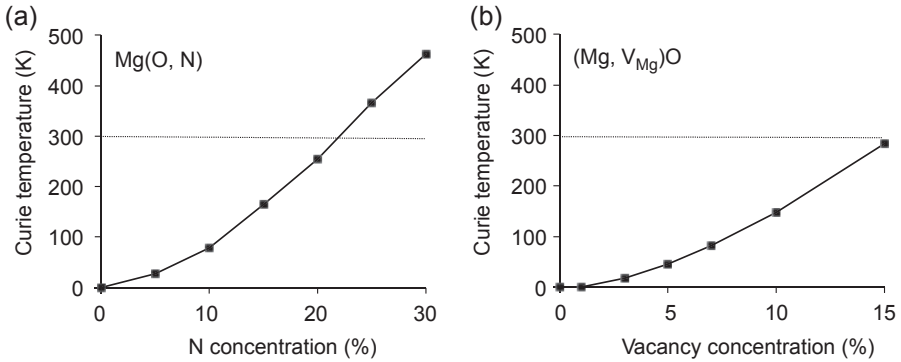


**Figure 1.23** The estimated  $T_C$  of (a)  $\text{Mg}(\text{O}, \text{N})$  using MC simulation and (b)  $(\text{Mg}, \text{V}_{\text{Mg}})\text{O}$ , by the MFA [114,115].

potential configuration of inhomogeneous dopant distribution using the calculated chemical pair interactions and MC simulations, which are already mentioned in the previous sections.

The chemical pair interactions between the dopants at sites  $i$  and  $j$  ( $V_{ij}$ ) were calculated using the calculated total energies, defined as  $E(\text{Mg}_{32}\text{O}_{32}) + E(\text{Mg}_{32}\text{O}_{31}\text{N}_1) - 2E(\text{Mg}_{32}\text{O}_{30}\text{N}_{2-ij})$  for  $\text{Mg}(\text{O}, \text{N})$  and  $E(\text{Mg}_{32}\text{O}_{32}) + E(\text{Mg}_{31}\text{V}_{\text{Mg}1}\text{O}_{32}) - 2E(\text{Mg}_{30}\text{V}_{\text{Mg}2-ij}\text{O}_{32})$  for  $(\text{Mg}, \text{V}_{\text{Mg}})\text{O}$ . Here, the VASP was used for calculations of the projector augmented wave (PAW) method [121] and the generalized gradient approximation (GGA) [122,123] exchange-correlation functional (PAW-GGA). An experimentally derived lattice constant with a rocksalt structure was also used and structural optimization was performed.

The present simulations showed that these materials favor phase separation because of the attractive pair interactions, and during crystal growth, spinodal decomposition can occur if the related temperatures are high enough for a sufficiently long time. Calculated  $V_{ij}$  shows that strong attractive interactions occurred between the first nearest neighbors in  $\text{Mg}(\text{O}, \text{N})$  and the second nearest neighbors in  $(\text{Mg}, \text{V}_{\text{Mg}})\text{O}$  (Fig. 1.24). The MC simulations show that self-organized nanoclusters of the *Dairiseki* phase appear under 3D crystal growth (Fig. 1.25) and nanowires of the *Konbu* phase appear under layer-by-layer crystal growth (Fig. 1.26).

This finding can be strengthened by comparing  $T_C$  between our theoretical estimations under the homogeneous conditions and recent experiments that report room-temperature ferromagnetic behaviors observed in  $\text{MgO}$  thin films with no magnetic elements. In our theoretical estimations, 15–20% doping concentrations are required for room-temperature ferromagnetism in  $\text{Mg}(\text{O}, \text{N})$  and  $(\text{Mg}, \text{V}_{\text{Mg}})\text{O}$  under homogeneous distribution conditions. On the other hand, experiments have reported ferromagnetism in 13%-N-doped  $\text{MgO}$  prepared via MBE has been observed [106] and ferromagnetism induced by a few percent of Mg vacancies in  $\text{MgO}$ , prepared with sputtering in an O atmosphere, also has been reported [112,113]. Considering these large discrepancies in  $T_C$  and their systems favorability of the formation of nanoclusters of dopants, it is strongly suggested that the magnetic properties observed

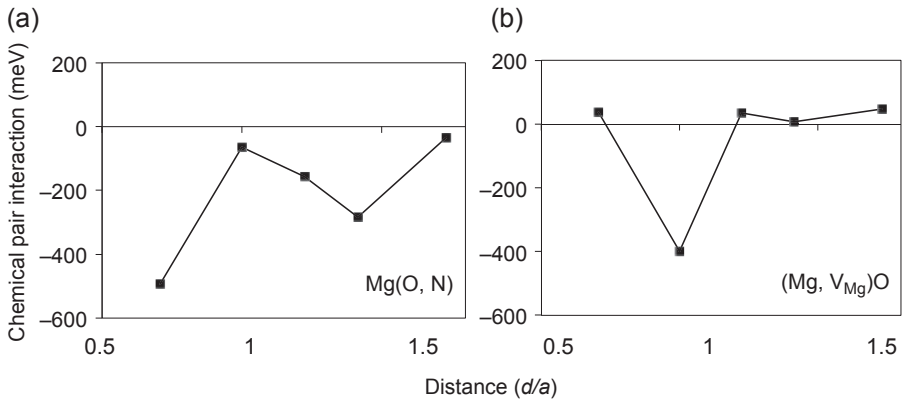


**Figure 1.24** The chemical pair interaction (a) between N atoms in Mg(O, N) and (b) between vacancies in (Mg,  $V_{Mg}$ )O.

From Seike M, Dinh VA, Fukushima T, Sato K, Katayama-Yoshida H. Spinodal nanodecomposition and high blocking temperature in MgO-based  $d^0$  ferromagnets. *Jpn J Appl Phys* 2012;51:050201.

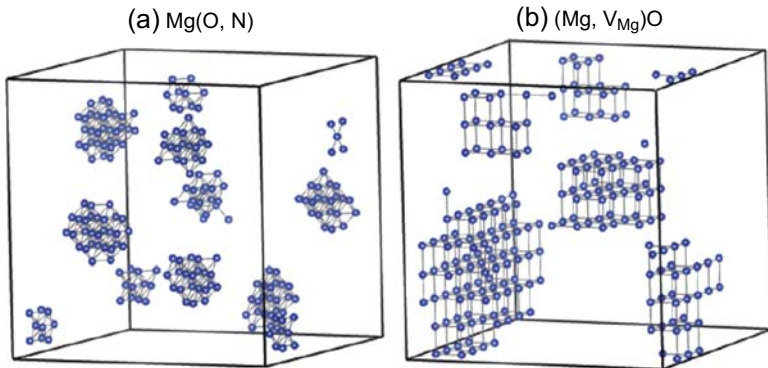


**Figure 1.25** Snapshots of the dopant configurations under 3D crystal growth for (a) Mg(O, N) after 5000 MC steps and for (b) (Mg,  $V_{Mg}$ )O after 20,000 MC steps. The dopant concentration is 5%. The lines between dopants represent first nearest neighbor bonds for the N-doped systems and second nearest neighbor bonds for (Mg,  $V_{Mg}$ )O.

From Seike M, Fukushima T, Sato K, Katayama-Yoshida H. Design of self-organized nanostructures to achieve high blocking temperatures in MgO-based  $d^0$  ferromagnets. *J Kor Phys Soc* 2013;62:1807.

in the hysteresis curves obtained for Mg(O, N) and (Mg,  $V_{Mg}$ )O in previous experimental studies originate from the superparamagnetic blocking phenomenon.

In addition, after a thorough study connecting our calculated results and the previously reported experimental data, we also propose that self-organized ferromagnetic nanowires of magnesium vacancies can be formed in MgO-based magnetic tunnel junctions (MTJs) [124]. This self-organization may provide a strong foundation for



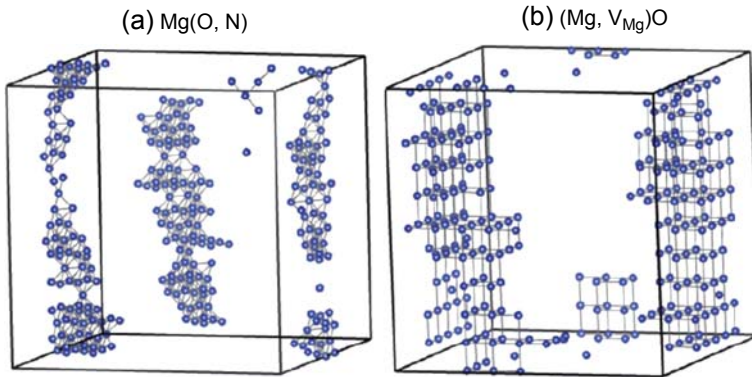


**Figure 1.26** Snapshots of the dopant configurations under layer-by-layer 2D crystal growth for (a) Mg(O, N) after 5000 MC steps and for (b) (Mg,  $V_{Mg}$ )O after 20,000 MC steps. The dopant concentration is 5%. The *lines* between dopants represent first nearest neighbor bonds for the N-doped systems and second nearest neighbor bonds for (Mg,  $V_{Mg}$ )O. From Seike M, Fukushima T, Sato K, Katayama-Yoshida H. Design of self-organized nanostructures to achieve high blocking temperatures in MgO-based  $d^0$  ferromagnets. *J Kor Phys Soc* 2013;62:1807.

a comprehensive understanding of the conductivity, tunnel barriers, and quantum oscillations of MgO-based MTJs; that is, these nanowires might play the role of spin filters to enhance the tunnel magnetic resistance (TMR) value, reduce tunnel barriers, and cause quantum oscillations of TMR by forming multiple paths for this tunneling. Therefore, we believe that it is worth reconsidering the microscopic origin [125,126] of the TMR and the tunneling spin current [127–129] by taking into account the role of nanowires of magnesium vacancies in the Fe/MgO/Fe MTJs. Additional experimental verification is needed before drawing firm conclusions, and further theoretical verification using a large-calculation framework is also desired to investigate the transport properties of these nanowires quantitatively.

In this section, based upon *ab initio* electronic structure calculation and multiscale simulation, we have discussed dynamically created nanostructures (spinodal nanodecomposition) and  $d^0$  ferromagnetism in MgO with N atoms or Mg vacancies ( $V_{Mg}$ ). First, we have shown that local magnetic moments in the materials are spontaneously formed by highly correlated narrow oxygen-2p bands ( $U > W$ ) and the ferromagnetic states are stabilized due to the kinetic energy gain from itinerant spin-polarized electrons, which result from the partial occupation of the narrow oxygen-2p bands. Next, we have discussed the chemical trends of the calculated exchange interactions and estimated Curie temperatures under a homogeneous distribution condition. Then, we have discussed the energetically favored configurations of dopant distribution using chemical pair interaction between dopants and MCS and it will be shown that self-organized nanoclusters of the dopants can be formed both in Mg(O, N) and (Mg,  $V_{Mg}$ )O under layer-by-layer crystal growth. In this context, the underlying mechanism for room-temperature  $d^0$  ferromagnetism from recent experimental reports

was also discussed. Finally, we have mentioned our recent proposal that this self-organization could be found in MgO-based MTJs and may provide the foundation for a comprehensive understanding of the conductivity, tunnel barriers, and quantum oscillations of the MTJs. The significance of these studies is in (1) pioneering the computational materials design of  $d^0$  ferromagnets, which has significantly contributed to developments in this novel research field; (2) presenting the materials design of  $d^0$  ferromagnets aimed at achieving high  $T_B$ ; and (3) elucidating the mechanism and magnetic properties associated with  $d^0$  ferromagnetism. These series of research outcomes provide not only an essential understanding of  $d^0$  ferromagnetism but also open a new route to creating environmentally friendly materials for spintronics without using magnetic elements.

## References

- [1] Katayama-Yoshida H, Sato K, Toyoda M, Dinh VA, Fukushima T, Kizaki H. Computational materials design in semiconductor nano-spintronics. In: Handbook of spintronic semiconductors. Pan Stanford Publishing Pte Ltd; 2010. p. 1–79 [chapter 1].
- [2] Sato K, Bergqvist L, Kudrnovsky J, Dederichs PH, Eriksson O, Turek I, et al. Electronic structure and magnetism of dilute magnetic semiconductors from first principles theory. *Rev Mod Phys* 2010;82:1633.
- [3] Katayama-Yoshida H, Sato K, Fukushima T, Toyoda M, Kizaki H, van Dinh A. Computational nano-materials design for the wide band-gap and high-TC semiconductor spintronics “SPINTRONICS”. In: Dietl T, Ohno H, Awschalom D, Kaminska M, editors. Semiconductors and semimetals, vol. 82. Elsevier Inc. and Academic Press; 2008. p. 433–54 [chapter 10].
- [4] Sato K, Toyoda M, Fukushima T, Dinh VA, Kizaki H, Katayama-Yoshida H. Computational materials design of ZnO-based semiconductor spintronics. In: Hong NH, editor. Magnetism in semiconducting oxides. Transworld Research Network; 2007. p. 1–21 [chapter 1].
- [5] Kasai H, Akai H, Katayama-Yoshida H. Introduction to computational materials design. Osaka: Osaka University Press; 2005.
- [6] Katayama-Yoshida H, Sato K, Fukushima T, Toyoda M, Kizaki H, Dinh VA, et al. Theory of ferromagnetic semiconductors. *Phys Status Solidi A* Jan 2007;204(1):15–32.
- [7] Furdyna JK. *J Appl Phys* 1988;64:R29.
- [8] Ohno H. *Science* 1998;281:951.
- [9] Zutic I, Fabian J, Sarma SD. *Rev Mod Phys* 2004;76:323.
- [10] Jungwirth T, Sinova J, Masek J, Kucera J, MacDonald AH. *Rev Mod Phys* 2006; 78:809.
- [11] Dietl T. *Nat Mater* 2010;9:965.
- [12] Sato K, Bergqvist L, Kudrnovsky J, Dederichs PH, Eriksson O, Turek I, et al. *Rev Mod Phys* 2010;82:1633.
- [13] Jungwirth T, Wunderlich J, Novak V, Olejnik K, Gallagher BL, Campion RP, et al. *Rev Mod Phys* 2014;86:855.
- [14] Dietl T, Ohno H. *Rev Mod Phys* 2014;86:187.
- [15] Dietl T, Ohno H, Matsukura F, Cibert J, Ferrand D. *Science* 2000;287:1019.
- [16] Kanamori J, Terakura K. *J Phys Soc Jpn* 2001;70:1433.

- 
- [17] Akai H. *Phys Rev Lett* 1998;81:3002.
- [18] Ohya S, et al. *Nature Phys* 2011;7:342.
- [19] Dobrowolska M, et al. *Nat Mater* 2012;11:444.
- [20] Chapler BC, et al. *Phys. Rev B* 2013;87:205314.
- [21] Belhadji B, et al. *J Phys: Condens Matter* 2007;19:436227.
- [22] Dederichs PH, Sato K, Katayama-Yoshida H. *Phase Transitions* 2005;78:851.
- [23] Sato K, Schweika W, Dederichs PH, Katayama-Yoshida H. *Phys Rev B* 2004;70:201202(R).
- [24] Liechtenstein AI, Katsnelson MI, Antropov VP, Gubanov VA. *J Magn Magn Mater* 1987;67:65.
- [25] Sato K, Fukushima T, Katayama-Yoshida H. *J Phys: Condens Matter* 2007;19:365212.
- [26] Bonanni A. *Semicond Sci Technol* 2007;22:R41.
- [27] Sato K, Katayama-Yoshida H. *Jpn J Appl Phys* 2007;46:L1120.
- [28] Bergqvist L, Sato K, Katayama-Yoshida H, Dederichs PH. *Phys Rev B* 2011;83:165201.
- [29] Fujii H, Sato K, Bergqvist L, Dederichs PH, Katayama-Yoshida H. *Appl Phys Express* 2011;4:043003.
- [30] Sato K, Fukushima T, Katayama-Yoshida H. *Jpn J Appl Phys* 2007;46:L682.
- [31] Fukushima T, et al. *Phys Rev B* 2014;90:144417.
- [32] Fukushima T, Shinya H, Fujii H, Sato K, Katayama-Yoshida H, Dederichs PH. *J Phys: Condens Matter* 2014 [accepted].
- [33] Kenmochi K, Seike M, Sato K, Yanase A, Katayama-Yoshida H. *Jpn J Appl Phys* 2004;43:L934.
- [34] Seike M, Sato K, Katayama-Yoshida H. *Jpn J Appl Phys* 2011;50:090204.
- [35] Seike M, Dinh VA, Fukushima T, Sato K, Katayama-Yoshida H. *Jpn J Appl Phys* 2012;51:050201.
- [36] Seike M, Fukushima T, Sato K, Katayama-Yoshida H. *Solid State Commun* 2013;167:14.
- [37] Sonoda S, Shimizu S, Sasaki T, Yamamoto Y, Hori H. *J Cryst Growth* 2002;237:1358.
- [38] Pearton SJ, Heo WH, Ivill M, Norton DP, Steiner T. *Semicond Sci Technol* 2004;19:R59.
- [39] Sato K, Katayama-Yoshida H, Dederichs PH. *Jpn J Appl Phys* 2005;44:L948.
- [40] Martínez-Criado G, Somogyi A, Ramos S, Campo J, Tucoulou R, Salome M, et al. *Appl Phys Lett* 2005;86:131927.
- [41] Gu L, Wu SY, Liu HX, Singh RK, Newman N, Smith DJ. *J Magn Magn Mater* 2005;290–291:1395.
- [42] Sato K, Fukushima T, Katayama-Yoshida H. *Jpn J Appl Phys* 2007;46:L1120.
- [43] Osorio-Guillén J, Zhao Y-J, Barabash SV, Zunger A. *Phys Rev B* 2006;74:035305.
- [44] Ducastelle F, Gautier F. *J Phys F* 1976;6:2039.
- [45] Turchi PE, Stocks GM, Butler WH, Nicholson DM, Gonis A. *Phys Rev B* 1988;37:5982.
- [46] Fukushima T, Sato K, Katayama-Yoshida H, Dederichs PH. *Jpn J Appl Phys* 2006;45:L416.
- [47] Binder K, Heermann DW. *Monte Carlo simulation in statistical physics*. Berlin: Springer; 2002.
- [48] Tay M, Wu YH, Han GC, Chong TC, Zheng YK, Wang SJ, et al. *J Appl Phys* 2006;100:063910.
- [49] Kuroda S, Nishizawa N, Takita K, Mitome M, Bando Y, Osuch K, et al. *Nat Mater* 2007;6:440.

- 
- [50] Jamet M, Barski A, Devillers T, Poydenot V, Dujardin R, Bayle-Guillemaud P, et al. *Nat Mater* 2006;5:653.
- [51] Aharoni A. *Introduction to the ferromagnetism*. Oxford Science Publications; 1995.
- [52] Dimitrov DA, Wysin GM. *Phys Rev B* 1996;54:9237.
- [53] Sato K, Fukushima T, Katayama-Yoshida H. *Jpn J Appl Phys* 2007;46:L682.
- [54] Theodoropoulou N, Hebard AF, Overberg ME, Abernathy CR, Pearton SJ, Chu SNG, et al. *Appl Phys Lett* 2001;78:3475.
- [55] Overberg ME, Abernathy CR, Pearton SJ, Theodoropoulou NA, McCarthy KT, Hebard AF. *Appl Phys Lett* 2001;79:1312.
- [56] Reed ML, El-Masry NA, Stadelmaier HH, Ritums MK, Reed MJ, Parker CA, et al. *Appl Phys Lett* 2001;79:3473.
- [57] Thaler GT, Overberg ME, Gila B, Frazier R, Abernathy CR, Pearton SJ, et al. *Appl Phys Lett* 2002;80:3964.
- [58] Ploog KH, Dhar S, Trampert A. *J Vac Sci Tech B* 2003;21:1756.
- [59] Kim KH, Li J, Jin SX, Lin JY, Jiang HX. *Appl Phys Lett* 2003;83:566.
- [60] Steckl AJ, Garter M, Lee DS, Heikenfeld J, Birkhahn R. *Appl Phys Lett* 1999;75:2184.
- [61] Lee DS, Steckl AJ. *Appl Phys Lett* 2002;81:2331.
- [62] Morishima S, Maruyama T, Tanaka M, Masumoto Y, Akimoto K. *Phys Status Solidi A* 1999;176:113.
- [63] Garter M, Scofield J, Birkhahn R, Steckl AJ. *Appl Phys Lett* 1999;74:182.
- [64] Nishikawa A, Kawasaki T, Furukawa N, Terai Y, Fujiwara Y. *Appl Phys Express* 2009; 2:071004.
- [65] Lee D, Nishikawa A, Terai Y, Fujiwara Y. *Appl Phys Lett* 2012;100:171904.
- [66] Wang R, Steckl AJ, Brown EE, Hommerich U, Zavada JM. *J Appl Phys* 2009;105: 043107.
- [67] Mitchell B, Lee D, Fujiwara Y, Dierolf V. *Appl Phys Lett* 2013;103:242105.
- [68] Mitchell B, Poplawsky J, Lee D, Koizumi A, Fujiwara Y, Dierolf V. *J Appl Phys* 2014; 115:204501.
- [69] Masago A, Fukushima T, Sato K, Katayama-Yoshida H. *Jpn J Appl Phys* 2014;53: 061001.
- [70] Masago A, Fukushima T, Sato K, Katayama-Yoshida H. *Appl Phys Express* 2014;7: 071005.
- [71] Wetzel C, Suski T, Ager III JW, Walukiewicz W, Fischer S, Meyer BK, et al. *Int Conf Phys Semicond* 1996;4:2929.
- [72] Yamamoto T, Katayama-Yoshida H. *Jpn J Appl Phys* 1997;36:L180.
- [73] Katayama-Yoshida H, Kato R, Yamamoto T. *J Cryst Growth* 2001;231:428.
- [74] Katayama-Yoshida H, Nishimatsu T, Yamamoto T, Orita N. *J Phys: Condens Matter* 2001;13:8901.
- [75] Amano H, Kito M, Hiramatsu K, Akasaki I. *Jpn J Appl Phys* 1989;28:L2112.
- [76] Kresse G, Joubert D. *Phys Rev B* 1999;59:1758.
- [77] Mishra JK, Langer URT, Shvarkov S, Wieck A, Hangleiter A. *Appl Phys Lett* 2013;102: 06115.
- [78] Sanna S, Schmidt WG, Frauenheim T, Gerstmann U. *Phys Rev B* 2009;80:104120.
- [79] Neugebauer J, de Walle CGV. *Appl Phys Lett* 1996;68:1829.
- [80] Mattila T, Nieminen RM. *Phys Rev B* 1996;54:16676.
- [81] Joseph M, Tabata H, Kawai T. *Jpn J Appl Phys* 1999;38:L1250.
- [82] Yamamoto T, Katayama-yoshida H. *Jpn J Appl Phys* 1999;38:L166.
- [83] Katayama-yoshida H, Yamamoto T. *Phys Status Solidi (B)* 1997;202:763.
- [84] Zener C. *Phys Rev B* 1951;81:440.

- [85] Masago A, Fukushima T, Sato K, Katayama-Yoshida H. *Appl Phys Express* 2014;7:121002.
- [86] Richardson FS, Riehl JP. *Chem Rev* 1977;77:773.
- [87] Riehl JP, Richardson FS. *Chem Rev* 1986;86:1.
- [88] Schadt M. *Annu Rev Matter Sci* 1977;27:305.
- [89] Steane A. *Rep Prog Phys* 1998;61:117.
- [90] Lunkley JL, Shirotani D, Yamanari K, Kaizaki S, Muller G. *J Am Chem Soc* 2008;130:13814.
- [91] Stainberg IZ. *Ann Rev Biophys Bioeng* 1978;7:113.
- [92] Suzuki M, Inobushi Y, Yabashi M, Ishikawa T. *J Synchrotron Radiat* 2014;21:466.
- [93] Meining CJ, Stir AV, McCombe BD, Chado I, Grabs P, Schmidt G, et al. *J Appl Phys* 2010;107:114510.
- [94] Sanchez-Carnero EM, Moreno F, Maroto BL, Agarrabeitia AR, Ortiz MJ, Vo BG, et al. *J Am Chem Soc* 2014;136:3346.
- [95] Zhang YJ, Oka T, Suzuki R, Ye JT, Iwasa Y. *Science* 2014;8:725.
- [96] Sircar N, Bougeard D. *Phys Rev B* 2014;89:041301(R).
- [97] Seike M, Fukushima T, Sato K, Katayama-Yoshida H. *Computational materials design of d<sup>0</sup> ferromagnetism in metal oxides (chapter contribution in new developments in metal oxides research)*. Nova Science Publishers Inc.; 2013. p. 109.
- [98] Seike M, Kenmochi K, Sato K, Yanase A, Katayama-Yoshida H. *New route to fabricate ferromagnetic semiconductors without transition metal elements*. *Jpn J Appl Phys* 2004;43:L579.
- [99] Kenmochi K, Seike M, Sato K, Sato K, Katayama-Yoshida H. *New class of diluted ferromagnetic semiconductors based on CaO without transition metal elements*. *Jpn J Appl Phys* 2004;43:L934.
- [100] Kenmochi K, Dinh VA, Sato K, Yanase A, Katayama-Yoshida H. *Materials design of transparent and half-metallic ferromagnets of MgO, SrO and BaO without magnetic elements*. *J Phys Soc Jpn* 2004;73:2952.
- [101] Yoshida H, Kenmochi K, Seike M, Sato K, Yanase A. *Transparent ferromagnetic compound containing no magnetic impurity such as transition metal or rare earth metal and forming solid solution with element having imperfect shell, and method for adjusting ferromagnetic characteristics thereof*. P2004-55017, WO2005/083161 A1, P2006-510484 (registered in Japan, 2011.3.25), US 2007/0178032 A1.
- [102] Dinh VA, Toyoda M, Sato K, Katayama-Yoshida H. *Exchange interaction and T<sub>C</sub> in alkaline-earth-metal-oxide-based DMS without magnetic impurities: first principle pseudo-SIC and Monte Carlo calculation*. *J Phys Soc Jpn* 2006;75:093705.
- [103] Dinh VA. *A new class of dilute magnetic semiconductors without transition metal elements*. Singapore: Pan Stanford Publishing Pte Ltd; 2010. p. 60–71.
- [104] Dinh VA, Sato K, Katayama-Yoshida H. *Dilute magnetic semiconductors based on wide bandgap SiO<sub>2</sub> with and without transition metal elements*. *Solid State Commun* 2005;136:1.
- [105] Kenmochi K, Sato K, Yanase A, Katayama-Yoshida H. *Materials design of ferromagnetic diamond*. *Jpn J Appl Phys* 2005;44:L51.
- [106] Yang C-H, Samant M, Parkin S. *Ferromagnetism in MgO by nitrogen doping*. APS March Meeting Abstract, p. V22.00004, <http://meetings.Aps.org/Meeting/MAR09/Event/98745S>; 2009.
- [107] Pan H, Yi JB, Shen L, Wu RQ, Yang JH, Lin JY, et al. *Room-temperature ferromagnetism in carbon-doped ZnO*. *Phys Rev Lett* 2007;99:127201.

- [108] Yu C-F, Lin T-J, Sun S-J, Chou H. Origin of ferromagnetism in nitrogen embedded ZnO: N thin films. *J Phys D* 2007;40:6497.
- [109] Venkatesan M, Fitzgerald CB, Coey JMD. Unexpected magnetism in a dielectric oxide. *Nature* 2004;430:630.
- [110] Hong NH, Sakai J, Poirot N, Brizé V. Room-temperature ferromagnetism observed in undoped semiconducting and insulating oxide thin films. *Phys Rev B* 2006;73:132404.
- [111] Hong NH, Poirot N, Sakai J. Ferromagnetism observed in pristine SnO<sub>2</sub> thin films. *Phys Rev B* 2008;77:033205.
- [112] Martínez-Boubeta C, Beltrán JI, Balcells LI, Konstantinović Z, Valencia S, Schmitz D, et al. Ferromagnetism in transparent thin films of MgO. *Phys Rev B* 2010;82:024405.
- [113] Araujo CM, Kapilashrami M, Jun X, Jayakumar OD, Nagar S, Wu Y, et al. Room temperature ferromagnetism in pristine MgO thin films. *Appl Phys Lett* 2010;96:232505.
- [114] Seike M, Sato K, Sato K, Katayama-Yoshida H. The magnetic properties of hole-doped MgO. *Jpn J Appl Phys* 2011;50:090204.
- [115] Seike M, Dinh VA, Sato K, Sato K, Katayama-Yoshida H. First-principles study of the magnetic properties of nitrogen-doped alkaline earth metal oxides. *Physica B* 2012;407:2875.
- [116] Liechtenstein AI, Katsnelson MI, Antropov VP, Gubanov VA. Local spin density functional approach to the theory of exchange interactions in ferromagnetic metals and alloys. *J Magn Magn Mater* 1987;67:65.
- [117] Sato K, Schweika W, Dederichs PH, Katayama-Yoshida H. Low-temperature ferromagnetism in (Ga, Mn)N: *ab initio* calculations. *Phys Rev B* 2004;70:201202(R).
- [118] Fukushima T, Sato K, Katayama-Yoshida H. Theoretical prediction of curie temperature in (Zn,Cr)S, (Zn,Cr)Se and (Zn,Cr)Te by first principles calculations. *Jpn J Appl Phys* 2004;43:L1416.
- [119] Sato K, Bergqvist L, Kudrnovský J, Dederichs PH, Eriksson O, Turek I, et al. First-principles theory of dilute magnetic semiconductors. *Rev Mod Phys* 2010;82:1633.
- [120] Seike M, Dinh VA, Fukushima T, Sato K, Katayama-Yoshida H. Spinodal nano-decomposition and high blocking temperature in MgO-based d<sup>0</sup> ferromagnets. *Jpn J Appl Phys* 2012;51:050201.
- [121] Kresse G, Joubert D. From ultrasoft pseudopotentials to the projector augmented-wave method. *Phys Rev B* 1999;59:1758.
- [122] Perdew JP, Yue W. Accurate and simple density functional for the electronic exchange energy: generalized gradient approximation. *Phys Rev B* 1986;33:8800.
- [123] Perdew JP, Burke K, Ernzerhof M. Generalized gradient approximation made simple. *Phys Rev Lett* 1996;77:3865.
- [124] Seike M, Fukushima T, Sato K, Katayama-Yoshida H. Design of self-organized nanostructures to achieve high blocking temperatures in MgO-based d<sup>0</sup> ferromagnets. *J Kor Phys Soc* 2013;62:1807.
- [125] [a] Seike M, Fukushima T, Sato K, Katayama-Yoshida H. Self-organized ferromagnetic nanowires in MgO-based magnetic tunnel junctions. *Solid State Commun* 2013;167:14. [b] Butler WH, Zhang X-G, Schulthess TC, Maclaren JM. Spin-dependent tunneling conductance of Fe|MgO|Fe sandwiches. *Phys Rev B* 2001;63:054416.
- [126] Mathon J, Umerski A. Theory of tunneling magnetoresistance of an epitaxial Fe/MgO/Fe(001) junction. *Phys Rev B* 2001;63:220403R.

- [127] Parkin SSP, Kaiser C, Panchula A, Rice PM, Hughes B, Samant M, et al. Giant tunnelling magnetoresistance at room temperature with MgO(100) tunnel barriers. *Nat Mater* 2004;3:862.
- [128] Yuasa S, Nagahama T, Fukushima A, Suzuki Y, Ando K. Giant room-temperature magnetoresistance in single-crystal Fe/MgO/Fe magnetic tunnel junctions. *Nat Mater* 2004;3:868.
- [129] Ikeda S, Hayakawa J, Ashizawa Y, Lee YM, Miura K, Hasegawa H, et al. Tunnel magnetoresistance of 604% at 300K by suppression of Ta diffusion in CoFeB/MgO/CoFeB pseudo-spin-valves annealed at high temperature. *Appl Phys Lett* 2008;93:082508.

# Electronic structure of magnetic impurities and defects in semiconductors: a guide to the theoretical models

2

*W.R.L. Lambrecht*

Department of Physics, Case Western Reserve University, Cleveland, OH, United States

## 2.1 Introduction

There is much incentive to imbue semiconductors with magnetic properties. In a semiconductor, the density of carriers can be controlled with great precision through doping and temperature control. The field of spintronics [1] is concerned with also controlling the spin of the electron. This leads to potentially new functionalities and new device concepts. Instead of moving charge carriers around, we now want to control in a general sense their spin orientations. Possibly, reorienting the spins requires less energy than moving them around between specific regions. Also, the spins may provide a net magnetization, which stays even if the device is switched off, and thus the potential of nonvolatile memory and integration of storage of information and manipulation of the information or computations. While spin-polarized carriers can be introduced in ordinary semiconductors using optical techniques (ie, using circularly polarized light), additional possibilities occur if the spin polarization in the semiconductor is introduced purely electrically through magnetic dopants. We can inject a net spin current and also a net spin accumulation in specific regions into a semiconductor from a metallic ferromagnetic contact. However, this process is inefficient, and we lose the spin coherence over a short length-scale because of the impedance mismatch between a semiconductor and a typical metal. Thus also for this purpose, magnetically ordered semiconductors are preferred.

Semiconducting properties—the property of having a bandgap—and ordered magnetism (which requires unpaired spins) do not naturally occur together, except in some special cases, such as rare-earth (RE) compounds, for example, GdN [2,3] and EuO [4–6]. The origin of the magnetism in these cases arises from the localized partially filled  $f$  shells. Thus to make semiconductors magnetic, we rely on doping them with magnetic elements, creating so-called dilute magnetic semiconductors (DMSs). Dilute paramagnetic semiconductor behavior has been studied first in II-VI materials [7]. Doping Mn on the group-II side, which occurs readily because Mn is divalent, leads to strong enhancement of the conduction band  $g$ -factor or Zeeman splitting in an external magnetic field due to the internal effective magnetic field created by the Mn local moments, strong Faraday rotation, and so on. Although the



moments in such a material can be aligned in an external field and saturated, they do not intrinsically order. On the other hand, when we dope Mn in a III-V semiconductor,  $\text{Mn}^{2+}$  plays a dual role of providing a magnetic moment but also acting as a p-type dopant. The carrier-mediated coupling via the holes can lead to ferromagnetic ordering of the Mn spins.

Since the first demonstrations of DMSs in Mn-doped InAs [8] and GaAs [9–12], there has been a worldwide interest in developing such materials with improved properties. A good review on Mn:GaAs can be found in Ref. [13]. The problem is that in order to dope magnetic elements into a semiconductor such as GaAs, we are forced to use nonequilibrium growth techniques with lower than optimal growth temperatures so as to prevent the formation of precipitates such as MnAs and MnGa. At the same time the Curie temperature ( $T_C$ ) of such systems depend on the effective interaction between impurities that are fairly far from each other in the dilute case and hence are usually found to be below room temperature. Only after much work,  $T_C$ s in  $\text{Mn}_x\text{Ga}_{1-x}\text{As}$  were raised to about 191 K [14–16]. Thus, in some sense, DMSs tend to be poor semiconductors and poor magnets. The holy grail of DMS research is indeed to find semiconductors, magnetic element combinations, and techniques to achieve above room temperature magnetic order without compromising the semiconductor quality of the materials.

To guide this development, an understanding of the electronic structure of magnetic impurities in semiconductors is a prerequisite. Questions we would like to understand are: what is the advantage or disadvantage of wide bandgap versus low bandgap semiconductors? What are the differences in behavior transition metal (TM) and RE magnetic dopants? What controls the magnetic moments of the dopants, and what is the origin of their exchange interactions, which leads to ordering these moments? What is the role of other defects introduced in the material by the doping process?

Theory has played an important role in this development, sometimes providing new directions to search, and sometimes, unfortunately misleading experiments due to an incomplete understanding of the limitations of the computational models [17]. The purpose of this chapter is to provide a guide to the theoretical models. As this field is strongly interdisciplinary with practitioners from materials science, chemistry, electrical engineering, as well as physicists, keeping up with the recent developments of modern computational methods can be a daunting task for the nonspecialist. Without being a practitioner of these methods, it is still important to be able to discern the relative merits of different approaches and the problems that these methods face for the systems under study. The present chapter makes an attempt at presenting an unbiased guide for the nonspecialist. Specific developments of specific materials systems, mostly from an experimental point of view, are presented in other chapters of this book. The purpose of this chapter is thus mostly pedagogic rather than describing the contributions of the author to this field.

We start with a discussion of the electronic energy levels of TMs and RE dopants, pointing out their key differences. Next, we discuss the different computational approaches within the general arena of so-called first-principles computations that are relevant to DMSs.

The underlying electronic structure of a single defect provides us with the first key property of magnetism, the magnetic moment of the defects. However, to obtain magnetic ordering the second key property is their interaction. The next section thus discusses various aspects of magnetic exchange interactions: how they are calculated, how they depend on distance between the impurities, and how to estimate macroscopic thermodynamic and statistical properties such as the  $T_C$  from them. Finally we also discuss the role of other defects in magnetism and in particular the possibility of  $d^0$  magnetism, that is, magnetism arising from defects without the elements containing partially filled shells, meaning without  $d$  or  $f$  open shells.

Ultimately, the purpose of magnetic semiconductors is to manipulate the spins in new devices. Therefore magnetic ordering in itself is not enough. The materials also must have sufficient conductivity and discernible effects of the magnetism on the transport properties. One of the most intriguing possibilities of spintronics is to develop quantum computing structures, in which we can exploit the quantum mechanical aspects of spin. A crucial aspect here is coherence times. This, however, goes beyond the scope of this chapter and will not be further discussed.

Since most of the rest of the book is dedicated to various TM-based systems, in the last section of this chapter, we present a case study of Gd-doped GaN and explain how the various elements discussed earlier come into play in this system. This section provides a review of this system, including work by the author and also by others.

## 2.2 Electronic structure of transition-metal and rare-earth elements in semiconductors

### 2.2.1 Basic energy level scheme

As is well known, the TM and RE elements derive their magnetic properties from their unfilled shells, respectively the  $3d$  shell and the  $4f$  shell. A key difference between RE and TM elements is that the RE elements (with some exceptions to be discussed later) correspond to a threefold valence if we ignore the  $f$  states. Thus, when placing such an element in a III-V semiconductor, it is an isovalent impurity, which typically does not produce defect energy levels in the gap. However, they can produce levels in the gap if they are combined with other defects in a complex [18], or are divalent (for example, Eu tends to be divalent) [19–21]. Interstitial sites are found to be less favorable but could produce defect levels [18,21]. The  $4f$  levels are so localized and shielded from the outer electrons that they obey essentially atomic physics. This means among other things that a many-electron theory is essential to describe them, which we postpone until the next subsection. TMs, in particular of the  $3d$  series, also have progressively more localized  $d$  states as we move to the right in the  $3d$  row, but they should still be considered valence electrons participating in the bonding.

As is well known, when a  $d$  state, which is fivefold degenerate in the free atom, is placed in a crystalline environment, its levels are split depending on the symmetry of the environment. This is traditionally described by means of crystal-field theory. On the other hand, the defect levels found in the gap of the semiconductor are not always

and, in fact, are usually not, composed mostly of these  $d$  orbitals. It depends on where these  $d$  states lie with respect to the semiconductor host element atomic levels. In a typical tetrahedrally bonded semiconductor, the valence bands (VBs) are bonding states between the anion  $p$  orbitals and the cation  $s$  and  $p$  orbitals, and are thus mostly anion  $p$ -like. The anion  $s$  states form a separate even deeper band that is of less importance for the semiconductor physics. The conduction bands, in contrast, are antibonding states and therefore dominated by the cation  $s$  and/or  $p$  orbitals. Which ones form the bottom of the conduction band depends strongly on whether the gap is direct or indirect. At the  $\Gamma$ -point the conduction bands are usually dominated by cation  $s$  states simply because  $s$  states lie below  $p$  states. For our purpose what matters is where the  $d$  states of the impurity lie relative to the anion  $p$  states, and more specifically, where their already spin-split  $d$  states lie with respect to the anion  $p$  and cation  $s$  states. The situation is quite different between traditional semiconductors such as GaAs, ZnSe, and the oxides or nitrides involving elements of the second row of the periodic table. The elements N and O have much deeper valence states than the higher rows, P, As, S, Se. Thus the majority spin TM  $d$  state typically lies below the anion  $p$  states for semiconductors with anions from rows 3 and beyond but may lie above or be resonant with the N- $p$  or O- $p$  levels. The minority spin  $d$  state, on the other hand, tends to lie above the anion  $p$  states. At the same time we have a downward trend for the  $d$  levels as we go through the  $d$  series from left to right. Thus various situations can occur.

Most TMs prefer to substitute the cation sites rather than the anion sites or interstitial sites. Therefore a good starting point for understanding the level scheme of a TM dopant in a semiconductor is to start from the cation vacancy. The latter is surrounded by anion dangling bonds. These can be thought of as  $sp^3$  hybrid orbitals of the anion which point toward the vacancy. These dangling bonds would normally interact with the cation dangling bonds, to form bonding (VB states) and antibonding conduction band states. The dangling bonds thus tend to lie in the forbidden gap. More precisely from the four dangling bonds we can make a linear combination  $(\phi_{d1} + \phi_{d2} + \phi_{d3} + \phi_{d4})/2$  of the orbitals all with the same phase, which has  $a_1$  symmetry using the language of group theory. What this means is a state that transforms into itself under all symmetry operations. This state usually has low enough energy (because of a small interaction among the dangling bonds across the vacancy) to form a state below the valence band maximum (VBM). In other words, it is resonant with the VB and does not form a state in the gap. In a tetrahedral symmetry environment, the other possibilities are to make combinations like  $(\phi_{d1} + \phi_{d2} - \phi_{d3} - \phi_{d4})/2$ , which have two positive and two negative signs. We can, in fact, make three linearly independent combinations of this type depending on which orbitals get the negative signs. As illustrated in Fig. 2.1, these linear combinations have the same properties as a  $p_x$ ,  $p_y$ , or  $p_z$  state at the center of the tetrahedron. In the language of group theory these are called  $t_2$  states. They belong to the irreducible representation  $t_2$  of the group  $T_d$ . This is just a fancy way of saying that they share the property of transforming into each other under operations of the group in the same way as do the vector components  $x$ ,  $y$ , and  $z$ . The  $t_2$  states for a triply degenerate state in the gap. However, now it depends on their filling. Depending on different charge states and whether we have a group-IV elemental semiconductor or a III-V or II-VI, this  $t_2$  level can have different

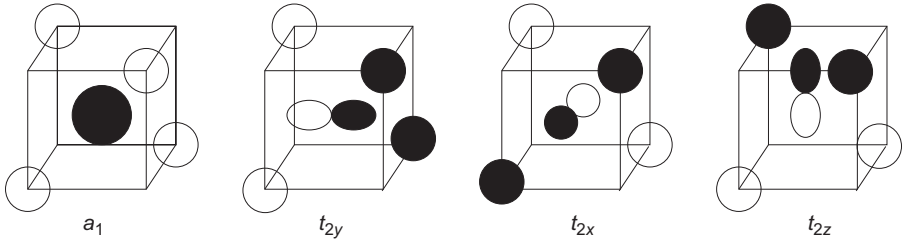


**Figure 2.1** Combinations of dangling bonds with different symmetry in a tetrahedral group.

occupations. The Jahn–Teller theorem then implies that if the state is degenerate the system can lower its energy by distorting, which leads to further splitting of the levels and lowering the energy of the filled states relative to those that remain empty. This completes our elementary discussion of the vacancy.

Interestingly, in a tetrahedron, the  $d$  states  $d_{xy}$ ,  $d_{xz}$ , and  $d_{yz}$  also transform into each other as a  $t_2$  state. In group theory language, we say “they belong to  $t_2$ .” We assume these notations are familiar to the reader from physics or chemistry. They refer to their angular behavior, which corresponds to the real spherical harmonics  $Y_{lm}(\theta, \phi)$ . The immediate consequence is that the dangling bonds of symmetry  $t_2$  can interact with the  $d$  states of the same symmetry but not with other  $d$  states. The other  $d$  states,  $d_{3z^2-r^2}$  and  $d_{x^2-y^2}$ , belong to the irreducible representation  $e$  of the group  $T_d$ .

So, now we are ready to discuss the levels schemes for a substitutional TM impurity. The TM- $d$  states split into  $e$  and  $t_2$  states with  $t_2$  above  $e$  in a tetrahedral environment. Second, there is a spin-splitting of each of those levels. Depending on whether the spin-splitting is larger or smaller than the crystal-field splitting, a different total spin may occur. For example, if the spin-splitting is larger than the crystal-field splitting in absolute value, then the ordering of the levels is  $e_+ < t_{2+} < e_- < t_{2-}$  and we have high-spin situation.

On the contrary if the crystal-field splitting is larger than the spin-splitting, we will have  $e_+ < e_- < t_{2+} < t_{2-}$  and a low-spin situation occurs. If the TM  $d$  states lie well below the anion  $p$  state, their bonding combination is mostly TM  $d$ -like and lies deep in the VB as a resonance. It is called a crystal-field resonance (CFR) state. This occurs typically for the majority spin  $d$  state in a traditional (not nitride) III-V compound. The corresponding antibonding states of  $t_2$  symmetry are mostly dangling bond-like but with some admixture of  $d$  orbital. They are called the dangling-bond hybrid (DBH). The  $e$  levels meanwhile do not interact, so they also lie in the VBM as a CFR. As an example, we show the interaction of the dangling bonds with the TM  $d$  states schematically in Fig. 2.2 for the case of  $\text{Mn}^{3+}$  with configuration  $3d^4$  on a cation site, say Ga in GaAs, and assuming the defect, which is an acceptor in a 3– charge state. In the neutral case, there would be three electrons in the dangling bond but now there are six. The CFR of both  $e_+$  and  $t_{2+}$  are occupied as well as the  $t_{2-}$ -DBH. The  $t_{2+}$  DBH is partially occupied. Note that in this example, the minority spin  $d$  states lie above the host dangling bonds and the majority spin  $d$  states lie below them.

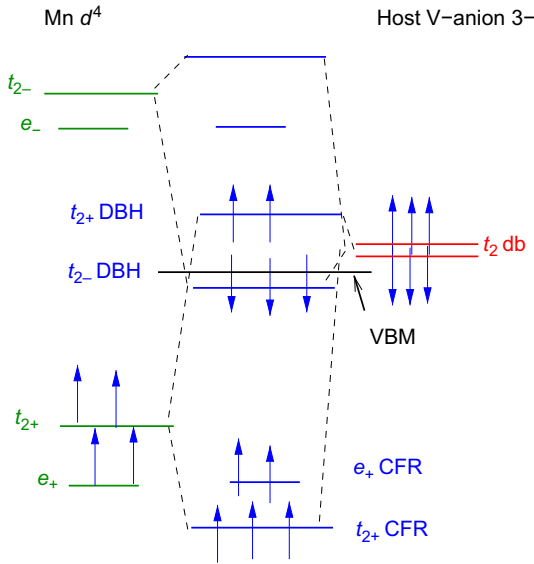


**Figure 2.2** Interaction scheme of dangling bonds with TM  $d$  states.

However, for nitrides or oxides the dangling bonds may lie below the TM  $d$  states for both majority and minority spin. It also depends on the TM. As we go from left to right, the TM  $d$  states become deeper. Thus we see that in traditional semiconductors, the majority spin levels in the gap are actually more dangling bond than TM  $d$ -like, while for wide bandgap semiconductors the states in the gap have stronger TM  $d$ -like character. The role of the CFR and dangling-bond-like state may be reversed. An example is Mn in GaN compared to Mn in GaAs as is clearly illustrated in Fig. 2.3, taken from Ref. [22]. An excellent review on these different possibilities can be found in Ref. [23].

Now, we again have to consider how these levels are filled and in addition we now have to consider Hund's rules to find out whether their spins will prefer to align anti-parallel or parallel with each other. These rules determine the total spin state of the defect and hence their magnetic moment. We may have either high-spin or low-spin configurations. This depends on whether the exchange splitting between up and down spin is larger than the  $e-t_2$  splitting of the levels in the gap, which depends on the degree of interaction with the anion dangling bonds. We do not attempt here to provide a complete description, only to explain what factors enter the level scheme. Typically, however, the spin-splitting is larger than the crystal-field splitting for a TM impurity in a semiconductor. The preceding is essentially a one-electron level picture. However, once we start talking about filling the levels we need to invoke a many-electron picture and discuss which multiplets can occur with different spin and different mixtures of electrons in the various one-electron states. These are also described in Ref. [23].

The important point is that even at this level, we already see that nitrides and oxides may be expected to behave quite differently from standard semiconductors.

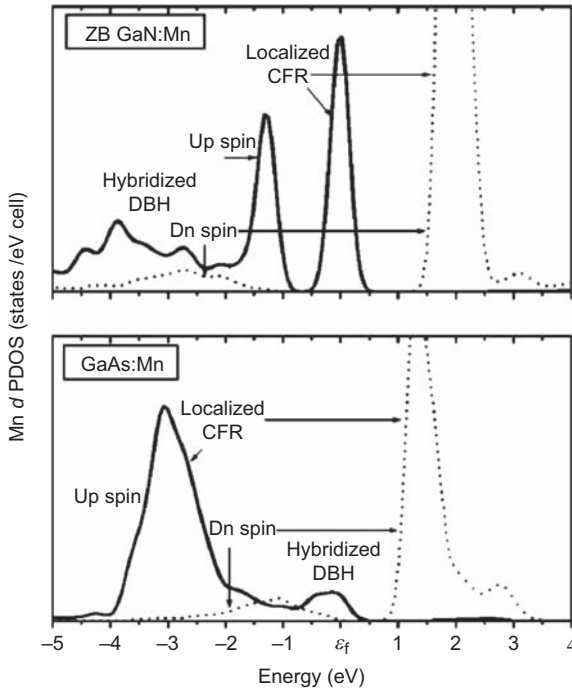


**Figure 2.3** Comparison of local density of states in Mn-doped GaN and Mn-doped GaAs, illustrating the reversal of the role of the CFR and DBH.

From Mahadevan P, Zunger A. First-principles investigation of the assumptions underlying Model-Hamiltonian approaches to ferromagnetism of  $3d$  impurities in III-V semiconductors. Phys Rev B 2004;69:115211. <http://dx.doi.org/10.1103/PhysRevB.69.115211>.

## 2.2.2 Multiplet splittings for $f$ electrons and Hund's rules

For a proper description of  $f$  electrons, a many-electron description is essential because they behave much more atomically than  $d$  electrons. The atomic theory for electronic states of different total orbital and spin angular momentum was developed long ago and can be found, for example, in the classic book by Condon and Shortley [24]. Combined with crystal-field theory and group theory, a full description was developed by Racah in a series of papers [25–30]. The different multiplet levels play an essential role in understanding the optical properties of RE-doped semiconductors. Optical transitions between the different multiplet states of the  $f$  electrons, which in the free atom are forbidden, become weakly allowed in a crystal environment. Because they are so atomic-like, they are shielded from the environment and thus particularly stable as function of temperature and provide very sharp luminescence lines. A useful overview of the multiplet levels in RE ions can be found in Dieke and Crosswhite [31]. The key question in this context is how a bandgap excitation is transferred to the  $f$  states manifold and leads to excited multiplets, which subsequently can decay radiatively. There is still no adequate first-principles theory for describing this energy transfer.

The multiplet theory describes a single RE ion with  $f$  electrons in its crystalline environment but provides no information on where the  $f$  electron manifolds lie with respect to the rest of the band structure. The problem is, how do we compare a many-electron state with a one-electron band picture? It is as if  $f$  electrons somehow live in a separate orthogonal space. Nonetheless, we are quite interested in how excitations are transferred to the  $f$  electron system. Of course, we could take the view that all excitations of a many-electron system are many-electron states, some simply involve excitation of one electron to a higher level, others are more complex. However, a unified framework for describing the different types of excitations seems desirable. We will see later that the dynamic mean field theory (DMFT) provides at least a framework for discussing the multiplets within a band structure scheme.

As already mentioned, the question of how the single electrons combine into different term states and combine their total spin and angular momenta also occurs for  $d$  states and is important to understand the optical properties of transitions between such states, so-called  $d-d$  transitions in the middle of the gap.

## 2.3 Computational methods dealing with strongly correlated electrons

### 2.3.1 Failures of density functional theory

We assume here that the reader has at least some familiarity with density functional theory (DFT) [32,33]. This theory provides in some sense the modern justification of a one-electron band structure picture. The starting point of DFT is to identify the electron density, rather than the many-electron wave functions, as the key quantity on which the properties of a many-electron system depends. It achieves this great simplification by focusing on the ground state of the system. Hohenberg and Kohn's theorem [32] states that the electron density in the ground state completely determines the external potential of that system and therefore, in principle, everything else. In other words, two systems with the same ground state density cannot have potentials that differ by more than a constant. This remarkable theorem then shifts the attention to finding the universal functional of interacting electrons that describes in principle all electronic systems. Unfortunately, the theory provides no prescription for how to determine this all-encompassing functional. Progress is made by making approximations. It is straightforward to write explicit expressions for the classical Coulomb interaction and the kinetic energy the electrons would have if they were not interacting and the interaction with the external potential (ie, the Coulomb interaction with the nuclei). These are three large contributions. The rest is then lumped together as the exchange-correlation functional. The latter is small when numerically compared to the other contributions and hence approximations for it can be made. The approximation most often made is the local density approximation (LDA). It assumes that the exchange-correlation energy per particle at each point in space can be approximated by the value it would have in an electron gas of the same density. The difference is that in the real system the density is varying from point to point while in an electron

gas, the density is constant. It would seem that this approximation would work only if the density varies slowly. However, it is found to work remarkably well even in real systems where the density is not slowly varying at all. This stems from the fact that it needs to describe only the average behavior and fulfills certain sum-rules. Together with the Kohn–Sham scheme [33], which replaces the real interacting system in a given potential by a fictitious system of noninteracting electrons in an effective potential with the same density, this requirement of having the same density provides a recipe for finding the potential as the self-consistent field potential. A one-electron Schrödinger equation is solved for the effective potential:

$$\left[-\frac{1}{2}\nabla^2 + v_{\text{eff}}(\mathbf{r})\right]\psi_i(\mathbf{r}) = \varepsilon_i\psi_i(\mathbf{r}) \quad [2.1]$$

Here we use atomic units ( $\hbar = e = m_e = 1$ ). The density is then given by summing the states according to the Aufbau principle:

$$n(\mathbf{r}) = \sum_i^{\text{occ}} |\psi_i(\mathbf{r})|^2 \quad [2.2]$$

and finally, given this density the effective potential is:

$$v_{\text{eff}}(\mathbf{r}) = v_{\text{ext}}(\mathbf{r}) + \int \frac{n(\mathbf{r}')}{|\mathbf{r} - \mathbf{r}'|} d^3\mathbf{r}' + v_{\text{xc}}(\mathbf{r}) \quad [2.3]$$

with the latter given by the functional derivative:

$$v_{\text{xc}}(\mathbf{r}) = \frac{\delta E_{\text{xc}}[n]}{\delta n(\mathbf{r})}. \quad [2.4]$$

These equations are then solved iteratively until convergence.

In spite of its great success for weakly correlated electronic systems, for example, semiconductors or simple metals, DFT fails to some degree for strongly correlated electron systems. Some of the failures are that the standard LDA and even the generalized gradient approximation (GGA) [34], which includes terms depending on  $\nabla n(\mathbf{r})$ , do not correctly cancel the self-interaction by the exchange term. Following, we will often say simply LDA when we mean LDA and GGA. They are sometimes called semilocal functionals and in terms of bandgaps have similar problems. The practical difference is that LDA tends to underestimate lattice constants while GGA generally overestimates lattice constants, each by a few percent.

One problem of LDA (and GGA) is that the solutions of the LDA avoid situations in which the electrons are localized, even when there should not really be a Coulomb penalty against this localization because it stems from a nonphysical self-interaction. This leads to underestimation of magnetic moments and in some cases, it predicts the wrong structures.



Another well-known failure is, of course, that we should not interpret the  $\varepsilon_i$  as band-structure energies or excitations for extracting or adding an electron to the system. If we do so anyway, we'll find that the bandgaps are strongly underestimated. The practical power of the DFT in the LDA or GGA lies in the fact that all electrons move in the same potential, which depends only on the density. This should be compared, for example, with the Hartree–Fock theory, in which each electron feels a different potential depending on what type of orbital state it is in. At the same time this is its weakness. What we have lost is the dependence of exchange–correlation energy on specific orbitals. While in principle, a much more complex, nonlocal functional could be devised to capture the different behavior of, for example,  $d$  or  $f$  electrons compared to more delocalized  $s$  and  $p$  electrons, it turns out that it is easier to describe it by expanding the functional to let it depend on orbitals. Most of the methods discussed next are of this type.

### 2.3.2 Hubbard $U$ correction: LDA + $U$ and SIC

The first approach to overcome the weakness of the LDA for strongly correlated electrons is the so-called LDA +  $U$  method [35–39]. This is a somewhat pragmatic approach, recognizing that correlation effects for localized orbitals can be captured by including strong on-site Coulomb interactions for such orbitals. This was the approximation suggested by John Hubbard in the model that now bears his name. The idea of LDA +  $U$  is to add these Hubbard  $U$  terms explicitly for a subset of strongly correlated orbitals but to merge this model somehow with standard DFT. Let's call this subset the  $d$  orbital, although it could also include the  $f$  electrons or even other orbitals. The basic variational quantities of the model then become the density plus the occupations of the  $d$  orbitals. The problem with the model is that the LDA already includes some of this correlation and so we must somehow subtract that contribution from the total. This is the so-called double-counting problem, and although different approaches have been proposed for it, it remains a weakness of the method. In any case, once the Hubbard  $U$  terms or a somewhat more detailed description of the on-site Coulomb interaction [37] between the different  $d$  orbitals is included, we solve the model in the mean field approximation. This is equivalent to a Hartree–Fock solution for these  $d$  orbitals, with the difference being that the Coulomb and exchange matrix elements between these orbitals are parameterized instead of self-consistently determined. It implies that now the  $d$  orbitals feel an additional potential from the other orbitals, not treated with  $U$  terms, and that this potential can even be different for different  $d$  orbitals. Their occupation numbers are effectively determined. So, what we have restored is an orbital-dependent picture but without the computational expense of a real Hartree–Fock calculation. At the same time we obtain how the occupation of these orbitals becomes self-consistent through its interaction with the other orbitals. Also, at the same time, it avoids the difficulties of a pure Hartree–Fock treatment, in the sense that the parameters, in particular the  $U$  value, include the screening by the other orbitals. This incorporates the main correlation effect that is missing in Hartree–Fock, which has only exchange. In other words, the exchange is really a screened exchange. The main advantage for magnetic systems

is that it improves on the orbital-independent local spin density functional approach (LSDA) in obtaining the magnetic moments and correct energy levels. The magnetic moments in fact result from the different occupation of up- and down-spin states together with the orbital polarization in an open shell system.

The advantage of the method is that it fits within DFT approaches with a slight extension, namely that the occupation numbers of the  $d$  orbitals are treated as separate degrees of freedom. It has a total energy expression, which is self-consistently linked with the effective potential through a variational principle. In other words,  $\partial E_{\text{tot}}^{\text{LDAU}} / \partial n_{m\sigma} = V_{m\sigma}$ .

There are several variants of the LSDA +  $U$  and LDA +  $U$  approaches. First of all, is some spin dependence already included in the functional as in LSDA or not, as in LDA? Second, how is the double counting treated? In the around mean field approach [35,40], the LDA and LDA +  $U$  agree with each other for the case that each  $d$  orbital has the same average occupation. In the fully localized limit [36,37], the LSDA and LSDA +  $U$  agree with each other for the case of the atomic limit with integer occupation numbers. This is the most used and also by most viewed as the most useful approach for cases with strong localization, for which LSDA +  $U$  is most needed in the first place. For intermediate cases, a mixture of both approaches has been proposed [41]. In its simplest form [39] the LDA +  $U$  adds a potential

$$V_{m\sigma} = U \left( \frac{1}{2} - n_{m\sigma} \right) \quad [2.5]$$

for orbital  $m$  of spin  $\sigma$ . In other words, if the occupation is 1, it shifts the level down by  $-U/2$  and if the level is empty it shifts it up by  $U/2$ . This provides a natural way to split up- and down-spin electrons and hence create a magnetic moment. For a more detailed account of the actual implementations, the reader is referred to the key papers. Generally, the method is formulated in a rotationally invariant way, without choosing a specific set of  $d_m$  orbitals, which depend on the choice of coordinates, by writing the method in terms of density matrices rather than occupation numbers. The method can be derived from the  $GW$  approach (explained in Section 2.3.4) under certain limiting assumptions.

An important aspect of the model is how to choose the  $U$  and  $J$  parameters that enter it. The  $U$  parameter basically describes the spherically symmetric Coulomb interaction between two  $d$  electrons but including the screening by other electrons. It describes the energy difference of extracting an electron from adding an electron to the  $d$  states. This very definition requires us to think in terms of an open system in which the  $d$  states are allowed to interact with other orbitals but with a constraint placed on the  $d$ -level occupation. Various approaches have been devised to obtain this energy difference from density functional calculations themselves but with a constrained DFT approach. In other words, we treat the  $d$  state to which an electron is added (or from which it is subtracted) locally as an impurity in the solid. This requires temporarily cutting off the interaction with the rest of the orbitals so that screening is provided only by the other electrons but not the  $d$  states themselves. This approach was first developed by Anisimov and Gunnarsson [42] and in a slightly different way by Dederichs et al. [43].

A modern, more or less equivalent scheme has been developed based on linear response by Cococcioni et al. [44]. A key observation in their approach is that in an exact theory the total energy should be a piecewise linear function of the occupation numbers. This is known as the Generalized Koopmans Theorem [45,46]. In other words, between integer occupations, the total energy should vary linearly but the slope can change discontinuously in each integer interval. The Kohn–Sham one-electron levels, which are  $\varepsilon_i = \partial E_{\text{tot}}/\partial n_i$  according to Janak’s theorem [47], are thus constant in each interval between integers but can jump discontinuously from one integer to another. The point is now that Hartree–Fock and LDA (or GGA) make errors of opposite sign on the dependence of the total energy on occupation number. In Hartree–Fock the curve is convex upward because it does not include the correlation self-energy, while in LDA it is concave downward because of the self-interaction error. With the appropriate choice of  $U$ , we can restore the correct linear dependence.

Although calculation schemes exist to self-consistently determine  $U$ , in practice it is often determined by comparison to experimental results; for example, the splitting of filled majority spin and empty minority spin bands, as determined via photoemission and inverse photoemission for some closely related reference system. Often, however, we treat  $U$  as an adjustable parameter and investigate how the results vary with  $U$ . The somewhat uncontrolled dependence on the  $U$  parameter and uncertainties associated with how well  $U$  is transferable from one system to another remain a problem in practice, judging the results obtained within this method.

The self-interaction correction approach (SIC) [48–51] achieves pretty much the same goals as the LDA +  $U$  with a somewhat different approach. The self-interaction term of LDA is explicitly removed for each orbital. Thus it also leads to an orbital-dependent functional. The method is somewhat more intricate to implement and has not been as widely adopted as the LDA +  $U$  approaches. While both methods originally were developed in the context of localized orbital methods such as the linearized muffin-tin orbital (LMTO) method and Green’s function or Korringa–Kohn–Rostoker (KKR) theory, the LDA +  $U$  is now also widely used in plane-wave-pseudopotential codes.

### 2.3.3 Hybrid functionals

As already mentioned, Hartree–Fock and LDA tend to make opposite errors. Hartree–Fock overestimates gaps and magnetic moments, whereas LDA underestimates them. It is thus natural to think of making a hybrid method of the two. Hybrid functionals were first devised and became popular with quantum chemists. The Becke hybrid functional [52–54] approach and some of its specific implementations, with names such as B3LYP, were tested widely on a benchmark set of small molecules and tend to provide accurate results if we do not stray too far from those systems. On the other hand, the Heyd–Scuseria–Ernzerhof [55,56] functional is based on the idea of range separation. It includes an effectively screened or truncated version of the Hartree–Fock exchange, which excludes the troublesome long-range part responsible for the difficulties of Hartree–Fock in periodic solids. It includes usually a fixed 0.25 fraction of range limited exact exchange combined with 75% PBE GGA

exchange and correlation. The fraction  $\alpha = 0.25$  is somewhat loosely justified by a perturbation theory argument [57] but is found to work well in practice. In particular, it was found to much improve bandgaps of most traditional semiconductors. Some people go beyond it and adjust the fraction of exact exchange to fit the bandgap exactly. However, it is then not clear that it will at the same time describe other properties correctly, such as a specific defect level. Another approach for defect studies is to adjust it so as to satisfy the Generalized Koopmans Theorem [45,46,58]. An important point to remember is that it is not clear that hybrid functional calculations would be always superior to LDA calculations. For example, for shallow defect systems, a hybrid functional might overcompensate the almost absent self-interaction problem and lead to artificially deep levels.

In practice, this method achieves the same goals as the LDA +  $U$  approach, namely to avoid the self-interaction error inherent in LDA/GGA. As the self-interaction error leads to too-delocalized states, it may also be expected to suppress magnetic moment formation. Thus the hybrid functional can overcome this problem. In practice, the method is significantly more time-consuming, but since it has been included in some of the most used plane wave-based band structure codes it has rapidly gained in popularity.

### 2.3.4 The GW method

Unlike both previous methods, which are classifiable as generalized Kohn–Sham scheme methods fitting with the general framework of DFT, the *GW* method is a many-body perturbation theory approach that focuses on obtaining better single particle excitation energies, in other words, band structures. The  $G$  and  $W$  in *GW* stand for the Green's function and screened Coulomb interaction, respectively, following simply the notations of the first paper by Lars Hedin [59,60] in which they were introduced. The idea is that even in a many-body system at least some of its excitations are closely related to the underlying noninteracting particle states, and as such called quasiparticle excitations. The Green's function, or propagator, is written in terms of a creation and annihilation operator at different times and time ordered. Thus it literally follows, creating a particle in the system and then at a later time destroying it, or alternatively destroying one first (ie, creating a hole), and then later creating it, or destroying the hole. As such, this time- and position-dependent Green's function describes how an extra electron or a hole propagates through the system in dynamic interaction with the other electrons. Their Fourier transform to the energy or frequency domain provides the energy of the quasiparticle and their spatial Fourier transform provides their crystal momentum so that it gives literally an energy band as it would be measured by photoemission (extracting a particle from the system or creating a hole) and inverse photoemission. Thus, unlike DFT, the solutions of the *GW* equations, or quasiparticle spectrum, provide a well-defined band structure closely related to specific experiments.

The difficulty of the many-body theory, of course, lies in including the interactions. Starting from a suitable independent particle or noninteracting system, the effects of the interactions on the particles is described in terms of a self-energy operator.

This is like an extra potential felt by the quasiparticle compared to the noninteracting particle, but is nonlocal and energy-dependent. The Hartree–Fock theory’s exchange term in this context is just a special case of a self-energy that happens to be energy-independent and containing only exchange, but not correlation effects. The self-energy (or rather its expectation value for a quasiparticle state) is a complex quantity whose real part describes the shift of the quasiparticle for the noninteracting particle, and its imaginary part describes its lifetime or energy broadening.

The self-energy concept is a general concept in many-body theory. The *GW* method is a specific approach to calculate it, in which, in fact the self-energy is given schematically as  $\Sigma = iGW$ , hence the name. More precisely, this should be written as  $\Sigma(1,2) = iG(1,2)W(1,2)$  where 1 stands for  $(\mathbf{r}_1, \sigma_1, t_1)$  (ie, the position, spin, and time variables of the particle) and 2 similarly for the same particle at a different position, spin, and time. Once transformed to energy domain, the equation becomes a convolution.

$$\Sigma(\mathbf{r}_1, \mathbf{r}_2, \omega) = \int \frac{d\omega'}{2\pi i} G(\mathbf{r}_1, \mathbf{r}_2, \omega - \omega') W(\omega') e^{i\delta\omega'} \quad [2.6]$$

The key feature of the *GW* theory is that it involves the screened Coulomb interaction. Thus, it includes the major effects of correlation, which are to screen the electron–electron interactions. The screened Coulomb interaction can be written in different ways, schematically

$$\begin{aligned} W(1,2) &= v(1,2) + \int d(34)v(1,3)P(3,4)W(4,2), \\ &= \int d(3)(1 - vP)^{-1}(1,3)v(3,2), \\ &= \int d(3)\epsilon^{-1}(1,3)v(3,2) \end{aligned} \quad [2.7]$$

It involves the inverse dielectric function  $\epsilon^{-1}$  or equivalently, the polarization operator  $P$ . The latter can in turn be calculated in terms of the one-electron Green’s function. So, the *GW* theory is clearly a functional theory in terms of the Green’s function as basic quantity rather than the density. In the so-called random phase approximation (RPA),  $P(1,2) = iG(1,2)G(1,2)$ . The preceding are all written as integral equations but once the real space functions are expanded in basis sets, they become algebraic matrix equations. The RPA neglects electron–hole interactions in the screening and more complex effects on the screening arising from the fact that the screening electrons themselves are subjected to electron–electron interactions. Formally, such effects may be incorporated through a vertex function and Hedin derived a self-consistent set of equation linking the vertex, self-energy, polarization, and Green’s function, which are however, too complicated to solve. Although some attempts have been made to incorporate additional screening effects in  $W$  through a time-dependent density functional exchange-correlation kernel [61,62], a full incorporation of the vertex effects has not yet been possible. Even at the *GW* level, the calculations are far more time-consuming than DFT calculations, even those with hybrid functionals.

Usually, we make the assumption that the LDA Kohn–Sham eigenstates are a good approximation for the quasiparticle wave functions and use a single-shot correction, written as  $G_0W_0$ , in which the effect of the self-energy term, or rather, its difference from the LDA exchange–correlation functional, is treated in first-order perturbation theory. Alternatively, sometimes we start from a hybrid functional point. In the quasiparticle self-consistent  $GW$  theory, or QSGW approach, we extract from the complex self-energy a new Hermitian, ie energy-independent but still nonlocal exchange–correlation potential, which thus defines a new starting point for the next iteration of the  $GW$  calculation. If we solve this iterative scheme self-consistently, then the final result becomes independent of the starting point and the Kohn–Sham eigenvalues approach the corresponding quasiparticle energies [63,64]. In solving the QSGW equations self-consistently, mixing between different one-particle states is included through the off-diagonal elements of the self-energy operator. Thus this form of the theory can describe even systems where the original noninteracting Hamiltonian provides a poor description of the interacting states of the system.

It also matters whether the  $GW$  theory is implemented on top of a pseudopotential framework or in an all-electron approach. The latter is clearly superior and, importantly, includes the effects of core–valence exchange and self-energy in a more accurate way. While  $G_0W_0$  originally was implemented in pseudopotential frameworks and seemed to provide quite accurate bandgaps for most semiconductors, it was later found that an all-electron scheme still underestimated it and the QSGW was found necessary to correct this. QSGW systematically overestimates gaps (typically by about 20%) because of its underscreening by the RPA. However, this error is very systematic, thus reducing the self-energy correction  $\Delta\Sigma$  by a factor of 0.8, sometimes called 0.8 $\Sigma$ , which provides almost perfect agreement with the gaps of most semiconductors. QSGW also provides a good starting point for many more complex, more strongly correlated systems such as TM oxides, but still suffers from larger overestimates in those cases. Furthermore, it has been appreciated [65,66] that in strongly ionic systems with large LO–TO splittings of the phonons, the lattice contribution to the polarization or dielectric screening function, arising from the long-range electric fields produced by the ionic motions, needs to be included in the screening of the electron–electron interaction, in calculating  $W$ .

It is important to point out that the  $GW$  theory as it stands is not yet a total energy theory. It is merely a theory to obtain the quasiparticle excitations. There exists a formulation of the total energy in terms of the one-particle Green’s function, for example, through the Luttinger–Ward identities, and since as we have seen,  $GW$  corresponds to the RPA for the screening, it leads to a so-called RPA theory for the total energy [64,67]. However, it is extremely difficult to converge computations within this framework, because, unlike DFT, which only involves sums over occupied states, it involves sums over all states, including the empty ones.

Also, we remind the reader that  $GW$  theory provides correct band structures, in the sense of band structures as mentioned by photoemission and inverse photoemission, but not of optical properties. In an optical experiment, the electron and hole are created simultaneously and are in interaction with each other, so it requires, formally, two-particle Green’s functions. That is what the Bethe–Salpeter equation

provides. It includes the effects of the electron–hole interaction, which leads, among other things, to bound-state excitons, but also to excitonic shifts of the peaks and line-shape changes of the optical absorption in the continuum above the gap.

Finally, *GW* calculations are much more complex than DFT calculations and as such applying them to defect systems or impurities as needed for DMS is still restricted by computational limitations. Applying them to large supercells as required to properly describe the dilute limit is difficult.

### 2.3.5 Dynamic mean field theory

Although *GW* theory provides a great step forward and is at present one of the most accurate approaches for electronic structure calculations, it still falls short to describe the complex behavior of strongly correlated many-body systems. Its strengths lie in describing the long-range effects of the Coulomb interaction, which, for example, are the main origin of the gap underestimation in semiconductors. However, it still may fail to describe the strong local correlation effects in *d*- or *f*-band systems. For instance, in tests on *f*-band systems, it was found that the empty *f* states are lying too high in the conduction band [68], sometimes by several eV. On the other hand, it may underestimate the binding energy of occupied *f*- or *d*-band states by a somewhat smaller amount. It does not allow a correct description of the spectral function in complex cases where, for example, a Kondo resonance occurs at the Fermi level in addition to the upper and lower Hubbard bands that the LDA + *U* or *GW* would obtain as the main quasiparticle states. Finally, it does not include the multiplet splitting effects, which are important for *f* electron systems.

The DMFT [69,70] provides a way to include these local correlation effects. The main approximation of DMFT is that it assumes a wave-vector-independent local self-energy  $\Sigma(\mathbf{k}, i\omega) \approx \Sigma(i\omega_n)$ . It is energy-dependent and for technical reasons usually evaluated along the imaginary energy axis at the so-called Matsubara frequencies from which the time-dependent Green's function can be obtained. The correlation effects are included locally on-site at some desired sophisticated level by treating the site as an impurity. The self-energy represents how the impurity level is changed by the correlation effects. Their effect is then included in the Green's function of the extended system through

$$G(\mathbf{k}, i\omega_n) = \frac{1}{i\omega_n + \mu - \varepsilon_k - \Sigma(i\omega_n)} \quad [2.8]$$

Locally, the lattice Green's function is required to coincide with the impurity Green's function. The coupling of this impurity to its environment then allows these local effects to be incorporated into the band structure. The local correlation problem is solved using a so-called impurity solver. The latter forms the heart of the DMFT calculation. It provides an accurate and sophisticated, possible, numerically almost exact calculation of the correlation problem locally, by means of a Quantum Monte Carlo or exact diagonalization approach.



The dynamical mean field theory derives its name from the fact that it treats the local time-dependent fluctuations while treating the spatial fluctuations in a mean field or averaging manner. Originally formulated as a way to treat the Hubbard model, it has been incorporated with DFT calculations in the same way as the LDA +  $U$  method. In that sense it can be viewed as a more sophisticated way of treating the Hubbard  $U$  terms in a dynamic way, including the time-dependent fluctuations. More recent work attempts to merge  $GW$  theory with DMFT.

For our purposes, an early version of DMFT, called the Hubbard-I approximation [71], is worth mentioning. It is particularly useful for treating  $f$  electron systems. It starts by including the multiplet effects locally on each site. In other words, it uses the correct many-body states of the  $f^n$  electron system classified according to their total angular momentum and spin in  $\mathbf{L} \cdot \mathbf{S}$  coupling. From these many-body states, we then calculate an atomic on-site one-electron Green's function. Its difference from the noninteracting local Green's function provides the self-energy. The latter is then inserted in the lattice Green's function. In other words, it treats how each of these multiplet states separately hybridizes with the other states in the system. The local projection of the lattice Green's function must agree with the impurity Green's function including the Coulomb correlation effects of the multiplet states. In the DMFT context, we may view the atomic multiplet calculation as a solution of the local impurity problem. Compared with LDA +  $U$ , which provided only an average static mean field approximation for the  $f$  electrons, the present scheme incorporates the various many-body states or multiplets explicitly. However, both share that they incorporate how these local states hybridize with the rest of the system. It provides a way to place the many-body states in the framework of a band structure, by focusing on the one-electron Green's function extracted from the many-body states. In other words, it helps us place where the  $f$ -electron states lie with respect to the rest of the band structure. In particular it allows us to calculate one-electron excitations of the type  $f^n s^m \rightarrow f^{n-1} s^{m+1}$ , where  $s$  represents all states besides  $f$  electrons. Examples of this approach can be found in [72–74]. As an example, we show in Fig. 2.4 how the DMFT calculation of the  $f^7$  multiplets and  $f^5$  compare with a full atomic multiplet splitting calculations including the  $3d$  core holes for the  $M_4$ ,  $M_5$  X-ray absorption spectra (XAS) and the X-ray photoemission spectroscopy (XPS) and N-2K X-ray emission spectra (XES), respectively, in EuN.

A somewhat different approach to include multiplet effects of  $f$  electrons in the context of band structure theory was proposed by Hourahine [75].

### 2.3.6 Concluding remarks

We realize that this bird's eye overview of recent developments in electronic structure theory is rather cursory. We deliberately avoided providing the technical details using a minimal number of equations and rather focused on the physical concepts. Needless to say it is not meant to be a true introduction to the methods, which can be found in many other review articles and books. Rather it is meant to serve as a conceptual introduction to give the reader some idea of the virtues and shortcomings of each approach. We hope it will be somewhat useful to the nonexpert reader.



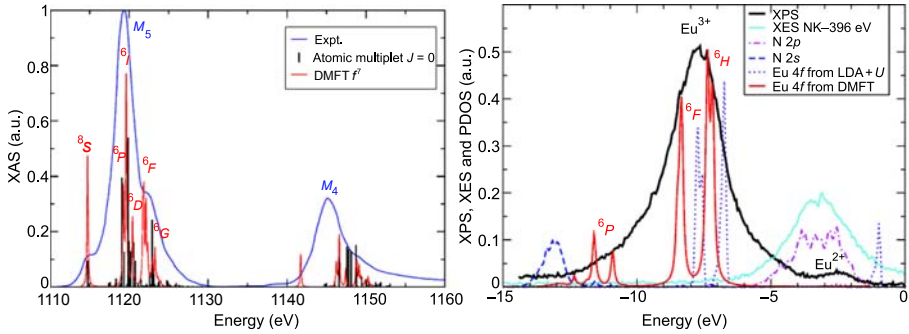


**Figure 2.4** Left: multiplet splittings of the  $\text{Eu}^{3+}f^7$  configuration obtained in DMFT, compared with the experimental XAS spectra. The atomic multiplet splittings in addition include the effects of the  $3d$  core holes. In XAS, an electron is excited from the  $3d$  core hole to the empty  $f$  states, so the  $\text{Eu}^{3+}f^6 \rightarrow f^7$  transition is exemplified. The advantage of the DMFT is that it lets us place the position of the  $f$  multiplets relative to the other bands in the system. Right: the N-2K XES spectra and XPS show the  $\text{Eu}^{3+}f^6 \rightarrow f^5$  transition multiplets. From Richter JH, Ruck BJ, Simpson M, Natali F, Plank NOV, Azeem M, et al. Electronic structure of EuN: growth, spectroscopy, and theory. *Phys Rev B* 2011;84:235120. <http://dx.doi.org/10.1103/PhysRevB.84.235120>.

## 2.4 Magnetism

### 2.4.1 Magnetic moments, ferromagnetic and antiferromagnetic coupling

#### 2.4.1.1 Introductory remarks

In the previous section, we focused on methods to obtain the electronic structure most closely related to spectroscopic experimental methods, such as photoemission and to some extent, optics. In this section, we focus on the magnetic quantities of interest. First of all, the difference in density of up- and down-spin electrons provides the magnetic moments. Of course, what we mean by up- and down-spin depends on the choice of coordinate axes for the spin; up and down mean simply that  $s_z = \pm 1/2$ , and how the spin axes are related to the crystal is determined by spin-orbit coupling. So, a noncollinear spin theory is required to even enable us to talk about spin directions. However, having an unpaired spin or local magnetic moment on the atoms is not sufficient to speak of magnetism. In particular, for impurities, they just would provide paramagnetic impurity centers, which for instance are detectable by electron paramagnetic resonance (EPR). However, in DMSs, we require in addition that these moments couple to each other and order in a ferromagnetic arrangement. Thus the next quantities of interest are the exchange couplings between the local moments. In this section we mainly review different approaches to calculate the exchange interactions between magnetic moments on different sites.

We should, at the outset, clarify the scope of this section. Often we also consider an orbital decomposition of magnetic moments. For instance we may consider the

$f$ -electron contribution to the magnetic moments or the  $f$ -electron spin. This local spin may then induce spin polarization in other bands. This is also an exchange effect and the parameters are also called exchange parameters but they are different from the ones mentioned earlier. The related splittings of some one-electron levels to other one-electron levels determine, for example, how the states near the gap become spin split whereas the exchange interactions we are mainly interested in here is the coupling from one  $f$  spin to another on a different site. Or more generally, how the local magnetic moments or any orbital part of it interacts with other ones on other sites. These exchange interactions affect the total energy of the system and tell us which arrangement of spins is favored in energy.

In other words, the concept is to replace the original problem of the electrons and their spins to an effective description of interacting spins or moments. This mapping to a spin Hamiltonian is the key first step to investigate the statistical finite temperature properties of the spins and hence magnetization and eventually magnetic effects on transport or spintronics.

The justification for such a scheme can be found in the different time scales for so-called longitudinal from transverse fluctuations of the spins [76]. The longitudinal fluctuations determine in some sense the magnitude of the local magnetic moments on each site. The transverse fluctuations determine how the orientation of the spins varies from site to site and thus how they order. The transverse fluctuations also determine the low energy excitations of the system, which are collective spin waves. There is a close analogy here with how atomic motions and electronic motions are decoupled via the adiabatic approximations. In fact, an adiabatic decoupling of the magnitude of the magnetic moments and the moment orientations have been described by Antropov et al. [76]. It provides among other things a justification for introducing an effective Heisenberg spin model for the electrons extracted from local spin density functional calculations. Just as in the usual adiabatic Born–Oppenheimer approximations, where the electronic structure provides an effective potential energy landscape for the atoms or ions or nuclei, the LSDA or one of the more sophisticated theories described in the previous section provides us the local magnetic moments (equivalent to the atoms) and their interactions; in other words, an effective spin Hamiltonian. The best known of these is the Heisenberg Hamiltonian. Just as we can then study the dynamics of the atoms by means of molecular dynamics or, for example, by finding the lowest energy-collective motions, the vibrational normal modes about their equilibrium positions or phonons, and can compare energies of different crystallographic phases, in the magnetic case from the spin Hamiltonian, we can study the different possible ordered phases and antiferromagnetic or ferromagnetic phases, and study their low energy excitations or spin waves, or magnons.

Our task is to see how this specifically applies to DMS systems. So, first we review computational techniques for mapping the electronic structure to an effective spin model. Then we discuss some particular aspects of DMS systems relating to their disordered nature, diluteness, and so on. Then we also discuss methods to obtain statistical mechanics, like finite temperature information from the effective spin model. Finally, we need to consider other aspects of the DMS, involving the atomic or crystallographic structure; for example, do the dilute atoms provide the spin order themselves and modify the underlying structure? How does this in turn affect the magnetic properties?

### 2.4.1.2 Mapping of total energy differences on a Heisenberg model

The most obvious and widely used approach to extract an effective spin model from electronic structure calculations is to simply postulate a generalized Heisenberg Hamiltonian with effective exchange interactions between the moments or equivalently spins of the magnetic atoms up to some distance between neighbors:

$$H_{\text{mag}} = - \sum_{\langle ij \rangle} J_{ij} S_i \cdot S_j \quad [2.9]$$

These spins can be classical spin vectors, or quantum mechanical spins; for example, for a  $\text{Mn}^{2+}$  impurity, we might pick  $S = 5/2$ . The interactions  $J_{ij}$  couple each neighboring spin pair. With this spin Hamiltonian, it is easy to write down the expression for the total energy of a given spin configuration. Now, we separately calculate the total energy differences of various spin configurations, typically within DFT in the LSDA or possibly with LSDA +  $U$  or a hybrid functional. If there are  $N$  distinct exchange parameters in the model, we need to calculate  $N + 1$  distinct spin configurations from first-principles so we have  $N$  total energy differences, which supposedly only differ because of the magnetic energy. Then we can map the calculated energy differences to the expressions of the spin model and by solving a set of linear equations, extract the exchange parameters.

For example, for two magnetic impurities, we typically choose a sufficiently large supercell, including only two magnetic atoms at some chosen distance from each other, and calculate the energy difference between their spins being parallel or antiparallel and extract from that the corresponding exchange interaction of this pair. Suppose we take spin vectors to be just unit classical vectors; then for the antiferromagnetic configurations, the energy is  $+J$  and for the ferromagnetic case it is  $-J$ , thus

$$E_{\text{AFM}} - E_{\text{FM}} = 2J \quad [2.10]$$

The assumption made in this approach is that longer range interactions that would couple spins in one unit cell with those in the next are negligible. We then repeat this for a few distances between the magnetic atoms and extract in this way a distance-dependent exchange interaction. Possibly we could distinguish different directions in the crystal. For nondilute systems, typically, we may have to consider a few different antiferromagnetic arrangements, such as ordering of spins in different directions, and the ferromagnetic case has a few parameters, such as first and second nearest spin interactions, which are mapped to the corresponding energy differences.

The advantage of the method is its simplicity. The disadvantage is that we make *a priori* assumptions about the model, and more importantly about the range of the interactions. It also completely neglects the fluctuations in the interactions arising possibly from different local environments of the impurity, the effect of the presence of one impurity on another pair, and so on. Another disadvantage is that this model only considers collinear spins to extract the energy parameters but later assumes

that they apply to the Heisenberg Hamiltonian where the spins can point in any direction. We thus focus on the large energy differences of spin configurations to extract the smaller energy scale of small rotations of the spins. Still, such calculations can give a first rough idea whether the spins tend to couple ferromagnetically or antiferromagnetically.

### 2.4.1.3 Liechtenstein's linear response theory

In the linear response theory [77], we consider a rotation of one spin away from the reference configuration, say the ferromagnetic one, by a small angle and calculate the induced torque on another, or rather the change in total energy to first order. That is,

$$J_{ij} \frac{\theta^2}{4} = \delta E_{ij} - \delta E_i - \delta E_j \quad [2.11]$$

where  $E_{ij}$  is the change in energy if we rotate the spin at site  $i$  by  $\theta/2$  and one at  $j$  by  $-\theta/2$ , and the  $\delta E_i$  is the change in energy to rotate a single spin by interacting with its environment. These total energy differences,  $\delta E_i$ , and such, can now be expressed analytically in terms of Green's functions. The reason is that we can calculate the total energy differences to first order using Andersen's force theorem in terms of frozen potentials with simply a rotation of the spin, without the need for a self-consistent redetermination of the charge and spin densities due to the spin rotation on one site. This allows us to write them in terms of the change in one-electron band energies alone, and the latter can in turn be written in terms of the phase shift formula of the total number of states, or Lloyd's formula in multiples scattering theory. The method is typically implemented in the context of the multiple scattering theory, KKR band structure theory, or the closely related LMTO method. In any case, the final result is that we obtain a closed expression for the exchange interaction in the form,

$$J_{ij} = \frac{2}{\pi} \int^{E_F} d\epsilon \text{ImTr} \left\{ \Delta t_i G_{ij}^\uparrow \Delta t_j G_{ji}^\downarrow \right\} \quad [2.12]$$

with  $\Delta t_i = (t_i^\uparrow - t_i^\downarrow)/2$ , with  $t_i^{\sigma(\epsilon)}$  the on-site  $t$ -matrix describing the scattering, and  $G_{ij}^{\sigma(\epsilon)}$  the Green's function connecting site  $i$  to  $j$  for a given spin. The advantage of this approach is that we make no *a priori* assumptions about the exchange interactions and can calculate them explicitly between any pair of magnetic atoms. If we apply this in a supercell approach we obtain  $J_{ij}(\mathbf{k})$  at any  $\mathbf{k}$  point of the supercell Brillouin zone. Using an inverse Fourier transform, we obtain the  $J_{i,j+\mathbf{T}}$  exchange interactions with atoms  $j$  in neighboring cells displaced by a lattice vector  $\mathbf{T}$ . Thus, we obtain interactions not only in the same unit cell but as far in the lattice as necessary. If we use  $N$   $\mathbf{k}$ -points, we can go out to  $N$  neighboring lattice vectors. An important advantage is that we obtain all the exchange interactions simultaneously from one calculation instead of having to study them one by one with different models. The upshot of this approach is that we can obtain long-range exchange interactions and explicitly test

how they decay. For example, if there are carrier-mediated interactions as in a metallic situation, we expect a slow  $1/r^3$  and oscillatory  $\cos 2k_{FF}$  exchange interactions as in the Ruderman–Kittel–Kasuya–Yosida (RKKY) model [78]. Using this approach, we generally find the exchange interactions to show significant fluctuations from site to site in a disordered system [79]. The method, for example, was applied to III-V DMSs, such as Mn:GaAs [79].

More generally, we may show that the exchange interactions correspond to the transverse spin susceptibility in a lumped atom-by-atom model rather than the continuous point-by-point in space model. The expressions for the spin susceptibility can be written in terms of the one-electron Green's function entering the *GW* theory or in terms of similar equations to those already used for the polarization function in the *GW* theory [80–82].

#### 2.4.1.4 *Disordered local moments theory*

Closely related to the preceding linear response method is the idea of disordered local moment theory [83–85]. The trouble with the direct DFT approaches is that they do not well describe the paramagnetic state above the ordering temperature. In that case, the magnetic moments are disordered in their orientation so there is no net magnetization, but the magnetic moments persist on each site. In a nonmagnetic calculation, we would have zero moment on each site. Describing the disordered orientation of the moments in a noncollinear way in a large enough cell to capture their randomness is challenging. Instead we can make use of effective medium-type theories, in this case the coherent potential approximation (CPA) [86]. In particular, within collinear magnetism theory, the problem of a disordered array of up and down spin states is equivalent to the alloy problem of two types of atoms and can be treated with the CPA. Generalizations of the CPA for noncollinear spins pointing in all directions, sometimes referred to as vector DLM or VDLM [87], or for fully relativistic theory including spin–orbit coupling are possible. This type of theory has been implemented in KKR [88] and LMTO programs [80,89,90] and provides a natural way to describe the paramagnetic state of randomly oriented moments. We can then apply the linear response theory with this disordered local moment state as reference instead of using a ferromagnetic reference system. This approach has been widely applied to DMS by Katayama-Yoshida et al. [84,85,91].

#### 2.4.2 *Spatial fluctuations of magnetic moments*

Using the previous linear response on large models with a random distribution of magnetic impurities has given important new insights in the nature of the exchange interactions in DMS. Typically, it was found for Mn in GaAs as an example that the individual interactions are longer range but significantly smaller than previously expected [79]. It means that what we previously had calculated with the direct approach of just focusing on the interaction energy of one spin pair at the time in a supercell is some average sum over many other long-range interactions with spin in neighboring cells. It turns out that the exchange interactions also show strong fluctuations between

pairs at the same distance from each other depending on the presence of the other spins in the system, which create a different local environment for each individual spin.

To illustrate, I will refer to some of our own work on exchange interactions of Mn atoms doped in ScN. In a first paper [92], we found fairly strong and mostly ferromagnetic interactions up to a few nearest neighbors when using the mapping approach to collinear spin configurations. Using the linear response theory [78], we found the individual interactions were an order of magnitude smaller but strongly fluctuating and long range. In this system, the small gap led to a metallic situation of free carriers in the LDA and we could discern the RKKY-like oscillations of exchange interactions. When adding a gap correction, the exchange interactions became exponentially decaying but still showed large fluctuations. Both are compared in Fig. 2.5. As an aside the motivation for studying Mn-doped ScN was that MnN and ScN share the same rock-salt crystal structure and a much larger solubility or the formation of fully mixed alloys between different TMs is possible in such systems. This leads possibly to a way to higher  $T_C$ s. The use of the linear response theory also allowed us to study the effect of doping on the system. For example, n-type doping could arise from nitrogen vacancies in such a system and would simply shift the Fermi level. We found that in order to obtain a maximum  $T_C$ , the doping must be kept below a certain threshold. Experimentally, this system has shown some ferromagnetic behavior [93] but the predicted high-temperature  $T_C$ s have not yet been realized experimentally.

Similar results were also found for Gd-doped GaN. As we will discuss in more detail in the last section, exchange interactions of Gd impurities with N and O interstitials at first appeared to be ferromagnetic when evaluated in fairly small supercells via the mapping approach, but upon closer inspection with the linear response approach were found to be strongly fluctuating in sign between ferromagnetic and antiferromagnetic leading to only short-range effective interactions.

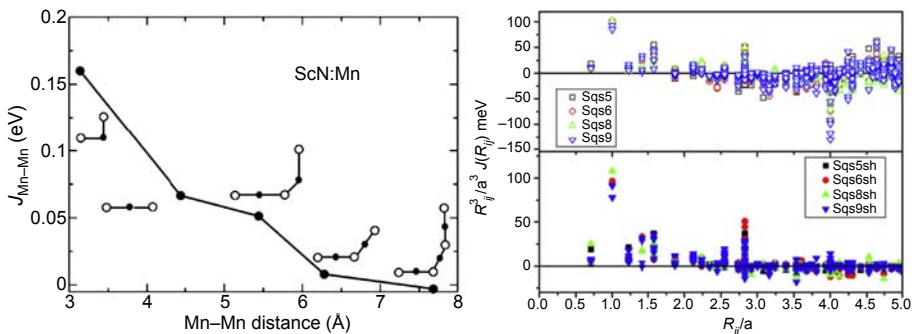


**Figure 2.5** Exchange interactions between Mn atoms in Mn:ScN. Left, (From Herwadkar A, Lambrecht WRL. Mn-doped ScN: a dilute ferromagnetic semiconductor with local exchange coupling. *Phys Rev B* 2005;72:235207. <http://dx.doi.org/10.1103/PhysRevB.72.235207>.) using direct mapping approach; right, (From Herwadkar A, Lambrecht WRL, van Schilfgaarde M. Linear response theoretical study of the exchange interactions in Mn-doped ScN: effects of disorder, band gap, and doping. *Phys Rev B* 2008;77:134433. <http://dx.doi.org/10.1103/PhysRevB.77.134433>.) using linear response approach.

### 2.4.3 Percolation theory

An important aspect of DMS is the randomness of the distribution of magnetic ions. In order to obtain an overall ferromagnetic order, a continuous network of coupled atoms must pervade the entire system, rather than only local clusters. This obviously requires sufficiently long-range exchange interactions, or, put another way, for a given range of the interactions, it requires a minimum critical concentration above which a connected network is established as opposed to disjoint islands or clusters of coupled magnetic moments. This requirement is described by *percolation* theory. In order to obtain ferromagnetic ordering in a DMS, the concentration of magnetic sites needs to be above the percolation threshold. This depends on the underlying lattice but also on the type of magnetic center. For instance, for a vacancy-induced magnetism (see a later subsection 2.5.2.8), the magnetic moments reside on the sites that are nearest neighbors to the vacancy instead of the site of the defect of impurity itself. This leads to a lower percolation threshold. Aspects of percolation theory with regard to DMS are discussed in Refs [85,94–96].

### 2.4.4 Effects of different underlying electronic structure methods

As we have mentioned in the previous section, the LDA has a tendency to avoid localized electronic distributions as a result of its incomplete cancellation of the self-interaction. This has important consequences for magnetism. For example, in reality the defect wave function might be localized on a single atom undergoing a local distortion of the system instead of spreading equally over the neighbors. The correct, more localized spin distribution then also leads to less overlap between adjacent magnetic centers and hence shorter range interaction, which means that a higher concentration of magnetic centers is required to reach the percolation threshold.

Another important point is that ferromagnetic coupling tends to occur in partially filled electron systems while antiferromagnetic superexchange tends to occur in completely filled level systems. This is a consequence of the Anderson Hasegawa model [97], which we now describe. Consider two magnetic atoms adjacent to each other. Their energy level scheme is depicted in Fig. 2.6. They have spin-dependent

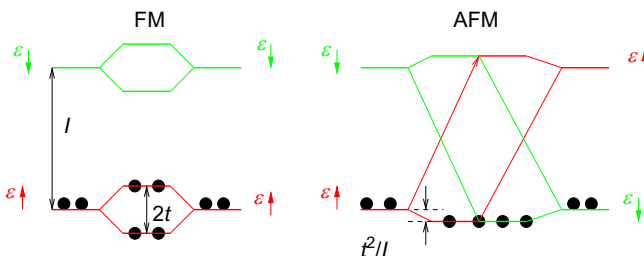


**Figure 2.6** Anderson Hasegawa model for superexchange versus ferromagnetic double exchange.

levels separated by an exchange energy,  $I$ . Now, we consider coupling via hopping from one to the other with a hopping energy,  $t$ . If the spins on the atoms are parallel,  $\epsilon_i^\uparrow$  couples with  $\epsilon_j^\uparrow$  into  $\epsilon^\uparrow \pm t$  and likewise the down-spin levels are  $\epsilon^\downarrow \pm t$  with  $\epsilon^\uparrow - \epsilon^\downarrow = I$ . On the other hand, if the spins on the neighboring sites are opposite, then the split into

$$\frac{\epsilon^\uparrow + \epsilon^\downarrow}{2} \pm \sqrt{\left(\frac{\epsilon^\uparrow - \epsilon^\downarrow}{2}\right)^2 + t^2}$$

or in second-order perturbation theory, assuming  $I \gg t$ , the lower level becomes  $\epsilon^\uparrow - t^2/I$ . Now, if each of these levels is  $n$ -fold degenerate and contains  $n$  electrons on each site, so that the up-spin level is entirely filled and the down-spin one is empty, then we have  $2n$  electrons, which fill both levels separated by  $2t$  in the ferromagnetic case, and hence there is no energy lowering of the total energy. On the other hand, in the antiferromagnetic arrangement, the  $2n$  electrons go into the lower level, and gain energy  $2nt^2/I$ , so the antiferromagnetic coupling is preferred in the half-filled shell case. However, if we have a partial occupation of the levels, then the lower level  $\epsilon^\uparrow - t$  has more electrons than the upper level  $\epsilon^\uparrow + t$  in the ferromagnetic case, and this energy gain is larger than for the antiferromagnetic case, where it is only  $t^2/I$  instead of  $t$ . So, partial occupations favor ferromagnetic coupling.

Now, the consequence of this for DMS is that LDA tends to underestimate binding energies of acceptors. Thus the magnetic impurity acceptor level might lie close to the VB and when considering their broadening into a band, overlaps with the latter, so that a partial occupation of the level results in ferromagnetic coupling. On the other hand, in a more accurate hybrid functional or LDA +  $U$  calculation, the level might be deeper and stay well isolated in the gap and entirely filled, leading to antiferromagnetic coupling.

Thus extreme caution is required when interpreting results from LDA calculations even for the sign of the exchange coupling. The overall message is that LDA tends to favor magnetism in this case, where the more accurate methods and more local spin densities preclude it. So, there are two opposite effects at work. The more localized nature of the wave functions in an orbital-dependent theory might produce stronger local moments, which seems to favor magnetism, but the more localized nature also means their exchange interactions are reduced, which means less tendency to ordering or possibly a change from ferromagnetic to antiferromagnetic coupling. The effects mentioned in this section were extensively discussed by Zunger et al. [17].

### 2.4.5 Calculating critical temperatures

Once we have the exchange interactions, we may apply statistical mechanics to find the ordering temperature. The simplest approach here is the mean field theory. The effects of the other spins are treated as an effective magnetic field and the problem then reduces to that of a spin in magnetic field for which the partition function can readily



be calculated. The average magnetic moment or spin then must obey a self-consistency condition in order to have a net spontaneous moment in the absence of an external field. This leads to a simple way of estimating the critical temperature, which, for example, for a ferromagnet is simply  $T_C = J/(S + 1)k_B$ . For  $S = 1/2$  this gives  $T_C = 2J/3k_B$ , with  $k_B$  Boltzmann's constant. Here  $J = \sum_j J_{ij}$  is a sum over all exchange interactions connected to a fixed atom  $i$  and eventually an average of all the magnetic atoms  $i$  in a disordered system is needed. However, mean field theory neglects fluctuations and hence overestimates  $T_C$ . It is well known that the higher the number of neighbors, the better mean field theory. It becomes exact for an infinite number of neighbors. For an fcc lattice with 12 neighbors, it tends to overestimate  $T_C$  by about 30% and in 2D systems with even fewer neighbors it becomes worse. Clearly, it can be expected to be especially problematic for dilute systems such as a DMS.

An exact solution is not known but Monte Carlo methods can provide quite accurate, essentially numerically exact predictions of the  $T_C$  in practice. Besides the Monte Carlo method, other techniques are useful because they are less time-consuming. The RPA for the calculation of critical temperatures [98] is based on the theory of spin-wave excitations and gives the critical temperature as

$$k_B T_C = \frac{2}{3} S(S + 1) \left( \frac{1}{N} \sum_{\mathbf{q}} \frac{1}{J(0) - J(\mathbf{q})} \right)^{-1} \quad [2.13]$$

where  $N$  is the number of spins, and  $J(\mathbf{q})$  is the Fourier transform of the exchange interactions. This is valid for an ordered periodic system. A local version of the random phase approximation suitable for disordered DMS was developed by Bouzerar et al. [99]. Another useful approach is the cluster variation method [78,100]. As mentioned earlier, in DMS, a crucial point is to include the percolation aspects. For further discussion we refer to Sato et al. [85].

## 2.4.6 Spinodal decomposition

So far we have assumed that the magnetic impurities are distributed randomly in the lattice and we have focused on the interactions and the formation of magnetic moments. On the other hand, a DMS is also a chemically inhomogeneous system and the important question is how the TM and/or RE impurities prefer to distribute themselves in the lattice under thermal equilibrium or more importantly during the growth process.

As is well known, the problem of alloying can be mapped on the Ising spin model and is thus a similar problem to that of magnetism itself. If an  $A$  atom prefers to surround itself with  $B$  atoms we tend to get ordered compounds; if  $A$  atoms prefer  $A$  atoms as nearest neighbors then we may tend to get phase separation. This is usually the case for TM impurities in semiconductors; their size and electronic structure character are sufficiently different that phase separation is to be expected. Furthermore the TM atoms tend to form different crystal structures with the group V or group III

atoms so that often in practice we find precipitates of different phases. Recognizing these when they are very small is a challenging experimental problem because they may not show up in X-ray diffraction when below a critical size. Even when the tetrahedrally bonded structure is maintained, we may expect TM-rich and TM-poor regions to phase separate. This is the problem of spinodal decomposition.

It has been studied extensively by Sato et al. [85] by direct numerical simulations. First, they used first-principles calculations of the phase separation behavior in typical TM-doped semiconductor systems, establishing that they have a phase diagram with a miscibility dome as a function of temperature and typically low miscibility at low temperatures. These are based on the Ising model mapping of the alloy problem and on CPA calculations. Second, using Monte Carlo simulations, they showed the occurrence of clusters of TM-rich regions either as isolated 3D clusters if the system is allowed to fully equilibrate or as elongated large clusters in the growth direction if only equilibration in each layer is allowed. If we allow the surface to come into equilibrium through surface diffusion but freeze in the surface distribution when building up the next layer in a growth simulation, we tend to find a columnar phase-separated situation. They dubbed the latter *Konbu* phases, after the Japanese word for kelp or seaweed because of their resemblance to seaweed, a popular food in Japan. See Fig. 2.7.

Third, they established the effects on the magnetic properties of these inhomogeneously distributed magnetic centers. In particular, they show that the hysteresis we obtain from such samples should be interpreted as superparamagnetism and they found that in particular, their so-called *Konbu* phases had a high superparamagnetic blocking temperature.

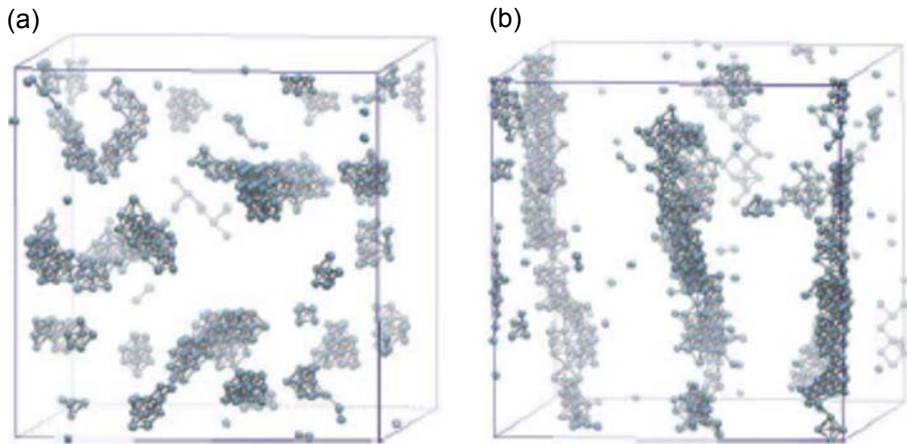


**Figure 2.7** Spinodal decomposition in TM-doped semiconductors leading either to isolated clusters in a 3D simulation (a) or to columnar clusters in a 2D growth simulation (b). From Sato K, Bergqvist L, Kudrnovský J, Dederichs PH, Eriksson O, Turek I, et al. First-principles theory of dilute magnetic semiconductors. *Rev Mod Phys* 2010;82:1633–1690. <http://dx.doi.org/10.1103/RevModPhys.82.1633>.

### 2.4.7 $d^0$ magnetism: role of defects in magnetism

Typically, ferromagnetism is associated with permanent magnetic moments arising from partially filled  $d$  or  $f$  shells. Ferromagnetism, however, was also found to occur in some systems without  $d$  or  $f$  electrons and was dubbed  $d^0$  magnetism. One of the first materials where this was discovered was  $\text{HfO}_2$ , a high-dielectric constant dielectric [101]. Soon, it was also found in other oxides, such as  $\text{MgO}$  and  $\text{ZnO}$  [102]. A good review of these systems can be found in Refs [103–105]. One possible origin of this type of magnetism is the presence of cation vacancies. It was pointed out that  $O-p$  and also  $N-p$  orbitals are nodeless and look very much like  $3d$  orbitals [106]. The fact that they are more localized than higher principal quantum number  $p$  states can lead to formation of magnetic moments. The strong exchange energy related to keeping parallel spins in these orbitals can lower the energy compared to alternative configurations in which electrons pair in singlet states. Venkatesan et al. [105,107] proposed a spin-split impurity band model, which gives rise to magnetism if it overlaps with either the majority or minority spin  $d$  bands but not otherwise, to explain the trends in magnetization in  $\text{ZnO}$  doped with various TM elements. The impurity band is thought of as a delocalized state with an effectively rather large Bohr radius, such as a shallow donor or acceptor, and thus magnetism can occur above a percolation threshold where these spread-out defect states overlap, which occurs for concentrations well below those for near-neighbor interactions. This idea is closely related to that of magnetic polarons. On the other hand, the surprise they found was that this magnetism is also very anisotropic. In a later paper, Coey et al. [104] proposed that this magnetism may essentially stem from extended defects, such as arising from grain boundaries, or dislocations or spinodal decomposition. The important point is that the magnetism in these systems occurs only in a small fraction of the sample near such defects. The actual mechanism they invoked is a charge transfer from a reservoir to a defect band, which thereby fulfills the Stoner criterion. We will see later that a related situation may occur in  $\text{Gd:GaN}$ .

### 2.4.8 Model exchange mechanisms

It is popular to assign exchange interactions between local moments to specific exchange mechanisms, such as Zener exchange, double exchange, direct or indirect exchange, superexchange, and so on. Our view on this is that it is the underlying electronic structure that determines the exchange interactions between local spins or magnetic moments. These exchange mechanisms are essentially simplifications of the latter in the context of some type of perturbation theory. Thus, identifying the exchange interactions with one of these models may be useful and may provide a deeper insight, but this is not always the case if we oversimplify the situation. Just giving a name to the type of mechanism in itself does not provide new insight. For example, we already compared antiferromagnetic superexchange with double exchange. This led us to the insight that filled systems tend to have antiferromagnetism, while ferromagnetism results from partially filled orbitals. The idea of double exchange as well as superexchange is usually related to the fact that other atoms such

as anions intervene between the magnetic atoms containing  $d$  electrons. There are then indirect couplings in second-order perturbation theory, which we can think of as hopping from the  $d$  orbital to the anion  $p$  state and back to another magnetic-atom  $d$  state. Essentially, this amounts to downfolding the interactions into a smaller subspace of the orbital of the magnetic atoms alone through indirect interactions via other orbitals. The Zener model [108–110] originally derived for TMs involves interaction between localized spins and conduction electrons. This is closely related to the so-called RKKY interaction [111–113], which is now a standard textbook model.

The Zener model became especially popular for DMS through the work of Dietl et al. [114]. That paper proposed among other things that higher critical temperature could be found in wide bandgap semiconductors, such as GaN and ZnO. However, this model was based on the idea that the TM ions do not thoroughly perturb the VBM, which can still be treated as in a p-type semiconductor and which interact with localized spins. As we have seen, this model is not justified because the TM  $d$  states in wide bandgap semiconductors form deep states in the gap.

The use of model systems, such as a localized spin interacting with conduction electron spins (or holes) has some advantages in that we can more completely treat disorder effects than in more realistic models. A big discussion [115,116] in Mn-doped GaAs has to do with the question whether the spins in the band tail above the VBM are actually localized in an impurity band or just form a continuous tail above the band. Although this question also closely depends on the nature of the defect states above the VBM being TM-like or dangling bond acceptor-like, even within the latter model, there is discussion on how localized they are when randomness is incorporated. Such questions are important from the point of view of spin transport. To the extent that such models are justified by first-principles, they are useful but in some cases they have been applied beyond the realm of validity. There has been an on-going discussion between the first-principles community, which advocates taking the explicit nature of the TM  $d$  states into account, and the model-Hamiltonian community, which describes the latter as a localized spin with some exchange coupling constant to the VB or acceptor-state spins. The localized spin model appears to be reasonably well justified for Mn:GaAs, for example, where the states in the gap are dangling-bond hybrid-like and thus to some extent like a normal acceptor but is not justified at all for Mn:GaN, where the states in the gap are deep states with Mn-3d character.

## 2.5 Case study: Gd in GaN

### 2.5.1 Introduction and experimental literature

Gd-doped GaN came on the scene with a splash in 2005 with a paper by Dhar et al. [117] that announced colossal magnetic moments of an order of  $4000 \mu_B$  per Gd atom. A few years earlier ferromagnetism had already been found by a Japanese group [118,119] in Gd-doped GaN but these samples contained of the order of a few percent Gd as is typical in DMS. The so-called colossal magnetic moments instead occurred in the case of extremely dilute Gd doping of the order of  $10^{15}/\text{cm}^3$  or parts per million.

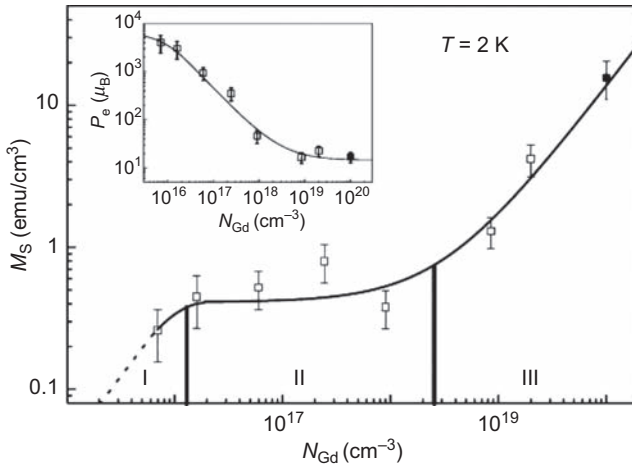


**Figure 2.8** Saturation magnetization and effective moment per Gd (inset) as function of Gd concentration in GaN.

From Dhar S, Pérez L, Brandt O, Trampert A, Ploog KH, Keller J, et al. Gd-doped GaN: a very dilute ferromagnetic semiconductor with a Curie temperature above 300 K. *Phys Rev B* 2005; 72:245203. <http://dx.doi.org/10.1103/PhysRevB.72.245203>.

Even in such extremely dilute samples, they found ferromagnetism to persist well above room temperature, in fact up to 780 K in some samples [120]. Clearly this paper caused a lot of consternation as well as skepticism. The data by Dhar et al. [120] are reproduced in Fig. 2.8. Several theoretical models were developed soon afterward but none could really explain the reported results quantitatively. The models are discussed in the next subsection.

Quite soon, it became clear from experimental studies that defects play an essential role in obtaining the huge magnetic moments. For example, if the Gd doping was introduced by implantation instead of during growth, the magnetic moment per Gd in the highly dilute limit was even higher [121,122]. Furthermore, annealing the samples decreased the magnetic moments. In other words, the more defects, the higher the magnetic moment. The question then became, what defects are responsible for the magnetic moments and for the ferromagnetism? In that sense the problem became closely related to that of so-called  $d^0$  magnetism. The role of the Gd then became in some sense secondary. In fact, explicit studies of the magnetic moments on Gd atoms by means of magnetic circular dichroism in X-ray absorption showed that the Gd localized magnetic moments were behaving paramagnetically and not following the overall magnetic moment in the system as measured by SQUID, which displays ferromagnetic hysteresis [123,124]. These studies also suggested that some of the Gd was residing in antisites, not on the Ga but on the N site. This, however, was found to be unfavorable by total energy calculations [125] and it was also shown that the X-ray linear dichroism data on which this claim was based could be explained perfectly assuming only Gd on Ga sites [126].

Kammermeier et al. [127] presented an EPR study and found no evidence for a ferromagnetic resonance. They found the signal to be dominated by a substrate SiC EPR signal. They did detect some signals corresponding to GdN in some of the samples with higher concentration. Later, Gehlhoff et al. [128] presented a detailed analysis of the expected  $\text{Gd}^{3+}$  ( $^8S_{7/2}$  ground state with  $S = 7/2$ ) resonant signal and strongly criticized the earlier EPR work by Kammermeier. They showed that the signals found by Kammermeier may all be related to  $\text{Gd}^{3+}$  but, unfortunately, because of the incomplete experimental study by Kammermeier et al. [127] of the magnetic field orientation dependence, the model could not be fully corroborated.

Different magnetic phases as function of temperature were found by Pérez et al. [129]. They distinguished three temperature regimes. Although the middle temperature regime with a critical temperature of about 70 K could correspond to GdN, they provided arguments against this interpretation. The magnetization maintained at high temperatures was ascribed to coupled magnetic clusters surrounding some of the Gd, while the intermediate temperature phase was tentatively associated by them to uncoupled clusters. Sapaga et al. [130] showed through circular dichroism of the photoluminescence that the Gd has an important effect in reversing the spin polarization of the conduction-band electrons even for low Gd concentrations. The PL line studied corresponds to a donor-bound exciton. This seems to relate to the  $s$ - $f$  coupling model discussed later.

Mishra et al. [131] studied the native defects introduced by Gd both in in-situ growth and implanted samples. Using photoconductivity and photothermoelectric power measurements, they found evidence for a large concentration of an acceptor-like defect being formed along with the Gd incorporated during growth. They tentatively identified this with Ga vacancies. For the implanted samples they also find evidence from the XRD measurements for a large defect cluster being formed around each Gd, and in that case,  $\text{Ga}_i$  and  $\text{N}_i$  were identified to be formed. This is mainly based on simulations of the implantation process, which identifies different zones that are either dominated by both interstitials or only  $\text{N}_i$  [122].

Not all studies agreed with the colossal magnetic moments. For example, the study of Gd-implanted metal-organic chemical vapor deposition (MOCVD) GaN by Hejtmanek et al. [132] found much smaller magnetic moments per Gd (of order  $0.7 \mu_B$ ) and showed that only the regions of the sample with small Gd concentration behaved ferromagnetically, while most of the sample near the surface behaved paramagnetically, on top of a large diamagnetic contribution from the substrate. Hite et al. [133] reported a positive effect of Si doping on the ferromagnetic properties of Gd:GaN. They did not, however, manage to quantify the magnetic moment per Gd. The Gd concentrations in the films were below the threshold of secondary ion mass spectroscopy detection, and estimated to be  $< 2 \times 10^{17} \text{cm}^{-3}$ . In a later paper, Hite et al. [134] showed a decrease in magnetic properties under proton irradiation. However, annealing recovered the magnetization.

Asahi et al. [135–137] continued to work on higher concentration Gd-doped GaN. They found signs of GdN precipitates for samples with higher than 7% Gd when grown at high temperature ( $700^\circ\text{C}$ ). In samples of the order 2–6% Gd, they found an increase in lattice constant  $c$  due to Gd, whereas Dhar et al. [120] found a decrease

in lattice constant. Both use molecular beam epitaxy growth but Dhar's group used SiC substrates and Asahi's group used sapphire substrates. Although there may be other differences, it is perhaps significant here that GaN on SiC is usually under tensile strain, while GaN on sapphire is under compressive strain. This results from the differences in thermal expansion coefficients. It seems plausible that under tensile strain, Ga vacancies are more readily formed and accompany the introduction of Gd, while under compressive strain, this is suppressed. As we will later see, Ga vacancies are found to play a key role in explaining the colossal moments.

The lattice constants came back down to GaN-like ones when the precipitation of GdN starts to occur, indicating a strain relieve mechanism. Extended X-ray absorption fine structure measurements provided evidence for incorporation of Gd on Ga sites in wurtzite GaN. These authors obtain magnetic moments per Gd of the order  $0.5-1 \mu_B$ . These are substantially smaller than the  $7 \mu_B$  expected for a  $Gd^{3+}$  ion indicating that perhaps not all the Gd is participating in the ferromagnetic signal. They are far from the colossal moments reported by Dhar et al. [117]. Interestingly, in some samples of high Gd concentration, Ishimaru et al. [138] observed an ordered superlattice of wurtzite, which they explained in terms of alternating layers with different Gd-Ga composition. This indicates some type of phase separation but without forming actual GdN. Takahashi et al. [139] reported an interesting temperature dependence from X-ray magnetic circular dichroism signals, indicating a low-temperature phase, a high-temperature paramagnetic phase, and a third ferromagnetic phase in the range 40–110 K. This should be compared with the temperature dependence studied by Dhar et al. [120] and Pérez et al. [129].

Asahi et al. [135,140] also studied superlattices of alternating GdGaN and GaN and found the magnetic moment per Gd to increase in thinner GdGaN layers and for thicker barrier layers of GaN. As they found the gap to be smaller in the GdGaN layers, the latter were concluded to act as quantum wells with higher electron concentration (or order up to  $10^{18} \text{ cm}^{-3}$ ) and thus the magnetization was attributed to a carrier-mediated coupling. Evidence for coupling between bandgap exciton-polarons to the Gd through a red-shift of the excitons in Gd-doped quantum wells versus undoped ones was presented by Almkohtar et al. [141]. In contrast, the low Gd concentration samples of Dhar et al. [117,120] were found to be mostly semiinsulating.

Larger concentrations of Gd were achieved by Asahi et al. [135,142] up to 12.5% by growing at lower temperatures and these samples showed magnetic moments of an order  $6 \mu_B$  per Gd, approaching the nominal moment for a  $Gd^{3+}$  [136]. These authors also studied Gd doping in InGaN layers and in InGaN/GaN superlattices [135,143]. These studies indicated that if Gd is incorporated in the lower gap InGaN layer where higher concentration of carriers occurs, the magnetization increased whereas in samples where the Gd was incorporated in the GaN barriers, the magnetization was decreased. They also confirmed the enhancement of magnetization by doping with Si.

Jamil et al. [144] reported Gd-doped GaN by MOCVD. They obtained magnetizations of order 40–50 emu/cm<sup>3</sup> but did not measure the Gd concentration independently, so we cannot convert it into moment per Gd. They found no increase when codoping with Si but a decrease when codoping with Mg and activating the Mg acceptors to make the material p-type. They found their material without codoping



to be already n-type (associated according to the authors to O-incorporation) and, remarkably, with higher mobilities than without Gd. They also reported circular polarization of electroluminescence from an InGaN/GaN quantum well sandwiched between p- and n-type GdGaN in an applied magnetic field in Faraday configuration (perpendicular to the films). The degree of circular polarization was interpreted as the result of spin polarization in the GaGdN and studied as a function of magnetic field. However, they report not to find a reversal under the reversal of the sign of the magnetic field. Thus, the meaning of this experimental result is unclear. In a subsequent paper [145], the same group used a different Gd precursor molecule in MOCVD, which was found to achieve higher Gd concentrations but without introducing any oxygen. These samples showed only very weak magnetism, indicating that the oxygen (or at least n-type doping) is essential to the ferromagnetism in Gd:GaN.

## 2.5.2 Models for explaining the magnetism

### 2.5.2.1 Sphere of influence model

The first model to explain the colossal magnetic moment behavior was proposed by Dhar et al. [117] in the first paper and elaborated on in a subsequent paper. The idea was that each Gd would create a sphere of influence around itself in which the spins are polarized. If the system is very dilute each sphere is completely separate from the others and the maximum magnetic moment per Gd occurs. If the spheres overlap, then each region could be part of two or more spheres and the relative moment per Gd goes down. So, this is essentially just a percolation-type theory, which explained the functional behavior with concentration but the question of what causes the magnetization around each Gd in the GaN matrix was left unanswered. In order to explain the observations, a sphere of influence of radius 30 nm was required.

### 2.5.2.2 $s$ - $f$ coupling model

The first attempt to address the origin of the polarization of the medium was by Dalpian and Wei [146]. They noted that in a tetrahedral environment,  $f$  electrons are allowed to interact with  $s$  electrons. This is in contrast to the octahedral environment of GdN, for example, where such interaction is forbidden by symmetry. They showed in small supercell calculations that the CBM, which is Ga-4s-like, becomes spin-split through the interaction with the  $f$  levels. The majority spin  $f$  level is occupied and lies some 8 eV below the Fermi level and pushes up the majority spin  $s$  level of the CBM. The minority spin  $f$  on Gd lies above the CBM and pushes minority spin  $s$  states down. Thus, an opposite spin polarization of the CBM to the magnetic moment of the  $f$  electrons of Gd is predicted. At first, we were concerned that their LDA calculations might have overestimated this effect because in LDA the  $f$  levels lie too close to the gap region. However with LSDA +  $U$  calculations, we obtained qualitatively similar effects. This is illustrated in Fig. 2.9.

As a next step, we attempted to explain more quantitatively how this could lead to magnetic moments much larger than that of Gd. If we combine the spin-splitting with n-type doping of the GaN, for example, through O impurities or Si impurities, then



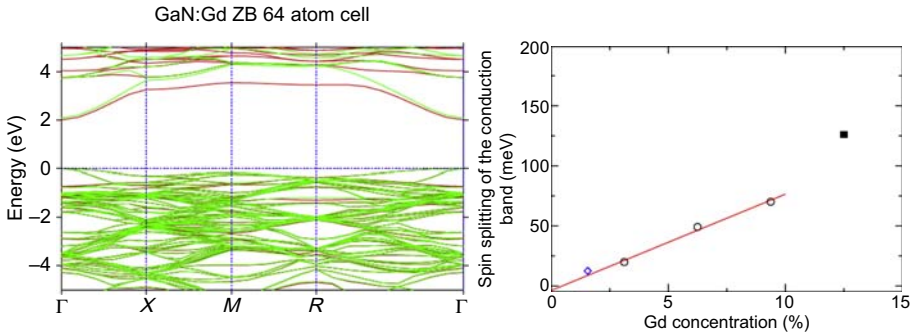


**Figure 2.9** Left: band structure of a 64-atom zinc-blende  $\text{GdGa}_{31}\text{N}_{32}$  supercell, showing the spin polarization of the conduction band. (From Lambrecht WRL, Larson P. Gadolinium and oxygen co-doping of gallium nitride: an LSDA +  $U$  study. In: Symposium I advances in III-V nitride semiconductor materials and devices. MRS proceedings, vol. 955; 2006. <http://dx.doi.org/10.1557/PROC-0955-I01-05>.) Right: spin-splitting of conduction band minimum (CBM) as a function of Gd concentration.

From Mitra C. Computational studies of gadolinium in nitrides: bulk GdN and Gd-doped GaN [Ph.D. thesis]. Case Western Reserve University; 2009.

these electrons could preferentially populate the minority spin CBM states [147]. As we already mentioned in the literature overview, there was indeed some evidence that n-type doping could increase the magnetization [133]. In Dhar's samples [117,120], the oxygen concentration reported to exceed that of Gd by maybe a factor of 1000. Thus conceptually, the large magnetic moments came from the n-type doping filling a spin-split CBM. Clearly, the highest magnetic moment would occur if the minority spin band were completely filled and the majority spin band would remain empty; in other words, if the Fermi level would lie right at the bottom of the majority-spin CBM. Using an isotropic effective mass parabolic band, we can then easily estimate that the density of electrons of one spin is given by  $n = (2m_*E_F/\hbar^2)^{3/2}/6\pi^2$ . The magnetic moment we can achieve in this model is determined by  $E_F = \Delta E_\sigma$  the spin-splitting of the CBM. In order to explain a magnetic moment of order  $4000 \mu_B$  with an n-type dopant concentration of an order  $10^{18}/\text{cm}^3$  and a Gd concentration or order  $10^{15}\text{cm}^{-3}$ , would require a spin-splitting  $\Delta E_\sigma \approx 50$  meV. The problem is, of course, that the spin-splitting is proportional to the concentration of Gd and in this dilute limit is way below this value, in fact, incalculably small. Chandrima Mitra [148] performed calculations of the splitting per Gd in different size supercells of decreasing Gd concentration and found the splitting to vary linearly with the concentration and hence to become negligible for the concentrations at the ppm level. So, this model cannot explain the colossal moments. Can it explain the ferromagnetism? In fact, it turns out that we and both Dalpian and Wei [146] found Gd spins to be antiferromagnetically coupled rather than ferromagnetically. In their paper Dalpian and Wei claimed that the coupling became ferromagnetic in the presence of n-type dopants but we found the opposite.

### 2.5.2.3 Ga vacancies

The next model was proposed by Liu et al. [149]. They proposed that Ga vacancies lead to a strong exchange between GaN-VBM N- $p$  states and the Gd- $d$  states that hybridize with the conduction band. They found a strong preference for FM coupling by an order 0.3–0.6 eV/Gd when including  $V_{\text{Ga}}$  next to Gd. The Ga vacancy is found in their calculations to have three minority spin bands in the gap above the VBM. They can support a maximum of 3  $\mu_{\text{B}}$ , which adds to the 7  $\mu_{\text{B}}$  of the  $\text{Gd}^{3+}$  half-filled  $4f$  shell. Thus they proposed the defect responsible for the colossal magnetic moment to be the  $V_{\text{Ga}}$ . In contrast, N-vacancies (n-type doping) led to only a small coupling to Gd magnetic moments and led to either small AFM or FM energy differences of order 1 meV/Gd only while Gd without vacancies gave a negligible energy difference between FM- and AFM-coupled spins on neighboring Gd. A contradiction appears how to explain the positive effect of Si on the magnetism, since the latter's n-type doping would compensate that of the vacancies. We note that all of these calculations assume only short-range magnetic interactions. The occurrence of vacancies in their paper was speculated to be related to the increase in lattice constant produced by the addition of Gd.

At about the same time, Dev et al. [150] also proposed Ga vacancies in GaN could support a magnetic moment between 0 and 3  $\mu_{\text{B}}$ . They emphasized that the N-2 $p$  orbitals are sufficiently localized to support a magnetic moment but at the same time the defect wave functions of these vacancies have a long-range tail that supports interactions between fairly distant neighbors. They found AFM coupling between neutral vacancies but FM coupling between negatively charged vacancies of charge  $-1$  or  $-2$ . They did not include Gd doping in their calculations explicitly but still proposed that the origin of magnetism in that case could be strongly enhanced by the presence of Ga vacancies. At the same time they also proposed ferromagnetism in C-doped ZnO could arise from cation vacancies.

The model of Ga vacancies was further pursued by Gohda and Oshiyama [151]. These authors used cells with up to 576 sites including 71 vacancies and found the magnetic moment to increase linearly with the number of Ga vacancies. They also studied the exchange interactions between pairs of  $V_{\text{Ga}}$ , pairs of  $\text{Gd}_{\text{Ga}}$ , and  $V_{\text{Ga}} - \text{Gd}_{\text{Ga}}$ . They found the latter to be ferromagnetic, while the  $V_{\text{Ga}} - V_{\text{Ga}}$  exchange interaction is smaller and could be antiferromagnetic in some cases depending on the exact positioning in the lattice of the vacancies relative to each other. The Gd–Gd interactions were found to be small. However, they also found complexes of Gd with nearby  $V_{\text{Ga}}$  to be favored, showing a definite binding between the two.

### 2.5.2.4 Critique of the vacancy model

Mitra and Lambrecht [152] criticized the vacancy model on the basis that none of the previous studies took into account the formation energy of vacancies, nor the plausible charge state of this defect. In fact, earlier work in the literature on native point defects in GaN [153,154] shows that the  $V_{\text{Ga}}$  in the neutral charge state is the defect with the highest energy of formation among all native point defects (with the exception of Ga-N antisites) in GaN and is as high as 9 eV. This makes it very difficult to explain the

occurrence of a large concentration of Ga vacancies. For example, we might seriously question how a sample with 576 atoms (or 288 cations) and 71 vacancies, almost 25% of the cation sites, are left vacant can still be stable. The whole rigidity of the lattice would be significantly deteriorated. The assumption here is that the large size of Gd disrupts the growth and causes the formation of vacancies. Gd would make the lattice constant increase and we might think that vacancies would tend to compensate for this effect. Mitra [148] calculated the increase in lattice constant due to a  $\text{Gd}_{\text{Ga}}$  and the decrease in lattice constant due to a  $V_{\text{Ga}}$  and estimated that about 20 vacancies would have to form per Gd in order to keep the lattice constant unchanged. In other words, the Gd increases the lattice constant far more than a  $V_{\text{Ga}}$  reduces it. However, there is no rule that lattice constants should be kept fixed, rather the total energy has to be minimized. Dhar et al. [121] reported a slight decrease in the c-lattice constant and unchanged a-lattice constant for only the highest level of Gd doping. However in Gd implanted samples, a slight increase in c-lattice constant was reported [120]. Also, in Asahi's work [135], an increase in c-lattice constant was reported. Thus in retrospect the fact that the lattice constant in Gd-doped GaN does not strongly increase is some indication that vacancies may form under the growth conditions of Dhar et al. [117,120] but not under all conditions and may explain some of the different behaviors in samples from different groups.

On the other hand, the question is, in what charge state do they occur? The actual samples of Gd-doped GaN are very resistive or semiinsulating, which suggests that the Fermi level lies in the middle of the bandgap. Under these circumstances, the  $V_{\text{Ga}}$  should be in a triple negative charge state according to the calculations of Limpijumngong et al. [154] and hence carry no magnetic moment! In order to have at least  $1 \mu_{\text{B}}$  we need to be in the  $2-$  charge state. The  $2-/\beta-$  transition level lies 1 eV above the VBM. This cannot be completely ruled out but then each  $V_{\text{Ga}}$  brings only one  $\mu_{\text{B}}$  and it becomes more difficult to explain the colossal magnetic moments. In any case, the energy of formation of a  $V_{\text{Ga}}$  stays very high unless the system becomes n-type and definitely the samples are not p-type as required to have large magnetic moments.

### 2.5.2.5 Interstitials

Based on similar considerations, Mitra and Lambrecht [152] rejected the  $V_{\text{Ga}}$  model and instead looked for other defects. Their reasoning was that the magnetic moments are related to nonbonding  $p$  orbitals and hence they looked for other defects such as interstitial N and interstitial O. They found indeed that these defects also provide acceptor-like levels in the gap with magnetic moments of  $3 \mu_{\text{B}}$  per N interstitial and  $2 \mu_{\text{B}}$  per oxygen interstitial. These defect levels lie higher in the gap and thus the neutral charge state in which the maximum magnetic moment occurs can be sustained with Fermi levels in the middle of the gap. Furthermore they showed that the magnetic moments of these interstitials were parallel to the Gd moment if they are next to each other, and finally, Gd–Gd exchange interactions as well as  $\text{N}_i$ – $\text{N}_i$  interactions were found to be substantially ferromagnetic up to at least second and possibly third neighbors as long as one of the  $\text{N}_i$  or  $\text{O}_i$  were nearest neighbor to a Gd. Finally, they proposed that  $\text{O}_i$  could prefer to move close to Gd and form complexes. On an

intuitive basis this relates to the well-known “gettering” effect of RE elements, such as Gd, which have a strong affinity for oxygen. For example, GdN is very unstable in air and quickly oxidizes. Also, Gd prefers to be octahedrally coordinated (as in GdN or Gd<sub>2</sub>O<sub>3</sub>) and the interstitial sites near Gd would essentially be like an octahedral neighbor. Of course oxygen in GaN normally prefers a substitutional site N<sub>O</sub> and in order to convert an O<sub>N</sub> to a O<sub>i</sub> next to a Gd, they had to assume a high N chemical potential.

Nonetheless the model seemed favorable for interstitials. Subsequently, some positive role of oxygen on the magnetism was reported from positron annihilation studies [155] but the occurrence of this oxygen as interstitial was not shown. They concluded however that n-type doping due to O<sub>N</sub> is unlikely in these samples as they had high resistivity. These authors found a remarkable instability of the samples as function of time. Over a period of a few years since growth, several samples lost their initial magnetism. They also did not find support for the vacancy-induced model as the samples with the most stable magnetism were the ones with lower Gd concentration and lower V<sub>Ga</sub> concentration.

Interstitial oxygen was also studied by Liu et al. [156]. These authors found only the so-called split interstitial configuration where an N-O dumb-bell sits on an N site close to one of the Gd, resulted in stable ferromagnetic coupling of the two Gd in the cell, while the channel site resulted in antiferromagnetic coupling. They also studied how these couplings change while adding electrons to simulate n-type doping. On the other hand, they found the split interstitial to have higher energy of formation than the channel site. The latter, however, is in contradiction with the result of Wright [157], who found the split interstitial to have lower energy. This reversal could possibly be due to the presence of Gd in Liu et al. [156], while Wright’s work is on the interstitials by themselves.

### 2.5.2.6 Analysis of exchange interactions

However, as we mentioned in earlier sections, the calculation of exchange interactions by the direct method or comparing total energies is not very reliable. Therefore we decided to study the exchange interactions in a more systematic way through linear response calculations. This was done in a collaboration with Alexander Thiess, a visiting German doctoral student in Lambrecht’s group, and most of the results were reported only in his doctoral thesis [158]<sup>1</sup>. Dr. Thiess had developed the KKR nanocode at the Forschungszentrum in Jülich, in collaboration with Dederichs and Zeller and Blügel. This Green’s function method allows us to study truly large unit cell sizes by exploiting various acceleration schemes and parallelization of the method on the Blue Gene computer architecture. Thus realistic samples of DMSs could be studied with a statistical sampling of the random placement of impurities in different concentrations. The linear response formula for exchange interactions was

<sup>1</sup> Recently also published in Thiess, A., Blügel, S., Dederichs, P.H., Zeller, R. Lambrecht, W.R.L., 2015. Systematic study of the exchange interactions in Gd-doped GaN containing N interstitials, O interstitials, or Ga vacancies. Phys. Rev. B 92, 104418 (Published 17 September 2015).

implemented in this code. Zinc-blende supercells of 512 atoms with various concentrations of interstitial N and O in addition to Gd were studied. A typical concentration would be 8 Gd out of 256 sites or 3.125% and 32 interstitial N sites, in a 512 atom cluster. For the interstitial O studies, 20 interstitial O were used and 3 Gd, so only 1% Gd.

The results confirmed the presence of  $N_i$ -induced defect levels in the gap but now showed a significant fluctuation of the levels as seen in their partial densities of states depending on the mutual interactions between them and the random fluctuations in the potential, resulting from different distances between impurities in a realistic sample with random placement of impurities (see Fig. 2.10). The two different interstitial sites, tetrahedral with lattice N as nearest neighbors or octahedral with Ga as nearest neighbors, showed different energy levels. The magnetic moments also show a significant distribution in values from  $-1$  to  $1$ ; in other words, not all are parallel and the moments were smaller than in the previous calculations by Mitra and Lambrecht [152]. We should keep in mind that these magnetic moments correspond to the muffin-tin region or sphere around the atom and may underestimate the true moments.

Most significantly, however, the exchange interactions between  $N_i$  were found to be mostly antiferromagnetic in nature and quite small, of an order 0 to  $-40$  meV as can be seen in Fig. 2.11. Likewise, exchange interactions between Gd and interstitial N were found to be predominantly antiferromagnetic. Only exchange interactions between the small induced moments on lattice N and nearest-neighbor interstitial N were found to be ferromagnetic. In the linear response method it is also straightforward to study the influence of the Fermi level position on the exchange interactions as they are given directly as an integral up to the Fermi level. From studying this, the origin of the antiferromagnetism was identified by Thiess as being superexchange. Essentially, the majority/minority spin levels of a given  $N_i$  are well separated as occupied/unoccupied, respectively. Under these circumstances we expect antiferromagnetic superexchange as the dominant interaction.

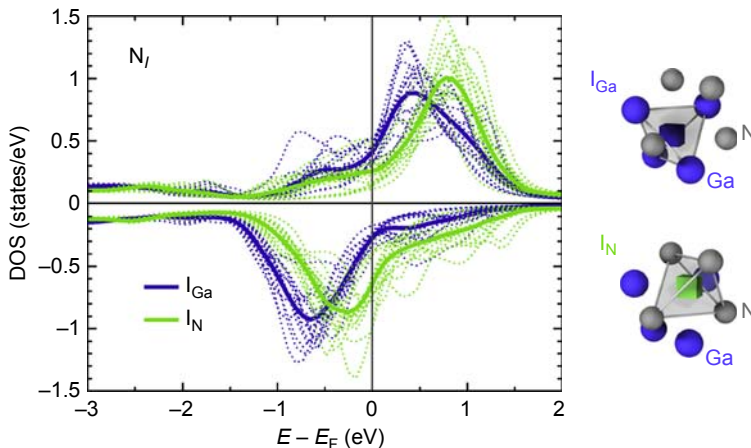


**Figure 2.10** Local density of states on two types of  $N_i$  in GaN.

From Thiess A. Development and application of a massively parallel KKR Green function method for large scale systems [Ph.D. thesis]. RWTH Aachen; 2011.

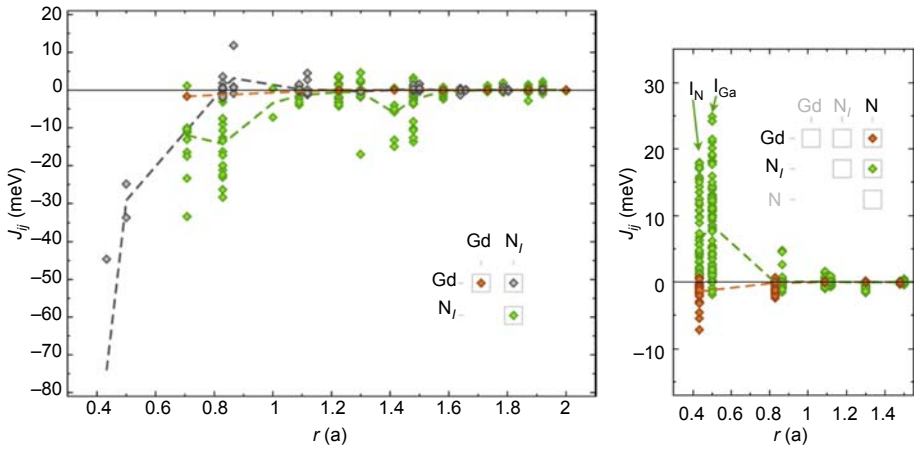


**Figure 2.11** Exchange interactions between (left) Gd and  $N_i$  and (right)  $N_i$  with lattice N, in Gd-doped GaN.

From Thies A. Development and application of a massively parallel KKR Green function method for large scale systems [Ph.D. thesis]. RWTH Aachen; 2011.

In retrospect the ferromagnetic exchange found by Mitra and Lambrecht [152] occurred for some specific  $N_i$  in which at least one of the N was right next to a Gd. In a randomly distributed impurity model and given the low concentration of Gd this is unlikely. Thus isolated  $N_i$  are actually not ferromagnetically but antiferromagnetically coupled. The Gd–Gd interaction was found to be negligible except for very close neighbors, consistent with earlier studies. In summary, no significant ferromagnetic coupling was found and most exchange interactions were found to be very short range and antiferromagnetic in nature.

For oxygen interstitials compared to N interstitials a slightly stronger tendency toward ferromagnetic coupling was found. Although there are still a lot of antiferromagnetic interactions at larger distance, there were about an equal number of ferromagnetic interactions. Again, only interactions with lattice N, which has only small induced moments, are positive, as can be seen in Fig. 2.12. The reasons lie in the smaller energy separation of majority and minority spin states of the interstitial O compared to the interstitial N. This leads to a competition between ferromagnetic double exchange and antiferromagnetic superexchange. Nonetheless these interactions are still too short range to explain an overall ferromagnetic behavior.

### 2.5.2.7 Ga-vacancy clusters

These negative results led us to reexamine the Ga vacancy model. Simulations were done for a model with 32  $V_{Ga}$  and 4  $Gd_{Ga}$ . The electronic structure revealed again defect states in the gap close to the VBM. An increasing partial density of states (PDOS) was found in the gap for N near to more than one  $V_{Ga}$  and the deepest levels occurred for N close to 3  $V_{Ga}$ . Examining the distribution of magnetic moments in this case, as seen in Fig. 2.13, immediately led to an important clue. The magnetic moment induced on N increased linearly with the number of nearest neighbor Ga atoms that were missing for this N.

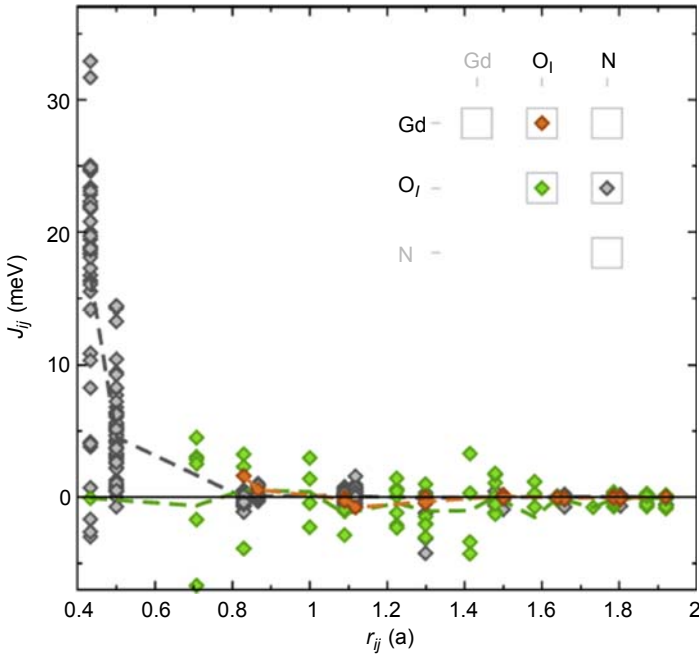


**Figure 2.12** Exchange interactions of interstitial O with Gd, lattice N, and other  $O_i$ . From Thiess A. Development and application of a massively parallel KKR Green function method for large scale systems [Ph.D. thesis]. RWTH Aachen; 2011.

Second, the model investigated, shown in Fig. 2.14 although the defects were introduced randomly, happened to have a somewhat clustered occurrence of the vacancies and the magnetic moments tended to be closely related to this vacancy cluster. This led

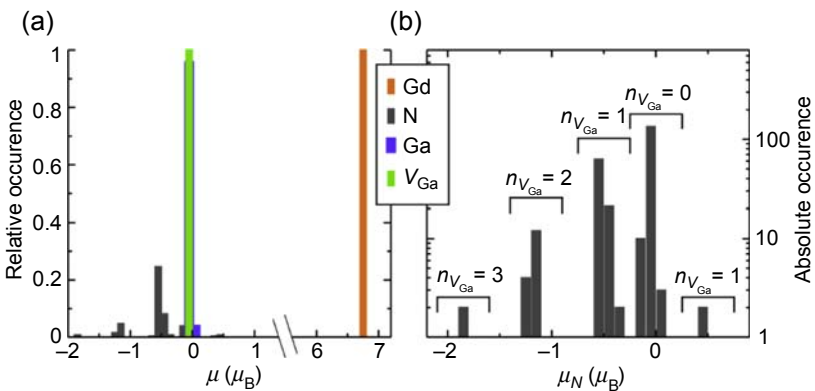


**Figure 2.13** Magnetic moments in  $Gd_{220}Gd_4N_{256}$  supercell, containing 4  $Gd_{rmGa}$ , and 32  $V_{Ga}$ . Note that the moments on N increase with the number of  $V_{Ga}$  they are nearest neighbor to. From Thiess A. Development and application of a massively parallel KKR Green function method for large scale systems [Ph.D. thesis]. RWTH Aachen; 2011.



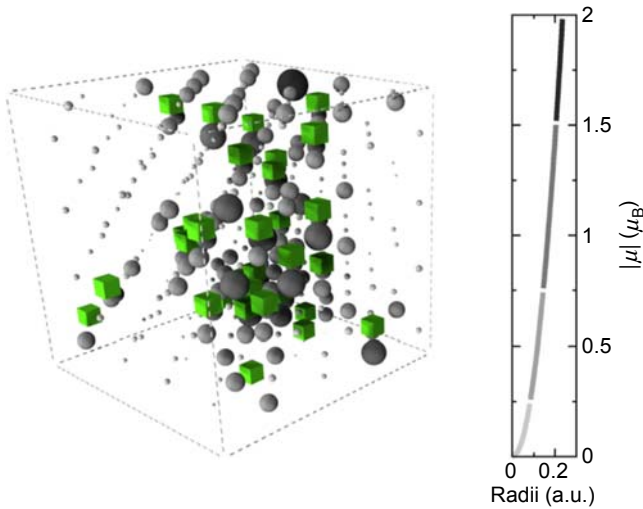


**Figure 2.14** Ga vacancies (*square green boxes*) in simulation cell and magnetic moments in N atoms near vacancies indicated by the size of the spheres. The more vacancies an N is close to the larger its magnetic moment. Also note the clustering of the moments and vacancies. From Thiess A. Development and application of a massively parallel KKR Green function method for large scale systems [Ph.D. thesis]. RWTH Aachen; 2011.

us to further study the occurrence of clusters as discussed in [Section 2.5.3](#). The magnetic moments of a  $V_{\text{Ga}}$  occur mostly on its nearest neighbor N sites.

Because of the small concentration of Gd in the cell, the most statistically significant exchange interactions to be studied are among N atoms in particular N atoms adjacent to  $V_{\text{Ga}}$ . The exchange interactions for the gallium vacancy case are shown in [Fig. 2.15](#).

These were found to be ferromagnetic and of order a few meV for near neighbors. They were larger if the vacancy occurred between the two N atoms. Gd-N atom interactions were also found to be ferromagnetic. Although in this case for the first time predominantly ferromagnetic interactions were found, they are still relatively short range only. Nonetheless there is an important difference between  $V_{\text{Ga}}$  and the other cases in terms of percolation theory.

### 2.5.2.8 Results of percolation theory

The fact that magnetic moments near  $V_{\text{Ga}}$  are located on the neighboring N rather than on the site of the vacancy itself, or by comparison with the  $\text{Gd}_{\text{Ga}}$  or  $\text{N}_i$  or  $\text{O}_i$  where the moment is located on the Gd or interstitial directly, has an important consequence for percolation theory. Ga vacancies that are fourth neighbor to each other still have N neighbors with magnetic moments on them that are nearest neighbors to each other, as can be seen in [Fig. 2.16](#).

Thus building a percolated network of  $V_{\text{Ga}}$  can be achieved at much lower concentration of vacancies than for magnetic moments directly located on the impurity site,



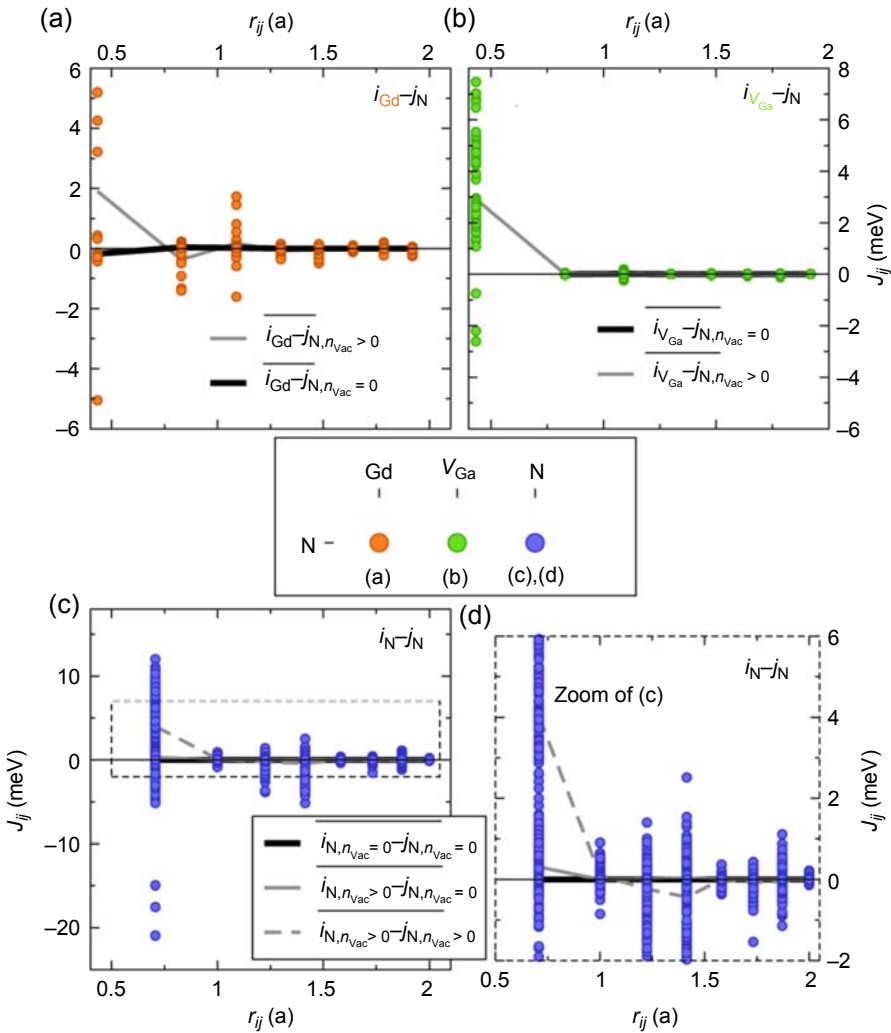


**Figure 2.15** Magnetic exchange interactions between Gd,  $V_{\text{Ga}}$ , and N. From Thiess A. Development and application of a massively parallel KKR Green function method for large scale systems [Ph.D. thesis]. RWTH Aachen; 2011.

which might only interact between nearest neighbors. Thiess determined the percolation threshold to be 4.8%, consistent with estimates of the percolation threshold in fcc lattices for fourth neighbor interactions of about 5% [85]. In contrast, for nearest neighbor interactions on an fcc lattice, the percolation threshold is about 20% [159]. Thus magnetism can occur for much lower concentrations of vacancies than other impurities. This was further confirmed by Thiess in his thesis by performing Monte Carlo simulations of the magnetization as function of temperature for different concentrations.

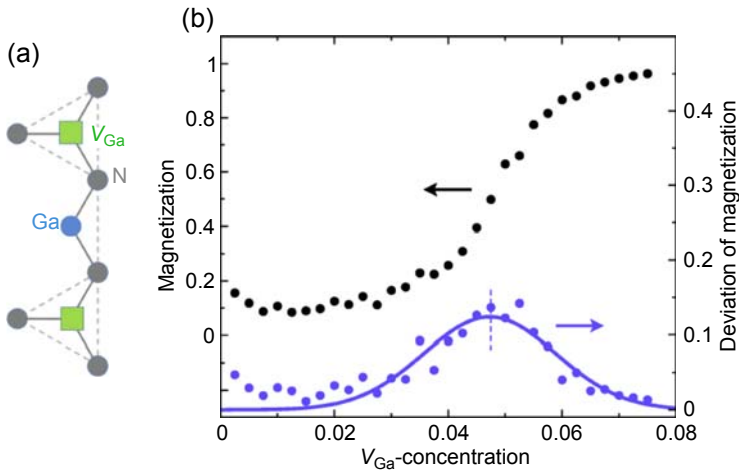


**Figure 2.16** Percolation with Ga vacancies. (a) Two  $V_{\text{Ga}}$  at fourth-nearest neighbor distance still have magnetic moment carrying N, which are nearest neighbor to each other. (b) Normalized magnetization of the largest cluster and its deviation in a Monte Carlo simulation of an 8000 atom GaN cell, taking into account  $V_{\text{Ga}}$  to be coupled when at a distance  $d < \sqrt{2}a$  with a, lattice constant. The peak in the deviation curve gives the percolation threshold.

From Thiess A. Development and application of a massively parallel KKR Green function method for large scale systems [Ph.D. thesis]. RWTH Aachen; 2011.

### 2.5.2.9 Fermi-level pinning near clusters

The previous results on  $V_{\text{Ga}}$  suggested strongly that  $V_{\text{Ga}}$  clustering could help to establish ferromagnetism. In fact, the more  $V_{\text{Ga}}$  an N is neighbor to, the larger its magnetic moment and the stronger the ferromagnetic exchange interactions. The clustering could resolve another puzzle mentioned earlier. In all the previous calculations, the vacancies were assumed to be in a neutral charge state. On the other hand, as discussed earlier, isolated  $V_{\text{Ga}}$  would be in a negative charge state if the Fermi level is in the middle of the gap or higher. However, if vacancies cluster then the Fermi level may become pinned by the vacancy states themselves. Likewise, any type of extended defects, or surfaces or grain boundaries, tend to pin the Fermi level. The Fermi level in a system is determined by the overall charge balance. On a macroscopic scale this is set by the average concentrations of various dopants and native defects, but near extended defects the local Fermi level can be pinned. In other words, the defect itself calls the shots locally and determines whether a state is occupied or not. Band bending then occurs near such defects, so that the overall Fermi level in the system is still uniform. This is well established way of thinking for surfaces and grain boundaries, and also for dislocations. We usually consider the Fermi level as an independent control parameter only for isolated point defects but not for such extended defects. As we have seen, only a neutral  $V_{\text{Ga}}$  can have a magnetic moment of  $3 \mu_{\text{B}}$ . The occurrence of vacancy clusters would thus invalidate one of our earlier objections against isolated vacancies, namely that they would be likely to be in a triple negative

charge state and hence without magnetic moment. As soon as the vacancies are allowed to cluster they are allowed to stay locally neutral and hence to have a magnetic moment.

### 2.5.3 Growth simulations of clustering

This led us to the question if vacancies are likely to cluster. To this end, Thiess performed growth simulations. Based on the local energies of atoms in the electronic structure simulations, it emerged that the energy of an N increases with the number of vacancies it has as neighbor and decreases with the number of Gd near to it. Kinetic Monte Carlo simulations were then carried out in the following manner. Atoms are deposited layer by layer. A fixed concentration of  $V_{\text{Ga}}$  and Gd per layer was allowed. We start from a complete (001) N layer in the zinc-blende structure. Ga or Gd or  $V_{\text{Ga}}$  are then deposited randomly in the prescribed concentrations and allowed to hop around, or exchange places with each other so as to minimize the energy based on the local energy rules. Because N atoms have different energy near a  $V_{\text{Ga}}$  or Gd or Ga, this leads to an optimal redistribution of the latter in the Ga-Gd layer. After the layer is finished, the next N layer is deposited and the procedure is repeated. After the layers are finished, they are not allowed to further relax. In other words, the surface configuration is frozen in. It was found that compared to random placement of the  $V_{\text{Ga}}$  significant clustering of vacancies occurred in this model. This is comparable to spinodal decomposition. Ga vacancies and Ga atoms phase separate. Clusters of different sizes and different geometric shapes were found to be incorporated in the simulation cell. While this model of growth is rather primitive and is not meant to simulate growth realistically, it led to interesting new overall simulation models on which the magnetic exchange interactions and magnetism could then be studied statistically.

For these magnetic simulations, which used the Monte Carlo metropolis algorithm, the Gd atoms were actually completely ignored. The exchange interactions and magnetic moments were assigned average values as obtained from the earlier calculations. In other words, N atoms nearest neighbors to  $V_{\text{Ga}}$  atoms were assigned a magnetic moment and only near-neighbor exchange interactions were included. Monte Carlo simulations of the magnetization as function of temperature were carried out for both a model in which vacancies were placed randomly and the growth model. Note that Monte Carlo simulations of two different types are combined here: first kinetic Monte Carlo simulations to simulate the clustering of vacancies and generate models of the distribution of vacancies. Second, Monte Carlo simulations of the magnetization are carried out in which the magnetic moments are allowed to flip so as to optimize the free energy at a given temperature of these moments, in interaction with each other through a prescribed set of exchange interactions. The resulting magnetization as function of temperature is obtained and lets us determine the transition temperature on a magnetic sample.

Interestingly, two temperature regimes could be discerned in these simulations. This is shown in Fig. 2.17. At first, the magnetization drops sharply but then a long tail persists. The latter has a higher magnetization remaining in the growth generated

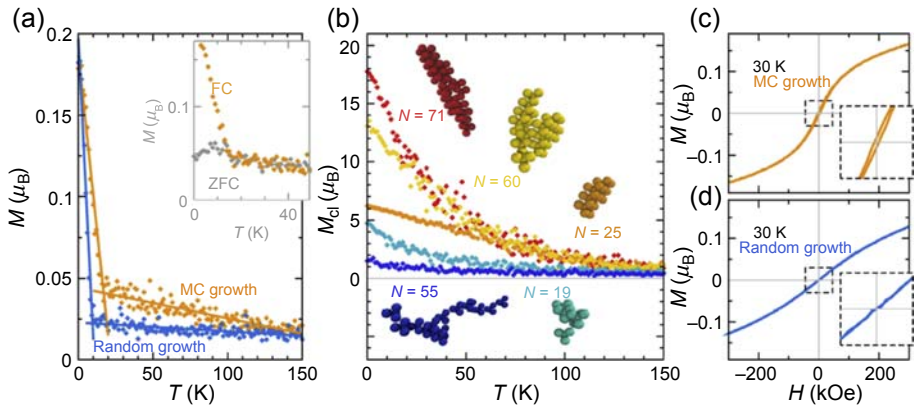


**Figure 2.17** (a) Normalized magnetization as function of temperature from Monte Carlo simulations of a random (RG) and growth generated model of GaN with  $V_{\text{Ga}}$ . The kinetic Monte Carlo generated model (MCG) has clustered vacancies. The inset shows zero-field and field-cooled magnetization curves. (b) Total magnetization of specific clusters occurring in the MCG model is color coded. (c) Hysteresis curves for RG and MCG models.

From Thiess A, Dederichs PH, Zeller R, Blügel S, Lambrecht WRL. Superparamagnetism in Gd-doped GaN induced by Ga-vacancy clustering. *Phys Rev B* 2012;86:180401. <http://dx.doi.org/10.1103/PhysRevB.86.180401> and unpublished. (Private communication with A. Thiess).

model. Calculations were also done starting from randomized spins or with the spins initially aligned. The latter compares in some sense to a field-cooled situation whereas the model starting from randomly oriented spins corresponds to zero-field cooling. Analysis of the results indicates that the first drop in magnetization versus temperature corresponds to a loss of the overall magnetization of the sample in which the clusters had originally aligned magnetizations, whereas in the high-temperature phase, the magnetic moments still persisted within the clusters but the correlation between clusters was lost. Further study of the magnetic moment in individual clusters showed that the cluster moment decay versus temperature depends crucially on the size and shape of the cluster. The more compact and three-dimensional the clusters, in other words, the higher the coordination of individual magnetic atoms with nearby ones, the slower the decay. The results strongly indicate that this system is superparamagnetic rather than truly ferromagnetic. The hysteresis found in the simulations only occurs for the clustered models. This hysteresis results from the finite time of the Monte Carlo simulations. This model does not include magnetic anisotropy effects, which play a role in the actual hysteresis phenomenon.

### 2.5.3.1 Experimental evidence for clustering and role of extended defects

The simulated magnetizations versus temperature show a remarkable resemblance to the experimental data of Dhar et al. [120], which also show two (or even three) temperature regions with distinct properties. These are reproduced here for convenience

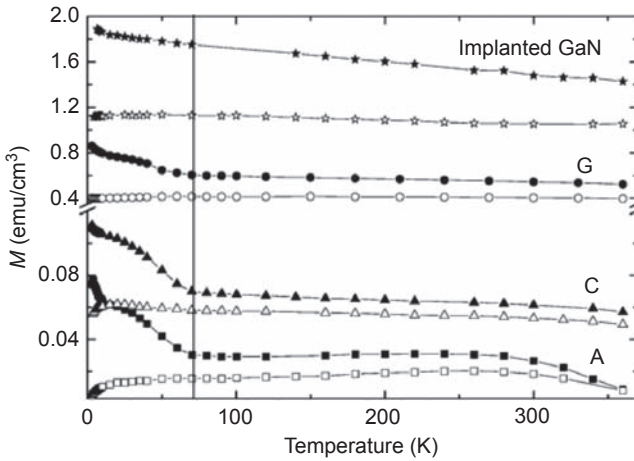


**Figure 2.18** Magnetization of Gd-doped GaN for different samples under field-cooled (*solid symbols*) and zero-field cooled conditions. The samples A–I have increasing of concentration of Gd.

From Dhar S, Pérez L, Brandt O, Trampert A, Ploog KH, Keller J, et al. Gd-doped GaN: a very dilute ferromagnetic semiconductor with a Curie temperature above 300 K. *Phys Rev B* 2005; 72:245203. <http://dx.doi.org/10.1103/PhysRevB.72.245203>.

in Fig. 2.18. The temperature cut-off of the initial rapid drop-off does not agree with experiments but the calculations were meant to simulate the qualitative behavior, not to actually reproduce experimental temperatures, which might depend more intricately on the exchange interactions. In fact, they seem to agree more with the first temperature phase in the experiment as identified by Pérez et al. [129]. The second temperature range in the experiment between 10 and 70 K could conceivably still be due to undetected regions of GdN, which have, after all, been found to be present in detectable concentrations for higher concentrations of Gd. The existence of a high-temperature tail would then be ascribed to superparamagnetism inside the clusters.

In the calculations, even a similar hysteresis under cycling the magnetic field was obtained. The latter narrow hysteresis curves were found only in the cluster growth model but not in the random model, which showed no hysteresis at all. This, however, should not be taken too seriously, because the actual physical mechanisms leading to hysteresis, such as magnetic anisotropy, were not included in the model. In the model the hysteresis may occur because the system does not get fully in equilibrium because of the short simulation times. Nonetheless, the difference between the two growth models has some significance and shows that the different degree of clustering plays a role. In the final version of the paper, the hysteresis curves were left out because of lack of space to adequately explain this. Nonetheless, it shows that the model with random  $V_{\text{Ga}}$  behaves essentially paramagnetically whereas the model with clusters behaves superparamagnetically. The two temperature regimes are a clear indication of the superparamagnetism located in clusters rather than an overall percolated

magnetism throughout the sample. These simulations showed that a cluster vacancy model is essential to explain the observed magnetic behavior versus temperature and the narrow hysteresis loops. As mentioned earlier an extended type of defect is also essential to explain why vacancies can stay neutral, pin the Fermi level, and hence maintain a magnetic moment at all.

### 2.5.3.2 Discussion

Although the growth model may be somewhat unrealistic and does not explain the concentration of vacancies, some key elements emerged from this study. In fact, the clustering itself is the key issue, not how it is obtained. The concentration of Ga vacancies was set as an input rather than an outcome of the simulations, but the fact that they tended to cluster is a significant outcome of the simulations. As such, they allow pinning of the Fermi level and hence keep the vacancies in a neutral charge state, which supports a large magnetic moment per vacancy. Second, the magnetic simulations of the magnetization in clustered versus unclustered models show clearly that the magnetization has two temperature regimes in agreement with the experiment and indicating first a loss of correlation of magnetic moments between clusters and later at higher temperature inside the clusters. So, the high-temperature magnetization seen in the real samples may also be assumed to be superparamagnetism inside clusters. The latter is further evidenced by the narrow hysteresis loops, which are characteristic of superparamagnetism. As discussed in the literature overview, ample evidence for the occurrence of a large amount of defects near Gd has been established and some of it points indeed to vacancies.

A disconcerting point of the result may be that the results seem to have little to do with Gd in the first place. Does it mean that just highly disordered GaN with clusters of Ga vacancies but no Gd would already be superparamagnetic? Clearly, this has not been found experimentally. We did find some tendency for Gd to cluster near the vacancy clusters and we may thus view the role of Gd as twofold. First, it seems to perturb the growth. We have already mentioned that it would tend to increase the lattice constant because of its large size, and formation of vacancies is a way to compensate for this overall lattice expansion. Second, in Gd implantation it is not surprising that vacancies would be created in fairly large amounts as this also happens with other energetic implantations. Also, its magnetic moments seem to provide a sort of trigger for initiating magnetic moments in nearby N next to Ga vacancies.

There are some further experimental indications in favor of the clustering model. First, positron annihilation experiments [155] did find fairly large Ga vacancy concentrations and indicate that they occur in clusters or voids. Unfortunately, the measurements do not provide further detail about the size of such voids or vacancy clusters. While these measurements did not find a clear correlation between the presence or absence of magnetism in the samples with the degree of clustering or presence of vacancies, they do provide at least evidence of vacancy clusters. Also the study by Mishra et al. [131] found the presence of native defects with an energy level closely above the VBM and hence compatible with Ga vacancies to be related to the magnetism in low-concentration Gd-doped samples.

We caution that besides vacancy clusters arising during growth as proposed in Thiess's model, other extended defects could play a significant role. For example, Kent et al. [161] observed a significant amount of dislocations oriented parallel to the growth direction. This study was focused on creating GdN/GaN superlattices and found a  $T_C$  consistent with GdN. However, magnetism persisted up to higher temperatures and was strongly anisotropic and therefore presumably related to the dislocation network. Some dislocations in GaN have empty cores and could thus be locally similar to vacancy clusters as studied by Thiess. The work of Dhar et al. [120] also shows significant amounts of dislocations in the samples. Furthermore, anisotropy was also detected in their samples [129], but in fact in their samples the easy axis was found to be in plane, rather than along the growth direction as found by Kent et al. [161].

### 2.5.4 Summary

In summary, the magnetism in Gd-doped GaN is a complex phenomenon. There seem to be two different regimes with rather different properties. At higher concentrations of Gd and assisted by n-type doping, there appears to exist a carrier-mediated magnetic interaction between Gd local moments maintaining ferromagnetic behavior at room temperature. In order to achieve high enough Gd concentrations without forming GdN precipitates, and activate the Gd so that the net magnetizations per Gd approach that of a  $Gd^{3+}$ , low-temperature growth (300 K) is required. However, no evidence of colossal magnetic moments is present in these samples and this magnetism appears to be similar to other DMS based on TM doping and explainable by standard carrier-mediated interactions. For a concentration of the order of 8–12%, significant splittings of the CBM of an order 50–80 meV are expected based on Mitra's [148] calculations. Shallow donor states due to Si or other shallow donors could then also be spin-split. The fact that even for the largest concentrations of Gd the net magnetic moment per Gd is still less than  $7 \mu_B$  and could result from the opposite spin polarization of the donor states to the Gd-4f. Nonetheless, these donor states could provide significant carrier-mediated coupling between the localized Gd moments. The shallow donors are quite extended and could provide long-range coupling. The fact that in this case and unlike most other DMSs we have electrons rather than holes achieving the coupling is interesting. Spin relaxation times in semiconductors tend to be longer from electrons than holes and thus an n-type DMS is potentially advantageous for spintronic transport applications.

On the other hand for extremely dilute concentrations the situation is different. We can fairly confidently say that the occurrence of magnetic moments exceeding those of the  $Gd^{3+}$  is related to defect magnetism rather than Gd. The Gd primarily acts to perturb the growth and create extended defects such as vacancy clusters or dislocation networks to which the Gd may segregate. Large concentrations of vacancies of the order of 10–20 per Gd would help the lattice constant of GaN to stay fixed and avoid tensile strain. Growth simulations indicate that Ga vacancies tend to cluster. Such extended defects can pin the Fermi level and locally keep  $V_{Ga}$  in the neutral charge state that is required to have the maximum magnetic moment per vacancy. The magnetic moments inside a cluster are then more strongly correlated than between



clusters and lead to a superparamagnetism rather than ferromagnetism. This is evidenced experimentally in the two temperature regimes of the decay of the magnetization as function of temperature and the narrow width of the hysteresis loops. The precise interplay of the Gd magnetic moments and the large vacancy clusters is still not fully understood. The nitrogen and oxygen interstitials are far less likely to contribute to ferromagnetism because their exchange interactions are too short-ranged. A key point here is that for a vacancy the magnetic moments occur on the N neighboring the vacancy and hence percolation is possible for a much lower concentrations of only 5% in spite of the vacancies themselves being fourth neighbors, the N attached to them are still nearest neighbors. If in addition there is indeed a tendency for vacancies to cluster and for Gd to segregate toward the surface of  $V_{\text{Ga}}$  clusters, then we start obtaining a coherent picture for the high-temperature magnetism and the colossal magnetic moments in extremely dilute samples. The positive effects of oxygen are unlikely to be due to interstitial O magnetic moments but rather due to the n-type doping effect of O, which can further produce some type of carrier-mediated exchange between cluster moments. Unfortunately, this inhomogeneous type of magnetism and the resulting potential fluctuations may also lead to localization and hence the semiinsulating nature of such samples. This means the carriers may stay away from the magnetic regions and this means they cannot be used for spintronics.

From a methodological point of view, the message from this case study is not to jump to conclusions. It is key to study the exchange interactions in a statistically meaningful manner and not based on a fortuitous close placement of the magnetic defects in each other's immediate proximity. The linear response method of calculating exchange interactions realistically and the use of large enough models with randomly placed defects and magnetic centers at realistic distances from each other was key in sorting out the behavior of these systems. Furthermore, the study by Thiess et al. [160] demonstrates the added insights we gain from combining first-principles calculations with Monte Carlo simulations of the actual magnetic properties and the interplay between the inhomogeneous distribution of magnetic centers in the system with their overall magnetic properties. This last point has also been strongly emphasized in the work of Sato et al. [85] for many TM-doped systems. The occurrence of spinodal decomposition in such systems is very similar to the occurrence of vacancy clusters found in the Gd:GaN system.

## Acknowledgments

First, I wish to thank the graduate students and post-doctorates who worked with me on various aspects of dilute magnetic semiconductors. Maosheng Miao worked on TM-doped SiC and on various transition metal nitrides. Paul Larson worked on LSDA +  $U$  in rare-earth nitrides and our first calculations on the Gd:GaN system. Aditi Herwadkar worked on the Mn-doped ScN system. Chandrima Mitra worked on the Gd-doped GaN. Tawinan Cheiwchanchamnangij worked on Gd-doped GaN site dependence. A special thanks goes to Alexander Thiess for letting me quote several of the results from his PhD that had not yet been published in journal form during the writing of this chapter, although see footnote page 79. Second, the work of our



group on dilute magnetic semiconductors was supported by NSF, Army Research Office at different times, and the work on point defects in semiconductors is currently supported by NSF and DOE.

## References

- [1] Žutić I, Fabian J, Das Sarma S. Spintronics: fundamentals and applications. *Rev Mod Phys* 2004;76:323–410. <http://dx.doi.org/10.1103/RevModPhys.76.323>.
- [2] Li DX, Haga Y, Shida H, Suzuki T, Kwon YS, Kido G. Magnetic properties of stoichiometric Gd monpnictides. *J Phys Condens Matter* 1997;9(48):10777. <http://stacks.iop.org/0953-8984/9/i=48/a=019>.
- [3] Granville S, Ruck BJ, Budde F, Koo A, Pringle DJ, Kuchler F, et al. Semiconducting ground state of GdN thin films. *Phys Rev B* 2006;73:235335. <http://dx.doi.org/10.1103/PhysRevB.73.235335>.
- [4] Matthias BT, Bozorth RM, Van Vleck JH. Ferromagnetic interaction in EuO. *Phys Rev Lett* 1961;7:160–1. <http://dx.doi.org/10.1103/PhysRevLett.7.160>.
- [5] Wachter P. Handbook on the physics and chemistry of rare earths, vol. 2. Amsterdam: Elsevier; 1979.
- [6] An JM, Belashchenko KD. Electronic structure and magnetic properties of Gd-doped and Eu-rich EuO. *Phys Rev B* 2013;88:054421. <http://dx.doi.org/10.1103/PhysRevB.88.054421>.
- [7] Nagata S, Galazka RR, Mullin DP, Akbarzadeh H, Khattak GD, Furdyna JK, et al. Magnetic susceptibility, specific heat, and the spin-glass transition in  $\text{Hg}_{1-x}\text{Mn}_x\text{Te}$ . *Phys Rev B* 1980;22:3331–43. <http://dx.doi.org/10.1103/PhysRevB.22.3331>.
- [8] Munekata H, Ohno H, von Molnar S, Segmüller A, Chang LL, Esaki L. Diluted magnetic III-V semiconductors. *Phys Rev Lett* 1989;63:1849–52. <http://dx.doi.org/10.1103/PhysRevLett.63.1849>.
- [9] De Boeck J, Oesterholt R, Van Esch A, Bender H, Bruynseraede C, Van Hoof C, et al. Nanometer-scale magnetic MnAs particles in GaAs grown by molecular beam epitaxy. *Appl Phys Lett* 1996;68(19):2744–6. <http://dx.doi.org/10.1063/1.115584>.
- [10] Ohno H, Shen A, Matsukura F, Oiwa A, Endo A, Katsumoto S, et al. (Ga,Mn)As: a new diluted magnetic semiconductor based on GaAs. *Appl Phys Lett* 1996;69(3):363–5. <http://dx.doi.org/10.1063/1.118061>.
- [11] Bockstal LV, Esch AV, Bogaerts R, Herlach F, van Steenberg A, Boeck JD, et al. Magnetic interactions with charge carriers in III-V diluted magnetic semiconductors. *Phys B Condens Matter* 1998;246–247(0):258–61. [http://dx.doi.org/10.1016/S0921-4526\(97\)00910-1](http://dx.doi.org/10.1016/S0921-4526(97)00910-1).
- [12] Van Esch A, Van Bockstal L, De Boeck J, Verbanck G, van Steenberg AS, Wellmann PJ, et al. Interplay between the magnetic and transport properties in the III-V diluted magnetic semiconductor  $\text{Ga}_{1-x}\text{Mn}_x\text{As}$ . *Phys Rev B* 1997;56:13103–12. <http://dx.doi.org/10.1103/PhysRevB.56.13103>.
- [13] Samarth N. An introduction to semiconductor spintronics. In: Ehrenreich H, Spaepen F, editors. *Solid state physics, Advances in research and applications*, vol. 58. Academic Press; 2004. p. 1–72.
- [14] Chen L, Yan S, Xu PF, Lu J, Wang WZ, Deng JJ, et al. Low-temperature magnetotransport behaviors of heavily Mn-doped (Ga,Mn)As films with high ferromagnetic transition temperature. *Appl Phys Lett* 2009;95(18):182505. <http://dx.doi.org/10.1063/1.3259821>.

- [15] Jungwirth T, Wang KY, Mašek J, Edmonds KW, König J, Sinova J, et al. Prospects for high temperature ferromagnetism in (Ga,Mn)As semiconductors. *Phys Rev B* 2005;72:165204. <http://dx.doi.org/10.1103/PhysRevB.72.165204>.
- [16] Wang H, Chen L, Zhao J. Enhancement of the Curie temperature of ferromagnetic semiconductor (Ga,Mn)As. *Sci China Phys Mech Astron* 2013;56(1):99–110. <http://dx.doi.org/10.1007/s11433-012-4959-3>.
- [17] Zunger A, Lany S, Raebiger H. The quest for dilute ferromagnetism in semiconductors: guides and misguides by theory. *Physics* 2010;3:53. <http://dx.doi.org/10.1103/Physics.3.53>.
- [18] Filhol J-S, Jones R, Shaw MJ, Briddon PR. Structure and electrical activity of rare-earth dopants in GaN. *Appl Phys Lett* 2004;84(15):2841–3. <http://dx.doi.org/10.1063/1.1710710>.
- [19] Svane A, Christensen NE, Petit L, Szotek Z, Temmerman WM. Electronic structure of rare-earth impurities in GaAs and GaN. *Phys Rev B* 2006;74:165204. <http://dx.doi.org/10.1103/PhysRevB.74.165204>.
- [20] Sanna S, Hourahine B, Gerstmann U, Frauenheim T. Efficient tight-binding approach for the study of strongly correlated systems. *Phys Rev B* 2007;76:155128. <http://dx.doi.org/10.1103/PhysRevB.76.155128>.
- [21] Sanna S, Schmidt WG, Frauenheim T, Gerstmann U. Rare-earth defect pairs in GaN: LDA +  $U$  calculations. *Phys Rev B* 2009;80:104120. <http://dx.doi.org/10.1103/PhysRevB.80.104120>.
- [22] Mahadevan P, Zunger A. First-principles investigation of the assumptions underlying Model-Hamiltonian approaches to ferromagnetism of 3d impurities in III-V semiconductors. *Phys Rev B* 2004;69:115211. <http://dx.doi.org/10.1103/PhysRevB.69.115211>.
- [23] Zunger A. Electronic structure of 3d transition-atom impurities in semiconductors. In: Ehrenreich H, Turnbull D, editors. *Solid state physics, Advances in research and applications*, vol. 39. Academic Press; 1986. p. 275–464.
- [24] Condon E, Shortley GH. *The theory of atomic spectra*. Cambridge University Press; 1959.
- [25] Racah G. Theory of complex spectra. I. *Phys Rev* 1942;61:186–97. <http://dx.doi.org/10.1103/PhysRev.61.186>.
- [26] Racah G. On a new type of vector coupling in complex spectra. *Phys Rev* 1942;61:537. <http://dx.doi.org/10.1103/PhysRev.61.537>.
- [27] Racah G. Theory of complex spectra. II. *Phys Rev* 1942;62:438–62. <http://dx.doi.org/10.1103/PhysRev.62.438>.
- [28] Racah G. On the configurations II's. *Phys Rev* 1942;62:523–5. <http://dx.doi.org/10.1103/PhysRev.62.523>.
- [29] Racah G. On the decomposition of tensors by contraction. *Rev Mod Phys* 1949;21:494–6. <http://dx.doi.org/10.1103/RevModPhys.21.494>.
- [30] Racah G. Theory of complex spectra. IV. *Phys Rev* 1949;76:1352–65. <http://dx.doi.org/10.1103/PhysRev.76.1352>.
- [31] Dieke GH, Crosswhite HM. The spectra of the doubly and triply ionized rare earths. *Appl Opt* 1963;2:675–86.
- [32] Hohenberg P, Kohn W. Inhomogeneous electron gas. *Phys Rev* 1964;136(3B):B864–71. <http://dx.doi.org/10.1103/PhysRev.136.B864>.
- [33] Kohn W, Sham LJ. Self-consistent equations including exchange and correlation effects. *Phys Rev* 1965;140(4A):A1133–8. <http://dx.doi.org/10.1103/PhysRev.140.A1133>.

- [34] Perdew JP, Burke K, Ernzerhof M. Generalized gradient approximation made simple. *Phys Rev Lett* 1996;77(18):3865–8. <http://dx.doi.org/10.1103/PhysRevLett.77.3865>.
- [35] Anisimov VI, Zaanen J, Andersen OK. Band theory and Mott insulators: Hubbard U instead of Stoner I. *Phys Rev B* 1991;44(3):943–54. <http://dx.doi.org/10.1103/PhysRevB.44.943>.
- [36] Anisimov VI, Solovyev IV, Korotin MA, Czyżyk MT, Sawatzky GA. Density-functional theory and NiO photoemission spectra. *Phys Rev B* 1993;48:16929–34. <http://dx.doi.org/10.1103/PhysRevB.48.16929>.
- [37] Liechtenstein AI, Anisimov VI, Zaanen J. Density-functional theory and strong interactions: orbital ordering in Mott-Hubbard insulators. *Phys Rev B* 1995;52(8):R5467–70. <http://dx.doi.org/10.1103/PhysRevB.52.R5467>.
- [38] Anisimov VI, Aryasetiawan F, Liechtenstein AI. First-principles calculations of the electronic structure and spectra of strongly correlated systems: the LDA +  $U$  method. *J Phys Condens Matter* 1997;9(4):767. URL <http://stacks.iop.org/0953-8984/9/i=4/a=002>.
- [39] Dudarev SL, Botton GA, Savrasov SY, Humphreys CJ, Sutton AP. Electron-energy-loss spectra and the structural stability of nickel oxide: an LSDA +  $U$  study. *Phys Rev B* 1998;57:1505–9. <http://dx.doi.org/10.1103/PhysRevB.57.1505>.
- [40] Czyżyk MT, Sawatzky GA. Local-density functional and on-site correlations: the electronic structure of  $\text{La}_2\text{CuO}_4$  and  $\text{LaCuO}_3$ . *Phys Rev B* 1994;49:14211–28. <http://dx.doi.org/10.1103/PhysRevB.49.14211>.
- [41] Petukhov AG, Mazin II, Chioncel L, Liechtenstein AI. Correlated metals and the LDA +  $U$  method. *Phys Rev B* 2003;67:153106. <http://dx.doi.org/10.1103/PhysRevB.67.153106>.
- [42] Anisimov VI, Gunnarsson O. Density-functional calculation of effective Coulomb interactions in metals. *Phys Rev B* 1991;43(10):7570–4. <http://dx.doi.org/10.1103/PhysRevB.43.7570>.
- [43] Dederichs PH, Blügel S, Zeller R, Akai H. Ground states of constrained systems: application to cerium impurities. *Phys Rev Lett* 1984;53:2512–5. <http://dx.doi.org/10.1103/PhysRevLett.53.2512>.
- [44] Cococcioni M, de Gironcoli S. Linear response approach to the calculation of the effective interaction parameters in the LDA +  $U$  method. *Phys Rev B* 2005;71(3):035105. <http://dx.doi.org/10.1103/PhysRevB.71.035105>.
- [45] Mori-Sánchez P, Cohen AJ, Yang W. Localization and delocalization errors in density functional theory and implications for band-gap prediction. *Phys Rev Lett* 2008;100(14):146401. <http://dx.doi.org/10.1103/PhysRevLett.100.146401>.
- [46] Perdew JP, Parr RG, Levy M, Balduz JL. Density-functional theory for fractional particle number: derivative discontinuities of the energy. *Phys Rev Lett* 1982;49:1691–4. <http://dx.doi.org/10.1103/PhysRevLett.49.1691>.
- [47] Janak JF. Proof that  $\partial E/\partial n_i = E_i$  in density-functional theory. *Phys Rev B* 1978;18(12):7165–8. <http://dx.doi.org/10.1103/PhysRevB.18.7165>.
- [48] Perdew JP, Zunger A. Self-interaction correction to density-functional approximations for many-electron systems. *Phys Rev B* 1981;23:5048–79. <http://dx.doi.org/10.1103/PhysRevB.23.5048>.
- [49] Svane A, Gunnarsson O. Localization in the self-interaction-corrected density-functional formalism. *Phys Rev B* 1988;37:9919–22. <http://dx.doi.org/10.1103/PhysRevB.37.9919>.
- [50] Svane A, Gunnarsson O. Transition-metal oxides in the self-interaction corrected density-functional formalism. *Phys Rev Lett* 1990;65:1148–51. <http://dx.doi.org/10.1103/PhysRevLett.65.1148>.

- [51] Lüders M, Ernst A, Däne M, Szotek Z, Svane A, Ködderitzsch D, et al. Self-interaction correction in multiple scattering theory. *Phys Rev B* 2005;71:205109. <http://dx.doi.org/10.1103/PhysRevB.71.205109>.
- [52] Becke AD. Density-functional thermochemistry. III. The role of exact exchange. *J Chem Phys* 1993;98:5648.
- [53] Becke AD. A new mixing of Hartree-Fock and local density-functional theories. *J Chem Phys* 1993;98(2):1372-7. <http://dx.doi.org/10.1063/1.464304>.
- [54] Becke AD. Density-functional thermochemistry. IV. A new dynamical correlation functional and implications for exact-exchange mixing. *J Chem Phys* 1996;104(3):1040-6. <http://dx.doi.org/10.1063/1.470829>.
- [55] Heyd J, Scuseria GE, Ernzerhof M. Hybrid functionals based on a screened Coulomb potential. *J Chem Phys* 2003;118(18):8207-15. <http://dx.doi.org/10.1063/1.1564060>.
- [56] Heyd J, Scuseria GE, Ernzerhof M. Erratum: "Hybrid functionals based on a screened Coulomb potential" [*J. Chem. Phys.* 118, 8207 (2003)]. *J Chem Phys* 2006;124(21):219906. <http://dx.doi.org/10.1063/1.2204597>.
- [57] Perdew JP, Ernzerhof M, Burke K. Rationale for mixing exact exchange with density functional approximations. *J Chem Phys* 1996;105(22):9982-5. <http://dx.doi.org/10.1063/1.472933>.
- [58] Lany S, Zunger A. Polaronic hole localization and multiple hole binding of acceptors in oxide wide-gap semiconductors. *Phys Rev B* 2009;80:085202. <http://dx.doi.org/10.1103/PhysRevB.80.085202>.
- [59] Hedin L. New method for calculating the one-particle Green's function with application to the electron-gas problem. *Phys Rev* 1965;139(3A):A796-823. <http://dx.doi.org/10.1103/PhysRev.139.A796>.
- [60] Hedin L, Lundqvist S. Effects of electron-electron and electron-phonon interactions on the one-electron states of solids. In: Seitz F, Turnbull D, Ehrenreich H, editors. *Solid state physics, advanced in research and applications*, vol. 23. (New York): Academic Press; 1969. p. 1-181.
- [61] Bruneval F, Sottile F, Olevano V, Del Sole R, Reining L. Many body perturbation theory using the density-functional concept: beyond the *GW* approximation. *Phys Rev Lett* 2005;94:186402. <http://dx.doi.org/10.1103/PhysRevLett.94.186402>.
- [62] Shishkin M, Marsman M, Kresse G. Accurate quasiparticle spectra from self-consistent *GW* calculations with vertex corrections. *Phys Rev Lett* 2007;99:246403. <http://dx.doi.org/10.1103/PhysRevLett.99.246403>.
- [63] van Schilfgaarde M, Kotani T, Faleev SV. Adequacy of approximations in *GW* theory. *Phys Rev B* 2006;74(24):245125. <http://dx.doi.org/10.1103/PhysRevB.74.245125>.
- [64] Kotani T, van Schilfgaarde M, Faleev SV. Quasiparticle self-consistent *GW* method: a basis for the independent-particle approximation. *Phys Rev B* 2007;76(16):165106. <http://dx.doi.org/10.1103/PhysRevB.76.165106>.
- [65] Bechstedt F, Seino K, Hahn PH, Schmidt WG. Quasiparticle bands and optical spectra of highly ionic crystals: AlN and NaCl. *Phys Rev B* 2005;72:245114. <http://dx.doi.org/10.1103/PhysRevB.72.245114>.
- [66] Botti S, Marques MAL. Strong renormalization of the electronic band gap due to lattice polarization in the *GW* formalism. *Phys Rev Lett* 2013;110:226404. <http://dx.doi.org/10.1103/PhysRevLett.110.226404>.
- [67] Harl J, Schimka L, Kresse G. Assessing the quality of the random phase approximation for lattice constants and atomization energies of solids. *Phys Rev B* 2010;81:115126. <http://dx.doi.org/10.1103/PhysRevB.81.115126>.

- [68] Chantis AN, van Schilfgaarde M, Kotani T. Quasiparticle self consistent GW method applied to localized 4f electron systems. *Phys Rev B* 2007;76:165126. <http://dx.doi.org/10.1103/PhysRevB.76.165126>.
- [69] Georges A, Kotliar G, Krauth W, Rozenberg MJ. Dynamical mean-field theory of strongly correlated fermion systems and the limit of infinite dimensions. *Rev Mod Phys* 1996;68:13–125. <http://dx.doi.org/10.1103/RevModPhys.68.13>.
- [70] Kotliar G, Savrasov SY, Haule K, Oudovenko VS, Parcollet O, Marianetti CA. Electronic structure calculations with dynamical mean-field theory. *Rev Mod Phys* 2006;78:865–951. <http://dx.doi.org/10.1103/RevModPhys.78.865>.
- [71] Lichtenstein AI, Katsnelson MI. *Ab initio* calculations of quasiparticle band structure in correlated systems: LDA++ approach. *Phys Rev B* 1998;57:6884–95. <http://dx.doi.org/10.1103/PhysRevB.57.6884>.
- [72] Richter JH, Ruck BJ, Simpson M, Natali F, Plank NOV, Azeem M, et al. Electronic structure of EuN: growth, spectroscopy, and theory. *Phys Rev B* 2011;84:235120. <http://dx.doi.org/10.1103/PhysRevB.84.235120>.
- [73] Savrasov SY, Haule K, Kotliar G. Many-body electronic structure of americium metal. *Phys Rev Lett* 2006;96:036404. <http://dx.doi.org/10.1103/PhysRevLett.96.036404>.
- [74] Pourousskii LV, Delaney KT, Van de Walle CG, Spaldin NA, Georges A. Role of atomic multiplets in the electronic structure of rare-earth semiconductors and semimetals. *Phys Rev Lett* 2009;102:096401. <http://dx.doi.org/10.1103/PhysRevLett.102.096401>.
- [75] Hourahine B. Excited multiplets of Eu in GaN. In: Symposium I magnetism and correlated electronic structure of nitrides-rare-earth and transition metals as constituents and dopants. MRS proceedings, vol. 1290; 2011. <http://dx.doi.org/10.1557/opl.2011.525>.
- [76] Antropov VP, Katsnelson MI, Harmon BN, van Schilfgaarde M, Kusnezov D. Spin dynamics in magnets: equation of motion and finite temperature effects. *Phys Rev B* 1996;54:1019–35. <http://dx.doi.org/10.1103/PhysRevB.54.1019>.
- [77] Liechtenstein A, Katsnelson M, Antropov V, Gubanov V. Local spin density functional approach to the theory of exchange interactions in ferromagnetic metals and alloys. *J Magn Magn Mater* 1987;67(1):65–74. [http://dx.doi.org/10.1016/0304-8853\(87\)90721-9](http://dx.doi.org/10.1016/0304-8853(87)90721-9).
- [78] Herwadkar A, Lambrecht WRL, van Schilfgaarde M. Linear response theoretical study of the exchange interactions in Mn-doped ScN: effects of disorder, band gap, and doping. *Phys Rev B* 2008;77:134433. <http://dx.doi.org/10.1103/PhysRevB.77.134433>.
- [79] Schilfgaarde MV, Mryasov ON. Anomalous exchange interactions in III-V dilute magnetic semiconductors. *Phys Rev B* 2001;63:233205. <http://dx.doi.org/10.1103/PhysRevB.63.233205>.
- [80] Ke L, Belashchenko KD, van Schilfgaarde M, Kotani T, Antropov VP. Effects of alloying and strain on the magnetic properties of Fe<sub>16</sub>N<sub>2</sub>. *Phys Rev B* 2013;88:024404. <http://dx.doi.org/10.1103/PhysRevB.88.024404>.
- [81] Antropov VP, van Schilfgaarde M, Brink S, Xu JL. On the calculation of exchange interactions in metals. *J Appl Phys* 2006;99(8). <http://dx.doi.org/10.1063/1.2176392>.
- [82] van Schilfgaarde M, Antropov VP. First-principles exchange interactions in Fe, Ni, and Co. *J Appl Phys* 1999;85(8):4827–9. <http://dx.doi.org/10.1063/1.370495>.
- [83] Akai H, Dederichs PH. Local moment disorder in ferromagnetic alloys. *Phys Rev B* 1993;47:8739–47. <http://dx.doi.org/10.1103/PhysRevB.47.8739>.
- [84] Chang YH, Park CH, Sato K, Katayama-Yoshida H. First-principles study of the superexchange interaction in (Ga,Mn)V (V = N, P, As, and Sb). *Phys Rev B* 2007;76:125211. <http://dx.doi.org/10.1103/PhysRevB.76.125211>.

- [85] Sato K, Bergqvist L, Kudrnovský J, Dederichs PH, Eriksson O, Turek I, et al. First-principles theory of dilute magnetic semiconductors. *Rev Mod Phys* 2010;82: 1633–90. <http://dx.doi.org/10.1103/RevModPhys.82.1633>.
- [86] Velický B. Theory of electronic transport in disordered binary alloys: coherent-potential approximation. *Phys Rev* 1969;184:614–27. <http://dx.doi.org/10.1103/PhysRev.184.614>.
- [87] Pujari B, Larson P, Antropov VP, Belashchenko KD. *Ab initio* construction of magnetic phase diagrams in alloys: the case of  $\text{Fe}_{1-x}\text{Mn}_x\text{Pt}$ . arXiv:1501.02794(cond-mat). 2015.
- [88] Faulkner JS, Stocks GM. Calculating properties with the coherent-potential approximation. *Phys Rev B* 1980;21:3222–44. <http://dx.doi.org/10.1103/PhysRevB.21.3222>.
- [89] Kudrnovský J, Drchal V. Electronic structure of random alloys by the linear band-structure methods. *Phys Rev B* 1990;41:7515–28. <http://dx.doi.org/10.1103/PhysRevB.41.7515>.
- [90] Kudrnovský J, Drchal V, Turek I, Khmelevskiy S, Glasbrenner JK, Belashchenko KD. Spin-disorder resistivity of ferromagnetic metals from first principles: the disordered-local-moment approach. *Phys Rev B* 2012;86:144423. <http://dx.doi.org/10.1103/PhysRevB.86.144423>.
- [91] Sato K, Dederichs PH, Katayama-Yoshida H. Curie temperatures of III-V diluted magnetic semiconductors calculated from first principles. *EPL Europhys Lett* 2003; 61(3):403. <http://stacks.iop.org/0295-5075/61/i=3/a=403>.
- [92] Herwadkar A, Lambrecht WRL. Mn-doped ScN: a dilute ferromagnetic semiconductor with local exchange coupling. *Phys Rev B* 2005;72:235207. <http://dx.doi.org/10.1103/PhysRevB.72.235207>.
- [93] Constantin C, Wang K, Chinchore A, Chia H-J, Markert J, Smith AR. Structural, magnetic and electronic properties of dilute MnScN(001) grown by RF nitrogen plasma molecular beam epitaxy. In: Symposium I magnetism and correlated electronic structure of nitrides rare-earth and transition metals as constituents and dopants. MRS proceedings, vol. 1290; 2011. <http://dx.doi.org/10.1557/opl.2011.178>.
- [94] Priour DJ, Das Sarma S. Clustering in disordered ferromagnets: the Curie temperature in diluted magnetic semiconductors. *Phys Rev B* 2006;73:165203. <http://dx.doi.org/10.1103/PhysRevB.73.165203>.
- [95] Priour DJ, Das Sarma S. Phase diagram of the disordered RKKY model in dilute magnetic semiconductors. *Phys Rev Lett* 2006;97:127201. <http://dx.doi.org/10.1103/PhysRevLett.97.127201>.
- [96] Kaminski A, Galitski VM, Das Sarma S. Ferromagnetic and random spin ordering in dilute magnetic semiconductors. *Phys Rev B* 2004;70:115216. <http://dx.doi.org/10.1103/PhysRevB.70.115216>.
- [97] Anderson PW, Hasegawa H. Considerations on double exchange. *Phys Rev* 1955;100: 675–81. <http://dx.doi.org/10.1103/PhysRev.100.675>.
- [98] Wang CS, Prange RE, Korenman V. Magnetism in iron and nickel. *Phys Rev B* 1982; 25:5766–77. <http://dx.doi.org/10.1103/PhysRevB.25.5766>.
- [99] Bouzerar G, Ziman T, Kudrnovsk J. Calculating the Curie temperature reliably in diluted III-V ferromagnetic semiconductors. *EPL Europhys Lett* 2005;69(5):812. <http://stacks.iop.org/0295-5075/69/i=5/a=812>.
- [100] Vaks V, Samolyuk G. On accuracy of different cluster models used in describing ordering phase transitions in fcc alloys. *J Exp Theor Phys* 1999;88(1):89–100. <http://dx.doi.org/10.1134/1.558769>.
- [101] Venkatesan M, Fitzgerald CB, Coey JMD. Thin films: unexpected magnetism in a dielectric oxide. *Nature* 2004;430(7000):630. <http://dx.doi.org/10.1038/430630a>.



- [102] Pham A, Assadi MHN, Zhang YB, Yu AB, Li S. Weak  $d^0$  magnetism in C and N doped ZnO. *J Appl Phys* 2011;110(12). <http://dx.doi.org/10.1063/1.3669491>.
- [103] Coey J. Ferromagnetism. *Solid State Sci* 2005;7(6):660–7. <http://dx.doi.org/10.1016/j.solidstatesciences.2004.11.012>. a tribute to Erwin Felix Bertaut.
- [104] Coey JMD, Stamenov P, Gunning RD, Venkatesan M, Paul K. Ferromagnetism in defect-ridden oxides and related materials. *New J Phys* 2010;12(5):053025. <http://stacks.iop.org/1367-2630/12/i=5/a=053025>.
- [105] Coey JMD, Venkatesan M, Fitzgerald CB. Donor impurity band exchange in dilute ferromagnetic oxides. *Nat Mater* 2005;4(2):173–9. <http://dx.doi.org/10.1038/nmat1310>.
- [106] Droghetti A, Pemmaraju CD, Sanvito S. Predicting  $d^0$  magnetism: self-interaction correction scheme. *Phys Rev B* 2008;78:140404. <http://dx.doi.org/10.1103/PhysRevB.78.140404>.
- [107] Venkatesan M, Fitzgerald CB, Lunney JG, Coey JMD. Anisotropic ferromagnetism in substituted zinc oxide. *Phys Rev Lett* 2004;93:177206. <http://dx.doi.org/10.1103/PhysRevLett.93.177206>.
- [108] Zener C. Interaction between the  $d$  shells in the transition metals. *Phys Rev* 1951;81:440–4. <http://dx.doi.org/10.1103/PhysRev.81.440>.
- [109] Zener C. Interaction between the  $d$ -shells in the transition metals. III. Calculation of the Weiss factors in Fe, Co, and Ni. *Phys Rev* 1951;83:299–301. <http://dx.doi.org/10.1103/PhysRev.83.299>.
- [110] Zener C, Heikes RR. Exchange interactions. *Rev Mod Phys* 1953;25:191–8. <http://dx.doi.org/10.1103/RevModPhys.25.191.2>.
- [111] Ruderman MA, Kittel C. Indirect exchange coupling of nuclear magnetic moments by conduction electrons. *Phys Rev* 1954;96:99–102. <http://dx.doi.org/10.1103/PhysRev.96.99>.
- [112] Kasuya T. A theory of metallic ferro and antiferromagnetism on Zener's model. *Prog Theor Phys* 1956;16(1):45–57. arXiv: <http://ptp.oxfordjournals.org/content/16/1/45.full.pdf+html>. <http://dx.doi.org/10.1143/PTP.16.45>. <http://ptp.oxfordjournals.org/content/16/1/45.abstract>.
- [113] Yosida K. Magnetic properties of Cu-Mn alloys. *Phys Rev* 1957;106:893–8. <http://dx.doi.org/10.1103/PhysRev.106.893>.
- [114] Dietl T, Ohno H, Matsukura F, Cibert J, Ferrand D. Zener model description of ferromagnetism in zinc-blende magnetic semiconductors. *Science* 2000;287(5455):1019–1022. arXiv: <http://www.sciencemag.org/content/287/5455/1019.full.pdf>. <http://dx.doi.org/10.1126/science.287.5455.1019>. <http://www.sciencemag.org/content/287/5455/1019.abstract>.
- [115] Jungwirth T, Sinova J, MacDonald AH, Gallagher BL, Novák V, Edmonds KW, et al. Character of states near the Fermi level in (Ga,Mn)As: impurity to valence band crossover. *Phys Rev B* 2007;76:125206. <http://dx.doi.org/10.1103/PhysRevB.76.125206>.
- [116] Mašek J, Máca F, Kudrnovský J, Makarovskiy O, Eaves L, Champion RP, et al. Microscopic analysis of the valence band and impurity band theories of (Ga,Mn)As. *Phys Rev Lett* 2010;105:227202. <http://dx.doi.org/10.1103/PhysRevLett.105.227202>.
- [117] Dhar S, Brandt O, Ramsteiner M, Sapega VF, Ploog KH. Colossal magnetic moment of Gd in GaN. *Phys Rev Lett* 2005;94:037205. <http://dx.doi.org/10.1103/PhysRevLett.94.037205>.

- [118] Asahi H, Zhou YK, Hashimoto M, Kim MS, Li XJ, Emura S, et al. GaN-based magnetic semiconductors for nanospintronics. *J Phys Condens Matter* 2004;16(48):S5555. <http://stacks.iop.org/0953-8984/16/i=48/a=011>.
- [119] Teraguchi N, Suzuki A, Nanishi Y, Zhou Y-K, Hashimoto M, Asahi H. Room-temperature observation of ferromagnetism in diluted magnetic semiconductor GaGdN grown by RF-molecular beam epitaxy. *Solid State Commun* 2002;122(12):651–3. [http://dx.doi.org/10.1016/S0038-1098\(02\)00228-4](http://dx.doi.org/10.1016/S0038-1098(02)00228-4).
- [120] Dhar S, Pérez L, Brandt O, Trampert A, Ploog KH, Keller J, et al. Gd-doped GaN: a very dilute ferromagnetic semiconductor with a Curie temperature above 300 K. *Phys Rev B* 2005;72:245203. <http://dx.doi.org/10.1103/PhysRevB.72.245203>.
- [121] Dhar S, Kammermeier T, Ney A, Prez L, Ploog KH, Melnikov A, et al. Ferromagnetism and colossal magnetic moment in Gd focused ion-beam-implanted GaN. *Appl Phys Lett* 2006;89(6):062503. <http://dx.doi.org/10.1063/1.2267900>.
- [122] Khaderbad MA, Dhar S, Prez L, Ploog KH, Melnikov A, Wieck AD. Effect of annealing on the magnetic properties of Gd focused ion beam implanted GaN. *Appl Phys Lett* 2007;91(7):072514. <http://dx.doi.org/10.1063/1.2770762>.
- [123] Ney A, Kammermeier T, Manuel E, Ney V, Dhar S, Ploog KH, et al. Element specific investigations of the structural and magnetic properties of Gd:GaN. *Appl Phys Lett* 2007;90(25). <http://dx.doi.org/10.1063/1.2750542>.
- [124] Ney A, Kammermeier T, Ney V, Ye S, Ollefs K, Manuel E, et al. Element specific magnetic properties of Gd-doped GaN: very small polarization of Ga and paramagnetism of Gd. *Phys Rev B* 2008;77:233308. <http://dx.doi.org/10.1103/PhysRevB.77.233308>.
- [125] Cheiwchanchamnangij T, Punya A, Lambrecht WRL. Site dependence of electronic structure of Gd impurities in GaN. In: Symposium I magnetism and correlated electronic structure of nitrides rare-earth and transition metals as constituents and dopants. MRS proceedings, vol. 1290; 2011. <http://dx.doi.org/10.1557/opl.2011.382>.
- [126] Cheiwchanchamnangij T, Lambrecht WRL. Calculated X-ray linear dichroism spectra for Gd-doped GaN. *Phys Rev B* 2011;84:205119. <http://dx.doi.org/10.1103/PhysRevB.84.205119>.
- [127] Kammermeier T, Dhar S, Ney V, Manuel E, Ney A, Ploog KH, et al. Paramagnetic and ferromagnetic resonance studies on dilute magnetic semiconductors based on GaN. *Phys Status Solidi (A)* 2008;205(8):1872–5. <http://dx.doi.org/10.1002/pssa.200824023>.
- [128] Gehlhoff W, Salameh B, Hoffmann A. Comment on “paramagnetic and ferromagnetic resonance studies on dilute magnetic semiconductors based on GaN” [*Phys Status Solidi A* 205, 1872 (2008)]. *Phys Status Solidi (A)* 2011;208(8):1953–6. <http://dx.doi.org/10.1002/pssa.201127125>.
- [129] Pérez L, Lau GS, Dhar S, Brandt O, Ploog KH. Magnetic phases and anisotropy in Gd-doped GaN. *Phys Rev B* 2006;74:195207. <http://dx.doi.org/10.1103/PhysRevB.74.195207>.
- [130] Sapega VF, Ramsteiner M, Dhar S, Brandt O, Ploog KH. Large spin splitting of GaN electronic states induced by Gd doping. 2005. arXiv:condmat/0509198.
- [131] Mishra JK, Dhar S, Khaderabad MA, Brandt O. Ferromagnetism in lightly Gd doped GaN: the role of defects. In: Symposium I magnetism and correlated electronic structure of nitrides rare-earth and transition metals as constituents and dopants. MRS proceedings, Vol. 1290; 2011. <http://dx.doi.org/10.1557/opl.2011.177>.



- [132] Hejtmek J, Knek K, Maryko M, Jirk Z, Sedmidubsk D, Sofer Z, Peina V, Hardtdegen H, Buchal C. On the magnetic properties of Gd implanted GaN. *J Appl Phys* 2008;103(7). <http://dx.doi.org/10.1063/1.2830644>.
- [133] Hite J, Frazier R, Davies R, Thaler G, Abernathy C, Pearton S, et al. Effect of Si Co doping on ferromagnetic properties of GaGdN. *J Electron Mater* 2007;36(4):391–6. <http://dx.doi.org/10.1007/s11664-006-0040-1>.
- [134] Hite JK, Allums KK, Thaler GT, Abernathy CR, Pearton SJ, Frazier RM, et al. Effects of proton irradiation on the magnetic properties of GaGdN and GaCrN. *New J Phys* 2008;10(5):055005. <http://stacks.iop.org/1367-2630/10/i=5/a=055005>.
- [135] Asahi H, Hasegawa S, Zhou Y, Emura S. Growth and characterization of transition-metal and rare-earth doped III-nitride semiconductors for spintronics. In: Symposium I magnetism and correlated electronic structure of nitrides rare-earth and transition metals as constituents and dopants. MRS proceedings, vol. 1290; 2011. <http://dx.doi.org/10.1557/opl.2011.585>.
- [136] Zhou YK, Choi SW, Emura S, Hasegawa S, Asahi H. Large magnetization in high Gd concentration GaGdN and Si-doped GaGdN grown at low temperatures. *Appl Phys Lett* 2008;92(6). <http://dx.doi.org/10.1063/1.2841657>.
- [137] Higashi K, Hasegawa S, Abe D, Mitsuno Y, Komori S, Ishikawa F, et al. Coherent growth of GaGdN layers with high Gd concentration on GaN(0001). *Appl Phys Lett* 2012;101(22). <http://dx.doi.org/10.1063/1.4767992>.
- [138] Ishimaru M, Higashi K, Hasegawa S, Asahi H, Sato K, Konno TJ. Strong atomic ordering in Gd-doped GaN. *Appl Phys Lett* 2012;101(10). <http://dx.doi.org/10.1063/1.4751245>.
- [139] Takahashi M, Hiromura Y, Emura S, Nakamura T, Zhou YK, Hasegawa S, et al. The third magnetic phase of GaGdN detected by SXMCD. *AIP Conf Proc* 2010;1199(1): 411–2. <http://dx.doi.org/10.1063/1.3295478>.
- [140] Zhou Y, Choi S, Kimura S, Emura S, Hasegawa S, Asahi H. Structural and magnetic properties of GaGdN/GaN superlattice structures. *Thin Solid Films* 2010;518(20): 5659–61. <http://dx.doi.org/10.1016/j.tsf.2009.10.032>. Special Section: Materials Today Asia Conference.
- [141] Almokhtar M, Emura S, Zhou YK, Hasegawa S, Asahi H. Photoluminescence from exciton-polarons in GaGdN/AlGaIn multi-quantum wells. *J Phys Condens Matter* 2011; 23(32):325802. <http://stacks.iop.org/0953-8984/23/i=32/a=325802>.
- [142] Zhou Y, Choi S, Kimura S, Emura S, Hasegawa S, Asahi H. High Gd concentration GaGdN grown at low temperatures. *J Supercond Nov Magn* 2007;20(6):429–32. <http://dx.doi.org/10.1007/s10948-007-0245-4>.
- [143] Tawil SNM, Kakimi R, Krishnamurthy D, Emura S, Tambo H, Hasegawa S, et al. Characterization of InGaGdN layers prepared by molecular beam epitaxy. *Phys Status Solidi (RRL) Rapid Res Lett* 2010;4(11):308–10. <http://dx.doi.org/10.1002/pssr.201004273>.
- [144] Jamil M, Zaidi T, Melton A, Xu T, Ferguson IT. Ga<sub>1-x</sub>Gd<sub>x</sub>N based spin polarized light emitting diode. In: Symposium I magnetism and correlated electronic structure of nitrides rare-earth and transition metals as constituents and dopants. MRS proceedings, vol. 1290; 2011. <http://dx.doi.org/10.1557/opl.2011.584>.
- [145] Melton AG, Liu Z, Kucukgok B, Lu N, Ferguson I. Properties of MOCVD-grown GaN: Gd films for spintronic devices. In: Symposium O compound semiconductors for generating, emitting and manipulating energy. MRS proceedings, vol. 1396; 2012. <http://dx.doi.org/10.1557/opl.2012.447>.

- [146] Dalpian GM, Wei S-H. Electron-induced stabilization of ferromagnetism in  $\text{Ga}_{1-x}\text{Gd}_x\text{N}$ . *Phys Rev B* 2005;72:115201. <http://dx.doi.org/10.1103/PhysRevB.72.115201>.
- [147] Lambrecht WRL, Larson P. Gadolinium and oxygen co-doping of gallium nitride: an LSDA +  $U$  study. In: Symposium I advances in III-V nitride semiconductor materials and devices. MRS proceedings, vol. 955; 2006. <http://dx.doi.org/10.1557/PROC-0955-101-05>.
- [148] Mitra C. Computational studies of gadolinium in nitrides: bulk GdN and Gd-doped GaN [Ph.D. thesis]. Case Western Reserve University; 2009.
- [149] Liu L, Yu PY, Ma Z, Mao SS. Ferromagnetism in GaN:Gd: a density functional theory study. *Phys Rev Lett* 2008;100:127203. <http://dx.doi.org/10.1103/PhysRevLett.100.127203>.
- [150] Dev P, Xue Y, Zhang P. Defect-induced intrinsic magnetism in wide-gap III nitrides. *Phys Rev Lett* 2008;100:117204. <http://dx.doi.org/10.1103/PhysRevLett.100.117204>.
- [151] Gohda Y, Oshiyama A. Intrinsic ferromagnetism due to cation vacancies in Gd-doped GaN: first-principles calculations. *Phys Rev B* 2008;78:161201. <http://dx.doi.org/10.1103/PhysRevB.78.161201>.
- [152] Mitra C, Lambrecht WRL. Interstitial-nitrogen and oxygen induced magnetism in Gd-doped GaN. *Phys Rev B* 2009;80:081202. <http://dx.doi.org/10.1103/PhysRevB.80.081202>.
- [153] Neugebauer J, Van de Walle CG. Atomic geometry and electronic structure of native defects in GaN. *Phys Rev B* 1994;50:8067–70. <http://dx.doi.org/10.1103/PhysRevB.50.8067>.
- [154] Limpijumnong S, Van de Walle CG. Diffusivity of native defects in GaN. *Phys Rev B* 2004;69:035207. <http://dx.doi.org/10.1103/PhysRevB.69.035207>.
- [155] Roeber M, Malindretos J, Bedoya-Pinto A, Rizzi A, Rauch C, Tuomisto F. Tracking defect-induced ferromagnetism in GaN:Gd. *Phys Rev B* 2011;84:081201. <http://dx.doi.org/10.1103/PhysRevB.84.081201>.
- [156] Liu Z, Yi X, Wang J, Kang J, Melton AG, Shi Y, et al. Ferromagnetism and its stability in n-type Gd-doped GaN: first-principles calculation. *Appl Phys Lett* 2012;100(23):232408. <http://dx.doi.org/10.1063/1.4717243>.
- [157] Wright AF. Substitutional and interstitial oxygen in wurtzite GaN. *J Appl Phys* 2005;98(10):103531. <http://dx.doi.org/10.1063/1.2137446>.
- [158] Thiess A. Development and application of a massively parallel KKR Green function method for large scale systems [Ph.D. thesis]. RWTH Aachen; 2011.
- [159] Kirkpatrick S. Percolation and conduction. *Rev Mod Phys* 1973;45:574–88. <http://dx.doi.org/10.1103/RevModPhys.45.574>.
- [160] Thiess A, Dederichs PH, Zeller R, Blügel S, Lambrecht WRL. Superparamagnetism in Gd-doped GaN induced by Ga-vacancy clustering. *Phys Rev B* 2012;86:180401. <http://dx.doi.org/10.1103/PhysRevB.86.180401>.
- [161] Kent TF, Yang J, Yang L, Mills MJ, Myers RC. Epitaxial ferromagnetic nanoislands of cubic GdN in hexagonal GaN. *Appl Phys Lett* 2012;100(15):152111. <http://dx.doi.org/10.1063/1.3702843>.

This page intentionally left blank

# Energetics, atomic structure, and magnetism of rare earth-doped GaN bulk and nanoparticles

3

*V. Kumar*

Dr. Vijay Kumar Foundation, Gurgaon, Haryana, India; Shiv Nadar University, Uttar Pradesh, India

*J.M. Zavada*

NYU Tandon School of Engineering, Brooklyn, NY, United States

## 3.1 Introduction

The great utility and versatility of semiconductor materials derive from the doping of such materials with impurity elements to achieve specific electronic properties. Typically, small amounts of the impurity element are added to the host material to produce such effects while maintaining basic semiconductor characteristics. In particular, doping of silicon (Si) with boron (B) or phosphorus (P) elements produces regions with either n-type or p-type conductivity, respectively. These regions enable formation of transistors that are the basis of modern microelectronic circuits (Casey, 1999). Similarly, doping of III-V compound semiconductors, such as gallium arsenide (GaAs) with Si or Mg, was essential in the development of electrically pumped lasers (LDs) and light emitting diodes (LEDs). In recent years, research activities have included efforts to develop multifunctional semiconductor materials through doping with optical or magnetic impurity elements. Also with the miniaturization of electronic devices, there is great interest to understand the properties of nanoparticles and other nanostructures of semiconductors and their doping with different elements. The goal of these efforts has been to produce materials with electrical, optical, and magnetic properties for memory, logic, and information processing capabilities. The developments in nano-materials of semiconductors have further widely expanded the scope of their applications such as in biological systems, sensors, imaging, and optical devices. For commercial applications such devices must be operational at room temperature (RT).

Incorporation and characterization of transition metal (TM) and rare earth (RE) atoms in semiconductors have been active areas of research for over 25 years. While TMs such as Mn have been used to develop materials for spintronics, the doping of RE atoms in IV and III-V semiconductor materials has been studied with the main thrust of developing efficient light sources and amplifiers for fiber optic communication systems. Initially, Er was the selected RE due to its intra- $4f$  shell transitions centered at 1540 nm. Si was the chosen semiconductor host material because of its importance in microelectronic chips. Most experiments involved ion implantation

to introduce Er atoms in Si wafers. While these experiments did succeed in producing Er-doped Si (Si:Er) material, several major obstacles were encountered. The solubility of Er in Si was quite low and there was a strong thermal quenching of the infrared (IR) light emission. It was found that codoping Er and O in a Si wafer increased solubility limits and improved IR emission (Favennec et al., 1990). The optimum ratio of O to Er was conjectured to be 4:1 forming a cage of O atoms around an Er atom. Such a configuration was thought to promote the formation of trivalent Er ions ( $\text{Er}^{3+}$ ) that are required for emission at 1540 nm (Takahei et al., 1994). Since Si is a group IV element, Er ions do not normally enter into their preferred 3+ valency. Even after numerous attempts at codoping, the IR emission at RT was still too low for practical applications. Another approach was to implant Er into  $\text{SiO}_2$  and to form Si:Er nanoparticles through post-implantation annealing. Research from these experiments showed an improved light emission and prototype LEDs were demonstrated. Nevertheless, Er-doped  $\text{SiO}_2$  layers were not stable under current injection and electroluminescence (EL) output could not be sustained. Consequently, other semiconductors, such as InP, GaAs, and GaP III-V compounds, were investigated as host materials. Er-implantation into these and other semiconductors indicated that thermal quenching of Er emission was reduced in wider band gap materials (Favennec et al., 1989). However, the IR emission at RT was still inefficient. Once again, O was investigated as a codopant and improved light emission and thermal stability were achieved (see Ohta et al., 2015, in this volume).

Concurrent to these research activities, advances in III-V nitride (III-N) semiconductor growth and processing technologies made possible the development of efficient blue LEDs and laser diodes (Nakamura et al., 2000). As a result, new investigations began using III-N semiconductors as host materials for Er. Initial results concerning Er and O coimplantation into gallium nitride (GaN) epilayers showed bright emission at 1540 nm and significantly less thermal quenching (Wilson et al., 1994). Rutherford backscattering measurements indicated that over 90% of Er atoms occupied group III sublattice sites. Photoluminescence (PL) measurements yielded optical emissions with characteristic  $\text{Er}^{3+}$  IR spectra confirming that the  $\text{Er}^{3+}$  ions were isoelectronic dopants. Subsequently, other methods, including molecular beam epitaxy (MBE), were used for doping GaN and AlN layers with Er and other RE atoms (MacKenzie et al., 1996; Steckl and Birkhahn, 1998; Hashimoto et al., 2003; Hite et al., 2006; Readinger et al., 2008). However, p-type GaN epilayers could not be produced using MBE and EL devices, and not true LEDs, were demonstrated (Steckl et al., 2002). In order to improve the observed luminescence, GaN thin films were codoped with Eu and Si using solid source MBE (Wang et al., 2009). They found that Si incorporation changed the GaN:Eu films from highly resistive to n-type conductive and had a significant effect on the integrated PL emission at 622 nm (see Fig. 3.1). While moderate Si doping levels produced nearly a 10-fold increase in PL intensity, higher Si doping levels, ~0.08–0.1 at.%, significantly quenched the PL intensity and lifetime.

With metal organic chemical vapor deposition (MOCVD), it was possible to fabricate both n-type and p-type epilayers, using Si and Mg doping, respectively. However, due to the very low vapor pressure of MO precursors, MOCVD was not a reliable technique for doping GaN epilayers with sufficient Er concentrations. Eventually, modified MOCVD techniques were developed and p-GaN:Mg/GaN:RE/n-GaN:Si heterojunctions were

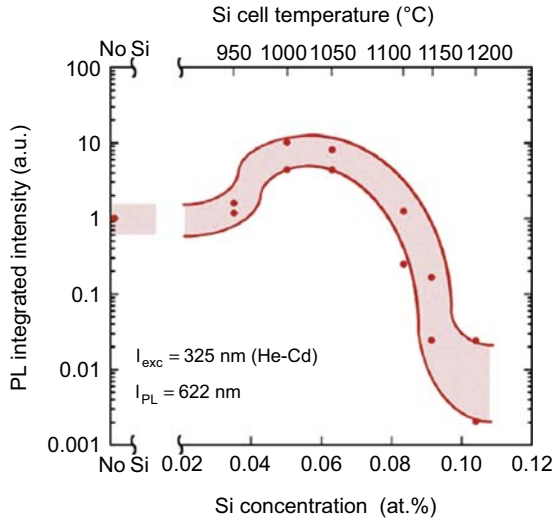


**Figure 3.1** Integrated PL intensity from GaN:Eu films at 622 nm as a function of Si concentration using above-band gap excitation at 325 nm.

After Wang, R., Steckl, A.J., Nepal, N., Zavada, J.M., 2010. Electrical and magnetic properties of GaN codoped with Eu and Si. *J. Appl. Phys.* 107, 013901.

fabricated leading to Er-LEDs, Eu-LEDs, and Gd-LEDs (Ugolini et al., 2006; Nishikawa et al., 2009; Hung et al., 2010; Kane and Ferguson, 2015, in this volume). The output power of the initial LEDs was on the order of a few  $\mu$ W with IR and green emissions for the Er-doped LEDs and red emission for the Eu-LEDs (Dahal et al., 2010; Nepal et al., 2015; Koizumi et al., 2015, in this volume). The active layers in these devices were very resistive and included rather high concentrations of O and hydrogen (H) from the MO precursors that were used. Experiments were made to reduce the O and H levels and to improve the conductivity of the RE-doped layers. GaN:Eu thin films with either Si or Mg resulted in improved light emission (Wang et al., 2009; Nishikawa et al., 2010). Gradually, researchers realized that nearby vacancies, impurity atoms, and electronic dopants play an important role in the excitation and optical emission from the RE ions.

Several research groups have studied the synthesis of GaN nano-powders doped with different RE atoms. Also lanthanide-doped upconversion nanoparticles have been studied (Bettinelli et al., 2015; Prodi et al., 2015; Wang and Liu, 2014). Using Na flux and combustion methods, GaN nano-powders doped with Eu, Er, Pr, Gd, and Tb were demonstrated (Hirata et al., 2001; El-Himri et al., 2004; Wu et al., 2005; Yamada et al., 2006; Nyk et al., 2006). These powders were to be used as phosphors to produce full color emissions. Their optical properties were measured using PL techniques and the results included green emission from Er-doped or Tb-doped GaN powders, and red emission from Eu-doped or Pr-doped GaN powders. However, the luminescence from these powders was not as intense as that from epi-grown RE-doped GaN films. The data clearly showed that impurity atoms in these nano-powders have a major effect on their optical properties.

In general, the luminescence from RE ions arises from intra-4*f* shell transitions that are forbidden in an isolated RE atom due to Laporte selection rules. Once RE atoms are incorporated into a host such as GaN, these transitions become allowed due to the internal electric field and hybridization of the electronic states of the RE atom with those of the host. The intensity of the luminescence strongly depends, not only on the host material, but also on impurities that are introduced intentionally, or unintentionally such as *N* vacancy (Mitchell et al., 2014). Understanding the influence of specific impurities and optimizing the complexes that are formed for enhanced light emission are critical for developing useful optoelectronic devices.

Besides the optical properties of RE atoms doped in different hosts, their 4*f*-shell electrons give rise to magnetic effects. Many permanent magnets are formed with alloys combining REs and TMs such as the strongest known magnet, Nd<sub>2</sub>Fe<sub>14</sub>B. Small concentrations of RE and TM atoms have been introduced into II-VI and III-V compounds to produce magnetic semiconductors. While these studies go back many years, it was only in 1989 that dilute magnetic semiconductors were demonstrated (Munekata et al., 1989). MBE was used for in situ doping of InAs and GaAs layers with Mn during growth. In these compounds, Mn acts as a p-type dopant and its unpaired 3*d* electrons lead to ferromagnetic properties. However, the Curie temperature ( $T_C$ ) for these materials has been limited to  $\sim 160$  K in spite of many attempts to reach higher temperatures. In 2000 a theoretical analysis suggested that wide band gap semiconductors, such as GaN or ZnO, doped with Mn would have a  $T_C > 300$  K (Dietl et al., 2000). Subsequently, several research groups demonstrated RT hysteretic behavior for Mn-doped GaN thin films (see El-Masry et al., 2015, in this volume). Furthermore, this analysis also motivated investigations into the magnetic properties of RE-doped III-N compounds. GaN thin films, grown by MBE, were doped with either Gd, Eu, Nd, or Tb, and magnetic effects at RT were observed (Teraguchi et al., 2002; Dhar et al., 2005a; Bang et al., 2002; Metcalfe et al., 2015, in this volume). Of particular note was the colossal effective magnetic moment,  $\mu_{\text{eff}}$  per Gd ion, reported for Gd-doped GaN epilayers and the ensuing controversy (Dhar et al., 2005b; Ney, 2015, in this volume; Lambrecht, 2015, in this volume). As with optical emission, codoping either GaN:Eu or GaN:Gd films with Si increased the RT magnetic properties (Wang et al., 2010; Hite et al., 2007). Hysteresis curves measured at RT for codoped GaN:(Eu,Si) films are shown in Fig. 3.2 indicating that incorporation of Si increases the saturation magnetization by a factor of  $\sim 9$ . GaN films, doped with Er, Gd, or Eu during MOCVD, were also studied and found to exhibit magnetic effects (Nepal et al., 2015; Kane and Ferguson, 2015; Koizumi et al., 2015, in this volume). For GaN:Er films, hysteretic curves were observed at RT with the saturation magnetization linearly dependent upon the Er concentration (Zavada et al., 2007). Similar effects were found for GaN:Gd films. Codoping GaN:Eu films with Mg led to higher values of  $\mu_{\text{eff}}$  per Eu ion.

In addition, Gd-doped GaN nano-powders were shown to exhibit Curie–Weiss behavior for the magnetic susceptibility (Nyk et al., 2006). However, magnetic properties in other GaN:RE nano-powders were not convincingly demonstrated. These experimental reports provide further evidence that both magnetic and optical properties are clearly dependent upon the impurities present in the RE-doped III-N materials. The magnetic interactions between the spins localized on RE ions as well as the

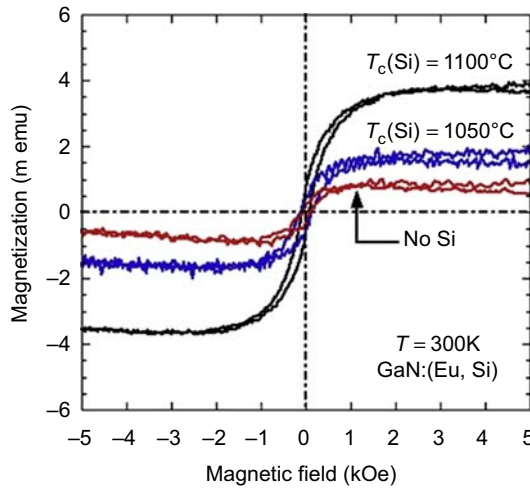


**Figure 3.2** Hysteresis curves measured at RT for codoped GaN:(Eu,Si) films grown at cell temperature  $T_c(\text{Si}) = 1100^\circ\text{C}$  and  $1050^\circ\text{C}$ . Data points for a GaN:Eu film are also shown. After Wang, R., Steckl, A.J., Nepal, N., Zavada, J.M., 2010. Electrical and magnetic properties of GaN codoped with Eu and Si. *J. Appl. Phys.* 107, 013901.

polarization induced around them will depend on the separation between the RE ions. Moreover, the magnetic moments on REs will in general get affected by the presence of other impurities/dopants as well as defects that may get created. This makes the study of these  $f$  electron systems difficult and therefore theoretical understanding of the magnetic properties of these RE-doped systems has been a challenge. These aspects also reemphasize the need to properly understand the structural effects due to RE doping in different hosts. In this chapter our emphasis is on GaN as a host material.

As mentioned earlier, GaN:Eu shows bright red emission at 622 nm due to  ${}^5\text{D}_0 \rightarrow {}^7\text{F}_2$  transition. Bulk GaN has wurtzite structure and as evidenced from the analysis of the emission spectra (Lozykowski et al., 2000), Eu atoms favor substitution at a Ga site in a  $3+$  state. On such a site there is axial  $\text{C}_{3v}$  symmetry. However, the presence of defects can have a strong influence on PL. Although there are numerous experimental studies, little progress has been made in the understanding of these materials from first principles calculations (O'Donnella and Hourahine, 2006; Svane et al., 2006; Goumri-Said and Kanoun, 2008). This is primarily due to the difficulties in dealing with  $f$  electron systems as well as the complex nature of the defect structures in these materials. Filhol et al. (2004) studied Eu-, Er-, and Tm-doped bulk GaN by treating RE atoms as trivalent and the remaining  $f$  electrons were treated as part of the core. Such an approach neglects the magnetic effects that would arise if all  $f$  electrons on RE atoms are considered as part of the valence. They found substitution of RE atoms on a Ga site to be energetically most favorable. Svane et al. (2006) performed a self-interaction corrected local spin density calculation to study RE doping in GaN, but they used small supercells with only up to 32 atoms to treat the RE-doped systems and



ignored atomic relaxation around the dopant. Later, calculations by [Bruno Cruz et al. \(2012\)](#) on larger supercells with about 100 atoms showed significant relaxation around RE ions. Such large supercells are also required to treat low doping concentration ( $\sim 1$  at.%) of RE atoms that are often used in experiments and have been shown to give high intensity emission ([Ishizumi et al., 2006](#)). Though larger concentration of Eu can be incorporated, experiments ([Sawahata et al., 2006](#)) show structural transition from crystalline to polycrystalline around 2–3.5 at.% doping of Eu in GaN.

[Sanna et al. \(2009\)](#) have studied RE-vacancy defect pairs in GaN using a local density approximation plus onsite Coulomb interaction  $U$  within a tight-binding approach. Their analysis showed that the RE dopants have a tendency to exist in a divalent state in the presence of defects such as  $N$  vacancy. The presence of defects near RE ions also reduces the local symmetry and can enhance the intra- $4f$  level transitions. In addition, defects can introduce shallow levels, which can act as assistant levels during transition. Doping of Gd has been also studied ([Nakhmanson et al., 2005](#)) in GaN, and the possibilities of ferromagnetism and antiferromagnetism have been explored. Codoping of Eu and Si in GaN has been studied from ab initio calculations ([Bruno Cruz et al., 2012](#)) as a 5–10 times increase in emission has been observed due to the increase in the PL lifetime.

In this chapter we review the results of ab initio calculations concerning the atomic structure and magnetic properties of bulk GaN as well as GaN nanoclusters, doped with selected RE atoms. The effects of codoping these materials with Si are also discussed. In [Section 3.2](#) we describe the calculation methods that were used in these investigations. The analysis of bulk GaN and the doping with Eu are presented in [Section 3.3](#) together with results from codoping with Si. Ab initio calculations by [Bruno Cruz et al. \(2012\)](#) showed that Eu doping in GaN becomes energetically favorable by the codoping of Si. The Si codoping breaks the local symmetry around Eu ions and leads to shallow states below the conduction band (CB) that can facilitate intra- $4f$  shell transitions. The excess of electrons in Si makes Eu behave as divalent and an enhancement in the magnetic moment as the half-filled  $4f$  states in  $\text{Eu}^{2+}$  produce an effective magnetic moment,  $\mu_{\text{eff}}$  of  $7.0 \mu_{\text{B}}$ , where  $\mu_{\text{B}}$  is the Bohr magneton. In [Section 3.4](#) we present results dealing with preferred atomic structures and magnetic behavior of GaN nanoclusters with different RE atoms substituting on Ga sites. The results of these studies can help to understand the behavior RE doping in larger nanoparticles. Note that doping of small size nanoclusters such as  $\text{Cd}_{13}\text{Se}_{13}$  with one or two Mn atoms has been achieved ([Yang et al., 2015](#); [Yu et al., 2010](#)). Such doped nanoclusters can be passivated and assembled into layers or other assemblies. While Mn-doped II-VI nanoclusters such as those of ZnSe have been also studied theoretically ([Nanavati et al., 2011](#)), for RE-doped nanoclusters, ab initio calculations were performed on  $(\text{GaN})_n$  nanoclusters, doped with Gd and Nd by [Kumar and Zavada \(2010\)](#), and Eu doping has been studied by [Kaur et al. \(2015\)](#). The atomic structures of such doped nanoclusters have been optimized by including all the  $4f$  electrons on RE atoms. Cage structures of these GaN nanoclusters were found to be lower in energy compared to bulk fragments that were fully optimized. Specific results show that Eu-doping in GaN nanoclusters is favorable compared with bulk GaN as a large fraction of atoms in a nanocluster lie on the surface where strain can be lower, in

contrast to bulk GaN where often Eu-doping is associated with  $N$  vacancy formation. Codoping of Si further facilitates Eu-doping as strain from an oversized Eu atom and an undersized Si atom is compensated. In [Section 3.5](#) we present summary of the main findings and a brief discussion.

## 3.2 Methods of calculation

Calculations on bulk GaN with RE and other codopants were performed ([Bruno Cruz et al., 2012](#)) using a  $3 \times 3 \times 3$  supercell of GaN wurtzite structure as shown in [Fig. 3.3\(a\)](#). It has 108 atoms, which are sufficient to study the effects of substitutional doping of  $\sim 1$  at.% REs often used in experiments. The results of these calculations for the local atomic structure and other electronic effects will also be good representatives of systems with even lower RE concentrations. The dopants (RE atoms and Si) were substituted on Ga sites and the positions of all the ions as well as the cell parameters were fully optimized without any symmetry constraint until the force on each ion became less than  $0.005 \text{ eV/\AA}$ . The electron–ion interaction was treated by using projector augmented wave pseudopotential method ([Blöchl, 1994](#)) as implemented in the Vienna Ab initio Simulation Package ([Kresse and Joubert, 1999](#)). The calculations were performed using high precision with the energy cutoff of 500 eV for the plane wave expansion and generalized gradient approximation (GGA) ([Perdew et al., 1992](#)) for the exchange–correlation energy. In these calculations the  $3d$  states of Ga were treated as valence states. The Brillouin zone was sampled by the  $\Gamma$  point for the ionic and electronic optimizations while a  $3 \times 3 \times 3$  Monkhorst and Pack  $\mathbf{k}$ -points mesh ([Monkhorst and Pack, 1976](#)) was used for the density of states calculations. In the case of RE-doped systems, the  $4f$  electrons were considered as part of the valence electrons and treated in a scalar relativistic manner with spin-polarized calculations. Due to the localized nature of the  $f$  electrons, the effects of onsite Coulomb interaction were also studied using a parameter  $U$  in  $GGA + U$  formalism. The value of the  $U$  parameter was taken following the literature on RE systems ([Goumri-Said and Kanoun, 2008](#); [Madsen and Novák, 2005](#); [Rubio-Ponce et al., 2008](#); [Steeneken et al., 2002](#)) in the range of 5–7.5 eV. Choosing slightly different values of  $U$  had only a small effect on the positions of the spin-up and spin-down  $4f$  states.

In the case of nanoclusters, a cubic cell of side  $20 \text{ \AA}$  was used with periodic boundary conditions and the Brillouin zone was represented by only the  $\Gamma$  point for  $\mathbf{k}$ -space integrations. The ionic positions were fully relaxed until the force on each ion became less than  $0.005 \text{ eV/\AA}$  and the energy was converged within  $0.0001 \text{ eV}$ . The valence configuration for Ga, N, Si, and Eu atoms was taken to be  $4s^2 4p^1$ ,  $2s^2 2p^3$ ,  $3s^2 3p^2$ , and  $5s^2 5p^6 4f^7 6s^2$ , respectively. Inclusion of  $3d$  electrons as valence on Ga gave overall a similar trend of the stability of different structures and generally the binding energy improved by about  $0.05 \text{ eV/atom}$ . Here the results obtained by considering three valence electrons on a Ga atom are given. The binding energy per atom,  $E_b$ , of different nanoclusters was calculated from  $(n_A E(A) + n_B E(B) + n_C E(C) + n_D E(D) - E(ABCD))/(n_A + n_B + n_C + n_D)$ . Here  $E(X)$ , ( $X = A, B, C, \text{ and } D$ ) is the energy of

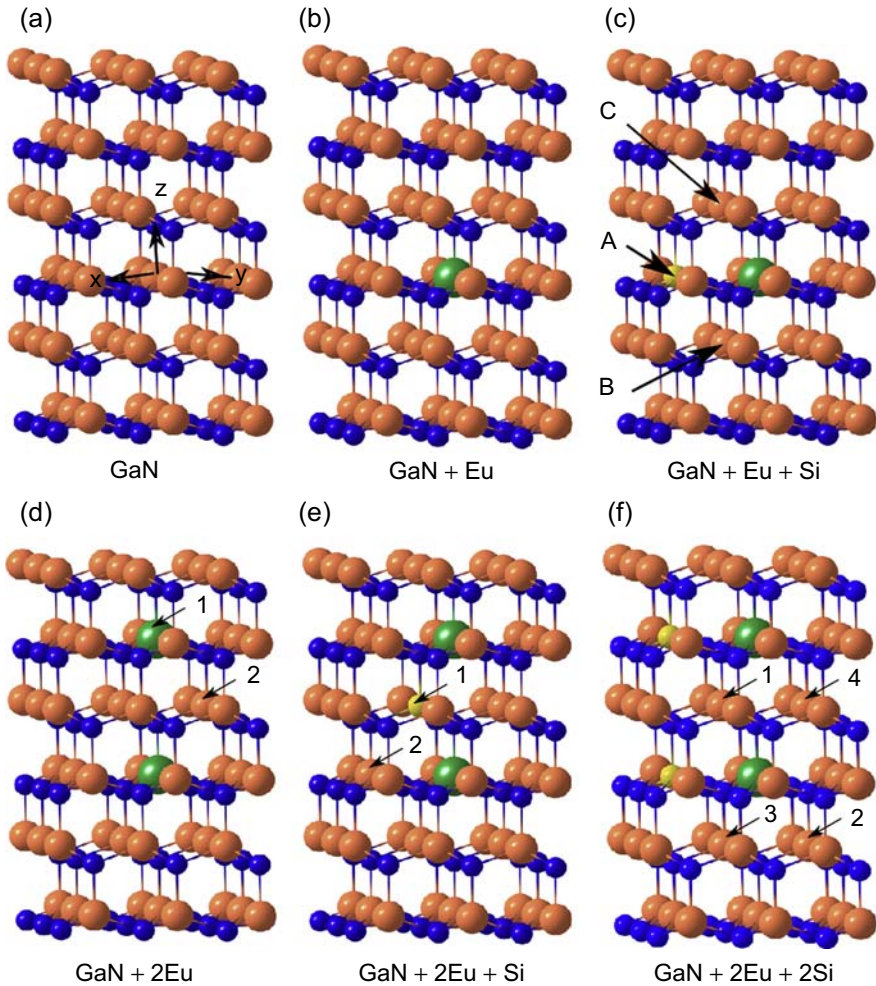


**Figure 3.3** (a) A  $3 \times 3 \times 3$  supercell of bulk GaN, (b) an Eu atom doped on a Ga site, (c) one Eu and one Si atom codoped on Ga sites, (d) two Eu atoms doped on Ga sites, (e) two Eu atoms and one Si atom codoped on Ga sites, and (f) two Eu and two Si atoms codoped on Ga sites in the lowest energy configurations. *Orange, blue, green, and yellow balls* show Ga, N, Eu, and Si atoms, respectively. In (c) three positions of a Si atom are shown as A, B, and C that are nearest neighbors of N atoms connected to a Eu atom. Site A has the lowest energy. In (d) 1 and 2 refer to two positions of Eu and in (e) two positions of Si. (f) Few low-lying configurations (1 and 2), (1 and 3), and (1 and 4) for two Si atoms keeping the Eu sites the same. The coordinate axes are shown in (a). After Bruno Cruz, A.V., Shinde, P.P., Kumar, V., Zavada, J.M., 2012. Phys. Rev. B 85, 045203.

a free  $X$  atom and  $E(ABCD)$ , the energy for a nanocluster with  $n_A$ ,  $n_B$ ,  $n_C$ , and  $n_D$  atoms of type A, B, C, and D, respectively. The formation energy for codoping was calculated from the formula  $\Delta H_D = E(\text{Ga}_{n-x}\text{N}_n\text{Eu}_x\text{D}_y) - E(\text{Ga}_{n-x}\text{N}_n\text{Eu}_x) - yE(\text{D})/N + xE(\text{Ga})/N$  where  $N = 2n$  is the total number of atoms in the nanocluster and  $E(X)$  is the energy of the system  $X$  with  $N$  atoms. For Si codoping the results show large formation energy

suggesting it to be highly favorable. We also discuss the results for the case of two RE atoms doped in nanoclusters to understand the magnetic interactions between the dopants.

### 3.3 Doping of bulk GaN with Eu and codoping with Si

In this section we discuss the results for the doping of one and two Eu atoms in the supercell of bulk GaN and also codoping with Si in the supercell. As a reference, we also present the results for pure GaN.

#### 3.3.1 Pure GaN and bulk GaN doped with Eu

For bulk GaN, the calculated lattice parameters in the wurtzite structure are  $a = 3.223 \text{ \AA}$  and  $c = 5.212 \text{ \AA}$  with  $c/a = 1.617$ . These are in very good agreement with the experimental values of 3.19 and 5.18  $\text{\AA}$  with  $c/a = 1.624$  (Edgar et al., 1999). The cohesive energy is calculated to be 4.373 eV/atom and it is also in good agreement with the experimental value of 4.53 eV/atom. The calculated band gap is 1.71 eV and it is significantly underestimated compared with the experimental value of 3.4 eV. This is due to the use of GGA. The valence band (VB) of GaN has mainly the  $2p$  states of N with an admixture of ( $4s, 4p$ ) states of Ga.

When a Eu atom is doped on a Ga site in a  $3 \times 3 \times 3$  supercell of GaN as shown in Fig. 3.3(b), the optimized atomic structure shows (Bruno Cruz et al., 2012) that there is a local  $C_{3v}$  symmetry around the Eu ion as it is also inferred from experiments. The nearest neighbor Eu–N bond length along the symmetry axis ( $z$ -axis) is 2.30  $\text{\AA}$  while the other three Eu–N bonds are 2.25  $\text{\AA}$  compared to the value of 1.96  $\text{\AA}$  for the Ga–N bond in bulk GaN. Therefore, the local symmetry around the Eu ion is reduced compared to the Ga ion in bulk GaN. Sanna et al. (2009) obtained the values of 2.27 and 2.24  $\text{\AA}$  using a tight-binding method. Therefore the doping of a Eu atom on a Ga site in GaN leads to about 15% outward relaxation in the bond lengths around Eu and also the deformation of the neighboring lattice structure as the Ga–N bonds nearest to the Eu atom are compressed (bond lengths of 1.92–1.94  $\text{\AA}$ ) while the second and third nearest Ga–N bonds from Eu have values in the range of 1.92–1.98 and 1.94–1.97  $\text{\AA}$ , respectively. These results show that the Eu doping affects bonds up to several neighbor distances. The lattice parameters  $a$  and  $c$  expand slightly to 3.237 and 5.227  $\text{\AA}$ , respectively, in agreement with the experimental result of Seo et al. (2008). Most importantly these calculations showed that there is a large energy cost of 1.84 eV due to the doping of a Eu atom in GaN and overall the cohesive energy of GaN:Eu decreases due to the deformation of the lattice. The strain energy of the deformation or the deformation energy of the structure is calculated by subtracting the energy of the pure bulk GaN from the energy of the deformed structure due to doping of Eu atom(s) but Eu replaced with Ga. The value of the deformation energy is 2.04 eV. Therefore we can say that from a chemical bonding point of view there is a small gain of 0.2 eV when Eu is doped in place of Ga but the deformation cost is very large. Further Eu atom on a Ga site in GaN is in a trivalent state and there are six unpaired  $4f$  electrons leading to a net magnetic moment of 6  $\mu_B$ . The spin-polarized density of

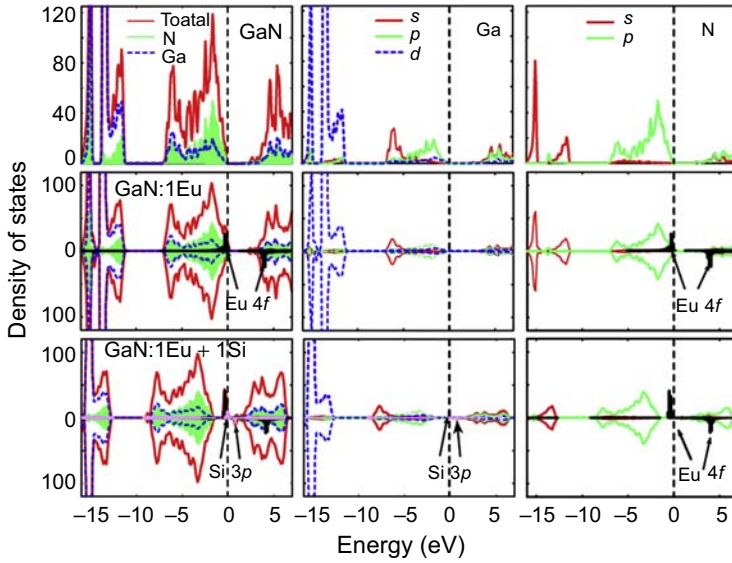


**Figure 3.4** Total (red curve), partial (filled green curve for N and broken curve for Ga) in the left column panels, and the angular momentum decomposed electronic densities of states (central and right column panels) for GaN, GaN doped with one Eu in the supercell, and GaN codoped with Eu and Si. For the Eu doping cases spin-polarized densities of states are shown (upper curves for up spin and lower curves for down spin).  $3p$  states of Si and  $4f$  states of Eu are marked. Vertical broken line shows the top of the valence band.

After Bruno Cruz, A.V., Shinde, P.P., Kumar, V., Zavada, J.M., 2012. Phys. Rev. B 85, 045203.

states (Fig. 3.4) shows that the spin-up  $4f$  states lie close to the top of the VB of GaN and have a hole while the spin-down  $4f$  unoccupied states lie above the band gap in the CB region. As the band gap is underestimated in GGA, it is likely that a more accurate description of the occupied and the unoccupied states could lead to the spin-down  $4f$  states lie close to the CB minimum since the bottom of the CB would move upward to increase the band gap (Svane et al., 2010). This can reduce the hybridization of the  $4f$  states of the RE atoms with the GaN states and lead to their narrower distribution.

For two Eu atoms in the supercell corresponding to about 2 at.% doping of Eu in bulk GaN, the most favorable positions are the consecutive Ga sites along the  $z$ -axis with a separation of 4.97 Å as shown by position 1 in Fig. 3.3(d). This is in contrast to the nearest neighbor Ga–Ga separation of 3.21 Å. This result shows that the Eu atoms avoid nearest neighbor Ga sites. The total cost to dope two Eu atoms is 3.01 eV and it is 0.67 eV less than twice the value for one Eu atom. This means that rather than keeping Eu atoms far away in the case of very small doping, it is energetically favorable to have a kind of clustering of Eu atoms. The deformation energy of the lattice due to two Eu atoms is 4.39 eV and this suggests that there is higher chemical bonding of two Eu atoms in GaN. This result of the formation of clustering of Eu atoms does not mean the formation of EuN as also inferred from experiments (Seo et al., 2008) because position 2 corresponding to the nearest neighbor Ga site



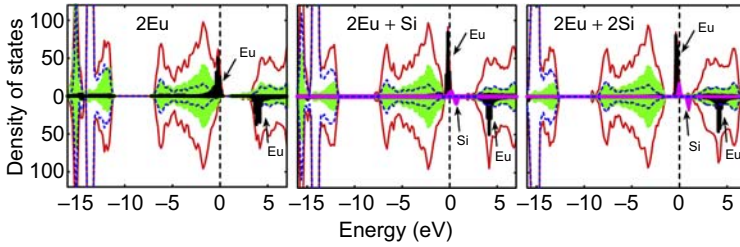


**Figure 3.5** The spin-polarized electronic densities of states (*upper curves for up spin and lower curves for down spin*) for the lowest energy configurations of GaN doped with two Eu atoms in the GaN supercell, two Eu and one Si, and two Eu and two Si atoms as shown in Fig. 3.3. *Full red curve* represents the total density of states. *Shaded green, dashed curve, shaded black curve, and shaded pink curve* represent N, Ga, Eu, and Si partial densities of states. *Vertical broken line* shows the top of the valence band.

After Bruno Cruz, A.V., Shinde, P.P., Kumar, V., Zavada, J.M., 2012. Phys. Rev. B 85, 045203.

in Fig. 3.3(d) for the second Eu lies 0.759 eV higher in energy as compared to the case where the second Eu atom is on position 1. In the lowest energy configuration, for one Eu atom three Eu–N bonds are 2.26 Å and one Eu–N bond is 2.33 Å while for another Eu atom three bonds are 2.26 Å and one bond is 2.39 Å. This leads to a compression of the nearest neighbor Ga–N bonds that are 1.91 and 1.95 Å while the bond lengths for the next nearest neighbor Ga–N bonds from Eu are in the range of 1.93–1.94 and 2.01 Å. There is a slight expansion in the lattice so that *a* and *c* parameters further increase to 3.250 and 5.239 Å, respectively, in agreement with the results of Seo et al. (2008) who reported a shift in the XRD peak position to slightly lower angle for 2 at.% Eu doping in GaN. Both the Eu ions are in 3+ states. As shown in Fig. 3.5, the spin-up 4*f* states have two holes and the band of the 4*f* states becomes slightly broader. There is low density of states near the bottom of the CB, which decreases the band gap. Such states could facilitate energy transfer from the host to the Eu impurity.

### 3.3.2 Codoping of Si and Eu in bulk GaN

Codoping of Si with Eu in bulk GaN was studied by Bruno Cruz et al. (2012). Experiments (Wang et al., 2009) have shown that a low concentration of Si of about 0.04 at.% does not improve the PL intensity of GaN:Eu much, but by increasing the Si concentration to about 0.05 at.%, the PL intensity increases 5 to 10 times while a further increase in the Si concentration to about 0.07 at.% decreases the PL emission and at about 0.1 at.% Si, the PL emission becomes ~1000 times lower (see Fig. 3.1). Around this concentration of Si, Eu concentration also has similar values and a broadband emission was obtained in the blue region. Note that for GaN:Eu there is red emission without Si codoping. Therefore the amount of Si codoping affects the properties of GaN:Eu very significantly. For Si codoping, Bruno Cruz et al. (2012) considered the Ga sites bonded to any of the three basal N atoms neighboring the Eu ion. There are

two neighboring Ga atoms (A-type sites in Fig. 3.3(c)) to such an N atom in the basal plane and one axial Ga atom (site B in Fig. 3.3(c)). There is another possible Ga site (site C in Fig. 3.3(c)) that is nearest neighbor to an axial N, which is nearest neighbor to the Eu ion. Codoping of Si at site A is about 0.68 eV (0.74 eV) lower in energy than at site B (C). In the lowest energy configuration A, the four Eu–N bonds lie in the range of 2.26–2.32 Å. Silicon codoping breaks the  $C_{3v}$  symmetry around the Eu ion and this could help in increasing the probability of intra 4f transitions. Significantly, Si codoping lowers the energy by 2.37 eV compared with pure GaN and by 4.22 eV compared with the case of one Eu-doped GaN in the supercell. Calculations show that the doping of a Si atom alone on a Ga site in the GaN supercell leads to a gain of 3.99 eV. This is less compared to the energy gain of 4.22 eV when Si is codoped with Eu atom in GaN. Therefore the energy gain is increased when Si is codoped with Eu. Accordingly, we can say that Si facilitates doping of Eu and it increases the stability of the doped system.

What leads to this behavior? A close look at the atomic structure shows that for Si doping alone, the Si–N bonds are shorter (three bonds of 1.803 Å in the basal plane and the axial Si–N bond length of 1.796 Å) compared with the Ga–N bond length of 1.96 Å in pure GaN. Therefore Si doping on a Ga site in GaN leads to an *expansion* of the neighboring Ga–N bonds to 2.03 Å. *This is the reverse of the compression we find for the Eu doping case.* Therefore, *codoping of Si and Eu can effectively reduce the strain and that is why Si codoping facilitates Eu in GaN.* From an electronic point of view, as Si is tetravalent, there is an extra electron from each Si added in the supercell. Calculations showed (Bruno Cruz et al., 2012) that this electron is transferred to Eu and accordingly the Eu ion behaves as divalent with the spin-up 4f states becoming fully occupied (Fig. 3.4). This also increases the magnetic moment on the Eu ion to  $7 \mu_B$ . The charge transfer to the Eu site pushes the 4f level upward and the spin-up 4f levels lie in the band gap above the VB of GaN. This also reduces the hybridization of the 4f states with the VB and they appear as sharp energy levels in the density of states plot. The optimized lattice parameters  $a$  and  $c$  become 3.235 and 5.219 Å, respectively. Accordingly with Si codoping there is a small *contraction* compared to the case of the doping of Eu atom alone. The spin-down 4f states also move up in the CB.

To further study the effects of different concentrations of Si codoping, Bruno Cruz et al. (2012) considered one and two Si atoms with two Eu atoms in the  $3 \times 3 \times 3$  GaN supercell. The Si atoms were substituted on Ga sites in such a manner (Figs. 3.3(e) and (f)) that Si and Eu atoms were connected through common N ions. For one Si codoping case Si was connected to both the Eu ions via N ions (site 1 in Fig. 3.3(e)). Also site 2 in Fig. 3.3(e) is energetically nearly degenerate with site 1. For the case of codoping of two Si atoms, the lowest energy configuration is shown in Fig. 3.3(f) and the two Si atoms are on sites 1 and 2 while the other configurations (1) + (3) and (1) + (4) lie about 0.25 and 0.35 eV higher in energy, respectively, compared with the lowest energy configuration. There is a higher gain of 4.96 eV for codoping of two Si atoms compared with 1.44 eV for codoping of one Si atom with two Eu atoms. The net magnetic moment is 13 and  $14 \mu_B$  for the codoping of one and two Si atoms along with two Eu atoms, respectively. This suggests ferromagnetic coupling between the spins on Eu

ions. Note that for only two Eu doping the net magnetic moment is  $12 \mu_B$ . Therefore Si codoping tends to increase the net magnetic moments. As in the case of codoping of one Si with one Eu, the  $4f$  states move up in the band gap in the case of codoping of two Si atoms as shown in Fig. 3.5. The hybridization of the occupied spin-up  $4f$  states with the VB is quite small compared to the case of two Eu doping alone. Also the separation between Eu ions increases to  $5.13 \text{ \AA}$  and this would further reduce the hybridization between the  $4f$  states of Eu ions and would likely lead to a weaker interaction between the two Eu ions. This will also weaken the magnetic coupling. As shown in Fig. 3.5, the peak in the density of states corresponding to  $4f$  states becomes narrower after Si codoping. Also there are shallow states near the bottom of the CB. Therefore from these results we can say that for very low codoping of Si, the effect on PL can be expected to be small as the  $4f$  states would remain very close to the top of the VB of GaN. With an increase in Si concentration the  $4f$  states will split-off the GaN VB maximum, become sharper, and have shallow states. These features could lead to enhancement in PL. With nearly equal concentration of Eu and Si, Eu ions will behave as divalent and this can explain the observation of broad blue emission. There are reports of blue emission from  $\text{Eu}^{2+}$  ions in AlN (Hirosaki et al., 2007)-and GaN-coated  $\text{SiO}_2$  nanoparticles GaN@ $\text{SiO}_2$  (Gautam and van Veggel, 2011).

As the distribution of the  $4f$  electronic states is narrow, Bruno Cruz et al. (2012) also considered the effects of onsite Coulomb interaction within  $GGA + U$  formalism taking an effective  $U$  value of 6 eV. The inclusion of  $U$  shifts the spin-up  $4f$  states deeper in the VB and the spin-down  $4f$  states upward in the CB. Therefore the hybridization between the  $4f$  states and the CB as well as the VB states increases and this makes the distribution of  $4f$  states broader. With Si codoping the occupied spin-up  $4f$  states shift again in the band gap and the distribution becomes even narrower compared with the case of  $U = 0$ . However, the effect of including  $U$  on the atomic structure is small. The cost of doping one and two Eu atoms in GaN supercell increases by 0.18 and 1.26 eV, respectively. However, with Si codoping the energy is lowered by 1.07 and 1.11 eV, respectively for 1Eu + 1Si and 2Eu and 2Si cases as compared to the case when  $U = 0$ .

### 3.4 Doping of rare earths in GaN nanoparticles

RE-doped compound semiconductor nanoparticles are of great interest for imaging, optoelectronic devices, thermal sensing, biomedical, and photovoltaic applications (Colvin et al., 1994; Bouzigues et al., 2011; O'Donnell and Hourahine, 2006; Dahal et al., 2009; Hirosaki et al., 2007, Wang and Steckl, 2003; Zhang et al., 2007; Steckl et al., 2002). Many of the photophysical properties of lanthanides are temperature dependent such as the emission intensity and the excited-state lifetime. The temperature sensitivity of the emission raises the exciting possibility of using nanoparticles for high-resolution contactless thermal sensing. Another exciting application is the photon upconversion, which makes use of the energy transfer between dopant ions. It is attracting great interest. In a host codoped with Yb and either Er or Tm, low-energy photons were absorbed by the  $\text{Yb}^{3+}$  ions, and higher-energy photons were emitted



by the  $\text{Er}^{3+}$  or  $\text{Tm}^{3+}$ . This has important implications for solar-cell efficiencies, which can be dramatically improved by using upconversion nanoparticles to harvest abundant near-IR radiation, which normally goes to waste, and convert it into photons with energies above the cell's semiconductor band gap. Core-shell nanoparticles are of interest as the distribution of the dopants can be manipulated.

Eu doping in GaN powders (Wu et al., 2006; Poitras et al., 2006), quantum dots (Hori et al., 2004a,b; Andreev et al., 2005), nanograins (Kudrawiec et al., 2006), and nanoparticles (Pan et al., 2012; Hori et al., 2006) as well as other REs in different nanoparticles including core-shell have been studied experimentally. However, there has been little theoretical progress to understand the effects associated with the doping of RE atoms in nanoparticles. The size of the nanoparticles in experiments is often about a few nm in diameter, which is difficult to treat from ab initio calculations. Such large nanoparticles are likely to have bulk atomic structure inside while their surfaces are likely to have reconstruction. Such reconstructions are also found on semi-infinite surfaces. Ab initio calculations on small nanoparticles/nanoclusters show that the atomic structures of the nanoclusters and small nanoparticles of about 1 nm diameter are often quite different from bulk. GaN nanoparticles with  $\sim 1$  nm diameter have fullerene-like structures (Kaur et al., 2012) in contrast to the wurtzite structure in bulk. The atomic structures of nanoparticles of semiconductors such as GaN with about 100 or more atoms have not been much explored. Kaur et al. (2012, 2013) studied the atomic and electronic structure of small GaN, AlN, and InN nanoparticles and it was shown that nanoparticles of GaN and AlN having up to 32 III-N molecules have empty cage structures while  $(\text{InN})_{32}$  was shown to have a rocksalt cubic structure. Bulk III-nitrides are known to undergo structural transition from wurtzite to rocksalt under pressure, but in InN nanoparticles this happens without the application of any pressure. The atomic structures of larger clusters/nanoparticles are still not well understood. Calculations (P. Kaur, S.S. Sekhon, and V. Kumar, unpublished.) on GaN clusters having up to about 200 atoms do show the preference for cage-type structures. A large fraction of atoms in these structures lie on the surface. This can give rise to a high probability of doping RE atoms since on the surface strain due to doping of another type of atom can be small. But in small nanoparticles, the bond lengths are generally shorter compared with the bulk and there is often a distribution of interatomic distances. This would lead to site selectivity and a proper understanding from ab initio calculations is necessary. The surface of even a large GaN nanoparticle can have significant  $sp^2$  bonding character as it has been also found on some surfaces of bulk GaN (Neugebauer, 2001). Therefore, an understanding of the RE doping in small GaN clusters could give useful information for understanding the behavior in large nanoparticles as well.

### **3.4.1 Doping of GaN nanoparticles with Eu and codoping with Si**

Eu-doped GaN nanoparticles and the effects of Si codoping on their stability and electronic structure have been studied by Kaur et al. (2015). They concluded that in nanoparticles, it may be energetically possible to dope Eu and other lanthanides in contrast to bulk and that codoping of, for example, Si could further facilitate the RE doping.

Therefore, similar to the behavior in bulk GaN as discussed earlier, codoping can be a useful approach to achieve stability of RE atoms in different hosts at the nanoscale. Mitchell et al. (2014) reported the formation of nitrogen vacancies in bulk GaN due to the size mismatch arising from Eu doping. In nanoparticles surface is an extended defect where strain can be lowered. Experiments have shown that the PL from RE-doped hosts is site specific (Fujiwara and Dierolf, 2014) and depends on the atomic structure and deviation from a symmetric environment around the Eu site. Therefore how Ga and N defects are arranged in the vicinity of the Eu ion has important implications for improved excitation efficiency. The codoping of Si or Mg ions is helpful in reducing the symmetry as well as the creation of proper defect sites around the RE ions in bulk GaN. This can be quite different in nanoparticles as there are often structural changes and there could be sites with different environments as compared to bulk. The doping could be inside or on the surface of the nanoparticles and we would like to understand whether codoping in nanoparticles would be similar to bulk GaN. Kaur et al. (2015) studied from ab initio calculations doping of a Eu atom in  $(\text{GaN})_n$  ( $n = 12, 13,$  and  $32$ ) nanoclusters as representatives of small sizes. In particular they asked the questions: (1) if Eu doping in GaN nanoclusters becomes energetically favorable in contrast to bulk; (2) if it would lead to a transition from an empty cage to a 3D-filled cage structure of GaN nanoclusters and, if so, whether Eu goes inside the nanoclusters or on the surface; and (3) the effect of Si codoping on the stability, charge distribution, and the electronic structure.

For the undoped small GaN nanoparticles/nanoclusters, empty cage formation similar to that of the BN cages is most favorable. In BN cages there are four-membered and six-membered rings unlike pentagons and hexagons in carbon fullerenes because of the polar covalent bonding between B and N, which does not favor odd-member rings. However, as we go down in the periodic table, clusters and small nanoparticles of group IV elements do not favor the formation of cage structures as does carbon. Instead filled fullerene cages become favorable as does Si. A similar behavior has been obtained (Kasuya et al., 2004) for CdSe nanoparticles. Doping of RE atoms can affect the atomic structure and in particular if filled cages become lower in energy compared with the empty cage structures without doping. Figs. 3.6 and 3.7 show the optimized atomic structures of  $n = 12, 13,$  and  $32$  nanoclusters doped with a Eu atom and for codoping of Eu and Si at different Ga sites in hexagons and rhombi. At a hexagonal site the bonding tends to be predominantly  $sp^2$  type while at a rhombus site the bonding becomes more  $sp^3$  like. The GaN bond length is shorter for  $sp^2$  bonding configuration compared with the value in  $sp^3$  configuration as it is also the case for carbon. This is important and it is likely to affect the preference for substitution of Eu and Si on Ga sites.

The smallest cage  $(\text{GaN})_{12}$  has eight hexagons and six rhombi and all the Ga sites are equivalent. When one Eu atom is doped on a Ga site, the cage is slightly distorted as the Eu–N bond is significantly longer (2.286 Å) than the Ga–N bonds. This leads to an outward relaxation around the Eu ion and similar to bulk GaN, the nearest neighbor Ga–N bonds become contracted in the range of 1.876–1.938 Å compared with 1.879–1.954 Å for the undoped  $(\text{GaN})_{12}$ . Because the Eu–N bond in  $(\text{GaN})_{12}$  nanoparticle is longer than 2.25 Å in bulk GaN, it indicates more outward relaxation

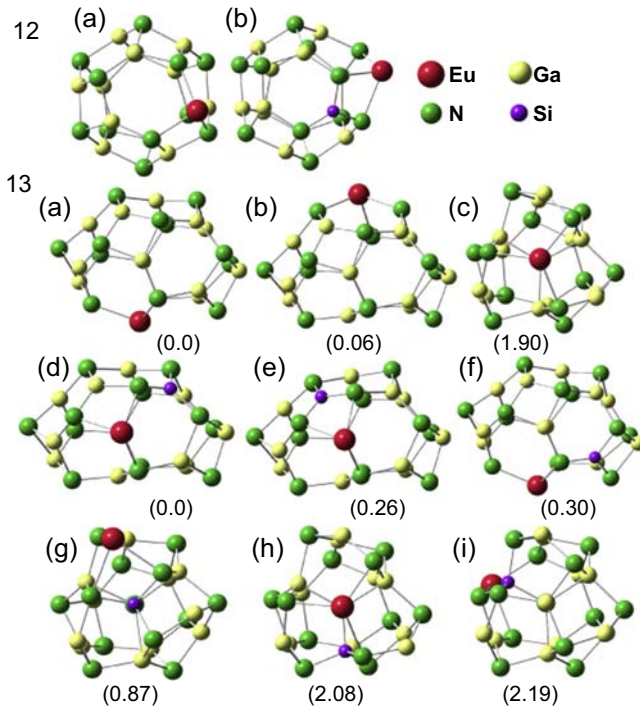


**Figure 3.6** Different isomers of empty and filled cage structures for Eu-doped and Eu + Si-codoped  $(\text{GaN})_n$  ( $n = 12$  and  $13$ ) nanoclusters. For  $(\text{GaN})_{12}$ , all Ga sites are equivalent and for Eu doping only one case is shown in 12(a). Codoping of Eu and Si is favored on Ga sites on the same rhombus as shown in 12(b). For  $n = 13$ , the lowest energy isomer is shown in 13(a) and the energy of the other isomers is given in brackets in eV. The energy of the lowest energy isomer has been taken as the reference. Cage structures 13(b) to 13(f) are favored over 3D structures (filled cage isomers) shown in 13(g) to 13(i).

After Kaur P., Sekhon, S.S., Zavada, J.M., Kumar, V., 2015. *J. Appl. Phys.* 117, 224301.

and lowering of the strain in nanoparticles. Its consequence is that Eu doping in GaN nanoparticles is energetically favorable by  $0.40 \text{ eV}$  in contrast to the cost of  $1.84 \text{ eV}$  in bulk GaN. The binding energy of the Eu-doped nanoclusters also increases, indicating enhanced chemical bonding by Eu doping.

Calculations on codoping of Si and Eu on Ga sites in  $(\text{GaN})_{12}$  show that the lowest energy isomer (Fig. 3.6, 12(b)) has Si on a Ga site that is nearest neighbor to the Eu atom such that both Si and Eu are on the same rhombus. This configuration is most favorable because as mentioned earlier, in a rhombus the bonding is more  $sp^3$ -like with longer Ga–N bonds compared with predominantly  $sp^2$  bonding in hexagons. The strain by an oversized Eu atom is lower at such a site. Furthermore, since the Si–N bond is short ( $1.692 \text{ \AA}$ ), the strain due to an oversized Eu and an undersized Si can be compensated when both Eu and Si are on nearest neighbor Ga sites. After Si codoping, the Eu–N (Si–N) bond length is  $2.337 \text{ \AA}$  ( $1.692 \text{ \AA}$ ) while the neighboring

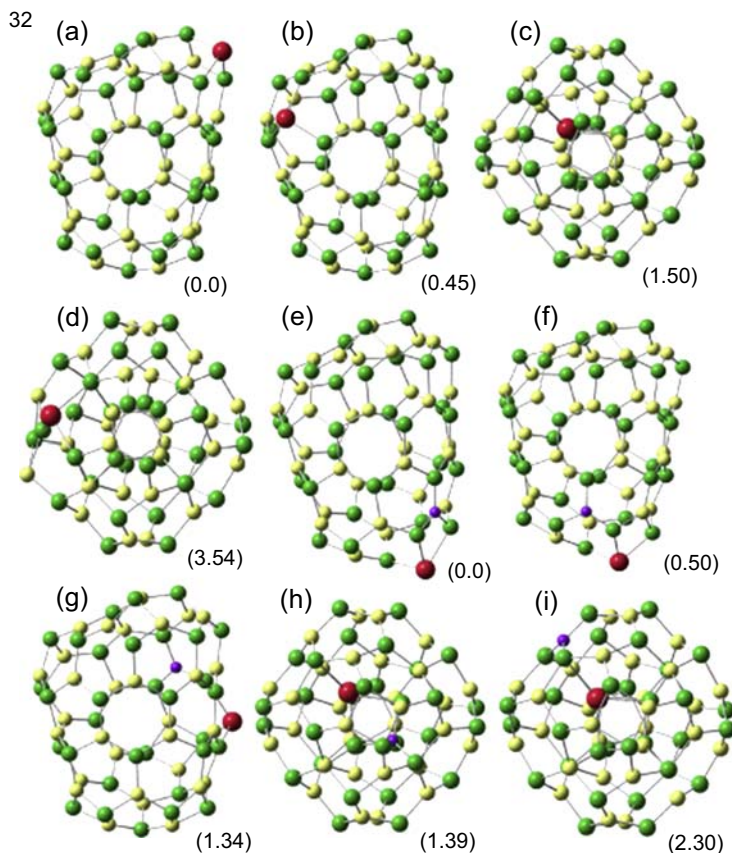


**Figure 3.7** Different empty (a, b, e, f, and g) and filled (c, d, h, and i) cage isomers of  $(\text{GaN})_{32}$  doped with Eu (a–d) and codoped with Eu and Si (e–i). Other details are the same as in Fig. 3.6. After Kaur, P., Sekhon, S.S., Zavada, J.M., Kumar, V., 2015. *J. Appl. Phys.* 117, 224301.

Ga–N bonds become slightly elongated with the bond lengths in the range of 1.883–1.928 Å. Si codoping with Eu leads to a large gain of 4.27 eV, making the nanoclusters energetically more favorable compared with Eu doping alone.

For  $n = 13$ , Eu doping was studied in empty and filled cage isomers and the optimized structures are shown in Fig. 3.6. In the filled cage, the Eu atom can bind with four N atoms (three on the cage and one inside) compared with three N atoms in an empty cage. In the empty cage (Fig. 3.6 (13a, b)), doping of Eu on a Ga site in a hexagon or a four-membered ring leads to only a small difference of 0.06 eV in energy with the hexagon slightly more favorable. For the filled cage, the optimized lowest energy structure is shown in Fig. 3.6 (13c) and it is 1.90 eV higher in energy than the empty cage isomer. This is due to the fact that the empty cage isomer of  $(\text{GaN})_{13}$  is 2.158 eV lower in energy (Kaur et al., 2012) than the filled cage. With Eu doping this difference is reduced.

With Si codoping, the optimized atomic structures are shown in Fig. 3.6 (13d–i). Calculations show that the empty cage with Eu at a rhombus site and Si at a distorted hexagonal site has the lowest energy (13d) while the isomer with both Eu and Si doped on the same rhombus (13e) is slightly (0.26 eV) higher in energy. The filled cage isomers (13g–i) lie 0.87–2.19 eV higher in energy. An interesting finding was that the energy difference between the empty and filled cage isomers reduces significantly as compared to only Eu doping case. This suggests that Si codoping can induce a transition to 3D structures for larger nanoparticles. This can be expected because Si favors  $sp^3$  bonding and in large GaN nanoparticles the bonding would be close to  $sp^3$  type.

For (GaN)<sub>32</sub> also, empty cage isomers (32a, b, e, f, and g) lie lower in energy than the filled cage isomers (32c, d, h, and i). With Eu doping the lowest energy isomer was shown to have Eu at a rhombus site (32a) and interestingly a gain of 0.40 eV compared with the undoped cage. The filled cage of (GaN)<sub>32</sub> has a distorted cuboidal unit inside  $n = 28$  cage (Kaur et al., 2012), and it lies 0.576 eV higher in energy than the empty cage isomer. Studies of different possibilities of Eu doping on a Ga site both inside and on the surface of the filled cage (32c, d) showed that these isomers are 1.50 eV (32c) and 3.54 eV (32d) higher in energy than the empty cage isomer. Furthermore, the isomer with Eu doping on the surface of the filled cage (32d) is much higher (3.54 eV) in energy compared with the isomer with Eu doped on a site inside the cage (1.50 eV) as shown in Fig. 3.7 (32c). These results can have important implications for the distribution of RE atoms in larger nanoparticles.

The previous result that an Eu atom is relatively more favorable inside the cage than on the surface could be due to more Eu–N bonds inside the cage and the fact that the cage is not tightly filled so that the strain inside is not large while on the surface, the bonds are contracted and this can make doping at the surface expansive. This result could have important implications for Eu or other RE doping in large 3D nanoparticles. As the chemical bonding between Eu and N is better than in Ga–N, sites with local  $sp^3$  bonding are more favorable. Also at such sites the bond length is longer compared to sites with local  $sp^2$  bonding. Nanoparticle surfaces can have significant  $sp^2$  bonding, and therefore doping at subsurface sites could be very likely. When Si is codoped (32e–i), an empty cage isomer with Eu and Si (32e) on the same rhombus has the lowest energy. Again the Eu–N bond (2.378 Å) and Si–N bond (1.680 Å) compensate strain in the nanoparticle. Empty cage isomer with Eu at a rhombus site and Si at a hexagon site (32f) lies 0.50 eV higher in energy, while an isomer with both Eu and Si in a hexagon (32g) has 1.34 eV higher energy. A filled cage isomer (Fig. 3.7 (32h)) with Eu and Si both in the core lies 1.39 eV higher in energy while another filled cage isomer (Fig. 3.7 (32i)) with Eu inside the cage and Si on the surface is 2.30 eV higher in energy than the minimum energy empty cage isomer. Silicon codoping with Eu in (GaN)<sub>32</sub> nanoparticles lowers its energy by 4.573 eV as also in bulk GaN. Therefore, Si codoping increases the stability of the nanoparticles also. The extra electron from Si changes Eu into a +2 charge state with  $4f^7$  electronic configuration and there is  $7 \mu_B$  magnetic moment. In general, Si codoping lowers the symmetry that could facilitate intra  $4f$  transitions. The formation energy for Si codoping in  $n = 12, 13,$  and 32 Eu-doped GaN nanoclusters is  $-2.705, -2.832,$  and  $-3.059$  eV, respectively.



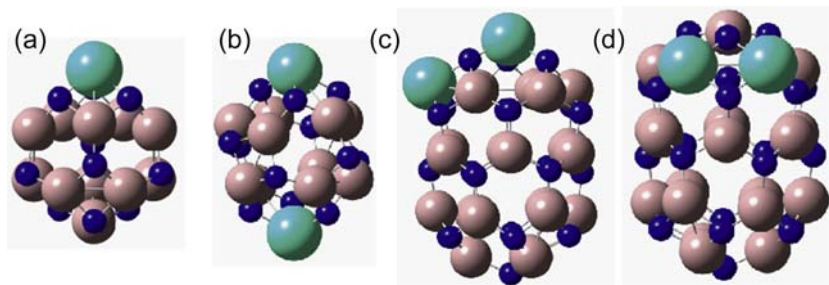


**Figure 3.8** The optimized atomic structures of (a) one Gd- or Nd-doped  $(\text{GaN})_{12}$ , (b) two Gd- or Nd-doped  $(\text{GaN})_{12}$ , (c) and (d) two Gd- or Nd-doped  $(\text{GaN})_{22}$ . For Gd the configuration (d) is about 0.08 eV lower in energy compared with the configuration in (c), both with  $14 \mu_B$  magnetic moment. Green, pink, and blue balls represent RE, Ga, and N atoms, respectively. After Kumar V., Zavada J.M., 2010. Proc. SPIE 7602, 7602 0E.

A large negative value suggests that Si codoping is strongly favorable in GaN nanoparticles and it becomes increasingly more favorable as the size grows.

### 3.4.2 Doping of GaN nanoparticles with Gd and Nd

Kumar and Zavada (2010) studied doping of Gd and Nd atoms in small  $(\text{GaN})_n$  cages with  $n = 12, 16,$  and  $22$ .  $(\text{GaN})_{16}$  has a cubic cage structure. These were shown to be lower in energy than bulk fragments. Substitution of one or two Gd or Nd atoms on Ga sites in these cages showed  $7 (3) \mu_B$  magnetic moment per Gd (Nd) in all cases as the RE atom behaves like a trivalent atom. Three electrons from either Gd or Nd participate in bonding with N and the remaining  $4f$  electrons give rise to the magnetic moments. The coupling between the spins is ferromagnetic but it is weak. For the doped case the cubic symmetry of the cage is broken. The spin-up  $4f$  levels of the Gd atom are fully occupied and lie about 3 eV below the highest occupied molecular orbital (HOMO) while the down-spin  $4f$  levels are completely unoccupied and lie about an eV above the lowest unoccupied molecular orbital (LUMO) due to large exchange splitting. This behavior is different from the case of Eu atom doping. Doping of Gd has also been studied in alumina nanoclusters (Rahane et al., 2012) and it has been found to be energetically favorable compared with the doping of Gd in bulk alumina. Each Gd atom has  $7 \mu_B$  magnetic moments and the magnetic coupling between two Gd dopants was found to be weak (Fig. 3.8).

## 3.5 Conclusions

Our work has focused on ab initio calculations of bulk GaN and  $(\text{GaN})_n$  nanoclusters doped with Eu, along with codoping of Si. The results clearly indicate that codoping of Si facilitates the inclusion of Eu in the wurtzite lattice as well as in the  $(\text{GaN})_n$  structures. The atomic structures of nanoclusters permit various atomic configurations

based on the number of specific atoms. In all of these studies, the magnetic effects are enhanced due to the codoping of Si. We have also treated  $(\text{GaN})_n$  nanoclusters doped with either Gd or Nd and found similar results.

In general, Eu doping leads to lowering of the local symmetry on a Ga site with significant deformation so that it is energetically highly unfavorable costing 1.84 eV. The lower symmetry can facilitate intra- $4f$  shell transitions. It has been found that codoping of Si lowers the energy and there is a net gain compared with pure GaN. Moreover Si codoping facilitates Eu doping since the gain is more than the sum of the gain and cost, respectively, due to the doping of Si and Eu individually. This is due to the compensation of strain from an oversized Eu atom and an undersized Si dopant. Also, there is a further reduction in the local symmetry around the Eu ion compared with Eu alone, and it can enhance intra- $4f$  transitions. Eu ions in GaN behave as trivalent species, but with the addition of tetravalent dopant Si, there is charge transfer to Eu and it behaves as divalent with the enhancement in the magnetic moments to  $7 \mu_B$  on each Eu, and there is ferromagnetic coupling between the spins on Eu ions. Si codoping reduces hybridization of the  $4f$  states of Eu with the host, making the  $4f$  states sharply distributed. This could lead to a long lifetime for luminescence, as observed. The electronic structure and the valence state of Eu are sensitive to the changes in Si concentration. Therefore, it can affect significantly the PL, as also was observed.

The results on  $(\text{GaN})_n$  nanoclusters show that Eu doping is energetically favorable compared with bulk GaN. In nanoparticles the strain is significantly reduced due to the presence of a surface. In nanoparticles there is generally a variation in the bond lengths and coordination number. It can lead to a variation in the bonding characteristics and selectivity in the distribution of RE atoms. Similar to bulk GaN, Si codoping further facilitates Eu doping with a large gain in energy.

While our calculations have dealt with only a subset of RE elements, namely Eu, Gd, and Nd, some generalizations emerge. Codoping with a smaller atom, such as Si, provides an interesting strategy to stabilize RE inclusion in GaN and other III-V nitride host materials. In our work, codoping GaN:Eu with Si produces a higher magnetic moment. Codoping GaN:Eu with other small atoms, such as Mg or O, is likely to facilitate the RE doping. However, it is not clear that the optical and magnetic properties will likewise be enhanced. Specific material systems consisting of a semiconductor and RE atom need to be addressed individually.

Our results indicate that spin-polarized LEDs, based on active regions of GaN:Eu, codoped with Si, are clearly feasible. The growth technology has certainly been established for fabrication of such structures (Koizumi et al., 2015, in this volume). One of the many questions that remain is whether the magnetic properties of such epilayers can be altered with application of an external electric field. Experiments need to explore this possibility. The  $(\text{GaN})_n$  nanoparticles offer many novel device applications. These powders can be imbedded in other materials to form optical and magnetic composites. The strain due to Eu doping as well as variations in local atomic structure will in general have reduced symmetry around a Eu ion in such nanoparticles and enhance intra  $4f$  level transitions. In addition, the nanoparticles may be deposited on Si electronic chips to produce multifunctional capabilities. In all of these examples, further analysis and experimental work is warranted.

## Acknowledgments

It is a pleasure to acknowledge the contributions of our collaborators A. V. Bruno Cruz, P. P. Shinde, P. Kaur, and S.S. Sekhon for the results and progress reported here. We are grateful to the staff of the Centre for Development of Advanced Computing for the use of their super-computing facilities and excellent support. V. K. thankfully acknowledges the financial support from the International Technology Centre—Pacific (ITC-PAC) for the work reported in this chapter.

## References

- Andreev, T., Monroy, E., Gayral, B., Daudin, B., Liem, N.Q., Hori, Y., Tanaka, M., Oda, O., Dang, D.L.S., 2005. *Appl. Phys. Lett.* 87, 021906.
- Bang, H., Morishima, S., Li, Z., Akimoto, K., Nomura, M., Yagi, E., 2002. *J. Appl. Phys.* 237–239, 1027.
- Bettinelli, M., Carlos, L., Liu, X., 2015. *Phys. Today* 68, 38.
- Blöchl, P.E., 1994. *Phys. Rev. B* 50, 17953.
- Bouzigués, C., Gacoin, T., Alexandrou, A., 2011. *ACS Nano* 5, 8488.
- Bruno Cruz, A.V., Shinde, P.P., Kumar, V., Zavada, J.M., 2012. *Phys. Rev. B* 85, 045203.
- Casey, H.C., 1999. *Devices for Integrated Circuits, Silicon and III-V Compound Semiconductors*. John Wiley & Sons, Inc.
- Colvin, V.L., Schlamp, M.C., Alivisatos, A.P., 1994. *Nature* 370, 354.
- Dahal, R., Ugolini, C., Lin, J.Y., Jiang, H.X., Zavada, J.M., 2009. *Appl. Phys. Lett.* 95, 111109.
- Dahal, R., Ugolini, C., Lin, J.Y., Jiang, H.X., Zavada, J.M., 2010. 1.54  $\mu\text{m}$  emitters based on erbium doped InGaN p-i-n junctions. *Appl. Phys. Lett.* 97, 141109.
- Dhar, S., Pérez, L., Brandt, O., Trampert, A., Ploog, K.H., Keller, J., Beschoten, B., 2005a. Gd-doped GaN: a very dilute ferromagnetic semiconductor with a Curie temperature above 300 K. *Phys. Rev. B* 72, 245203.
- Dhar, S., Brandt, O., Ramsteiner, M., Sapega, V.F., Ploog, K.H., 2005b. Colossal magnetic moment of Gd in GaN. *Phys. Rev. Lett.* 94, 037205.
- Dietl, T., Ohno, H., Matsukura, F., Cibert, J., Ferrand, D., 2000. Zener model description of ferromagnetism in zinc-blende magnetic semiconductors. *Science* 287 (5455), 1019–1022.
- Edgar, J.H., Strite, S., Akasaki, I., Amano, H., Wetzell, C. (Eds.), 1999. *Properties, Processing and Applications of Gallium Nitride and Related Semiconductors*. IEE-INSPEC, Hertfordshire.
- El-Himri, A., Perez-Coll, D., Nunez, P., Martin, I.R., Lavin, V., Rodriguez, V.D., 2004. *J. Solid State Chem.* 177, 4213.
- El-Masry, N.A., Zavada, J.M., Nepal, N., Bedair, S.M., 2015. Ferromagnetic behavior in transition metal doped III-N semiconductors (Chapter 12, This Volume).
- Favennec, P.N., Lharidon, H., Salvi, M., Moutonnet, D., Leguillou, Y., 1989. Luminescence of erbium implanted in various semiconductors: IV, III-V and II-VI materials. *Electron. Lett.* 25, 718.
- Favennec, P.N., L'Haridon, H., Moutonnet, D., Salvi, M., Gauneau, M., 1990. Optical activation of  $\text{Er}^{3+}$  implanted in silicon by oxygen impurities. *Jpn. J. Appl. Phys.* 29, L524.
- Filhol, J.-S., Jones, R., Shaw, M.J., Briddon, P.R., 2004. *Appl. Phys. Lett.* 84, 2841.
- Fujiwara, Y., Dierolf, V., 2014. *Jpn. J. Appl. Phys.* 53 (Part 1), 05FA13.
- Gautam, A., van Veggel, F.C.J.M., 2011. *Chem. Mater.* 23, 4817.



- Goumri-Said, S., Kanoun, M.B., 2008. *J. Phys. D Appl. Phys.* 41 (035004).
- Hashimoto, M., Yanase, A., Asano, R., Tanaka, H., Bang, H., Akimoto, K., Asahi, H., 2003. *Jpn. J. Appl. Phys.* 42 (Part 2), L1112.
- Hirata, G.A., Ramos, F., Garcia, R., Bosze, E.J., Mckittrick, J., Contreras, O., 2001. *Phys. Stat. Sol A* 188, 179.
- Hirosaki, N., Xie, R.-J., Inoue, K., Sekiguchi, T., Dierre, B., Tamura, K., 2007. *App. Phys. Lett.* 91, 061101.
- Hite, J., Thaler, G.T., Khanna, R., Abernathy, C.R., Pearton, S.J., Park, J.H., Steckl, A.J., Zavada, J.M., 2006. Optical and magnetic properties of Eu-doped GaN. *J. Appl. Phys. Lett.* 89, 132119.
- Hite, J., Frazier, R.M., Davies, R.P., Thaler, G.T., Abernathy, C.R., Pearton, S.J., Zavada, J.M., Brown, E., Hömmerich, U., 2007. Effect of Si Co-doping on ferromagnetic properties of GaGdN. *J. Elec. Mat.* 36, 391.
- Hori, Y., Andreev, T., Jalabert, D., Monroy, E., Dang, L.S., Daudin, B., Tanaka, M., Oda, O., 2006. *Appl. Phys. Lett.* 88, 053102.
- Hori, Y., Biquard, X., Monroy, E., Jalabert, D., Enjalbert, F., Dang, L.S., Tanaka, M., Oda, O., Daudin, B., 2004a. *Appl. Phys. Lett.* 84, 206.
- Hori, Y., Jalabert, D., Andreev, T., Monroy, E., Tanaka, M., Oda, O., Daudin, B., 2004b. *Appl. Phys. Lett.* 84, 2247.
- Hung, I.H., Lai, Y.H., Feng, Z.C., Gupta, S., Zaidi, T., Ferguson, I., Lu, W., 2010. *Proc. SPIE* 7784, 77840H.
- Ishizumi, A., Sawahata, J., Akimoto, K., Kanemitsu, Y., 2006. *Appl. Phys. Lett.* 89, 191908.
- Kane, M.H., Gupta, S., Ferguson, I.T., 2015. Transition metal and rare earth doping in GaN (Chapter 10, This Volume).
- Kasuya, A., Sivamohan, R., Barnakov, Y.A., Dmitruk, I.M., Nirasawa, T., Romanyuk, V.R., Kumar, V., Mamykin, S.V., Tohji, K., Jeyadevan, B., Shinoda, K., Kudo, T., Terasaki, O., Liu, Z., Belosludov, R.V., Sundararajan, V., Kawazoe, Y., 2004. *Nat. Mater.* 3, 99.
- Kaur, P., Sekhon, S.S., Kumar, V., 2012. *Phys. Rev. B* 85, 085429.
- Kaur, P., Sekhon, S.S., Kumar, V., 2013. *J. Chem. Phys.* 138, 114310.
- Kaur, P., Sekhon, S.S., Kumar, V., Unpublished.
- Kaur, P., Sekhon, S.S., Zavada, J.M., Kumar, V., 2015. *J. Appl. Phys.* 117, 224301.
- Koizumi, A., Mitchell, B., Dierolf, V., Fujiwara, Y., 2015. Growth of Eu-doped GaN and its magneto-optical properties (Chapter 8, This Volume).
- Kresse, G., Joubert, D., 1999. *Phys. Rev. B* 59, 1758.
- Kudrawiec, R., Nyk, M., Podhorodecki, A., Misiewicz, J., Streck, W., Wołczyrz, M., 2006. *Appl. Phys. Lett.* 88, 061916.
- Kumar, V., Zavada, J.M., 2010. *Proc. SPIE* 7602, 7602 0E.
- Lambrecht, W.R.L., 2015. Electronic structure of magnetic impurities and defects in semiconductors: a guide to the theoretical models (Chapter 2, This Volume).
- Lozykowski, H.J., Jadwisnienczak, W.M., Han, J., Brown, I.G., 2000. *Appl. Phys. Lett.* 77, 767.
- Madsen, G.K.H., Novák, P., 2005. *Europhys. Lett.* 69, 777.
- MacKenzie, J.D., Abernathy, C.R., Pearton, S.J., Hommerich, U., Wu, X., Schwartz, R.N., Wilson, R.G., Zavada, J.M., 1996. Er doping of ALN during growth by metalorganic molecular beam epitaxy. *Appl. Phys. Lett.* 69, 2083–2085.
- Metcalf, G.D., Readinger, E.D., Woodward, N., Dierolf, V., Nepal, N., Zavada, J.M., 2015. Optical and magnetic characterization of III-N: Nd grown by MBE (Chapter 9, This Volume).
- Mitchell, B., Poplawsky, J., Lee, D., Koizumi, A., Fujiwara, Y., Dierolf, V., 2014. *J. Appl. Phys.* 115, 204501.

- Monkhorst, H.J., Pack, J.D., 1976. *Phys. Rev. B* 13, 5188.
- Munekata, H., Ohno, H., von Molnar, S., Segmüller, A., Chang, L.L., Esaki, L., 1989. Diluted magnetic III-V semiconductors. *Phys. Rev. Lett.* 63, 1849.
- Nakamura, S., Pearton, S., Fasol, G., 2000. *The Blue Laser Diode: The Complete Story*. Springer.
- Nakhmanson, S.M., Buongiorno Nardelli, M., Bernholc, J., 2005. *Phys. Rev. B* 72, 115210.
- Nanavati, S., Sundararajan, V., Mahamuni, S., Ghaisas, S.V., Kumar, V., 2011. *Phys. Rev. B* 84, 045306.
- Nepal, N., Jiang, H.X., Lin, J.Y., Mitchell, B., Dierolf, V., Zavada, J.M., 2015. MOCVD growth of Er-doped III-N and optical-magnetic characterization (Chapter 7, This Volume).
- Neugebauer, J., 2001. *Phys. Status Solidi B* 227, 93.
- Ney, A., 2015. Gadolinium-doped gallium-nitride (GaN: Gd): synthesis routes, structure, and magnetism (Chapter 6, This Volume).
- Nishikawa, A., Kawasaki, T., Furukawa, N., Terai, Y., Fujiwara, Y., 2009. *Appl. Phys. Express* 2, 071004.
- Nishikawa, A., Furukawa, N., Kawasaki, T., Terai, Y., Fujiwara, Y., 2010. *Appl. Phys. Lett.* 97, 05113.
- Nyk, M., Kudrawiec, R., Strek, W., Misiewicz, J., 2006. *Opt. Mater.* 28, 767.
- O'Donnella, K.P., Hourahine, B., 2006. *Eur. Phys. J. Appl. Phys.* 36, 91.
- Ohta, H., Okubo, S., Fujiwara, Y., 2015. Electron spin resonance studies of GaAs:Er, O (Chapter 5, This Volume).
- Pan, X., An, X., Zhang, Z., Zhou, J., Xie, E., 2012. *J. Alloys Compd* 519, 67.
- Perdew, J.P., Chevary, J.A., Vosko, S.H., Jackson, K.A., Pederson, M.R., Singh, D.J., Fiolhais, C., 1992. *Phys. Rev. B* 46, 6671.
- Poitras, C.B., Wu, H., Turner, A.C., Spencer, M.G., Lipson, M., 2006. *Appl. Phys. Lett.* 89, 111912.
- Prodi, L., Rampazzo, E., Rastrelli, F., Speghinic, A., Zaccheronia, N., 2015. *Chem. Soc. Rev.* 44, 4922.
- Rahane, A.B., Deshpande, M.D., Kumar, V., 2012. *J. Phys. Chem. C* 116, 6115.
- Readinger, E.D., Metcalfe, G.D., Shen, H., Wraback, M., 2008. GaN doped with neodymium by plasma-assisted molecular beam epitaxy. *Appl. Phys. Lett.* 92, 061108.
- Rubio-Ponce, A., Conde-Gallardo, A., Olguin, D., 2008. *Phys. Rev. B* 78, 035107.
- Sanna, S., Schmidt, W.G., Frauenheim, Th, Gerstmann, U., 2009. *Phys. Rev. B* 80, 104210.
- Seo, J., Chen, S., Sawahata, J., Mitome, M., Akimoto, K., 2008. *J. Cer. Proc. Res.* 9, 68.
- Steckl, A.J., Birkhahn, R., 1998. Visible emission from Er-doped GaN grown by solid source molecular beam epitaxy. *Appl. Phys. Lett.* 73, 1700–1702.
- Steckl, A.J., Heikenfeld, J.C., Lee, D.S., Garter, M.J., Baker, C.C., Wang, Y.Q., Jones, R., 2002. Rare-earth-doped GaN: growth, properties, and fabrication of electroluminescent devices. *IEEE J. Sel. Top. Quantum Electron* 8, 749.
- Steeneken, P.G., Tjeng, L.H., Elfimov, I., Sawatzky, G.A., Ghiringhelli, G., Brookes, N.B., Huang, D.-J., 2002. *Phys. Rev. Lett.* 88, 047201.
- Svane, A., Christensen, N.E., Gorczyca, I., van Schilfgaarde, M., Chantis, A.N., Kotani, T., 2010. *Phys. Rev. B* 82, 115102.
- Svane, A., Christensen, N.E., Petit, L., Szotek, Z., Temmerman, W.M., 2006. *Phys. Rev. B* 74, 165204.
- Sawahata, J., Seo, J., Chen, S., Takiguchi, M., Saito, D., Nemoto, S., Akimoto, K., 2006. *Appl. Phys. Lett.* 89, 192104.
- Takahei, K., Taguchi, A., Horikoshi, Y., Nakata, J., 1994. Atomic configuration of the Er-O luminescence center in Er-doped GaAs with oxygen codoping. *J. Appl. Phys.* 76, 4332.

- Teraguchi, N., Suzuki, A., Nanishi, Y., Zhou, Y.K., Hashimoto, M., Asahi, H., 2002. Room-temperature observation of ferromagnetism in diluted magnetic semiconductor GaGdN grown by RF-molecular beam epitaxy. *Solid State Commun.* 122, 651.
- Ugolini, C., Nepal, N., Lin, J.Y., Jiang, H.X., Zavada, J.M., 2006. Erbium-doped GaN epilayers synthesized by metal-organic chemical vapor deposition. *Appl. Phys. Lett.* 89, 151903.
- Wang, F., Liu, X., 2014. *Acc. Chem. Res.* 47, 1378.
- Wang, R., Steckl, A.J., Brown, E.E., Hommerich, U., Zavada, J.M., 2009. Effect of Si co-doping on  $\text{Eu}^{3+}$  luminescence in GaN. *J. Appl. Phys.* 105, 043107.
- Wang, R., Steckl, A.J., Nepal, N., Zavada, J.M., 2010. Electrical and magnetic properties of GaN codoped with Eu and Si. *J. Appl. Phys.* 107, 013901.
- Wang, Y.Q., Steckl, A.J., 2003. *Appl. Phys. Lett.* 82, 502.
- Wilson, R.G., Schwartz, R.N., Abernathy, C.R., Pearton, S.J., Newman, N., Rubin, M., Fu, T., Zavada, J.M., 1994. 1.54- $\mu\text{m}$  photoluminescence from Er-implanted GaN and AlN. *Appl. Phys. Lett.* 65, 992.
- Wu, H., Poitras, C.B., Lipson, M., Spencer, M., Hunting, J., DiSalvo, F., 2005. *Appl. Phys. Lett.* 86, 191918.
- Wu, H., Poitras, C.B., Lipson, M., Spencer, M.G., Hunting, J., DiSalvo, F.J., 2006. *Appl. Phys. Lett.* 88, 011921.
- Yamada, T., Nanbu, H., Yamane, H., Kohiro, K., Tsuchida, Y., 2006. *Jpn. J. Appl. Phys.* 45, L194.
- Yang, J., Fainblat, R., Kwon, S.G., Muckel, F., Yu, J.H., Terlinden, H., Kim, B.H., Iavarone, D., Choi, M.K., Kim, I.Y., Park, I., Hong, H.-K., Lee, J., Son, J.S., Lee, Z., Kang, K., Hwang, S.-J., Bacher, G., Hyeon, T., 2015. *J. Am. Chem. Soc.* 137, 12776.
- Yu, J.H., Liu, X., Kweon, K.E., Joo, J., Park, J., Ko, K.-T., Lee, D.W., Shen, S., Tivakornasithorn, K., Son, J.S., Park, J.-H., Kim, Y.-W., Hwang, G.S., Dobrowolska, M., Furdyna, J.K., Hyeon, T., 2010. *Nat. Mater.* 9, 47.
- Zhang, L., Liu, F.Q., Liu, C., 2007. *Appl. Phys. Lett.* 91, 143514.
- Zavada, J.M., Nepal, N., Ugolini, C., Lin, J.Y., Jiang, H.X., Davies, R., Hite, J., Abernathy, C.R., Pearton, J., Brown, E.E., Hommerich, U., 2007. Optical and magnetic behavior of erbium-doped GaN epilayers grown by metal-organic chemical vapor deposition. *Appl. Phys. Lett.* 91, 054106.

## Part Two

# **Magnetic semiconductors based on rare earth/transition metals**

This page intentionally left blank

# Prospects for rare-earth-based dilute magnetic semiconductor alloys and hybrid magnetic rare-earth/semiconductor heterostructures

*S. Dong, J.K. Furdyna, X. Liu*

University of Notre Dame, Notre Dame, IN, United States

## 4.1 Introduction

### 4.1.1 Objectives and background

In this chapter we will consider the possibility of incorporating rare-earth (RE) elements into semiconductor lattices with an eye on designing new dilute magnetic semiconductor (DMS) materials. Among the qualities of RE elements that make them attractive for this purpose are their large magnetic moments (see [Table 4.1](#)), which may be exploited for designing magnetic properties of these materials. To proceed in this direction, we have the opportunity to build on our extensive experience with the family of already established DMSs, and especially on the rich literature involving  $\text{II}_{1-x}\text{Mn}_x\text{VI}$  and  $\text{III}_{1-x}\text{Mn}_x\text{V}$  alloys. However, in considering the options made possible by involving the REs in this role, we should also recall that the earliest magnetic semiconductors (in this case binary compounds rather than ternary alloys) were in fact based on RE elements; for example, EuS and EuSe ([Proceedings, 1970](#); [Enz et al., 1962](#); [Vanhouten, 1962](#); [Reed and Fahey, 1971](#)). In exploring this subject we can additionally build on the already existing rich literature in the area of incorporating RE ions in semiconductor lattices, which has been carried out for the purpose of a wide range of optical effects ([Kumta and Risbud, 1994](#); [Zavada and Zhang, 1995](#); [Steckl et al., 2002](#); [Kenyon, 2002](#); [Bunzli et al., 2007](#); [Steckl et al., 2007](#)). We illustrate this latter aspect by [Fig. 4.1](#), which shows interlevel transition energies of several REs incorporated in dilute amounts into the GaN lattice for laser applications ([Steckl et al., 2007](#)). While this latter effort is unrelated to magnetic properties, it contributes significantly to our know-how regarding the incorporation of RE ions into the semiconductor lattice, which may thus be exploited for purposes discussed in this chapter.

Originally the field of DMSs started out with  $\text{II}_{1-x}\text{Mn}_x\text{VI}$  alloys ([Furdyna and Kossut, 1988](#); [Furdyna, 1988](#); [Gaj and Kossut, 2011](#)). The success of this family of materials was based on the ease of incorporating Mn ions by substitution for the group-II elements in the parent II-VI semiconductor lattice, owing to the preference

**Table 4.1 Atomic, covalent, and ionic radii, and magnetic moments of rare earths (Lide, 2004)**

	Atomic radii (pm)	Covalent radii (pm)	Ionic radii (pm) coordination number = 8			Magnetic moment ( $\mu_B$ ) $\mu_{\text{eff}} = g\sqrt{J(J+1)}\mu_B^a$		
			RE <sup>2+</sup>	RE <sup>3+</sup>	RE <sup>4+</sup>	RE <sup>2+</sup>	RE <sup>3+</sup>	RE <sup>4+</sup>
La	187.9	207		118			0	
Ce	183.2	204		114	97		2.54	0
Pr	182.8	203		114	96		3.58	2.54
Nd	182.1	201		112			3.62	
Pm	181.1	199		110			2.68	
Sm	180.4	198	127	109		0 (3.4)	0.85	
Eu	204.2	198	125	107		7.94	0 (3.4)	
Gd	180.1	196		106			7.94	
Tb	178.4	194		104	88		9.72	7.94
Dy	177.4	192		103			10.63	
Ho	176.6	192		102			10.58	
Er	175.7	189		100			9.58	
Tm	174.6	190	108	99		4.54	7.56	
Yb	193.9	187	107	98		0	4.54	
Lu	173.5	187		97			0	

<sup>a</sup>g is the Lande factor and  $J$  is the total angular momentum.

of this element for the divalent state. We note parenthetically that, although Mn played a dominant role in these early DMS studies, it was also possible to extend the concepts established in that work to transition metals (TMs) other than Mn (eg, Co) in the II-VI lattice (Lewicki et al., 1989). These alloys are examples of isovalent incorporation of magnetic cations, and are typically paramagnetic, tending toward antiferromagnetism as the concentration of magnetic ions becomes large. We will use these alloys as a conceptual precursor for considering their ternary RE analogs in Section 4.2.1.

The field of DMSs acquired new impetus with the emergence of ferromagnetic (FM) DMS alloys such as  $\text{In}_{1-x}\text{Mn}_x\text{As}$  and  $\text{Ga}_{1-x}\text{Mn}_x\text{As}$  (Dietl et al., 2009; Ohno et al., 1991, 1996; VanEsch et al., 1997; Ohno, 1999). These  $\text{III}_{1-x}\text{Mn}_x\text{V}$  materials differ qualitatively from the  $\text{II}_{1-x}\text{Mn}_x\text{VI}$  family in that now the Mn ions, while still retaining their preferred divalent state, substitute for a group-III element (ie, the substitution in this case is heterovalent), bringing not only magnetic moments into the system, but also becoming acceptors. The holes arising from the acceptor nature of  $\text{Mn}^{2+}$  then provide an RKKY-like medium of exchange between magnetic moments

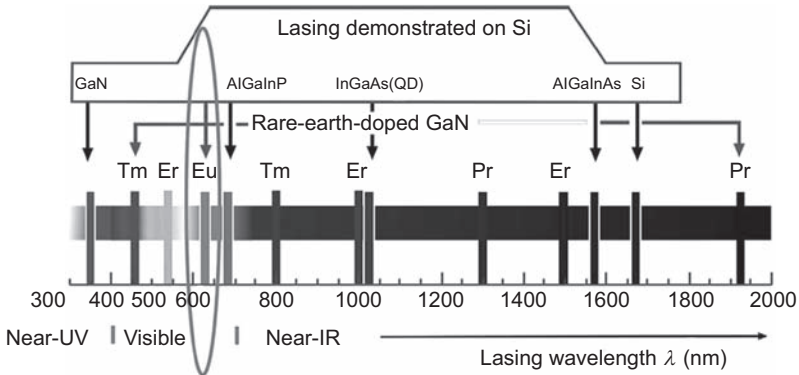


**Figure 4.1** Wavelength scale indicating emissions obtained from various REs incorporated into the GaN lattice. The figure also compares these RE emissions with lasing wavelengths from several well-known semiconductor materials.

Adapted from Steckl, A.J., Park, J.H., Zavada, J.M., 2007. Prospects for rare earth doped GaN lasers on Si. *Materials Today* 10, 20–27.

localized on the Mn ions, resulting in ferromagnetism (Mahadevan et al., 2004). In Fig. 4.2 we illustrate the quality of FM properties of these alloys in the form of specularly square hysteresis loop observed in  $\text{Ga}_{1-x}\text{Mn}_x\text{As}$  (Cho et al., 2008). Such non-isovalent incorporation of the magnetic element in  $\text{III}_{1-x}\text{Mn}_x\text{V}$  systems can then serve

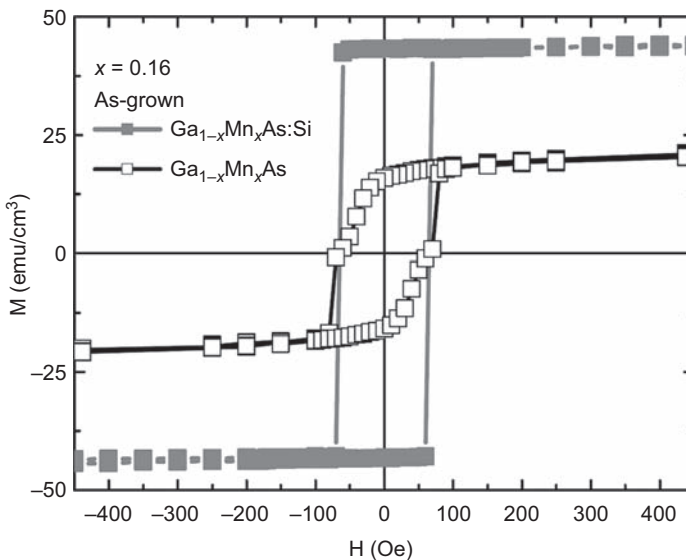


**Figure 4.2** Hysteresis loops observed at 5 K in  $\text{Ga}_{0.84}\text{Mn}_{0.16}\text{As}$  and  $\text{Ga}_{0.84}\text{Mn}_{0.16}\text{As}:\text{Si}$  films grown by low-temperature MBE. Magnetic field is applied along the in-plane (100) easy axis of the films.

After Cho, Y.J., Yu, K.M., Liu, X., Walukiewicz, W., Furdyna, J.K., 2008. Effects of donor doping on  $\text{Ga}_{1-x}\text{Mn}_x\text{As}$ . *Applied Physics Letters* 93, 262505.



as a model for considering analogous nonisovalent RE incorporation into a semiconductor matrix. Prospects for such systems will be considered in [Section 4.2.2](#).

#### **4.1.2 Properties of rare-earth ions relevant to formation of dilute magnetic semiconductors**

In contemplating the prospects for creating RE-containing magnetic semiconductor alloys, we first need to consider specific properties of the RE ions. First, all lanthanide REs can exist in the trivalent state; additionally, the valency of Sm, Eu, Tm, and Yb can be 2+ ([Dietl, 1994](#)), while Ce, Pr, and Tb can have a valency of 4+, which can be exploited in designing various options for bonding and coordination in RE-based DMS alloys. Another property of the REs is the large value of their covalent radii, which typically lie in a very narrow range, as shown in [Table 4.1](#). These are large radii, which may stand in the way of forming semiconductor alloys with RE concentrations that are sufficient for achieving significant magnetism. Here, however, we can build on experience already established with incorporating alien ions into the III-V lattice by low temperature (nonequilibrium) epitaxy, as has been done very successfully in the case of the  $\text{III}_{1-x}\text{Mn}_x\text{V}$  FM alloys. On the other hand, this size is nicely compatible with semiconducting systems based on Ba and, of course, on La, so that RE ions can be readily substituted for these elements in order to introduce magnetic moments into the material in question. We will discuss this as we consider the various possibilities in [Sections 4.2 and 4.5](#).

We should also note here that most binary RE compounds, particularly pnictides and chalcogenides, tend to be either FM or antiferromagnetic (AFM). This feature will prove important when we consider the effect of magnetic RE-based inclusions or nanoscale insertions on the overall magnetic properties of RE-based semiconductor systems, in a manner analogous to inclusion of MnAs in GaMnAs ([De Boeck et al., 1996](#)), or of Co in ZnO ([Sawicki et al., 2013](#)), which are known to play an important role in determining the magnetism of the resulting composite structure ([Bonanni and Dietl, 2010](#)). RE analogs of such inhomogeneous systems will be considered in [Section 4.4](#).

Finally, let us also consider the case of already well-established DMSs based on TMs such as  $\text{Zn}_{1-x}\text{Co}_x\text{Se}$ ,  $\text{Ga}_{1-x}\text{Mn}_x\text{As}$ , or  $\text{Pb}_{1-x}\text{Mn}_x\text{Te}$ , into which we additionally introduce RE ions. The coexistence of  $4f$  and  $3d$  electrons in such a system is expected to bring entirely novel situations, with interesting implications for spintronic applications. Specifically, magnetic interactions occurring in such RE–TM intermetallic alloys will now involve the following mechanisms: (1) a relatively weak RE–RE interaction, (2) a much stronger TM–TM interaction, and (3) RE–TM interaction, with a strength intermediate between (1) and (2) ([Buschow, 1977](#)). In the past 10 years many novel phenomena have been observed in systems of this type, in which both the ion radius and the spin reversal of the RE ions can strongly affect the spin configuration/reorientation of the TM ions (eg, controllable spin flop ([Kimura et al., 2003](#)), spin-induced current ([Katsura et al., 2005](#)), antisymmetric Dzyaloshinskii–Moriya interaction ([Cheong and Mostovoy, 2007](#))), thus providing intriguing opportunities for exploration of new types of spintronic functionalities.

### 4.1.3 Chapter organization

The present chapter is organized as follows. We first consider the possible effects of substitutional incorporation of RE ions into semiconductor lattices (both isovalent and heterovalent) in the form of homogeneous single-phase alloys. Next, we will discuss inhomogeneous semiconductor systems containing REs, where the inhomogeneity arises either from spinodal decomposition or from precipitation of phases other than the host matrix. We will then consider heterostructures comprised of RE and semiconductor constituents. Following this, we will discuss the newly emerging systems of layered pnictide and chalcogenide DMSs, whose complex crystal structure appears particularly suitable for RE incorporation. And, finally, we will briefly introduce the basics of AFM spintronics, which is now acquiring increasing attention, and which holds out special opportunities for systems based on REs.

## 4.2 Single-phase magnetic semiconductor alloys based on rare earths

### 4.2.1 Magnetic semiconductors with isovalent rare-earth incorporation

Extensive studies of DMSs began in the 1970s, focused primarily on  $\text{II}_{1-x}\text{Mn}_x\text{VI}$  ternary alloys such as  $\text{Hg}_{1-x}\text{Mn}_x\text{Te}$  and  $\text{Cd}_{1-x}\text{Mn}_x\text{Te}$  (Furdyna, 1988). In these systems the magnetic ion (Mn) enters the system with the same valency (2+) as that of the cations which it replaces, thus acting as a pseudo-group-II element. Systems of this type can be fabricated by bulk techniques (such as Bridgman crystal growth) up to impressively high concentrations of Mn (eg, in excess of  $x = 0.65$  in the case of  $\text{Cd}_{1-x}\text{Mn}_x\text{Te}$ ); and, with the advent of epitaxial methods, the range of Mn incorporation has been extended to higher values of  $x$ , even including  $x = 1.0$ . These systems were of interest for their magneto-optical properties (giant Faraday rotation (Bartholomew et al., 1986), wave function mapping in quantum structures (Lee et al., 1999), formation of novel magnetic structures such as spin superlattices (Dai et al., 1991), a wide range of magnetotransport phenomena (Wojtowicz and Mycielski, 1983; Wojtowicz et al., 1985)), specific magnetic properties (spin glass and AFM ordering (Galazka et al., 1980; Nagata et al., 1980), including entirely new AFM structures (Giebultowicz et al., 1990, 1994)), and novel device functionalities, such as the spin transistor (Betthausen et al., 2012) device. The dramatic magneto-optical potential of these materials is illustrated in Fig. 4.3, which shows the giant Faraday rotation in  $\text{CdMnTe}$  that reaches angles in excess of tens of thousands of degrees (Bartholomew et al., 1986).

#### 4.2.1.1 Rare-earth alloys based on II-VI semiconductor lattice

The success of fabrication of  $\text{II}_{1-x}\text{Mn}_x\text{VI}$  ternaries, and the wide range of new magnetic, magneto-optical, and magnetotransport effects that they exhibit (Furdyna, 1988; Furdyna and Kossut, 1988), encourage the possibility of extending these

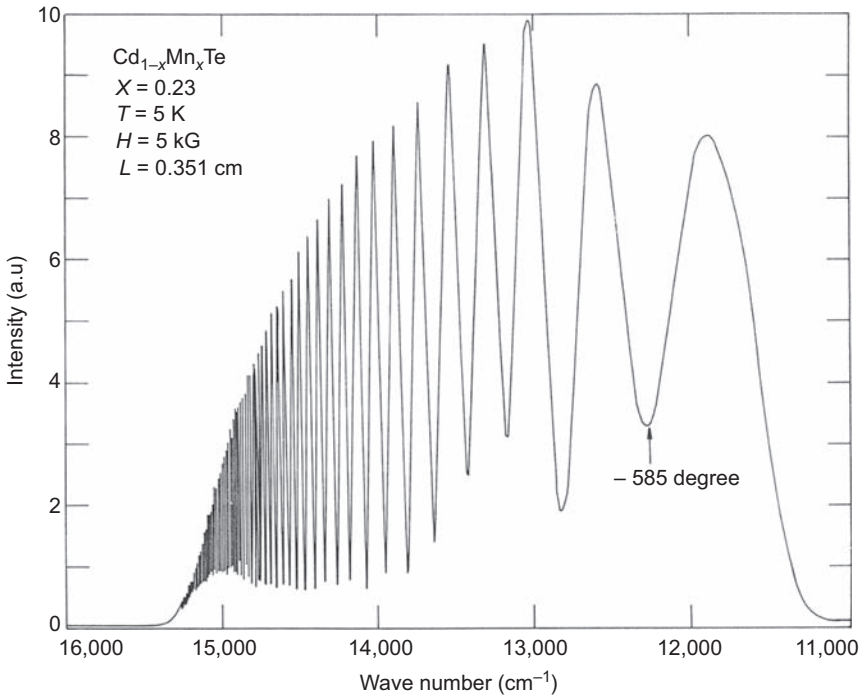


**Figure 4.3** Transmission as a function of wave number through a  $\text{Cd}_{1-x}\text{Mn}_x\text{Te}$  slab ( $x = 0.23$ ) sandwiched between two linear polarizers, displaying giant Faraday rotation. At  $15,000 \text{ cm}^{-1}$  the rotation exceeds  $-8000$  degree. The measurements were carried out at  $5 \text{ K}$  at  $5 \text{ T}$ . After Bartholomew, D.U., Furdyna, J.K., Ramdas, A.K., 1986. Interband Faraday rotation in diluted magnetic semiconductors:  $\text{Zn}_{1-x}\text{Mn}_x\text{Te}$  and  $\text{Cd}_{1-x}\text{Mn}_x\text{Te}$ . *Physical Review B* 34, 6943–6950.

systems to their RE-based analogs. In this connection we will first consider  $\text{Eu}^{2+}$ , for two reasons. First, the Eu ion is capable of existing in the divalent state, and is thus expected to be particularly attractive for forming II-VI-based alloys by substituting for the group-II element in analogy with  $\text{Mn}^{2+}$ . And second, it also resembles  $\text{Mn}^{2+}$  in that its  $f$ -shell is exactly half full, similar to the  $d$ -shell of Mn. This then suggests that in principle  $\text{Eu}^{2+}$  can be used to extend the II-VI-based family of DMSs by bringing in its large magnetic moment of  $\sim 7$  Bohr magnetons into the DMS family.

We should note here, however, that the possibility of incorporating REs in a II-VI lattice in divalent state as described earlier, in analogy to  $\text{Mn}^{2+}$  and  $\text{Co}^{2+}$  ions, is at best speculative, since so far we only have evidence for the presence of REs in trivalent state in this structure (Mukherjee et al., 2010). For example, as shown in Fig. 4.4, luminescence from Tb and Eu incorporated in ZnS nanoparticles is ascribed to  $\text{Tb}^{3+}$  and  $\text{Eu}^{3+}$ . This situation, however, involves REs incorporated in extremely dilute amounts. Since we have no knowledge of the preferred valency REs when they enter the II-VI lattice at concentrations required for achieving significant magnetic behavior, we have

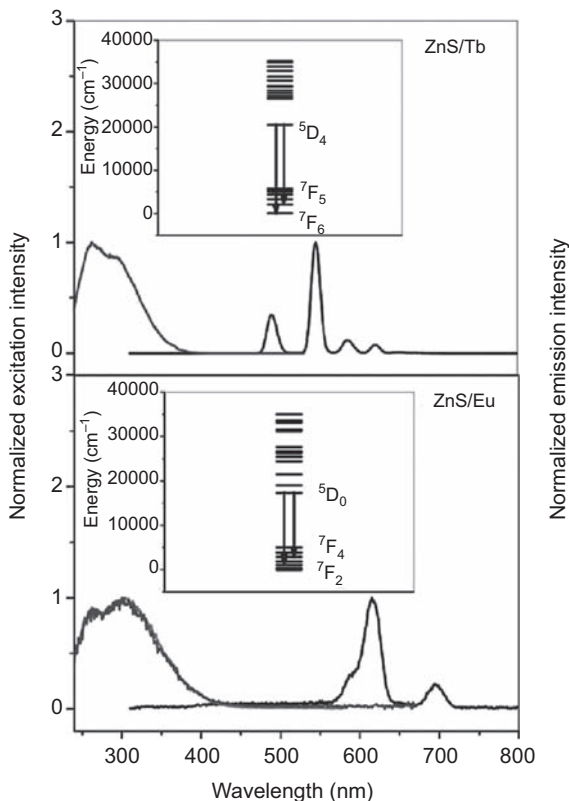


**Figure 4.4** Examples of optoelectronic processes in REs embedded in II-VI semiconductor nanoparticles, showing normalized time-gated excitation and emission spectra for ZnS/Tb (*upper panel*); and for ZnS/Eu (*lower panel*). Insets show electronic transitions associated with the 490 and 545 nm bands for ZnS/Tb, and with 616 and 696 nm bands for ZnS/Eu. It is inferred from these data that both RE elements are in their trivalent state.

After Mukherjee, P., Shade, C.M., Yingling, A.M., Lamont, D.N., Waldeck, D.H., Petoud, S.P., 2010. Lanthanide sensitization in II–VI semiconductor materials: a case study with terbium(III) and europium(III) in zinc sulfide nanoparticles. *The Journal of Physical Chemistry A* 115, 4031–4041.

included the discussion of isovalent RE ions in this structure for the sake of completeness.

Another problem that we will unavoidably face in attempts to incorporate the alien RE ion (such as  $\text{Eu}^{2+}$ ) in a tetrahedrally bonded crystalline host is the accommodation of the size of its covalent radius (see [Table 4.1](#)), which is much larger than that of most elements used for creating traditional DMSs. Given, however, the success of growing highly lattice-mismatched  $\text{II}_{1-x}\text{Mn}_x\text{VI}$  alloys from solution (eg,  $\text{Cd}_{1-x}\text{Mn}_x\text{S}$  ([Counio et al., 1998](#))) or by epitaxy (eg,  $\text{Be}_{1-x}\text{Mn}_x\text{Te}$  ([Nakamura et al., 2004](#); [Sawicki et al., 2002](#))), it would be expected that alloys such as  $\text{Cd}_{1-x}\text{Eu}_x\text{Te}$  or  $\text{Cd}_{1-x}\text{Eu}_x\text{Se}$  in zinc

blende or wurtzite crystal phases could also be achieved, at least for low values of  $x$  ( $x < 0.05$ ) (Raola and Strouse, 2002). We should note that this range of  $x$  is precisely the composition region where magneto-optical properties of such alloys are most interesting. In this context we can additionally consider low-temperature epitaxial growth, where incorporation of lattice-mismatched ions can be enormously increased by reducing the surface mobility of these ions during deposition. If this approach is successful, Sm and Yb (which, as noted, can exist in  $2+$  valency) can also be considered as candidates for tetrahedrally bonded  $\text{II}_{1-x}(\text{RE})_x\text{VI}$  DMSs.

#### 4.2.1.2 Rare-earth alloys based on III-V and group-IV semiconductor lattice

Studies of isovalent DMSs were largely limited to materials involving the replacement of group-II elements in the II-VI lattice by divalent ions such as  $\text{Mn}^{2+}$  or  $\text{Co}^{2+}$ . As already noted, all RE elements can exist in the trivalent state, which makes them of particular interest as candidates for forming  $\text{III}_{1-x}(\text{RE})_x\text{V}$  ternaries. We should note here that much work on incorporating REs in the III-V host lattice has already been done, primarily focused on their photoluminescent properties (Zavada and Zhang, 1995; Steckl et al., 2002, 2007; Kenyon, 2002; Steckl et al., 2007). In most of these cases it was found that the RE elements form complexes, whose formation depends critically on growth and/or annealing procedures. Photoluminescence excitation spectroscopy (Wagner et al., 1984; Ennen et al., 1987; Morishima et al., 2000) (as seen in Fig. 4.5) and Zeeman splitting analysis of photoluminescence (Aszodi et al., 1985) have shown that the dominant RE centers in III-V compounds correspond to trivalent RE ions, presumably on the group-III cation site. However, more work is clearly needed to gain further insight into magnetic properties of  $\text{III}_{1-x}(\text{RE})_x\text{V}$  ternaries alloys (Overberg et al., 2001; Bang et al., 2003). As an example, consider trivalent Gd, which in many ways is magnetically similar to the divalent Eu (or, for that matter, to Mn), in that it has a half-filled  $f$  shell, and can thus be considered as a promising candidate for replacing group-III ions in the III-V lattice, in close analogy to the isovalent  $\text{II}_{1-x}\text{Mn}_x\text{VI}$  systems. We can thus envision forming ternary isovalent alloys such as  $\text{Ga}_{1-x}\text{Gd}_x\text{As}$  (Shiraoka et al., 2008),  $\text{Ga}_{1-x}\text{Gd}_x\text{N}$ , and  $\text{Al}_{1-x}\text{Gd}_x\text{N}$  (Teraguchi et al., 2002; Pérez et al., 2006; Han et al., 2006; Dhar et al., 2006; Choi et al., 2006). Again, the large covalent radius of Gd is likely to stand in the way of sufficient degree of miscibility of Gd in the III-V matrix in equilibrium crystal growth; but, as mentioned in the case of Eu in the II-VI lattice, we have the possibility of using low-temperature epitaxy to enhance Gd incorporation. Again, other trivalent REs may also be considered here, particularly those with ultra-large magnetic moments (such as  $\text{Dy}^{3+}$ ) (Zhou et al., 2003), which may offer attractive properties in the form of inter-ion magnetic exchange interactions, thus leading to new magnetic properties.

Similarly, it is interesting that the rare-earth elements Ce, Pr, and Tb can adopt a  $+4$  valence state, which immediately suggests their potential for forming isovalent magnetic alloys based on group-IV elemental semiconductors such as  $\text{Ge}_{1-x}\text{Ce}_x$ ,  $\text{Sn}_{1-x}\text{Tb}_x$ , and so on. At the present time little is known to contribute to this discussion, but again the flexibility of epitaxial methods, including low-temperature

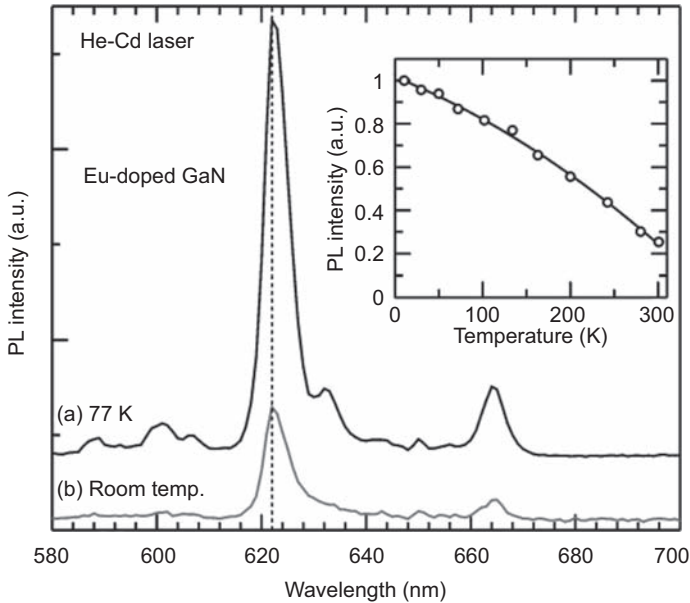


**Figure 4.5** Photoluminescence (PL) spectra observed on Eu-doped GaN specimen measured at 77 K (curve (a)) and room temperature (curve (b)). Intensity of the 622 nm PL peak is shown as a function of temperature in the inset. Note that the PL from the Eu ions embedded in GaN survives to room temperature.

After Morishima, S., Maruyama, T., Akimoto, K., 2000. Epitaxial growth of Eu-doped GaN by gas source molecular beam epitaxy. *Journal of Crystal Growth* 209, 378–381.

and atomic-layer epitaxy, or ion implantation followed by pulsed laser annealing (Scarpulla et al., 2003), may be helpful in this regard. This, however, awaits further exploration.

#### 4.2.1.3 Advanced tetrahedrally bonded structures

All systems just considered form either in zinc blende or in wurtzite structures, both of which are bonded tetrahedrally. It is possible to extend this discussion also to more complex tetrahedrally bonded systems, such as chalcopyrites, famatinites, and ordered vacancy compounds (Parthé, 1964; Shay and Wernick, 1975; MacKinnon, 1981; Siebentritt and Rau, 2006), which we will briefly touch upon. Consider, for example, the chalcopyrite compound  $\text{CdGeAs}_2$ . Following the logic of our preceding discussion, it is possible to consider alloys formed by substituting for Cd in this system, as has been successfully done with Mn to form the chalcopyrite DMS alloy  $(\text{Cd}_{1-x}\text{Mn}_x)\text{GeAs}_2$  (Kilanski et al., 2014). This alloy has shown excellent magnetic properties very analogous to  $\text{II}_{1-x}\text{Mn}_x\text{VI}$  alloys, and we can thus immediately envision the possibilities that this approach opens to divalent REs, in analogy with  $\text{Mn}^{2+}$ . Furthermore, in this same manner we can consider substituting REs with +4 valency for Ge in this and related systems; and, perhaps more importantly, isovalent

substitution of trivalent REs in (I)(III)(VI)<sub>2</sub> chalcopyrites such as CuInS<sub>2</sub> or AgInTe<sub>2</sub>. While these considerations are admittedly very speculative, if such systems are formed, they are very likely to display DMS characteristics analogous to the isovalent combinations discussed earlier. It is therefore worth noting that substitution of REs into this crystal structure has already been demonstrated, as shown in Fig. 4.6 (Tsuji et al., 2001).

Among the tetrahedrally bonded crystals, ordered vacancy compounds (OVCs) appear to be especially promising for RE incorporation into the semiconductor lattice. The OVC structure is shown in Fig. 4.7. As seen in the figure, this structure is similar to the chalcopyrite (also shown in the figure), but with vacancies replacing ions in a regular progression (Bernard and Zunger, 1988). To appreciate the structural properties of OVC compounds and their relevance to the present chapter, consider the OVC compound CdIn<sub>2</sub>Se<sub>4</sub>. This structure is in many ways analogous to an I-III-VI<sub>2</sub> chalcopyrite, where now the combination of a vacancy and a group-II element together act as two group-I ions (see Fig. 4.7). As an example, consider the chalcopyrite CuInS<sub>2</sub> in which one-half of the copper sites are replaced by vacancies, and the other half by Cd ions in such a way that the Cd-vacancy combination acts as two Cu ions. Thus in the OVC structure 25% of the fcc cation sublattice is occupied by vacancies. Since, as seen in Table 4.1, covalent radii of REs are much larger than those of most elements comprising typical semiconductor lattices, it is reasonable to expect that this feature

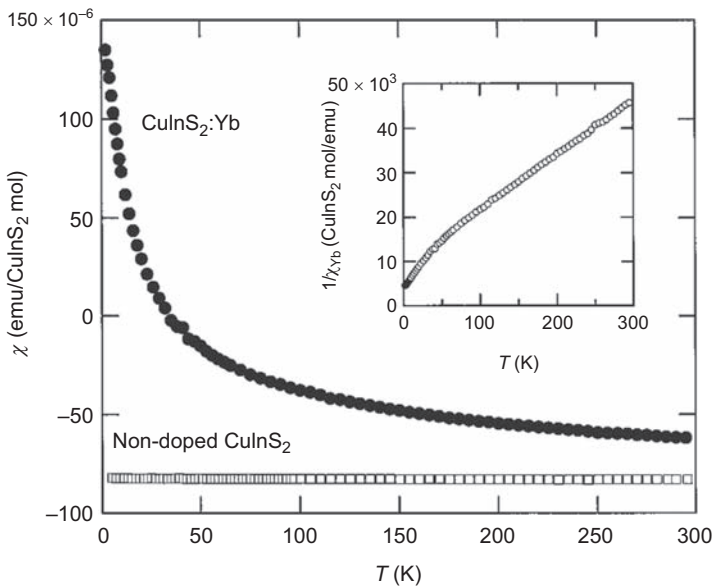


**Figure 4.6** Temperature dependence of magnetic susceptibility  $\chi$  of the chalcopyrite CuInS<sub>2</sub> crystal doped with Yb, with  $\chi$  for undoped CuInS<sub>2</sub> shown for comparison. The inset shows the inverse of the Yb contribution to the susceptibility in CuInS<sub>2</sub>:Yb.

After Tsujii, N., Imanaka, Y., Takamasu, T., Kitazawa, H., Kido, G., 2001. Photoluminescence of Yb<sup>3+</sup>-doped CuInS<sub>2</sub> crystals in magnetic fields. *Journal of Applied Physics* 89, 2706–2710.



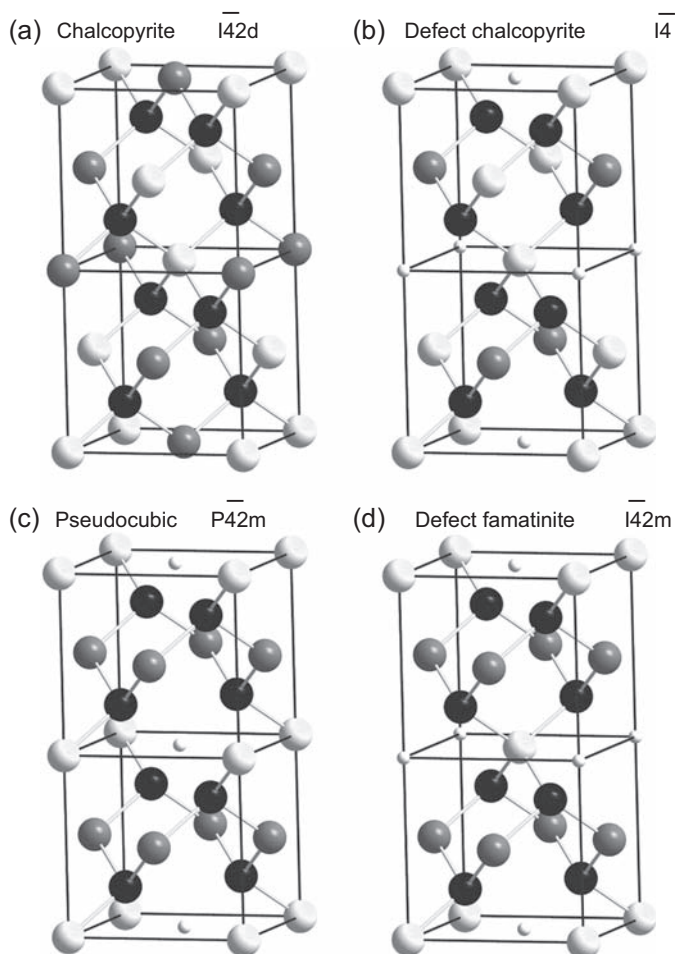


**Figure 4.7** Possible crystal structures (b–d) of OVCs of the type II-III<sub>2</sub>-VI<sub>4</sub> (eg, CdIn<sub>2</sub>Se<sub>4</sub>). The closely related chalcopyrite structure (such as CuInSe<sub>2</sub>) is also shown for comparison in panel (a).

will provide the necessary “elbow room” for incorporating the RE ions into this tetrahedrally bonded structure. In particular, such OVC structure appears suitable for substitutional isovalent incorporation of both divalent and trivalent REs. This is of course a speculative, but nevertheless plausible direction for accommodating REs in a wide range of semiconductor systems.

#### 4.2.1.4 Alloys based on IV-VI semiconductor lattice

In contrast with the somewhat speculative possibilities of significant RE incorporation in tetrahedrally bonded crystal structures considered in the preceding sections, the



family of  $\text{IV}_{1-x}\text{RE}_x\text{VI}$ s alloys (which crystallize in the lead-salt structure) is now well established, and has been studied quite extensively both as bulk crystals and in the form of a variety of multilayers. Extensive work carried out on  $\text{IV}_{1-x}\text{Eu}_x\text{VI}$ -based systems has already led to fascinating new magnetic effects (Story, 1997, 2002; Krenn et al., 1999; Dobrowolski et al., 2003). In particular, throughout nearly their entire Eu composition ranges studied so far,  $\text{Pb}_{1-x}\text{Eu}_x\text{Te}$  (Krenn et al., 1999),  $\text{Pb}_{1-x}\text{Eu}_x\text{Se}$  (Bindilatti et al., 1996; Isber et al., 1997),  $\text{Pb}_{1-x}\text{Eu}_x\text{S}$  (Bindilatti et al., 1998), and  $\text{Sn}_{1-x}\text{Eu}_x\text{Te}$  (Errebbahi et al., 2002) crystals are Curie–Weiss paramagnets revealing only very weak AFM  $f$ – $f$  exchange interactions between the magnetic moments of the  $\text{Eu}^{2+}$  ions. Additionally, in thick  $\text{Pb}_{1-x}\text{Eu}_x\text{Te}$  epitaxial layers with  $x > 0.8$  a transition to long-range AFM order is observed below 10 K, similar to the well-known terminal ( $x = 1$ )  $\text{EuTe}$  compound. The evolution of magnetic properties of  $\text{Pb}_{1-x}\text{Eu}_x\text{Te}$  as a function of Eu content is shown in Fig. 4.8. The presence of AFM exchange coupling between nearest magnetic neighbors in such IV–VI DMSs with Eu (as well as with Mn or Gd) is experimentally evidenced by the Curie–Weiss temperature dependence of the magnetic susceptibility, as well as by the characteristic step-like behavior of the magnetization as a function of magnetic field observed at low temperatures. Given the success of the rock-salt Eu-based chalcogenides, it is tempting to also consider the incorporation of other RE ions in IV–VI semiconductor lattices.

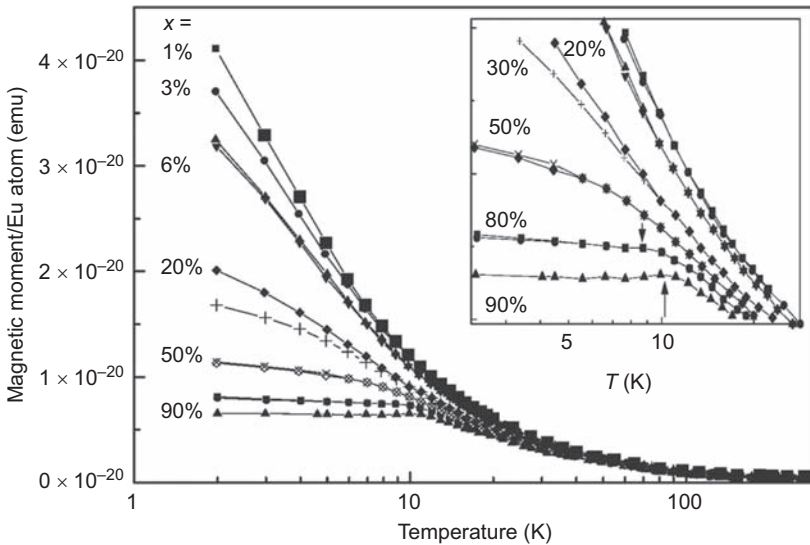


**Figure 4.8** Magnetic moment per single magnetic ion of  $\text{Pb}_{1-x}\text{Eu}_x\text{Te}$  as a function of temperature for an in-plane magnetic field of 1.0 T and for various concentrations of Eu. Insert: Magnified scale showing the AFM phase transition (arrows) for  $\text{Pb}_{1-x}\text{Eu}_x\text{Te}$  samples with  $x > 0.80$ . The plot for  $\text{EuTe}$  ( $x = 1$ ) is indistinguishable from that for the  $x = 0.9$  sample. After Krenn, H., Herbst, W., Pascher, H., Ueta, Y., Springholz, G., Bauer, G., 1999. Interband Faraday and Kerr rotation and magnetization of  $\text{Pb}_{1-x}\text{Eu}_x\text{Te}$  in the concentration range  $0 < x \leq 1$ . *Physical Review B* 60, 8117–8128.

## 4.2.2 Homogeneous magnetic alloys based on heterovalent rare-earth incorporation

Experience with epitaxial formation of  $\text{III}_{1-x}\text{Mn}_x\text{V}$  DMSs has shown that a large fraction of heterovalent incorporation of  $\text{Mn}^{2+}$  in the III-V lattice is not only possible, but that it constitutes a unique form of generating ferromagnetism through high-level electrical doping of the host semiconductor, which in turn creates magnetic exchange paths between the magnetic ions. In full realization that the possibilities we consider next are at this point speculative, we will nevertheless consider several circumstances that hold promise, as they represent direct analogs of the already well-established magnetic  $\text{III}_{1-x}\text{Mn}_x\text{V}$  DMSs. Again, success with these scenarios will in large measure depend on our ability to form systems of this type by nonequilibrium methods, such as low-temperature epitaxy extensively used in the formation of  $\text{III}_{1-x}\text{Mn}_x\text{V}$  DMS alloys or, alternatively, by ion implantation followed by rapid annealing, which has also been highly successful in achieving ferromagnetism in  $\text{III}_{1-x}\text{Mn}_x\text{V}$  alloys (Scarpulla et al., 2003).

### 4.2.2.1 Alloys based on III-V semiconductor lattice

As noted earlier, the field of DMSs has acquired added momentum with the advent of  $\text{III}_{1-x}\text{Mn}_x\text{V}$  FM semiconductors, and particularly of  $\text{Ga}_{1-x}\text{Mn}_x\text{As}$ , where Mn enters the III-V lattice in its preferred divalent state, thus constituting both a source of magnetic ions and of electrical carriers (holes). As in the preceding section, we now look for analogs of  $\text{III}_{1-x}\text{Mn}_x\text{V}$  alloys in the form of  $\text{III}_{1-x}\text{RE}_x\text{V}$  ternaries, in the hope of obtaining RE-based FM semiconductors. Again Eu is the prime candidate in this context, in that it can form a system that closely parallels the already widely studied FM  $\text{III}_{1-x}\text{Mn}_x\text{Vs}$ . Specifically, if Eu enters the system  $\text{III}_{1-x}\text{Eu}_x\text{Vs}$  in divalent state, it is expected to act as an acceptor, so that at Eu concentrations  $x$  exceeding 0.01 it may potentially form a FM system, in close analogy to, for example,  $\text{Ga}_{1-x}\text{Mn}_x\text{As}$ . As with that latter case, we expect that we will need to rely on low-temperature epitaxy or on ion implantation followed by pulsed laser annealing to achieve concentrations sufficient for achieving this goal. We should emphasize, however, that this remains an open question, particularly because current results with dilute Eu doping of the III-V hosts indicate that Eu enters the lattice in the trivalent state. Nevertheless, this issue still remains open, since there is no information regarding the behavior of Eu ions (and especially regarding their valence state) at concentrations that lead to measurable magnetic properties.

### 4.2.2.2 Alloys based on II-VI semiconductor lattice

In this section we will consider the substitution of trivalent REs for group-II ions in the II-VI lattice. It was already mentioned that in studies carried out so far the REs tend to enter this lattice in the trivalent state, as seen in Fig. 4.4. This case is new, in that it does not have well-established analogs among the DMSs considered so far (Coey et al., 2005). The trivalent RE, for example,  $\text{Gd}^{3+}$ , upon substitution for the group-II ion is expected to form a donor. Little is known about magnetism mediated by electrons

in the semiconductor lattice (Coey et al., 2005), so that this variant is somewhat speculative. It was proposed that FM exchange can in this case be mediated by shallow-donor electrons that form bound magnetic polarons, which at sufficient concentrations overlap to create a spin-split impurity band. Given the natural preference of REs for their trivalent state, this is a particularly important situation, and hopefully more work will be done in this area toward the realization of polaron-induced magnetism in RE-doped II-VI semiconductors.

#### 4.2.2.3 *Final comment on heterovalent incorporation of rare earths*

As a comment note on this section, we note that the central issue related to heterovalent incorporation of REs in the semiconductor lattice was the possibility that such incorporation will provide a source of magnetic moments as well as charge carriers into the system, which in turn would lead to novel magnetic properties, in analogy to the behavior widely observed in  $\text{III}_{1-x}\text{Mn}_x\text{V}$  FM semiconductors. This may not be possible in all cases considered previously. For example, as already pointed out, so far evidence exists that all REs studied so far in this context prefer to enter the III-V lattice in trivalent state, at least when they are introduced in very dilute concentrations, thus precluding heterovalent incorporation. If this preference persists to concentrations of interest in magnetism, there is of course also the option of codoping the material with appropriate impurities (as is routinely done in the case of  $\text{III}_{1-x}\text{Mn}_x\text{Vs}$  by using, eg, Be doping) to enable carrier-mediated magnetic exchange. It is somewhat premature to pursue this hypothetical issue here, but we should notice that this issue will naturally arise in Section 4.5.

### 4.3 Inhomogeneous and mixed-phase magnetic rare-earth systems

The foregoing discussion was based on the possibility of forming homogeneous alloys, analogous to  $\text{Ga}_{1-x}\text{Mn}_x\text{As}$  or  $\text{Zn}_{1-x}\text{Mn}_x\text{Te}$ , but with RE elements in place of TMs. There also exists, however, the possibility of achieving attractive magnetic properties based on the fluctuation of magnetic content, either as a quantitative variation of the concentration of magnetic species without changing phase of the alloy that results from spinodal decomposition (Sato et al., 2005, 2007; Fukushima et al., 2006; Katayama-Yoshida et al., 2007; Dietl, 2006), or by formation of second-phase magnetic insertions in the semiconductor host. Examples of the latter option are, for example, inclusions of FM MnAs in GaMnAs (De Boeck et al., 1996), Co in ZnCoO (Sawicki et al., 2013), or Fe-rich clusters in GaFeN (Bonanni, 2007), which form due to precipitation of an element or a compound that does not dissolve in the multicomponent system during its growth. This option is especially important in the present situation, since many REs may not be fully miscible in a semiconductor matrix (largely because of the mismatch in ion size). This is not necessarily a drawback, since fluctuations of concentration as well as precipitation of second-phase magnetic inclusions may also

be of great interest in the context of spintronics. Specifically, such magnetic islands are likely to affect electric currents via spin–spin interactions with charge carriers, and can be exploited for controlling these currents using spin–spin interaction. As an introduction to magnetic properties of such composite media with magnetic inclusions, we will use the ZnO:Co system discussed in the very enlightening paper of [Sawicki et al. \(2013\)](#). While this paper focuses on the inclusion of Co into the ZnO matrix, it serves to illustrate the variety of effects in such an inhomogeneous medium, which should also be applicable to semiconductor systems with RE-containing inclusions. [Sawicki et al. \(2013\)](#) show that, depending on growth conditions (and particularly on growth temperature), three types of magnetic media can form based on such magnetic admixtures, all of which are interesting in the context of spintronics in various ways. We thus begin by discussing the behavior observed in these ZnO:Co combinations as an analog for possible mixed RE-semiconductor composites.

First, at very low concentrations of Co in this system there occurs a dilute solid solution of  $\text{Zn}_{1-x}\text{Co}_x\text{O}$ . In this specific case, and in the absence of a very high concentration of free carriers to serve as a medium of exchange, we simply have a paramagnetic system due to the presence of magnetic ions, very much as in the thoroughly studied  $\text{II}_{1-x}\text{Mn}_x\text{VI}$  DMSs in the  $x \ll 1$  limit. The paramagnetism of the system may in fact be additionally weakened if the preferred coupling between the magnetic ions is AFM (as it is the case of the  $\text{II}_{1-x}\text{Mn}_x\text{VIs}$ ). Whether the latter is true or not, magnetic susceptibility of such a system is expected to rapidly weaken with temperature. We have already discussed the magnetic properties of such solutions earlier in the chapter, and we recall this here mainly because a multinary system that we are now considering is likely to consist of such a dilute alloy as a matrix that also contains the magnetically concentrated inclusions of interest in this section.

The second case involves precipitation of magnetic inclusions, such as Co in ZnO discussed in [Sawicki et al. \(2013\)](#) (or, indeed, of MnAs in  $\text{Ga}_{1-x}\text{Mn}_x\text{As}$  ([De Boeck et al., 1996](#))). Such Co precipitates represent superspins of tens to hundreds of Bohr magnetons, in other words, of many spins ferromagnetically coupled within a nano-sized volume. The resulting composite medium then forms a superparamagnetic material comprised of an ensemble of such superspins. Since each nanoprecipitate is typically a single domain, such precipitates retain their FM properties up to temperatures that correspond to the Curie temperature of the precipitated material. We should note that such superparamagnetic media are also of interest for spintronic applications because of their large magnetic susceptibility alongside very small coercive fields ([Sawicki et al., 2013](#)).

For specificity we have used here the example of Co metal as a precipitate, but in the absence of full miscibility magnetic ions can equally well precipitate as binary compound, that may be FM or AFM. Interestingly, AFM precipitates will be important in this context, particularly in the nanoscale limit, since in such ultrasmall cases they may also carry sizable net magnetic moments, as discussed later in this chapter, thus leading to superparamagnetism.

As an example of such inclusions involving REs, let us consider precipitates of ErAs in III-V lattices. ErAs is a semimetal with a cubic rock-salt structure ( $a_{\text{ErAs}} = 0.573$  nm) and is known to grow epitaxially on arsenide zinc-blende

semiconductors (Palmstrom et al., 1988). We will return to this again in the next section in the context of multilayer growth. Here we focus on composites of ErAs nanoparticles embedded in epitaxial GaAs or  $\text{In}_{1-x}\text{Ga}_x\text{As}$  layers, fabricated either as random nanoparticle distributions or by overgrowing nanometer-size islands of ErAs with the host semiconductor (Kadow et al., 1999; Driscoll et al., 2003; Klenov et al., 2005a; Zide et al., 2005). Depending on growth conditions, such ErAs inclusions can enter the host lattice in their natural rock-salt structure, as shown from the high-angle annular dark-field (HAADF) images in Fig. 4.9; or they can be induced by the surrounding matrix to acquire the zinc-blende structure of the host, as seen in Fig. 4.10. For conditions under which these cases occur the reader is referred to Kadow et al. (1999), Driscoll et al. (2003), Klenov et al. (2005a), and Zide et al. (2005).

However, the most interesting point addressed in Sawicki et al. (2013) pertains to interfaces that automatically exist in such multiple-phase composites. In the specific case discussed by Sawicki et al., the interface of ZnCoO with its nonmagnetic substrate is preferentially decorated by nanoprecipitates of Co (or possibly of intermetallic FM compound CoZn). The density of such precipitated FM nanocrystals is adequate (ie, the distances between the interfacial nanocrystals are sufficiently small) for the super-spins localized on these inclusions to interact ferromagnetically by dipole–dipole interactions, thus resulting in 2D FM layers. As noted earlier, each constituent nanocrystal of such a 2D assembly is itself a single domain representing tens to hundreds of

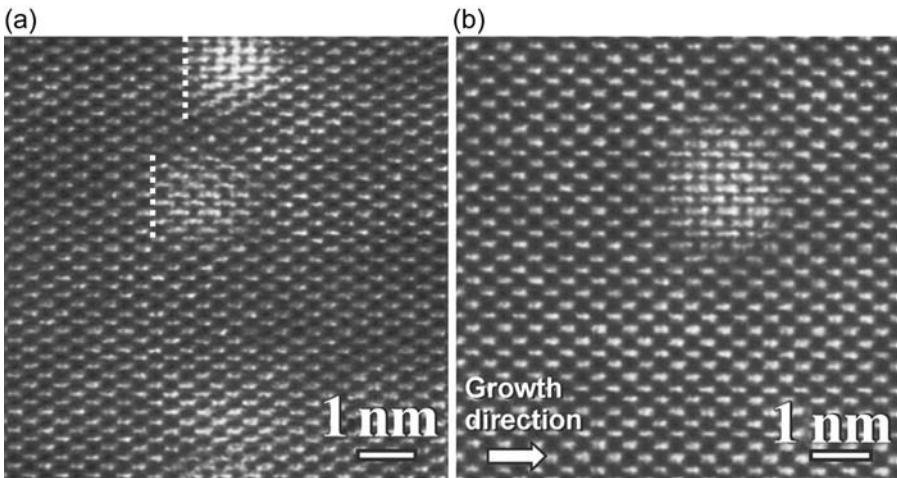


**Figure 4.9** HAADF-STEM micrographs of rock-salt ErAs particles in a zinc-blende  $\text{In}_{0.53}\text{Ga}_{0.47}$  matrix obtained by deposition of Er layers of (a) 1.2 ML and (b) 1.4 ML ErAs, respectively. The interface between the particle and the matrix on the substrate side is indicated by dotted lines in (a). The arrow shows the growth direction. For growth details see Klenov et al. (2005a).

After Klenov, D.O., Driscoll, D.C., Gossard, A.C., Stemmer, S., 2005a. Scanning transmission electron microscopy of ErAs nanoparticles embedded in epitaxial  $\text{In}_{0.53}\text{Ga}_{0.47}\text{As}$  layers. Applied Physics Letters 86, 111912.

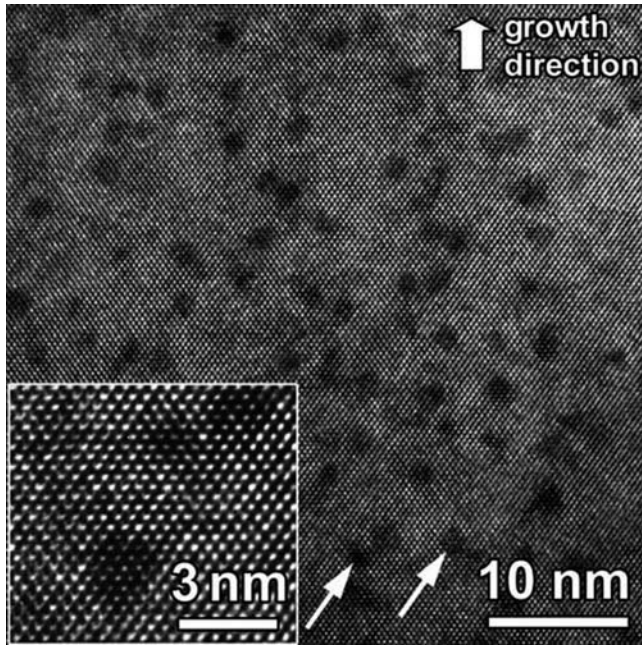


**Figure 4.10** High-resolution cross-sectional transmission electron micrograph (TEM) of ErAs particles in an  $\text{In}_{0.53}\text{Ga}_{0.47}\text{As}$  matrix, indicating formation of nanometer-size particles with crystal structure of the surrounding matrix. The spatial distribution of the particles appears to be essentially random. For clarity, several particles are pointed out by *arrows*.

After Zide, J.M., Klenov, D.O., Stemmer, S., Gossard, A.C., Zeng, G., Bowers, J.E., Vashaee, D., Shakouri, A., 2005. Thermoelectric power factor in semiconductors with buried epitaxial semimetallic nanoparticles. *Applied Physics Letters* 87, 112102.

Bohr magnetons, that persists essentially unchanged well above room temperature. As pointed out in [Sawicki et al. \(2013\)](#), it is advantageous that such an assembly does not require free carriers to achieve its collective ferromagnetism, since—because in a nonconducting matrix the inclusions are electrically insulated from one another—this minimizes eddy current losses, making such FM media especially attractive for non-dissipative device applications.

As noted, attempts to introduce REs into a semiconducting matrix may result in precipitation of inclusions of elemental REs or of RE compounds, with behaviors that very likely are similar to those discussed earlier. When the inclusions are FM, and when their density is sufficiently high, dipolar interactions between such magnetic inclusions can occur at interfaces, or even in the bulk. The key here of course is the understanding and control of growth conditions. We should mention parenthetically that the prominent occurrence of 2D ferromagnetism due to precipitate ensembles at interfaces (as observed [Sawicki et al. \(2013\)](#)) may be enhanced further because of the tendency of easy axes of the nanoparticles to lie in the interface plane, which



additionally facilitates in-plane dipole–dipole interactions. These properties constitute an attractive feature for designing planar spintronic devices.

In the previous discussion we have primarily focused on precipitation of discrete crystal phases that are different in structure from the semiconductor matrix (eg, Co in ZnO, such as the ErAs inclusions in Fig. 4.9). We add parenthetically that in the growth of multicomponent alloys we can also encounter inhomogeneities due to the formation of regions with the same crystal structure, but differing in composition due to a miscibility gap, due to the process of spinodal decomposition (Sato et al., 2005, 2007; Fukushima et al., 2006; Katayama-Yoshida et al., 2007). For example (as presumably is the case in Figs. 4.9 and 4.10), in growing an alloy of Ga, RE, and N, we can obtain regions of  $\text{Ga}_{1-y}\text{RE}_y\text{N}$  in a matrix of  $\text{Ga}_{1-x}\text{RE}_x\text{N}$ , with  $y \gg x$  (Bonanni, 2007). It may well happen that  $y$  is sufficiently large to render the  $\text{Ga}_{1-y}\text{RE}_y\text{N}$  FM (as would be the case in  $\text{Ga}_{1-y}\text{Gd}_y\text{N}$  at high values of  $y$ ). In that case, the previous discussion of magnetic properties of the ensemble applies equally well.

## 4.4 Heterostructures of semiconductor and magnetic rare-earth compounds

In addition to random distributions of magnetic species in a nonmagnetic semiconducting matrix discussed earlier, we can also envision attractive magnetic effects arising in composite media comprised of nonmagnetic and magnetic components, such as multilayers and so-called digital alloys. Many of these structures have been successfully exploited in systems involving semiconductor/TM combinations, and in this section we will consider the RE-based analogs of such systems.

### 4.4.1 Superlattice and multilayer semiconductor/rare-earth combinations

It has already been noted that the lattice constant of ErAs (which forms in the cubic rock-salt structure) is very close to that of the zinc-blende GaAs, allowing the formation of AFM ErAs inclusions (either rock salt or zinc blende) within the zinc-blende GaAs host. Such inclusions are crystallographically coherent, as seen in Figs. 4.9 and 4.10. This lattice match has also been exploited to form actual layered heterostructures (Palmstrom et al., 1988; Klenov et al., 2005b; Zhu et al., 1990; Crook et al., 2011; Sands et al., 1990), as shown in Fig. 4.11. While ErAs itself is AFM, this (as has already been pointed out) does not preclude spintronic functionalities (Allen et al., 1989; Petukhov et al., 1996; Watanabe et al., 2004). For example, AFM ErAs layers may play a useful role to enable exchange bias in spintronic devices (eg, those using thin-film Fe/GaAs combinations). We note here that Fe also has a fortuitous lattice match with GaAs, and has been widely studied for this lucky structural match between the semiconductor GaAs and the metallic FM Fe (Yoo et al., 2009, 2010; Khym et al., 2012; Tivakornsasithorn et al., 2014). Furthermore, it is now recognized that AFM systems can be useful for spintronic applications, as will be discussed in Section 4.6, and the

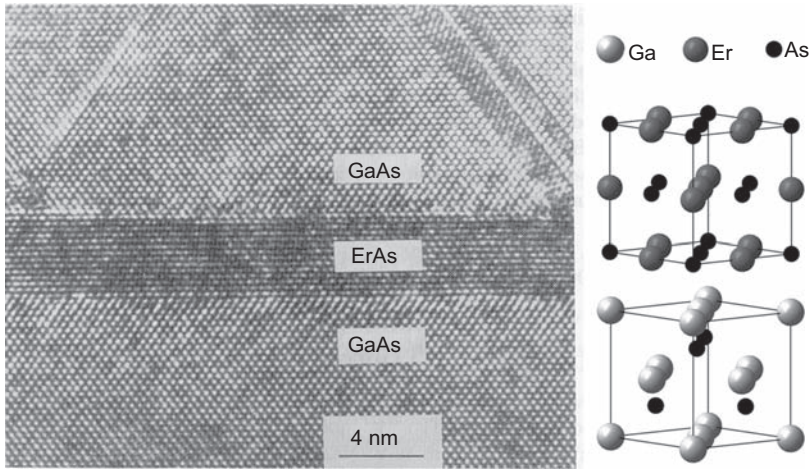


**Figure 4.11** Cross-sectional high-resolution TEM image of a GaAs/ErAs/GaAs multilayer structure. Note that the ErAs layer forms a rock-salt structure that is coherent with the zinc blende lattice of GaAs; and that the coherence survives also after deposition of the ErAs layer, with only minor formation of a few defects. Structures of the coexisting crystal forms are shown on the right.

After Sands, T., Palmstrøm, C.J., Harbison, J.P., Keramidis, V.G., Tabatabaie, N., Cheeks, T.L., Ramesh, R., Silberberg, Y., 1990. Stable and epitaxial metal/III-V semiconductor heterostructures. *Materials Science Reports* 5, 99–170.

convenient structural compatibility of the AFM ErAs with GaAs may prove quite valuable as a prototype for studying this aspect of spintronic applications.

It is relevant to note in this connection that, as mentioned in [Section 4.2.1](#), much work has already been done in combining lead-salt semiconductors with REs. Work in this area has also been very fruitfully extended to multilayer systems such as EuTe/PbTe ([Springholz and Bauer, 1993](#); [Giebultowicz et al., 1995](#); [Heremans and Partin, 1988](#); [Kepa et al., 2003](#)), EuS/PbS ([Stachow-Wójcik et al., 1999](#); [Story et al., 2001](#); [Swirkowicz and Story, 2000](#)), and others, which exhibit fascinating characteristics of their own. As an example, we illustrate this in [Fig. 4.12](#) ([Dobrowolski et al., 2003](#)), where multilayers of EuS/PbS exhibit FM behavior, which can be controlled by varying the thickness of the constituent layers.

#### 4.4.2 Digital alloys using rare-earth compounds

Digital alloys are formed by repeatedly depositing ultrathin magnetic layers (typically a monolayer) on a nonmagnetic host material to form a superlattice. Successful examples of this have already been achieved in the form of GaSb/Mn, InAs/Mn, and GaAs/Mn systems, where the Mn layers are used to form the digital insertions ([McCombe et al., 2003](#); [Luo et al., 2004](#)). The case of GaSb/Mn is particularly interesting, since it has been shown to retain its FM properties to temperatures above 300 K ([Chen et al., 2002](#)), as shown in [Fig. 4.13](#).



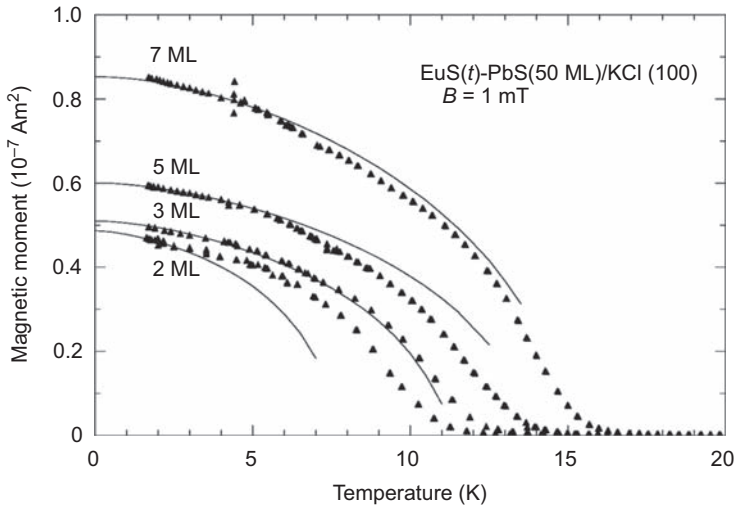


**Figure 4.12** Temperature dependence of the magnetization of EuS-PbS multilayers with varying thicknesses  $t$  of the ferromagnetic EuS layers (indicated in the figure) (for detail see [Stachow-Wójcik et al. \(1999\)](#) and [Story et al. \(2001\)](#)). The PbS spacer thickness is 15 nm (about 50 ML). Solid lines represent results of theoretical calculations of spin wave excitations performed by [Swirkowicz and Story \(2000\)](#).

After Dobrowolski, W., Kossut, J., Story, T., 2003. II-VI and IV-VI diluted magnetic semiconductors new bulk materials and low-dimensional quantum structures. In: Buschow, K.H.J. (Ed.), *Handbook of Magnetic Materials*, vol. 15. Elsevier Science.

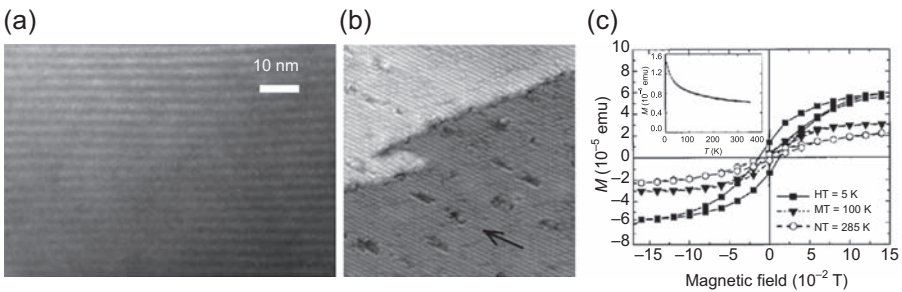


**Figure 4.13** (a) TEM image of a Mn/GaSb digital alloy with a repeat unit of Mn (0.5 ML)/GaSb (12 ML). *Dark lines* correspond to Mn-containing layers. (b) Cross-sectional scanning tunneling microscope images showing discrete MnSb islands (indicated by *arrow*), which suggest that ferromagnetic MnSb islands are incorporated in the same (zinc blende) phase as the host lattice, rather than in the form of second-phase precipitates. (c) Hysteresis loops of the digital-alloy sample. Temperature dependence of the remanent magnetization is shown in the inset.

After Chen, X., Na, M., Cheon, M., Wang, S., Luo, H., McCombe, B.D., Liu, X., Sasaki, Y., Wojtowicz, T., Furdyna, J.K., Potashnik, S.J., Schiffer, P., 2002. Above-room-temperature ferromagnetism in GaSb/Mn digital alloys. *Applied Physics Letters* 81, 511–513.

The success of these systems based on TM insertions leads us to suggest that a similar approach with REs may also have promise for achieving ferromagnetism in such composite systems (Klenov et al., 2005a). There are essentially three possibilities that may occur. Considering digital Gd insertions in GaN as an example (see Fig. 4.14) (Kent et al., 2012), such digital insertion may retain the magnetic properties of the elemental RE in its bulk form; it may form a GdN rock-salt phase by bonding with the anions of the host seen in the middle-upper panel (where rock salt is the natural phase of bulk GdN); or it may bond with N, but be coerced by the surrounding atoms to form the same crystal phase as the host (in this case, wurtzite). Indeed, magnetic characterization in Kent et al. (2012) indicates that two magnetic phases are present in the digital structure described in that work, one due to the rock-salt FM GdN with Curie temperature of 70 K and a second, anisotropic phase (a prominent out-of-plane easy axis) whose magnetization persists past room temperature (Kent et al., 2012).

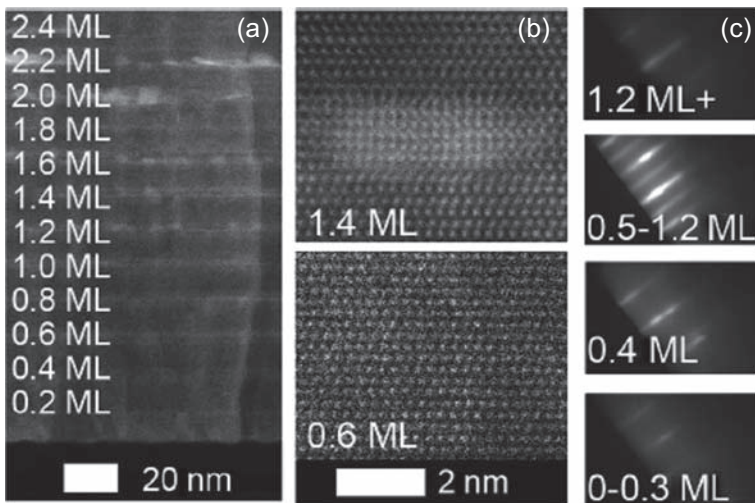


**Figure 4.14** (a) Cross-sectional z-contrast HAADF-STEM image of a digital GdN/GaN multilayer. (b) Atomic resolution STEM images for selected layers occurring in such digital growth. The top image shows a GdN nanoparticle of clearly cubic structure surrounded by a continuous GaN wurtzite matrix. For comparison, the bottom atomic resolution image shows the normal wurtzite structure prior to island formation. (c) RHEED patterns taken during the growth of GdN layers for different thicknesses, showing the evolution of the surface reconstruction from  $1 \times 2$  to  $2 \times 4$  reconstruction and back to the  $1 \times 2$  with increasing layer thicknesses. For additional details see Kent et al. (2012).

After Kent, T.F., Yang, J., Yang, L., Mills, M.J., Myers, R.C., 2012. Epitaxial ferromagnetic nanoislands of cubic GdN in hexagonal GaN. Applied Physics Letters 100, 152111.

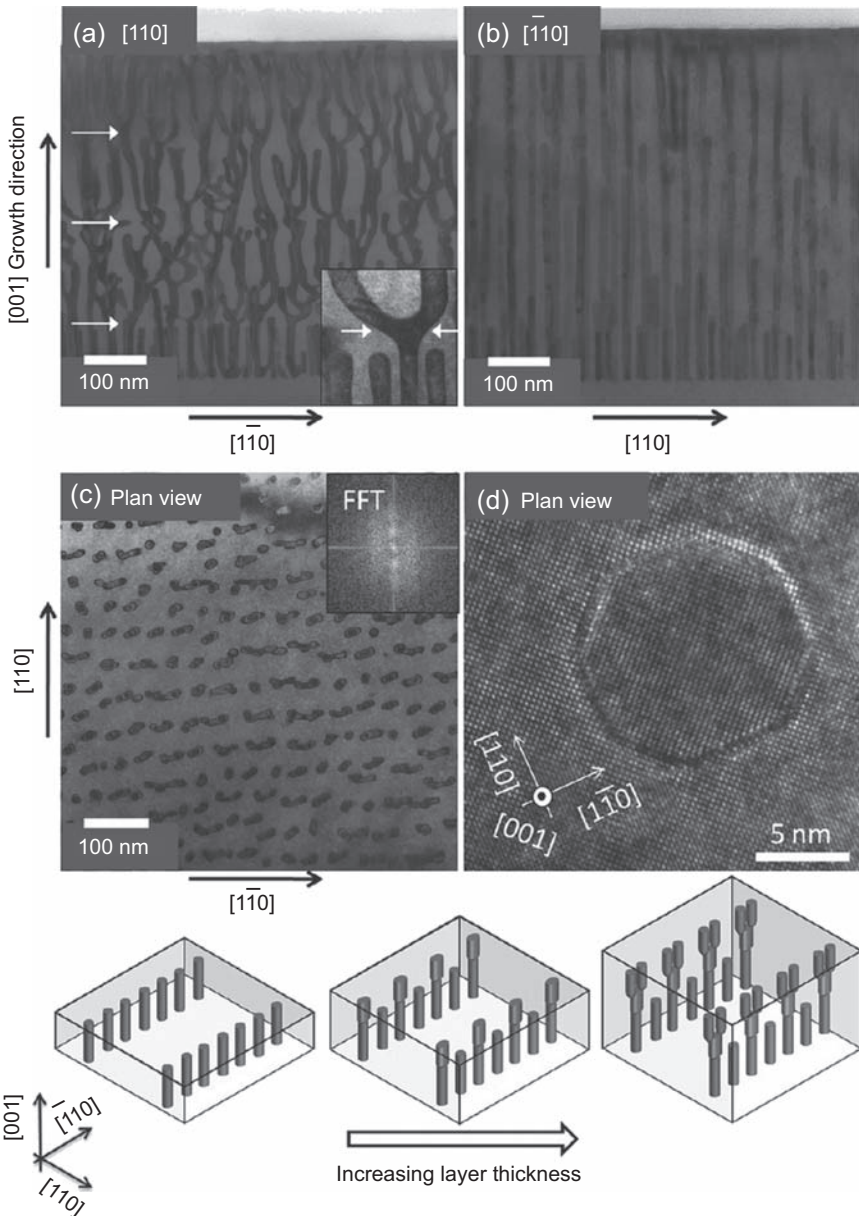


**Figure 4.15** Bright-field TEM images of a 250 nm thick  $\text{Ga}_{0.9}\text{Er}_{0.1}\text{Sb}$  (001) layer observed (a) along cross-sectional  $[110]$  zone axis, (b) along cross-sectional  $[\bar{1}10]$  zone axis, and (c) along plan-view  $[001]$  zone axis. (d) High-resolution plan-view TEM image of a single ErSb nanorod, showing a mixture of  $\{010\}$  and  $\{110\}$  facets. Bottom: schematic diagrams depicting evolution of nanorod branching with increasing layer thickness.

After Kawasaki, J.K., Schultz, B.D., Lu, H., Gossard, A.C., Pamstrom, C.J., 2013. Surface-mediated tunable self-assembly of single crystal semimetallic ErSb/GaSb nanocomposite structures. *Nano Letters* 13, 2895–2901.

### 4.4.3 Complex rock-salt/zinc-blende composites involving rare earths

It has already been pointed out in [Section 4.3](#) that rock-salt RE compounds can be combined with zinc-blende semiconductors in various ways, as seen, for example, in [Figs. 4.9–4.11](#). Such combinations of two different crystal structures can also lead to very complex novel morphologies of the RE-species coexisting with the zinc-blende host, as illustrated by the ErSb structures in a  $\text{Ga}_{1-x}\text{Er}_x\text{Sb}$  matrix shown in [Fig. 4.15](#) ([Kawasaki et al., 2013](#)). If the RE compound is FM, we can immediately envision novel possibilities for magnetic interactions (including percolation) that may lead to interesting spintronic functionalities. Additionally, if the parent RE compound is itself AFM, this does not preclude the possibility that in such complex morphologies as shown in [Fig. 4.15](#) such RE species will carry a nonzero magnetic moment, and will thus be of interest in the spintronic context.

## 4.5 Rare-earth-based layered chalcogenides and pnictides, including mixed anion systems

In the preceding sections we focused on semiconductors that form in the zinc-blende, wurtzite, and rock-salt crystal structures, since until most recently those materials were of primary interest in the formation of DMSs. In 2013–2015, however, entirely new classes of DMSs began to emerge in the form of layered chalcogenides and pnictides, many of them based on RE elements. Importantly, these materials include a wide range of oxychalcogenides and oxypnictides, which are wide-gap materials, opening the way to DMS systems that are transparent to wavelengths in the visible and the near ultraviolet ([Zhu et al., 2010](#); [Wildman et al., 2012](#); [Tuxworth and Evans, 2014](#); [Luo et al., 2014](#)). This class of materials builds heavily on developments first encountered in the area of high-temperature superconductors ([Johnston, 2010](#)), so that the vast experience already acquired in that field has also served to guide the development of this new class of DMSs. While these materials are also basically homogeneous single-phase alloys, like those considered in [Section 4.2](#), we discuss them separately because of their distinct layer nature and highly complex crystallographic structure.

In discussing their properties we will, for convenience, use the nomenclature that has been widely used to describe these complex systems in the contexts in which they were first discovered ([Zhen et al., 2013](#)). Thus we will designate  $\text{LaZnAsO}$  (and therefore also the related  $(\text{La}_{1-y}\text{Sr}_y)(\text{Zn}_{1-x}\text{Mn}_x)\text{AsO}$ ) as a 1111 system ([Ding et al., 2014](#)),  $\text{BaZn}_2\text{As}_2$  (and therefore  $(\text{Ba}_{1-x}\text{K}_x)(\text{Zn}_{1-y}\text{Mn}_y)_2\text{As}_2$ ) as a 122 system ([Zhao et al., 2013](#)), and so on. By way of example, we list selected DMSs from this class along with their Curie temperature,  $T_C$  or Neel temperature,  $T_N$  in [Table 4.2](#). Many such systems are in fact already based on REs, indicating that these structures are likely to be compatible with the REs in terms of bonding and ionic size; their layered nature suggests added flexibility for accommodating the large sizes of the lanthanide-series ions.

**Table 4.2 Examples of layered ferromagnetic and antiferromagnetic alloys (Man et al., 2014)**

	Ferromagnetic	Antiferromagnetic
111	Li(Zn,Mn)As $T_C \sim 50$ K	LiMnAs $T_N \sim 393$ K
1111	(La,Ba)(Zn,Mn)AsO $T_C \sim 40$ K	LaMnAsO $T_N \sim 317$ K
122	(Ba,K)(Zn,Mn) <sub>2</sub> As <sub>2</sub> $T_C \sim 180$ K	BaMn <sub>2</sub> As <sub>2</sub> $T_N \sim 625$ K
32522	Sr <sub>3</sub> La <sub>2</sub> O <sub>5</sub> (Zn,Mn) <sub>2</sub> As <sub>2</sub> $T_C \sim 40$ K	Hypothetical Sr <sub>3</sub> La <sub>2</sub> O <sub>5</sub> Mn <sub>2</sub> As <sub>2</sub>
42622	Sr <sub>4</sub> Ti <sub>2</sub> O <sub>6</sub> (Zn,Mn) <sub>2</sub> As <sub>2</sub> $T_C \sim 250$ K	Hypothetical Sr <sub>4</sub> Ti <sub>2</sub> O <sub>6</sub> Mn <sub>2</sub> As <sub>2</sub>

$T_C$ , Curie temperature;  $T_N$ , Neel temperature.

To illustrate the novel features that characterize these new DMSs, for specificity we will first discuss two examples of this new class in some detail. In our opinion the materials described next lay the ground for forming analogous systems involving REs.

#### 4.5.1 Example of dilute magnetic semiconductors with 122 structure

To illustrate the novelty that such systems bring to the field of DMS, we begin this section by first describing a 122 structure based on a magnetic TM, which illustrates the enormous promise of this class of materials. It is encouraging in the present context that compounds of this type have been shown to accommodate a wide range of magnetic TM ions (Mn, Co, Fe, Cr), which attests to their flexibility, and which suggests that compounds of this type may also play a role as hosts for REs. By way of example we will consider the 122 layered semiconducting compound BaZn<sub>2</sub>As<sub>2</sub>, in which a fraction of the Zn<sup>2+</sup> ions is substitutionally replaced by Mn<sup>2+</sup>, thus introducing a magnetic component into the system; and a fraction of the divalent Ba sublattice is substitutionally replaced by monovalent K, which thus acts as a p-type dopant (Deng et al., 2011; Zhao et al., 2013). The resulting (Ba<sub>1-x</sub>K<sub>x</sub>)(Zn<sub>1-y</sub>Mn<sub>y</sub>)<sub>2</sub>As<sub>2</sub> alloy retains the layered structure of the parent ternary compound (see Fig. 4.16), becoming a layered FM DMS system in which the magnetic moments localized on the Mn ions are presumably coupled via itinerant holes, in loose analogy with GaMnAs. Unlike GaMnAs, however, in this compound the magnetic and the electronic doping can be controlled independently of one another. Furthermore, referring to the structure of BaZn<sub>2</sub>As<sub>2</sub> shown in Fig. 4.16, we note that the magnetic Mn ions exist in different layers from the acceptors, thus representing a very different system in terms of magnetic interactions from DMSs studied so far in either the II-VI, III-V, or IV-VI families.

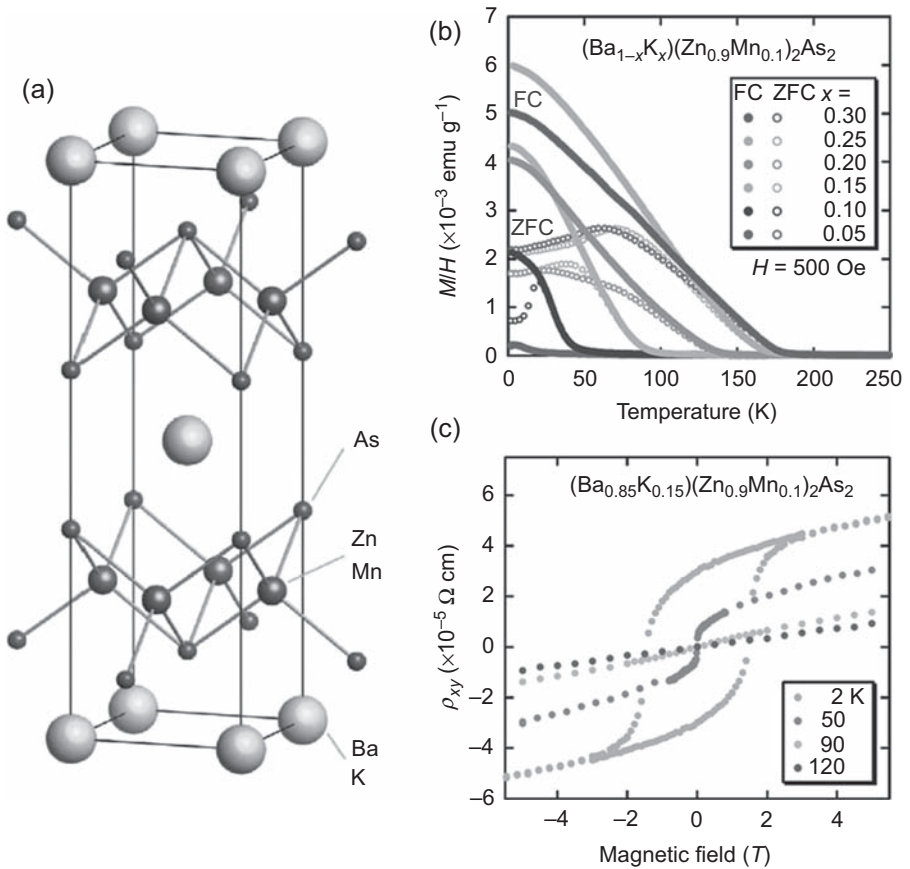


**Figure 4.16** (a) Crystal structure of the layered  $(Ba_{1-x}K_x)(Zn_{1-y}Mn_y)_2As_2$  122 system. (b) dc magnetization observed in  $(Ba_{1-x}K_x)(Zn_{0.90}Mn_{0.10})_2As_2$  specimens with various K-doping levels  $x$  used to control charge carriers, measured in zero-field and field-cooled modes. (c) Hall effect measurements observed on a  $(Ba_{0.85}K_{0.15})(Zn_{0.90}Mn_{0.10})_2As_2$  specimen ( $\rho_{xy}$  is the Hall resistivity). This specimen has a Curie temperature of 90 K. Note the very small coercive field seen at  $T = 50$  K, which rapidly grows to an astounding value of  $\sim 1.0$  T as it approaches  $T = 2$  K.

After Zhao, K., Deng, Z., Wang, X., Han, W., Zhu, J., Li, X., Liu, Q., Yu, R., Goko, T., Frandsen, B., 2013. New diluted ferromagnetic semiconductor with Curie temperature up to 180 K and isostructural to the ‘122’ iron-based superconductors. *Nature Communications* 4, 1442.

The magnetic properties of the magnetic semiconductor  $(Ba_{1-x}K_x)(Zn_{1-y}Mn_y)_2As_2$  are quite unique, as shown in the pioneering work of [Deng et al. \(2011\)](#) and [Zhao et al. \(2013\)](#). The material is FM, with an impressive Curie temperature of about 180 K and an astounding coercivity of about 1.0 T. Importantly, these values were obtained in early attempts to grow this material, thus holding out the hope that with future efforts at optimization the values just mentioned can be further improved.



The results obtained on  $(\text{Ba}_{1-x}\text{K}_x)(\text{Zn}_{1-y}\text{Mn}_y)_2\text{As}_2$  are especially interesting in the context of the present chapter. First, since the growth of this system is already well established, the presence of Ba (whose covalent radius is close of that of the REs) holds promise that the structural constraints of this alloy may in principle be able to accommodate a wide range of REs. It should be particularly interesting to attempt to substitute  $\text{Eu}^{2+}$  for Zn, which, as mentioned, may be made possible due to the large Ba ion in adjacent atomic layer. Alternately, we can consider the possibility of forming (RE)  $\text{Zn}_2\text{As}_2$  in an analogous structure to  $\text{BaZn}_2\text{As}_2$ , but replacing either Zn by monovalent ions or As by group-IV ions to provide the holes required for achieving FM coupling between the magnetic moments localized at the RE sites. This is something of a guess at the present time, but the exciting DMS properties already discovered in this 122 structure make attempts of such variations highly worthwhile.

#### 4.5.2 Example of dilute magnetic semiconductor with 1111 structure

As another important example, consider the structure shown in Fig. 4.17, which in keeping with our adopted nomenclature we will refer to as 1111. Let us consider the system from Fig. 4.17 in more detail. This system is obtained by replacing a fraction of La in the parent  $\text{LaCuSO}$  system by Sr for the purposes of p-type doping, and a fraction of Cu by Mn for introducing magnetic moments into the lattice, to form the  $\text{La}_{1-x}\text{Sr}_x\text{Cu}_{1-y}\text{Mn}_y\text{SO}$  DMS alloy system. As in the preceding 122 example, in this system we can independently vary the concentration of carriers (by controlling the parameter  $x$ ) and magnetic moment concentration (by controlling  $y$ ). Furthermore, similar to the 122 system that we discussed, free carriers and magnetic moments exist in separate layers, thus providing a very different coupling situation between the spins of free carriers and of magnetic moments that is the case in, for example,  $\text{Ga}_{1-x}\text{Mn}_x\text{As}$ . Magnetic properties of this 1111 system are extremely promising, in that a very high Curie temperature of over 190 K has been achieved in what is still rather early work on this system (Yang et al., 2013). It is most especially interesting that such robust ferromagnetism as seen in Fig. 4.17 (and also Fig. 4.16) is obtained in systems where carriers and magnetic moments are localized in different layers of the material.

While in this specific system the REs are not used as a means of providing magnetic moments into the system, the presence of La suggests that other lanthanides can also be fitted into a lattice of this type, thus affecting magnetic properties of the system at hand. In this connection we also note that, if a TM such as Mn is also present in the system, then replacing La by another RE (or alkaline earth ion) can lead to change in the valence state on Mn, thus dramatically affecting the magnetic properties of the entire system. As an example, following the reasoning established in studies of colossal magnetoresistance, substitution of La by, for example, Sr may lead to the conversion of a fraction of the  $\text{Mn}^{3+}$  population to  $\text{Mn}^{4+}$ . We base this possibility on the fact that in  $\text{LaMnO}_3$  Mn is 3+, and in  $\text{SrMnO}_3$  Mn is 4+. Interestingly, when  $\text{Mn}^{3+}$  and  $\text{Mn}^{4+}$  coexist in this type of perovskite system, strong FM ordering can be obtained via double exchange in the  $\text{Mn}^{3+}-\text{O}^{2-}-\text{Mn}^{4+}$  configuration (Okimoto et al., 1995). Of course, because of its valence state, Sr can additionally modulate the type and the

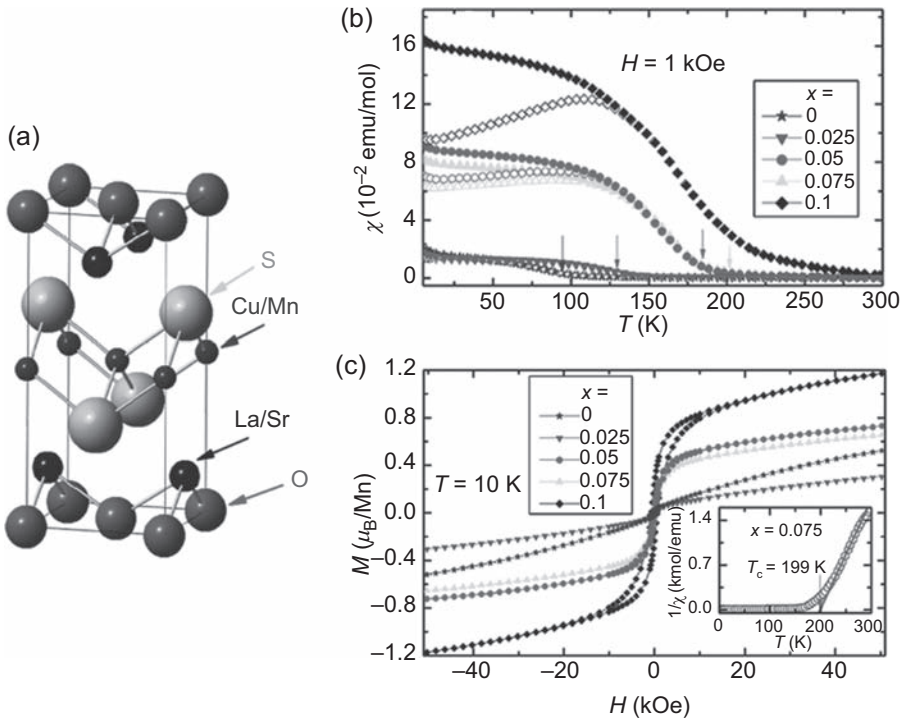


**Figure 4.17** (a) Crystal structure of the layered La<sub>1-x</sub>Sr<sub>x</sub>Cu<sub>1-y</sub>Mn<sub>y</sub>SO 1111 oxychalcogenide system. (b) Temperature dependence of dc magnetic susceptibility  $\chi$  measured in  $H = 1$  kOe on La<sub>1-x</sub>Sr<sub>x</sub>Cu<sub>0.925</sub>Mn<sub>0.075</sub>SO specimens for a series of Sr concentrations  $x$  (where *solid symbols* indicate field cooled, and *open symbols* zero field cooled measurements). (c) Field dependence of magnetization measured at 10 K for the same set of samples as in (b). Inset: plot of  $1/\chi$  versus  $T$ , showing determination of the Curie temperature.

After Yang, X., Li, Y., Shen, C., Si, B., Sun, Y., Tao, Q., Cao, G., Xu, Z., Zhang, F., 2013. Sr and Mn co-doped LaCuSO: a wide band gap oxide diluted magnetic semiconductor with  $T_C$  around 200 K. *Applied Physics Letters* 103, 022410.

concentration of charge carrier, as is the case in superconductors such as La<sub>2-x</sub>Sr<sub>x</sub>CuO<sub>4</sub> (Xu et al., 2000). And, continuing this line of reasoning, if we replace Sr<sup>2+</sup> by Ce<sup>4+</sup>, the type of doping is expected to change from p to n, as expected from the fact that Ce-containing compounds tend to be n-type (Mitra et al., 2001). These options serve to illustrate the rich menu of novel possibilities available for designing and controlling the magnetic properties of these new complex materials by manipulating their RE content.

It should be emphasized that the system at hand is unique in a number of ways that may be attractive in various spintronic situations. It is a wide-gap semiconductor, thus opening the door to DMS application in short-wavelength optoelectronics. It is a strongly p-type layered oxide, which is unique, given the difficulties in p-type doping of wide-gap materials such as ZnO. And its 1111 structure is the same as that of many



1111 Fe-based superconductors, thus suggesting the possibility of integrating this DMS material with superconductors and other related systems.

### **4.5.3 General prospects for layered rare-earth-based pnictides, chalcogenides, and oxide systems**

As seen in Table 4.2, a number of such layered systems already exist as promising DMS materials, many in fact having unprecedented magnetic properties. After discussing two specific examples in the preceding subsections, we now summarize some of the features that characterize this group of materials generally. As illustrated earlier, many of these materials allow decoupling of their spin and charge doping. They typically are p-type semiconductors, which is particularly important from the viewpoint of strong magnetic exchange interactions between charge carriers and localized magnetic moments. Some of the systems already studied have enormous coercive fields, making them completely unique in the field of DMS. Furthermore, many of these systems are wide-gap semiconductors, exhibiting important excitonic effects (Hiramatsu et al., 2003)—a feature that does not occur in FM semiconductors such as  $\text{Ga}_{1-x}\text{Mn}_x\text{As}$ . Because of the characteristics of the crystal structure in which they form, these new materials offer the opportunity of integrating their spin properties with superconducting, thermoelectric, and multiferroic properties occurring in related structures. And, finally, many of these new materials are oxides, thus opening the door to carrier-mediated magnetism in this latter class of materials. The broad range of novel properties of these materials, along with the expected structural flexibility of such layered chalcogenides and pnictides, makes them particularly attractive as a platform for accommodating REs with an eye on forming new RE-based DMSs.

## **4.6 Spintronic possibilities with antiferromagnetic rare-earth compounds**

So far we have focused on RE/semiconductor combinations by assuming that the RE constituent orders ferromagnetically in such alloys. Recently, however, there has been increasing interest in also considering AFM materials as viable candidates for spintronic applications (Wadley et al., 2013; Barthem et al., 2013; Sando et al., 2013; Beleanu et al., 2013). These possibilities are especially relevant in the present context, since a large number of naturally occurring RE compounds (eg, RE monopnictides) are AFM (Duan et al., 2007). We will therefore include this topic in the present chapter, and will briefly speculate on several examples involving this interesting possibility.

Although the use of AFM materials in spintronic applications may at first glance appear to be a contradiction in terms because of the vanishing dc magnetic moment in a typical antiferromagnet, bear in mind that the AFM system is dramatically different from a nonmagnetic system. A simple antiferromagnet can be pictured as consisting of two magnetically ordered sublattices,  $M_1$  and  $M_2$ , which are strongly

exchange-coupled to one another in such a way that  $M_1$  and  $M_2$  exactly cancel each other, resulting in zero magnetization. However, both the inherent order of the sublattices and the exchange coupling that exists between them can be tapped into serving spintronic functions by device design, as has been now shown by a large number of highly imaginative approaches (Gomonay and Loktev, 2014; Li et al., 2013; Tveten et al., 2013). While this field is still very new, and deals with systems that are in many ways more complex than simple ferromagnets, important advances have already been made in this area, including experimental demonstration of the viability of AFM-based spintronic effects (Cava et al., 2011; Sinova and Žutić, 2012; Wang et al., 2012, 2013). We will describe some of these advances as illustrations of the promise that this new field holds for spintronics.

The usefulness of AFM structures in spintronics is based on several arguments. The most obvious application of an AFM material is the phenomenon of exchange bias, already widely used in applications such as spin valves (Park et al., 2011). This, however, also requires the presence of a ferromagnet interfaced with the AFM component. Going beyond that, consider an interface of an antiferromagnet with another material (which can be a ferromagnet, another antiferromagnet, or a magnetically neutral layer). Such an interface necessarily involves breaking of magnetic symmetry, and thus may result in a finite magnetic moment associated with the discontinuity. This then can be harnessed in a number of situations that we will discuss next. A related opportunity of obtaining a finite net magnetic moment from an antiferromagnet exists in the case of small AFM particles embedded in a nonmagnetic medium that has already been mentioned. Such nanoparticles naturally contain symmetry-breaking discontinuities, but on the nanoscale may additionally involve an imbalance in the numbers of oppositely oriented spins, both effects resulting in a finite magnetic moment of the nanoparticle that renders it weakly FM (Manukyan et al., 2014). This will be especially important in cases where AFM precipitates are present (similar to the cases considered in Section 4.3, but where now we expect to have weakly FM instead of fully FM particles).

Several types of structures involving AFM materials can be of interest in this context: systems based on exchange bias, spin valves, tunnel structures, and structures involving processes based on spin transfer torque, as described in the excellent review of Gomonay and Loktev (2014). As an example, consider a current of electrons flowing through an AFM/FM bilayer shown schematically in Fig. 4.18. The current is spin-polarized by the FM layer, and transfers some of its magnetic moment to the AFM region through which it passes. As a consequence, the AFM region acquires a net magnetic moment (in the form of rotation of its sublattices  $M_1$  and  $M_2$ , which now no longer cancel), as shown in Fig. 4.18(b). It is encouraging that many of the options anticipated theoretically have already been achieved in the laboratory (Park et al., 2011; Wang et al., 2012, 2013; Sando et al., 2013). Although the discussions in the literature are largely focused on metallic systems (such as Cr), this is a practical rather than a fundamental distinction, and semiconductors with AFM interactions involving REs are equally interesting in this context as important candidates for spintronic applications. Since both the field of AFM spintronics and of RE DMSs at their formative stages, it

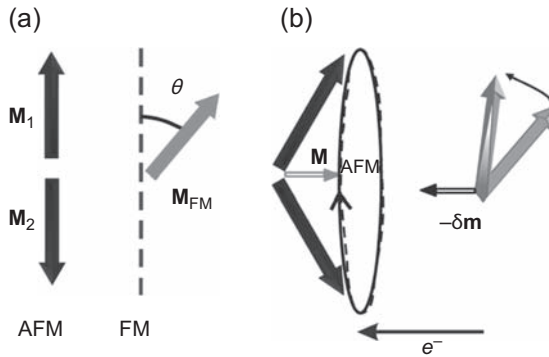


**Figure 4.18** An example of effects on magnetic properties of an AFM/FM bilayer induced by a current. *Broad arrows* show the orientation of magnetic moments of sublattices  $M_1$  and  $M_2$  in the AFM region, and of magnetization vector  $M_{FM}$  in the FM layers. (a) Magnetizations in the AFM/FM bilayer in the absence of the current. (b) When a current of electrons whose spins are polarized in the FM layer flows (from the left, as shown by the *horizontal arrow*), it transfers an increment of its magnetic moment  $\delta m$  to the AFM region, giving rise to a net magnetization  $M_{AFM}$  of that region in the form of rotation of the vectors  $M_1$  and  $M_2$ , as shown schematically in (b).

After Gomonay, E.V., Loktev, V.M., 2014. Spintronics of antiferromagnetic systems (review article). *Low Temperature Physics* 40, 17–35.

is of course premature to pursue this subject in greater detail, but it is important to bear in mind that both fields hold opportunities that are mutually promising.

## 4.7 Conclusions

In this chapter we discussed a wide spectrum of possibilities for achieving promising RE-based DMS systems, including single-phase magnetic semiconductor alloys, inhomogeneous and mixed-phase RE-based magnetic systems, hybrid heterostructures comprised of semiconductor and magnetic RE compounds, and the new generation of RE-based layered semiconducting chalcogenides and pnictides. Additionally, we considered the possibility of AFM RE compounds to achieve spintronic functionalities. Taken together, the field RE-based DMS alloys and hybrid magnetic RE/semiconductor heterostructures appears to hold in store highly promising prospects for spintronic applications, making it worthwhile to undertake further exploration of new RE-based materials, new approaches to their crystal growth, and ultimately of new optical and spintronic devices based on these systems.

However, as in most emerging fields, many challenges must still be overcome before this field can be considered for practical device applications. Among the greatest is the perennial problem of the Curie temperature, which still remains too low for practical use in RE-based magnetic semiconductors achieved so far. We should note parenthetically, however, that alloys such as  $(Ba,K)(Zn,Mn)_2As_2$  have achieved

impressively high Curie temperatures (along with enormous coercivities) even in early attempts at their formation, making it tempting to explore related 122 alloys based on REs. Even if these obstacles are overcome, we must also consider whether devices involving dilute magnetic RE-based semiconductors can be practical in industry. Here one of the issues is the question of integration of such alloys with established semiconductor systems due to considerable lattice mismatch. Again, however, we find it encouraging that many of the new RE-based semiconductors belong to the family of layered structures (such as the 122 system already mentioned), which appear to be quite forgiving where issues with lattice mismatch are involved. Thus, although there is still a long way to go to achieve the goals of practicality for the new systems discussed in this chapter, the authors feel that the door for this new area is already open and waiting.

## References

- Allen, S.J., Tabatabaie, N., Palmstrom, C.J., Hull, G.W., Sands, T., Derosa, F., Gilchrist, H.L., Garrison, K.C., 1989. ErAs epitaxial layers buried in GaAs: magnetotransport and spin-disorder scattering. *Physical Review Letters* 62, 2309–2312.
- Aszodi, G., Weber, J., Uihlein, C., Pu-lin, L., Ennen, H., Kaufmann, U., Schneider, J., Windscheif, J., 1985. Zeeman analysis of the ytterbium luminescence in indium phosphide. *Physical Review B* 31, 7767–7771.
- Bang, H., Sawahata, J., Piao, G., Tsunemi, M., Yanagihara, H., Kita, E., Akimoto, K., 2003. Magnetic properties of rare-earth-doped GaN. *Physica Status Solidi (C)* 2874–2877.
- Barthem, V.M.T.S., Colin, C.V., Mayaffre, H., Julien, M.H., Givord, D., 2013. Revealing the properties of Mn<sub>2</sub>Au for antiferromagnetic spintronics. *Nature Communications* 4, 2892.
- Bartholomew, D.U., Furdyna, J.K., Ramdas, A.K., 1986. Interband Faraday rotation in diluted magnetic semiconductors: Zn<sub>1-x</sub>Mn<sub>x</sub>Te and Cd<sub>1-x</sub>Mn<sub>x</sub>Te. *Physical Review B* 34, 6943–6950.
- Beleanu, A., Kiss, J., Kreiner, G., Köhler, C., Mühler, L., Schnelle, W., Burkhardt, U., Chadov, S., Medvediev, S., Ebke, D., Felser, C., Cordier, G., Albert, B., Hoser, A., Bernardi, F., Larkin, T.I., Pröpper, D., Boris, A.V., Keimer, B., 2013. Large resistivity change and phase transition in the antiferromagnetic semiconductors LiMnAs and LaOMnAs. *Physical Review B* 88, 184429.
- Bernard, J.E., Zunger, A., 1988. Ordered-vacancy-compound semiconductors: pseudocubic CdIn<sub>2</sub>Se<sub>4</sub>. *Physical Review B* 37, 6835–6856.
- Bethhausen, C., Dollinger, T., Saarikoski, H., Kolkovsky, V., Karczewski, G., Wojtowicz, T., Richter, K., Weiss, D., 2012. Spin-transistor action via tunable Landau-Zener transitions. *Science* 337, 324–327.
- Bindilatti, V., Oliveira, N.F., Shapira, Y., McCabe, G.H., Liu, M.T., Isber, S., Charar, S., Averous, M., McNiff, E.J., Golacki, Z., 1996. Magnetization steps in Pb<sub>1-x</sub>Eu<sub>x</sub>Se: determination and identification of the dominant antiferromagnetic exchange constant. *Physical Review B* 53, 5472–5480.
- Bindilatti, V., ter Haar, E., Oliveira, N.F., Liu, M.T., Shapira, Y., Gratens, X., Charar, S., Isber, S., Masri, P., Averous, M., Golacki, Z., McNiff, E.J., 1998. Magnetization steps in Pb<sub>1-x</sub>Eu<sub>x</sub>S: exchange and anisotropic interactions. *Physical Review B* 57, 7854–7862.

- Bonanni, A., 2007. Ferromagnetic nitride-based semiconductors doped with transition metals and rare earths. *Semiconductor Science and Technology* 22, R41–R56.
- Bonanni, A., Dietl, T., 2010. A story of high-temperature ferromagnetism in semiconductors. *Chemical Society Reviews* 39, 528–539.
- Bunzli, J.C.G., Comby, S., Chauvin, A.S., Vandevyver, C.D.B., 2007. New opportunities for lanthanide luminescence. *Journal of Rare Earths* 25, 257–274.
- Buschow, K., 1977. Intermetallic compounds of rare-earth and 3d transition metals. *Reports on Progress in Physics* 40, 1179.
- Cava, R.J., Jungwirth, T., Novák, V., Martí, X., Cukr, M., Máca, F., Shick, A., Mašek, J., Horodyská, P., Němec, P., 2011. Viewpoint: a useful pyramid scheme. *Physical Review B* 83, 035321.
- Chen, X., Na, M., Cheon, M., Wang, S., Luo, H., McCombe, B.D., Liu, X., Sasaki, Y., Wojtowicz, T., Furdyna, J.K., Potashnik, S.J., Schiffer, P., 2002. Above-room-temperature ferromagnetism in GaSb/Mn digital alloys. *Applied Physics Letters* 81, 511–513.
- Cheong, S.-W., Mostovoy, M., 2007. Multiferroics: a magnetic twist for ferroelectricity. *Nature Materials* 6, 13–20.
- Cho, Y.J., Yu, K.M., Liu, X., Walukiewicz, W., Furdyna, J.K., 2008. Effects of donor doping on  $\text{Ga}_{1-x}\text{Mn}_x\text{As}$ . *Applied Physics Letters* 93, 262505.
- Choi, S.W., Zhou, Y.K., Emura, S., Lee, X.J., Teraguchi, N., Suzuki, A., Asahi, H., 2006. Magnetic, optical and electrical properties of GaN and AlN doped with rare-earth element Gd. *Physica Status Solidi (C)* 3, 2250–2253.
- Coey, J.M.D., Venkatesan, M., Fitzgerald, C.B., 2005. Donor impurity band exchange in dilute ferromagnetic oxides. *Nature Materials* 4, 173–179.
- Counio, G., Gacoin, T., Boilot, J.P., 1998. Synthesis and photoluminescence of  $\text{Cd}_{1-x}\text{Mn}_x\text{S}$  ( $x \leq 5\%$ ) nanocrystals. *Journal of Physical Chemistry B* 102, 5257–5260.
- Crook, A.M., Nair, H.P., Ferrer, D.A., Bank, S.R., 2011. Suppression of planar defects in the molecular beam epitaxy of GaAs/ErAs/GaAs heterostructures. *Applied Physics Letters* 99, 072120.
- Dai, N., Luo, H., Zhang, F.C., Samarth, N., Dobrowolska, M., Furdyna, J.K., 1991. Spin superlattice formation in  $\text{ZnSe}/\text{Zn}_{1-x}\text{Mn}_x\text{Se}$  multilayers. *Physical Review Letters* 67, 3824–3827.
- De Boeck, J., Oesterholt, R., Van Esch, A., Bender, H., Bruynseraede, C., Van Hoof, C., Borghs, G., 1996. Nanometer-scale magnetic MnAs particles in GaAs grown by molecular beam epitaxy. *Applied Physics Letters* 68, 2744–2746.
- Deng, Z., Jin, C., Liu, Q., Wang, X., Zhu, J., Feng, S., Chen, L., Yu, R., Arguello, C., Goko, T., 2011.  $\text{Li}(\text{Zn,Mn})\text{As}$  as a new generation ferromagnet based on a I–II–V semiconductor. *Nature Communications* 2, 422.
- Dhar, S., Kammermeier, T., Ney, A., Pérez, L., Ploog, K.H., Melnikov, A., Wieck, A.D., 2006. Ferromagnetism and colossal magnetic moment in Gd-focused ion-beam-implanted GaN. *Applied Physics Letters* 89, 062503.
- Dietl, T., 1994. (Diluted) magnetic semiconductors. In: Mahajan, S., Moss, T.S. (Eds.), *Handbook on Semiconductors*, vol. 3, part 1. North-Holland.
- Dietl, T., 2006. From our readers: self-organized growth controlled by charge states of magnetic impurities. *Nature Materials* 5, 673.
- Dietl, T., Awschalom, D.D., Kaminska, M., Ohno, H. (Eds.), 2009. *Spintronics, Semiconductors and Semimetals*, vol. 82. Academic Press.
- Ding, C., Gong, X., Man, H., Zhi, G., Guo, S., Zhao, Y., Wang, H., Chen, B., Ning, F., 2014. The suppression of Curie temperature by Sr doping in diluted ferromagnetic semiconductor  $(\text{La}_{1-x}\text{Sr}_x)(\text{Zn}_{1-y}\text{Mn}_y)\text{AsO}$ . *EPL (Europhysics Letters)* 107, 17004.

- Dobrowolski, W., Kossut, J., Story, T., 2003. II-VI and IV-VI diluted magnetic semiconductors new bulk materials and low-dimensional quantum structures. In: Buschow, K.H.J. (Ed.), Handbook of Magnetic Materials, vol. 15. Elsevier Science.
- Driscoll, D.C., Hanson, M.P., Mueller, E., Gossard, A.C., 2003. Growth and microstructure of semimetallic ErAs particles embedded in an  $\text{In}_{0.53}\text{Ga}_{0.47}\text{As}$  matrix. *Journal of Crystal Growth* 251, 243–247.
- Duan, C.-G., Sabirianov, R.F., Mei, W.N., Dowben, P.A., Jaswal, S.S., Tsymbal, E.Y., 2007. Electronic, magnetic and transport properties of rare-earth monopnictides. *Journal of Physics: Condensed Matter* 19, 315220.
- Ennen, H., Wagner, J., Müller, H.D., Smith, R.S., 1987. Photoluminescence excitation measurements on GaAs:Er grown by molecular-beam epitaxy. *Journal of Applied Physics* 61, 4877–4879.
- Enz, U., Vanhouten, S., Fast, J.F., Smit, J., 1962. Magnetism of EuS, EuSe and EuTe. *Philips Research Reports* 17, 451.
- Errebhahi, A., Charar, S., Terki, F., Fau, C., Isber, S., Tabbal, M., Christidis, T.C., Ravot, D., Tedenac, J.C., Golacki, Z., 2002. Investigation of the effect of annealing on the magnetic properties of  $\text{Sn}_{1-x}\text{Eu}_x\text{Te}$  single crystals. *Journal of Magnetism and Magnetic Materials* 247, 55–61.
- Fukushima, T., Sato, K., Katayama-Yoshida, H., Dederichs, P.H., 2006. Spinodal decomposition under layer by layer growth condition and high Curie temperature quasi-one-dimensional nano-structure in dilute magnetic semiconductors. *Japanese Journal of Applied Physics Part 2-Letters & Express Letters* 45, L416–L418.
- Furdyna, J.K., 1988. Diluted magnetic semiconductors. *Journal of Applied Physics* 64, R29–R64.
- Furdyna, J.K., Kossut, J. (Eds.), 1988. Diluted Magnetic Semiconductors, Semiconductors and Semimetals, vol. 25. Academic Press, Inc., Boston.
- Gaj, J.A., Kossut, J. (Eds.), 2011. Introduction to the Physics of Diluted Magnetic Semiconductors, Springer Series in Materials Science, vol. 144. Springer.
- Galazka, R.R., Nagata, S., Keesom, P.H., 1980. Paramagnetic-spin-glass-antiferromagnetic phase transitions in  $\text{Cd}_{1-x}\text{Mn}_x\text{Te}$  from specific heat and magnetic susceptibility measurements. *Physical Review B* 22, 3344–3355.
- Giebultowicz, T.M., Faschinger, W., Nunez, V., Klosowski, P., Bauer, G., Sitter, H., Furdyna, J.K., 1994. Antiferromagnetic spin ordering and interlayer magnetic correlations in MnTe/CdTe superlattices. *Journal of Crystal Growth* 138, 877–883.
- Giebultowicz, T.M., Klosowski, P., Samarth, N., Luo, H., Rhyne, J.J., Furdyna, J.K., 1990. Antiferromagnetic phase transition in  $\text{Cd}_{1-x}\text{Mn}_x\text{Se}$  epilayers. *Physical Review B* 42, 2582–2585.
- Giebultowicz, T.M., Nunez, V., Springholz, G., Bauer, G., Chen, J., Dresselhaus, M.S., Furdyna, J.K., 1995. Interlayer coupling in (111) EuTe/PbTe AFM multilayers. *Journal of Magnetism and Magnetic Materials* 140–144, part 1, 635–636.
- Gomonay, E.V., Loktev, V.M., 2014. Spintronics of antiferromagnetic systems (review article). *Low Temperature Physics* 40, 17–35.
- Han, S.Y., Hite, J., Thaler, G.T., Frazier, R.M., Abernathy, C.R., Pearton, S.J., Choi, H.K., Lee, W.O., Park, Y.D., Zavada, J.M., Gwilliam, R., 2006. Effect of Gd implantation on the structural and magnetic properties of GaN and AlN. *Applied Physics Letters* 88, 042102.
- Heremans, J., Partin, D.L., 1988. Magnetic properties of EuTe-PbTe superlattices. *Physical Review B* 37, 6311–6314.
- Hiramatsu, H., Ueda, K., Takafuji, K., Ohta, H., Hirano, M., Kamiya, T., Hosono, H., 2003. Intrinsic excitonic photoluminescence and band-gap engineering of wide-gap p-type

- oxychalcogenide epitaxial films of  $\text{LnCuOCh}$  ( $\text{Ln} = \text{La}, \text{Pr}, \text{and Nd}$ ;  $\text{Ch} = \text{S}$  or  $\text{Se}$ ) semiconductor alloys. *Journal of Applied Physics* 94, 5805–5808.
- Isber, S., Masri, P., Charar, S., Gratens, X., Misra, S.K., 1997. The effect of the crystal field on magnetization steps due to exchange-coupled  $\text{Eu}^{2+}$  open and closed triplets in  $\text{Pb}_{1-x}\text{Eu}_x\text{Se}$ . *Journal of Physics-Condensed Matter* 9, 10023–10032.
- Johnston, D.C., 2010. The puzzle of high temperature superconductivity in layered iron pnictides and chalcogenides. *Advances in Physics* 59, 803–1061.
- Kadow, C., Fleischer, S.B., Ibbetson, J.P., Bowers, J.E., Gossard, A.C., Dong, J.W., Palmstrom, C.J., 1999. Self-assembled ErAs islands in GaAs: growth and subpicosecond carrier dynamics. *Applied Physics Letters* 75, 3548–3550.
- Katayama-Yoshida, H., Sato, K., Fukushima, T., Toyoda, M., Kizaki, H., Dinh, V.A., Dederichs, P.H., 2007. Computational nano-materials design for high- $T_C$  ferromagnetism in wide-gap magnetic semiconductors. *Journal of Magnetism and Magnetic Materials* 310, 2070–2077.
- Katsura, H., Nagaosa, N., Balatsky, A.V., 2005. Spin current and magnetoelectric effect in noncollinear magnets. *Physical Review Letters* 95, 057205.
- Kawasaki, J.K., Schultz, B.D., Lu, H., Gossard, A.C., Pamstrom, C.J., 2013. Surface-mediated tunable self-assembly of single crystal semimetallic ErSb/GaSb nanocomposite structures. *Nano Letters* 13, 2895–2901.
- Kent, T.F., Yang, J., Yang, L., Mills, M.J., Myers, R.C., 2012. Epitaxial ferromagnetic nanoislands of cubic GdN in hexagonal GaN. *Applied Physics Letters* 100, 152111.
- Kenyon, A.J., 2002. Recent developments in rare-earth doped materials for optoelectronics. *Progress in Quantum Electronics* 26, 225–284.
- Kepa, H., Springholz, G., Giebultowicz, T.M., Goldman, K.I., Majkrzak, C.F., Kacman, P., Blinowski, J., Holl, S., Krenn, H., Bauer, G., 2003. Magnetic interactions in EuTe epitaxial layers and EuTe/PbTe superlattices. *Physical Review B* 68, 024419.
- Khym, S., Yoo, T., Lee, H., Lee, S., Lee, S., Liu, X.Y., Furdyna, J.K., Lee, D.U., Kim, E.K., 2012. Multi-valued planar hall resistance manipulated by current induced magnetic field in Fe films grown on GaAs(001) substrates. *Applied Physics Express* 5, 093004.
- Kilanski, L., Górska, M., Dynowska, E., Podgórn, A., Avdonin, A., Dobrowolski, W., Fedorchenko, I.V., Marenkin, S.F., 2014. Homogeneous limit of  $\text{Cd}_{1-x}\text{Mn}_x\text{GeAs}_2$  alloy: electrical and magnetic properties. *Journal of Applied Physics* 115, 133917.
- Kimura, T., Goto, T., Shintani, H., Ishizaka, K., Arima, T., Tokura, Y., 2003. Magnetic control of ferroelectric polarization. *Nature* 426, 55–58.
- Klenov, D.O., Driscoll, D.C., Gossard, A.C., Stemmer, S., 2005a. Scanning transmission electron microscopy of ErAs nanoparticles embedded in epitaxial  $\text{In}_{0.53}\text{Ga}_{0.47}\text{As}$  layers. *Applied Physics Letters* 86, 111912.
- Klenov, D.O., Zide, J.M., Zimmerman, J.D., Gossard, A.C., Stemmer, S., 2005b. Interface atomic structure of epitaxial ErAs layers on (001)  $\text{In}_{0.53}\text{Ga}_{0.47}\text{As}$  and GaAs. *Applied Physics Letters* 86, 241901.
- Krenn, H., Herbst, W., Pascher, H., Ueta, Y., Springholz, G., Bauer, G., 1999. Interband Faraday and Kerr rotation and magnetization of  $\text{Pb}_{1-x}\text{Eu}_x\text{Te}$  in the concentration range  $0 < x \leq 1$ . *Physical Review B* 60, 8117–8128.
- Kumta, P.N., Risbud, S.H., 1994. Rare-earth chalcogenides – an emerging class of optical-materials. *Journal of Materials Science* 29, 1135–1158.
- Lee, S., Dobrowolska, M., Furdyna, J.K., Ram-Mohan, L.R., 1999. Wave-function mapping in multiple quantum wells using diluted magnetic semiconductors. *Physical Review B* 59, 10302–10308.

- Lewicki, A., Schindler, A.I., Furdyna, J.K., Girit, W., 1989. Magnetic susceptibility of  $\text{Zn}_{1-x}\text{Co}_x\text{S}$  and  $\text{Zn}_{1-x}\text{Co}_x\text{Se}$  alloys. *Physical Review B* 40, 2379–2382.
- Li, X., Cao, T., Niu, Q., Shi, J., Feng, J., 2013. Coupling the valley degree of freedom to antiferromagnetic order. *Proceedings of the National Academy of Sciences* 110, 3738–3742.
- Lide, D.R., 2004. *CRC Handbook of Chemistry and Physics*. CRC Press.
- Luo, H., Kim, G.B., Cheon, M., Chen, X., Na, M., Wang, S., McCombe, B.D., Liu, X., Sasaki, Y., Wojtowicz, T., Furdyna, J.K., Boishin, G., Whitman, L.J., 2004. Ferromagnetic GaSb/Mn digital alloys. *Physica E-Low-Dimensional Systems & Nanostructures* 20, 338–345.
- Luo, Y., Pourovskii, L., Rowley, S., Li, Y., Feng, C., Georges, A., Dai, J., Cao, G., Xu, Z.a., Si, Q., 2014. Heavy-fermion quantum criticality and destruction of the Kondo effect in a nickel oxypnictide. *Nature Materials*.
- MacKinnon, A., 1981. Ternary semiconductors. In: Treusch, J. (Ed.), *Festkörperprobleme*, vol. 21. Springer Berlin Heidelberg.
- Mahadevan, P., Zunger, A., Sarma, D.D., 2004. Unusual directional dependence of exchange energies in GaAs diluted with Mn: is the RKKY description relevant? *Physical Review Letters* 93, 177201.
- Man, H., Qin, C., Ding, C., Wang, Q., Gong, X., Guo, S., Wang, H., Chen, B., Ning, F., 2014.  $(\text{Sr}_3\text{La}_2\text{O}_5)(\text{Zn}_{1-x}\text{Mn}_x)_2\text{As}_2$ : a bulk form diluted magnetic semiconductor isostructural to the “32522” Fe-based superconductors. *Europhysics Letters* 105, 67004.
- Manukyan, K.V., Chen, Y.-S., Rouvimov, S., Li, P., Li, X., Dong, S., Liu, X., Furdyna, J.K., Orlov, A., Bernstein, G.H., Porod, W., Roslyakov, S., Mukasyan, A.S., 2014. Ultrasmall  $\alpha\text{-Fe}_2\text{O}_3$  superparamagnetic nanoparticles with high magnetization prepared by template-assisted combustion process. *Journal of Physical Chemistry C* 118, 16264–16271.
- McCombe, B.D., Na, M., Chen, X., Cheon, M., Wang, S., Luo, H., Liu, X., Sasaki, Y., Wojtowicz, T., Furdyna, J.K., Potashnik, S.J., Schiffer, P., 2003. Novel ferromagnetism in digital GaAs/Mn and GaSb/Mn alloys. *Physica E-Low-Dimensional Systems & Nanostructures* 16, 90–98.
- Mitra, C., Raychaudhuri, P., John, J., Dhar, S., Nigam, A., Pinto, R., 2001. Growth of epitaxial and polycrystalline thin films of the electron doped system  $\text{La}_{1-x}\text{Ce}_x\text{MnO}_3$  through pulsed laser deposition. *Journal of Applied Physics* 89, 524–530.
- Morishima, S., Maruyama, T., Akimoto, K., 2000. Epitaxial growth of Eu-doped GaN by gas source molecular beam epitaxy. *Journal of Crystal Growth* 209, 378–381.
- Mukherjee, P., Shade, C.M., Yingling, A.M., Lamont, D.N., Waldeck, D.H., Petoud, S.P., 2010. Lanthanide sensitization in II–VI semiconductor materials: a case study with terbium(III) and europium(III) in zinc sulfide nanoparticles. *The Journal of Physical Chemistry A* 115, 4031–4041.
- Nagata, S., Galazka, R.R., Mullin, D.P., Akbarzadeh, H., Khattak, G.D., Furdyna, J.K., Keesom, P.H., 1980. Magnetic susceptibility, specific heat and the spin-glass transition in  $\text{Hg}_{1-x}\text{Mn}_x\text{Te}$ . *Physical Review B* 22, 3331–3343.
- Nakamura, A., Kato, N., Yamakawa, I., Akimoto, R., 2004. Magnetic field enhanced luminescence in ZnSe/BeMnTe multiple quantum wells with a type II band alignment. *Journal of Luminescence* 108, 65–68.
- Ohno, H., 1999. Properties of ferromagnetic III-V semiconductors. *Journal of Magnetism and Magnetic Materials* 200, 110–129.
- Ohno, H., Munekata, H., Vonmolnar, S., Chang, L.L., 1991. New III-V diluted magnetic semiconductors (invited). *Journal of Applied Physics* 69, 6103–6108.



- Ohno, H., Shen, A., Matsukura, F., Oiwa, A., Endo, A., Katsumoto, S., Iye, Y., 1996. (Ga,Mn)As: a new diluted magnetic semiconductor based on GaAs. *Applied Physics Letters* 69, 363–365.
- Okimoto, Y., Katsufuji, T., Ishikawa, T., Urushibara, A., Arima, T., Tokura, Y., 1995. Anomalous variation of optical spectra with spin polarization in double-exchange ferromagnet:  $\text{La}_{1-x}\text{Sr}_x\text{MnO}_3$ . *Physical Review Letters* 75, 109.
- Overberg, M., Lee, K.N., Abernathy, C.R., Pearson, S.J., Hobson, W.S., Wilson, R.G., Zavada, J.M., 2001. Characterization and annealing of Eu-doped GaN. *Materials Science and Engineering: B* 81, 150–152.
- Pérez, L., Lau, G.S., Dhar, S., Brandt, O., Ploog, K.H., 2006. Magnetic phases and anisotropy in Gd-doped GaN. *Physical Review B* 74, 195207.
- Palmstrom, C.J., Tabatabaie, N., Allen, S.J., 1988. Epitaxial growth of ErAs on (100)GaAs. *Applied Physics Letters* 53, 2608–2610.
- Park, B., Wunderlich, J., Marti, X., Holý, V., Kurosaki, Y., Yamada, M., Yamamoto, H., Nishide, A., Hayakawa, J., Takahashi, H., 2011. A spin-valve-like magnetoresistance of an antiferromagnet-based tunnel junction. *Nature Materials* 10, 347–351.
- Parthé, E., 1964. *Crystal Chemistry of Tetrahedral Structures*. Gordon and Breach, New York.
- Petukhov, A.G., Lambrecht, W.R.L., Segall, B., 1996. Spin-dependent resonant tunneling through semimetallic ErAs quantum wells in a magnetic field. *Physical Review B* 53, 3646–3649.
- Proceedings of the symposium on magnetic semiconductors, 1970. *IBM Journal of Research and Development* 14, 205–340.
- Raola, O.E., Strouse, G.F., 2002. Synthesis and characterization of Eu-doped cadmium selenide nanocrystals. *Nano Letters* 2, 1443–1447.
- Reed, T.B., Fahey, R.E., 1971. Growth of EuO, EuS, EuSe and EuTe single crystals. *Journal of Crystal Growth* 8, 337.
- Sands, T., Palmstrøm, C.J., Harbison, J.P., Keramidis, V.G., Tabatabaie, N., Cheeks, T.L., Ramesh, R., Silberberg, Y., 1990. Stable and epitaxial metal/III-V semiconductor heterostructures. *Materials Science Reports* 5, 99–170.
- Sando, D., Agbelele, A., Rahmedov, D., Liu, J., Rovillain, P., Toulouse, C., Infante, I.C., Pyatakov, A.P., Fusil, S., Jacquet, E., Carrétéro, C., Deranlot, C., Lisenkov, S., Wang, D., Le Breton, J.M., Cazayous, M., Sacuto, A., Juraszek, J., Zvezdin, A.K., Bellaiche, L., Dkhil, B., Barthélémy, A., Bibes, M., 2013. Crafting the magnonic and spintronic response of  $\text{BiFeO}_3$  films by epitaxial strain. *Nature Materials* 12, 641–646.
- Sato, K., Fukushima, T., Katayama-Yoshida, H., 2007. Super-paramagnetic blocking phenomena and room-temperature ferromagnetism in wide band-gap dilute magnetic semiconductor (Ga,Mn)N. *Japanese Journal of Applied Physics Part 2-Letters & Express Letters* 46, L682–L684.
- Sato, K., Katayama-Yoshida, H., Dederichs, P.H., 2005. High Curie temperature and nano-scale spinodal decomposition phase in dilute magnetic semiconductors. *Japanese Journal of Applied Physics Part 2-Letters & Express Letters* 44, L948–L951.
- Sawicki, M., Guzewicz, E., Lukasiewicz, M.I., Proselkov, O., Kowalik, I.A., Lisowski, W., Dluzewski, P., Wittlin, A., Jaworski, M., Wolska, A., Paszkowicz, W., Jakiela, R., Witkowski, B.S., Wachnicki, L., Klepka, M.T., Luque, F.J., Arvanitis, D., Sobczak, J.W., Krawczyk, M., Jablonski, A., Stefanowicz, W., Sztenkiel, D., Godlewski, M., Dietl, T., 2013. Homogeneous and heterogeneous magnetism in (Zn,Co)O: from a random antiferromagnet to a dipolar superferromagnet by changing the growth temperature. *Physical Review B* 88, 085204.

- Sawicki, M., Le van, K., Hansen, L., Ferrand, D., Molenkamp, L.W., Waag, A., Dietl, T., 2002. Magnetic characterisation of highly doped MBE grown  $\text{Be}_{1-x}\text{Mn}_x\text{Te}$  and bulk  $\text{Zn}_{1-x}\text{Mn}_x\text{Te}$ . *Physica Status Solidi B-Basic Research* 229, 717–721.
- Scarpulla, M.A., Dubon, O.D., Yu, K.M., Monteiro, O., Pillai, M.R., Aziz, M.J., Ridgway, M.C., 2003. Ferromagnetic  $\text{Ga}_{1-x}\text{Mn}_x\text{As}$  produced by ion implantation and pulsed-laser melting. *Applied Physics Letters* 82, 1251–1253.
- Shay, J.L., Wernick, J.H., 1975. Ternary chalcopyrite semiconductors: growth, electronic properties, and applications. In: *International Series in the Science of the Solid State*, vol. 7. Pergamon.
- Shiraoka, H., Miyagawa, H., Higuchi, S., Fujii, K., Takahashi, N., Watanabe, Y., Oda, K., Tsurumachi, N., Nakanishi, S., Itoh, H., Koshiba, S., 2008. MBE growth of diluted magnetic semiconductor gadolinium-doped GaAs. *Transactions of the Materials Research Society of Japan* 33 (2).
- Siebentritt, S., Rau, U., 2006. Wide-gap chalcopyrites. *Springer Series in Materials Science* 86. Springer Berlin Heidelberg.
- Sinova, J., Žutić, I., 2012. New moves of the spintronics tango. *Nature Materials* 11, 368–371.
- Springholz, G., Bauer, G., 1993. Molecular beam epitaxy of strained  $\text{PbTe}/\text{EuTe}$  superlattices. *Applied Physics Letters* 62, 2399–2401.
- Stachow-Wójcik, A., Story, T., Dobrowolski, W., Arciszewska, M., Galazka, R.R., Kreijveld, M.W., Swuste, C.H.W., Swagten, H.J.M., de Jonge, W.J.M., Twardowski, A., Sipatov, A.Y., 1999. Ferromagnetic transition in  $\text{EuS-PbS}$  multilayers. *Physical Review B* 60, 15220–15229.
- Steckl, A.J., Heikenfeld, J.C., Lee, D.S., Garter, M.J., Baker, C.C., Wang, Y.Q., Jones, R., 2002. Rare-earth-doped GaN: growth, properties, and fabrication of electroluminescent devices. *IEEE Journal of Selected Topics in Quantum Electronics* 8, 749–766.
- Steckl, A.J., Park, J.H., Zavada, J.M., 2007. Prospects for rare earth doped GaN lasers on Si. *Materials Today* 10, 20–27.
- Story, T., 1997. IV-VI semimagnetic semiconductors with rare earth ions. *Acta Physica Polonica A* 92, 663–672.
- Story, T., 2002. Semimagnetic semiconductors based on lead chalcogenides. In: Khokhlov, D. (Ed.), *Lead Chalcogenides: Physics and Applications*, vol. 18. Taylor & Francis.
- Story, T., Arciszewska, M., Chernyshova, M., Dobrowolski, W., Mac, W., Twardowski, A., Swirkowicz, R., Sipatov, A.Y., 2001. The effect of stress on magnetic properties of ferromagnetic  $\text{EuS-PbS}$  and  $\text{EuS-PbSe}$  semiconductor structures. In: Miura, N., Ando, T. (Eds.), *Proceedings of the 25th International Conference on the Physics of Semiconductors*, Pts I and II.
- Swirkowicz, R., Story, T., 2000. Spin waves and temperature dependence of magnetization in strained  $\text{EuS}$  films. *Journal of Physics: Condensed Matter* 12, 8511.
- Teraguchi, N., Suzuki, A., Nanishi, Y., Zhou, Y.-K., Hashimoto, M., Asahi, H., 2002. Room-temperature observation of ferromagnetism in diluted magnetic semiconductor  $\text{GaGdN}$  grown by RF-molecular beam epitaxy. *Solid State Communications* 122, 651–653.
- Tivakornsasithorn, K., Liu, X., Li, X., Dobrowolska, M., Furdyna, J.K., 2014. Magnetic anisotropy in ultrathin Fe films on GaAs, ZnSe, and Ge (001) substrates. *Journal of Applied Physics* 116, 043915.
- Tsujii, N., Imanaka, Y., Takamasu, T., Kitazawa, H., Kido, G., 2001. Photoluminescence of  $\text{Yb}^{3+}$ -doped  $\text{CuInS}_2$  crystals in magnetic fields. *Journal of Applied Physics* 89, 2706–2710.

- Tuxworth, A., Evans, J., 2014. Synthesis, structure and properties of the oxychalcogenide series  $A_4O_4TiSe_4$  ( $A = Sm, Gd, Tb, Dy, Ho, Er$  and  $Y$ ). *Journal of Solid State Chemistry* 210, 188–194.
- Tveten, E.G., Qaiumzadeh, A., Tretiakov, O.A., Brataas, A., 2013. Staggered dynamics in antiferromagnets by collective coordinates. *Physical Review Letters* 110, 127208.
- VanEsch, A., VanBockstal, L., DeBoeck, J., Verbanck, G., vanSteenbergen, A.S., Wellmann, P.J., Grietens, B., Bogaerts, R., Herlach, F., Borghs, G., 1997. Interplay between the magnetic and transport properties in the III-V diluted magnetic semiconductor  $Ga_{1-x}Mn_xAs$ . *Physical Review B* 56, 13103–13112.
- Vanhouten, S., 1962. Magnetic interaction in  $EuS$ ,  $EuSe$ , and  $EuTe$ . *Physics Letters* 2, 215–216.
- Wadley, P., Novák, V., Champion, R.P., Rinaldi, C., Martí, X., Reichlová, H., Železný, J., Gazquez, J., Roldan, M.A., Varela, M., Khalyavin, D., Langridge, S., Kriegner, D., Mácá, F., Mašek, J., Bertacco, R., Holý, V., Rushforth, A.W., Edmonds, K.W., Gallagher, B.L., Foxon, C.T., Wunderlich, J., Jungwirth, T., 2013. Tetragonal phase of epitaxial room-temperature antiferromagnet  $CuMnAs$ . *Nature Communications* 4.
- Wagner, J., Windscheif, J., Ennen, H., 1984. Photoluminescence excitation spectroscopy on  $InP:Yb$ . *Physical Review B* 30, 6230–6231.
- Wang, Y.Y., Song, C., Cui, B., Wang, G.Y., Zeng, F., Pan, F., 2012. Room-temperature perpendicular exchange coupling and tunneling anisotropic magnetoresistance in an antiferromagnet-based tunnel junction. *Physical Review Letters* 109, 137201.
- Wang, Y.Y., Song, C., Wang, G.Y., Zeng, F., Pan, F., 2013. Insensitivity of tunneling anisotropic magnetoresistance to non-magnetic electrodes. *Applied Physics Letters* 103, 202403.
- Watanabe, A., Itoh, H., Inoue, J.I., 2004. Magnetoresistance in ferromagnet/semimetal/ferromagnet junctions. *Japanese Journal of Applied Physics Part 1-Regular Papers Short Notes & Review Papers* 43, 540–546.
- Wildman, E.J., Skakle, J.M., Emery, N., Mclaughlin, A.C., 2012. Colossal magnetoresistance in  $Mn^{2+}$  oxypnictides  $NdMnAsO_{1-x}F_x$ . *Journal of the American Chemical Society* 134, 8766–8769.
- Wojtowicz, T., Gawron, T.R., Robert, J.L., Raymond, A., Bousquet, C., Mycielski, A., 1985. Hopping conduction studies of  $p-Hg_{1-x}Mn_xTe$  in high magnetic fields: unusual anisotropy of resistivity. *Journal of Crystal Growth* 72, 385–388.
- Wojtowicz, T., Mycielski, A., 1983. Magnetic susceptibility, specific heat and the spin-glass transition in  $Hg_{1-x}Mn_xTe$ . *Physica B & C* 117, 476–478.
- Xu, Z., Ong, N., Wang, Y., Kakeshita, T., Uchida, S., 2000. Vortex-like excitations and the onset of superconducting phase fluctuation in underdoped  $La_{2-x}Sr_xCuO_4$ . *Nature* 406, 486–488.
- Yang, X., Li, Y., Shen, C., Si, B., Sun, Y., Tao, Q., Cao, G., Xu, Z., Zhang, F., 2013. Sr and Mn co-doped  $LaCuSO$ : a wide band gap oxide diluted magnetic semiconductor with  $T_C$  around 200 K. *Applied Physics Letters* 103, 022410.
- Yoo, T., Khym, S., Lee, H., Chung, S., Lee, S., Liu, X., Furdyna, J.K., 2010. Asymmetry in the planar Hall resistance of Fe films grown on vicinal GaAs substrates. *Journal of Applied Physics* 107, 09c505.
- Yoo, T., Khym, S., Yea, S.Y., Chung, S., Lee, S., Liu, X., Furdyna, J.K., 2009. Four discrete Hall resistance states in single-layer Fe film for quaternary memory devices. *Applied Physics Letters* 95, 202505.
- Zavada, J.M., Zhang, D.H., 1995. Luminescence properties of erbium in III–V compound semiconductors. *Solid-State Electronics* 38, 1285–1293.

- Zhao, K., Deng, Z., Wang, X., Han, W., Zhu, J., Li, X., Liu, Q., Yu, R., Goko, T., Frandsen, B., 2013. New diluted ferromagnetic semiconductor with Curie temperature up to 180 K and isostructural to the '122' iron-based superconductors. *Nature Communications* 4, 1442.
- Zhen, W., Yao, C., Huai-Xin, Y., Huan-Fang, T., Zhi-Wei, W., Chao, M., Zhen, C., Jian-Qi, L., 2013. Microstructure and structural phase transitions in iron-based superconductors. *Chinese Physics B* 22, 087409.
- Zhou, Y.K., Kim, M.S., Teraguchi, N., Suzuki, A., Nanishi, Y., Asahi, H., 2003. Optical and magnetic properties of the DyN/GaN superlattice. *Physica Status Solidi (B)* 240, 440–442.
- Zhu, J.-X., Yu, R., Wang, H., Zhao, L.L., Jones, M., Dai, J., Abrahams, E., Morosan, E., Fang, M., Si, Q., 2010. Band narrowing and Mott localization in iron oxychalcogenides  $\text{La}_2\text{O}_2\text{Fe}_2\text{O}(\text{Se},\text{S})_2$ . *Physical Review Letters* 104, 216405.
- Zhu, J.G., Carter, C.B., Palmstrom, C.J., Mounier, S., 1990. Microstructure of epitaxially grown GaAs/ErAs/GaAs. *Applied Physics Letters* 56, 1323–1325.
- Zide, J.M., Klenov, D.O., Stemmer, S., Gossard, A.C., Zeng, G., Bowers, J.E., Vashaee, D., Shakouri, A., 2005. Thermoelectric power factor in semiconductors with buried epitaxial semimetallic nanoparticles. *Applied Physics Letters* 87, 112102.

This page intentionally left blank

# Electron spin resonance studies of GaAs:Er,O

5

H. Ohta, S. Okubo  
Kobe University, Kobe, Japan

Y. Fujiwara  
Osaka University, Suita, Osaka, Japan

## 5.1 Introduction and previous studies

Rare earth elements are playing important roles in wide areas of application [1]. For instance, Nd or Sm ions are used in high-strength permanent magnets, especially the Nd-Fe-B permanent magnet is known as the strongest permanent magnet, which gives 1 T [2]. Not only the magnetic properties but their optical properties are also widely used for applications; for instance, Eu and Tb are used in energy-efficient fluorescent lamps, and Er is used as an amplifier in fiber optics.

The  $\text{Er}^{3+}$  ion especially has a unique feature: an intra-4f-shell transition from its first excited state ( ${}^4\text{I}_{13/2}$ ) to its ground state ( ${}^4\text{I}_{15/2}$ ) corresponding to the photoluminescence (PL) at 1.5  $\mu\text{m}$ . Since this wavelength matches the low-loss window in the absorption spectrum of silica fiber,  $\text{Er}^{3+}$  ion is very attractive for silica fiber-based optical communication. Furthermore, since the PL at 1.5  $\mu\text{m}$  from  $\text{Er}^{3+}$  ion is based on the atomic intra-4f-shell transition, it is stable against temperature or environment when the  $\text{Er}^{3+}$  ion is incorporated in host materials. Therefore,  $\text{Er}^{3+}$  ion is very attractive for optical applications.

Among various host materials the semiconductor has some advantages because its growth technique is at the state-of-art level and designing the optical elements is possible. However, although silicon has the advantages of low-cost and well-established growth techniques, its energy transfer efficiency to  $\text{Er}^{3+}$  ion by the host excitation is low due to its indirect band gap [3]. On the other hand, GaAs has several advantages, such as direct band gap, structural stability, and advanced growth techniques. Ennen et al. [3] observed PL of Er-doped GaAs with photoexcitation beyond the band gap of GaAs. They observed PL spectra at around 1.54  $\mu\text{m}$  with apparent fine structures reflecting the weak interaction of 4f electrons with their crystalline environment at 20K. However, Er atoms doped in GaAs with O codoping by the organometallic vapor-phase epitaxy (OMVPE) turned out to exhibit much simplified, sharp, and high-efficient PL at 1.54  $\mu\text{m}$  compared to the PL of GaAs doped only with Er atoms [4,5]. This luminescent Er center in GaAs:Er,O sample is suggested as Er-2O center, where  $\text{Er}^{3+}$  ion substitutes the Ga site with two adjacent oxygen atoms, by Takahei et al. [4]. They studied PL spectra of AlGaAs:Er,O samples with different Al concentration. Considering the higher tendency of O to react with Al

rather than Ga, they revealed that many new Er centers are formed by small inclusion of Al, and came up with the suggestion of Er-2O center with detailed discussion [4,6]. This suggestion of Er-2O center was also supported by the polarized PL and fluorescence extended X-ray absorption fine structure (EXAFS) measurements [7]. EXAFS measurement can provide distance distributions of atoms around Er ion atom in GaAs:Er,O, and the experimental result turned out to be rather consistent with the Er-2O configuration. Katsuno et al. also discussed the detailed local structure of Er-2O center by calculating the energy splitting of states  $^4I_{15/2}$  and  $^4I_{13/2}$  using the crystal theory [8] in order to interpret the PL measurement result on GaAs:Er,O under a high-pulsed magnetic field up to 60 T [9]. Katsuno's result was also consistent with Er-2O center. From all these results, the formation of Er-2O center is rather established in GaAs:Er,O.

However, the detailed site selective PL spectroscopy revealed more than 10 different kinds of Er centers in GaAs:Er,O [10,11]. It suggested that the host-excited PL spectrum of GaAs:Er,O is dominated by only one kind of Er center, and other Er centers can be excited only under direct 4f-shell excitation. Therefore, further study remained to identify the slight difference in the atomic structure between luminescent and nonluminescent Er-2O centers.

Electron spin resonance (ESR) is known as a sensitive probe to identify the local environment around the magnetic ion. Ishiyama et al. performed X-band (9.05 GHz) ESR measurements on GaAs:Er,O grown by MOCVD at 4.2K [12]. They observed four kinds of anisotropic  $\text{Er}^{3+}$  ESR lines (A, B, C, and D), which newly appeared and showed stronger intensity by oxygen codoping. From the angular dependence in the (1–10) plane, they suggested that B and C centers have orthorhombic  $C_{2v}$  symmetry corresponding to Er-2O centers, while A center has lower symmetry, and D center has trigonal  $C_{3i}$  symmetry. Typical ESR spectra observed by Ishiyama et al. [12] are shown in Fig. 5.1. Moreover, Ishiyama et al. performed ESR measurements under the illumination with 632 nm He-Ne laser light [12]. Typical examples for A and B centers are shown in Fig. 5.2. The ESR intensity of B center decreased under the illumination by about 30%, while A, C, and D centers showed no changes in their intensities. From these results they suggested that B center corresponded to the dominant Er luminescent center because the decrease of ESR intensity for B center was observed due to the explanation that the 4f shell of only B center is excited under host photoexcitation while those of A, C, and D centers were not excited.

To get information about the dynamics of the photoexcitation process, K. Nakamura et al. performed pump and probe measurements on GaAs:Er,O ( $[\text{Er}] = 8.7 \times 10^{18} \text{cm}^{-3}$ ) at room temperature and 12K [13]. Time-resolved reflectivity results showed an abrupt increase in amplitude followed by a steep decrease to negative, followed by fast and slow recovery processes to zero. They discussed that the observed fast recovery process ( $T_{\text{fast}} = 22 \text{ ps}$  at 12K) corresponded to the capture process of electron by the trap, which was calculated to be 23 ps at 12K. Here they assumed the electron-like trap. They also calculated the energy transfer process of electron–hole pair to the  $\text{Er}^{3+}$  intra-4f-shell as 54 ps, which was comparable to the observed slow recovery process ( $T_{\text{slow}} = 38 \text{ ps}$ ). Y. Fujiwara et al. extended similar

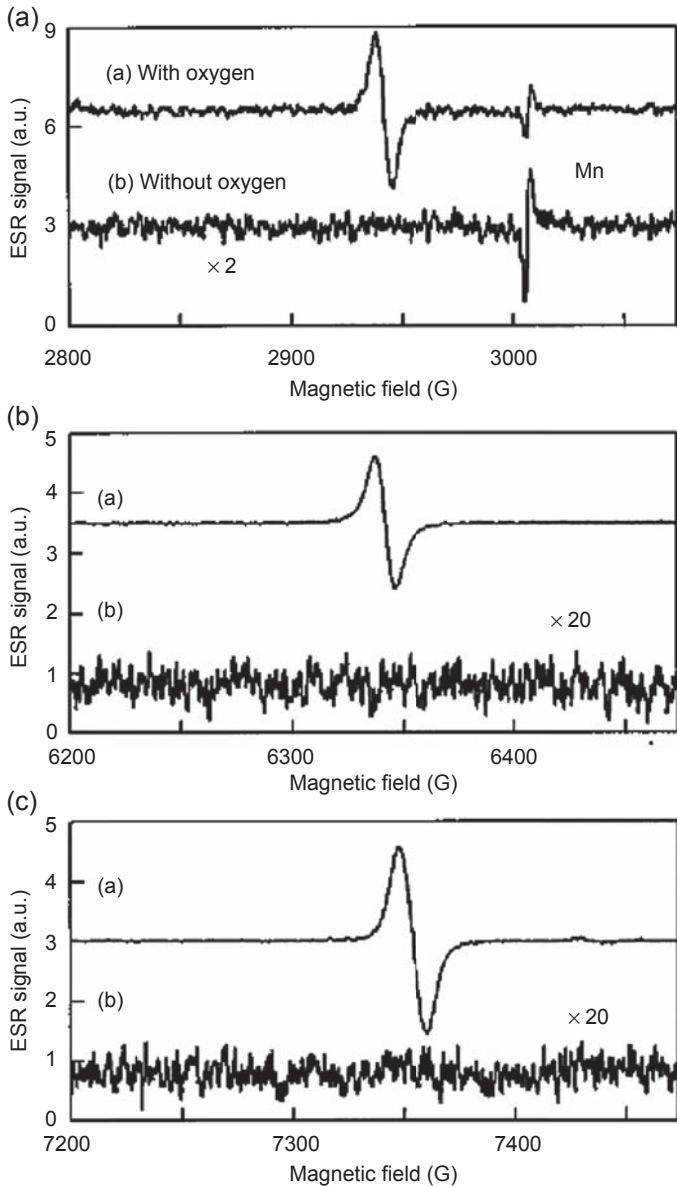


**Figure 5.1** Typical ESR lines (A, B, and C) observed at 4.2K for Er-doped GaAs with oxygen codoping (a) and without oxygen codoping (b). ESR signals are derivative curves of ESR absorption lines due to the magnetic field modulation.

Adapted from Ishiyama T, Katayama E, Murakami K, Takahei K, Taguchi A. J Appl Phys 1998; 84:6782.



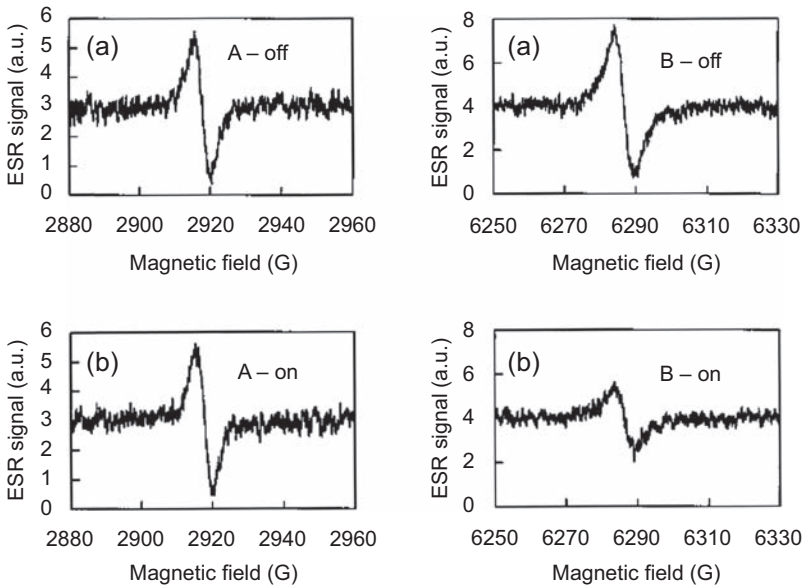


**Figure 5.2** Typical ESR signals for the A and B centers under no illumination (a) and under illumination (b) observed at 4.2K. The Er and O concentrations in the sample were  $[Er] = 2.5 \times 10^{17} \text{ cm}^{-3}$ ,  $[O] = 7.0 \times 10^{17} \text{ cm}^{-3}$ .

Adapted from Ishiyama T, Katayama E, Murakami K, Takahei K, Taguchi A. *J Appl Phys* 1998; 84:6782.

measurements to other GaAs:Er,O with the Er concentration of  $10^{18}$ – $10^{19} \text{ cm}^{-3}$  [14]. It was shown that the electron–hole pair formation time is shorter for the samples with higher Er concentration. Here they assumed the hole-like trap. This means that we need other experimental evidence to distinguish if the electron-like trap or hole-like trap is formed in GaAs:Er,O.

As shown in this introduction, the details of PL mechanism in GaAs:Er,O were not really understood up to this stage. For instance, does the Er-2O center form the electron-like trap or hole-like trap, or which Er-2O center is the dominant Er luminescent center? Therefore, to get deeper insight into the PL mechanism in GaAs:Er,O, extended ESR measurements, such as the extended angular dependence, temperature dependence, and carrier dependence measurements, have been performed.

## 5.2 Sample preparations

Two low-pressure OMVPE growth systems (OMVPE I and OMVPE II) with different types of reactors were utilized in this work. OMVPE I has a specially designed reactor with a vertical four-barrel structure. Advantages of this growth system have been

described previously [15]. OMVPE II has a conventional horizontal reactor. The reactor pressure was kept at 76 Torr. The samples were grown on (001)-just semi-insulating GaAs substrates or (001) Si-doped GaAs substrates, misoriented 2 degree off to  $\langle 110 \rangle$  direction. Triethylgallium (TEGa) and tertiarybutylarsine (TBAs) were used as source materials for GaAs growth. Er was doped with trisopropylcyclopentadienylerbium ( $\text{Er}(i\text{-PrCp})_3$ ). The Er source was maintained at a constant temperature of  $90^\circ\text{C}$  under  $1.01 \times 10^4$  Pa and introduced into the reactor by an  $\text{H}_2$  flow through a source cylinder.  $\text{O}_2$  of 38.4 ppm in Ar gas was used as an  $\text{O}_2$  source.  $\text{H}_2\text{S}$  and diethylzinc (DEZn) were also used for p- and n-type doping sources, respectively (Table 5.1).

Fig. 5.3 shows Er-related PL spectrum in GaAs codoped with Er and O, which is compared with that in GaAs doped with Er. PL measurements were carried out with the samples directly immersed in liquid He at 4.2K. The photoexcitation source was a continuous wave mode  $\text{Ar}^+$  laser operating at 515 nm with a beam diameter of 1 mm and an incident power of 180 mW. The luminescence of the sample was dispersed using a grating monochromator and detected with a liquid nitrogen-cooled Ge pin photodiode using a chopper and a lock-in amplifier. In Er-doped GaAs, there are many emission lines, reflecting coexistence of various Er centers not identified. In GaAs:Er,O, the Er-related PL spectrum reveals strong emission lines from an Er-2O center as reported previously [4].

We investigated the dependence of Er-related PL spectra on growth conditions. The spectrum is almost independent of Er concentration up to  $2 \times 10^{19} \text{ cm}^{-3}$  and the  $\text{O}_2$  content in the growth ambient up to 0.8 ppm. However, the formation of the

**Table 5.1 GaAs:Er,O- and carrier-doped samples studied by ESR in Kobe**

Sample#	Growth system	$T_g$ ( $^\circ\text{C}$ )	[Er] ( $\text{cm}^{-3}$ )	[O] ( $\text{cm}^{-3}$ )	Carrier density
GA05544	OMVPE I	540	$6.3 \times 10^{18}$	$7.0 \times 10^{18}$	I
GA05569			$1.0 \times 10^{19}$	$3.0 \times 10^{19}$	$7 \times 10^{17}$ (p)
GA055BN			$4.3 \times 10^{19}$	$9.8 \times 10^{18}$	$5 \times 10^{18}$ (p)
GA05522			$8.3 \times 10^{17}$	$9.2 \times 10^{17}$	—
GA05529			$9.2 \times 10^{18}$	$3.8 \times 10^{18}$	—
GA030278	OMVPE II	545	$1.0 \times 10^{17}$	—	—
GA040396			$7.0 \times 10^{17}$	—	$5.6 \times 10^{14}$ (n)
GA050462			$4.0 \times 10^{18}$	—	I
GA050461			$1.0 \times 10^{19}$	—	$5.7 \times 10^{16}$ (p)

(—) means not measured.

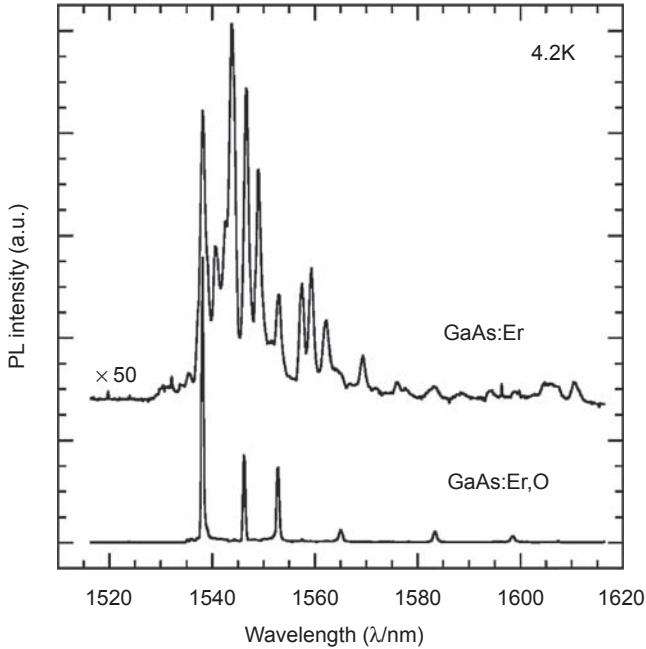


**Figure 5.3** Comparison of Er-related PL spectra in Er-doped and Er,O-codoped GaAs. In Er,O-codoped GaAs, the PL spectrum is dominated by strong emission lines from an Er-2O center.

Adapted from Fujiwara Y. *Mater Trans* 2005;46:1969.

Er-2O center is greatly influenced by growth temperature [5]. The growth temperature dependence of the PL spectra is shown in Fig. 5.4. The PL spectrum changes drastically between 543 and 585°C, suggesting that there is a threshold growth temperature. In samples grown at temperatures higher than 585°C, the Er-2O emission lines become weak and the PL spectrum is dominated by emission lines from other Er centers. This result means that the formation of the Er-2O center is strongly suppressed above the threshold growth temperature.

Effects of Zn- or S-doping on Er-related PL properties have also been investigated in GaAs:Er,O [17]. Fig. 5.5(a) shows the PL spectrum in Zn-doped GaAs:Er,O with hole concentration of  $1.2 \times 10^{18} \text{ cm}^{-3}$ , which is compared with that in GaAs:Er,O without Zn. Identical emission lines due to an Er-2O center are clearly observed in both samples. The Er-related PL spectrum in S-doped GaAs:Er,O with electron concentration of  $3.4 \times 10^{17} \text{ cm}^{-3}$  is also shown in Fig. 5.5(b). The Er-2O emission lines become weak and the PL spectrum is dominated by emission lines from other Er centers, suggesting that the formation of the Er-2O center is greatly suppressed by the doping of S.

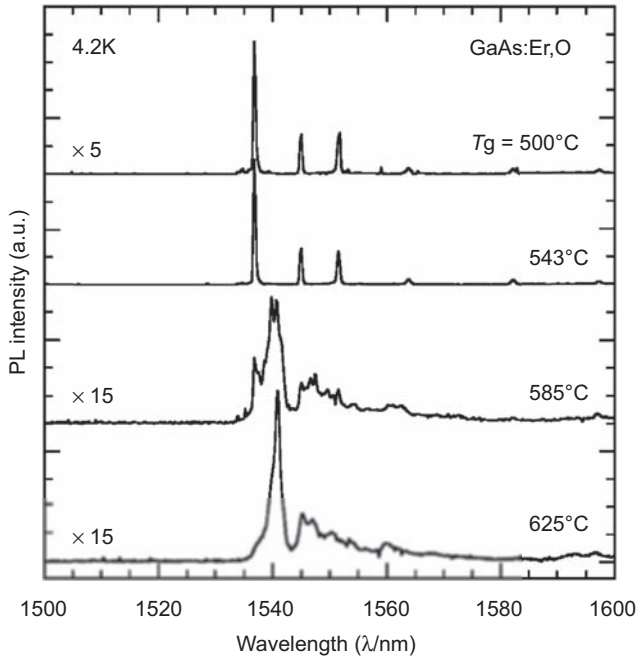


**Figure 5.4** Growth temperature dependence of Er-related PL spectra in Er,O-codoped GaAs. The spectral shape changes drastically between 543 and 585°C, suggesting that there is a threshold growth temperature. Above the temperature, formation of the Er-2O center is greatly suppressed.

Adapted from Fujiwara Y. *Mater Trans* 2005;46:1969.

## 5.3 Electron spin resonance results in Kobe

### 5.3.1 Fundamental properties of GaAs:Er,O (GA05544, without charge carrier) studied by electron spin resonance [18]

X-band (about 9.49 GHz) ESR measurements of GaAs:Er,O (GA05544) were performed in the temperature region from 4.5 to 13K using a Bruker ESR spectrometer EMX081 with a TE103 rectangular cavity and Oxford He flow cryostat ESR900 at Kobe University [18]. The external field was swept up to 9000 G.

To check the symmetry of ESR lines, ESR measurements were performed for three different configurations as shown in Fig. 5.6 [18] while only the configuration (a) was done previously [12]. Fig. 5.7 shows the observed angular dependence for the configuration (a) at 8K. Three ESR signals A, B, and C are observed and showed the consistent angular dependence as observed previously [12]; even the Er concentration is one order of magnitude higher than the previous measurement [12]. The ESR measurements were also performed for the configuration (b), which was not performed

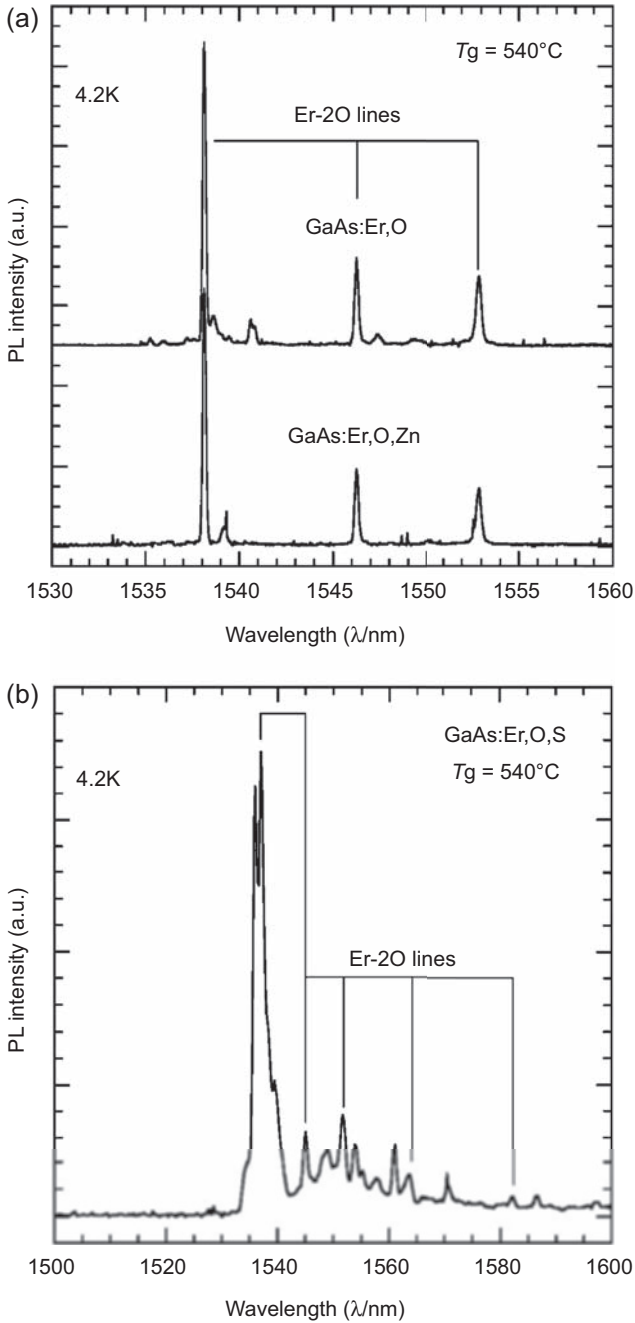


**Figure 5.5** PL spectra in Zn-doped GaAs:Er,O (a) and S-doped GaAs:Er,O (b). The spectrum in GaAs:Er,O without Zn is also shown for comparison. Identical Er-2O lines are observed in both samples. The formation of the Er-2O center is greatly suppressed by S doping. Adapted from Fujiwara Y. *Mater Trans* 2005;46:1969.

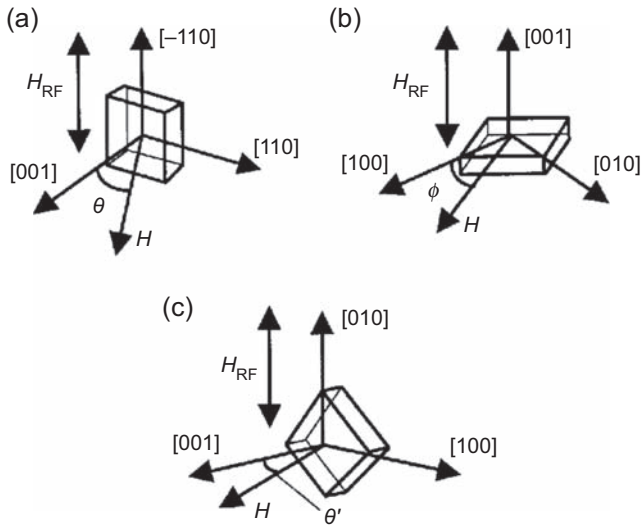


**Figure 5.6** Experimental configurations employed in the study of GaAs:Er,O (GA05544). (a)  $\theta$  is the angle in degrees between the magnetic field and the [001] direction in the  $(-110)$  plane. (b)  $\phi$  is the angle in degrees between the magnetic field and the [100] direction in the (001) plane. (c)  $\theta'$  is the angle in degrees between the magnetic field and the [001] direction in the (010) plane.

Adapted from Yoshida M, Hiraka K, Ohta H, Fujiwara Y, Koizumi A, Takeda Y. *J Appl Phys* 2004;96:4189.

in the previous report [12]. We found new ESR lines  $B'$  and  $C'$  as shown in Fig. 5.8. As the resonance fields of  $B'$  and  $C'$  signals coincide with those of  $B$  and  $C$  signals, respectively, for  $\theta = 0$  ( $H//[100]$ ),  $B'$  and  $C'$  signals were considered to be equivalent to the  $B$  and  $C$  signals, respectively. Since  $B'$  and  $C'$  signals largely shift to the lower field side by changing  $\phi$  slightly as shown in Fig. 5.8, we can expect a very large principal  $g$ -value  $g_1$  along a direction perpendicular to the [100] direction, which was not considered in the previous report [12]. Therefore, we can say that the symmetry of  $B$  and  $C$  centers are lower than  $C_{2v}$  symmetry, which was proposed previously [12]. The details of this discussion can be found in Ref. [18]. The suggested  $g_1 = 16.5$  is a hint to consider the origin of  $A$ ,  $B$ , and  $C$  centers in GaAs:Er,O which will be discussed in Section 5.4.1.

Temperature dependences in ESR measurements were observed by us for the first time [18]. The result is shown in Fig. 5.9. To our surprise the ESR intensities showed a maximum around 8K and decreased to zero below 8K, which clearly suggests that the  $B$  and  $C$  centers are not isolated paramagnetic centers but nonmagnetic at lowest temperature. The Er pair model is discussed in Section 5.4.2 as the possible origin of this temperature dependence.

Temperature dependences of line width were also observed for the first time [18]. The result is shown in Fig. 5.10. The line widths remain constant up to 8K and increase

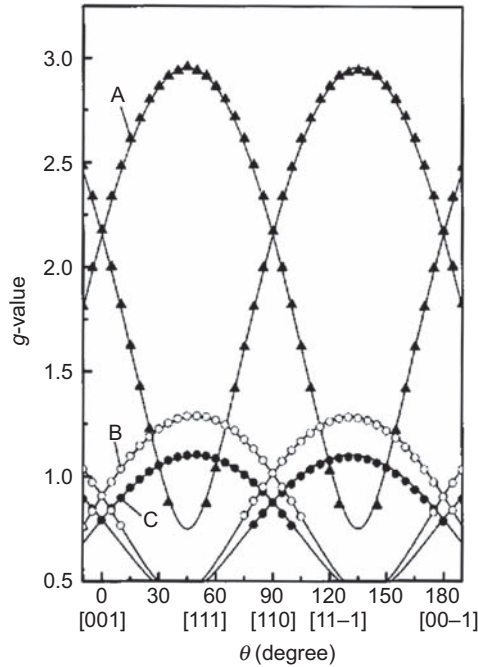


**Figure 5.7** Angular dependence of the  $g$ -values of GaAs:Er,O (GA05544) in the  $(-110)$  plane for A (solid triangle), B (open circle), and C (solid circle) from  $\theta = -10$  to  $190$  degrees in  $5$  degree steps at  $8\text{K}$ .

Adapted from Yoshida M, Hiraka K, Ohta H, Fujiwara Y, Koizumi A, Takeda Y. *J Appl Phys* 2004;96:4189.

rapidly above  $8\text{K}$ . Therefore, low temperature measurement using He flow cryostat is essential to observe ESR signals in GaAs:Er,O.

In order to get information about the effect of photoexcitation of the host on the ESR spectra of A, B, and C centers, ESR measurements under He-Ne laser illumination were performed [18]. The result at  $8\text{K}$  is shown in Fig. 5.11. In order to check the heating effect, the temperature dependences with and without illumination were compared. As a result very small change for C center seems to be a heating effect while the observed change for B center is concluded as intrinsic. However, the decrease of ESR intensity under illumination for B center turned out to be smaller than the 30% decrease observed previously [12]. Possible origin of this effect based on our new model is discussed in Section 5.4.3.

### 5.3.2 Zn codoping (hole carriers) effect on electron spin resonance [19]

Zn codoping effects to ESR signals were also studied at  $8\text{K}$  under the configuration (a) in Fig. 5.6. Here Zn codoping introduces hole carriers into GaAs:Er,O. ESR

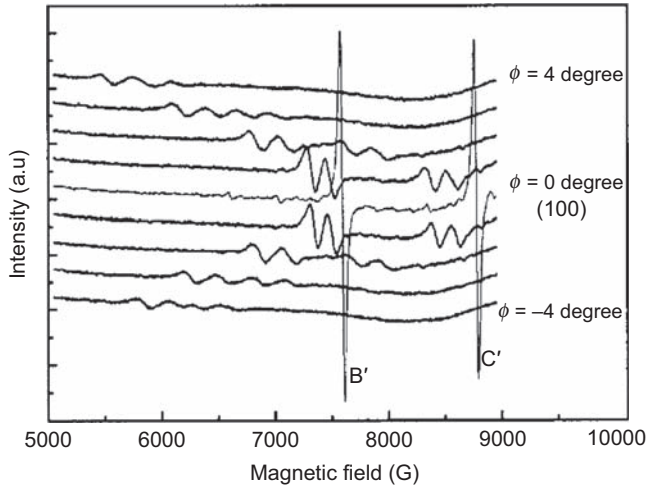


**Figure 5.8** ESR spectra of GaAs:Er,O (GA05544) at 8K for various field directions from  $\phi = -4$  to 4 degrees in 1 degree steps.

Adapted from Yoshida M, Hiraka K, Ohta H, Fujiwara Y, Koizumi A, Takeda Y. J Appl Phys 2004;96:4189.

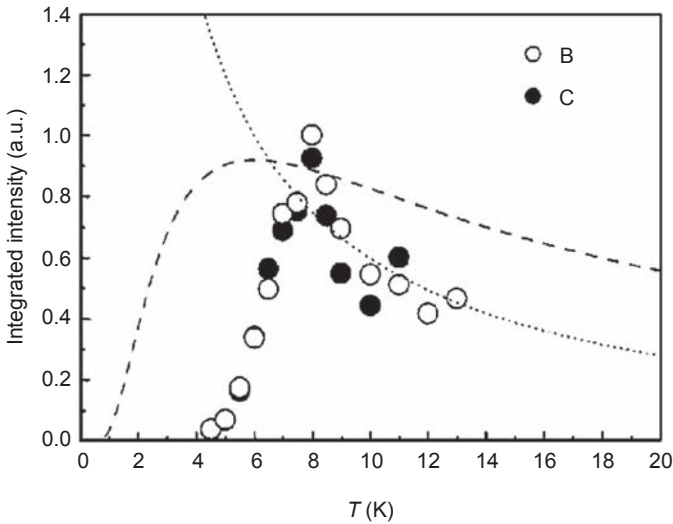


**Figure 5.9** Temperature dependence of the integrated ESR intensities of B (*open circle*) and C (*solid circle*) signals. The *dotted* and *dashed* lines are calculated for typical temperature dependences of ground and excited states of paramagnetic center, respectively.

Adapted from Yoshida M, Hiraka K, Ohta H, Fujiwara Y, Koizumi A, Takeda Y. J Appl Phys 2004;96:4189.



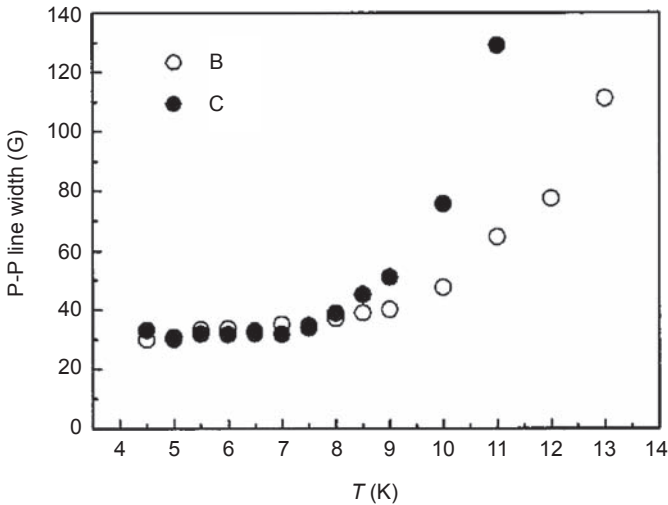


**Figure 5.10** Temperature dependence of the peak-to-peak line widths of B (*open circle*) and C (*solid circle*) signals.

Adapted from Yoshida M, Hiraka K, Ohta H, Fujiwara Y, Koizumi A, Takeda Y. *J Appl Phys* 2004;96:4189.

measurements were performed on GaAs:Er,O (GA05544) and GaAs:Er,O,Zn (GA05569 and GA055BN) samples at 8K. Although Zn concentration was not precisely identified, GA055BN is expected to have higher Zn concentration than GA05569 because the flow rate of the Zn source was higher for GA055BN during the OMVPE process.

A, B, and C signals were observed for all Zn codoped samples with similar angular dependence as observed for GaAs:Er,O [12,18]. This implies that the local atomic configuration of A, B, and C centers are not affected by the Zn codoping.

On the other hand, the Zn codoping has a drastic effect on the ESR intensity as shown in Fig. 5.12. Especially the ESR intensity of C signal almost disappears as the Zn (hole carrier) concentration increases, which has a strong correlation with the decrease of PL intensity by the increase of Zn codoping [19]. The possible model to interpret these effects based on our new model is discussed in Section 5.4.3.

### 5.3.3 Electron spin resonance study of Er concentration dependence

#### 5.3.3.1 GaAs:Er,O without charge carrier [20,21]

Er concentration dependence is studied by ESR for samples GA030278 ( $[Er] = 1.0 \times 10^{17} \text{ cm}^{-3}$ ), GA05522 ( $[Er] = 8.3 \times 10^{17} \text{ cm}^{-3}$ ), and GA05529 ( $[Er] = 9.2 \times 10^{18} \text{ cm}^{-3}$ ). No charge carrier exists in these samples. Angular dependence measurements were performed for the configuration in Fig. 5.6(a) at 8.0K, and angular

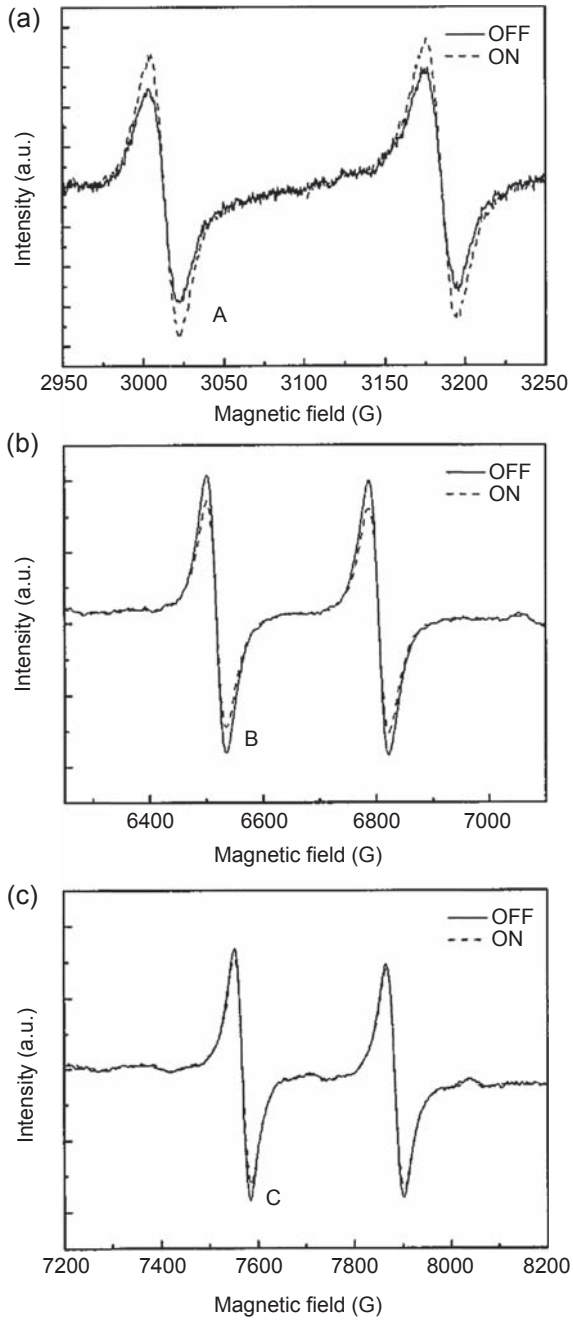


**Figure 5.11** ESR spectra for (a) A, (b) B, and (c) C under illumination (*dashed line, ON*) and in the dark (*solid line, OFF*) at 8K.

Adapted from Yoshida M, Hiraka K, Ohta H, Fujiwara Y, Koizumi A, Takeda Y. *J Appl Phys* 2004;96:4189.

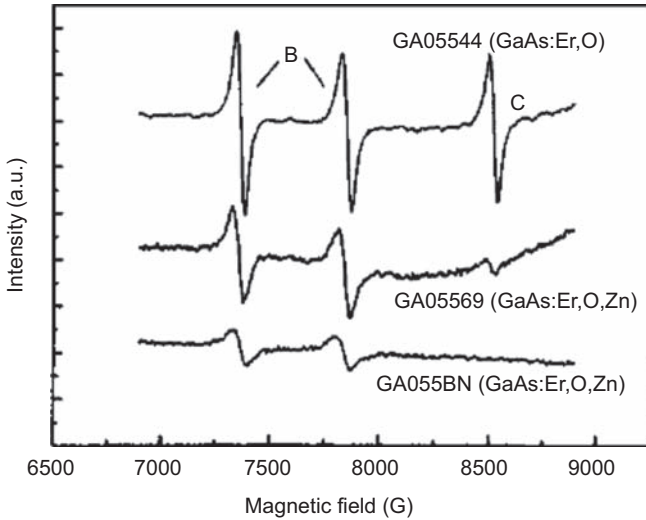


**Figure 5.12** ESR spectra of B and C for GaAs:Er,O (GA05544) and GaAs:Er,O,Zn (GA05569 and GA055BN) at 8K. The magnetic field was applied approximately along the [001] direction.

Adapted from Yoshida M, Hiraka K, Ohta H, Fujiwara Y, Koizumi A, Takeda Y. *J Appl Phys* 2005;97:023909.

dependences of  $g$ -values for A, B, and C centers turned out to be similar with the previous reports [12,18]. This result suggests that the local atomic configuration of A, B, and C centers are not affected by the change of Er concentration.

Temperature dependence ESR measurements were also performed for all three samples. The temperature dependence of integrated intensity of B and C signals showed a maximum around 8K, which was a similar behavior observed in the previous reports [12,18]. Fig. 5.13 shows the temperature dependence of line width for B and C centers. Observed temperature dependence is similar to what was observed in the previous reports [12,18]. In order to discuss the Er concentration dependence of line width, the line width calculation was performed on the assumptions that  $\text{Er}^{3+}$  ions are homogeneously distributed in the sample and the dominant interaction between  $\text{Er}^{3+}$  ions is the magnetic dipole–dipole interaction [20]. From the theoretical equation, the line width should increase in proportion to the spin density [22]. However, the experimental result suggests that the line width increases only twice when the spin density is increased 10 times. One of the ways to interpret this discrepancy is the existence of exchange interaction. The exchange interaction will reduce the line width through the exchange narrowing effect [23,24], and this leads to the Er pair model discussed in Section 5.4.2.

Line shape analyses of signal B were performed for GA05522 ( $[\text{Er}] = 8.3 \times 10^{17} \text{ cm}^{-3}$ ) and GA05529 ( $[\text{Er}] = 9.2 \times 10^{18} \text{ cm}^{-3}$ ) as shown in Fig. 5.14 [20], and for GA030278 ( $[\text{Er}] = 1.0 \times 10^{17} \text{ cm}^{-3}$ ) as shown in Fig. 5.15 [21]. Generally the line shape becomes Lorentzian (Gaussian) if the dominant interaction

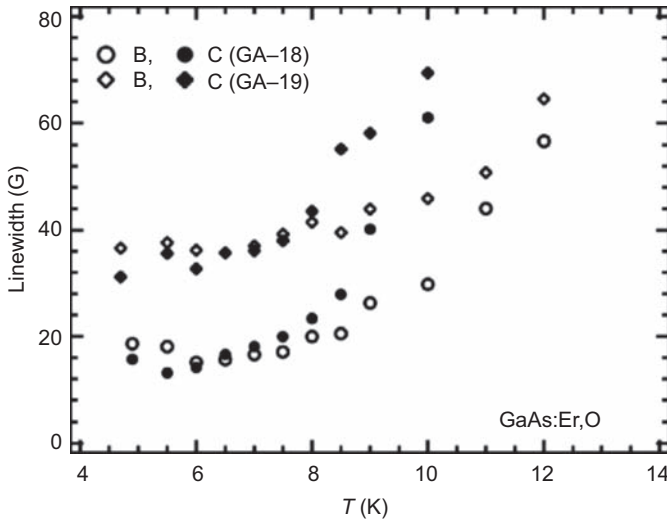


**Figure 5.13** Temperature dependence of peak-to-peak line width. The *open (closed) circles* and *open (closed) diamonds* correspond to signal B (C) of GA05522 ( $[\text{Er}] = 8.3 \times 10^{17} \text{ cm}^{-3}$ ) and GA05529 ( $[\text{Er}] = 9.2 \times 10^{18} \text{ cm}^{-3}$ ), respectively. The magnetic field is applied approximately along the [110] direction.

Adapted from Fujisawa M, Asakura A, Elmasry F, Okubo S, Ohta H, Fujiwara Y. *J Appl Phys* 2011;109:053910.

is the exchange (magnetic dipole–dipole) interaction. The experimental results in [Figs. 5.14 and 5.15](#) clearly show that the line shape of signal B is Lorentzian for all three samples. Therefore, the existence of exchange interaction is expected for signal B in GaAs:Er,O without charge carrier, and this result also supports the Er pair model discussed in [Section 5.4.2](#).

[Fig. 5.16](#) shows the relative integrated intensity, which is normalized by the total number of Er atoms in each sample, as a function of Er concentration. There is a tendency that all the normalized intensities decrease around the Er concentration of  $10^{18} \text{ cm}^{-3}$ , which is in correlation with the decrease of PL [\[25\]](#).

### 5.3.3.2 GaAs:Er,O with charge carriers [\[26\]](#)

Er concentration dependence is studied by ESR for n-type GA040396 ( $[\text{Er}] = 7.0 \times 10^{17} \text{ cm}^{-3}$ ,  $n = 5.6 \times 10^{14} \text{ cm}^{-3}$ ), high-resistance GA050462 ( $[\text{Er}] = 4.0 \times 10^{18} \text{ cm}^{-3}$ ), and p-type GA050461 ( $[\text{Er}] = 1.0 \times 10^{19} \text{ cm}^{-3}$ ,  $p = 5.7 \times 10^{16} \text{ cm}^{-3}$ ). Here charge carrier type should also be considered. Angular dependence measurements were performed for the configuration in [Fig. 5.6\(a\)](#) at 8K, and angular dependences of  $g$ -values for A, B, and C centers turned out to be similar to the previous reports [\[12,18\]](#). This result suggests that the local atomic configuration of A, B, and C centers are not affected by the change of Er concentration and the charge carrier type.

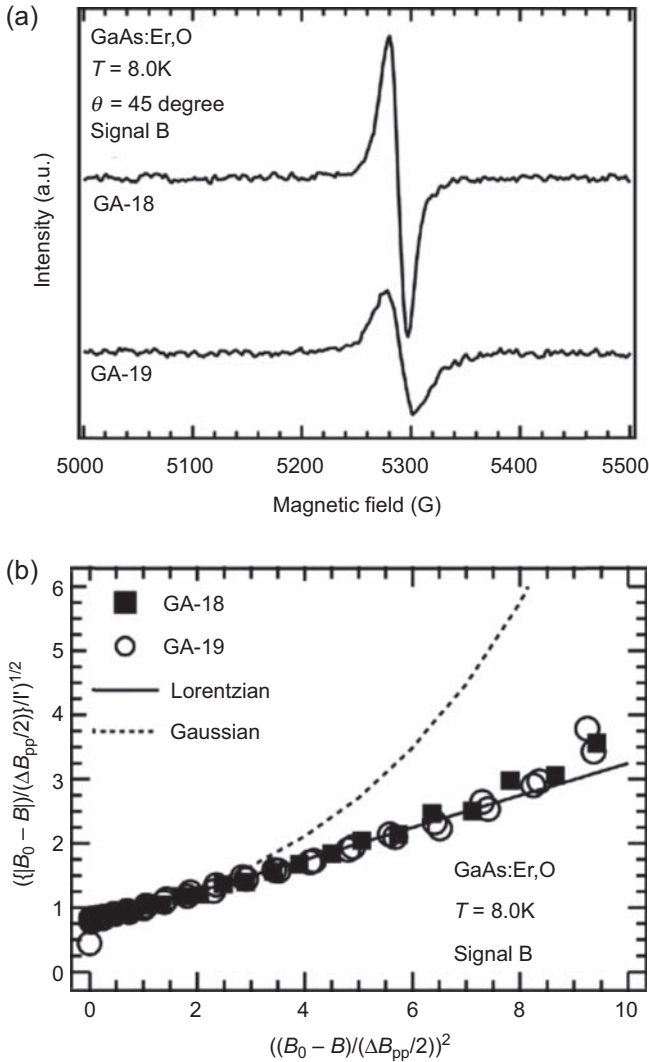


**Figure 5.14** (a) ESR spectra B of GA-18 (GA05522,  $[\text{Er}] = 8.3 \times 10^{17} \text{ cm}^{-3}$ ) and GA-19 (GA05529,  $[\text{Er}] = 9.2 \times 10^{18} \text{ cm}^{-3}$ ) observed at  $T = 8.0\text{K}$ . The magnetic field is applied 45 degrees from the [001] direction in the  $(-110)$  plane. (b) Line shape of B signals observed at  $T = 8.0\text{K}$ . Closed squares and open circles correspond to GA-18 and GA-19, respectively. Solid and dashed lines correspond to Lorentzian and Gaussian line shapes, respectively.  $B_0$  and  $\Delta B_{pp}$  are the resonance field and the line width, respectively.

Adapted from Fujisawa M, Asakura A, Elmasry F, Okubo S, Ohta H, Fujiwara Y. J Appl Phys 2011;109:053910.

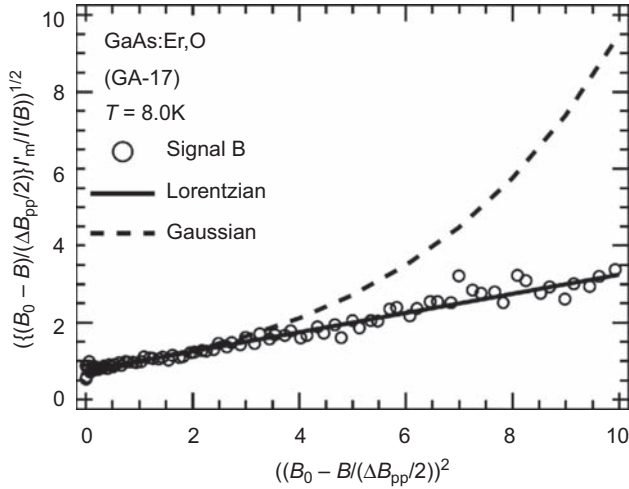


**Figure 5.15** Comparison between the experimental absorption line for GaAs:Er,O (GA-17 (GA030278, [Er] =  $1.0 \times 10^{17}$  cm<sup>-3</sup>)) and the theoretical curves. *Open circles* correspond to the experimental data of signal B observed at  $T = 8.0\text{K}$ . *Solid and dashed lines* correspond to Lorentzian and Gaussian line shapes, respectively.  $B_0$  and  $\Delta B_{pp}$ ,  $I'_m$  and  $I'(B)$  are the resonance field, the line width, the peak intensity, and the magnetic field dependence of the absorption intensity, respectively.

Adapted from Fujisawa M, Asakura A, Elmasry F, Okubo S, Ohta H, Fujiwara Y. J Phys Conf Ser 2010;200:062005.

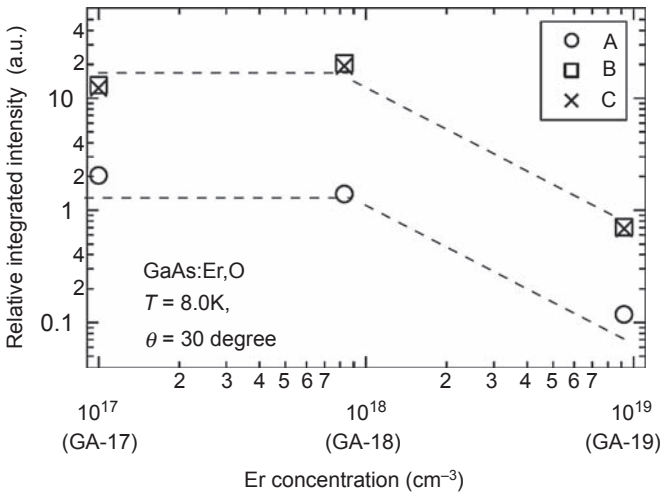


**Figure 5.16** Relative integrated intensity of GaAs:Er,O as a function of Er concentration at 8.0K. The integrated intensity was normalized by the total number of Er atoms in each sample. The left (*center, right*) side data near  $10^{17}$  ( $10^{18}$ ,  $10^{19}$ ) cm<sup>-3</sup> are obtained from the experiments for GA-17 (GA-18, GA-19). The *broken lines* are included as visual guides.

Adapted from Fujisawa M, Asakura A, Elmasry F, Okubo S, Ohta H, Fujiwara Y. J Phys Conf Ser 2010;200:062005.

Temperature dependence ESR measurements were also performed for all three samples. The temperature dependence of integrated intensity of B and C signals showed a maximum around 7K, which was a similar behavior observed in the previous reports [18,20]. Fig. 5.17 shows the temperature dependence of line width for B and C centers. Observed temperature dependence is similar to what was observed in the previous reports [18,20]. Here the line width calculation was also performed on the assumptions that  $\text{Er}^{3+}$  ions are homogeneously distributed in the sample and the dominant interaction between  $\text{Er}^{3+}$  ions is the magnetic dipole–dipole interaction [20]. From the theoretical calculation, the line width should have the ratio of 1:7:21 for GA-17-n, GA-18-n, and GA-19-p. However, the experimental result in Fig. 5.17 shows a much smaller increase. One of the ways to interpret this discrepancy is the existence of exchange interaction. The exchange interaction will reduce the line width through the exchange narrowing effect [23,24], and this again leads to the Er pair model discussed in Section 5.4.2.

Line shape analyses of signal B were performed for all three samples as shown in Fig. 5.18 [26]. Generally the line shape becomes Lorentzian (Gaussian) if the dominant interaction is the exchange (magnetic dipole–dipole) interaction. The experimental results in Fig. 5.18 show that the line shape of signal B is closer to the

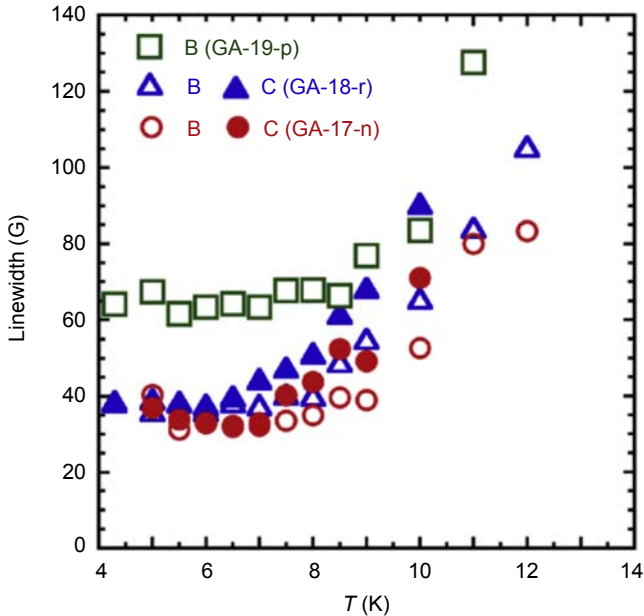


**Figure 5.17** Temperature dependence of peak-to-peak line width. The *open (closed) circles*, *open (closed) triangles*, and *open squares* correspond to signal B (C) of n-type GA-17-n (GA040396,  $[\text{Er}] = 7.0 \times 10^{17} \text{ cm}^{-3}$ ,  $n = 5.6 \times 10^{14} \text{ cm}^{-3}$ ), high-resistance GA-18-r (GA050462,  $[\text{Er}] = 4.0 \times 10^{18} \text{ cm}^{-3}$ ), and p-type GA-19-p (GA050461,  $[\text{Er}] = 1.0 \times 10^{19} \text{ cm}^{-3}$ ,  $p = 5.7 \times 10^{16} \text{ cm}^{-3}$ ), respectively. The magnetic field is applied approximately along the [110] direction.

Adapted from Elmasry F, Okubo S, Ohta H, Fujiwara Y. J Appl Phys 2014;115:193904.

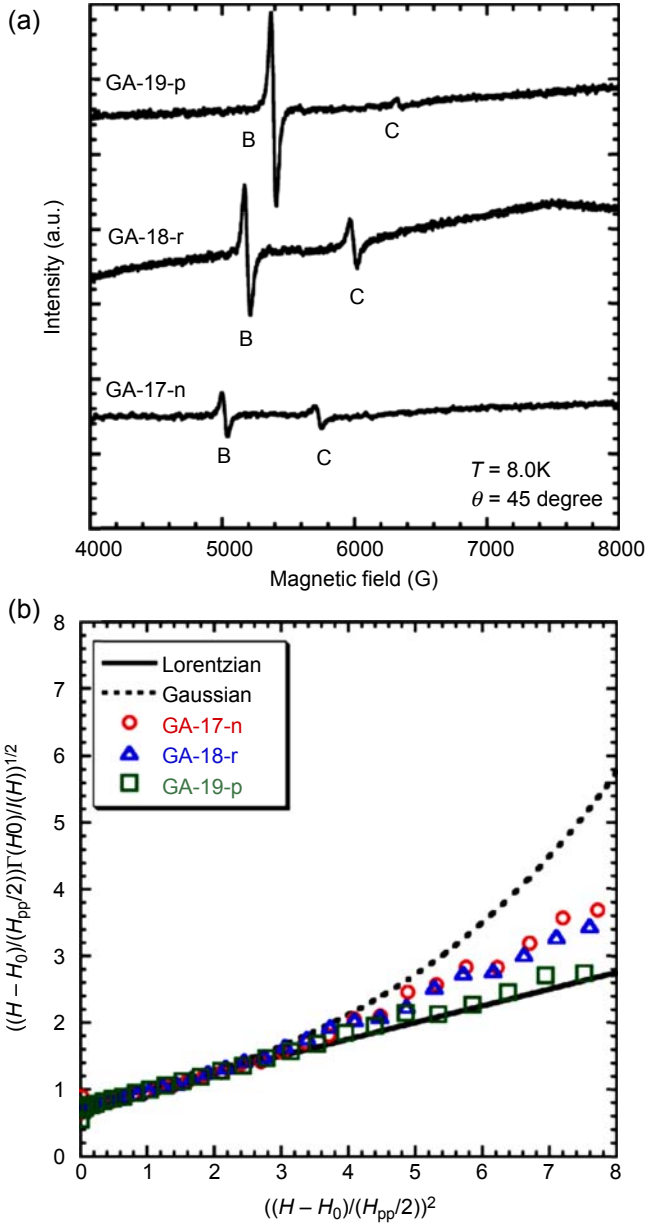


**Figure 5.18** (a) ESR spectra B and C of n-type GA-17-n (GA040396,  $[\text{Er}] = 7.0 \times 10^{17} \text{ cm}^{-3}$ ,  $n = 5.6 \times 10^{14} \text{ cm}^{-3}$ ), high-resistance GA-18-r (GA050462,  $[\text{Er}] = 4.0 \times 10^{18} \text{ cm}^{-3}$ ), and p-type GA-19-p (GA050461,  $[\text{Er}] = 1.0 \times 10^{19} \text{ cm}^{-3}$ ,  $p = 5.7 \times 10^{16} \text{ cm}^{-3}$ ) observed at  $T = 8.0\text{K}$ . The magnetic field is applied 45 degrees from the [001] direction in the (-110) plane. (b) Line shape of B signals observed at  $T = 8.0\text{K}$ . Open circles, triangles, and squares correspond to GA-17-n, GA-18-r, and GA-19-p, respectively. Solid and dashed lines correspond to Lorentzian and Gaussian line shapes, respectively.  $H_0$  and  $H_{pp}$  are the resonance field and the line width, respectively.

Adapted from Elmasy F, Okubo S, Ohta H, Fujiwara Y. J Appl Phys 2014;115:193904.



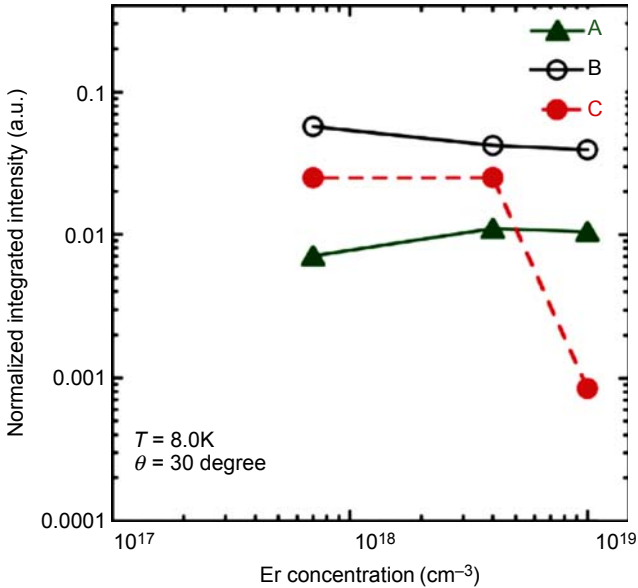


**Figure 5.19** ESR integrated intensity for A, B, and C centers as a function of Er concentration. The ESR intensity is normalized by the total number of Er atoms in each sample. The magnetic field is applied 30 degrees from the [001] direction in the  $(-110)$  plane. Adapted from Elmasry F, Okubo S, Ohta H, Fujiwara Y. *J Appl Phys* 2014;115:193904.

Lorentzian, and there is a tendency that it moves to the Lorentzian side as the Er concentration increases. Therefore, the existence of exchange interaction is also expected for signal B in GaAs:Er,O with charge carriers, and this result also supports the Er pair model discussed in Section 5.4.2.

Fig. 5.19 shows the relative integrated intensity, which is normalized by the total number of Er atoms in each sample, as a function of Er concentration. Drastic decrease is observed only for the signal C of p-type GA-19-p (GA050461,  $[\text{Er}] = 1.0 \times 10^{19} \text{ cm}^{-3}$ ,  $p = 5.7 \times 10^{16} \text{ cm}^{-3}$ ). This behavior is rather similar to the case of Zn codoped GaAs:Er,O, and will be discussed in connection with the proposed model in Section 5.4.3.

## 5.4 Discussion and proposed models

### 5.4.1 Origin of A, B, and C electron spin resonance centers

Since A, B, and C ESR centers are observed in all ESR measurements of GaAs:Er,O with similar angular dependences, the possible origin of A, B, and C ESR centers will be discussed. Most early angular dependence ESR measurements were done in the  $(-110)$  plane and suggested the  $C_{2v}$  symmetry for ESR centers [12,27]. However,

Yoshida et al. performed the angular dependence ESR measurement in the (001) plane and found new ESR lines [18]. The analyses of their results suggested that the new lines are related to ESR lines observed in the ( $-110$ ) plane and the local symmetry of A, B, and C ESR centers are lower than the  $C_{2v}$  symmetry [18]. This suggestion is consistent with the previous Zeeman analysis, which showed that the symmetry of the luminescent Er-2O center deviates from  $C_{2v}$  [28]. Moreover, the extended analyses also suggested the existence of large principal  $g$ -value ( $g_1 = 16.5$ ) nearly along the  $[-110]$  direction. Then the situation became easier to understand why we observe different A, B, and C ESR centers in the ( $-110$ ) plane. Since  $g_1$  has a very large  $g$ -value of 16.5, small deviation of  $g_1$  axis from the  $[-110]$  direction gives a large projection difference of  $g$ -value in the ( $-110$ ) plane. Therefore, the difference among observed A, B, and C ESR centers can be attributed to the difference in the deviation of  $g_1$  direction from the  $[-110]$  direction. They also suggested that the two oxygen atoms or two arsenic atoms for the Er-2O center should lie along the  $g_1$  direction and give rise to the very anisotropic  $g_1$  value. Therefore, specific atoms can deviate from the  $\langle 110 \rangle$  direction in various ways, resulting in the various Er-2O centers, which are consistent with PLE spectroscopy suggesting many kinds of Er-2O centers [10,11].

#### 5.4.2 Er pair model

Temperature dependence of ESR intensity down to 4.2K was first observed for A ESR center by Yoshikawa et al. [27] and for B and C ESR centers by Yoshida et al. [18]. Surprisingly, all ESR intensities did not show the paramagnetic behavior, which shows the monotonic increase of intensity as temperature decreases, but showed a maximum around 8K. This behavior is universal for all measured samples as shown in Section 5.3. Yoshida et al. [18] proposed the Er pair model to interpret this temperature dependence. If two Er ions are situated close together and coupled antiferromagnetically, the ground state will be a singlet and the ESR intensity decreases at very low temperature. If the temperature increases comparable to the gap between the magnetic excited state and the singlet ground state, the ESR intensity shows a maximum due to the increase of population at the magnetic excited state. If the temperature increases further, the populations in Zeeman split magnetic excited states become comparable and the ESR intensity decreases. Therefore, this model can interpret the temperature dependence of ESR intensity shown in Section 5.3 qualitatively. Moreover, there are several other evidences to support this Er pair model. First, the concentration dependence of line width of B and C ESR centers is far from the theoretically calculated line width [22], assuming the magnetic dipole–dipole interaction and the uniform distribution of Er ions in GaAs [20,26]. This result implies that Er ions are not uniformly distributed and Er pairs may exist in GaAs. Second, the line shape analyses of B ESR center show the Lorentzian line shape not the Gaussian [20,21,26]. In ESR the Lorentzian line shape appears when the exchange interaction is dominant, and the Gaussian line shape appears when the magnetic dipole–dipole interaction is dominant [23]. Therefore, the observation of Lorentzian line shape is the strong indication that there exists the exchange interaction, and the only way to have the exchange interaction is via Er ion pairs. However, we should point out that there should be no exchange

coupling among A, B, and C ESR centers because they are separately observed. If there is an exchange interaction between two centers, the exchange narrowing effect will average out two ESRs into one ESR [23].

### 5.4.3 Proposed model for the trap level

Energy transfer from light excited GaAs host to  $\text{Er}^{3+}$  ion was studied by pump and probe measurement [13,14]. The electron–hole pair creation at the trap level inside the gap of GaAs host and the energy transfer time were discussed. They also suggested that the trap level is coming from the Er-2O center but the energy transfer can be interpreted either by an electron-like trap [13] or a hole-like trap [14]. The nature of trap level will be discussed from the carrier effects on PL and ESR intensity in GaAs:Er,O.

We will start with the carrier effect on PL in GaAs:Er,O. First we assume that the Er-2O center forms the hole-like trap as shown in Fig. 5.20. In the case of n-type charge carriers as shown in Fig. 5.20(a), the hole-like trap is empty. When a free-electron and a free-hole are generated by the light excitation on the GaAs host, the hole-like trap level captures a photogenerated hole and becomes positively charged. The attractive potential of the trap level on a photogenerated hole is coming from the large strain field produced by the size difference between the  $\text{Er}^{3+}$  ion

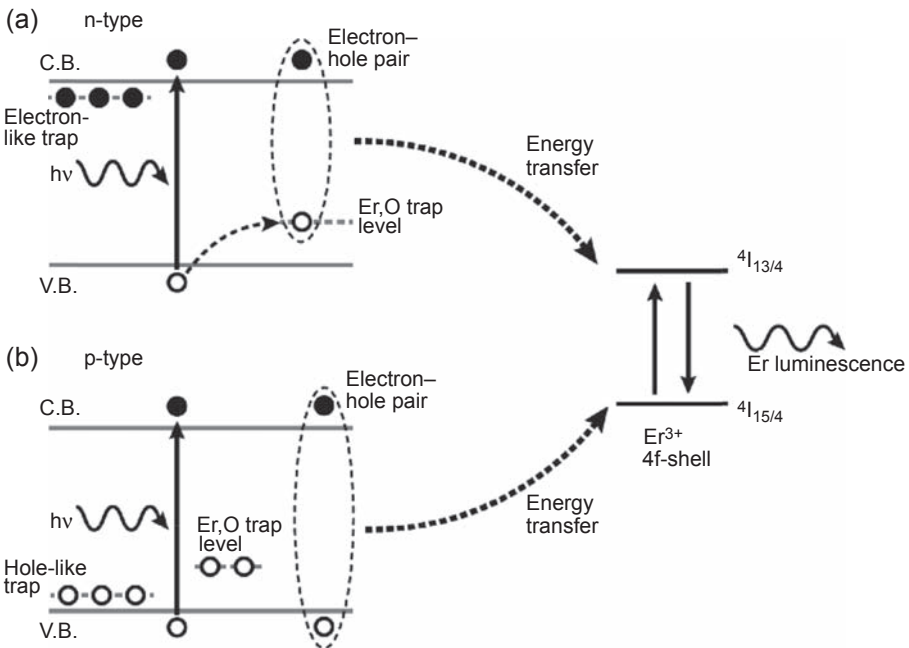


**Figure 5.20** Host-excited PL model (a) in the case of n-type charge carriers (b) in the case of p-type charge carriers.

(0.096 nm) and  $\text{Ga}^{3+}$  ion (0.062 nm) [29]. Then the positively charged trap level attracts a photogenerated electron in the conduction band through the Coulomb force and the electron–hole pair is created. This electron–hole pair recombines at the Er-2O center and the part of recombination energy is transferred to the  $\text{Er}^{3+}$  4f-shell for the 4f excitation. The excited 4f-shell relaxes from its first excited state ( $^4I_{13/2}$ ) to the ground state ( $^4I_{15/2}$ ) and it emits PL at 1.5  $\mu\text{m}$ . As the electron–hole pair recombination occurs at the Er-2O center, the efficiency to excite the  $\text{Er}^{3+}$  4f-shell will be very high.

On the other hand, in the case of p-type charge carriers as shown in Fig. 5.20(b), the hole-like trap is already occupied by holes even before the light excitation on the GaAs host. Then consider the situation when a free-electron and a free-hole are generated by the light excitation on the GaAs host. As the photogenerated electron in the conduction band sees many positive traps all over in the real space, the recombination of photogenerated electron with the photogenerated hole in the valence band is more preferable. Then the part of recombination energy is transferred to  $\text{Er}^{3+}$  4f-shell for the 4f excitation. However, the efficiency to excite the  $\text{Er}^{3+}$  4f-shell will be very low in this case because the electron–hole pair recombination occurs mainly not at the Er-2O center. Then the reduction of PL is expected in the case of p-type carriers.

Our observation of PL discussed in Section 5.2, where the PL intensity is reduced in the case of p-type charge carriers than in the case of n-type charge carriers, coincides well with this assumption of the hole-like trap for the Er-2O center. Moreover, if we assume that the Er-2O center forms the electron-like trap, the whole discussion on the carrier effect will be opposite and the reduced PL intensity is expected for the case of n-type carriers, which is inconsistent with our observed results in Section 5.2.

Next we will discuss the charge carrier effect on ESR based on the model described in Fig. 5.20. As discussed in Section 5.3 the ESR intensity decrease of signal C is very significant for p-type samples [26] including the Zn doping GaAs:Er,O (p-type) samples [19]. Especially the ESR intensity of the C center decreases dramatically with increasing the doping amount of Zn [19], which corresponds to the increase of p-type carriers. This mechanism is not clearly established by the experiments. However, the one possible mechanism is that, when the hole goes into  $\text{Er}^{3+}$  ion ( $4f^{11}$ ), the electronic state changes to  $\text{Er}^{4+}$  ( $4f^{10}$ ). The electronic state of  $\text{Er}^{4+}$  ion is comparable to  $\text{Ho}^{3+}$  ion ( $4f^{10}$ ). The  $\text{Ho}^{3+}$  ion is known to have more anisotropic  $g$ -values than  $\text{Er}^{3+}$  ion [24,30]. Therefore, the ESR signal may move outside of our X-band ESR measurement range and it results in the decrease of ESR signal intensity for p-type samples as observed in our experiments.

Then the question may arise why the ESR intensity decreases only for the signal C and not for the signal B by the increase of p-type carriers. As already discussed in Section 5.4.1, slightly different local structures are expected between the B and C centers from the angular dependence of  $g$ -values. Therefore, it is reasonable to expect different energy levels for B and C centers. If we assume a deeper hole-like trap level for the C center than for the B center, the doped p-type carriers tend to go into the trap level of the C center first and give rise to the decrease of ESR intensity of the C center. Determination of precise local structures of the B and C centers may be the future issue to support this proposed model. Finally the proposed trap level model is schematically summarized in Fig. 5.21.

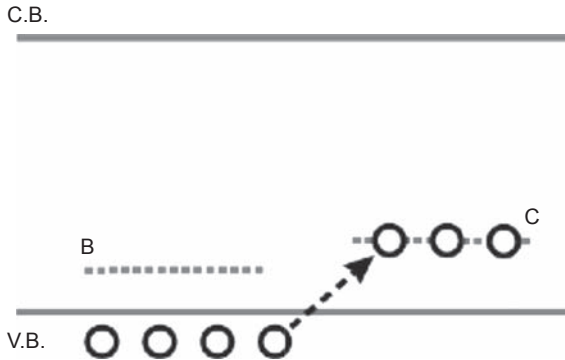


**Figure 5.21** Proposed trap level model for B and C centers.

A final comment may be addressed about the main host-excited PL center. Ishiyama et al. suggested that the luminescent Er center (PLE line No. 9 [11]) corresponds to either the B or C ESR center from the classification of Er concentration dependence of ESR and PLE intensities [12]. Then as discussed in Sections 5.2 and 5.3, there is a strong correlation between the decrease of PL and the decrease of ESR intensity of the C center by the increase of p-type carriers. Together with this fact and the possible mechanism discussed with Figs. 5.20 and 5.21, it is more likely that the C center has the higher energy transfer efficiency to the  $\text{Er}^{3+}$  4f-shell after the electron–hole pair recombination than the B center. Therefore, the C center may be the main host-excited PL center while the microscopic origin to interpret the different energy transfer efficiency between B and C centers is not clear at the moment. On the other hand, it is reported that there is decrease of ESR intensity of the B center by the light illumination of GaAs:Er,O with He-Ne laser while there is no change for the ESR intensity of the C center [12,18]. As the ESR measuring time is the order of minutes, which is much longer than the electron–hole recombination time and energy transfer time of the order of psec, we have to consider the steady state under the He-Ne laser illumination. If the energy transfer efficiency to the  $\text{Er}^{3+}$  4f-shell with the electron–hole pair recombination is higher at C center than B center as discussed earlier, the averaged time for the hole to stay at the Er-2O trap level is longer for the B center than the C center. Then the ESR intensity of the B center decreases compared to that of the C center on average, which is consistent with the ESR experiments under the illumination of GaAs:Er,O with He-Ne laser. In conclusion, the ESR C center can be considered as the main host-excited PL center from our model illustrated in Fig. 5.21.

## 5.5 Summary

ESR studies of GaAs codoped with Er and O atoms (GaAs:Er,O) with and without carriers are presented. ESR studies include the detailed angular dependence, the temperature dependence, the effect of illumination, and Er concentration dependence

measurements. Moreover, the line width calculations and the line shape analyses are performed. Considering these ESR results and analyses, the origin of A, B and C ESR centers, Er pair model, and the proposed model for the trap level are discussed.

## References

- [1] Jha AR, editor. Rare earth materials: properties and applications. Taylor and Francis Group; 2014.
- [2] Sagawa M, Fujimura S, Togawa N, Yamamoto H, Matsuura Y. *J Appl Phys* 1984;55:2083.
- [3] Ennen H, Schneider J, Pomrenke G, Axmann A. *Appl Phys Lett* 1983;43:943.
- [4] Takahei K, Taguchi A. *J Appl Phys* 1993;74:1979.
- [5] Fujiwara Y, Kawamoto T, Koide T, Takeda Y. *Phys B* 1999;273–274:770.
- [6] Takahei K, Taguchi A, Horikoshi Y, Nakata J. *J Appl Phys* 1994;76:4332.
- [7] Tabuchi M, Ofuchi H, Kubo T, Takahei K, Takeda Y. *Mater Sci Forum* 1997;258–263:1571.
- [8] Katsuno H, Ohta H, Portugall O, Ubrig N, Fujisawa M, Fatma E, et al. *J Lumin* 2011;131:2294.
- [9] Ohta H, Portugall O, Ubrig N, Fujisawa M, Katsuno H, Fatma E, et al. *J Low Temp Phys* 2010;159:203.
- [10] Takahei K, Taguchi A. *J Appl Phys* 1995;77:1735.
- [11] Takahei K, Taguchi A, Hogg RA. *J Appl Phys* 1997;82:3997.
- [12] Ishiyama T, Katayama E, Murakami K, Takahei K, Taguchi A. *J Appl Phys* 1998;84:6782.
- [13] Nakamura K, Takemoto S, Terai Y, Koizumi A, Fujiwara Y. *Phys B* 2006;376–377:556–9.
- [14] Fujiwara Y, Terai Y, Nishikawa A. *J Phys Conf Ser* 2009;165:012025.
- [15] Fujiwara Y, Nonogaki Y, Oga R, Koizumi A, Takeda Y. *Appl Surf Sci* 2003;216:564.
- [16] Fujiwara Y. *Mater Trans* 2005;46:1969.
- [17] Fujiwara Y, Koizumi A, Inoue K, Urakami A, Yoshikane T, Takeda Y. *Materials Research Society Symposium Proceedings*. In: Weaver BD, Manasreh MO, Jagadish CC, Zollner S, editors. *Progress in semiconductors II—electronic and optoelectronic applications*, vol. 744. Pittsburgh: Materials Research Society; 2003. p. 149–54.
- [18] Yoshida M, Hiraka K, Ohta H, Fujiwara Y, Koizumi A, Takeda Y. *J Appl Phys* 2004;96:4189.
- [19] Yoshida M, Hiraka K, Ohta H, Fujiwara Y, Koizumi A, Takeda Y. *J Appl Phys* 2005;97:023909.
- [20] Fujisawa M, Asakura A, Elmasry F, Okubo S, Ohta H, Fujiwara Y. *J Appl Phys* 2011;109:053910.
- [21] Fujisawa M, Asakura A, Elmasry F, Okubo S, Ohta H, Fujiwara Y. *J Phys Conf Ser* 2010;200:062005.
- [22] Van Vleck JH. *Phys Rev* 1948;74:1168.
- [23] Poole Jr CP. *Electron spin resonance: a comprehensive treatise on experimental techniques*. 2nd ed. New York: Dover; 1997.
- [24] Abragam A, Bleaney B, editors. *Electron paramagnetic resonance of transition ions*. New York: Dover; 1983.
- [25] Fujiwara Y, private communication.

- [26] Elmasry F, Okubo S, Ohta H, Fujiwara Y. *J Appl Phys* 2014;115:193904.
- [27] Yoshikawa J, Urakawa C, Ohta H, Koide T, Kawamoto T, Fujiwara Y, et al. *Phys E* 2001;10:395.
- [28] Haase D, Dornen A, Takahei K, Taguchi A. *Mater Res Soc Symp Proc* 1996;422:179.
- [29] Philips JC, editor. *Bonds and bands in semiconductors*. New York: Academic Press; 1973.
- [30] Kirton J. *Phys Rev* 1965;139:A1930.

# Gadolinium-doped gallium-nitride: synthesis routes, structure, and magnetism

6

A. Ney

Johannes Kepler University, Linz, Austria

## 6.1 Introduction

The race toward a dilute magnetic semiconductor (DMS) that exhibits room-temperature (RT) ferromagnetism has been in progress for about 15 years, sparked by the theoretical prediction that the two wide band-gap semiconductors GaN and ZnO would show a Curie temperature ( $T_C$ ) above 300 K if doped with 5% of Mn and a large hole concentration of  $1 \times 10^{20}/\text{cm}^3$  (Dietl et al., 2000). Despite apparent experimental evidence that RT magnetic order was already reported by many groups shortly after the theoretical prediction, the subject remained unusually controversial in the following years. Dietl (2010) summarizes that after 10 years of research the existence of ferromagnetism is well established for GaAs:Mn and related systems but it remains the major goal in the field to achieve  $T_C$ s at or above 300 K. Around the same time a review of a large group of theorists summarize: “The results of ab initio calculations seem to suggest that it is rather unlikely to obtain  $T_C$  values as high as room temperature or above in this range” (Sato et al., 2010). Nonetheless persistent experimental claims of  $T_C$ s above 300 K for a range of DMS materials can be found up to today. Thus it is worth trying to get a broader view on a given materials systems and compare a range of samples from different sources to elucidate whether these reports are characteristic of the DMS material itself (system-specific) or if only peculiarities of a given specimen are reported (sample-specific). Only in the former case can we consider those findings to be useful for future potential applications in spintronic devices that have to be operational at ambient conditions.

Meanwhile a range of DMS materials with a potential  $T_C$  above RT were reviewed in a comprehensive way, for example, ZnO:Co (Ney et al., 2010a), and in most of these cases two points turned out to be crucial: (1) exclusion of secondary magnetic phases, where transmission electron microscopy (TEM) and synchrotron-based techniques like X-ray absorption spectroscopy (XAS) were found to be advantageous; and (2) magnetic characterization beyond the standard superconducting quantum interference device (SQUID) magnetometry to evidence ferromagnetism. Using the X-ray magnetic circular dichroism (XMCD) technique, (1) and (2) can be combined in an elegant way because this approach combines the chemical sensitivity of XAS with the possibility to probe the magnetic properties with element specificity using XMCD. The aim of this chapter is therefore to focus on a range of GaN:Gd samples that were fabricated by different synthesis routes on different substrates in different



laboratories. While for most of these samples a standard SQUID characterization was made, only a few of them were investigated with more advanced experimental techniques trying to unravel the microscopic origin of the integral magnetic properties of the various specimen.

### 6.1.1 A brief overview for GaN:Gd

The first claim of RT-ferromagnetism in GaN:Gd was made by [Teraguchi et al. \(2002\)](#). However, rare-earth doping of GaN was primarily the focus because of its importance in optoelectronics and thus this report received only little interest from the DMS community in the beginning. This has drastically changed, when ferromagnetism far above 300 K was reported even at very dilute doping levels down to  $10^{16}$  Gd/cm<sup>3</sup>. Moreover the magnetic order was reported to be caused by effective magnetic moments of the order of 1000  $\mu_B$  per Gd atom ([Dhar et al., 2005a](#)) and a heuristic model relying on magnetically polarized spheres of influence was invoked to explain these unusual findings ([Dhar et al., 2005a,b](#)). [Röver et al. \(2008\)](#) confirmed the existence of the colossal magnetic moments in the ultra-dilute limit a few years later. Similar results, with even higher effective magnetic moments, were also reported for Gd ion-implanted hexagonal (wurtzite structure) GaN ([Dhar et al., 2006](#)). On the other hand, in cases where Gd-ions were implanted into cubic (zincblende structure) GaN, only paramagnetism was found ([Lo et al., 2007](#)). Therefore it was speculated that a combination of implantation-related defects and the polar nature of the wurtzite lattice may promote the magnetic order.

Besides the claims of colossal effective moments, the presence of RT-ferromagnetism was also found by other experimentalists up to Gd concentrations of 8.9% ([Zhou et al., 2008](#)). Other groups paid special attention to the correlation of ferromagnetism with the preparation conditions ([Hite et al., 2006](#)), especially regarding the robustness of the observed RT ferromagnetism with respect to defects ([Hite et al., 2008](#)). The interrelation of RT ferromagnetism with defects is also underlined by the existence of variable range hopping transport in ferromagnetic (FM) GaN:Gd ([Bedoya-Pinto et al., 2009](#)). Especially the latter finding is worth commenting on since the samples with the colossal moments studied by [Dhar et al. \(2005a,b\)](#) were also highly resistive, which is in contrast to the initial theoretical prediction where a high hole concentration was the prerequisite for robust magnetic order ([Dietl et al., 2000](#)). More recently, also reproducibility-issues and long-time degradation of the magnetic properties of GaN:Gd were reported ([Roever et al., 2011](#)). It should be noted that in all these papers the magnetic characterization was predominantly based on integral SQUID magnetometry.

In parallel to these experimental reports theoretical groups tried to shed light on the possible origin of the claimed ferromagnetism. Theory was initially suggesting an antiferromagnetic order via sf-coupling which can be tuned to be FM by electron doping ([Dalpian and Wei, 2005](#)), which however was not consistent with the insulating samples reported by [Dhar et al. \(2005a,b\)](#). Later, it was reported that Ga vacancies could be responsible for the ferromagnetism in Gd:GaN ([Liu et al., 2008](#); [Gohda and Oshiyama, 2008](#)) and even in undoped GaN ([Dev et al., 2008](#)). The importance of the role of defects was consistent with the experimental observation that the magnetic properties of

ion-implanted and thus potentially more defective GaN:Gd were enhanced (Dhar et al., 2006) compared to samples grown by molecular beam epitaxy (MBE) (Dhar et al., 2005a,b). However, these theoretical predictions were criticized because of the large number of defects, which had to be invoked, and the high energy of formation of Ga vacancies. Therefore interstitial N or O on octahedral sites was proposed as an alternative explanation to mediate ferromagnetism (Mitra and Lambrecht, 2009). This prediction was consistent with the reported oxygen concentration of  $10^{18}/\text{cm}^3$ , which was held responsible for the high resistivity of the GaN:Gd MBE samples exhibiting the colossal magnetic moments (Dhar et al., 2005a,b).

Summarizing, a defect-based explanation for the reported ferromagnetism in GaN:Gd seems to be plausible. This scenario can explain large variations from sample to sample and the importance of the fabrication method. In addition, the absence of carrier-mediated ferromagnetism as reported from early on by experimentalists is in contrast to other DMS, for example, for GaAs:Mn where carrier-mediated ferromagnetism is satisfyingly explained by theory and verified by experiments (see, eg, Dietl et al. (2000) and Dietl (2010)). It is therefore worth trying a systematic synopsis over a range of published experimental results that deal with the magnetic properties of GaN:Gd to try to test the hypothesis of defect-induced magnetic order in this DMS compound.

## 6.2 General considerations and experimental methods

In the course of this chapter a range of experimental methods will be employed. The XAS-based methods will briefly be described and discussed in this section. It also includes some detailed technical remarks on the standard SQUID magnetometry to highlight possible pit-falls. However, we will start with some general considerations about magnetic properties and recall some well-known but important facts about magnetism.

### 6.2.1 Generals remarks about magnetic properties

First, the various categories of possible magnetic properties that will be used throughout this chapter are listed. The term “ferromagnetic” will be used only if it can be experimentally demonstrated by more than one method or evidence that long-range magnetic order with a remanent magnetization, magnetic anisotropy, and a magnetic hysteresis are present. All these properties shall vanish at  $T_C$  and the system becomes paramagnetic (PM). At  $T_C$  a peak in the susceptibility should be present and the specific heat should exhibit an anomaly. A PM material is characterized by noninteracting atomic moments of a few  $\mu_B$  and the absence of both remanence and hysteretic behavior down to the lowest temperatures ( $\sim 1$  K) where dipolar interaction starts to play a role. For well-isolated magnetic impurities in a symmetric environment the magnetization can be described by the Brillouin function ( $B_J$ ). However, it should be recalled that PM can also be anisotropic, which has explicitly been reported in DMS systems having the wurtzite structure like GaN:Mn (Stefanowicz et al., 2010) and ZnO:Co (Ney et al., 2010b). Note that for these  $3d$  dopants in a wurtzite matrix  $B_J$  does not properly describe the magnetization curves.

The term “superparamagnetic” (SPM) is used in cases when a magnetic hysteresis and a remanence are observed at low temperatures. Both vanish above a certain temperature above which the PM response is indicative of larger effective magnetic moments compared to the atomic moments in a PM sample. This is typically asserted by the presence of a clear blocking behavior (separation of field-cooled (FC) versus zero-field-cooled (ZFC)  $M(T)$  curves with a clear maximum in the ZFC curve) and an anhysteretic, S-shaped  $M(H)$  curve at elevated temperatures, which typically can be described by a Langevin function. SPM is typically present if a non-, or weakly (dipolar) interacting ensemble of small FM nanoparticles is studied. In the context of DMS materials it is crucial to note that the vast majority of presented data throughout the literature is merely indicative of SPM rather than FM, with the exception of GaAs:Mn, where FM is well established in the earlier sense. It should also be noted that SPM in DMS systems can have different microscopic origins. On the one hand, if a coalescence model of spheres of influence is considered (Dhar et al., 2005a,b), SPM-like signatures are expected. The blocking temperature would correspond to the temperature where the magnetic coupling between the spheres of influence breaks down. Within such a scenario, SPM would be an intrinsic property of the material. On the other hand, small FM inclusions (precipitations or nanoclusters) more naturally constitute SPM behavior. Such nanoclusters can originate from different sources: (1) phase separation of dopant atoms; (2) decoration of grain boundaries with dopant atoms beyond the solubility limit; (3) magnetic contaminations due to sample-handling such as wafer cutting by the manufacturer, cleaving, improper tweezers-handling, improper sample mounting, or even using a marker pen to label the samples on the backside; and finally (4) dopant-rich regions in a dopant-poor host matrix such as in the Mn:Ge system (eg, Bougeard et al., 2006). Whereas (4) can be considered as an intrinsic property of the material as well, (1–3) will be regarded as extrinsic and therefore not as a real physical property of the material in question. Note that it is experimentally extremely difficult to rule out (1) and (2) since small nanoclusters are hard to be detected using standard X-ray diffraction (XRD) and a search of nanoclusters using TEM can be rather tedious (see, eg, Ney et al., 2010a). Sample contamination issues summarized in (3) will be discussed in more detail along with SQUID magnetometry in the following.

### 6.2.2 SQUID magnetometry

Very sensitive magnetometry represents an essential tool to study the magnetic properties of a range of different sample systems. Many DMS samples studied throughout the literature have in common that they are all deposited on a substrate and the data presented in most publications are already corrected for the magnetic response of the substrate, or even for the studied sample volume. This is especially true for GaN-based DMS because large single crystals of GaN are not available. The vast majority of experiments are based on magnetic characterizations performed by SQUID magnetometry and in particular the commercial SQUID magnetometer MPMS (XL) from Quantum Design. Using the MPMS SQUID is widely spread mainly

due to its high degree of user-friendly automation and reliability as well as the lack of commercial alternatives. The SX-700 from Cryogenic can be found less frequently and thus it is worth summarizing a few technical details about the standard usage of the MPMS SQUID magnetometer that are very important when small magnetic signals of a DMS layer have to be separated from the large diamagnetic background of the substrate. [Stamenov and Coey \(2006\)](#) have pointed out that the second-order gradiometer, which detects the magnetic moment of the given sample in a SQUID magnetometer is already prone to errors because of the finite sample size while the MPMS assumed a point dipole and they provided some correction factors. Note that some variants of the SX-700 offer to correct the data for higher order multipoles. However, this mainly concerns the quantitative accuracy of the results, and later, a correction table for arbitrary sample sizes for the MPMS gradiometer was provided ([Sawicki et al., 2011](#)).

Along another line of possible pitfalls it was discussed that especially  $\text{Al}_2\text{O}_3$  (sapphire) substrates can exhibit ferromagnetism themselves ([Salzer et al., 2007](#)), which may originate from residual contaminations from the manufacturer. However, even after thorough cleaning of the substrates, a small apparently FM hysteresis can be detected ([Sawicki et al., 2011](#)). By comparing diamagnetic and PM substrates and by properly quenching the superconducting magnet to eliminate residual trapped flux, [Sawicki et al. \(2011\)](#) could demonstrate that it is inevitable to pick up some residual flux in the superconducting magnet of the order of 0.5 mT while tracing a complete magnetization curve  $M(H)$ . Since the actual magnetic field is not directly measured in any commercial SQUID magnetometer, this leads to an apparent FM hysteresis on diamagnetic substrates of the order of  $2\text{--}4 \times 10^{-7}$  emu ([Sawicki et al., 2011](#)). Note that throughout this chapter the old cgs electromagnetic unit (emu) is used rather than SI units because this is the standard throughout most of the existing literature;  $10^3$  emu correspond to a magnetic moment of  $1 \text{ Am}^2 = 1 \text{ J/T}$ . [Fig. 6.1](#) exemplarily shows the typical performance of the SQUID magnetometer when a magnetically clean GaN film grown on c-sapphire is measured. Throughout the entire chapter the diamagnetic contribution is already corrected as follows: the slope of the  $M(H)$  curves between 2 T and the highest field is derived at 300 K and this diamagnetic susceptibility is subsequently subtracted from all  $M(H)$  and  $M(T)$  data. The rather noisy  $M(H)$  curves at 300 and 5 K are virtually identical indicating an almost step-like feature over a wide field range of  $\pm 4$  T ([Fig. 6.1](#), left) while the enlarged part of the  $M(H)$  ([Fig. 6.1](#), middle) exhibits a virtually temperature-independent apparent hysteresis of the order of 0.4 micro-emu ( $\mu\text{emu}$ ). The temperature-dependent measurement  $M(T)$  shown in [Fig. 6.1](#), right, is a typical sequence, which will be used throughout this chapter. For this the sample is either cooled in a high magnetic field (4, 4.5, or 5 T) down to the lowest temperature, field-cooled, and then measured in a field of 10 mT while warming or the sample is cooled in zero external field, zero-field-cooled, and then measured at 10 mT while warming. Coinciding FC and ZFC curves are indicative of a PM sample while a separation between the two can either indicate SPM or FM behavior. In the case of the GaN/sapphire sample in [Fig. 6.1](#), FC and ZFC coincide and are close to zero. Since the diamagnetism has already been subtracted, the absence of any signal, especially the characteristic  $1/T$  behavior of a PM, indicates that this sample is purely diamagnetic from the  $M(T)$

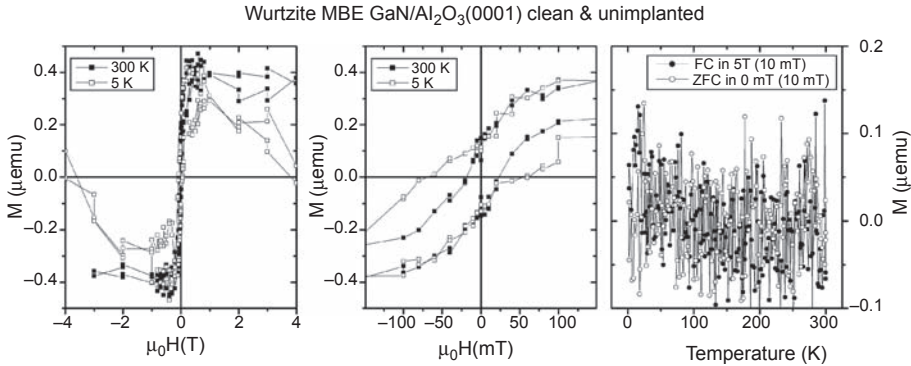


**Figure 6.1** Residual magnetic  $M(H)$  curves (left) of undoped GaN/sapphire as measured by SQUID at 300 K (*full squares*) and 5 K (*open squares*) after subtraction of the diamagnetic background. The enlarged low field region (middle) shows that the apparent hysteresis and remanence are temperature independent.  $M(T)$  curves (right) measured under FC (*full circles*) or ZFC (*open circles*) do not exhibit any sizable signal.

Data adapted from Sawicki, M., Stefanowicz, W., Ney, A., 2011. Sensitive SQUID magnetometry for studying nanomagnetism. *Semicond. Sci. Technol.* 26, 064006, <http://dx.doi.org/10.1088/0268-1242/26/6/064006>.

behavior underlining that the apparent hysteresis in the  $M(H)$  data is an artifact stemming from the superconducting magnet (Sawicki et al., 2011).

On the other hand, there are studies that discuss the influence of stainless-steel tweezers handling on the magnetic properties of the samples (Abraham et al., 2005) or that highlight possible contamination of the sample holder (typically clear drinking straws) and of other means of sample mounting (Bonanni et al., 2007). Nonetheless, the measurements in Fig. 6.1 were performed with great care using the standard sample mounting (ie, the clear drinking straws), and all samples should be held in place inside the straw without any other means than by clamping them in-between the two walls of the straw without puncturing or cutting the straw. Note that it is extremely crucial that the entire mounting of the actual sample is magnetically extremely homogeneous along the sample transport. Besides these sample-mounting issues, which are also discussed in detail by Sawicki et al. (2011), cutting the samples to a suitable size for the SQUID measurements is a potential source of magnetic contamination. This is illustrated in Fig. 6.2, where an ammonia-assisted MBE-grown GaN film on sapphire is measured in the as-cleaved state (full symbols), and after thorough cleaning by etching in HCl and subsequent cleaning in an ultrasonic bath using acetone, ethanol, and deionized water for 5 min each (open symbols). The observed hysteresis in the as-cleaved state is of the order of 2 (emu, which roughly corresponds to an Fe contamination of about a few nanograms, which most likely stems from the stainless-steel rod of the diamond stencil, and some material is abraded by the harder sapphire; the same would also be possible for SiC but less likely for softer substrates like Si. The raw data in Fig. 6.2, middle, indicate that there is a characteristic feature at fields where the total signal including diamagnetism goes to zero. The fact, that the apparent sample

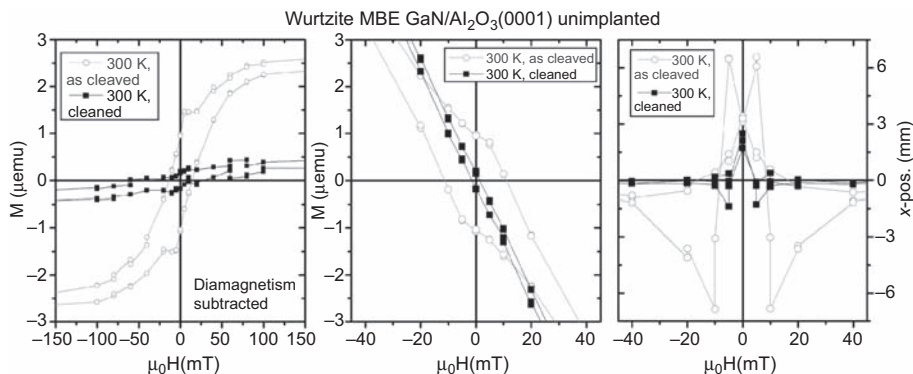


**Figure 6.2**  $M(H)$  curve (left) of undoped GaN/sapphire recorded at 300 K in the as-cleaved state (*open gray circles*) and after cleaning in HCl (*full black squares*) after subtraction of the diamagnetic background and before (middle). The kink in the  $M(H)$  curves is indicative of magnetic (edge-) contamination of the sample and it occurs where the total signal goes through zero and the respective fitted  $x$ -position of the SQUID signal (right) in the iterative regression mode exhibits a characteristic up/down behavior.

Data adapted from Sawicki, M., Stefanowicz, W., Ney, A., 2011. Sensitive SQUID magnetometry for studying nanomagnetism. *Semicond. Sci. Technol.* 26, 064006, <http://dx.doi.org/10.1088/0268-1242/26/6/064006>.

position of the as-cleaved sample in Fig. 6.2, right, exhibits a clear up/down feature around the field where the total signal goes to zero, is a good indication that the origin of the signal is located at the edges of the sample, thus underlining that magnetic contamination originating from sample cleavage is the source of this magnetic signal; see Sawicki et al. (2011) for more details. The above discussion should illustrate that extreme care has to be exercised if one wants to base the claim of the existence of FM in DMS samples exclusively on integral SQUID magnetometry. In cases where ion implantation is used to dope a DMS, one can measure first the unimplanted sample piece and then remeasure it after ion implantation. In any case a reference sample without magnetic dopants should be mandatory. We will come back on to these issues later in this chapter.

### 6.2.3 XAS-based techniques

For the study of multiconstituent magnetic materials, the power of XAS is well known (see, eg. Stöhr and Siegmann, 2006, Chapter 9). Near-edge XAS (XANES) excites a core level electron to an unoccupied final state and the dipolar selection rules stipulate that depending on the chosen absorption edge different unoccupied orbitals can be probed. For example, at the so-called K-edge a  $1s$  core electron is excited into the unoccupied  $p$ -states, which in the case of the Ga K-edge, are the relevant orbitals for the chemical bonding in GaN. On the other hand at the Gd L-edges a  $2p$  core electron is excited predominantly into the unoccupied  $d$ -states. All absorption edges are located at well-separated characteristic energies, a fact



that constitutes the element specificity of all XAS-based techniques. By selecting the photon energy of the incident (synchrotron) light, we can choose which atomic species to probe. In addition the shape of the XANES is characteristic for the oxidation state (valence) of the constituent atoms. In addition, since GaN crystallizes in the wurtzite structure, which has a uniaxial crystal symmetry with fairly directional covalent bonding, this leads to a splitting of the tetrahedrally coordinated cations and anions by the surrounding crystal field so that there is a clear directional dependence of the density of unoccupied final states, which can be probed with linear polarized X-rays in such a way that the  $E$  vector of the light is either parallel ( $E \parallel c$ ) or perpendicular ( $E \perp c$ ) to the  $c$ -axis of the crystal. The difference between these two spectra is that the so-called X-ray linear dichroism (XLD) has a characteristic shape for the wurtzite structure, which allows the local structural environment of even dilute species to be probed in a highly sensitive way.

The power of XLD to quantitatively determine the fraction of absorbing atomic species incorporated at specific lattice sites was first demonstrated for GaN:Mn where the XLD was recorded and simulated for the Ga and Mn K-edges, respectively (Sarigiannidou et al., 2006). In addition, atom-specific sensitivity over a micron depth scale is available using XAS in the hard X-ray regime, allowing full characterization of epitaxial films with a range of thicknesses, especially, their interfaces to the substrate. Finally, XMCD directly probes their magnetic properties with element specificity since the circular polarization is transferred to a finite spin polarization of the photoelectron, which in turn senses the unoccupied states spin-selectively. Thus the difference between left and right circular polarization is a measure for the spin-imbalance of the unoccupied final states and thus the magnetism (Stöhr and Siegmann, 2006, p. 389 ff.). Note that at the K-edge the initial state ( $1s$ ) has no angular momentum ( $l = 0$ ) and thus the XMCD only exists if the final  $p$ -states possess a finite orbital moment (Stöhr and Siegmann, 2006, p. 398). All XAS measurements presented here were taken at the ESRF beamline ID12 in total fluorescence yield. The XANES/XLD measurements were carried out at 300 K and a quarter wave plate was used to flip the linear polarization of the synchrotron light from vertical (ie,  $E \parallel c$ ) to horizontal ( $E \perp c$ ); the angle of incidence was 10 degrees with respect to the sample surface. The XLD was taken as the direct difference of the normalized XAS with  $E \perp c$  and  $E \parallel c$ ; the linear polarization was flipped back and forth three times at each energy point of the spectra. The XANES was derived from the weighted average of the two XAS spectra. The XMCD measurements were taken down to 6 K as the direct difference of XANES spectra recorded with right and left circular polarized light for  $H = 6$  T typically under grazing incidence of 15 degrees. To minimize artifacts, the direction of the external magnetic field was reversed as well. Element-specific XMCD(H) curves were typically recorded at fixed photon energy of the maximum of the XMCD spectrum by recording the difference of the X-ray absorption between left and right circular polarized light as a function of the external field. In general, the high sensitivity, element specificity, and nondestructive nature of these X-ray-based methods allow us to draw clear and unambiguous conclusions about the electronic, magnetic, and structural properties of DMS materials on a local scale.

## 6.3 GaN:Gd samples with colossal magnetic moments

### 6.3.1 MBE-grown wurtzite GaN:Gd/SiC(0001)

GaN:Gd epitaxial films with a low nominal Gd concentration ( $\leq 0.05\%$ ) have been grown using ammonia-assisted MBE directly on SiC(0001) substrates. Details of the sample characterization using in situ reflection high-energy electron diffraction, XRD, and secondary ion mass spectroscopy (SIMS) are reported in the literature (Dhar et al., 2005a,b). These samples belong to a growth series for which colossal magnetic moments have been claimed at low Gd concentrations of the order of  $10^{16}/\text{cm}^3$ . They are typically highly resistive and contain about  $10^{18}/\text{cm}^3$  of oxygen. Fig. 6.3 presents a reanalysis of the SQUID data of one sample with  $6 \times 10^{16}/\text{cm}^3$  Gd (sample C in the original work). The data by Dhar et al. (2005a) were originally presented in  $\text{emu}/\text{cm}^3$  and the film thickness was determined by SIMS to be 600 nm (Dhar et al., 2005b). To extract the raw data in emu the sample area has to be assumed and a typical sample size for SQUID magnetometry is about  $5 \times 3 \text{ mm}^2$ . Using these numbers we can back-calculate the original data to derive the actual measured magnetic moment of the sample in emu. Fig. 6.3 displays the resulting  $M(H)$  curves at 300 and 2 K (left) and the  $M(T)$  curves under FC and ZFC conditions (middle) as well as the dependence of the magnetization as a function of Gd concentration (right) for which the identical volume for the various GaN:Gd layers has been assumed.

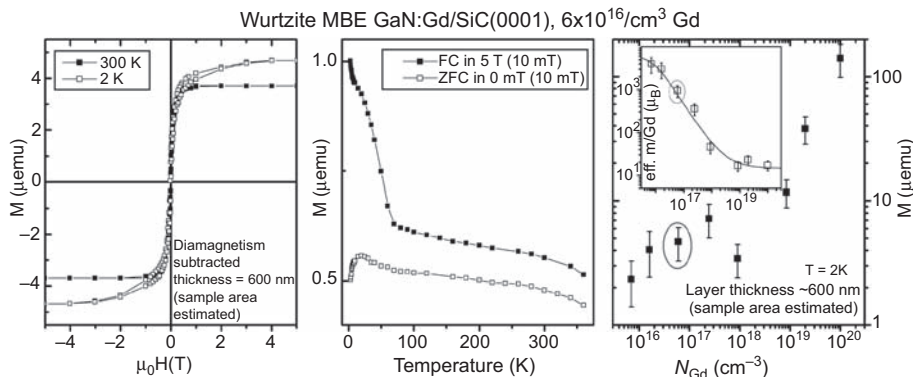


**Figure 6.3**  $M(H)$  curves (left) of MBE-grown GaN:Gd/SiC(0001) measured at 300 K (*full squares*) and 2 K (*open squares*) after subtraction of the diamagnetic background. The measurement signal has been back-calculated from the published data by assuming a typical sample area of  $3 \times 5 \text{ mm}^2$  and a film thickness of 600 nm taken from the published SIMS profile. The corresponding  $M(T)$  curves under FC (*full squares*) and ZFC (*open squares*) are shown in the middle. Assuming an identical sample volume for the sample series from Dhar et al. (2005a) we can recalculate the total signal as measured by SQUID for the entire concentration series (right) revealing that the colossal effective moments per Gd (inset) correlate with a magnetic signal of less than  $7 \mu\text{emu}$  at 2 K.

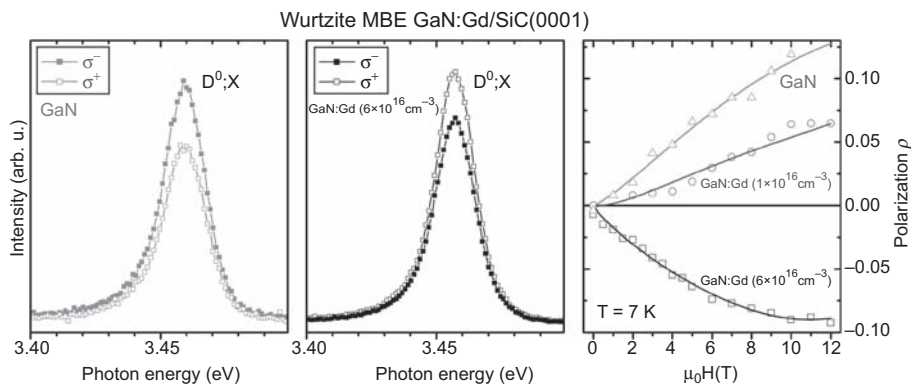
Reanalysis of data from Dhar, S., Brandt, O., Ramsteiner, M., Sapega, V.F., Ploog, K.H., 2005a. Colossal magnetic moment of Gd in GaN. Phys. Rev. Lett. 94, 037205, <http://dx.doi.org/10.1103/PhysRevLett.94.037205>.



From this plot it is obvious that all samples below a Gd concentration of  $10^{19}/\text{cm}^3$  exhibit a total magnetic signal of less than  $8 \mu\text{emu}$ , which is already close to the typical size of sample handling artifacts as shown in Fig. 6.2. However, assuming that the entire magnetic signal stems from the Gd, the colossal magnetic moments of up to a few  $1000 \mu\text{B}$  result as shown in the inset of Fig. 6.3, right. On the other hand, above  $10^{18}/\text{cm}^3$  Gd only the well-known atomic moment of Gd of about  $7.7 \mu\text{B}$  is derived.

A similar result is reported by Roever et al. (2011), where GaN:Gd was fabricated by plasma-assisted MBE (PAMBE) on GaN buffer layers grown by metal organic chemical vapor deposition (MOCVD) on c-sapphire substrates. Their results could be modeled by an atomic moment of the Gd plus a constant additional magnetic moment of  $2.5 \times 10^{19} \mu\text{B}/\text{cm}^3$  independent of the Gd concentration, which however was found to degrade on the timescale of years (Roever et al., 2011, Fig. 6.1(b)). From that, Roever et al. (2011) conclude that “uncontrollable parameters seem to be responsible for the FM properties.” Only the role of oxygen is found to apparently promote the magnetic properties. Unfortunately, such low oxygen concentrations are not accessible to element-selective techniques such as O K-edge XMCD studies. Note that even in alleged FM ZnO:Co layers, where oxygen is present in stoichiometric quantities and not on the impurity level, no sizable O K-edge XMCD has been found (Tietze et al., 2008). Therefore, it seems to be unlikely that direct experimental evidence can be provided for this hypothesis. The situation is even worse in for the Gd dopant itself, where concentrations as low as  $1 \times 10^{16}/\text{cm}^3$  would have to be sensed by XMCD. In any case, the attribution of a local magnetic moment of several hundreds  $\mu\text{B}$  to a single atom is unphysical, thus, from early on it was speculated that the surrounding semiconductor matrix must carry some finite magnetic moment that would be the source of these colossal effective magnetic moments. Therefore, it is an experimental alternative to probe the band structure of the GaN:Gd sample using magneto-photoluminescence (PL). The PL spectra of the series of GaN:Gd samples shown in Fig. 6.4 are dominated by the donor-bound exciton ( $D^0;X$ ) transition at a photon energy of 3.458 eV.

The donor most likely being responsible for this transition is oxygen, which was evidenced to be present by SIMS. Since these donors are most likely distributed homogeneously over the entire GaN matrix, the properties of the electronic band structure can be probed from this oxygen-dominated PL. Fig. 6.4 shows the PL spectra at 10 T and 7 K for an undoped GaN reference sample (left) and the  $6 \times 10^{16}/\text{cm}^3$  Gd sample (middle), which was already shown in Fig. 6.3. All data in Fig. 6.4 have already been reported by Ney (2010) but originate from an unpublished work by Sapega et al. (2005). The observed ( $D^0;X$ ) emission is polarized in both samples, which is evident from the difference in intensities of the two circularly polarized  $\sigma^-$  (full squares) and  $\sigma^+$  (open squares) components. Most importantly, the polarization for GaN:Gd sample has the opposite sign of the one in the GaN reference sample clearly evidencing an influence of the Gd doping on the magneto-PL. Fig. 6.4 (right) displays the field dependence of the ( $D^0;X$ ) polarization for the two samples together with an intermediate Gd concentration. With regard to the possible origin of the magnetic signal as measured by SQUID the field dependence of the magneto-PL is of interest.



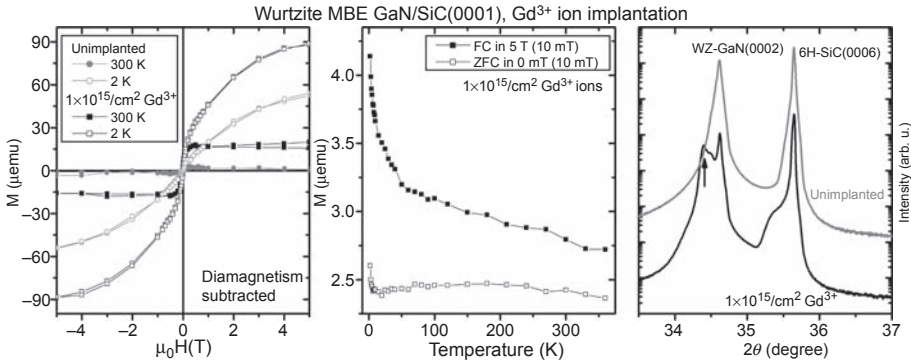
**Figure 6.4** Circularly polarized PL spectra of the donor-bound exciton ( $D^0;X$ ) for an undoped GaN reference sample (left) and the GaN:Gd sample from Fig. 6.3. Both samples were measured at 7 K and 10 T in the Faraday configuration ( $B \parallel c$ ). Circular polarization  $\rho$  of the ( $D^0;X$ ) emission as a function of the external magnetic field at 7 K (right) for the reference GaN sample (triangles) and two Gd:GaN films with  $1 \times 10^{16}/\text{cm}^3$  of Gd (circles) and the sample from Fig. 6.3 (squares).

Figure adapted from Ney, A., 2010. Element specific versus integral structural and magnetic properties of Co:ZnO and Gd:GaN probed with hard X-ray absorption spectroscopy. *Materials* 3, 3565–3613, <http://dx.doi.org/10.3390/ma3063565>.

It is obvious that even at very low temperatures the magnetic polarization at remanence is rather small if present at all and it increases with the external magnetic field in a Brillouin-like fashion. Furthermore, Sapega et al. (2005) report that the polarization decreases rapidly with increasing temperature. Therefore the magnetic properties as seen by the ( $D^0;X$ ) transition, that is, the oxygen-affected part of the band structure of GaN:Gd, is of PM character and therefore cannot account for the  $M(H)$  and  $M(T)$  behavior at 300 K. More generally speaking, Fig. 6.4 provides indirect experimental evidence that magnetically active oxygen cannot be the origin of either the colossal magnetic moments or the ferromagnetism. It also represents a first hint that the Gd may actually behave paramagnetically in this type of sample. Turning back to Fig. 6.3, only the difference between the  $M(H)$  curve at 2 K and at 300 K may originate from Gd, while the remaining larger fraction of the magnetic signal would have to be associated with the constant additional magnetic moment inferred by Roever et al. (2011), which was previously invoked by the heuristic model of magnetically polarized spheres of influence by Dhar et al. (2005a).

### 6.3.2 Gd ion-implanted wurtzite molecular beam epitaxy GaN:Gd/Si(0001)

Another elegant way of disentangling the origin of the colossal magnetic moments in GaN:Gd is the use of ion implantation. This opens the possibility to measure a pristine piece of GaN before and after implantation to minimize the risk of unintentional



**Figure 6.5**  $M(H)$  curves (left) of unimplanted MBE-grown GaN/SiC(0001) (circles) and after implantation of  $1 \times 15 \text{ Gd}^{3+}/\text{cm}^2$  (squares) measured at 300 K (full symbols) and 2 K (open symbols) after subtraction of the diamagnetic background. Here the magnetic signal is not divided by the sample volume. The corresponding  $M(T)$  curves under FC (full squares) and ZFC (open squares) of the implanted sample are shown in the middle. The X-ray diffraction (right) reveals the development of a pronounced shoulder at the low angle side (arrow) of the GaN(0002) reflection.

Reanalysis of data from Dhar, S., Kammermeier, T., Ney, A., Pérez, L., Ploog, K.H., Melnikov, A., Wieck, A.D., 2006. Ferromagnetism and colossal magnetic moment in Gd-focused ion-beam-implanted GaN. *Appl. Phys. Lett.* 89, 062503, <http://dx.doi.org/10.1063/1.2267900>.

magnetic contamination of the sample. For such an experiment (Dhar et al., 2006), an undoped 600 nm thick wurtzite GaN film has been grown by ammonia-assisted MBE directly on SiC(0001). In Fig. 6.5 (left) the  $M(H)$  curves (gray circles) of the unimplanted sample are shown for 300 K (open circles) and 2 K (closed circles). From the data it is obvious that hardly any magnetic signal is present at 300 K while a clear PM-like signal can be detected at 2 K. This signal is most likely caused by PM impurities in the SiC substrate as well as unintentional PM defects in the GaN layer. The latter should represent a negligible contribution, since high purity Ga sources were used and the volume of the substrate is by about three orders of magnitude larger than that of the GaN layer. Fig. 6.5 also shows the basic structural properties of the layer before implantation (gray line, right) evidencing that the wurtzite GaN grows c-oriented with very good crystalline quality.

Subsequently, the GaN layer was focused on an ion-beam implanted with  $\text{Gd}^{3+}$  ions with 300 keV kinetic energy and a dose of  $1 \times 10^{15}/\text{cm}^2$  resulting in an average implantation depth of 100 nm and an average volume concentration of  $1 \times 10^{20} \text{ Gd}/\text{cm}^3$ . Note that this high Gd concentration did not lead to colossal effective magnetic moments, which were only found at much lower Gd doses. However, room-temperature FM-like signals were evidenced by SQUID for all three studied Gd doses (Dhar et al., 2006). Fig. 6.5 summarizes only the highest Gd fluence (black squares) with an FM-like  $M(H)$  signal at 300 K (left, full black squares) and a superposition of PM and FM-like behavior at 2 K (left, open squares). FC and ZFC curves are well separated up to 300 K (Fig. 6.5, middle), indicating robust magnetic order up to elevated temperatures.

The overall signal size at 300 K is around 15  $\mu\text{emu}$ , which is about five times as large as the sample handling artifacts as shown in Fig. 6.2 and thus the results were taken seriously.

The XRD of the implanted GaN:Gd sample with the highest dose is also shown in Fig. 6.5 (right). A clear shoulder toward smaller angles (ie, larger lattice spacing) is visible both for the GaN as well as the SiC reflection. These shoulders are characteristic for implantation-induced defects which obviously extend even into the substrate. In other words, the entire thickness of the GaN layer is structurally affected by the implantation process. This can be taken as an indication that the claimed FM originates from defects. However, Dhar et al. (2006) state that the two samples implanted at lower doses do not exhibit defect-related features in XRD. On the other hand, the magnetic signal of those samples was associated with colossal magnetic moments up to  $10^5 \mu_B$  and magnetic order up to 300 K. Thus it appears that both desirable magnetic properties are in fact not caused by the implantation-induced defects but merely existing in spite of these defects.

In the light of the preceding discussion it is obvious that the claims of colossal magnetic moments and the existence of room-temperature magnetic order is based only on SQUID magnetometry and colossal moments occur only in samples with very low Gd content, leading to the situation that a large magnetic moment is obtained when a small magnetic signal is divided by an extremely small number of Gd atoms. Although most of the error-bars provided in the original publications are rather small, we should keep in mind that these do not take into account effects that may influence the raw magnetic signal picked up by the SQUID, such as (1) the possible artifact level, which is admittedly difficult to be assessed on a meaningful quantitative basis and (2) the PM signal from substrate and GaN matrix, which also contribute to the saturation magnetization at 2 K, which is used to extract numbers for the effective magnetic moment per Gd atom (Dhar et al., 2005a,b, 2006). In the case of the highest Gd concentration the background signal (2) is already half of the total signal as visible in the way the data are presented in Fig. 6.5 (left). Besides these cautious considerations, the findings of Dhar et al. (2005a,b, 2006) sparked a lot of interest in the DMS community and many efforts were undertaken to understand the origin of these unusual magnetic properties and/or reproduce the results, which has led to a series of ion implantation experiments that will be briefly summarized in the following section.

## 6.4 Gd ion implantation into various GaN samples

The use of ion implantation to fabricate DMS materials has the advantage that the identical piece of sample can be measured before and after the implantation process, thus minimizing the risk of unintentional magnetic contamination. Note that the GaN/sapphire layer shown in Figs. 6.1 and 6.2 was actually a sample that was measured before Sm ion implantation (Lo et al., 2014) to assure magnetic cleanliness. Nonetheless even after ion implantation strict magnetic cleanliness has to be assured (see Section 6.2.2). The disadvantage is that the dopant concentration, which is achievable using ion implantation, is restricted to less than 1% to avoid complete amorphization of the

implanted layer. Therefore, these samples are difficult to study using XMCD since the absorption signal is usually too small to be sensed with sufficient statistics to record good quality dichroic spectra. In the case of the ion-implanted GaN:Gd films discussed later, measuring XMCD at the Gd  $L_3$ -edge to investigate element-selective magnetic properties was tried, but even at the highest implantation doses of  $1 \times 10^{15}/\text{cm}^2$ , which corresponds to a dopant concentration of 0.23% for typical implantation depths, the XANES was so small that a reliable XMCD could not be extracted. Therefore all GaN:Gd samples that were fabricated by ion implantation and presented in this section could only be investigated using SQUID except one sample where the anomalous Hall effect could be measured in addition.

#### 6.4.1 Gd ion implantation into zincblende MBE-grown GaN/SiC(001)

A 700 nm thick GaN layer was grown by MBE on a 3C-SiC(001) substrate at  $720^\circ\text{C}$ . Under this growth condition, the GaN layer grows in the zincblende structure as evidenced by XRD (Fig. 6.6, right, gray line). In contrast to the wurtzite GaN grown by MBE, which is highly resistive, the zincblende GaN layer is typically n-type, and the impurity concentration is around  $1 \times 10^{18}/\text{cm}^3$  (Lo et al., 2007). The sample was then cut into pieces, one of which was kept unimplanted as a reference, and the others were implanted with  $\text{Gd}^{3+}$  ions at RT with constant ion energy of 300 keV. The doses presented here were  $1 \times 10^{14}/\text{cm}^2$  and  $1 \times 10^{15}/\text{cm}^2$  and the projected range of the Gd ion

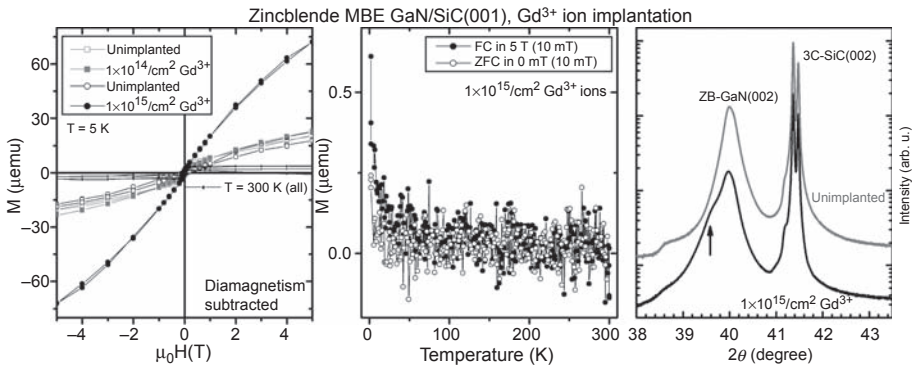


**Figure 6.6**  $M(H)$  curves (left) of cubic GaN/SiC at 5 K before (*open symbols*) and after (*full symbols*) implantation of  $1 \times 10^{14}$   $\text{Gd}^{3+}/\text{cm}^2$  (*gray squares*) and  $1 \times 10^{15}$   $\text{Gd}^{3+}/\text{cm}^2$  (*black circles*) after subtraction of the diamagnetic background. The  $M(T)$  curves (middle) reveal no significant separation between FC (*full circles*) and ZFC (*open circles*) conditions, thus demonstrating paramagnetic behavior. The X-ray diffraction (right) reveals the development of a pronounced shoulder at the low angle side (*arrow*) of the GaN(002) reflection.

Parts of the data are adapted from Lo, F.-Y., Melnikov, A., Reuter, D., Wieck, A.D., Ney, V., Kammermeier, T., Ney, A., Schörmann, J., Potthast, S., As, D.J., Lischka, K., 2007. Magnetic and structural properties of Gd-implanted zinc-blende GaN. *Appl. Phys. Lett.* 90, 262505, <http://dx.doi.org/10.1063/1.2753113>.

in the samples is 100 nm (Lo et al., 2007). This results in an average Gd concentration in the sample of  $1 \times 10^{19}/\text{cm}^3$  and  $1 \times 10^{20}/\text{cm}^3$ , the latter corresponding to a Gd concentration of 0.23%. All samples were measured using SQUID and the resulting M(H) curves at 5 K are shown in Fig. 6.6, left, before (open symbols) and after (full symbols) implantation for the low (gray squares) and high (black circles) Gd concentration. It can be clearly seen that the unimplanted samples exhibit PM behavior that is a bit weaker than for the implanted wurtzite films (Fig. 6.5, left), which presumably stems from unintentional PM impurities in the substrate as well. The implantation of  $1 \times 10^{14}$  Gd/cm<sup>2</sup> does not lead to a significant increase of the PM signal. Only for the dose of  $1 \times 10^{15}$  Gd/cm<sup>2</sup> is a clear increase of the magnetization visible. Nonetheless, no significant opening of a hysteresis is visible.

The absence of FM or SPM is further evidenced by the M(T) curves recorded under FC (full circles) and ZFC (open circles) conditions shown in Fig. 6.6, middle, where no separation between the two curves is visible beyond the noise level of the experiment. However, the XRD of the highest Gd dose shown in Fig. 6.6, right (black line), shows that a Gd-implantation related shoulder at the GaN (002) reflex develops, which is similar to the one seen in the wurtzite sample but less pronounced, which again can be associated with the creation of defects. While Lo et al. (2007) presented M(T) data indicative of a weak separation of FC and ZFC curves below 60 K, the measurements shown in Fig. 6.6, middle, were recorded with a much higher point density and they do not confirm the original observation. Therefore we can conclude that Gd implantation into zincblende GaN does not lead to anything but a PM behavior of the implanted Gd atoms and the creation of implantation-related defects evidenced by XRD.

Lo et al. (2007) attributed the absence of strong magnetic order in the nonpolar zincblende GaN as an indication that the spontaneous polarization in the polar wurtzite GaN may play a decisive role for the magnetic order. This would be also consistent with the fact that the zincblende GaN layer is more conductive than the wurtzite GaN layer. On the other hand, the difference between the implantation series into wurtzite and zincblende GaN is that for the latter each piece was measured before and after ion implantation while in the former only one of the implanted pieces was measured in the SQUID prior to the implantation and no unimplanted reference was kept. It is therefore a theoretical possibility that the findings for the Gd implantation of the wurtzite GaN may be at least partially associated with unintentional magnetic contamination of the measured pieces. For this reason further Gd implantation series have been carried out for wurtzite GaN.

#### **6.4.2 Gd ion implantation into wurtzite molecular beam epitaxy grown GaN/Si(111)**

Shvarkov et al. (2014) presented a comprehensive study on the magnetic properties of Gd-doped GaN, which comprises a range of different fabrication methods including a good summary of results from the literature, which shall not be summarized here. In the context of the Gd ion implantation of GaN layers only two results shall be highlighted in this and the preceding section. First a concentration series of



Gd ion implantation into MBE-grown wurtzite GaN films on Si(111) substrates shall be presented. The entire series exactly reproduces the series of Dhar et al. (2006) regarding implantation conditions, Gd doses, and the absence of any annealing treatment. The only discrepancy is the chosen substrate, namely Si(111) instead of SiC(0001) (Shvarkov et al., 2014). Since XRD data have neither been published nor are accessible to the author, Fig. 6.7 only summarizes the M(H) SQUID data of the concentration series (left) as published by Shvarkov et al. (2014), as well as M(T) curves recorded under FC and ZFC conditions for the highest Gd concentration (right).

It can be seen from Fig. 6.7, that the unimplanted reference is magnetically very clean, showing only a maximum PM signal of less  $1 \mu\text{emu}$  at 5 K. The Gd ion implantation does not alter the magnetic signal significantly for the two lower doses of  $1 \times 10^{13}/\text{cm}^2$  and  $1 \times 10^{14}/\text{cm}^2$ , which is similar to the findings of the implantation series of the zincblende GaN layers (see Fig. 6.6, left). Only the highest Gd dose of  $1 \times 10^{15}/\text{cm}^2$  yields a sizable PM signal, which could be shown to be well described by a Brillouin function for  $S = 7/2$  (Shvarkov et al., 2014, Fig. 6.6). In addition, the absence of any significant separation between FC and ZFC M(T) curves in Fig. 6.7, right, underlines that the implantation of Gd only leads to PM properties, which is in stark contrast to the findings of Dhar et al. (2006). At first glance it may be tempting to attribute this discrepancy to the choice of the substrate, however, a wurtzite MBE-grown GaN layer should exhibit the same magnetic properties upon Gd ion implantation no matter whether it has been grown on SiC(0001) or Si(111). A discussion of an altered strain state of the layers can also be disregarded considering the typical

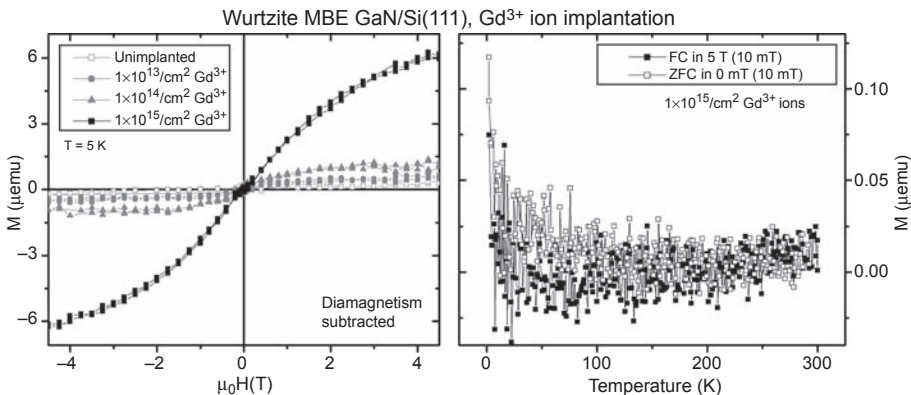


**Figure 6.7** M(H) curves (left) of a Gd ion implantation series of GaN/Si(111) at 5 K after subtraction of the diamagnetic background. Only for the highest Gd dose of  $1 \times 10^{15}/\text{cm}^2$  (black squares) is a significant paramagnetic response visible. The M(T) curves (right) under FC (full squares) and ZFC (open squares) conditions reveal no separation and are indicative of the absence of any long-range magnetic order.

Figure adapted from Shvarkov, S., Ludwig, A., Wieck, A.D., Cordier, Y., Ney, A., Hardtdegen, H., Haab, A., Trampert, A., Ranchal, R., Herfort, J., Becker, H.-W., Rogalla, D., Reuter, D., 2014. Magnetic properties of Gd-doped GaN. Phys. Status Solidi B 251, 1673–1684, <http://dx.doi.org/10.1002/pssb.201350205>.

layer thicknesses of a few hundred nanometers. Only the intrinsic growth-related defects of the GaN layer may serve as an explanation; however, after ion implantation, the resulting layer is much more defective than before so that this explanation also appears to be unlikely. The only difference is that Si is magnetically much cleaner in terms of PM impurities than SiC and also much softer and thus easier to be cleaved with less risk of unintentional magnetic contaminations.

Further insight may be gained by a more quantitative analysis of the unimplanted and Gd ion-implanted MBE wurtzite GaN samples on SiC(0001) (Fig. 6.5, left) and on Si(111) (Fig. 6.7, left). In both samples the same amount of Gd ion has been implanted and the difference between the maximum magnetization at 4.5 T is about 30  $\mu\text{emu}$  for the former and only 5  $\mu\text{emu}$  for the latter case. If we disregard the residual magnetic signal of 15  $\mu\text{emu}$  at 300 K, we would have to explain a discrepancy of a factor of 6 in magnetic moment of the Gd. However, if we assume that the signal of 15  $\mu\text{emu}$  at 300 K in Fig. 6.5, left, stems from unintentional magnetic contaminations, the difference between the unimplanted and Gd ion-implanted samples reduces to 15  $\mu\text{emu}$ ; therefore only a factor of 3 has to be explained compared to the sample on Si (111). This discrepancy can be made plausible by small differences in the sample area as well as the higher measurement temperature of 5 K compared to 2 K for the sample on SiC(0001). Either way, the magnetization at 300 K for the Gd ion-implanted GaN/SiC(0001) cannot be directly associated with the Gd itself but only with either a magnetic polarization of the GaN, which persist up to RT or unintentional magnetic contamination. In any case this brief discussion shall underline the difficulties in making SQUID magnetometry a reliable quantitative measure of magnetic moments in multiconstituent samples like DMS layers grown on a substrate.

### 6.4.3 *Gd ion implantation into wurtzite molecular beam epitaxy grown GaN/AlGaIn-based HEMT on Si(111)*

Shvarkov et al. (2014) also report an investigation of Gd ion implantation into a GaN/AlGaIn-based high electron mobility transistor (HEMT) grown by MBE on Si(111) to follow up on earlier work that tried to record the anomalous Hall effect to prove or disprove the existence of FM in such systems by an independent experimental evidence beyond SQUID. Details of the experiment can be found in the original publication (Shvarkov et al., 2014). For the purpose of this chapter Fig. 6.8 summarizes the most important findings. The SQUID investigation of a wurtzite MBE-grown GaN/AlGaIn HEMT on Si(111) is reported before (gray circles) and after Gd ion implantation with a dose of  $3 \times 10^{11}/\text{cm}^2$  (black squares). The  $M(H)$  curves at 300 K (full symbols) and 5 K (open symbols) are shown in Fig. 6.8, left, and it can be seen that the implantation of a small dose of Gd ions leads to a weak PM signal that is superimposed to a temperature-independent background signal, which is also found in the unimplanted sample. The  $M(T)$  curves under FC and ZFC conditions are displayed in Fig. 6.8, middle, and a weak increase of the magnetization can be seen. In addition, the weak separation between FC and ZFC, which is visible up to about 150 K, can be found both in the unimplanted as well as in the Gd ion-implanted sample. In addition, Fig. 6.8 includes anomalous Hall effect data (transversal magnetoresistivity, right) of a comparable



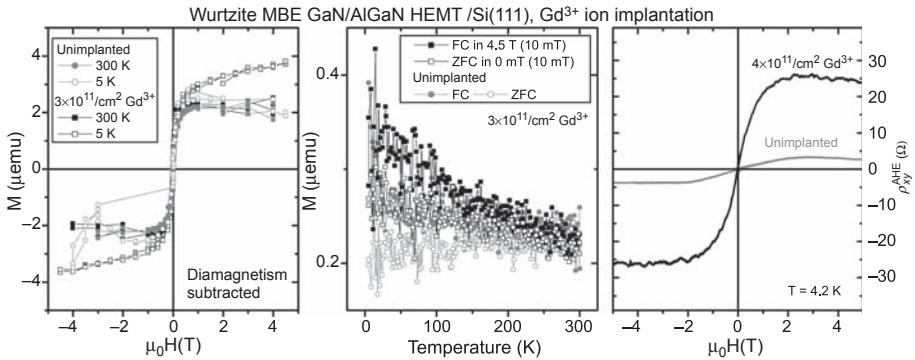


**Figure 6.8**  $M(H)$  curves (left) for the unimplanted GaN grown on a GaN/AlGaIn-based HEMT on Si(111) (gray circles) and the sample implanted with a dose of  $3 \times 10^{11} \text{ Gd}^{3+}/\text{cm}^2$  (black squares) measured at 300 K (full symbols) and 5 K (open symbols). Upon Gd implantation only an additional paramagnetic signal is visible. The comparison of  $M(T)$  curves (middle) under FC (full symbols) and ZFC (open symbols) of the unimplanted (gray circles) and Gd ion-implanted sample (black squares) reveals no significant change of the magnetic behavior upon ion implantation except a small paramagnetic contribution. Paramagnetism is confirmed by transversal magnetoresistivity  $\rho_{xy}$  measurements (right) as function of  $H$  after subtraction of the linear part for the unimplanted (gray line) and the sample implanted with  $4 \times 10^{11} \text{ Gd}^{3+}/\text{cm}^2$  (black line).

Figure adapted from Shvarkov, S., Ludwig, A., Wieck, A.D., Cordier, Y., Ney, A., Hardtdegen, H., Haab, A., Trampert, A., Ranchal, R., Herfort, J., Becker, H.-W., Rogalla, D., Reuter, D., 2014. Magnetic properties of Gd-doped GaN. *Phys. Status Solidi B* 251, 1673–1684, <http://dx.doi.org/10.1002/pssb.201350205>.

sample implanted with  $4 \times 10^{11} \text{ Gd}/\text{cm}^3$  recorded at 4.2 K, which was derived after subtraction of the linear contribution from the classical ordinary Hall effect (Shvarkov et al., 2014). Already in the unimplanted sample a small nonlinear contribution is visible, which becomes much more pronounced upon Gd implantation. However, the resulting field dependence does not show any evidence of a hysteretic behavior and a shape characteristic of a PM. Since also no magnetoresistance is detected in these samples (Shvarkov et al., 2014, Fig. 6.12) the findings of the magneto-transport investigations are consistent with the results obtained by SQUID and no experimental evidence is found for FM at any temperature. Thus the findings on the Gd-implanted GaN/AlGaIn-based HEMT corroborate the findings for the Gd-implanted GaN layers on Si(111) as presented in Fig. 6.7.

#### 6.4.4 Discussion of the magnetic properties of Gd-implanted GaN samples

It should be noted that there are also other reports of FM in Gd-implanted GaN grown by MOCVD. Han et al. (2006) report room-temperature FM for Gd-implanted GaN with doses up to  $\sim 4 \times 10^{14} \text{ Gd}/\text{cm}^2$ . However, they do not report the existence of colossal magnetic moments. The presented data of Han et al. (2006, Fig. 6.3(b))

look rather similar as the ones shown in Fig. 6.3, left—a strong S-shaped  $M(H)$  curve with a narrow hysteresis is found at 300 K and a small PM-like contribution is superimposed at low temperatures. These findings were critically discussed within the original work, also again with the possibility of the formation of secondary phases. However, no SQUID data are shown for an unimplanted reference sample. A second claim of FM of Gd-implanted MOCVD GaN is made by Davies et al. (2010). They report a strongly anisotropic FM, in fact, the samples seem to exhibit FM at 300 K when measured parallel to the surface normal of the  $c$ -oriented films while they essentially show no magnetic signature when measured in the film plane (Davies et al., 2010, Fig. 6.2). Interestingly, the reported magnetization is by far smaller ( $5 \times 10^{-4}$  emu/cm<sup>3</sup>) than those of Dhar et al. (2006), who find  $\sim 4$  emu/cm<sup>3</sup>. This discrepancy of four orders of magnitude obviously cannot be assigned to very different sample volumes. Unfortunately, although Davies et al. (2010) report to have measured the samples up to 5 T, only data between +100 mT and -100 mT are shown. If we would try to estimate the size of the raw signal measured by the SQUID by using a typical sample volume, we would end up with tiny signals of the order of  $10^{-9}$  to  $10^{-10}$  emu, far below the manufacturer's specifications of the MPMS SQUID magnetometer. In addition, the paper does not report details of the used sample geometry or sample mounting for the in-plane versus out-of-plane measurements, which is typically a nontrivial problem (Sawicki et al., 2011). Therefore the situation for Gd-implanted GaN samples remain inconclusive and speculative.

No experimental evidence for FM is provided beyond SQUID magnetometry and the understanding of the data on a quantitative basis remains awkward in most cases. In a few reports, only PM behavior of the implanted Gd ions is evidenced and corroborated by anomalous Hall effect measurements (Shvarkov et al., 2014). Therefore it remains unclear how to explain the differences in the magnetic properties in the various Gd-implanted GaN samples reported so far and thus to unravel the microscopic origin of the strong FM signatures found in these samples.

Summarizing this section, the confirmation of the original claims made by Dhar et al. (2005a,b, 2006) was only presented by Roever et al. (2008) for MBE-grown samples; however, with reproducibility issues and time-dependent effects (Roever et al., 2011). In contrast, the situation in Gd-implanted samples remains controversial and inconclusive, since the typical Gd concentrations in implanted samples are too low to be studied by element-selective methods, only a set of MBE-grown GaN:Gd samples can be used for a detailed investigation using XANES, XLD, and XMCD.

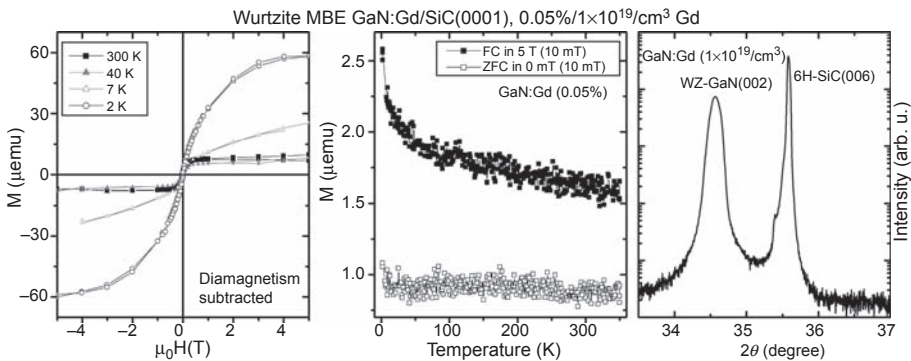
## 6.5 Synchrotron-based investigations on molecular beam epitaxy grown GaN:Gd

To assure sufficiently high Gd concentrations that facilitate synchrotron-based investigations a selection of three samples will be discussed: one sample contains 0.05% of Gd and was grown by ammonia-assisted MBE on SiC(0001) together with the sample series presented in Fig. 6.3. The two other samples were grown by plasma-assisted MBE on an MOVPE-grown GaN buffer on  $c$ -sapphire substrates;

one contains  $\sim 0.4\%$  Gd and the other has a slightly smaller Gd concentration of  $\sim 0.15\%$  but it was codoped with hydrogen.

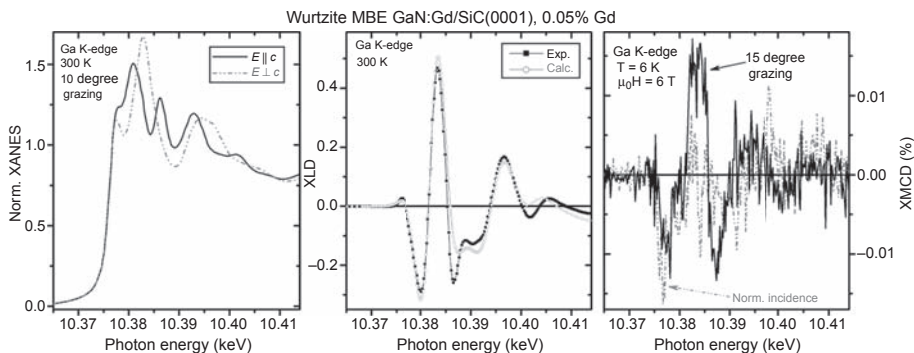
### 6.5.1 Molecular beam epitaxy GaN:Gd on SiC(0001)

Fig. 6.9 compiles a summary of the standard characterization of the magnetic and structural properties of the GaN:Gd sample grown by ammonia-assisted MBE on SiC(0001) containing 0.05% ( $\sim 2 \times 10^{19}/\text{cm}^3$ ) of Gd using SQUID and XRD, respectively. The  $M(H)$  curves (Fig. 6.9, left) have a clear S-shape at 300 K and in addition a PM-like signal is superimposed at 2 K, which is decreasing very fast with temperature: already at 40 K the data are virtually identical to the ones at 300 K. The  $M(T)$  curves (middle) show a separation between FC and ZFC curves, which indicates long-range magnetic order up to at least 350 K. XRD (right) confirms the good crystalline quality of the layer, and the defect-related shoulders as seen for the ion-implanted samples is absent. Thus this sample seems to perfectly fit into the series of room-temperature FM in GaN:Gd specimen grown by ammonia-assisted MBE on SiC(0001) (Dhar et al., 2005a,b). In this sample the Gd concentration is sufficiently large to record reliable XANES and thus the XLD and XMCD at the Gd  $L_3$ -edge. Therefore, the local structural and magnetic properties not only of the Ga but also of the Gd subspecies can be investigated in this sample (Ney et al., 2007, 2008). Fig. 6.10 (left) displays the Ga K-edge XANES recorded with the linear polarization of the synchrotron light parallel



**Figure 6.9**  $M(H)$  curves (left) of MBE-grown GaN:Gd/SiC(0001) with 0.05% Gd measured at 300 K (full squares), 40 and 7 K (open and full gray triangles), and 2 K (open circles) after subtraction of the diamagnetic background. The corresponding  $M(T)$  curves under FC (full squares) and ZFC (open squares) are shown in the middle revealing a clear separation up to 350 K. The X-ray diffraction (right) of a comparable sample with  $1 \times 10^{19}$  Gd/cm $^3$  indicates a good crystalline quality via the GaN(002).

Parts of the data are adapted from Ney, A., Kammermeier, T., Manuel, E., Ney, V., Dhar, S., Ploog, K.H., Wilhelm, F., Rogalev, A., 2007. Element specific investigations of the structural and magnetic properties of Gd:GaN. Appl. Phys. Lett. 90, 252515, <http://dx.doi.org/10.1063/1.2750542>; Dhar, S., Pérez, L., Brandt, O., Trampert, A., Ploog, K.H., Keller, J., Beschoten, B., 2005b. Gd-doped GaN: a very dilute ferromagnetic semiconductor with a Curie temperature above 300 K. Phys. Rev. B 72, 245203, <http://dx.doi.org/10.1103/PhysRevB.72.245203>.



**Figure 6.10** XANES (left) spectra recorded at the Ga K-edge of the sample in Fig. 6.9 recorded at 300 K with the E-vector of the linear polarized synchrotron light parallel (*solid line*) and perpendicular (*dash-dotted line*) to the *c*-axis of the wurtzite crystal. The resulting XLD signal is shown in the middle together with the simulated spectrum from Ney et al. (2007). The respective XMCD signal at the Ga K-edge (right) is recorded with circular light at 6 T and 6 K under grazing and normal incidence revealing only a very weak magnetic polarization of the Ga.

Adapted from Ney, A., Kammermeier, T., Manuel, E., Ney, V., Dhar, S., Ploog, K.H., Wilhelm, F., Rogalev, A., 2007. Element specific investigations of the structural and magnetic properties of Gd:GaN. *Appl. Phys. Lett.* 90, 252515, <http://dx.doi.org/10.1063/1.2750542>; Ney, A., Kammermeier, T., Ney, V., Ye, S., Ollefs, K., Manuel, E., Dhar, S., Ploog, K.H., Arenholz, E., Wilhelm, F., Rogalev, A., 2008. Element specific magnetic properties of Gd-doped GaN: very small polarization of Ga and paramagnetism of Gd. *Phys. Rev. B* 77, 233308, <http://dx.doi.org/10.1103/PhysRevB.77.233308>.

(full line) and perpendicular (dash-dotted line) to the *c*-axis of the GaN wurtzite crystal. The difference of the two spectra is the XLD, which reflects the local anisotropy of the unoccupied final states of the Ga. These spectra could be successfully simulated using the known structural parameters of bulk-like GaN (Ney et al., 2007). In addition, also the XMCD at the Ga K-edge was recorded at 6 K and 6 T (Fig. 6.10, right). XMCD at the Ga K-edge directly probes the  $4p$  orbital contribution to the total magnetic moment of the Ga and thus the magnetic polarization of the host crystal. A very small XMCD signal of the order of 0.013% at the Ga K-edge for 15-degree grazing and normal incidence can be detected (Ney et al., 2008). From a more quantitative analysis we can associate the size of the XMCD signal with magnetic moment of at most  $1 \times 10^{-5} \mu_B/\text{Ga atom}$  (Ney et al., 2008). This is significantly smaller than the polarization of  $\sim 1 \times 10^{-3} \mu_B$  inferred by the magnetically polarized spheres of influence (Dhar et al., 2005a). Note that for these Gd concentrations the model by Dhar et al. (2005a) would predict the entire sample to be filled by spheres of influence, the maximum possible magnetic polarization of the GaN host crystal. Therefore the magnetic signal recorded by integral SQUID magnetometry cannot be attributed to the magnetic polarization of the Ga. Together with the null result of the magneto-PL (Fig. 6.4), we have to conclude that the integral magnetic signal recorded by SQUID cannot be caused by a magnetic polarization of the GaN host.

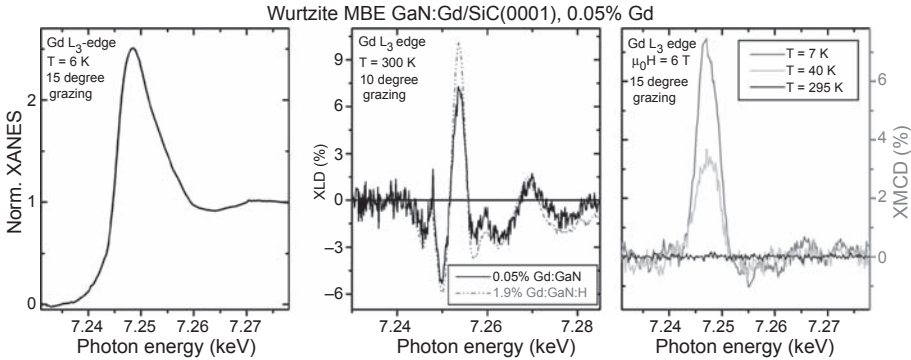


**Figure 6.11** XANES (left) spectra recorded at the Gd  $L_3$ -edge of the sample in Figs. 6.9 and 6.10. The size and shape of the XLD signal at 300 K (middle) is indicative of  $\sim 85\%$  of the Gd substituting for Ga (Ney et al., 2007) and is displayed together with the hydrogen-codoped sample of Fig. 6.13. The XMCD spectrum at the Gd  $L_3$ -edge (right) is recorded with circular light at 6 T under grazing incidence at 7 K (gray line) and 40 K (light gray line). No XMCD can be recorded at 295 K (dark gray line), which demonstrates that the SQUID signal at 300 K does not originate from the Gd itself.

Data adapted from Ney, A., 2010. Element specific versus integral structural and magnetic properties of Co:ZnO and Gd:GaN probed with hard X-ray absorption spectroscopy. Materials 3, 3565–3613, <http://dx.doi.org/10.3390/ma3063565>.

Fig. 6.11 (left) shows the XANES recorded at the Gd  $L_3$ -edge as well as the XLD (middle) of this sample together with the hydrogen-codoped sample, which will be discussed further, later. Simulations have indicated that the size of the XLD can be associated with the fact that  $\sim 15\%$  of the Gd does not substitute for Ga (Ney et al., 2007) and thus may form secondary phases. A clear XMCD can be recorded at the Gd  $L_3$ -edge at 7 and 40 K (Fig. 6.11, right). In contrast, no sizable XMCD is found at 295 K. Therefore the Gd sublattice cannot be responsible for the SQUID signal at more elevated temperatures. A more quantitative analysis reveals that the maximum XMCD signal at 7 K of about 7% only corresponds to the atomic moment of  $\sim 8 \mu_B/\text{Gd}$  (Ney et al., 2007). This corroborates the findings of Dhar et al. (2005a) and Roever et al. (2011), that the Gd indeed carries its atomic magnetic moment in these samples. However, a closer inspection of the element-selective XMCD(H) curves in Fig. 6.12 reveals slight deviations from an ideal PM behavior. In Fig. 6.12 (left) the XMCD(H) curves recorded at the Gd  $L_3$  edge at 7 and 40 K are shown, and reveal a hysteretic PM-like behavior corroborated by the data shown in the inset, where the low-field regime was measured at 15 K. The magnetic behavior of the Gd sublattice is obviously clearly distinct from the integral magnetization measurements by SQUID shown in Fig. 6.9 (left). The XMCD(H) curves at 7 K (middle) and 40 K (right) cannot be fitted by a single Brillouin function  $B_J$  (Ney et al., 2007). Only a superposition of  $B_J$  with  $J = 7/2$  and a Langevin function  $L_\mu$  with an effective moment of  $50 \mu_B$  can successfully describe the data at both temperatures, where the best fit is achieved for 85% of the atomic-like  $B_J$  contribution and 15% of Gd being present as SPM clusters, hence exhibiting a small supermoment consistent with the XLD findings (Ney, 2010).

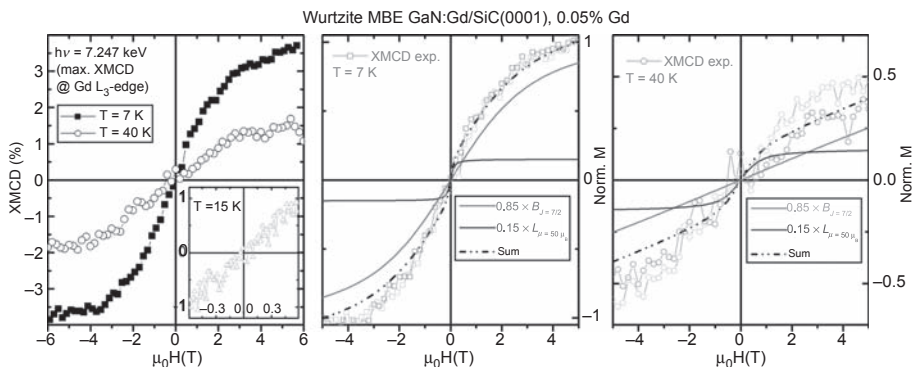


**Figure 6.12** XMCD(H) curves (left) recorded at the Gd  $L_3$ -edge at 7 K (*full squares*) and 40 K (*open circles*). The inset reveals anhysteretic behavior at 15 K. Modeling (see text for details) of the XMCD  $M(H)$  curves (*gray open symbols*) using a superposition of a Brillouin ( $B_J$ ) and a Langevin ( $L_M$ ) function at 7 K (middle) and 40 K (right).

Data adapted from Ney, A., 2010. Element specific versus integral structural and magnetic properties of Co:ZnO and Gd:GaN probed with hard X-ray absorption spectroscopy. *Materials* 3, 3565–3613, <http://dx.doi.org/10.3390/ma3063565>.

Since the Curie temperature of GdN is around 60 K, phase separate GdN clusters can only account for the low temperature part of the separation of the FC versus ZFC curves in Fig. 6.9 (middle). Further, the  $T_C$  of metallic Gd is around 291 K. Therefore also small SPM metallic Gd clusters cannot account for the clear separation in the  $M(T)$  curves, which persists up to at least 350 K. Although secondary phases were indirectly evidenced by a quantitative analysis of the element-specific XMCD(H) curves and a reduced XLD, they do not provide a satisfactory explanation of the SQUID data. Also a magnetic polarization of the Ga as measured by XMCD (Fig. 6.10, right) or the O-related defects as measured by magneto-PL (Fig. 6.4) do not reveal an alternative explanation. The same is true for additional investigations using electron PM resonance (Ney, 2010). Therefore the origin of the weak separation of the  $M(T)$  curves under FC and ZFC conditions in Fig. 6.9 (middle) of only  $0.6 \mu\text{emu}$  remains unclear. At present either an artifact from improper sample handling or directly from the superconducting magnet of the SQUID may be the most likely explanation. No additional experimental evidence beyond SQUID for the existence of FM at and above 300 K has been reported.

### 6.5.2 PAMBE GaN:Gd grown on MOCVD GaN buffer on $\text{Al}_2\text{O}_3(0001)$

Finally two GaN:Gd samples shall be discussed, where the combined structural and magnetic characterization leads to a conclusive picture. Fig. 6.13 summarizes the characterization of a GaN:Gd sample with 0.15% Gd doping an additional hydrogen codoping to improve the growth and thus the phase purity of the resulting layer. The SQUID measurements of the  $M(H)$  (left) and  $M(T)$  curves (middle) clearly reveal pure PM



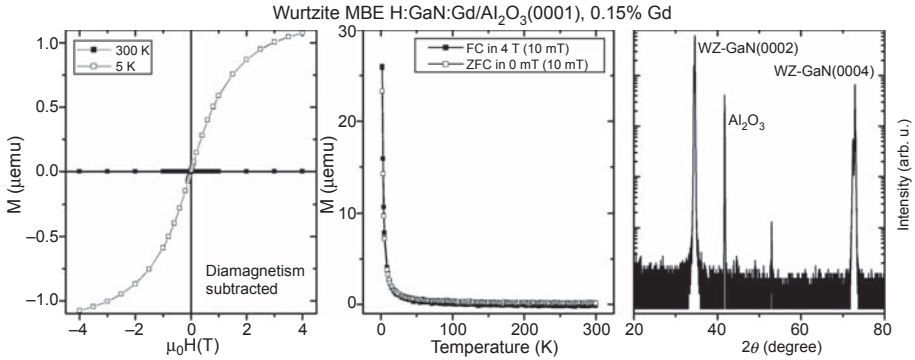


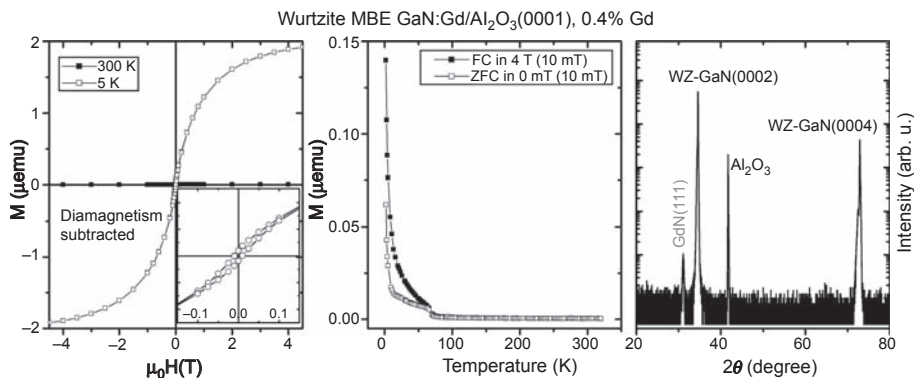
**Figure 6.13**  $M(H)$  curves (left) of MBE-grown H:GaN:Gd/GaN/sapphire with 0.15% Gd measured at 300 K (*full squares*) and 2 K (*open squares*) after subtraction of the diamagnetic background. The corresponding  $M(T)$  curves under FC (*full squares*) and ZFC (*open squares*) are shown in the middle revealing paramagnetism. The wide-angle X-ray diffraction (right) indicates a good crystalline quality and no secondary phases.

Data adapted from Ney, A., 2010. Element specific versus integral structural and magnetic properties of Co:ZnO and Gd:GaN probed with hard X-ray absorption spectroscopy. *Materials* 3, 3565–3613, <http://dx.doi.org/10.3390/ma3063565>.

behavior of this sample and XRD (right) confirms the absence of any secondary phase. Note that the finite amount of PM impurities in the sapphire substrate lead to small deviations of the integral  $M(H)$  curves from an ideal Brillouin-like PM. However, the almost perfectly coinciding FC and ZFC curves underline the PM character of this sample.

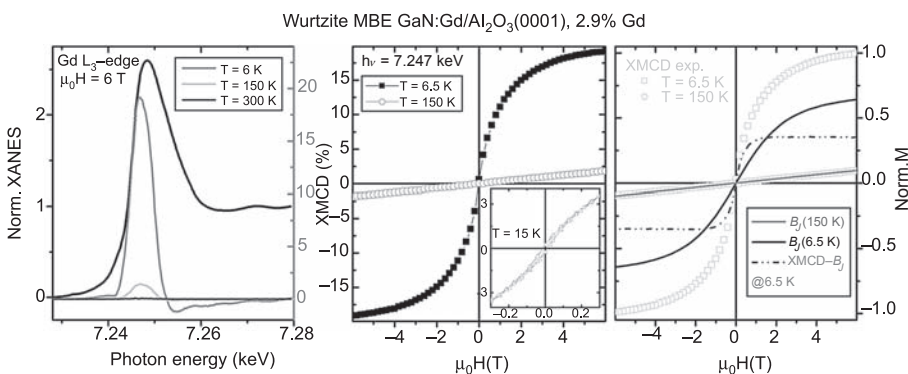
Fig. 6.14 shows another PAMBE-grown Ga:Gd layer on GaN/c-sapphire where no hydrogen codoping was done. In addition the Gd concentration was further increased to 0.4%. The resulting magnetic and structural properties are in stark contrast to the previous sample. The  $M(H)$  curves in Fig. 6.14 (left) show a much stronger curvature at 5 K and an opening of a small hysteresis at low magnetic fields (inset). The  $M(T)$  curves recorded under FC and ZFC conditions (middle) are clearly separated below  $\sim 60$  K, which is superimposed on a PM-like component. No separation is visible above  $\sim 60$  K consistent with the negligible  $M(H)$  signal at 300 K. The XRD investigation in Fig. 6.14 (right) evidences the formation of a secondary crystallographic phase, which is identified to be GdN. Given the  $T_C$  of GdN these two results consistently point toward GdN as secondary phase in this sample.

Fig. 6.15 presents a more quantitative analysis using the element-selective XMCD( $H$ ) curves recorded at the Gd  $L_3$ -edge. The XMCD spectra recorded in an external field of 6 T at 6, 150, and 300 K at the Gd  $L_3$ -edge are shown in Fig. 6.15 (left). The maximum XMCD signal at 6 K is about 20%, thus exceeding the atomic moment of  $8 \mu_B/\text{Gd}$  in Fig. 6.11 (right). The XMCD is strongly reduced at 150 K and is not observable any more at 300 K. In Fig. 6.15 (middle) the  $M(H)$  curves recorded at 6 and 150 K are shown revealing PM-like behavior; however, the inset reveals a small magnetic hysteresis at 15 K, which is in agreement with the SQUID data.



**Figure 6.14**  $M(H)$  curves (left) of MBE-grown GaN:Gd/GaN/sapphire with 0.4% Gd measured at 300 K (*full squares*) and 2 K (*open circles*) after subtraction of the diamagnetic background. The inset reveals a small hysteresis at 15 K. The corresponding  $M(T)$  curves under FC (*full squares*) and ZFC (*open squares*) are shown in the middle revealing a separation below  $\sim 60$  K. The wide-angle X-ray diffraction (right) indicates a good crystalline quality of the GaN(0002) and an additional phase identified as GdN(111).

Data adapted from Ney, A., 2010. Element specific versus integral structural and magnetic properties of Co:ZnO and Gd:GaN probed with hard X-ray absorption spectroscopy. *Materials* 3, 3565–3613, <http://dx.doi.org/10.3390/ma3063565>.



**Figure 6.15** XANES and XMCD of the sample of Fig. 6.14 recorded at the Gd L<sub>3</sub>-edge at 6 T and various temperatures (left). XMCD( $H$ ) curves recorded at the Gd L<sub>3</sub>-edge at 6.5 K (*full squares*) and 150 K (*open circles*). The inset reveals weak hysteretic behavior at 15 K consistent with Fig. 6.14. Modeling (see text for details) of the XMCD( $H$ ) curves (*gray open symbols*) using the Brillouin function  $B_J$  (right).

Data adapted from Ney, A., 2010. Element specific versus integral structural and magnetic properties of Co:ZnO and Gd:GaN probed with hard X-ray absorption spectroscopy. *Materials* 3, 3565–3613, <http://dx.doi.org/10.3390/ma3063565>.



In Fig. 6.15 (right), two different contributions to the XMCD(H) curves at 6 K can be disentangled by the following procedure: Since at 150 K the sample is PM according to the SQUID  $M(T)$  results, an atomic-like magnetic moment can be assumed for all Gd atoms. Thus the  $M(H)$  curve at 150 K is modeled using  $B_J$  with  $J = S = 7/2$  (ie, an ideal Brillouin-like PM) and adjusted to the experimental XMCD  $M(H)$  data (gray line). From this fitted  $B_J$  the expected PM response at 6 K can be back-calculated (dark gray line in Fig. 6.15, right). The second magnetic contribution can thus be derived by subtracting the scaled Brillouin function ( $x*B_J = 7/2$  (6K)) from the XMCD(H) data. This difference is plotted as a dash-dotted line for  $x = 0.7$  in Fig. 6.15 (right). The resulting  $M(H)$  curve resembles a Langevin  $L_\mu$  function with an effective moment of  $\mu \sim 50 \mu_B$ , which can be associated with an SPM behavior of the phase separated GdN clusters. By using the element-selective XMCD(H) curves we can obviously try to quantify the fraction of the phase separated Gd in this sample to be  $\sim 30\%$ . In turn Fig. 6.15 (right) illustrates that a superposition of  $B_J$  and  $L_\mu$  can lead to an effective magnetization curve, which still resembles PM behavior. Only a careful inspection of the curvature of the  $M(H)$  curve together with a detailed temperature-dependent study yields a consistent picture. Note that such an analysis is much more meaningful when performed for element-selective magnetometry such as XMCD.

## 6.6 Summary of magnetic properties of GaN:Gd

This comprehensive overview on the magnetic and structural properties of a range of GaN:Gd samples prepared by different synthesis allows us to draw the following conclusions. The seemingly exceptional magnetic properties of GaN:Gd grown by ammonia-assisted MBE on SiC(0001) as measured by integral SQUID magnetometry cannot be confirmed by complementary experimental techniques such as magneto-PL or XMCD. The magnetic polarization of the Ga is by two orders of magnitude too small to account for the colossal effective magnetic moments; the Gd sublattice magnetization is PM and the magneto-PL is only indicative of PM as well. Furthermore, signs of the formation of secondary magnetic phases are found by a detailed quantitative analysis for two samples with a rather high Gd concentration grown via different MBE-based routes. Reproducibility issues as addressed by Roever et al. (2011) for a large series of PAMBE-grown GaN:Gd samples raise additional doubts that GaN:Gd is indeed a FM DMS material.

The absence of FM order in GaN:Gd is supported by a large set of Gd ion-implanted GaN samples grown on various substrates. Only in one case, namely for hexagonal MBE-grown GaN on SiC(0001), room-temperature FM with colossal magnetic moments is reported while in all other cases only PM is found for the as-implanted samples. In one case PM is corroborated by the anomalous Hall effect, via the magneto-transport properties. At first sight these findings may point toward a special role played by the SiC substrate. However, a critical inspection of the available results shows that the exceptional magnetic properties of GaN:Gd were exclusively measured by integral SQUID magnetometry and the absolute size of the measured magnetic moment of the actual

specimen is rather close in magnitude to experimental artifacts like unintentional magnetic contamination by improper sample handling or the special properties of the superconducting magnet used for conventional SQUID magnetometry.

It is therefore of utmost importance to base any claim of room-temperature FM in DMS materials on more than one experimental evidence. The presence of an especially small and narrow magnetic hysteresis in a SQUID experiment is necessary, but not a sufficient criterion for the existence of FM. The present findings for the GaN:Gd system may also explain in general, why hardly any spintronic device based on DMS materials operational at RT has been successfully demonstrated yet, despite numerous claims of room-temperature FM in DMS that can be found throughout the literature.

## References

- Abraham, D.W., Frank, M.M., Guha, S., 2005. Absence of magnetism in hafnium oxide films. *Appl. Phys. Lett.* 87, 252502. <http://dx.doi.org/10.1063/1.2146057>.
- Bedoya-Pinto, A., Malindretos, J., Roeber, M., Mai, D.D., Rizzi, A., 2009. Variable range hopping transport in ferromagnetic GaGdN epitaxial layers. *Phys. Rev. B* 80, 195208. <http://dx.doi.org/10.1103/PhysRevB.80.195208>.
- Bonanni, A., Kiecana, M., Simbrunner, C., Li, T., Sawicki, M., Wegscheider, M., Quast, M., Przybylinka, H., Navarro-Quezada, A., Jakiela, R., Wolos, A., Jantsch, W., Dietl, T., 2007. Paramagnetic GaN:Fe and ferromagnetic (Ga,Fe)N: the relationship between structural, electronic, and magnetic properties. *Phys. Rev. B* 75, 125210. <http://dx.doi.org/10.1103/PhysRevB.75.125210>.
- Bougeard, D., Ahlers, S., Trampert, A., Sircar, N., Abstreiter, G., 2006. Clustering in a precipitate-free GeMn magnetic semiconductor. *Phys. Rev. Lett.* 97, 237202. <http://dx.doi.org/10.1103/PhysRevLett.97.237202>.
- Dalpian, G.M., Wei, S.-H., 2005. Electron-induced stabilization of ferromagnetism in Ga<sub>1-x</sub>Gd<sub>x</sub>N. *Phys. Rev. B* 72, 115201. <http://dx.doi.org/10.1103/PhysRevB.72.115201>.
- Davies, R.P., Gila, B.P., Abernathy, C.R., Pearton, S.J., Stanton, C.J., 2010. Defect-enhanced ferromagnetism in Gd- and Si-coimplanted GaN. *Appl. Phys. Lett.* 96, 212502. <http://dx.doi.org/10.1063/1.3437085>.
- Dev, P., Xue, Y., Zhang, P., 2008. Defect-induced intrinsic magnetism in wide-gap III nitrides. *Phys. Rev. Lett.* 100, 117204. <http://dx.doi.org/10.1103/PhysRevLett.100.117204>.
- Dhar, S., Brandt, O., Ramsteiner, M., Sapega, V.F., Ploog, K.H., 2005a. Colossal magnetic moment of Gd in GaN. *Phys. Rev. Lett.* 94, 037205. <http://dx.doi.org/10.1103/PhysRevLett.94.037205>.
- Dhar, S., Pérez, L., Brandt, O., Trampert, A., Ploog, K.H., Keller, J., Beschten, B., 2005b. Gd-doped GaN: a very dilute ferromagnetic semiconductor with a Curie temperature above 300 K. *Phys. Rev. B* 72, 245203. <http://dx.doi.org/10.1103/PhysRevB.72.245203>.
- Dhar, S., Kammermeier, T., Ney, A., Pérez, L., Ploog, K.H., Melnikov, A., Wieck, A.D., 2006. Ferromagnetism and colossal magnetic moment in Gd-focused ion-beam-implanted GaN. *Appl. Phys. Lett.* 89, 062503. <http://dx.doi.org/10.1063/1.2267900>.
- Dietl, T., Ohno, H., Matsukara, F., Cibert, J., Ferrand, D., 2000. Zener model description of ferromagnetism in zinc-blende magnetic semiconductors. *Science* 287, 1019–1022. <http://dx.doi.org/10.1126/science.287.5455.1019>.
- Dietl, T., 2010. A ten-year perspective on dilute magnetic semiconductors and oxides. *Nat. Mater.* 9, 965–974. <http://dx.doi.org/10.1038/nmat2898>.

- Gohda, Y., Oshiyama, A., 2008. Intrinsic ferromagnetism due to cation vacancies in Gd-doped GaN: first-principles calculations. *Phys. Rev. B* 78, 161201(R). <http://dx.doi.org/10.1103/PhysRevB.78.161201>.
- Han, S.Y., Hite, J., Thaler, G.T., Frazier, R.M., Abernathy, C.R., Pearton, S.J., Choi, H.K., Lee, W.O., Park, Y.D., Zavada, J.M., Gwilliam, R., 2006. Effect of Gd implantation on the structural and magnetic properties of GaN and AlN. *Appl. Phys. Lett.* 88, 042102. <http://dx.doi.org/10.1063/1.2167790>.
- Hite, J.K., Frazier, R.M., Davies, R., Thaler, G.T., Abernathy, C.R., Pearton, S.J., Zavada, J.M., 2006. Effect of growth conditions on the magnetic characteristics of GaGdN. *Appl. Phys. Lett.* 89, 092119. <http://dx.doi.org/10.1063/1.2337082>.
- Hite, J.K., Allums, K.K., Thaler, G.T., Abernathy, C.R., Pearton, S.J., Frazier, R.M., Dwivedi, R., Wilkins, R., Zavada, J.M., 2008. Effects of proton irradiation on the magnetic properties of GaGdN and GaCrN. *New J. Phys.* 10, 055005. <http://dx.doi.org/10.1088/1367-2630/10/5/055005>.
- Liu, L., Yu, P.Y., Ma, Z., Mao, S.S., 2008. Ferromagnetism in GaN:Gd: a density functional theory study. *Phys. Rev. Lett.* 100, 127203. <http://dx.doi.org/10.1103/PhysRevLett.100.127203>.
- Lo, F.-Y., Melnikov, A., Reuter, D., Wieck, A.D., Ney, V., Kammermeier, T., Ney, A., Schörmann, J., Potthast, S., As, D.J., Lischka, K., 2007. Magnetic and structural properties of Gd-implanted zinc-blende GaN. *Appl. Phys. Lett.* 90, 262505. <http://dx.doi.org/10.1063/1.2753113>.
- Lo, F.-Y., Huang, C.-D., Chou, K.-C., Guo, J.-Y., Liu, H.-L., Ney, V., Ney, A., Shvarkov, S., Pezzagna, S., Reuter, D., Chia, C.-T., Chern, M.-Y., Wieck, A.D., Massies, J., 2014. Structural, optical, and magnetic properties of highly-resistive Sm-implanted GaN thin films. *J. Appl. Phys.* 116, 043909. <http://dx.doi.org/10.1063/1.4891226>.
- Mitra, C., Lambrecht, W.R.L., 2009. Interstitial-nitrogen- and oxygen-induced magnetism in Gd-doped GaN. *Phys. Rev. B* 80, 081202(R). <http://dx.doi.org/10.1103/PhysRevB.80.081202>.
- Ney, A., Kammermeier, T., Manuel, E., Ney, V., Dhar, S., Ploog, K.H., Wilhelm, F., Rogalev, A., 2007. Element specific investigations of the structural and magnetic properties of Gd:GaN. *Appl. Phys. Lett.* 90, 252515. <http://dx.doi.org/10.1063/1.2750542>.
- Ney, A., Kammermeier, T., Ney, V., Ye, S., Ollefs, K., Manuel, E., Dhar, S., Ploog, K.H., Arenholz, E., Wilhelm, F., Rogalev, A., 2008. Element specific magnetic properties of Gd-doped GaN: very small polarization of Ga and paramagnetism of Gd. *Phys. Rev. B* 77, 233308. <http://dx.doi.org/10.1103/PhysRevB.77.233308>.
- Ney, A., Opel, M., Kaspar, T.C., Ney, V., Ye, S., Ollefs, K., Kammermeier, T., Bauer, S., Nielsen, K.-W., Goennenwein, S.T.B., Engelhard, M.H., Zhou, S., Potzger, K., Simon, J., Mader, W., Heald, S.M., Cezar, J.C., Wilhelm, F., Rogalev, A., Gross, R., Chambers, S.A., 2010a. Advanced spectroscopic synchrotron techniques to unravel the intrinsic properties of dilute magnetic oxides: the case of Co:ZnO. *New J. Phys.* 12, 013020. <http://dx.doi.org/10.1088/1367-2630/12/1/013020>.
- Ney, A., Kammermeier, T., Ollefs, K., Ye, S., Ney, V., Kaspar, T.C., Chambers, S.A., Wilhelm, F., Rogalev, A., 2010b. Anisotropic paramagnetism of Co-doped ZnO epitaxial films. *Phys. Rev. B* 81, 054420. <http://dx.doi.org/10.1103/PhysRevB.81.054420>.
- Ney, A., 2010. Element specific versus integral structural and magnetic properties of Co:ZnO and Gd:GaN probed with hard X-ray absorption spectroscopy. *Materials* 3, 3565–3613. <http://dx.doi.org/10.3390/ma3063565>.
- Roever, M., Mai, D.-D., Bedoya-Pinto, A., Malindretos, J., Rizzi, A., 2008. Electron stabilized ferromagnetism in GaGdN. *Phys. Status Solidi C* 5, 2352–2354. <http://dx.doi.org/10.1002/pssc.200778560>.

- Roever, M., Malindretos, J., Bedoya-Pinto, A., Rizzi, A., Rauch, C., Tuomisto, F., 2011. Tracking defect-induced ferromagnetism in GaN:Gd. *Phys. Rev. B* 84, 081201(R). <http://dx.doi.org/10.1103/PhysRevB.84.081201>.
- Salzer, R., Spemann, D., Esquinazi, P., Höhne, R., Setzer, A., Schindler, K., Schmidt, H., Butz, T., 2007. Possible pitfalls in search of magnetic order in thin films deposited on single crystalline sapphire substrates. *J. Magn. Magn. Mater.* 317, 53–60. <http://dx.doi.org/10.1016/j.jmmm.2007.04.015>.
- Sapega, V.F., Ramsteiner, M., Dhar, S., Brandt, O., Ploog, K.H., 2005. Large spin splitting of GaN electronic states induced by Gd doping. Unpublished work, arXiv:cond-mat/0509198v1.
- Sarigiannidou, E., Wilhelm, F., Monroy, E., Galera, R.M., Bellet-Amalric, E., Rogalev, A., Goulon, J., Cibert, J., Mariette, H., 2006. Intrinsic ferromagnetism in wurtzite (Ga,Mn)N semiconductor. *Phys. Rev. B* 74, 041306(R). <http://dx.doi.org/10.1103/PhysRevB.74.041306>.
- Sato, K., Bergqvist, L., Kudrnovský, J., Dederichs, P.H., Eriksson, O., Turek, I., Sanyal, B., Bouzerar, G., Katayama-Yoshida, H., Dinh, V.A., Fukushima, T., Kizaki, H., Zeller, R., 2010. First-principles theory of dilute magnetic semiconductors. *Rev. Mod. Phys.* 82, 1633–1690. <http://dx.doi.org/10.1103/RevModPhys.82.1633>.
- Sawicki, M., Stefanowicz, W., Ney, A., 2011. Sensitive SQUID magnetometry for studying nanomagnetism. *Semicond. Sci. Technol.* 26, 064006. <http://dx.doi.org/10.1088/0268-1242/26/6/064006>.
- Stamenov, P., Coey, J.M.D., 2006. Sample size, position, and structure effects on magnetization measurements using second-order gradiometer pickup coils. *Rev. Sci. Instrum.* 77, 015106. <http://dx.doi.org/10.1063/1.2149190>.
- Shvarkov, S., Ludwig, A., Wieck, A.D., Cordier, Y., Ney, A., Hardtdegen, H., Haab, A., Trampert, A., Ranchal, R., Herfort, J., Becker, H.-W., Rogalla, D., Reuter, D., 2014. Magnetic properties of Gd-doped GaN. *Phys. Status Solidi B* 251, 1673–1684. <http://dx.doi.org/10.1002/pssb.201350205>.
- Stefanowicz, W., Sztenkiel, D., Faina, B., AGrois, A., Rovezzi, M., Devillers, T., Navarro-Quezada, A., Li, T., Jakiela, R., Sawicki, M., Dietl, T., Bonanni, A., 2010. Magnetism of dilute (Ga,Mn)N. *Phys. Rev. B* 81, 235210. <http://dx.doi.org/10.1103/PhysRevB.81.235210>.
- Stöhr, J., Siegmann, H.C., 2006. *Magnetism from Fundamentals to Nanoscale Dynamics*. Springer, Berlin Heidelberg New York.
- Teraguchi, N., Suzuki, A., Nanishi, Y., Zhou, Y.K., Hashimoto, M., Asahi, H., 2002. Room-temperature observation of ferromagnetism in diluted magnetic semiconductor GaGdN grown by RF-molecular beam epitaxy. *Solid State Commun.* 122, 651–653. [http://dx.doi.org/10.1016/S0038-1098\(02\)00228-4](http://dx.doi.org/10.1016/S0038-1098(02)00228-4).
- Tietze, T., Gacic, M., Schütz, G., Jakob, G., Brück, S., Goering, E., 2008. XMCD studies on Co and Li doped ZnO magnetic semiconductors. *New J. Phys.* 10, 055009. <http://dx.doi.org/10.1088/1367-2630/10/5/055009>.
- Zhou, Y.K., Choi, S.W., Emura, S., Hasegawa, S., Asahi, H., 2008. Large magnetization in high Gd concentration GaGdN and Si-doped GaGdN grown at low temperatures. *Appl. Phys. Lett.* 92, 062505. <http://dx.doi.org/10.1063/1.2841657>.

This page intentionally left blank

# MOCVD growth of Er-doped III-N and optical-magnetic characterization

7

*N. Nepal*

U.S. Naval Research Laboratory, Washington, DC, United States

*H.X. Jiang, J.Y. Lin*

Texas Tech University, Lubbock, TX, United States

*B. Mitchell*

University of Mount Union, Alliance, OH, United States

*V. Dierolf*

Lehigh University, Bethlehem, PA, United States

*J.M. Zavada*

NYU Tandon School of Engineering, Brooklyn, NY, United States

## 7.1 Introduction

Dilute magnetic semiconductors (DMS) form a class of materials that combine properties of a semiconductor host with magnetic effects due to an impurity dopant. While the concept of DMS materials was known for a long time, it was only in 1989 that researchers were able to demonstrate such materials in GaAs and InAs films doped with Mn (Munetaka et al., 1989). These films possessed all the requisite properties and held high potential for many novel electronic-magnetic devices. However, the Curie temperature ( $T_C$ ) for such magnetic effects was well below room temperature (RT), precluding practical applications. Even after many innovative approaches,  $T_C$  for these materials is still limited to  $\sim 160\text{K}$ . In 2000 a theoretical study predicted that p-type wide bandgap semiconductors doped with Mn could form a DMS system (Dietl et al., 2000). A number of research investigations proceeded and ferromagnetic (FM) behavior was reported for Mn-doped GaN films. These research efforts are described in other chapters in this volume.

Shortly afterward, several research groups began investigating doping GaN films with lanthanide rare earth (RE) elements. These elements have been widely studied in connection with light-emitting sources for solid state lasers, optical displays, and optical communication components. The special optical properties of the RE elements arise from transitions of the  $4f$  shell electrons. Due to the asymmetric nature of the  $4f$  shell wave function and inhomogeneous nucleus screening, the  $4f$  shell is concatenated and resides nearer to the nucleus than the filled  $5s$  and  $5p$  shells. Since the outer,

complete 5s and 5p shells shield the inner 4f electrons from the surrounding host environment, the energy levels of the 4f shell remain relatively unperturbed when placed into a solid state host (Hufner, 1978). Intra 4f-shell transitions in trivalent RE ions lead to narrow emissions ranging from the ultraviolet light (UV) through the visible to the infrared (IR).

Erbium (Er) is an especially important RE element for optical telecommunication systems. The trivalent ion ( $\text{Er}^{3+}$ ) has an emission at 1.54  $\mu\text{m}$ , from the  ${}^4\text{I}_{13/2} \rightarrow {}^4\text{I}_{15/2}$  transitions of 4f electrons, that corresponds to the absorption minimum of silica-based optical fibers. Research in Er-doped materials is of high technological importance and has resulted in development of Er-doped fiber amplifiers (EDFA) and Er-based fiber lasers [1–4]. In addition, the unpaired 4f electrons produce a magnetic moment and have made Er an important constituent of permanent magnetic alloys.

In this chapter, we address the growth, characterization, and device properties of Er-doped GaN and InGaN films that were produced by metal-organic chemical vapor deposition (MOCVD). In Section 7.2 we describe the challenges that were faced with in situ Er doping of III-N films and the approach that was made to accomplish this goal. The photoluminescence (PL) characterization of these films is presented in Section 7.3 together with electroluminescence (EL) data from prototype light-emitting diodes (LEDs). Results of magnetic measurement of the Er-doped III-N films are given in Section 7.4 and a summary of these findings is provided in Section 7.5.

## 7.2 MOCVD growth of Er-doped III-N films

The Er-doped III-N films materials and device structures were prepared using a custom-built MOCVD system with specific adaptations to accommodate the Er precursor. High-purity metal-organic (MO) precursors were obtained from Epichem Inc. and Strem Chemical Inc. and stored in stainless steel bubblers. Trimethylgallium (TMG) and trimethylindium (TMI) were used for the Ga and In sources, respectively, and transported by an inert carrier gas (typically hydrogen or nitrogen) into a heated reaction zone containing a suitable growth substrate. The group-V element, typically a hydride like  $\text{NH}_3$ , was separately transported to the induction heated reaction zone. In an ideal MOCVD growth, the group-III and the N sources have negligible chemical interaction before encountering the reaction zone above the substrate. Then the precursors pyrolyze in the reaction zone due to the elevated temperatures, and the group-III and N atoms are adsorbed onto the surface, resulting in growth of the III-N epilayer. Silane ( $\text{SiH}_4$ ), obtained from BOC Edwards (20 ppm in 6 grades  $\text{H}_2$ ), was used to supply Si as an n-type dopant, while bicyclopentadienylmagnesium ( $\text{Cp}_2\text{Mg}$ ) was obtained from Epichem and used to supply Mg as the p-type dopant. Tri-isopropylcyclopentadienylerbium (TRIPER) was obtained from Strem Chemical Inc. and used as the Er source. Blue Ammonia (99.99994%), obtained from Airgas Inc., was passed through an Aeronex purifier and used as the N source. Ultrahigh-purity H (99.999%) was passed through a palladium and the Aeronex purifier and served as the transport gas. High-purity liquid N was passed through the gas purifier and used as an alternative transport gas. All MO bubblers were placed in Polystat recirculating refrigeration units to maintain the sources at constant temperature and vapor pressure.

Gas protocol stations were employed for all other gases to maintain gas pressure. Computer-controlled Swagelok BN and HB series pneumatic valves in conjunction with MKS mass flow controllers (MFCs) were employed to control precursor flow rate ratios and gas directions. Swagelok VCR gasket seals were used to maintain a leak-free system. The growth chamber consisted of a horizontal-flow quartz reactor (created by Technical Glass Products Inc.), a Boron Nitride coated graphite susceptor, a quartz positioning rod, and a quartz thermocouple tube. A Huttinger TIG 10/100 RF generator in combination with a 4-inch, 8-turn copper coil was used to provide heating during the epilayer growth. A type-R thermocouple (Platinum/Rhodium alloy) and a DP460 control unit created by OMEGA was used for temperature monitoring and control.

There was a major challenge with use of the Er MO precursors. Due to the large atomic mass of Er, most of these precursors have an extremely low vapor pressure at RT making it virtually impossible to attain sufficiently high Er doping concentrations ( $N_{\text{Er}}$ ) for device applications. Attempts have been made to increase the volatility of Er precursors by attaching O or S chains to the Er compound. However, these elements have a parasitic effect on the optical and electrical properties of III-N materials. While TRIPEr does not contain either O or S, this precursor has a very low vapor pressure RT. The vapor pressures of the MOCVD precursors (TMGa, TMIIn, TMAI,  $\text{Cp}_2\text{Mg}$ , TMIIn, and TRIPEr) used for III-N growth are displayed in Fig. 7.1. Data points were calculated based on the Clausius–Clapeyron relation with values taken from SAFC (<http://www.safcglobal.com/>) and Strem Chemicals (<http://www.strem.com/>).

The very low vapor pressure of TRIPEr, in comparison with the other sources, prevented the standard gas flow arrangements for MOCVD III-N growth. To overcome this obstacle the Er source was immersed in a silicone oil bath at temperatures between 65 and 140°C. Higher temperatures were not possible due to the fact that heated silicone oil produces formaldehyde (a carcinogenic) in the presence of air at temperatures exceeding 150°C. Most of the Er-doped III-N growth was done at a bubbler temperature

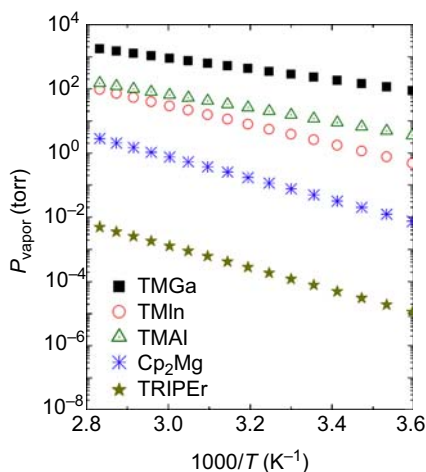


**Figure 7.1** Vapor pressure as function of the reciprocal of the bubbler temperature for the metal-organic precursors: TMGa, TMIIn, TMAI,  $\text{Cp}_2\text{Mg}$ , and TRIPEr.



of 100°C at which the vapor pressure of TRIPeR was  $\sim 0.028$  torr. Furthermore, in order to prevent Er condensation in the stainless system, a special heating system was applied to the valves and tubing. The system consisted of several rubber, current-carrying, heating tapes acquired from Cole Parmer with adjustable heat output. The tapes were secured to the doping line by a foil tape with a high temperature epoxy. Several thermistors and a controller were attached directly to the stainless steel tubing via a thermal bonding compound allowing for direct temperature measurement. During growth of Er-doped epilayers, the temperature of the transport line was kept above bubbler temperature. To achieve higher doping concentrations, the pressure of the Er bubbler was adjusted with respect to the other precursors. In addition, the MFC was placed upstream of the MO bubbler, thereby controlling the pressure inside the bubbler by the reactor pressure. This allowed the ratio of the carrier gas to source gas to be reduced, and the gas phase concentration of the source in the reaction zone to increase. Consequently, the Er doping concentration for low pressure MOCVD III-N growth was substantially increased. More detailed information of the MOCVD system for growth of Er-doped III-N films can be found in (Ugolini et al., 2006; Feng et al., 2012).

### 7.2.1 MOCVD growth of GaN:Er films

To establish the basic properties of Er-doped GaN (GaN:Er) films, simple material structures were grown by MOCVD on commercial sapphire substrates. The (0001) sapphire substrates were  $\sim 430$   $\mu\text{m}$  thick, and had a root mean square (RMS)  $z$ -profile deviation of 0.5 nm. Before growth, the substrates were cleaned using acetone, isopropanol, and deionized water in an ultrasonic bath. After insertion into the reaction chamber, the substrates were heat treated at 1150°C for 10 min. Growth of the epilayers began with a thin GaN buffer layer, followed by a 1.2  $\mu\text{m}$  GaN template, and then a 0.5  $\mu\text{m}$  GaN:Er layer. The GaN template and Er-doped layer were grown at 10 torr and at a growth temperature ( $T_G$ ) of 1040°C, which was estimated based on readings from a thermocouple placed inside the graphite susceptor. Fig. 7.2(a) is a schematic of a typical GaN:Er structure.

To monitor in situ growth and surface morphology, a 670 nm Epieye reflectometer from ORS ltd. was used. For a fixed laser wavelength, polarity, and incident angle, the thickness  $d$  of the epilayer could be determined by:

$$n\lambda_m = d \sin \theta, \quad [7.1]$$

where  $n$  is an integer,  $\lambda_m$  is the wavelength inside the material, and  $\theta$  is the angle of reflection. With an increase in strain or surface roughness of the film, the reflected intensity decreased. The intensity profile of the reflectance pattern for a typical multilayer GaN:Er structure during growth is shown in Fig. 7.2(b), where the changes in intensity are due to different layers in the structure. In Fig. 7.2(c),  $T_{\text{Susceptor}}$  indicates the susceptor temperature profile during growth.

Secondary Ion Mass Spectrometry (SIMS) measurements were made to determine the Er concentration as a function of growth conditions. The atomic depth profiles shown in Fig. 7.3 indicate that concentrations up to  $N_{\text{Er}} \sim 2 \times 10^{21} \text{ cm}^{-3}$  were

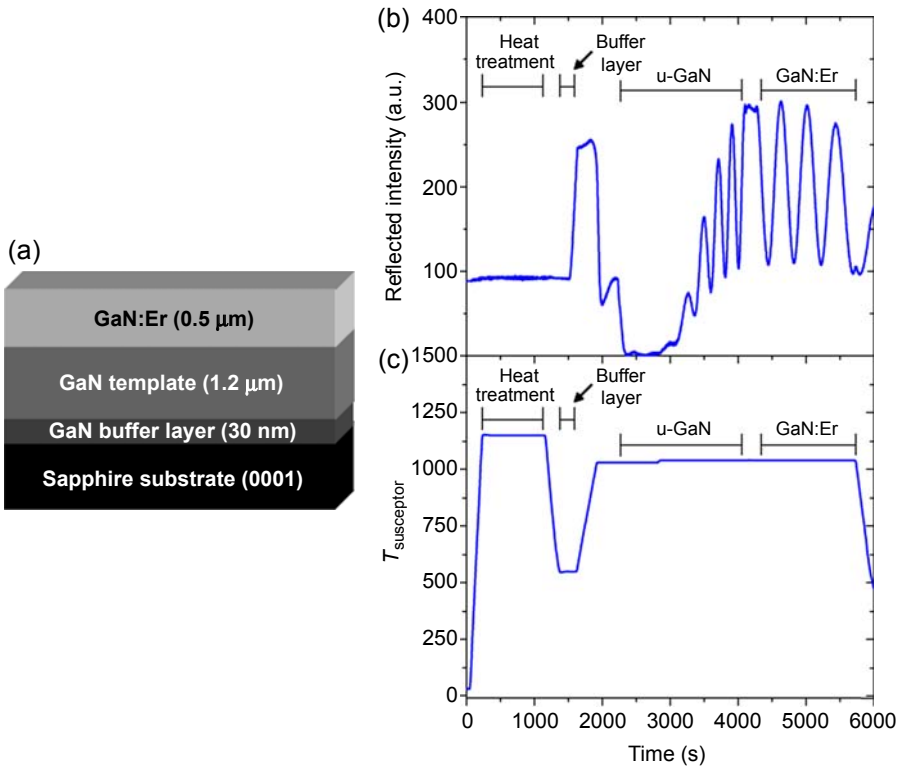


**Figure 7.2** (a) Schematic diagram of a typical GaN:Er multilayer sample; (b) the reflected intensity pattern versus growth time; and (c) the susceptor temperature profile. The brackets indicate regions of different layers in the structure.

Source: Adapted from Ugolini, C.R., 2008. Optical and Structural Properties of Er-doped GaN/InGaN Materials and Devices Synthesized by Metal Organic Chemical Vapor Deposition (thesis). Kansas State University.

achieved. This concentration is comparable to that previously reported for  $N_{\text{Er}}$  levels in GaN synthesized by molecular beam epitaxy (MBE) (Steckl et al., 1998), and much larger than reported values of Er in InP, GaAs, or Si (Isshiki et al., 1991; Koizumi et al., 2003). The C and H concentrations, shown in Fig. 7.3, were relatively low,  $\sim 5 \times 10^{18} \text{ cm}^{-3}$ , similar to values reported for high-quality undoped GaN [29]. The oxygen concentration, which can be parasitic to electrical and optical properties, was below the detection limit in GaN:Er.

In Fig. 7.4 atomic force microscopy (AFM) images are shown of the surface of an undoped GaN epilayer and those of GaN:Er samples having Er concentrations of  $2 \times 10^{20} \text{ cm}^{-3}$  and  $2 \times 10^{21} \text{ cm}^{-3}$ . The surface of the GaN:Er epilayer with  $N_{\text{Er}} = \sim 2 \times 10^{21} \text{ cm}^{-3}$  suffers a large degradation in surface smoothness, with the RMS value  $\sim 56 \text{ nm}$  in the vertical direction. However, the sample with  $N_{\text{Er}} = \sim 2 \times 10^{20} \text{ cm}^{-3}$  has an RMS value  $\sim 2 \text{ nm}$ , which is comparable to that  $\sim 1.0 \text{ nm}$  for the undoped GaN.

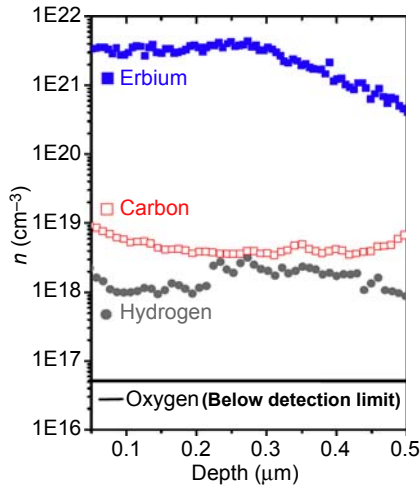


**Figure 7.3** SIMS atomic depth profiles for Er, C, H, and O in a GaN:Er sample grown by MOCVD.

Source: Adapted from Dahal, R., Lin, J.Y., Jiang, H.X., Zavada, J., 2010b. Er-doped GaN and InGaN for optical communications. In: O'Donnell, K., Dierolf, V. (Eds.), *Topics in Applied Physics: Rare Earth Doped III-nitrides for Optoelectronic and Spintronic Applications*. Springer, The Netherlands, pp. 115–157.

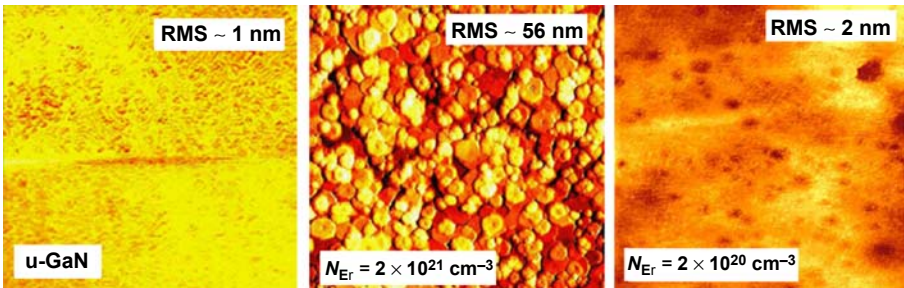


**Figure 7.4** AFM images of the surfaces of undoped GaN and GaN:Er samples. The Er concentration is indicated in the lower left corner and the RMS value in the top right corner of each image. The surface quality of the GaN:Er sample with  $N_{\text{Er}} \sim 2 \times 10^{20} \text{ cm}^{-3}$  is comparable to that of undoped GaN.

Source: Adapted from Ugolini, C.R., 2008. *Optical and Structural Properties of Er-doped GaN/InGaN Materials and Devices Synthesized by Metal Organic Chemical Vapor Deposition* (thesis). Kansas State University.

The crystalline ordering in GaN:Er and high-quality undoped GaN samples was examined using XRD measurements. In Fig. 7.5 the  $\theta$ – $2\theta$  XRD rocking curves of the (002) peak for two samples, one undoped and the other with  $N_{\text{Er}} = \sim 2 \times 10^{21} \text{ cm}^{-3}$ , are shown. As can be seen, the full width at half maximum (FWHM) for each sample is nearly identical. Consequently, incorporation of Er, even to a high concentration, does not significantly change the crystalline ordering.

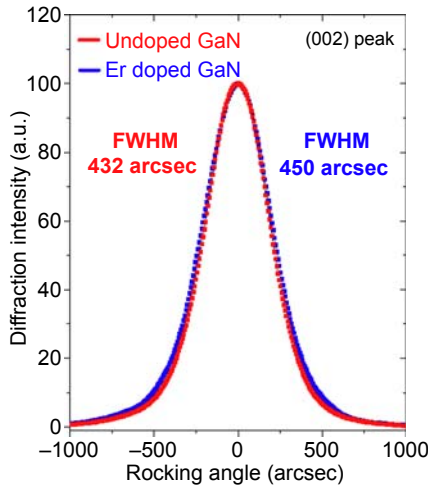


**Figure 7.5** XRD rocking curves for an undoped GaN sample and for GaN:Er, with  $N_{\text{Er}} = \sim 2 \times 10^{21} \text{ cm}^{-3}$ . The FWHM of each (002) peak is nearly the same.

Source: Adapted from Dahal, R., Lin, J.Y., Jiang, H.X., Zavada, J., 2010b. Er-doped GaN and InGaN for optical communications. In: O'Donnell, K., Dierolf, V. (Eds.), *Topics in Applied Physics: Rare Earth Doped III-nitrides for Optoelectronic and Spintronic Applications*. Springer, The Netherlands, pp. 115–157.

## 7.2.2 MOCVD growth of InGaN:Er films

InGaN alloys are very important for blue and green LEDs as well as for multijunction solar cell devices and optical communication components. Compared with GaN, these alloys have a lower bandgap energy that can be tailored to fit the specific application. Through ternary alloying, the RT bandgap  $E_G$  of  $\text{In}_x\text{Ga}_{1-x}\text{N}$  alloys can be adjusted to cover a wide range of emission energies (Nakamura et al., 2000):

$$E_G(x) = [0.7x + 3.42(1 - x) - 1.43x(1 - x)] \text{ eV} \quad [7.2]$$

where  $x$  is the mole fraction of In,  $E_G(0) = E_G(\text{GaN}) = 3.42 \text{ eV}$ , and  $E_G(1) = E_G(\text{InN}) = 0.7 \text{ eV}$ . However, growth of high-quality InGaN with large In fractions is still very challenging. Due to the much lower bond energy between In and N (Edgar, 1994), the growth temperature  $T_G$  for InGaN must be about 200–300°C lower than that for GaN. At such temperatures, the crystalline quality and surface of the InGaN films become slightly degraded, and dislocations are readily incorporated into the epilayer. Furthermore, synthesis of InGaN epilayers requires using large In/Ga precursor ratios and slow growth rates. These changes in growth conditions present complex obstacles for the realization of InGaN materials for practical applications. Investigation of Er-doped InGaN (InGaN:Er) films is critical for the formation of heterojunction III-N structures that can be used for LEDs and optical amplifiers at 1.54  $\mu\text{m}$ .

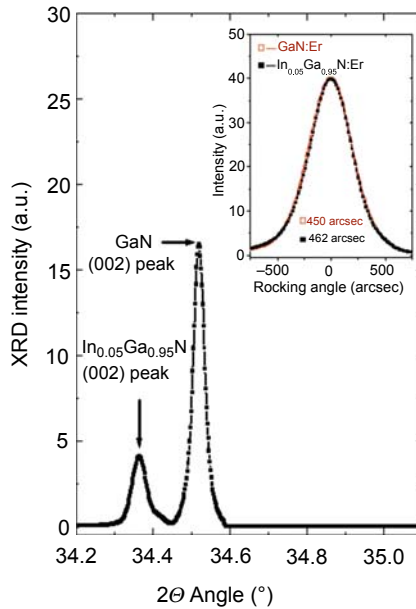


**Figure 7.6** XRD scan of the (002) peak of an  $\text{In}_{0.05}\text{Ga}_{0.95}\text{N}:\text{Er}$  film. Distinct peaks can be seen at 34.36 and 34.52 degree corresponding to the diffraction peaks of  $\text{In}_{0.05}\text{Ga}_{0.95}\text{N}$  and GaN. The inset contains the comparison of the rocking curves of  $\text{In}_{0.05}\text{Ga}_{0.95}\text{N}:\text{Er}$  and GaN:Er films. The FWHM is indicated beneath the curves.

Source: Adapted from Sedhain, A., Ugolini, C., Lin, J.Y., Jiang, H.X., Zavada, J.M., 2009. Photoluminescence properties of erbium doped InGaN epilayers. *Appl. Phys. Lett.* 95, 041113.

MOCVD growth of InGaN:Er films proceeded along similar lines to that for GaN:Er described in Section 7.2.1. The InGaN:Er epilayers were grown on (0001) sapphire substrates following the same substrate preparation. Growth began with thin GaN buffer layer and 1.2  $\mu\text{m}$  GaN template layer, followed by a 300 nm InGaN:Er layer. The growth temperature layer was  $T_G = 760^\circ\text{C}$  using pressures between 10 and 50 torr.

A  $\theta-2\theta$  XRD scan of the (002) peak of an  $\text{In}_{0.05}\text{Ga}_{0.95}\text{N}:\text{Er}$  is shown in Fig. 7.6 indicating diffraction peaks corresponding to  $\text{In}_{0.05}\text{Ga}_{0.95}\text{N}$  and GaN. The XRD rocking curve of the  $\text{In}_{0.05}\text{Ga}_{0.95}\text{N}:\text{Er}$  film was nearly the same as that of GaN:Er, as shown in the inset. The In fraction of the InGaN:Er epilayers was determined from the diffraction peaks in the XRD scan indicating a bandgap  $E_G(0.05) \sim 3.44$  eV. AFM measurements of the surface of the film resulted in an RMS value approximately twice that of the GaN:Er (2 nm) in Fig. 7.4. SIMS depth profiles of Er showed that  $N_{\text{Er}}$  for  $\text{In}_{0.05}\text{Ga}_{0.95}\text{N}:\text{Er}$  grown at  $760^\circ\text{C}$  was about an order lower than that in a GaN:Er epilayer grown at  $1040^\circ\text{C}$  (Sedhain et al., 2009).

It was possible to increase the In fraction in the InGaN alloy by employing slower growth rates, larger growth pressures, and larger  $\text{NH}_3$  fluxes without changing  $T_G$ . This was done in attempts to optimize the Er optical emission. However, higher In fractions led to poorer crystal quality and lower optical emission efficiency.

### 7.2.3 III-N:Er growth on alternative substrates

One of the major issues facing growth of III-N films is the lack of a native substrate for such growth. Initially, III-N synthesis focused on using sapphire ( $\text{Al}_2\text{O}_3$ ) or SiC substrates in spite of the large lattice mismatch, which led to high dislocation densities (Nakamura et al., 2000). In addition, differences in thermal expansion coefficients between the substrate and epilayer induced thermal strain, producing epilayers with cracks and other associated defects. Many different approaches, including selective area growth (SAG) and epitaxial lateral overgrowth, were investigated to reduce the lattice mismatch with the substrate and to minimize the dislocation density in the III-N films.

We have studied MOCVD synthesis of GaN:Er on four different templates: AlN/ $\text{Al}_2\text{O}_3$ , GaN/ $\text{Al}_2\text{O}_3$ , c-GaN bulk, and GaN/Si(111). In each case, undoped GaN epilayers with a thickness of  $\sim 500$  nm were grown on the templates, followed by the simultaneous growth of 500 nm thick GaN:Er epilayers at 10 torr and  $T_G = 1040^\circ\text{C}$ . In Fig. 7.7 the  $\theta-2\theta$  XRD scans of the four samples are shown. The use of different templates resulted in shifts in the diffraction peaks relative to the reference position of bulk c-GaN. The GaN:Er film grown on the c-GaN bulk substrate showed almost no strain. However, the XRD scans of the GaN:Er films grown on other templates were elongated due to biaxial stress. The shift in peak position increased with greater lattice mismatch.

Experiments were also conducted to grow InGaN:Er epilayers on different templates, GaN/AlN/Si(001), GaN/AlN/Si(111), GaN/AlN/ $\text{Al}_2\text{O}_3$ , and directly on Si(001). Thin films were grown simultaneously at  $T_G \sim 760^\circ\text{C}$  and a growth pressure  $\sim 100$  torr. SAG techniques were used to prepare the GaN/AlN/Si(001) templates in order to suppress dislocations and prevent cracks. The In content of the films was determined from

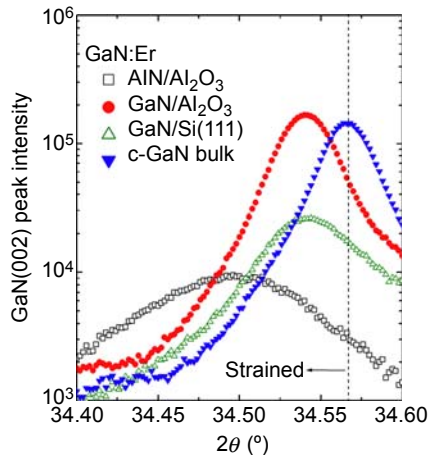


**Figure 7.7** XRD scan of the (002) peaks for GaN:Er layers grown on different templates indicating induced strain due to lattice mismatch. With increased strain the diffraction peaks shifted to smaller angles relative to the c-GaN bulk position.

Source: Adapted from Feng, I.W., Li, J., Sedhain, A., Lin, J.Y., Jiang, H.X., Zavada, J., 2010. Enhancing erbium emission by strain engineering in GaN heteroepitaxial layers. Appl. Phys. Lett. 96, 031908.

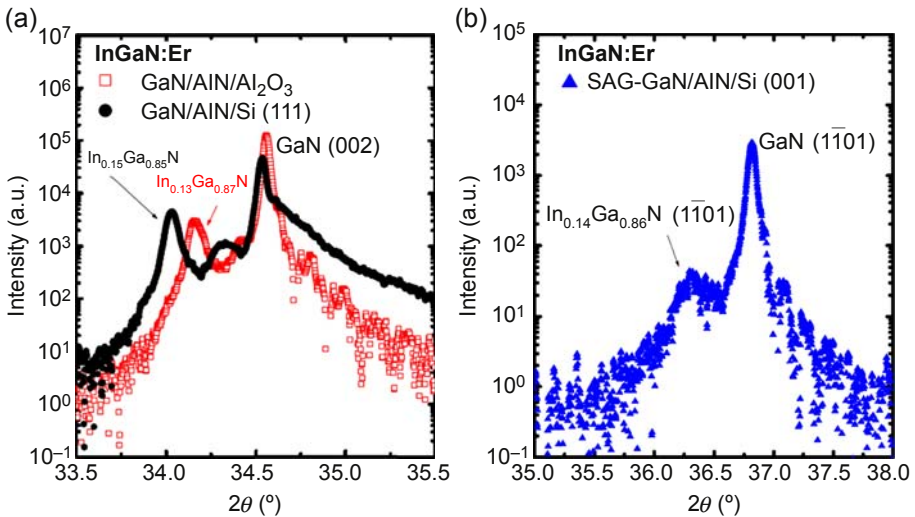


**Figure 7.8** XRD spectra for growth of InGaN:Er layers grown on different templates: (a) InGaN and GaN(002) peaks appear in the scans for In<sub>0.15</sub>Ga<sub>0.86</sub>N/GaN/AlN/Si(111) and In<sub>0.13</sub>Ga<sub>0.86</sub>N/GaN/AlN/Al<sub>2</sub>O<sub>3</sub>; and (b) a wurtzite In<sub>0.14</sub>Ga<sub>0.86</sub>N(1101) peak for the film on the SAG GaN/AlN/Si(001).

Source: Adapted from Feng, I.W., 2013. Erbium Doped III-Nitride Semiconductors: Material Synthesizing and Applications, Texas Tech University.

the peak positions in the XRD measurements. No peak corresponding to single crystal InGaN was detected for the sample grown on Si(001). However, as shown in Fig. 7.8(a), InGaN XRD(002) peaks, at  $2\theta = 34.04$  and  $34.16$  degree, were detected for In<sub>0.15</sub>Ga<sub>0.86</sub>N/GaN/AlN/Si(111) and In<sub>0.13</sub>Ga<sub>0.86</sub>N/GaN/AlN/Al<sub>2</sub>O<sub>3</sub>, respectively. A wurtzite In<sub>0.14</sub>Ga<sub>0.86</sub>N(1101) reflection at  $2\theta = 36.29$  degree, shown in Fig. 7.8(b), was detected for the SAG InGaN:Er/GaN/AlN/Si(001) sample. Nonuniform distribution of strain or the different growth rates may explain the small difference in In content among InGaN:Er samples grown on these three templates.

The successful demonstration of epitaxial growth of Er-doped InGaN on Si(001) substrates laid the ground work for the realization of new types of  $1.54 \mu\text{m}$  optical emitters and amplifiers (Dahal et al., 2009) on Si, which are compatible with standard processes of complementary metal-oxide-semiconductor technology used for digital electronics and computer chips.

## 7.3 Optical properties

### 7.3.1 Photoluminescence characterization

In this work, a specialized time-resolved PL system was assembled to study optical properties of Er-doped III-N semiconductors. The PL system consists of a frequency-doubled, and -tripled, 100 fs Ti:sapphire laser operating with an average



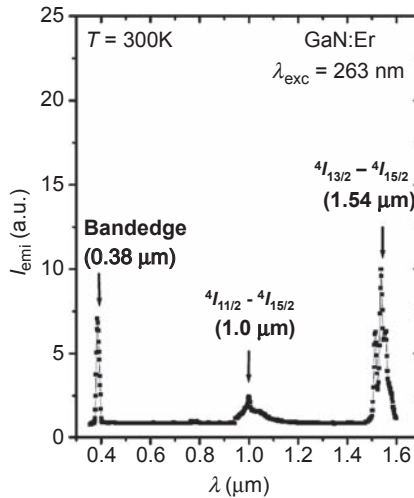


**Figure 7.9** PL spectrum of GaN:Er, measured at 300K, using laser excitation at 263 nm and detected over a broad spectral range from UV to IR.

Source: Adapted from Dahal, R., Lin, J.Y., Jiang, H.X., Zavada, J., 2010b. Er-doped GaN and InGaN for optical communications. In: O'Donnell, K., Dierolf, V. (Eds.), *Topics in Applied Physics: Rare Earth Doped III-nitrides for Optoelectronic and Spintronic Applications*. Springer, The Netherlands, pp. 115–157.

power of 150 mW at wavelengths of 263 and 395 nm, with a repetition rate of 76 Hz. PL detection was accomplished in the IR (800–1700 nm) region using an InGaAs detector and in the UV–visible (185–800 nm) region with a multichannel plate photomultiplier tube, in conjunction with a 1.3 m monochromator. A Janis cryostat system capable of producing temperatures of 10–800K was used in order to probe the PL emission as a function of ambient temperature.

The PL spectrum of a GaN:Er epilayer, covering the visible to IR region, is shown in Fig. 7.9. The Er concentration was  $\sim 10^{21} \text{ cm}^{-3}$  and the measurement was made at 300K using a laser excitation wavelength ( $\lambda_{\text{exc}}$ ) of 263 nm. Two sharp emission peaks were observed at wavelengths of 1.0 and 1.54  $\mu\text{m}$ , with an FWHM of 10.2 and 11.8 nm, respectively. The first peak corresponds to the radiative intra- $4f$  transitions of  $\text{Er}^{3+}$  from the  ${}^4I_{11/2} \rightarrow {}^4I_{15/2}$  and the second from the  ${}^4I_{13/2} \rightarrow {}^4I_{15/2}$  levels. At RT the PL intensity of the 1.54  $\mu\text{m}$  emission was  $\sim 4$  times that of the 1.0  $\mu\text{m}$  line. Virtually no visible emission lines were observed in PL spectrum for GaN:Er epilayers grown by MOCVD. This is in contrast to results of GaN:Er material produced by ion-implantation or by MBE, in which  $\text{Er}^{3+}$  emissions at 537 and 558 nm are observed from  $4f$  transitions between the  ${}^2H_{11/2}$  and  ${}^4S_{3/2}$  levels to the ground state (Steckl and Birkhahn, 1998; Son et al., 2004). In addition, the dominant bandedge emission of GaN:Er is at  $\sim 3.23 \text{ eV}$ , which is red-shifted by  $\sim 0.19 \text{ eV}$  from that of undoped GaN (Dahal et al., 2010b). This red-shift appears related to the formation of  $\text{Er}_{\text{Ga}}-\text{V}_{\text{N}}$  complexes and the recombination between bound electrons at the complexes and free holes in the valence band.



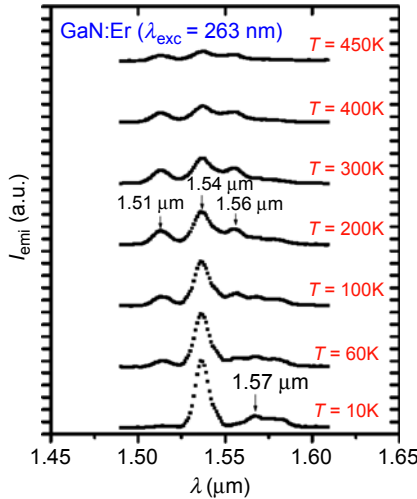


**Figure 7.10** PL spectra of GaN:Er in the 1.54  $\mu\text{m}$  region in GaN:Er as a function of temperature between 10 and 450K for  $\lambda_{\text{exc}} = 263 \text{ nm}$ .

Source: Adapted from Ugolini, C.R., 2008. Optical and Structural Properties of Er-doped GaN/InGaN Materials and Devices Synthesized by Metal Organic Chemical Vapor Deposition (thesis). Kansas State University.

It was also found that the PL intensity of the 1.54  $\mu\text{m}$  emission was more than 10 times larger with above-bandgap excitation at 263 nm than with below-bandgap excitation at 395 nm. This indicates that the generation of electron–hole pairs via above-bandgap excitation results in a more efficient energy transfer to  $\text{Er}^{3+}$  ions than that through defect centers in the epilayers (Wu et al., 1997).

The thermal quenching of PL emission, between 10 and 450K, was measured in the 1.54  $\mu\text{m}$  region as shown in Fig. 7.10. While the 1.54  $\mu\text{m}$  emission line was dominant at low temperatures, two additional emission peaks appeared, at 1.51 and 1.56  $\mu\text{m}$ , as the temperature increased. These peaks originate from the splitting of the  $^4\text{I}_{13/2}$  manifold due to the  $\text{C}_{3v}$  nature of the crystal field in the GaN host (Makarova et al., 2008).

As previously reported, the thermal quenching of the Er-based PL emission is much less in wide bandgap semiconductor (WBGs) hosts than in smaller bandgap semiconductors (Favannec et al., 1989). In Fig. 7.11, the integrated PL intensity ( $I_{\text{int}}$ ) of the 1.54  $\mu\text{m}$  emission for  $\lambda_{\text{exc}} = 263 \text{ nm}$  is plotted as a function of temperature. Only a 20% decrease in  $I_{\text{int}}$  was observed between 10 and 300K, which represents one of the lowest reported values of thermal quenching for any RE-doped III-V semiconductor (MacKenzie et al., 1998). The  $I_{\text{int}}$  data in Fig. 7.11 were fitted by the Arrhenius relation:

$$I_{\text{int}} = \frac{I_0}{1 + ce^{-E_0/kT}} \quad [7.3]$$

where  $I_0$  is the integrated intensity at low temperature,  $c$  is a fitting constant,  $E_0$  is the activation energy of the thermal quenching, and  $k$  is Boltzmann's constant. From the

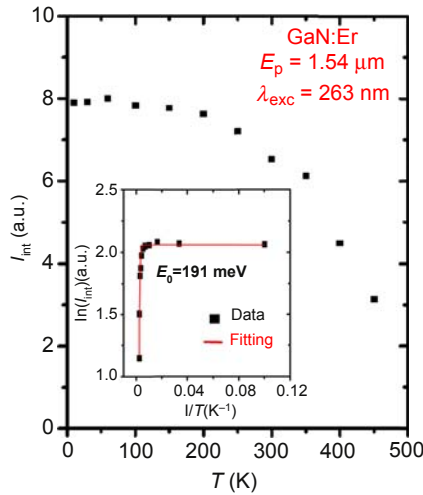


**Figure 7.11** Plot of the integrated PL intensity of the 1.54  $\mu\text{m}$  emission of GaN:Er as a function of temperature between 10 and 450 K for  $\lambda_{\text{exc}} = 263$  nm. In the inset an Arrhenius plot shows the best fitting using  $E_0 = 191$  meV.

Source: Adapted from Dahal, R., Lin, J.Y., Jiang, H.X., Zavada, J., 2010b. Er-doped GaN and InGaN for optical communications. In: O'Donnell, K., Dierolf, V. (Eds.), *Topics in Applied Physics: Rare Earth Doped III-Nitrides for Optoelectronic and Spintronic Applications*. Springer, The Netherlands, pp. 115–157.

Arrhenius plot shown in the inset,  $E_0$  was determined to be  $\sim 191 \pm 8$  meV, which is almost the same as the magnitude of the red-shift in the bandedge emission.

Both values of the experimentally measured red-shift of the bandedge PL emission and the activation energy of thermal quenching are in good agreement with a density functional study by Fihol et al. (2004). They showed that  $\text{Er}_{\text{Ga}}-\text{V}_{\text{N}}$  complexes in GaN:Er produce a half-filled energy level at approximately 0.2 eV below the conduction band. Our experimental results also match well with DLTS measurements by Song et al. (2005), who found a defect level at 188 meV below the conduction band in Er-implanted GaN. Thus, it is reasonable to conclude that the energy transfer between electrons bound to the  $\text{Er}_{\text{Ga}}-\text{V}_{\text{N}}$  complex and the 4f electrons of  $\text{Er}^{3+}$  ions is the dominant excitation mechanism of the 1.54  $\mu\text{m}$  emission in MOCVD-grown GaN:Er using above-bandgap excitation.

These results also provide a better understanding regarding the low degree of thermal quenching found in GaN:Er. It is well established that for semiconductors, effective donor levels increase with increasing bandgap energy. For smaller bandgap semiconductors, the majority of electrons bound to the Er-related traps are thermally excited into the conduction band at RT since their binding energy is small. Thus, electrons cannot efficiently transfer energy to the 4f electrons via an Auger-like process. For WBGs hosts, such as GaN, the energy levels are deeper and electrons remain bound to the  $\text{Er}_{\text{Ga}}-\text{V}_{\text{N}}$  at higher temperatures. While Auger energy transfer between bound electrons and 4f electrons can still occur, the subsequent thermal quenching is dramatically reduced.

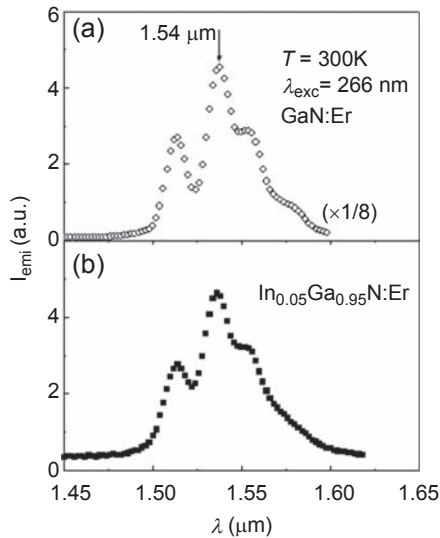


**Figure 7.12** Comparison of the PL spectra of GaN:Er (a) and  $\text{In}_{0.05}\text{Ga}_{0.95}\text{N:Er}$  (b) measured at 300K for  $\lambda_{\text{exc}} = 263 \text{ nm}$ .

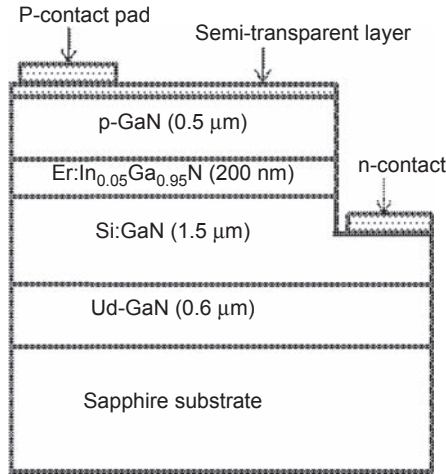
Source: Adapted from Sedhain, A., Ugolini, C., Lin, J.Y., Jiang, H.X., Zavada, J.M., 2009. Photoluminescence properties of erbium doped InGaN epilayers. *Appl. Phys. Lett.* 95, 041113.

Fig. 7.12 is a comparison of the PL spectra of GaN:Er (a) and  $\text{In}_{0.05}\text{Ga}_{0.95}\text{N:Er}$  (b) measured at 300K for  $\lambda_{\text{exc}} = 263 \text{ nm}$ . The Er concentration in  $\text{In}_{0.05}\text{Ga}_{0.95}\text{N:Er}$  was comparable to that in GaN:Er,  $N_{\text{Er}} \sim 10^{21} \text{ cm}^{-3}$ , as determined by SIMS. While the PL spectra are very similar, the  $1.54 \mu\text{m}$  emission intensity from  $\text{In}_{0.05}\text{Ga}_{0.95}\text{N:Er}$  is almost an order of magnitude lower than that from GaN:Er even though both epilayers had comparable crystalline quality and surface morphology. In general, InGaN:Er epilayers with higher In content resulted in a lower PL emission intensity.

### 7.3.2 Electroluminescent devices

One of the main advantages of using a semiconductor material as a host for RE ions is that heterojunctions can be formed leading to electrical excitation of the  $4f$  electrons. This electrical excitation can occur either through electron–hole recombination, under forward bias (Koizumi et al., 2015, in this volume), or by impact excitation, with reverse bias (Heikenfeld et al., 1999; Morishima et al., 1999). In either case energy is transferred to the RE ion with subsequent optical emission.

We have fabricated and characterized several different p-i-n semiconductor multi-layer structures in which the i-layer was doped with Er (Ugolini, 2008; Feng, 2013; Dahal et al., 2010a,b). The p-i-n diodes were grown on (0001) sapphire substrates as were used for the GaN:Er and InGaN:Er epilayer studies. A schematic of one of the fabricated p-GaN/InGaN:Er/n-GaN LEDs is shown Fig. 7.13. The active region was a 200 nm thick  $\text{In}_{0.05}\text{Ga}_{0.95}\text{N:Er}$  epilayer. Growth of the p-i-n diodes began with a thin



**Figure 7.13** Schematic diagram of a p-GaN/InGaN:Er/n-GaN LED with a 200 nm thick  $\text{In}_{0.05}\text{Ga}_{0.95}\text{N}:\text{Er}$  epilayer as the active region.

Source: Adapted from Dahal, R., Ugolini, C., Lin, J.Y., Jiang, H.X., Zavada, J.M., 2010a.

1.54  $\mu\text{m}$  emitters based on erbium doped InGaN p-i-n junctions. *Appl. Phys. Lett.* 97, 141109.

GaN buffer layer, followed by a 0.6  $\mu\text{m}$  undoped GaN layer grown at 1040°C. Then 1.5  $\mu\text{m}$  thick Si-doped GaN layer, with electron concentration  $n = 5 \times 10^{18} \text{ cm}^{-3}$  and mobility  $\mu = 250 \text{ cm}^2/\text{V s}$ , was deposited. This was followed by growth of the  $\text{In}_{0.05}\text{Ga}_{0.95}\text{N}:\text{Er}$  active layer with Er concentration  $\sim 2 \times 10^{19} \text{ cm}^{-3}$ , and a 0.5  $\mu\text{m}$  thick Mg-doped p-type GaN layer with hole concentration,  $p = 3 \times 10^{17} \text{ cm}^{-3}$  and mobility,  $\mu = 10 \text{ cm}^2/\text{V s}$ . To activate the Mg acceptors in the p-layers, the structures were annealed in  $\text{N}_2$  ambient at 550°C for 30 min. XRD  $\theta-2\theta$  scans of the (002) peak were used to determine the In content and assess the crystalline quality of the multi-layer structure. The LED fabrication process started with deposition of a thin semitransparent current spreading layer of Ni/Au (5/10 nm) by e-beam evaporation. Devices with mesa size of  $300 \times 300 \mu\text{m}^2$  were defined by etching down to n-type GaN (0.8  $\mu\text{m}$  deep from top) using a chlorine-based inductively coupled plasma technique. Then the semi-transparent p-contact was annealed for 30 min in air at 450°C to obtain the ohmic characteristics for the p-contact. Finally, the n-contact, Ti/Al/Ti/Au (30/100/20/150 nm), and the p-contact pad Ni/Au (30/200 nm) were deposited by e-beam evaporation using optical lithography and lift-off techniques.

EL was observed when a forward bias was applied to the diode. The EL emission was characterized using a custom-built probe station, which consisted of a Keithley 2400 series source meter to apply variable bias and an Olympus SZ61 Optical microscope for device positioning. An Ocean Optics QP-600-mixed bifurcated fiber was used to transfer the EL emission to an IR InGaAs detector and to an Ocean Optics PC2000 visible spectrometer. The EL spectrum, measured at RT under 20 mA current injection and a forward bias of 12.5 V is shown in Fig. 7.14. In contrast to the PL spectrum shown in Fig. 7.9, which had emission peaks only at

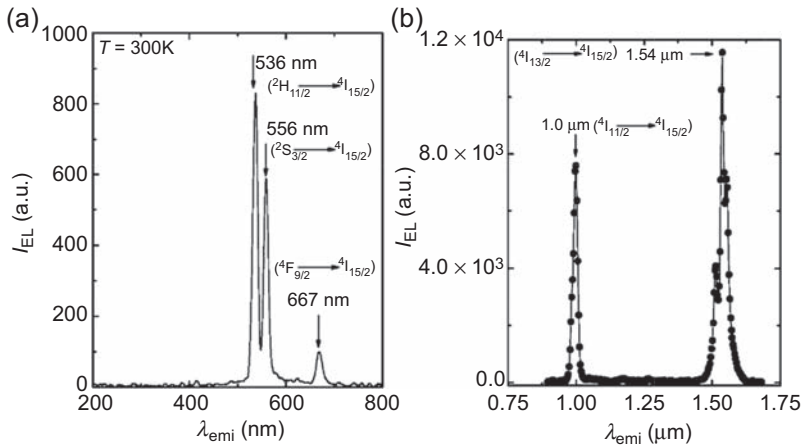


**Figure 7.14** EL spectra of the a p-GaN/In<sub>0.05</sub>Ga<sub>0.95</sub>N:Er/n-GaN LED measured at RT in (a) the visible region and (b) the near-IR region under a current injection of 20 mA with a forward bias of 12.5 V.

Source: Adapted from Dahal, R., Ugolini, C., Lin, J.Y., Jiang, H.X., Zavada, J.M., 2010a. 1.54  $\mu\text{m}$  emitters based on erbium doped InGaN p-i-n junctions. *Appl. Phys. Lett.* 97, 141109.

1.0 and 1.54  $\mu\text{m}$ , emission lines at visible wavelengths of 536, 556, and 667 nm were also observed in the EL spectrum (see Fig. 7.14(b)). These peaks are due to transitions from the higher  $4f$  energy levels to the  $^4I_{15/2}$  ground state. The appearance of these additional emissions peaks indicates that the excitation process for the p-i-n diode was different than the PL mechanism involved in above-bandgap optical excitation.

Under 20 mA current injection, the integrated emitted power over the near-IR emissions was  $\sim 2 \mu\text{W}$ , which was about twice that in the visible region. The output power from the Er-doped InGaN LEDs was comparable to initial results for Eu-doped GaN LEDs (Nishikawa et al., 2010). EL spectra from the Er-doped InGaN LED, measured at RT in the region between 900 and 1700 nm under different input currents, are shown in Fig. 7.13. In the inset, intensities of the emission lines at 1.0 and 1.54  $\mu\text{m}$  can be seen to increase monotonically up to  $\sim 70$  mA (Fig. 7.15).

Other Er-doped III-N LEDs were designed and fabricated, including p-i-n homojunctions having GaN:Er and GaN:Er + Mg epilayers as the active regions (Feng, 2013). In general, EL spectra from these LEDs contained emissions in both the visible and near-IR limiting power output at the desired 1.54  $\mu\text{m}$  region.

## 7.4 Magnetic properties of III-N:Er thin films

Several different techniques were used to measure the magnetic properties of the III-N:Er films grown by MOCVD. These include superconducting quantum

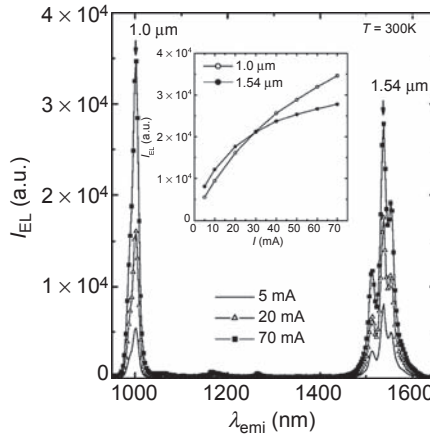


**Figure 7.15** EL spectra in the near-IR of an Er-doped InGaN LED under different levels of injection currents. In the inset, the EL intensities of 1.0 and 1.54  $\mu\text{m}$  emissions are shown as a function of injection current.

Source: Adapted from Dahal, R., Ugolini, C., Lin, J.Y., Jiang, H.X., Zavada, J.M., 2010a.

1.54  $\mu\text{m}$  emitters based on erbium doped InGaN p-i-n junctions. Appl. Phys. Lett. 97, 141109.

interference device (SQUID) measurements, alternating gradient magnetometry (AGM), and combined excitation emission spectroscopy (CEES) in conjunction with an applied magnetic field.

In SQUID measurements, a high sensitivity magnetometer utilizes the properties of electron-pair wave coherence and Josephson junctions to detect very small magnetic fields. A natural result of the phase coherence over long distances is the quantization of magnetic flux in a superconducting ring. The working principle of the SQUID is based on this property of a superconducting ring. The SQUID measurement is performed by moving a sample through the superconducting detection coils that are in a loop with the SQUID chip. As the sample moves through the coils, the magnetic moment of the sample induces an electric current in the detection coils and this change in current produces a voltage, which is then converted into the magnetic response from the sample. In our experiments, an SQUID magnetometer by Quantum Design was used to measure the magnetic moments of samples. Since the operation of the SQUID requires cryogenic temperatures (4K), liquid helium was needed as the medium for cooling, making the operational costs expensive. After the III-N samples were ultrasonically cleaned in solvents and dried by blowing nitrogen, they were loaded in the SQUID chamber using a straw as a sample holder. The applied magnetic field ( $H_a$ ) was vertical to the sample surface, which was normally the easy axis of magnetization (Nepal et al., 2009b).

With AGM, electromagnets are used to produce an alternating magnetic field gradient across a region in which a sample is placed. The sample is mounted at one end of a vertical cantilever, the other end of which is attached to the bottom of a piezoelectric transducer (see schematic diagram in Fig. 7.16). The alternating field gradient

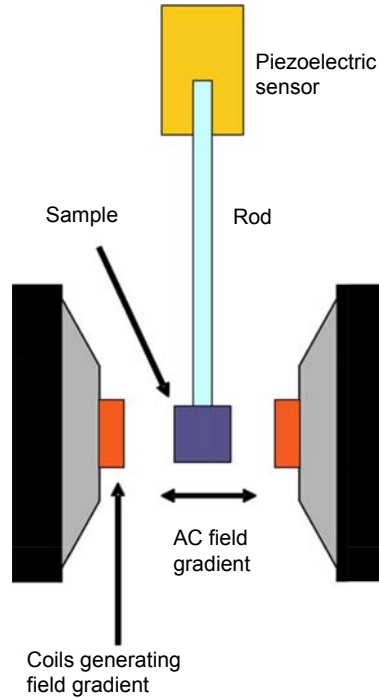


**Figure 7.16** Schematic of an alternating gradient magnetometer. The force on the sample is generated by a set of coils, and the motion of the sample is proportional to its magnetization. Source: Adapted from Luen, M.O., 2009. Spintronics: Towards Room Temperature Ferromagnetic Devices via Mn and Rare Earth Doped GaN (thesis). North Carolina State University.

exerts an oscillatory force on the sample, and the bending of the transducer produces a voltage proportional to the amplitude of the oscillation. The AGM needs to be operated at the resonant frequency of the cantilever system, which depends upon the weight of the sample. The sensitivity of the instrument is limited by thermal noise in the mechanical oscillator, and typical sensitivities are comparable to cryogenic magnetometers ( $\sim 10^{-12} \text{ Am}^2$ ). A DC field also may be applied during measurements, to allow the magnetization as a function of the electric field to be determined. Often a heater or cryostat also is fitted to permit both field and temperature variation of the magnetization to be determined.

CEES measurements employ the capability of CCD-based spectrometers to collect emission spectra from a sample in a rapid fashion while tuning the laser wavelength in small steps. The data collection process is computer controlled and the 2D-data set of emission intensities as a function of excitation and emission energies can be collected. The data can be depicted by contour or image plots resembling geographic maps. This technique has been applied to Er-doped  $\text{LiNbO}_3$  to allow systematic determination of different defect sites and to identify specific transitions involving the same defect site (Dierolf and Sandmann, 2007). In the present investigations, this technique was used

together with an applied magnetic field to probe the magnetic influence on the optical emission of the III-N:Er specimens (Woodward et al., 2011).

#### 7.4.1 Magnetic properties of GaN:Er

A set of GaN:Er samples was grown by MOCVD on (0001) c-plane sapphire substrates as described in Section 7.2.3. The Er concentrations were in the range of  $N_{\text{Er}} \sim 2\text{--}10 \times 10^{20} \text{ cm}^{-3}$  as determined by SIMS. The electrical properties were determined by van der Pauw Hall effect measurements and found to be comparable to those of high-quality undoped MOCVD GaN films. XRD spectra from the GaN:Er samples, as well as the spectrum from an undoped GaN epilayer, are displayed in Fig. 7.17. All the samples were of high crystallinity and there was no indication of second phase formation, even with  $N_{\text{Er}} \sim 10^{21} \text{ cm}^{-3}$ . However, splitting of the  $K_{\alpha 1}$  and  $K_{\alpha 2}$  lines was observed indicating an increase in in-plane strain for  $N_{\text{Er}}$  above  $\sim 3 \times 10^{20} \text{ cm}^{-3}$ .

For the SQUID measurements,  $H_a$  was normal to the sample surface, diamagnetic properties of the substrate and holder were subtracted out, and the data normalized to sample volume. Each of the GaN:Er epilayers displayed hysteretic behavior at RT consistent with FM ordering. The magnetization ( $M$ ) data as a function of temperature  $T$  of the sample having  $N_{\text{Er}} \sim 10^{21} \text{ cm}^{-3}$  are summarized in Fig. 7.18. The data points show the results of the zero-field-cooled (ZFC) and field-cooled (FC) SQUID measurements done with  $H_a = 200 \text{ Oe}$ . The measurements clearly indicate that the temperature at which the ZFC/FC curves meet, the blocking temperature  $T_B$ , is above 300K. This is further evidence of the high degree of crystallinity of the GaN:Er epilayers grown by

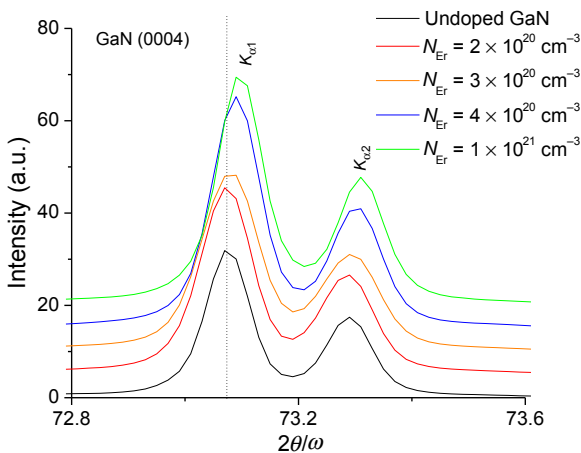


**Figure 7.17** XRD spectra from an undoped GaN epilayer and GaN:Er samples having different Er concentrations. For  $N_{\text{Er}}$  above  $\sim 3 \times 10^{20} \text{ cm}^{-3}$  the in-plane strain increased.

Source: Adapted from Ugolini, C.R., 2008. Optical and Structural Properties of Er-Doped GaN/InGaN Materials and Devices Synthesized by Metal Organic Chemical Vapor Deposition (thesis). Kansas State University.



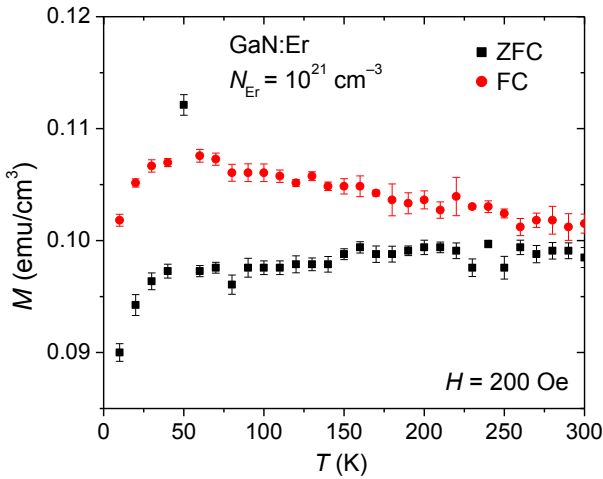


**Figure 7.18** SQUID measurements, in an applied field of 200 Oe, as a function of temperature from the GaN:Er sample with  $N_{\text{Er}} \sim 10^{21} \text{ cm}^{-3}$ . FC and ZFC magnetization data points are shown.

Source: Adapted from Zavada, J.M., Nepal, N., Ugolini, C., Lin, J.Y., Jiang, H.X., Davies, R., Hite, J., Abernathy, C.R., Pearton, J., Brown, E.E., Hommerich, U., 2007. Optical and magnetic behavior of erbium-doped GaN epilayers grown by metal-organic chemical vapor deposition. *Appl. Phys. Lett.* 91, 054106.

MOCVD. SQUID measurements were also performed on an undoped GaN sample to eliminate the possibility that spurious TM impurities might be responsible for the magnetic response. No magnetic hysteresis was observed in the undoped sample (Zavada et al., 2007).

The dependence of the saturation magnetization ( $M_S$ ) on the Er concentration is shown in Fig. 7.19. For measurements at 10K the  $M_S$  has a linear dependence on  $N_{\text{Er}}$ . At 300K, values for  $M_S$  are nearly the same for  $N_{\text{Er}} \leq 3 \times 10^{20} \text{ cm}^{-3}$ . However, for the sample having  $N_{\text{Er}} \sim 10^{21} \text{ cm}^{-3}$ , there is a noticeable decrease in  $M_S$ , which may be due to effects of increased dislocations or defects that are present with higher doping levels.

#### 7.4.1.1 Strain-induced effects

The magnetic properties of GaN:Er epilayers grown on different substrates (see Section 7.2.3) were examined using AGM and resonant CEES combined with an applied magnetic field. The AGM measurements were made at RT with the magnetic field applied first normal to the sample surface and subsequently parallel to the sample surface. The diamagnetic properties of the substrate and holder were subtracted out and the data normalized to sample volume. Results of these measurements for different GaN:Er samples are presented in Fig. 7.20. The in-plane hysteretic data (Fig. 7.20(a)) show that the GaN:Er sample grown on the GaN/Al<sub>2</sub>O<sub>3</sub> template had the highest  $M_S$  value. This was followed by the sample grown on the GaN/Si (111). The other films displayed either

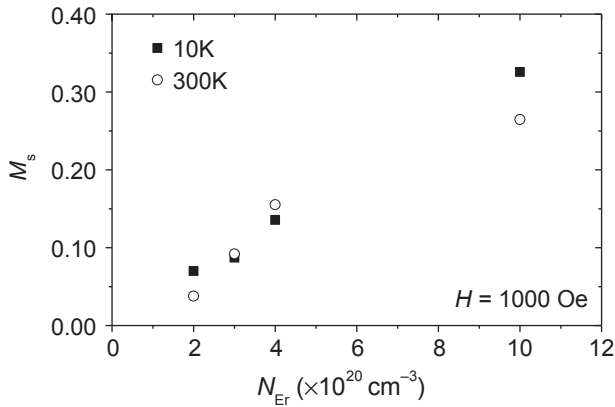


**Figure 7.19** Plot of the data points showing the dependence of the saturation magnetization ( $M_s$ ) on the Er concentration. There was a decrease in  $M_s$  at 300K for the sample with  $N_{Er} \sim 10^{21} \text{ cm}^{-3}$ .

Source: Adapted from Zavada, J.M., Nepal, N., Ugolini, C., Lin, J.Y., Jiang, H.X., Davies, R., Hite, J., Abernathy, C.R., Pearton, J., Brown, E.E., Hommerich, U., 2007. Optical and magnetic behavior of erbium-doped GaN epilayers grown by metal-organic chemical vapor deposition. *Appl. Phys. Lett.* 91, 054106.

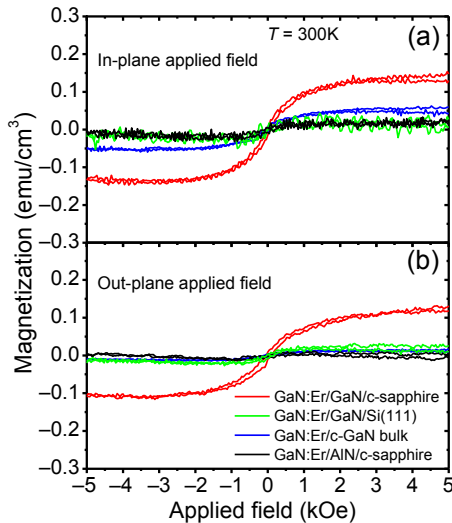


**Figure 7.20** Results of AGM measurements made at RT for GaN:Er epilayers grown on different templates: (a) in-plane data and (b) out-of-plane data. In both orientations of the applied field, magnetization was highest for the GaN:Er sample grown on the GaN/Al<sub>2</sub>O<sub>3</sub> template.

Source: Adapted from Woodward, N.T., Nepal, N., Mitchell, B., Feng, I.W., Li, J., Jiang, H.X., Lin, J.Y., Zavada, J.M., Dierolf, V., 2011. Enhanced magnetization in erbium doped GaN thin films due to strain induced electric fields. *Appl. Phys. Lett.* 99, 122506.

weak or paramagnetic behavior. The broad XRD spectrum for the GaN:Er layer grown on the AlN/Al<sub>2</sub>O<sub>3</sub> template may have been a result of significant disorder in the film, which inhibited magnetic ordering. The out-of-plane hysteretic data (Fig. 7.20(b)) were similar, with  $M_S$  being highest for the epilayer grown on the GaN/Al<sub>2</sub>O<sub>3</sub> template and negligible for the other samples.

Based on estimate of the GaN:Er material volume involved in these measurements, an effective magnetic moment ( $\mu_{\text{eff}}$ ) for the two orientations was obtained for this GaN:Er sample. The in-plane  $\mu_{\text{eff}}$  was  $\sim 0.24 \mu_B$  and the out-of-plane  $\mu_{\text{eff}} \sim 0.22 \mu_B$ , where  $\mu_B$  is the Bohr magneton, indicating  $\sim 7.2\%$  magnetic activation of Er atoms. The presence of a magnetic moment in both the in-plane and out-of-plane orientations is an indication that this epilayer was in a transitional state of stress (El-Masry et al., 2015, in this volume).

The substrate dependence of the magnetization that is induced by different substrates raises the question on how this behavior is reflected in the spectroscopic properties of the Er ions. To this end, we used CEES, which has been proven to be a powerful tool to identify different incorporation sites and the variation of their environment (Dierolf, 2010; Woodward et al., 2011). To illustrate this capability, Fig. 7.21 shows, as an example, data for a GaN:Er sample was grown on the GaN/Al<sub>2</sub>O<sub>3</sub> template. The CEES data were obtained at  $T = 4\text{K}$  using liquid He-flow cryostat by scanning a 980 nm external cavity laser in the spectral region of the  $^4I_{15/2}$  to  $^4I_{11/2}$  transition and recording the resulting emission around 1.5  $\mu\text{m}$  corresponding to the transition between the  $^4I_{13/2}$  to  $^4I_{15/2}$  state. The resulting 2D-data set is depicted as an image plot. Despite the multitude of transition peaks in the measurements, all transitions can be accounted by taking thermally excited states into consideration. The corresponding level scheme is shown as an inset of Fig. 7.21. It should also be noted that there is clear evidence of fluorescence line narrowing (FLN). This is reflected in the excitation/emission features that are tilted in the CEES image. This is most apparent in the feature on the very right within the dotted square in Fig. 7.21. Such a line narrowing effect is a clear indication of an inhomogeneously broadened spectral line that results from Er centers that are slightly different in the local environment in a continuous way. Variations in local intrinsic strain are a likely candidate for these variations. The differences in spectra are best quantified by taking the spectral differences between the emission transitions from level B2 to A1 and B2 to A3, as a measure (Dierolf, 2010).

In Fig. 7.22(a), we compare a small region of the CEES data for two samples grown on different substrates. The image plot represents a zoomed-in representation of the same data as in Fig. 7.21 for the sample grown on a GaN/Al<sub>2</sub>O<sub>3</sub> template, while the contour lines indicate the data for a sample grown on bulk c-GaN. We clearly see how different the spectral features are both in position as well as in the extent of the features. In particular, the tilted feature is shifted from one sample to another, indicating the same incorporation site but with different strain environments for the two samples. Arrows indicate the shifts of the maxima. This finding becomes even more apparent if we take spectra for an excitation transition that has no FLN and that leads to wider emission lines that reflect the average splitting of A1 and A3 in their emission maxima. Fig. 7.22(b) shows a comparison of three samples grown on different

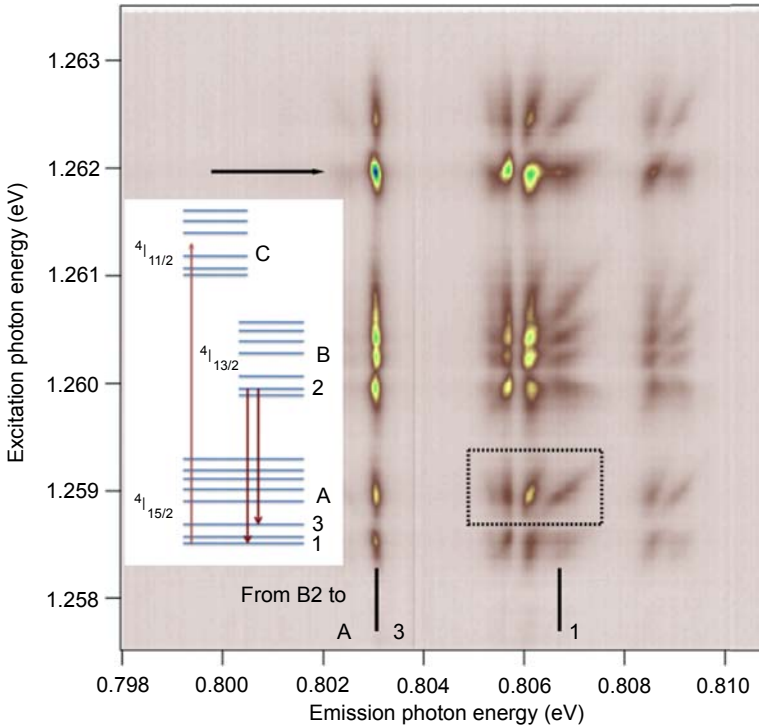


**Figure 7.21** CEES of GaN on sapphire in situ doped with Er. The inset shows a schematic of the excitation and emission transitions. The dotted area is the region that is shown in more detail in Fig. 7.22. Transitions from the level B2 to A1 and A3 are indicated by lines. The excitation for which the FLN is small is indicated by an arrow, and is used for Fig. 7.22.

Source: Adapted from Woodward, N.T., Nepal, N., Mitchell, B., Feng, I.W., Li, J., Jiang, H.X., Lin, J.Y., Zavada, J.M., Dierolf, V., 2011. Enhanced magnetization in erbium doped GaN thin films due to strain induced electric fields. *Appl. Phys. Lett.* 99, 122506.

substrates. While the peaks for the transition between levels B2 and A3 are almost identical, the transition to A1 is shifted dramatically, giving rise to a sample-dependent splitting of the A1 and A3 level, indicated by an arrow in Fig. 7.22(b), which can be correlated to different average strain fields. It is important to note that the values of these shifts vary in a similar way as the magnetization shown in Fig. 7.20.

Applying a magnetic field will split the spectral lines of Er ions as described in Chapter 9 for Nd-doping of GaN (Metcalf et al., 2015, in this volume). Fig. 7.23 shows the spectra obtained under an applied field of 1 T parallel to the *c*-axis of a GaN:Er sample and compares it to the spectrum in the absence of a field. It should be noted that even for a rather small field the magnetically induced Zeeman splitting of lines becomes comparable to the Stark-type level splitting caused by the crystal field. As a consequence, the Zeeman splittings are no longer linear in the magnetic field, and moreover no longer symmetric around the zero-field lines. Both are a consequence of avoided level crossings. The former also explains why *g*-factors for the

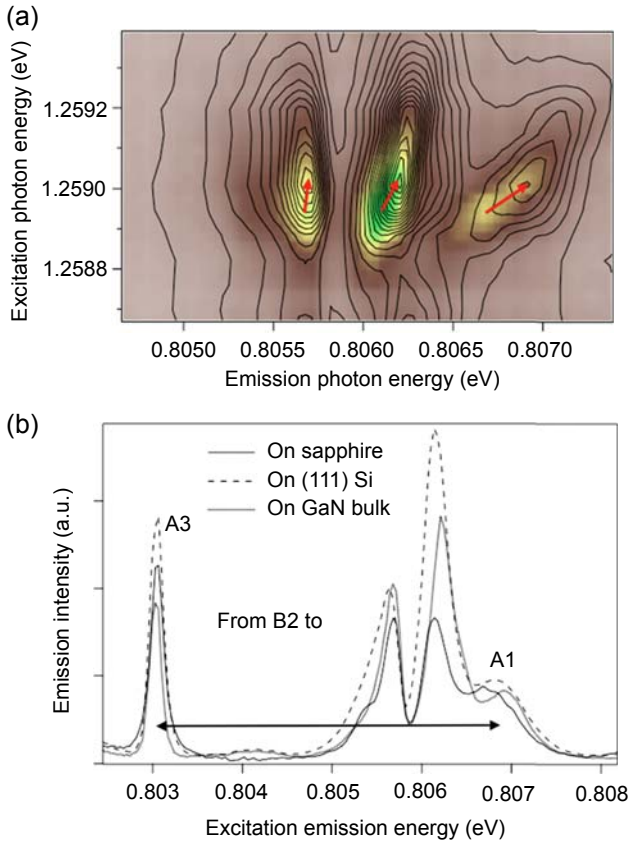


**Figure 7.22** (a) Excerpt of CEES for samples grown on sapphire (image) and on bulk GaN (black contour lines) for an area that shows pronounced FLN. Arrows indicate the shifts of the maxima of the respective lines between samples. (b) Emission spectra taken for layers grown on three different substrates excited at a transition for which little fluorescence line narrowing occurs (see arrow in Fig. 7.21). The arrow indicates the splitting between the A1 and A3 levels, which characterizes the strain.

Source: Adapted from Woodward, N.T., Nepal, N., Mitchell, B., Feng, I.W., Li, J., Jiang, H.X., Lin, J.Y., Zavada, J.M., Dierolf, V., 2011. Enhanced magnetization in erbium doped GaN thin films due to strain induced electric fields. *Appl. Phys. Lett.* 99, 122506.

ground state that are reported in literature depend on the magnetic field under which they are obtained. For instance, [Konopka et al. \(2011\)](#) report values of  $g_{\parallel} = 2.96$  and  $g_{\perp} = 8.806$  for the ground state; whereas, [Wolos et al. \(2003\)](#) report  $g_{\parallel} = 2.86$  and  $g_{\perp} = 7.645$ . Collecting CEES data under application of a magnetic field allows the determination of the  $g$ -factors. The values obtained at 1 T are summarized in [Table 7.1](#).

In the presence of considerable strain and inhomogeneous broadening, such as in the GaN:Er samples grown on different substrates that were discussed earlier, the

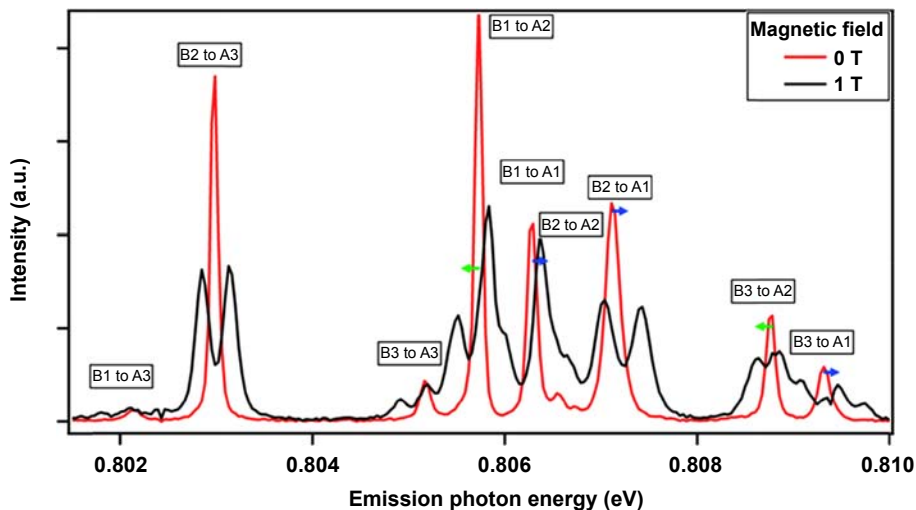


**Figure 7.23** Emission spectra obtained at 4K for applied magnetic fields of 0 and 1 T, perpendicular to the  $c$ -axis. The respective transitions are labeled. Arrows indicate the shift of the centers of the gravity of the peaks with increasing magnetic field. Note that transitions that terminate on A1 shift to higher energies, while those that terminate on A2 shift to lower energies.

strong overlap of Stark-split levels does not allow for a substrate-dependent determination of  $g$ -factors. However, a very noticeable difference arises when fields are applied parallel and antiparallel to the  $c$ -axis, which is the growth direction. Fig. 7.24(a) shows the emission spectra at 6.6 T, with its complicated splitting behavior, for GaN:Er epilayer grown on bulk  $c$ -GaN. The splitting and the relative strength of the peaks are independent of the direction of the magnetic field. This behavior, which is

**Table 7.1** Values of  $g$ -factors, as determined by CEES under application of a magnetic field, for the ground state of Er ions in GaN films

Crystal field level	$g$ -Factor B-field//to $c$ -axis	$g$ -Factor B-field $\perp$ to $c$ -axis
B3	$4.04 \pm 0.20$	$4.52 \pm 0.23$
B2	$7.96 \pm 0.40$	0
B1	$2.88 \pm 0.14$	$5.70 \pm 0.29$
A3	$5.27 \pm 0.26$	$4.83 \pm 0.24$
A2	$9.28 \pm 0.46$	0
A1 (ground state)	$2.88 \pm 0.14$	$6.94 \pm 0.35$

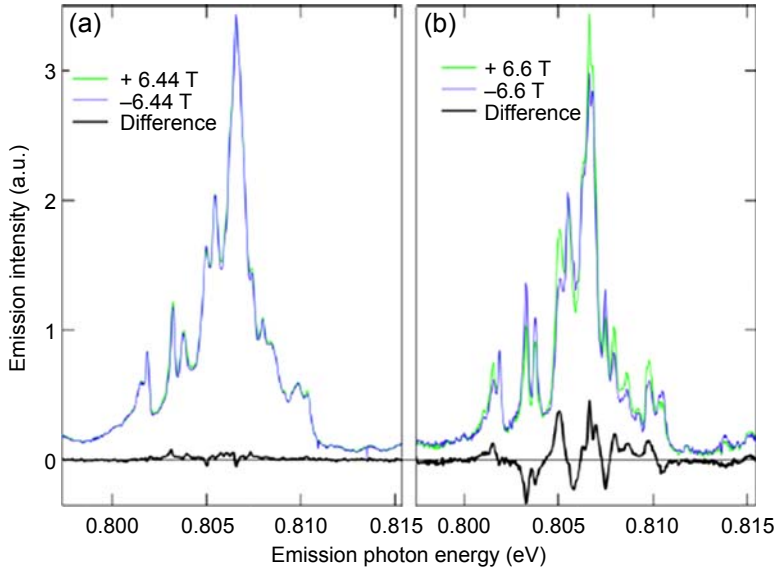


**Figure 7.24** Emission spectra of Er ions, excited at the spectral position, indicated in Fig. 7.22, under application of a magnetic field parallel and antiparallel to the growth axis of the GaN:Er layer grown on (a) c-GaN bulk substrate and (b) the GaN/Al<sub>2</sub>O<sub>3</sub> template. The emission difference spectra, black curves, clearly demonstrate the changes brought about by the residual strain in the layer grown on sapphire.

Source: Adapted from Woodward, N.T., Nepal, N., Mitchell, B., Feng, I.W., Li, J., Jiang, H.X., Lin, J.Y., Zavada, J.M., Dierolf, V., 2011. Enhanced magnetization in erbium doped GaN thin films due to strain induced electric fields. *Appl. Phys. Lett.* 99, 122506.

generally expected, is changed dramatically for the GaN:Er epilayer grown on sapphire (see Fig. 7.24(b)). In this case, the relative strength of the transitions is quite different for the two antiparallel field directions, while the splitting still remains independent of the direction. Apparently, in this sample, the magnetic states of the Er ion are dependent on the growth direction. Such coupling between growth direction and magnetic field states can only be provided by an internal electric field that is provided through a piezoelectric effect induced by the lattice mismatch.

These strain-induced fields are drastically different when a layer is grown on bulk c-GaN or on a GaN/Al<sub>2</sub>O<sub>3</sub> template. The electric field breaks the symmetry, which is then reflected in the dependence of the transition strength on the field direction. This clearly demonstrates a coupling of the Er<sup>3+</sup>-states to the host. Further evidence from the influence of the strain comes from the fact that the changes in relative transition strength are most pronounced for transitions that are also shifted most significantly for different strain environments (see Fig. 7.24). Comparison with other piezoelectric materials such as LiNbO<sub>3</sub> and LiTaO<sub>3</sub>, for which no difference is observed, reveals that this behavior is quite unique and demonstrates that a special coupling exists between the magnetic Er ion and the semiconductor host such as GaN.

The results of these experiments provide strong evidence that FM behavior of GaN:Er epilayers grown by MOCVD, is directly proportional to the stress in the thin films induced by lattice mismatch with the substrate. Hysteretic data from such films are in general agreement with optical emission intensities taken in PL measurements and with the strain-induced spectral shifts found in our CEES measurements shifts. In addition, PL spectra taken in the presence of an applied magnetic field indicate the magnetic states of the Er ion are coupled to the electronic states of the host. The strongest effect is observed for states that are also most sensitive to strain. This correlation suggests that the coupling of the magnetic states to the host can be modified by strain.

#### 7.4.2 Magnetic properties of InGaN:Er

We have also investigated the magnetic properties of InGaN:Er epilayers, with different In content, and grown on (0001) c-plane sapphire substrates as described in Section 7.2.3. These epilayers had a thickness of  $\sim 0.5 \mu\text{m}$  and were subsequently characterized by AGM and CEES techniques. Results of AGM measurements made at RT for InGaN:Er epilayers, with  $x = 0.11, 0.13, 0.15,$  and  $0.18,$  are shown in Fig. 7.25. In-plane hysteretic behavior was found for each of the samples, with the Ms being nearly linearly proportional to the In content. Even though the crystalline quality and surface of the InGaN films was degraded with higher In content, the  $\text{In}_{0.18}\text{Ga}_{0.82}\text{N}$  epilayer had the strongest magnetic response. A similar behavior was found for Tm-doped AlGaN films showing that the magnetic behavior was correlated with compositional fluctuation of Al content (Nepal et al., 2009a). Alloy disordering appears to lead to potential energy fluctuations that produce a strong localization effect that enhances magnetic ordering. As in the case of GaN:Er epilayers grown on different substrates, InGaN:Er with higher In content may also have increased biaxial stress that also promotes FM behavior.

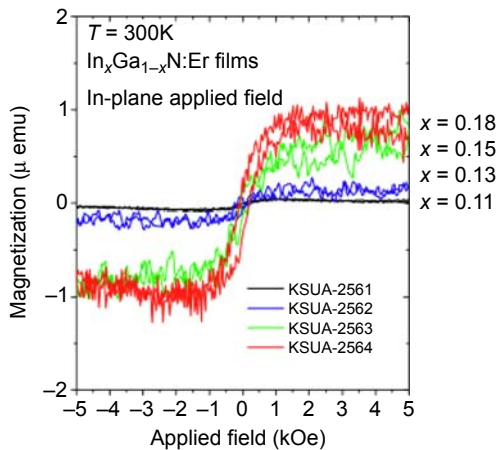


**Figure 7.25** AGM measurements made at RT for InGaN:Er epilayers grown on sapphire and having different In content. The saturation magnetization was found to be nearly linearly proportional to the In content.



Stachowicz et al. studied the local lattice disorder in these InGaN:Er epilayers using the 1.54 emission of the  $\text{Er}^{3+}$  ions. The Er concentration in these layers was  $\sim 2.3\%$ . Based on site selective optical spectroscopy and PL excitation spectroscopy, they found that there were two classes of the emitting Er centers. One was nearly the same as in GaN:Er, except for nonuniform broadening. The other center had new emission features that were not present in GaN:Er layers. These emission features were interpreted as originating from Er-complexes involving one or more In atoms in the second coordination sphere. The observed fluorescence line broadening and wavelength shifts in the emission wavelength indicated the extent of the disorder in the metallic sublattice (Stachowicz et al., 2014).

### 7.4.3 Influence of light on magnetic properties

In general, there was a direct correspondence between the magnetic and optical properties of the III-N:Er epilayers as a function of Er concentration. As  $N_{\text{Er}}$  increased, so did the PL intensity at 1.54  $\mu\text{m}$  as well as the  $M_{\text{S}}$  value, measured at 10 and 300K. However, the PL spectrum, with its distinctive characteristics of the  $4f$  transitions between the  $^4\text{I}_{15/2}$  and  $^4\text{I}_{13/2}$  levels, was very dependent upon the excitation wavelength. It was found that either a laser diode at 370 nm, or an LED at 371 nm, was a very efficient source for excitation of the  $\text{Er}^{3+}$  ions in GaN and InGaN epilayers (Dahal et al., 2008). In addition, since the magnetic properties were related to coupling between electrons bound at the complex and those in the host, experiments were undertaken to determine whether incident photons could affect the magnetic measurements. Several GaN:Er samples, with  $N_{\text{Er}} \sim 2\text{--}10 \times 10^{20} \text{ cm}^{-3}$ , were examined at RT using AGM without and with illumination of an LED at 371 nm. The magnetic field was applied parallel to the GaN:Er sample surface and a commercially available nitride LED, Nichia model NSHU550B, was used as the optical source during AGM measurements (Nepal et al., 2009b). The LED power output was  $\sim 2 \text{ mW}$  at 371 nm and the full width half maximum was 15–20 nm. The GaN:Er samples were mounted at a distance of about 1 mm from the LED's surface, as shown in the schematic in Fig. 7.26. The diamagnetic properties of the substrate and holder were subtracted out and the data normalized to sample volume.

Without illumination (LED-off), the GaN:Er specimens displayed RT hysteretic behavior consistent with FM ordering, whereas with illumination (LED-on) an increase in  $M_{\text{S}}$  was observed for all samples. In Fig. 7.27(a) hysteretic data taken at RT are presented for the GaN:Er sample with  $N_{\text{Er}} \sim 2 \times 10^{20} \text{ cm}^{-3}$  under LED-off and LED-on conditions. While the coercivity remained constant, there was an increase of approximately  $0.8 \mu \text{ emu}$  in  $M_{\text{S}}$  when the sample was illuminated. The measured increase in magnetization,  $\Delta M_{\text{S}} = M_{\text{S}}(\text{on}) - M_{\text{S}}(\text{off})$ , for each of the samples is plotted in Fig. 7.27(b) as a function of Er concentration. Also plotted are the  $M_{\text{S}}(\text{off})$  values. The largest increase was observed for the sample with the lowest Er concentration. The other samples had a higher initial  $M_{\text{S}}$  value but a slightly lower  $\Delta M_{\text{S}}$  of  $\sim 0.7 \mu \text{ emu}$ . While the measured coercivity was unchanged under LED-off/LED-on conditions, the  $M_{\text{S}}$  returned to its original levels when the LED was turned off.

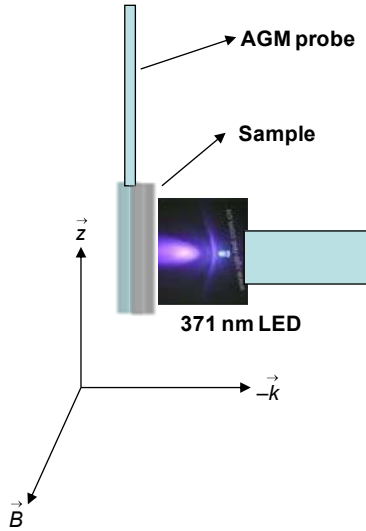


**Figure 7.26** Illustration of the placement of the LED source and a GaN:Er sample. The sample was at a distance of  $\sim 2$  mm from LED surface during AGM measurements.

Source: Adapted from Nepal, N., Zavada, J.M., Dahal, R., Ugolini, C., Sedhain, A., Lin, J.Y., Jiang, H.X., 2009b. Optical enhancement of room temperature ferromagnetism in Er-doped GaN epilayers. Appl. Phys. Lett. 95, 022510.

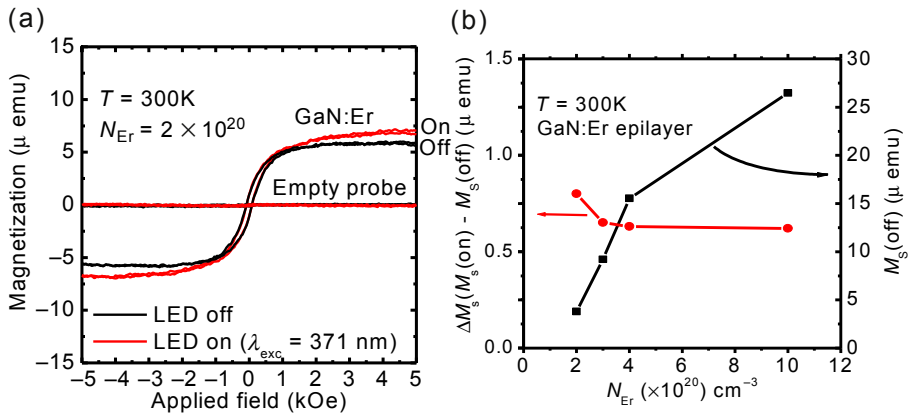


**Figure 7.27** AGM measurements at RT showing (a) hysteretic behavior under LED-off and LED-on conditions for a GaN:Er sample with  $N_{Er} \sim 2 \times 10^{20} \text{ cm}^{-3}$  and (b) the measured  $\Delta M_S$  and  $M_S(\text{off})$  values plotted as a function of Er concentration.

Source: Adapted from Nepal, N., Zavada, J.M., Dahal, R., Ugolini, C., Sedhain, A., Lin, J.Y., Jiang, H.X., 2009. Optical enhancement of room temperature ferromagnetism in Er-doped GaN epilayers. Appl. Phys. Lett. 95, 022510.

The results of these experiments indicate that electron-hole pairs created by incident photons from the LED source facilitate FM ordering in GaN:Er layers. While the data support a carrier-mediated mechanism for the RT FM behavior observed in these Er-doped films, it is unclear whether positive or negative carriers are dominant. In addition, the photon flux of the LED may have been the limiting factor in these experiments and use of a laser source may have produced larger increases in  $M_S$ .

## 7.5 Summary

We have demonstrated that MOCVD is a reliable technique for synthesis of high-quality Er-doped GaN and InGaN epilayers. PL measurements showed low thermal quenching of emission around 1.54  $\mu\text{m}$  even up to RT. Prototype EL devices with InGaN:Er active layers were fabricated and processed into LED devices. Hysteric behavior at RT was observed for both GaN:Er and InGaN:Er epilayers. The optical and magnetic properties of these films were shown to be dependent upon the stress produced due to lattice mismatch during MOCVD growth on different substrates. These effects indicate the coupling of the optical and magnetic states of the Er ions to the semiconductor host. These results indicate the possible use of externally induced strain to control optical and FM behavior. CEES measurements showed that applied magnetic fields may alter optical emission of the Er ions. Illumination of GaN-Er epilayers at a wavelength of 371 nm produced an enhancement of magnetic properties suggesting a carrier-mediated mechanism. Consequently, magnetic control of optical properties and optical control of magnetic properties have been demonstrated for III-N:Er films grown by MOCVD. Similar results may occur for other RE-doped III-N semiconductor films. Considering the fact that the majority of Er ions enter into a defect-related complex ( $\text{Er}_{\text{Ga}}-\text{V}_{\text{N}}$ ), the presented results emphasize the critical role of the electrically active complexes on the optical and magnetic effects. While the Er ion itself is quite insensitive to the lattice environment, such defect-related complexes appear very sensitive in their formation kinetics and energetics, in their configuration, and in their energy level positions within band structure of the III-N host. Moreover, these complexes are very sensitive to their charge state, which can be manipulated by creating free carriers using above-bandgap light irradiation.

## Acknowledgments

The authors thank Dr. N. El-Masry for her helpful comments concerning portions of this work that were performed in her lab at NCSU under grants from the US Army Research Office (W911NF-06-1-0134) and the National Science Foundation (EECS-0823894). NN gratefully acknowledges the ARO/NRC postdoctoral fellowship program. The work at Texas Tech University was partially supported by National Science Foundation through grant ECCS-1200168. JYL and HXJ acknowledge the support of the Linda Whitacre and Edward Whitacre endowed chair positions through the AT&T Foundation. Work at Lehigh University was supported by a Lehigh

University FIG grant and by the National Science Foundation through grant ECCS-1239679. Support from NSF grant DMR-1008075 was used to perform measurements on  $\text{LiNbO}_3$  and  $\text{LiTaO}_3$  for comparison.

## References

- Dahal, R., Ugolini, C., Lin, J.Y., Jiang, H.X., Zavada, J.M., 2008. Current-injected 1.54  $\mu\text{m}$  light emitting diodes based on erbium-doped GaN. *Appl. Phys. Lett.* 93, 033502.
- Dahal, R., Ugolini, C., Lin, J.Y., et al., 2009. Erbium-doped GaN optical amplifiers operating at 1.54 microns. *Appl. Phys. Lett.* 94, 111109.
- Dahal, R., Ugolini, C., Lin, J.Y., Jiang, H.X., Zavada, J.M., 2010a. 1.54  $\mu\text{m}$  emitters based on erbium doped InGaN p-i-n junctions. *Appl. Phys. Lett.* 97, 141109.
- Dahal, R., Lin, J.Y., Jiang, H.X., Zavada, J., 2010b. Er-doped GaN and InGaN for optical communications. In: O'Donnell, K., Dierolf, V. (Eds.), *Topics in Applied Physics: Rare Earth Doped III-nitrides for Optoelectronic and Spintronic Applications*. Springer, The Netherlands, pp. 115–157.
- Dietl, T., Ohno, H., Matsukura, F., Cibert, J., Ferrand, D., 2000. Zener model description of ferromagnetism in zinc-blende magnetic semiconductors. *Science* 287 (5455), 1019–1022.
- Dierolf, V., Sandmann, C., 2007. Combined excitation emission spectroscopy of defects for site-selective probing of ferroelectric domain inversion in lithium niobate. *J. Lumin.* 125, 67–79.
- Dierolf, V., 2010. Combined excitation emission spectroscopy (CEES) of RE ions in gallium nitride. In: O'Donnell, K., Dierolf, V. (Eds.), *Topics in Applied Physics: Rare Earth Doped III-nitrides for Optoelectronic and Spintronic Applications*. Springer, The Netherlands, pp. 221–268.
- Edgar, J., 1994. *Properties of Group-iii-Nitrides*. Institution of Electrical Engineers.
- El-Masry, N.A., Zavada, J.M., Nepal, N., Bedair, S.M., 2015. Ferromagnetic behavior in transition metal doped III-N semiconductors (Chapter 12, This Volume).
- Favennec, P.N., L'Haridon, H., Salvi, M., Moutonnet, D., Le Guillou, Y., 1989. *Electron. Lett.* 25, 718.
- Feng, I.W., Li, J., Sedhain, A., Lin, J.Y., Jiang, H.X., Zavada, J., 2010. Enhancing erbium emission by strain engineering in GaN heteroepitaxial layers. *Appl. Phys. Lett.* 96, 031908.
- Feng, I.W., Li, J., Lin, J.Y., Jiang, H.X., Zavada, J., 2012. Effects of growth pressure on erbium doped GaN infrared emitters synthesized by metal organic chemical vapor deposition. *Opt. Mater. Express* 2, 1095–1100.
- Feng, I.W., 2013. *Erbium Doped III-Nitride Semiconductors: Material Synthesizing and Applications*. Texas Tech University.
- Fihol, J.S., Jones, R., Shaw, M.J., Briddon, P.R., 2004. *Appl. Phys. Lett.* 84, 2841.
- Heikenfeld, J., Garter, M., Lee, D., Birkhahn, R., Steckl, A., 1999. Red light emission by photoluminescence and electroluminescence from Eu-doped GaN. *Appl. Phys. Lett.* 75, 1189–1191.
- Hufner, S., 1978. *Optical Spectra of Transparent Rare Earth Compounds*. Academic Press, New York.
- Isshiki, H., Kobayashi, H., Yugo, S., Kimura, T., Ikoma, T., 1991. *Appl. Phys. Lett.* 58, 484.
- Koizumi, A., Fujiwara, Y., Urakami, A., Inoue, K., Yoshikane, T., Takeda, Y., 2003. *Appl. Phys. Lett.* 83, 4521.

- Koizumi, A., Mitchell, B., Dierolf, V., Fujiwara, Y., 2015. Growth of Eu-doped GaN and its magneto-optical properties (Chapter 8, This Volume).
- Konopka, A., Greulich-Weber, S., Dierolf, V., Jiang, H.X., Gerstmann, U., Rauls, E., Sanna, S., Schmidt, W.G., 2011. Microscopic structure and energy transfer of vacancy-related with erbium in wide-gap semiconductors. *Opt. Mater.* 33, 1041–1044.
- Luen, M.O., 2009. Spintronics: Towards Room Temperature Ferromagnetic Devices via Mn and Rare Earth Doped GaN. North Carolina State University.
- MacKenzie, J.D., Abernathy, C.R., Pearton, S.J., Hömmerich, U., Seo, J.T., Wilson, R.G., Zavada, J.M., 1998. *Appl. Phys. Lett.* 72, 2710.
- Makarova, K., Stachowicz, M., Glukhanyuk, V., Kozanecki, A., Ugolini, C., Lin, J.Y., Jiang, H.X., Zavada, J.M., 2008. Spectroscopic studies of Er-centers in MOCVD grown GaN layers highly doped with Er. *Mater. Sci. Eng. B* 146, 193–195.
- Metcalfe, G.D., Readinger, E.D., Woodward, N., Dierolf, V., Nepal, N., Zavada, J.M., 2015. Optical and magnetic characterization of III-N: Nd grown by MBE (Chapter 9, This Volume).
- Morishima, S., Maruyama, T., Tanaka, M., Masumoto, Y., Akimoto, K., 1999. *Phys. Status Solidi A* 176, 113.
- Munekata, H., Ohno, H., von Molnar, S., Segmüller, A., Chang, L.L., Esaki, L., 1989. Diluted magnetic III-V semiconductors. *Phys. Rev. Lett.* 63, 1849.
- Nakamura, S., Pearton, S.J., Fasol, G., 2000. *The Blue Laser Diode: The Complete Story.* Springer.
- Nepal, N., Zavada, J.M., Lee, D.S., Steckl, A.J., Sedhain, A., Lin, J.Y., Jiang, H.X., 2009a. Deep UV photoluminescence of Tm-doped AlGaIn alloys. *Appl. Phys. Lett.* 94, 111103.
- Nepal, N., Zavada, J.M., Dahal, R., Ugolini, C., Sedhain, A., Lin, J.Y., Jiang, H.X., 2009b. Optical enhancement of room temperature ferromagnetism in Er-doped GaN epilayers. *Appl. Phys. Lett.* 95, 022510.
- Nishikawa, A., Furukawa, N., Kawasaki, T., Terai, Y., Fujiwara, Y., 2010. *Appl. Phys. Lett.* 97, 051113.
- Sedhain, A., Ugolini, C., Lin, J.Y., Jiang, H.X., Zavada, J.M., 2009. Photoluminescence properties of erbium doped InGaIn epilayers. *Appl. Phys. Lett.* 95, 041113.
- Steckl, A.J., Garter, M., Birkhahn, R., Scofield, J., 1998. *Appl. Phys. Lett.* 73, 2450.
- Steckl, A.J., Birkhahn, R., 1998. Visible emission from Er-doped GaN grown by solid source molecular beam epitaxy. *Appl. Phys. Lett.* 73, 1700–1702.
- Son, C.S., Kim, S., Kim, Y.H., Han, I.K., Kim, Y.T., Wakahara, A., Choi, I.H., Lopez, H.C., 2004. *J. Korean Phys. Soc.* 45, 955.
- Song, S.F., Chen, W.D., Zhang, C., Bian, L., Hsu, C.C., Lu, L.W., Zhang, Y.H., Zhu, J., 2005. *Appl. Phys. Lett.* 86, 152111.
- Stachowicz, M., Kozanecki, A., Lin, J.Y., Jiang, H.X., Zavada, J.M., 2014. Probing of local alloy disorder in InGaIn using Er<sup>3+</sup> ions. *Opt. Mater.* 36, 1730.
- Ugolini, C.R., 2008. Optical and Structural Properties of Er-doped GaN/InGaIn Materials and Devices Synthesized by Metal Organic Chemical Vapor Deposition. Kansas State University.
- Ugolini, C., Nepal, N., Lin, J.Y., Jiang, H.X., Zavada, J.M., 2006. Erbium-doped GaN epilayers synthesized by metal-organic chemical vapor deposition. *Appl. Phys. Lett.* 89, 151903.
- Woodward, N.T., Nepal, N., Mitchell, B., Feng, I.W., Li, J., Jiang, H.X., Lin, J.Y., Zavada, J.M., Dierolf, V., 2011. Enhanced magnetization in erbium doped GaN thin films due to strain induced electric fields. *Appl. Phys. Lett.* 99, 122506.
- Wu, X., Hommerich, U., MacKenzie, J.D., Abernathy, C.R., Pearton, S.J., Schwartz, R., Wilson, R.G., Zavada, J.M., 1997. *Appl. Phys. Lett.* 70, 2126.

- 
- Wolos, A., Palczewska, M., Wilamowski, Z., Kaminska, M., Twardowski, A., Bockowski, M., Grzegory, I., Porowski, S., 2003. S-d exchange interaction in GaN: Mn studied by electron paramagnetic resonance. *Appl. Phys. Lett.* 83, 5428.
- Zavada, J.M., Nepal, N., Ugolini, C., Lin, J.Y., Jiang, H.X., Davies, R., Hite, J., Abernathy, C.R., Pearton, J., Brown, E.E., Hommerich, U., 2007. Optical and magnetic behavior of erbium-doped GaN epilayers grown by metal-organic chemical vapor deposition. *Appl. Phys. Lett.* 91, 054106.

This page intentionally left blank

# Growth of Eu-doped GaN and its magneto-optical properties

8

*A. Koizumi*

Osaka University, Suita, Osaka, Japan

*B. Mitchell*

University of Mount Union, Alliance, OH, United States

*V. Dierolf*

Lehigh University, Bethlehem, PA, United States

*Y. Fujiwara*

Osaka University, Suita, Osaka, Japan

## 8.1 Introduction

Trivalent europium ( $\text{Eu}^{3+}$ ) ions have been widely used as red-emitting phosphors for cathode ray tubes and fluorescent lamps. In these applications, the ions are doped in an insulator, and red emission is obtained mainly through optical excitation. Eu-doped GaN (GaN:Eu) has been extensively studied because it has excellent luminescence properties in the red spectral region, resulting from the specific optical properties of rare-earth (RE) materials, such as sharp, intense, and temperature-insensitive emission peak owing to the intra- $4f$  shell transitions of the  $\text{Eu}^{3+}$  ions [1–9]. The progress in the GaN:Eu optical applications is shown in Fig. 8.1. The fabrication of GaN:Eu layers has initially mainly been performed by ion implantation on a GaN template with post-thermal annealing or by in situ doping using molecular beam epitaxy [1–3,5,10]. These studies produced red emission [1–3] and a stimulated emission [5,10] from the Eu ions by optical excitation of the GaN:Eu layers. More importantly, electroluminescence (EL) was observed from indium-tin-oxide (ITO)/GaN:Eu/undoped GaN grown on  $p$ -type Si(111) substrates [1] and metal-insulator-semiconductor (MIS) structures of indium (In)/GaN:Eu/undoped GaN grown on  $n$ -type Si(111) substrates [2]. Although both studies showed a red emission with current injection, the applied voltage was as high as 46 V for the ITO/GaN:Eu sample, and the emission efficiency was low for the In/GaN:Eu sample because of the low efficiency of impact excitation of the  $\text{Eu}^{3+}$  ions by hot carriers, which is dominant in these devices. To reduce the operating voltage, it was necessary to use a  $p$ - $n$  junction diode structure to inject the current into an active layer and achieve energy transfer from the GaN host to the Eu ions. The fabrication of a GaN-based red light-emitting diode (LED) using in situ Eu-doped GaN grown between  $p$ - and  $n$ -GaN by organometallic vapor-phase epitaxy (OMVPE) has



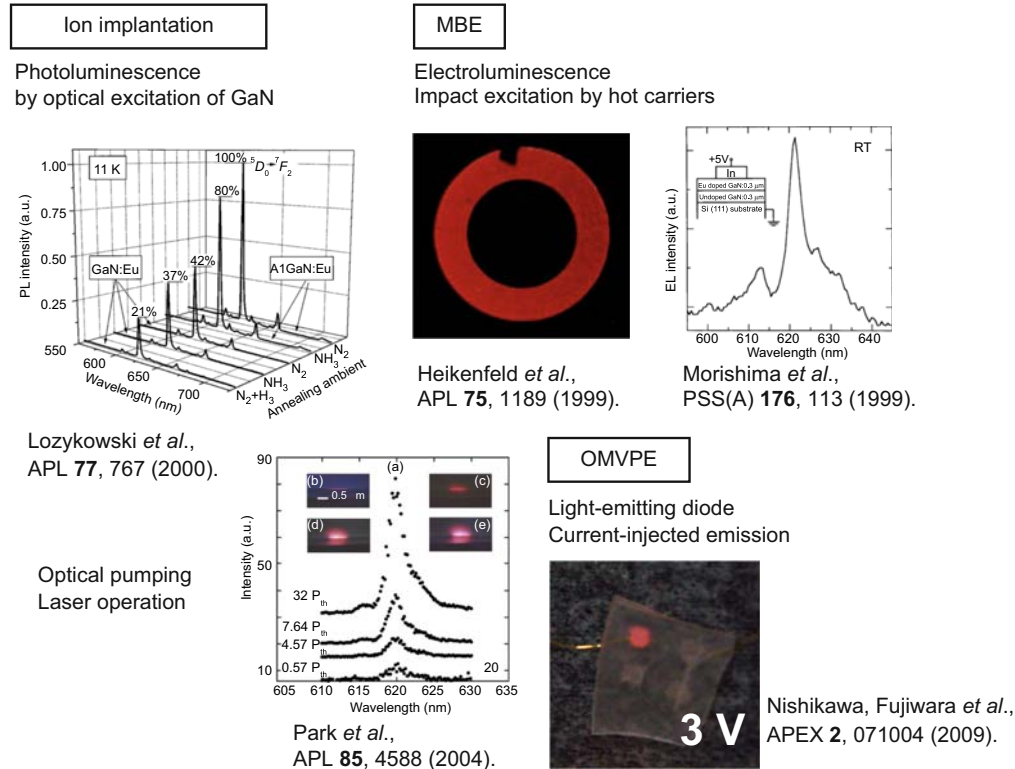


**Figure 8.1** Progress in GaN:Eu optical applications [1–6].

been demonstrated [6]. A sharp red emission with a wavelength near 620 nm and a full width at half maximum of less than 10 nm is obtained in the GaN:Eu LED operating by low-voltage current injection at room temperature (RT).

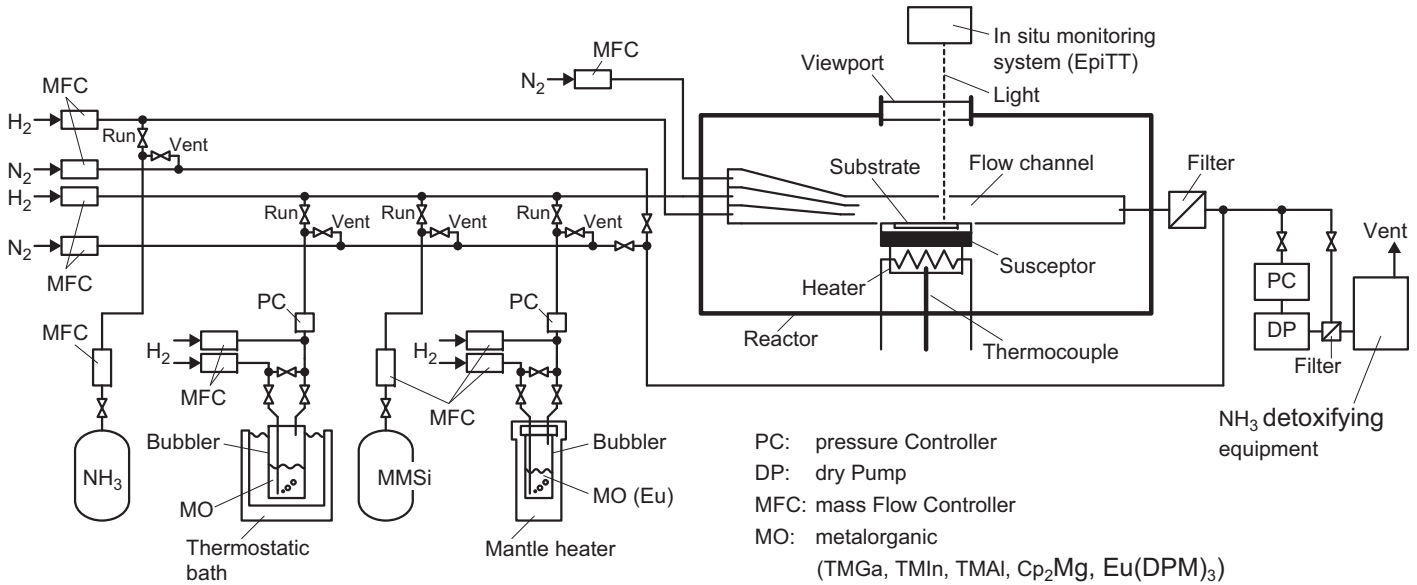
In this chapter, we will describe the growth of GaN:Eu by OMVPE with various growth conditions and their application to LEDs. After that we discuss the nature of efficient Eu luminescent centers as investigated by site selective optical techniques, and evaluate their corresponding optical and magneto-optical properties. In particular, the influence of intrinsic and/or extrinsic defects such as  $V_N$ ,  $V_{Ga}$ , and O on these properties will be discussed.

## 8.2 Growth of Eu-doped GaN by OMVPE

### 8.2.1 OMVPE growth of Eu-doped GaN

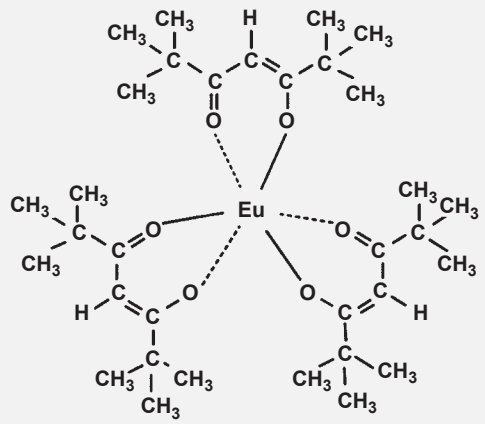
OMVPE is a common growth method for GaN and other compound semiconductors. At present, almost all commercially available GaN photonic devices are grown by the OMVPE method. In situ doping during OMVPE growth of GaN is a convenient method to introduce  $\text{Eu}^{3+}$  ions into GaN, which can be done in a controlled manner, with reproducible profiles. However, there have been only a few reports on OMVPE-grown GaN:Eu [11,12]. One of the difficulties involved in growing GaN:Eu by OMVPE is the lack of a suitable metal-organic precursor for Eu doping. Although there are several candidate precursors, the vapor pressure of an Eu precursor is generally much lower than that of conventional metal-organic precursors. This means that special precautions are required when transporting the Eu precursor to the reactor chamber, such as heating of the transfer lines to avoid its condensation [6].

Fig. 8.2 shows a schematic diagram of the horizontal OMVPE system with the three-layered laminar flow gas injection (Taiyo Nippon Sanso SR-2000) [13] used in this study. Both the bubbling and carrier gas was  $\text{H}_2$  purified with an Ag-Pd purifier. The growth is monitored using an in situ monitoring system (LayTec EpiTT), which can measure the true temperature and the layer thickness. Metal-organic precursors for Ga, Al, In, and Mg were trimethylgallium (TMGa), trimethylaluminum (TMAI), trimethylindium (TMIn), and bis(cyclopentadienyl)magnesium ( $\text{Cp}_2\text{Mg}$ ), respectively, which were maintained in a thermostatic bath to control their vapor pressure. Ammonia ( $\text{NH}_3$ ) and monomethylsilane (MMSi) were used for N and Si source gases, respectively. The optimal ratio of the TMGa and ammonia supply rates was determined to be 6400 [14].  $\text{Eu}^{3+}$  ions were doped using tris(dipivaloylmetanate)europium ( $\text{Eu}(\text{DPM})_3$ ), also known as tris(2,2,6,6-tetramethyl-3,5-heptanedionato)europium ( $\text{Eu}(\text{thd})_3$ ) [15]. The chemical structure and physical properties of  $\text{Eu}(\text{DPM})_3$  are shown in Table 8.1. The Eu precursor was maintained at 135–145°C under 103 kPa and the transfer lines were maintained at 10°C higher temperature than the Eu precursor to avoid condensation of Eu precursor during transportation. Since  $\text{Eu}(\text{DPM})_3$  has a melting point of 188°C, it is used as a solid source material and supplied by sublimation of the solid at operating temperature. Sublimation from the solid can limit the transport rate. The surface area of the solid precursor changes with time, resulting in a transport



**Figure 8.2** Schematic diagram of the horizontal OMVPE system.

**Table 8.1 Chemical structure and physical properties of Eu(DPM)<sub>3</sub> [15]**

Chemical structure	
Molecular weight	701.8
Melting point	188°C
Vapor pressure at 135°C	0.82 Pa
Clausius-Clapeyron equation $\log P = a + b/T$ ( $P$ : Torr, $T$ : Kelvin)	$a = 18.959, b = 8640.1$ K

rate or an effective vapor pressure that decreases with time during both storage and use. Therefore, the temperature of Eu precursor was sometimes adjusted to maintain a constant Eu concentration while keeping the carrier gas flow rate constant.

The growth sequence of a sample for photoluminescence (PL) measurements was initiated by the low-temperature growth of a 30-nm-thick GaN buffer on a sapphire (0001) substrate, which was followed by successive growth of a 2–3- $\mu\text{m}$ -thick undoped GaN layer, a 300- or 400-nm-thick GaN:Eu layer, and a 10-nm-thick GaN capping layer. Eu concentration was  $(3\text{--}7) \times 10^{19} \text{ cm}^{-3}$  in GaN:Eu, which was measured by synchrotron-radiation-excited X-ray fluorescence performed at the bending-magnet beamline BL14B2 at SPring-8 with a Si(111) double crystal monochromator using synchrotron radiation from the 8 GeV storage ring [16]. A GaN:Eu sample measured by secondary ion mass spectrometry is used as a reference standard.

The LED structure (Fig. 8.3) consists of a 20-nm-thick Mg-doped GaN contact layer and an 80-nm-thick Mg-doped GaN layer with an Mg-doping concentration of  $7 \times 10^{19} \text{ cm}^{-3}$ . This was followed by a 20-nm-thick Mg-doped  $\text{Al}_{0.1}\text{Ga}_{0.9}\text{N}$  electron-blocking layer, a 300-nm-thick Eu-doped GaN layer and a 3- $\mu\text{m}$ -thick  $n$ -type Si-doped GaN layer, with a Si-doping concentration of  $4 \times 10^{18} \text{ cm}^{-3}$ . Thermal annealing was performed in nitrogen ambient at a temperature of 800°C for 10 min to activate the Mg acceptor atoms. Pd/Au or In electrodes were formed on the  $p$ -type layer, while an In electrode was formed on the  $n$ -type layer. The light output power of the EL from the LED was measured with an integrating sphere spectrometer (LMS-100).

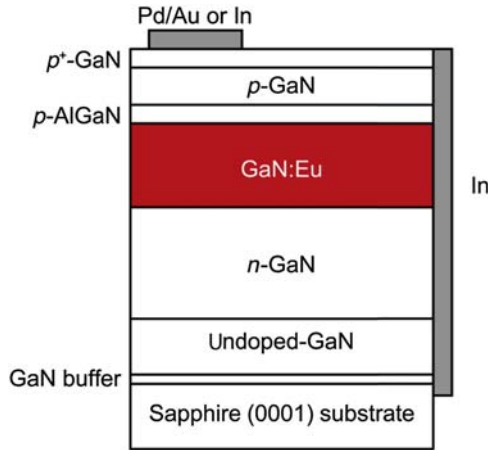


**Figure 8.3** Schematic drawing of GaN:Eu LED structure.

### 8.2.2 Effects of growth conditions and device structures on Eu luminescence properties

The growth temperature has a strong influence on the Eu incorporation in GaN. Fig. 8.4 shows PL spectra of the GaN:Eu grown at different temperatures under low pressure (10 kPa) [17]. The growth temperature dependences of PL intensity and Eu concentration are also shown. The highest 621 nm emission intensity was observed in the sample grown at 1000°C. For temperatures over 1000°C, the Eu concentration decreases with increasing growth temperature, which is a result of desorption of Eu atoms from the growth surface. Therefore, the decrease in the PL peak intensity over 1000°C is caused by the decrease in the Eu concentration in the layer. On the other hand, the PL intensity

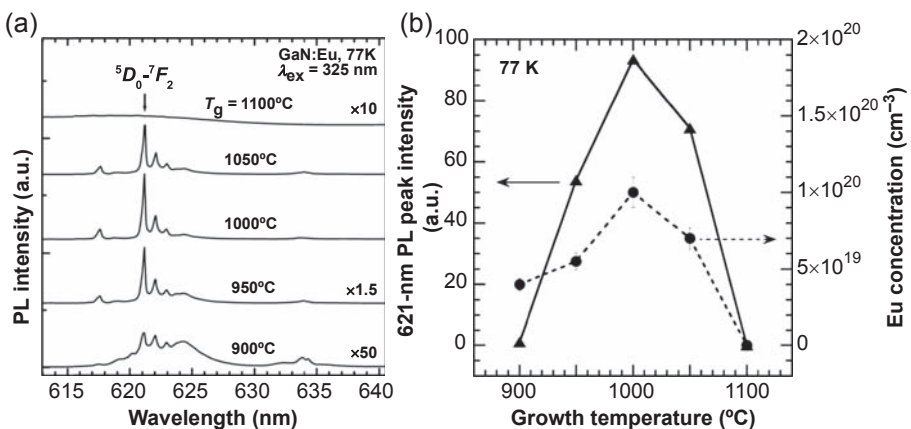


**Figure 8.4** (a) PL spectra of the GaN:Eu grown at various temperatures; (b) 621-nm PL intensity and Eu concentration as a function of the growth temperature [17].

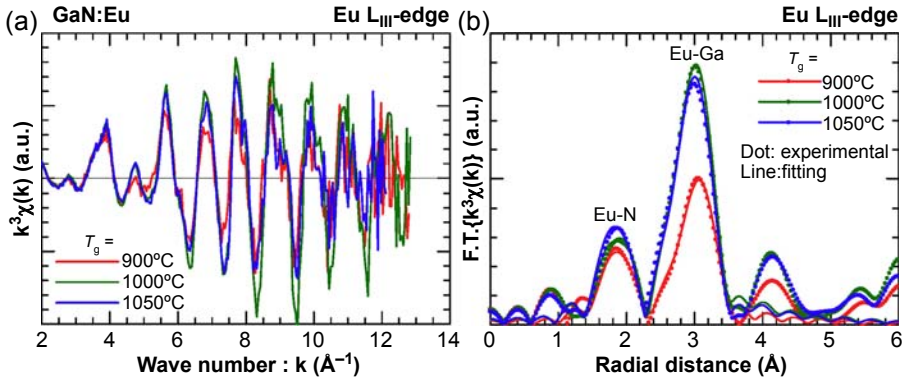


**Figure 8.5** Eu L<sub>III</sub>-edge EXAFS spectra (a) and Fourier transformed Eu L<sub>III</sub>-edge EXAFS spectra (b) for the Eu-doped GaN layers [18].

remarkably decreased with decreasing growth temperature from 1000 to 900°C, despite a Eu concentration reduction of only ~50%. This is attributed to an increase in the amount of Eu<sup>3+</sup> ions that were incorporated into different environments in the GaN, as well as a reduction in the energy-transfer efficiency from GaN host-material to Eu<sup>3+</sup> ions attributed to nonradiative centers [17].

The local structures around Eu atoms were investigated by fluorescence X-ray absorption fine structure measurement [18]. Fig. 8.5(a) and (b) shows Eu L<sub>III</sub>-edge extended X-ray absorption fine structure (EXAFS) spectra and Fourier transform of Eu L<sub>III</sub>-edge EXAFS spectra, respectively, for the Eu-doped GaN measured at the SPring-8 [18]. By curve fitting, a model of substitutional Eu ions on Ga site in GaN was fitted best for all the samples. Thus, it is considered that the Eu atoms are essentially all substituted onto a Ga site within the GaN lattice. Additionally, results of Rutherford backscattering/channeling (RBS/C) measurements also indicate that Eu is incorporated entirely on substitutional Ga sites with a slight displacement that is highest in the sample grown at 900°C. This result suggests that a large fraction of incorporated Eu ions remain optically inactive [19]. Moreover, the Debye-Waller factor, which corresponds to the degree of disorder of the sample grown at 900°C, is larger than that of the samples grown at 1000 and 1050°C.

Fig. 8.6 shows the EL spectra of an LED using GaN:Eu as a function of applied voltage [6]. The emission at 621 nm was dominant in the EL spectra under applied forward bias. No luminescence was observed in the reverse bias conditions. Therefore, the observed emission under the forward bias condition was not due to the impact excitation of the Eu<sup>3+</sup> ions by hot carriers, but rather was caused by the energy transfer from the GaN host to the Eu<sup>3+</sup> ions. At a dc current of 20 mA, the output power, integrated over the <sup>5</sup>D<sub>0</sub>-<sup>7</sup>F<sub>2</sub> transition region was 1.3 μW; the corresponding external quantum efficiency (EQE) was 0.001%.

It is also possible to grow GaN with high crystal quality under high reactor pressures [20]. The impact of growth at atmospheric pressure can be summarized as increasing the number of optically active Eu centers and enhancing efficient energy

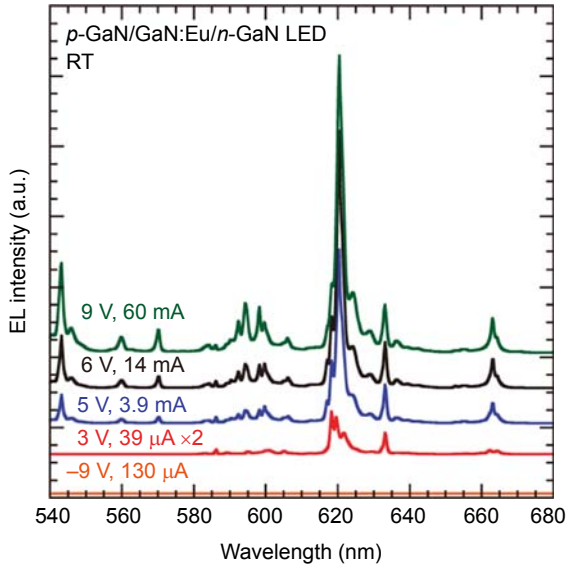


**Figure 8.6** EL spectra of GaN:Eu LED with different applied voltages [6].

transfer, while further reducing nonradiative processes in the GaN host [14,21]. Although Eu concentration of atmospheric pressure GaN:Eu (AP-GaN:Eu) was lower than that of low-pressure GaN:Eu (LP-GaN:Eu), the integrated PL and EL intensities of the AP-GaN:Eu samples were 10 times higher than that of the LP-GaN:Eu samples. The temperature dependence of time-resolved PL measurements, shown in Fig. 8.7, reveals that the improved PL intensity can be attributed to the high crystal quality of the AP-GaN:Eu as compared to that of the LP-GaN:Eu. Fig. 8.8 shows the EL spectrum in the LED with a GaN:Eu grown at 100 kPa and the spectrum for the 10 kPa LED measured at RT. In the LED doped with Eu at atmospheric pressure, the output

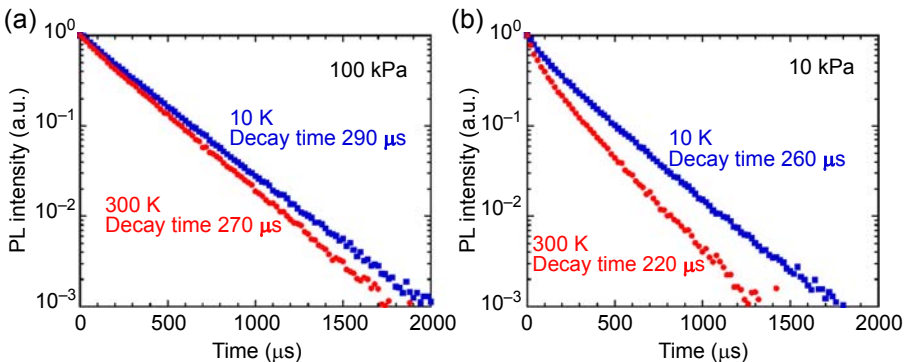


**Figure 8.7** Decay profiles of the Eu emission in (a) AP- and (b) LP-GaN:Eu, measured at 10 and 300 K [21].

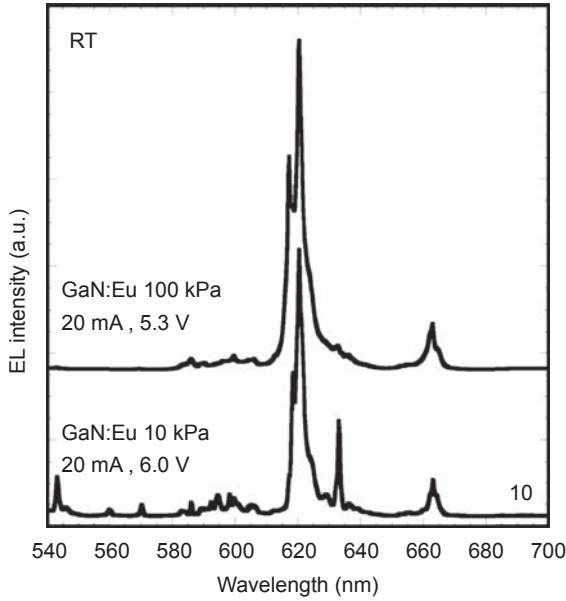


**Figure 8.8** EL spectra of GaN:Eu LED grown at 10 and 100 kPa [14].

power integrated over the  ${}^5D_0$ - ${}^7F_2$  transition region was  $17 \mu\text{W}$  at a DC current of 20 mA; the corresponding EQE was 0.04% [14].

The light output power also increased with the GaN:Eu active layer thickness as there were more Eu ions contributing to the emission [22]. Fig. 8.9 shows light output power and EQE as a function of injected current for the LEDs with different active

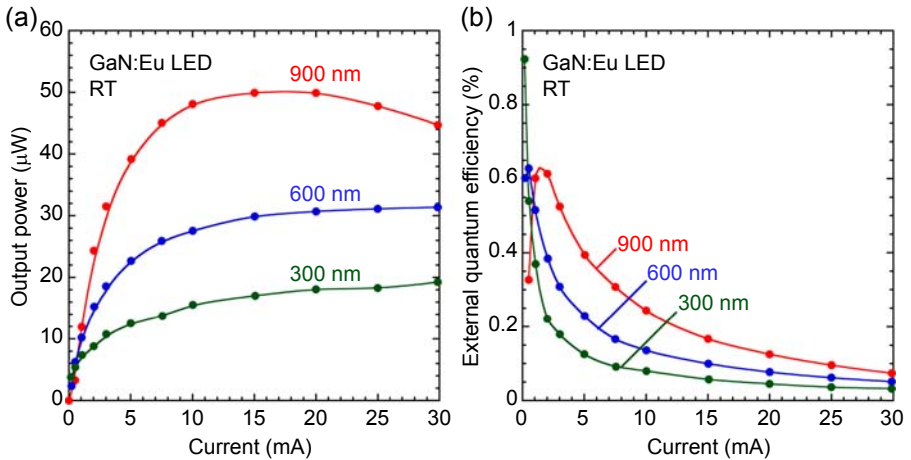


**Figure 8.9** Light output (a) and external quantum efficiency (b) of LEDs with different thickness of Eu-doped GaN active layer [22].



layer thickness. The maximum light output power of 50  $\mu\text{W}$  was obtained for the LED with a 900 nm active layer thickness with an injected current of 20 mA; the corresponding EQE was 0.12%. At present, the maximum light output power is 93  $\mu\text{W}$  with an injected current of 20 mA, which is the highest value ever reported [23]. The corresponding EQE is 0.23%. The fact that higher EQE values are observed at low current conditions [23] and that the emission efficiency can be enhanced by pulse-controlled injected charges using a rectangular pulse drive [24] indicates that there is a bottleneck of the output power due to the number of optically active Eu ions and their energy-transfer efficiency from the GaN host. The energy-transfer efficiency is effected by the local environments around the Eu ions, which can include intrinsic and/or extrinsic defects [25,26]. The nature of Eu incorporation and its impact on the luminescence and magnetic properties of the system will be discussed in the next section.

## 8.3 Nature of Eu incorporation into GaN: structural, optical, and magneto-optical properties

### 8.3.1 Overview of Eu sites and local defect assignment of the majority center

OMVPE growth of GaN introduces a number of defects including gallium and nitrogen vacancies as well as oxygen and carbon, which sit on nitrogen sites. These defects can localize and couple to the Eu ion creating various defect environments or sites. These environments can be distinguished by differences in the excitation and emission spectra caused by variations in the perturbations they induce on the Eu ions.

To distinguish these centers, the technique of combined excitation emission spectroscopy (CEES) [27] was utilized, where the Eu ions are resonantly excited from the  ${}^7F_0$  level to the  ${}^5D_0$  level. This transition is normally forbidden in free ions due to the violation of angular momentum conservation. However, once the ions are placed into a crystal field, second-order perturbation effects due to the local defect configurations can relax this rule, especially for excitations that contain both  $\pi$  and  $\sigma$  polarizations to the  $c$ -axis [28,29]. Since the transition occurs between two  $J = 0$  levels, there is only one excitation energy for each environment, meaning that the number of centers can be determined by the number of resonant excitation peaks. Using this technique at least eight different environments have been identified in OMVPE-grown GaN:Eu, labeled OMVPE 1–8, which are identified in Fig. 8.10 [26,30].

The red emission centered at 621 nm is a result of transitions from the  ${}^5D_0$  to the  ${}^7F_2$ . The  ${}^7F_2$  level has a degeneracy of 5, meaning that in the presence of external electric and magnetic fields this level can split into, at most, five separate levels. The presence of the crystal field in GaN can also remove this degeneracy, where the symmetry of the field felt by the Eu ion determines the number of splittings, referred to as crystal field multiplets. In a defect-free GaN environment, the Eu ion will exist in  $C_{3v}$  symmetry, which partially removes the degeneracy of the  ${}^7F_2$  level, and separates it into three crystal field multiplets.

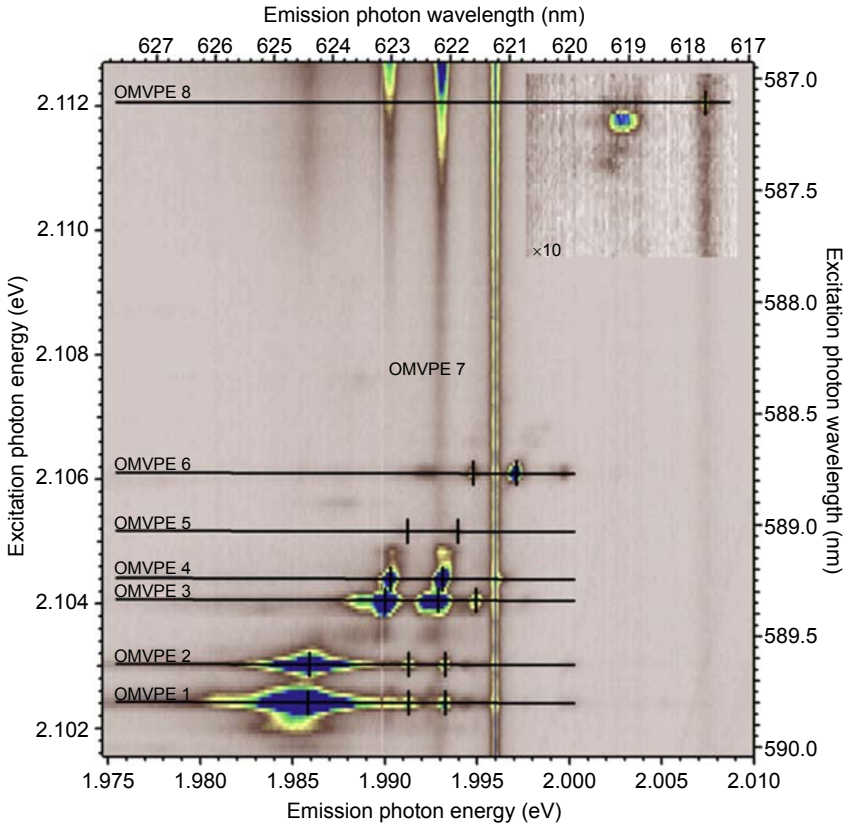


**Figure 8.10** Zero-phonon CEEs of GaN:Eu taken at 10 K, which shows the eight different incorporation centers that can form under these growth conditions [30].

Inspection of Fig. 8.11 reveals that the Eu centers OMVPE 1 and 2 have identical emission spectra that both contain far too many peaks ( $>5$ ) if they are to be attributed to a single Eu ion. This indicates that these two centers are actually a coupled pair that transfers energy between each other. As expected, these centers become less prominent, and are eventually absent as the Eu concentration is lowered, and clustering is less likely to occur.

In this excitation wavelength region, the emission intensity is related to the degree of perturbation felt by the Eu and hence the emission strength is not directly proportional to the number of centers. However, by taking into consideration the center-specific excitation cross-sections and emission lifetime, the relative numbers of each center have been analyzed by Wakamatsu et al. [26]. The proportional number of centers is taken to be

$$N_{\text{Eui}} \propto \left( \frac{\sigma_i \phi_i \tau_{\text{rad}} + 1}{\phi_i \sigma_i} \right) I_i \quad [8.1]$$

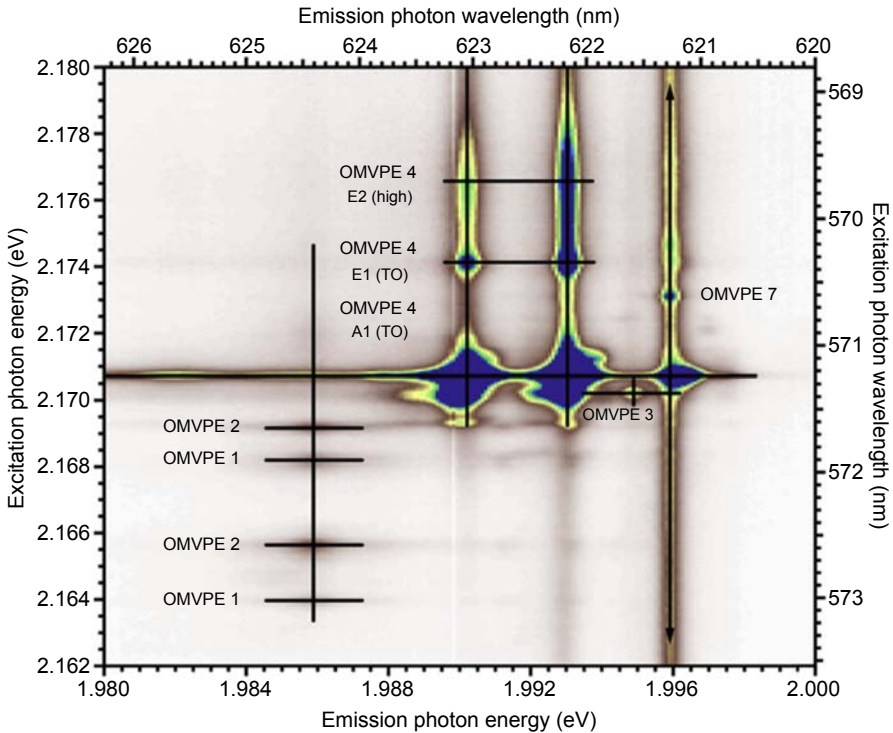


**Figure 8.11** CEES of the phonon-assisted excitation region in GaN:Eu, taken at 10 K. In this region, the ratio of the emission intensities from the various incorporation centers can be used as an indication of the relative abundance of each center [30].

where  $\sigma_i$  is the cross-section,  $\phi_i$  is the photon flux,  $\tau_{\text{rad}}$  is the radiative lifetime, and  $I_i$  is the emission intensity. While this method is quantitatively more accurate, it can be time-consuming to analyze the relative number of centers for a large volume of samples grown under different conditions.

To make this process more efficient, the property of phonon-assisted transitions can be utilized. When Eu ions couple to bulk phonons in GaN the excitation selection rule for  $J = 0$  to  $J = 0$  transitions is relaxed, and the emission lifetimes and excitation cross-sections of the various centers become comparable. This allows for the relative number of centers to be estimated by their relative emission intensities [30]. The excitation wavelength range for the phonon-assisted region is higher in energy by the amount of the common bulk phonon in GaN  $\approx 60$  meV (see Fig. 8.11).

As the sample quality has improved, it has been determined that two of these centers, OMVPE 4 and 7, commonly referred to as Eu1 and Eu2, respectively, represent 90–95% of the Eu incorporation, and play the largest role in the luminescent properties that are crucial for LED applications [26,30,31]. Of these two, Eu1 is commonly referred to as the majority center since it has a concentration that is  $>80\%$  in all GaN:Eu samples.

While resonant excitation is useful for determining the relative number of the centers, it does not provide information on how well energy is transferred from electron–hole (e–h) pair recombination within the host to the Eu ion, as is the case during device operation. To simulate this, (e–h) pairs are generated by exciting the GaN above the bandgap, using a 325 nm He–Cd laser. By comparing the resulting emission intensities for each center under He–Cd excitation, with the relative numbers as determined by CEES, the effective excitation efficiency of each center can be determined. It has been observed that the excitation efficiency of Eu1 and Eu2 can be modified by altering the growth environment, and modifying the concentration of intrinsic defects in GaN.

The majority center (Eu1) has been attributed to a center where the Eu ion contains a  $V_N$  as a nearest neighbor [32,33]. This vacancy can sit in two different configurations, each of which puts the Eu ion in a different crystal field symmetry. The first configuration is where the  $V_N$  sits axially above the Eu, and the other is at one of three equivalent off-center positions. These configurations have crystal field symmetries of  $C_{3v}$  and  $C_{1h}$ , respectively. For  $C_{3v}$  symmetry, group theory predicts that a  $J = 2$  level will split into three crystal field levels [28,34,35]. Two of the dipole transitions, from  $J = 0$  to  $J = 2$ , will exhibit both  $\pi$  and  $\sigma$  polarization, while the other will only be  $\pi$  polarized. Since two of the levels remain degenerate, they are expected to split under the application of a magnetic field applied parallel to the  $c$ -axis of the crystal. This is summarized for  $C_{3v}$  in Fig. 8.12.

$C_{1h}$  is a lower symmetry group than  $C_{3v}$ , and therefore the degeneracy for the  $J = 2$  state will be completely removed and will split into five crystal field levels. For this

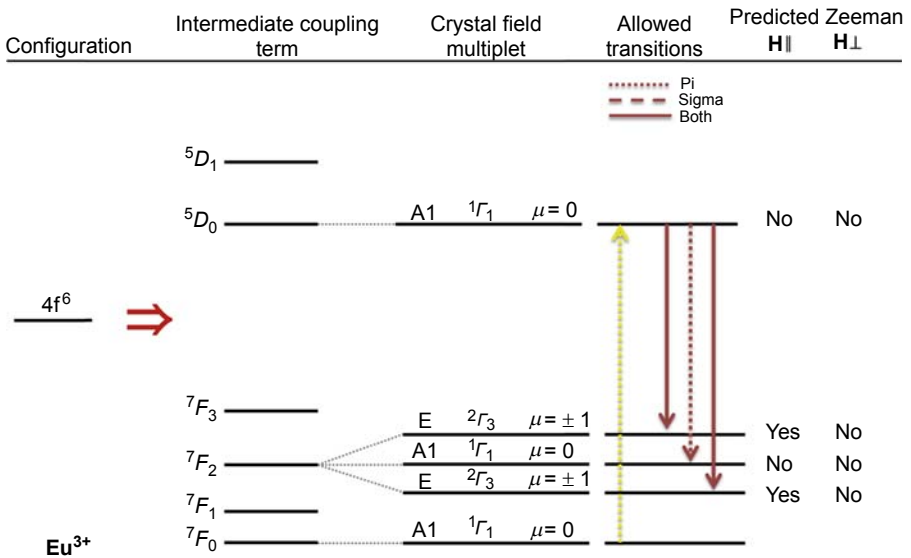


**Figure 8.12** Energy level diagram for the 580 nm excitation and 621 nm emission in GaN:Eu. The crystal field representations allowed dipole transition polarizations, and predicted effects of the Zeeman interaction are also given [33].

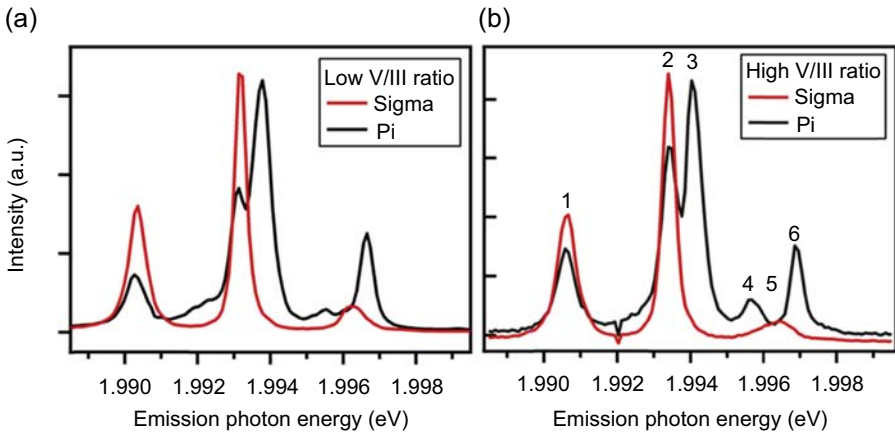


**Figure 8.13** Overlapped  $\sigma$ - and  $\pi$ -polarized emission spectra from the Eu1 center taken at 10 K. Six emission peaks are observed, where two of the peaks have both  $\sigma$  and  $\pi$  components. The peaks are labeled 1–6 for easy reference [32].

symmetry, three of the transitions will be  $\sigma$  polarized and two will be  $\pi$ . Since all the degeneracy is removed, there can be no further splitting of these levels in the presence of a magnetic field.

As mentioned in Section 8.2.1, the optimal ratio of the Ga to N source supply rates (a.k.a. the V/III ratio) was 6400; however, by lowering the Ga supply rate, the local structures around the Eu ions can be further modified [32]. These variations can be used to further help in distinguishing the assignment of the emission peaks to the various centers. Using two different geometries both the  $\pi$ - and  $\sigma$ -polarized emission can be collected and separated using linear polarizers. The resonantly excited  $\pi$  and  $\sigma$  emission spectra of Eu1, for samples grown with a V/III ratio of 3200 and 6400, are given in Fig. 8.13(a) and (b), respectively. The emission peaks for Eu1 are labeled 1–6 for easy reference.

It is apparent that there is overlap between two of the  $\pi$  and  $\sigma$  emission peaks, as expected. Moreover, when the two samples are compared, the relative ratio of the peak intensities changes between some peaks, while not for others. This indicates that there simultaneously exist two distinct centers that are very similar in nature and hence can be excited at the same resonant energy. Table 8.2 lists each peak with its respective emission photon energy and polarization characterization.

### 8.3.2 Evaluation of the magneto-optical properties of Eu1

How do these Eu centers behave under the application of magnetic field? As opposed to some RE ions such as Nd and Er, the Eu levels have even spin quantum numbers and are hence not necessarily Kramers-degenerate. To investigate the magneto-optical properties of the system, magnetic fields are applied both parallel and perpendicular

**Table 8.2 Emission photon energies of peaks 1–6 along with their respective polarizations [32]**

Peak #	Peak energy (eV)	Polarization
1	1.99062	$\pi$ and $\sigma$
2	1.99321	$\pi$ and $\sigma$
3	1.99402	$\pi$
4	1.99562	$\pi$
5	1.99633	$\sigma$
6	1.99696	$\pi$

to the  $c$ -axis using a magnetic cryostat capable of reaching temperatures as low as 30 K. Although no splitting is expected from applied magnetic field perpendicular to the  $c$ -axis, a significant repulsion of peaks 2 and 3 is observed, and becomes stronger as the field is increased (Fig. 8.14(a)). In this figure, the two polarizations have not been separated in order to clearly show the interaction between all the transitions.

In order to bring out this effect, the data are rescaled such that emission intensity of peak 1, which exhibits no shift due to the magnetic field, remains constant, and the zero field spectra was then subtracted from every subsequent higher field spectra (Fig. 8.14(b)). The interaction between peak 2 and peak 3 becomes apparent for field strengths greater than 3 T.

Fig. 8.15 shows the emission spectra of Eu1 (containing both polarizations) as the magnetic field strength is raised. Peak 3, which normally exhibits strictly  $\pi$ -polarized emission, shifts to higher energies and increases in intensity relative to peak 2.

To shed some light on this effect, the  $\pi$ - and  $\sigma$ -polarized emission under applied fields of 0 and 6 T are separated and shown in Fig. 8.16. For the  $\sigma$ -polarized emission, none of the three peaks is expected to split but we observe that peak 1 does shift to lower energies. More importantly, a fourth emission peak appears. Upon inspection of the  $\pi$ -polarized emission spectra under application of a 6 T magnetic field, it can be seen that this emission peak overlaps with peak 3, which is strictly  $\pi$  polarized under zero field conditions. Thus we can conclude that upon application of a magnetic field, the strict polarizations predicted by group theory are no longer maintained.

The determination of whether or not a particular transition is allowed for a given polarization is based on the irreducible representations of the crystal field interaction. Once the magnetic field is strong enough that magnetic interaction is comparable to that of the crystal field interaction, these representations cease to uniquely define the state of the electron. As a result the strict transition polarizations are lost and a mixing of the polarization states is observed. In order to quantify the strength of the magnetic interaction in this case we need to determine at what magnetic field strength this effect is observed.

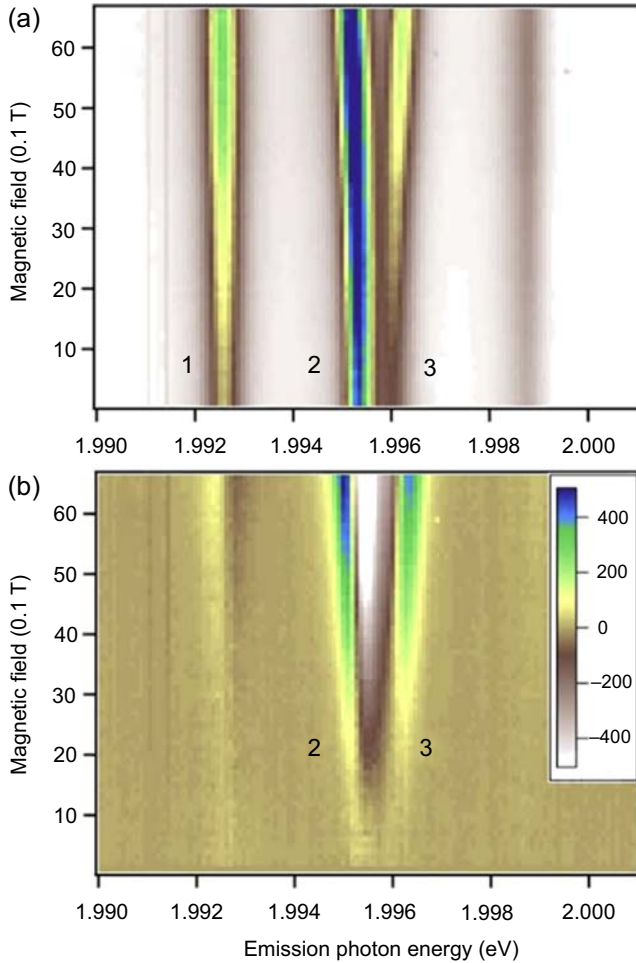


**Figure 8.14** Unpolarized Eu1 spectra taken at 0.1 T intervals from 0 to 6.5 T, at 30 K. (a) Raw data (b) data with the emission intensity normalized and the 0 T emission spectra subtracted out. The only changes that result from the application of the magnetic field are between peaks 2 and 3 [33].

To this end, we define the difference  $\Delta_i$  in normalized peak intensities of peak 2 and peak 3 as

$$\Delta_i = \frac{I_i(B)}{I_2(B) + I_3(B)} - \frac{I_i(0)}{I_2(0) + I_3(0)}, \quad [8.2]$$

and plot them as a function of magnetic field in Fig. 8.17. The data was fit with a sigmoid function, and from this it can be inferred that the magnetic field begins to influence the zero field crystal field states around 3 T, and saturates around 6 T.

For magnetic fields applied parallel to the  $c$ -axis, we expect emission peaks 1 and 2 to split since they are twofold degenerate for  $C_{3v}$  symmetry. Fig. 8.18 shows



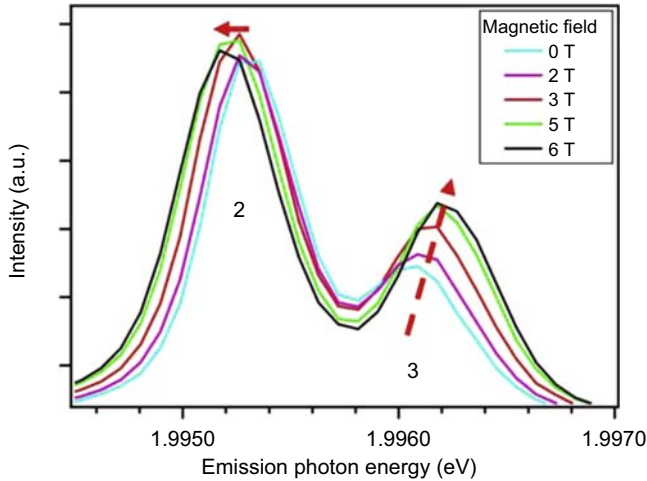


**Figure 8.15** Unpolarized emission spectra under increasing magnetic fields, applied perpendicular to the  $c$ -axis, at 30 K. Peaks 2 and 3 shift away from each other and their relative ratio decreases with increasing field strength [33].

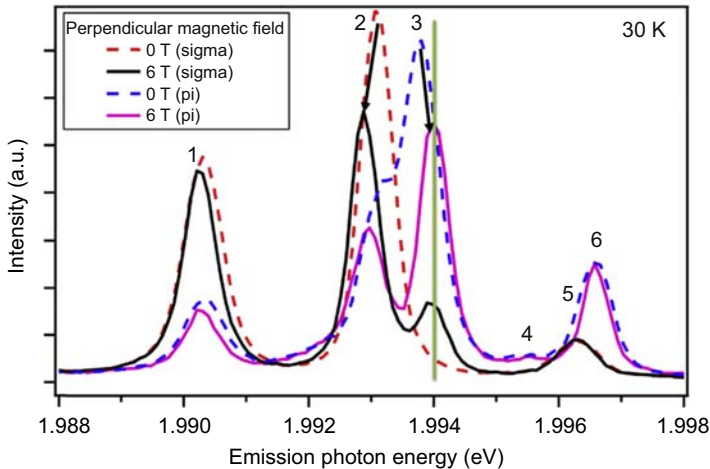


**Figure 8.16** Emission spectra showing the effect of applying a 6 T magnetic field perpendicular to the  $c$ -axis at 30 K. Peak 3 and peak 4 appear to shift away from each other in the  $\pi$ -polarized emission spectra. For the  $\sigma$  emission, the 6 T field breaks down the strict polarizations of some transitions and a peak corresponding to peak 4 appears and shifts with increasing magnetic field [32].

the  $\sigma$ -polarized emission under magnetic fields of 0 and 6 T. It can be seen that while peaks 1 and 2 split as expected, there is also an apparent splitting of peak 5. For the latter, we again have the same situation that we encountered before.

In fact, we find for peak 5 that under increasing magnetic field strengths, it really does not split but is shifting to higher energies while a new peak appears (Fig. 8.19). This new peak becomes distinguishable for applied fields greater than 3 T, and increasing in intensity analogous to the perpendicular field case. Once the  $\pi$  and  $\sigma$



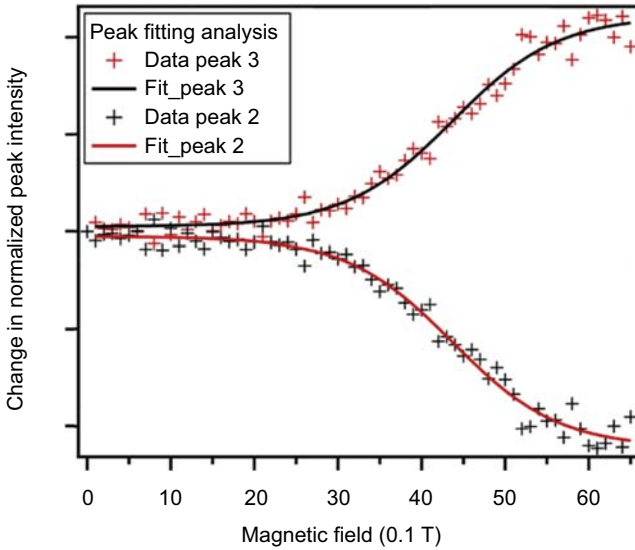


**Figure 8.17** Plot of the changes in normalized peak intensity as a function of magnetic field strength, for peaks 2 and 3. The polarization state mixing does not take full effect until 3 T, and saturates around 6 T [33].

emission spectra at 6 T are overlapped, it appears that the “new” peak coincides with the normally  $\pi$ -polarized peak 6 (Fig. 8.19).

Putting all of this together, we can find the 10 emission peaks that are expected for two distinct Eu centers with all the degeneracy removed. Only peaks 1 and 2 show Zeeman splitting while all other apparent splitting is a result of polarization mixing of states due to the application of a strong external magnetic field.

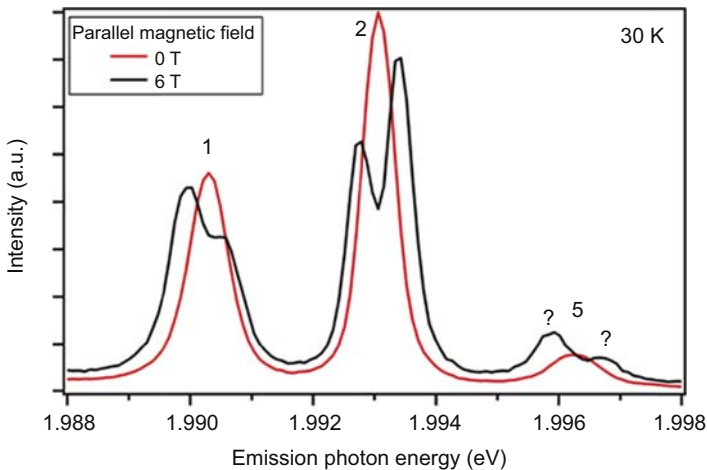


**Figure 8.18** Emission spectra showing the effect of applying a 6 T magnetic field parallel to the  $c$ -axis, at 30 K. All three peaks appear to split. The left two peaks have calculated  $g$ -factors of 1.79 and 1.83, respectively [33].

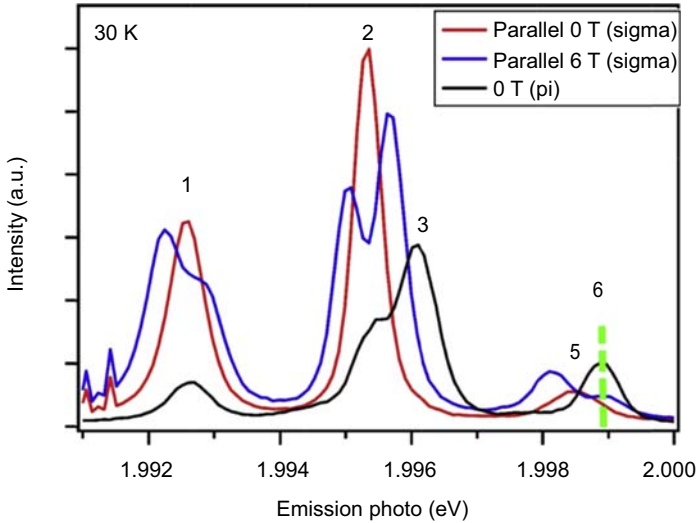


**Figure 8.19** Emission spectra for the 0 and 6 T magnetic fields applied parallel to the  $c$ -axis, at 30 K. The  $\pi$ -polarized emission for 0 T is also included, and it appears that the right-most peak for the 6 T field spectra appears to coincide with peak 6 [33].

Finally, we mention an interesting effect of applying a magnetic field on the emission intensity. When a magnetic field is applied and subsequently removed, the intensity of the emission never returns to its initial level (Fig. 8.20). This has been observed by Li et al., who tried to explain this as the conversion of  $\text{Eu}^{3+}$  to  $\text{Eu}^{2+}$  due to the capture of  $(e-h)$  pairs created during indirect excitation [36]. However, this phenomenon was

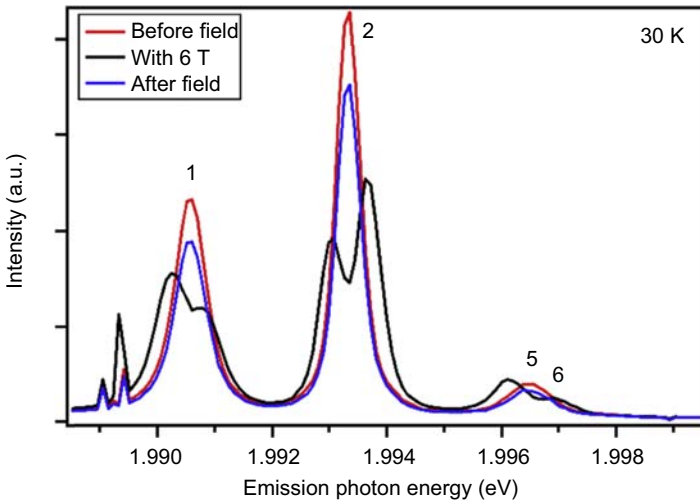


**Figure 8.20** Emission spectra taken at 0 T, 6 T, and after the field is removed for a parallel magnetic field, taken at 30 K. The intensity does not return to its original value once the field is removed [33].

also observed under resonant excitation, and thus cannot be explained by the capture of (e-h) pairs. Instead, this could be a result of the defect- or strain-mediated ferromagnetism found in GaN:Eu. The effect is reversed once the sample is brought to RT.

## 8.4 Summary and conclusions

Despite the fact that the ground state of  $\text{Eu}^{3+}$  has a zero  $J$  value ( ${}^7F_0$ ), which nominally has no magnetic moment, various studies reveal interesting magnetic properties. In addition to the distinct Zeeman splittings of the  ${}^7F_2$  state and hysteretic changes in transition probabilities mentioned in the previous sections, there have also been observations of other interesting phenomena:

1. Under cycling of the magnetic field, the intensity of the Eu emission is decreased. This occurs both for resonant and above bandgap excitation [36] and hence has to be related to the transition probability or efficiency of the emission transitions. As we have seen, slightly different centers are present in the samples that differ just by the location of the nitrogen vacancy. These centers may indeed have different emission efficiencies. One possibility that should be considered is a potential magneto-strictive effect that can induce a structural modification in which the nitrogen vacancy is moved to a different position relative to the Eu ion. At this point, the evidence is very indirect. Alternatively, the effect could be more local and connected with a modification of the electronic states of the Eu ion under application of the magnetic field, which could alter the selection rules associated with those transitions. Under these conditions, the energetics of the Eu- $V_N$  configuration may change, enabling a conversion. To directly demonstrate the center rearrangement, magneto-strictive effect, or modified defect energetics just suggested, more experimental and theoretical studies are needed.
2. Remnant magnetization has been observed by Wang et al. [37]. This magnetization is increased significantly as a result of codoping with Si. Since the ground state should not have a magnetic moment, this effect could be driven by the presence of defect and the fact that the Eu ion indeed attracts additional defects (such as  $V_N$ , Mg, and Si) that function as donors or acceptors. We should further keep in mind that while the total spin  $J$  is expected to be zero (assuming a pure  $LS$  coupling scheme), the  $L$  and  $S$  are not zero and can induce a magnetization in the presence of a coupling mechanism with another spin. Masago et al. have speculated that defect complexes consisting of Eu, O, and Mg could modify the ground state sufficiently such that it has a finite magnetic moment [38]. Another potential explanation for the observed magnetization is the potential presence of  $\text{Eu}^{2+}$  at surfaces and interfaces, where this ionization state becomes more favorable.
3. Utilizing the visible Eu emission for trivalent Eu ions, Kachkanov et al. [39] found a magnetic circular dichroism in the  $\text{Eu}^{3+}$  specific X-ray absorption. This elegant detection method clearly connects this unexpected effect with the  $\text{Eu}^{3+}$  ions. While in their paper they speculate about the role of the  ${}^7F_2$  states, the defect-induced effects discussed earlier could be responsible for the effect as well.

In summary, it turns out that Eu is by no means a magnetically boring ion in GaN. The presence of RT magnetic effects (magnetization, dichroism), in combination with the excellent luminescence properties, makes this material a prime candidate to explore devices that are magnetically controlled, not only in their intensity, but also the nature of their emission polarization.

## Acknowledgments

Part of this work was supported by JSPS KAKENHI Grant Numbers 19GS1209, 24226009, and 26820113. This work was also supported by the Frontier Research Base for Global Young Researchers, Osaka University, from the Ministry of Education, Culture, Sports, Science, and Technology of Japan. The synchrotron radiation experiments were performed at the BL14B2 beamline of SPring-8 with the approval of the Japan Synchrotron Radiation Research Institute (JASRI) (Proposal Numbers 2011A1747 and 2011A1864). The work at Lehigh was supported by the National Science Foundation grant (ECCS-1140038).

## References

- [1] Heikenfeld J, Garter M, Lee DS, Birkhahn R, Steckl AJ. *Appl Phys Lett* 1999;75:1189.
- [2] Morishima S, Maruyama T, Tanaka M, Masumoto Y, Akimoto K. *Phys Status Solidi A* 1999;176:113.
- [3] Lozykowski HJ, Jadwisieniczak WM, Han J, Brown IG. *Appl Phys Lett* 2000;77:767.
- [4] Steckl A, Heikenfeld J, Lee D, Garter M, Baker C, Wang Y, et al. *IEEE J Sel Top Quantum Electron* 2002;8:749.
- [5] Park JH, Steckl AJ. *Appl Phys Lett* 2004;85:4588.
- [6] Nishikawa A, Kawasaki T, Furukawa N, Terai Y, Fujiwara Y. *Appl Phys Express* 2009; 2:071004.
- [7] Sekiguchi H, Takagi Y, Otani T, Matsumura R, Okada H, Wakahara A. *Jpn J Appl Phys* 2013;52:08JH01.
- [8] Miranda SMC, Edwards P, O'Donnell K, Boćkowski B, Alves E, Roqan I, et al. *Phys Status Solidi C* 2014;11:253.
- [9] de Boer WDAM, McGonigle C, Gregorkiewicz T, Fujiwara Y, Tanabe S, Stallinga P. *Sci Rep* 2014;4:5235.
- [10] Park JH, Steckl AJ. *J Appl Phys* 2005;98:056108.
- [11] Pan M, Steckl AJ. *Appl Phys Lett* 2003;83:9.
- [12] Laski J, Klinedinst K, Raukas M, Mishra KC, Tao J, McKittrick J, et al. *J Electrochem Soc* 2008;155:J315.
- [13] Uchida K, Tokunaga H, Inaishi Y, Akutsu N, Matsumoto K, Itoh T, et al. *Mater Res Soc Symp Proc* 1997;449:129.
- [14] Nishikawa A, Furukawa N, Kawasaki T, Terai Y, Fujiwara Y. *Appl Phys Lett* 2010;97:05113.
- [15] Sicre JE, Dubois JT, Eisentraut KJ, Sievers RE. *J Am Chem Soc* 1969;91:3476.
- [16] Honma T, Oji H, Hirayama S, Taniguchi Y, Ofuchi H, Takagaki M. *AIP Conf Proc* 2010; 1234:13.
- [17] Kawasaki T, Nishikawa A, Furukawa N, Terai Y, Fujiwara Y. *Phys Status Solidi C* 2010; 7:2040.
- [18] Ofuchi H, Honma T, Kawasaki T, Furukawa N, Nishikawa A, Fujiwara Y. *e-J Surf Sci Nanotechnol* 2011;9:51.
- [19] Lorenz K, Alves E, Roqan IS, O'Donnell KP, Nishikawa A, Fujiwara Y, et al. *Appl Phys Lett* 2010;97:111911.
- [20] Watanabe A, Takahashi H, Tanaka T, Ota H, Chikuma K, Amano H, et al. *Jpn J Appl Phys* 1999;38:1159.
- [21] Furukawa N, Nishikawa A, Kawasaki T, Terai Y, Fujiwara Y. *Phys Status Solidi A* 2011; 208:445.

- 
- [22] Nishikawa A, Furukawa N, Lee D, Kawabata K, Matsuno T, Harada R, et al. *MRS Proc* 2012;1342:9.
- [23] Fujiwara Y, Dierolf V. *Jpn J Appl Phys* 2014;53:05FA13.
- [24] Ishii M, Koizumi A, Fujiwara Y. *Appl Phys Lett* 2014;105:171903.
- [25] Woodward N, Poplawsky J, Mitchell B, Nishikawa A, Fujiwara Y, Dierolf V. *Appl Phys Lett* 2011;98:011102.
- [26] Wakamatsu R, Lee D, Koizumi A, Dierolf V, Fujiwara Y. *J Appl Phys* 2013;114:043501.
- [27] Fleischman Z, Munasinghe C, Steckl AJ, Wakahara A, Zavada J, Dierolf V. *Appl Phys B* 2009;97:607.
- [28] Wybourne B. Coupled products of annihilation and creation operators in crystal energy level problems. In: Crosswhite HM, Moos HW, editors. *Optical properties of ions in crystals*. New York: Interscience Publishers; 1967.
- [29] Downer MC, Burdick GW, Sardar DK. *J Chem Phys* 1988;89:1787.
- [30] Woodward N, Nishikawa A, Fujiwara Y, Dierolf V. *Opt Mater* 2011;33:1050.
- [31] Roqan IS, O'Donnell KP, Martin RW, Edwards PR, Song SF, Vantomme A, et al. *Phys Rev B* 2010;81:085209.
- [32] Mitchell B, Poplawsky J, Lee D, Koizumi A, Fujiwara Y, Dierolf V. *J Appl Phys* 2014; 115:204501.
- [33] Mitchell B. The role of defect complexes in the magneto-optical properties of rare earth doped gallium nitride [Doctoral thesis]. PA: Lehigh University; 2014.
- [34] Tinkham M. *Group theory and quantum mechanics*. New York: McGraw-Hill; 1964.
- [35] Wybourne BG. *Spectroscopic properties of rare earths*. New York: Interscience Publishers; 1965.
- [36] Li Y, Yu S, Meng X, Liu Y, Zhao Y, Liu F, et al. *J Phys D: Appl Phys* 2013;46:215101.
- [37] Wang R, Steckl AJ, Nepal N, Zavada JM. *J Appl Phys* 2010;107:013901.
- [38] Masago A, Fukushima T, Sato K, Katayama-Yoshida H. *Appl Phys Express* 2014;7: 121002.
- [39] Kachkanov V, Wallace MJ, van der Laan G, Dhesi SS, Cavill SA, Fujiwara Y, et al. *Sci Rep* 2012;2:969.

# Optical and magnetic characterization of III-N:Nd grown by molecular beam epitaxy

*G.D. Metcalfe*

U.S. Army Research Laboratory, Sensors and Electron Devices Directorate, Adelphi, MD, United States

*E.D. Readinger*

International Rectifier Corp., St. Paul, MN, United States

*N. Woodward, V. Dierolf*

Lehigh University, Bethlehem, PA, United States

*N. Nepal*

U.S. Naval Research Laboratory, Washington, DC, United States

*J.M. Zavada*

NYU Tandon School of Engineering, Brooklyn, NY, United States

## 9.1 Introduction

Rare-earth (RE)-doped semiconductors are well studied for their potential applications in optical fiber telecommunications, light-emitting displays and devices, solid-state lasers, and spintronics (Steckl et al., 2002). After Favennec et al. (1989) demonstrated a reduction in thermal quenching of the luminescence in Er-doped materials with increasing bandgap, interest in wide bandgap semiconductors as host material flourished, particularly in wurtzite group III-nitride semiconductors, which have strong ionic bonds that can enhance the probability of the otherwise forbidden  $4f$  intra-subshell transitions in the  $RE^{3+}$  ion with substitutional occupation of the group III site (Steckl et al., 2002; Steckl and Birkhahn, 1998). Of the III-nitride semiconductors, AlN has the widest bandgap of 6.2 eV, allowing for higher energy RE transitions as well as a decrease of thermal quenching of the emission intensity (Slack et al., 1987). AlN also has the highest thermal conductivity (3.19 W/cm K at 300 K) (Slack et al., 1987) among the III-nitrides, which is  $>10$  times higher than yttrium aluminum garnet (YAG) at room temperature (RT), to allow efficient heat removal from the active media, a requirement for maximizing performance of high power/high temperature devices. Despite its smaller bandgap of 3.4 eV, GaN is the most mature of the binary III-nitrides with a thermal conductivity of 1.3 W/cm K at 300 K (Sichel and Pankove, 1977).

As for the dopant, work on RE ions such as Er (MacKenzie et al., 1996) for emission at 1.54  $\mu\text{m}$  and Eu and Tb for visible emission (Jaswieniczak et al., 2001) in III-N materials have been reported. Neodymium (Nd) is another excellent RE dopant for optical applications, as demonstrated by the great success in solid-state lasers such as Nd:YAG and Nd:YVO<sub>4</sub> lasers. These lasers have attained power levels higher than from any other four-level material (Koechner, 1999). Nd also has an even larger emission cross-section than Er. Nd has also found important technological uses in the class of strong, compact magnets based on Nd compounds. In particular, Nd<sub>2</sub>Fe<sub>14</sub>B is one of the strongest permanent magnets and is used in applications requiring small, strong magnetic fields, such as microphones, headphones, and computer hard disks. We therefore focus our discussions in this chapter on Nd-doped GaN and AlN with a particular emphasis on the system's potential for applications, such as spintronics and quantum information processing. Consequently, Nd-doped semiconductors could have an important technological impact as well as providing a rich topic for materials and device physics research.

This chapter is structured as follows: in Section 9.2 we discuss in situ RE doping through plasma-assisted molecular beam epitaxy (PA-MBE) and pertinent characterization; in Section 9.3, we present experimental results from optically characterized Nd-doped nitride semiconductors, including the Stark energy sublevels of Nd<sup>3+</sup> ions in GaN and AlN as determined by luminescence spectra; in Section 9.4 we present magnetic characterization of III-N:Nd; and conclude in Section 9.5 with discussions on future applications of RE semiconductors.

## 9.2 Molecular beam epitaxy growth

### 9.2.1 III-nitrides:Nd background

Two main techniques exist for the introduction of RE dopants into the semiconductor matrix: ion implantation and in situ doping during growth or deposition. Nd has previously been incorporated into GaN through ion implantation (Kim et al., 1998) and reactive cosputtering deposition (Kim et al., 2003a,b). Ion implantation has limitations due to damage effects and nonuniform doping profiles. In many cases, a postimplantation annealing is required due to the amorphization of the GaN lattice; however, annealing will not completely recover the damage. The maximum yield for ion implantation, where yield is defined as an RE ion sitting on a group III site, is (70 to 90)% and is dependent on the RE element. For ion-implanted Nd in GaN, the majority of Nd<sup>3+</sup> ions sit on the Ga substitutional site; however, four other sites associated with impurities and defects are also identified within the GaN matrix (Kim et al., 1998). Three in situ growth techniques have been demonstrated for RE incorporation into semiconductors: reactive cosputtering deposition, MBE, and metal-organic chemical vapor deposition (MOCVD). For reactive cosputtering of GaN with RE atoms, a postgrowth anneal ( $\geq 700$  °C) in nitrogen is often necessary in order to achieve photoluminescence (PL) emission (Kim and Holloway, 2004a,b; Kim et al., 2003a,b). Nevertheless, RT

emission from cosputtered GaN:Nd is observed under electrical stimulus. MOCVD has been successful in doping GaN films with Er (Chapter 7) and Eu (Chapter 8). MBE has been used to dope GaN with several different RE atoms including Eu (Steckl and Birkhahn, 1998) and Gd (Chapter 11). Our efforts have focused on using MBE to dope Nd into GaN and AlN epilayers.

### 9.2.2 III-nitrides:Nd molecular beam epitaxy growth

The MBE growth of Nd-doped nitrides has been performed at the US Army Research Laboratory. The MBE chambers utilize solid source materials for all group III and dopant elements coupled with a plasma-assisted ultrahigh-purity nitrogen source. One MBE chamber, an Applied EPI GENII, is outfitted with standard group III sources: Ga, In, and Al, as well as a Nd source for RE-doping experimentation. Active nitrogen is supplied by a Veeco UNI-bulb™ rf plasma source, which provides the necessary nitrogen species (N, N<sub>2</sub><sup>\*</sup>, and ions) for epitaxial growth. The growth module was equipped with an electron gun and phosphorus screen to perform reflective high-energy electron diffraction (RHEED), which provides an in situ tool for monitoring the growth surface.

All III-N layers throughout these studies were grown on single side polished *c*-plane sapphire. To improve the radiative heating and temperature uniformity across the sapphire substrate, a nominally 2 μm thick layer of titanium was sputter deposited on the backside. Substrates were thoroughly solvent cleaned (acetone, methanol, and isopropanol), etched using boiling aqua regia, and thoroughly rinsed in deionized water prior to loading into the MBE system. Once loaded in the MBE entry/exit chamber a mild degassing took place at 200 °C. Further degassing of the substrates in an outgas or buffer chamber saw a set point temperature of 600 °C while waiting for the chamber pressure to drop below  $1 \times 10^{-8}$  torr.

All solid sources were calibrated in situ prior to each growth using an ion gauge (beam flux monitor) that provides a beam equivalent pressure that is proportional to the atom flux at the substrate surface. All growth commenced with a low temperature (200 °C) nitridation of the sapphire substrate, where RHEED provided verification of a continuous AlN nucleation layer. Following the sapphire nitridation, an AlN buffer layer of ~25 nm was grown at 900 °C, as measured by a thermocouple. For GaN samples the AlN buffer is followed by a 200 nm undoped GaN base layer and an Nd-doped ~1 μm GaN layer with various Nd concentrations. The AlN Nd-doped samples consist of an AlN buffer layer (8–25 nm) followed by a 0.4 or 0.6 μm-thick Nd-doped AlN layer (Metcalf et al., 2011). The Nd neodymium cell temperature is adjusted while maintaining fixed growth conditions (growth temperature and III-N growth rate) to control the dopant incorporation. The maximum growth rate for III-nitrides using the rf plasma source is fixed by the conditions of the plasma, referred to as nitrogen limited growth. The growth of these Nd-doped III-N films proceeds under slightly nitrogen-rich conditions at fixed substrate growth temperature, in analogy to the work of Steckl et al. (2002) on the incorporation of Er into GaN for optimal PL emission. The rf plasma power was kept



between 250 and 350 W and a nitrogen flow of 0.6–1.2 sccm. The target growth rate was 200 nm/h, which required a N<sub>2</sub> flow of 0.6 sccm and corresponded to a chamber pressure of  $\sim 9 \times 10^{-6}$  torr.

### 9.2.3 III-nitrides:Nd material characterization

Immediately following growth, all III-N epilayers are evaluated by X-ray diffraction (XRD), and transmission and reflectance with a UV–Vis–NIR spectrophotometer to assess the nitride matrix. Quantitative analysis of the Nd concentration was attained by Rutherford backscattering spectroscopy and secondary ion mass spectrometry (SIMS) and then correlated with PL and PL excitation (PLE) data.

GaN samples are grown with a fixed growth rate at two temperatures, the Nd cell temperature is varied from (850 to 1000) °C, and the Ga flux, measured as beam equivalent pressure, is varied from  $9.8 \times 10^{-6}$  to  $5.6 \times 10^{-7}$  torr. Quantification of the SIMS data is performed using two standards, GaN epilayers grown by PA-MBE and hydride vapor phase epitaxy (HVPE) GaN that are both implanted with the same dose of Nd. The SIMS profiling tracks the Ga and Nd signals and assumes the Ga signal is associated with a fully dense stoichiometric GaN film. The average Nd doping concentration, over the bulk of the film thickness, is converted to Nd atomic percent (at%) within the GaN matrix. A set of Nd:GaN samples was prepared with different Nd concentration ( $C_{Nd}$ ) ranging from 0.004 to 8.0 at%. The SIMS data for two different Ga fluxes is plotted versus inverse temperature in Fig. 9.1. From the data in Fig. 9.1, the activation energy for Nd vapor over the temperature range of interest is determined to be  $\sim 7.4$  eV. The Nd at% found by the SIMS profiles gives good data for correlating the optical properties of the GaN epilayers as well as the crystalline quality of the epilayers as found by XRD. A variety of growth conditions are evaluated to determine the most ideal growth parameters for the desired optical and thermally conductive properties.

The typical XRD scans over a  $\theta$  range of 14–22 degree (see Fig. 9.2) and uses the (0006) sapphire peak (20.84 degree) as a reference peak among all samples. The peak at 17.27 degree is the (0002) GaN peak. The shoulder is due to the AlN buffer layer. In GaN:Nd epilayers with Nd > 1 at% an additional peak is observed for which the position does not align with that for NdN nor Nd metal clusters. The peak may be related to a ternary alloy of Ga–Nd–N. The average X-ray rocking curve of the GaN(0002) reflection yields a full width at half maximum of  $\sim 1400$  arcsec, which is consistent with the use of nitrogen-rich growth conditions shown to be favorable for RE optical emission from the GaN matrix (Steckl et al., 2002). The transmittance and reflectance spectra, collected over a wavelength range of (300 to 1500) nm, reveal that the band-edge of the GaN is unaffected by the addition of Nd. Measuring the optical transmittance at 1  $\mu$ m reveals that samples with  $\geq 1$  at% exhibit an optical transmittance that is reduced by as much as (60 to 80) % over that of epilayers with less Nd. This along with the extra peak in the XRD data suggests a new phase present in the GaN epilayers, whether it's a ternary Nd-Ga-N alloy, crystals of NdN, or clusters of Nd metal.

For the incorporation of Nd in III-N epilayers nitrogen-rich growth conditions are most favorable because the Nd and Ga (or Al) have little competition for the same

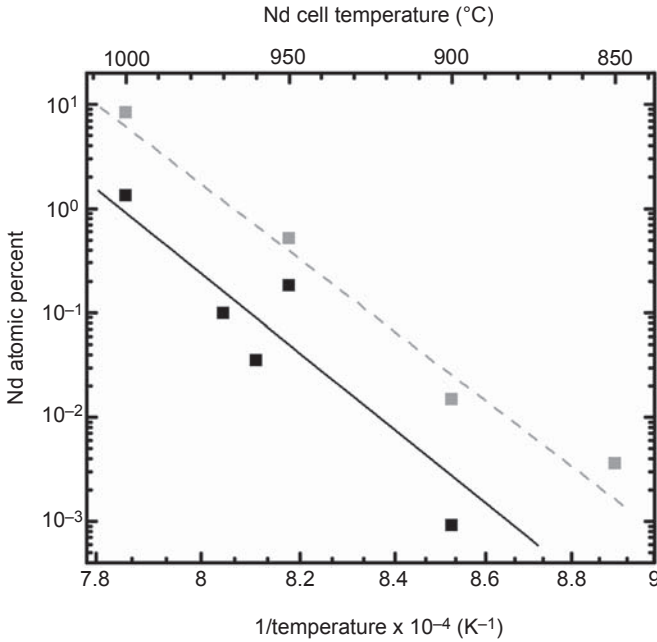


**Figure 9.1** The Nd at% from SIMS data from two different Ga flux conditions plotted versus inverse cell temperature. The *black* (*gray*) data points correspond to a beam equivalent pressure of  $\sim 3.5 \times 10^{-7}$  torr ( $\sim 1.4 \times 10^{-7}$  torr). The fits aid the eye in seeing the relationship between the data for the two Ga fluxes.

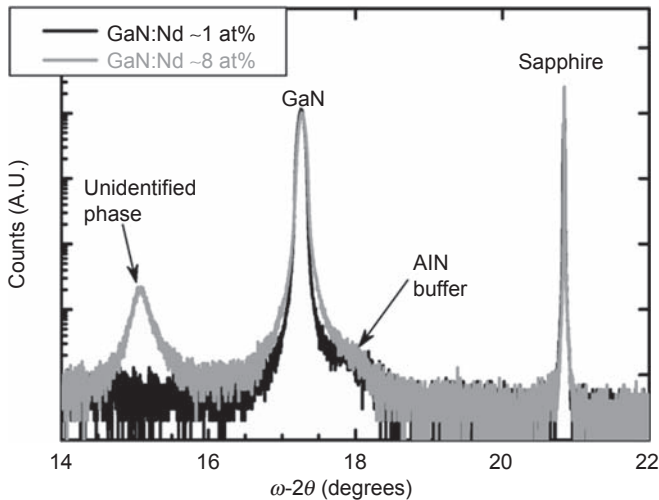


**Figure 9.2** Two XRD scans of GaN:Nd layers, one with 1 at% Nd and the other with 8 at%, showing the GaN(0002) reflection relative to the sapphire substrate (0006) reflection.

lattice site due to the excess of nitrogen (Readinger et al., 2008b). Optically these samples produce significant PL intensities of the Nd  $4f$  transitions under above-bandgap excitation. The regular near-band-edge emission of the GaN host is significantly suppressed for both low Nd at% as well as Nd at% greater than 1. As an example, Fig. 9.3 shows the strong emission observed at RT from GaN:Nd epilayers with Nd concentrations of  $\sim 0.1$  and  $\sim 0.6$  at%. The samples were excited above the bandgap with a pump laser at 266 nm. The characteristic peaks from the  $4f$  transitions from the  ${}^4F_{3/2}$  level to the  ${}^4I_{9/2}$  and  ${}^4I_{11/2}$  manifolds are shown between 1.30 and 1.36 eV (910–950 nm) and between 1.08 and 1.13 eV (1100–1150 nm), respectively. These Nd transitions are red-shifted with respect to the same transitions in a Nd:YAG matrix due to the difference in the GaN crystal field. The intensity of the strongest PL peak (1106 nm) for the  ${}^4F_{3/2} \rightarrow {}^4I_{11/2}$  transition is plotted in Fig. 9.4 versus the Nd concentration in the epilayer. The PL intensity increases with increasing Nd concentration up to  $\leq 0.5$  at%. At higher Nd concentrations, the PL intensity decreases. This may be linked with the occurrence of an additional phase mentioned earlier. Even for the GaN matrix an onset of a concentration quenching effect is expected for higher concentrations and the closer proximity of Nd atoms.

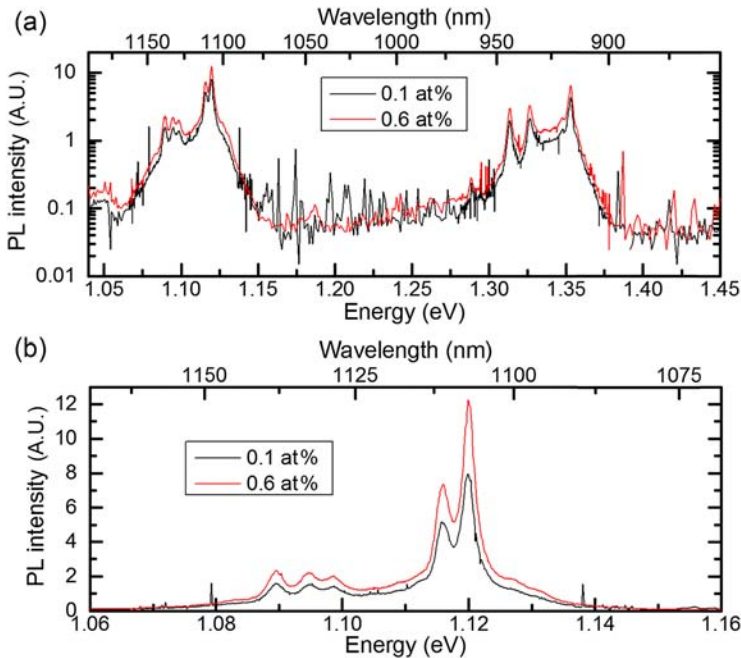


**Figure 9.3** Room-temperature PL intensity spectra due to laser excitation at 266 nm for Nd:GaN samples prepared with a Nd concentration of  $\sim 0.1$  at% (*black curves*) and  $\sim 0.6$  at% (*red curves*). (a) The PL intensity is plotted on a logarithmic scale for the  ${}^4F_{3/2} \rightarrow {}^4I_{9/2}$  and  ${}^4F_{3/2} \rightarrow {}^4I_{11/2}$  transitions. (b) The PL intensity is plotted on a linear scale for the  ${}^4F_{3/2} \rightarrow {}^4I_{11/2}$  transitions.

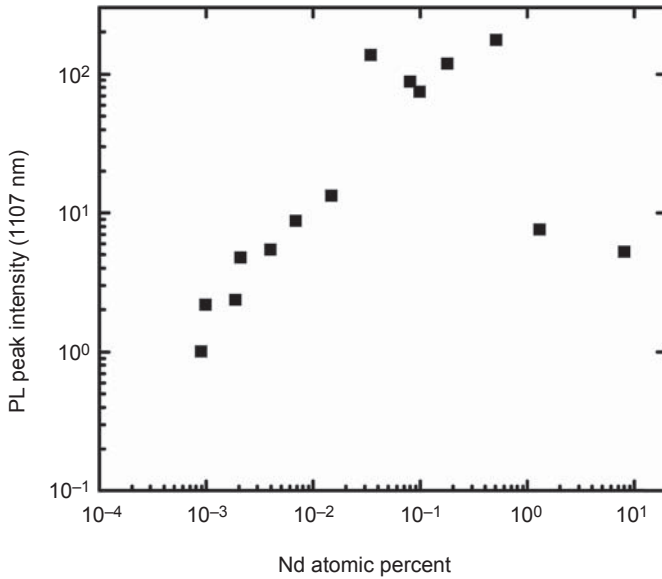


**Figure 9.4** The PL intensity for the 1106 nm peak within the  ${}^4F_{3/2} \rightarrow {}^4I_{11/2}$  manifold versus the Nd at% as determined by SIMS. A maximum in PL intensity corresponds with near 1 at% Nd within the GaN.

## 9.3 Optical characterization

### 9.3.1 Background

RE-doped GaN and AlN have been optically studied for decades using techniques such as PL (Kim et al., 1998; Silkowski et al., 1996), electroluminescence (Kim and Holloway, 2004a), and cathode-luminescence (Jadwisiensczak et al., 2001), but much of the research has focused on materials doped by reactive ion sputtering or ion implantation. Primarily due to the high density of sputtering or implantation related defects in the host material, reduced luminescence efficiency, and  $\text{Nd}^{3+}$  ions occupying multiple sites, it has been difficult to spectrally resolve the Stark levels of the  $4f$  states (Kim et al., 1998; Kim and Holloway, 2004a). The ability to in situ dope RE into III-N semiconductors with enhanced substitutional doping at the group III site (Readinger et al., 2008a) as described previously has allowed the detection and resolution of the Stark energy levels. For instance, luminescence detected from in situ Er-doped AlN samples was orders of magnitude greater than from ion-implanted Er in AlN (MacKenzie et al., 1996). For  $\text{Nd}^{3+}$  ions, the sublevels of the  ${}^4I_{9/2}$ ,  ${}^4I_{11/2}$ ,  ${}^4I_{13/2}$ ,  ${}^4F_{3/2}$ ,  ${}^4F_{5/2}$ ,  ${}^2H_{9/2}$ ,  ${}^4F_{7/2}$ ,  ${}^4S_{3/2}$ ,  ${}^4G_{5/2}$ , and  ${}^4G_{7/2}$  manifolds shown in the energy diagram in Fig. 9.5 were identified in PA-MBE-grown GaN (Metcalf et al., 2009a,b) and AlN (Metcalf et al., 2011) by PL, PLE spectroscopy, and combined excitation-emission spectroscopy (CEES). The manifolds are labeled using the conventional notation of  ${}^{2S+1}L_J$ , where  $S$  is the total spin,  $L$  is the total orbital angular momentum, and  $J$  is

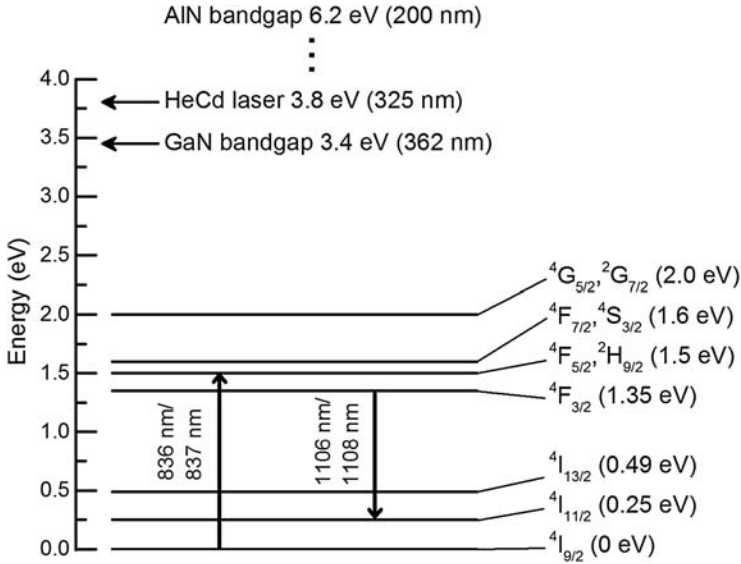


**Figure 9.5** Energy levels of Nd in situ doped in GaN and AlN.

the total angular momentum. Site-selective spectroscopy studies using CEES with confocal microscopy (Dierolf and Sandmann, 2007) determined that the majority of the emission occurs from one dominant site, along with minority incorporation sites (Metcalf et al., 2009a). Table 9.1 shows the crystal-field split energy levels of the  $\text{Nd}^{3+}$  ions in GaN (AlN) for the main incorporation site A (a) and two minority sites B (b) and C (c). Note that not all samples demonstrated the same minority sites, but all samples demonstrated the same dominant site. Although the  $4f$  electrons are well shielded from the host material, weak electron–phonon interactions were also observable. The separation between the higher level  $^{2S+1}L_J$  states  $^4F_{5/2}$ ,  $^2H_{9/2}$ ,  $^4F_{7/2}$ ,  $^4S_{3/2}$ ,  $^4G_{5/2}$ , and  $^4G_{7/2}$  are based on Gruber et al. (2011).

### 9.3.2 Conventional photoluminescence studies

For conventional PL studies, the III-N:Nd samples studied in (Metcalf et al., 2011, 2009a,b; Readinger et al., 2008a) were mounted in a closed-loop helium cryostat system for temperature-dependent PL and PLE measurements. A Nd:YVO<sub>4</sub>-pumped continuous wave (CW) Ti:Sapphire laser tunable between (750 to 950) nm and with an excitation density of  $\sim 20 \text{ kW/cm}^2$  was used for below bandgap excitation. To pump above the GaN bandgap, a CW HeCd laser at 325 nm with an excitation density of  $\sim 0.1 \text{ kW/cm}^2$  was utilized. The subsequent luminescence was collected into a 1 m focal length spectrometer and focused onto a liquid nitrogen cooled Ge detector. The CEES data was acquired at  $T = 4 \text{ K}$  with an Argon laser-pumped dye laser. The 3D data set of emission intensity as a function of excitation and emission energies was collected using a liquid nitrogen cooled-CCD array mounted onto a 0.25 m focal length spectrometer.

**Table 9.1 Crystal-field split energy levels of Nd<sup>3+</sup> ions in GaN (AlN) for the main incorporation site *A* (*a*) and two minority sites *B* (*b*) and *C* (*c*) as determined by PL, PLE, and CEES measurements (the *g*-factors for various levels are also included)**

$2S+1L_J$ manifold	Crystal field quantum	Sites in GaN					Sites in AlN		
		<i>A</i> (meV)	<i>B</i> (meV)	<i>C</i> (meV)	$\perp$ <i>g</i> -value <sub>exp</sub>	$\parallel$ <i>g</i> -value <sub>exp</sub>	<i>a</i> (meV)	<i>b</i> (meV)	<i>c</i> (meV)
$^4I_{9/2}$	3/2	0	0	0	4.03	0.12	0	0	0
	1/2	5.9	13.2	12	0.14	2.91	13.3	21.6	11.8
	1/2	26.1			2.51	0	23.3	31.1	14.5
	1/2	30.4	30.7	32	0.09	—	36.4	42.7	—
	3/2	39.5	32.2	46	4.12	0	50.2	61.6	70.7
$^4I_{11/2}$	1/2	232.8					236.6		
	3/2	236.8					241.5		
	1/2	241.6					244.6		
	1/2	244.7					249.7		
	3/2	257.9					264.1		
$^4I_{13/2}$	1/2	263.5					270.4		
	1/2	477.2					480.8		
	1/2	479.2					486.8		
	3/2	483.2					490.1		

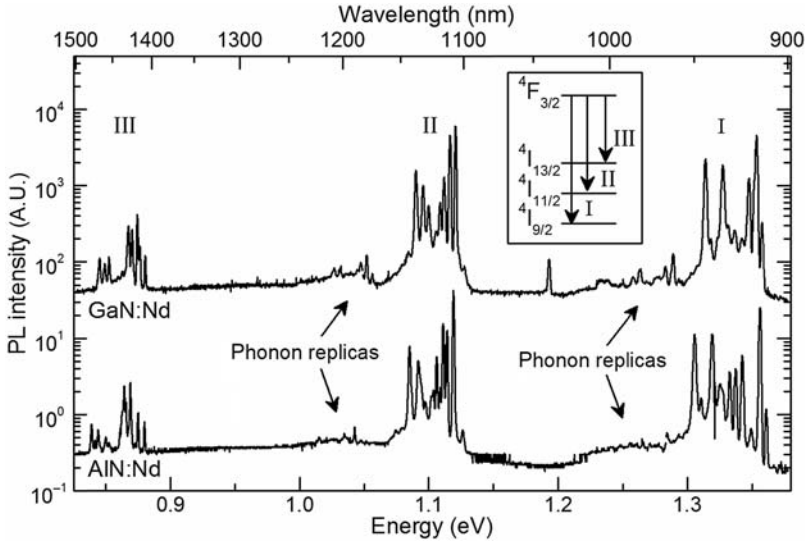
Continued

Table 9.1 Continued

$2S+1L_J$ manifold	Crystal field quantum	Sites in GaN					Sites in AlN		
		<i>A</i> (meV)	<i>B</i> (meV)	<i>C</i> (meV)	$\perp$ <i>g</i> -value <sub>exp</sub>	$\parallel$ <i>g</i> -value <sub>exp</sub>	<i>a</i> (meV)	<i>b</i> (meV)	<i>c</i> (meV)
$^4F_{3/2}$	1/2	486.2	1347.8	1353.85	0.46	0.26	491.6		
	3/2	501.0					511.9		
	1/2	504.2					514.0		
	1/2	508.4					516.8		
	1/2	1353.5					1355.8		
	3/2	1357.7					1360.9		
$^4F_{5/2}$	1/2	1470.8					1477.5		
	3/2	1476.6					1480.5		
	1/2	1479.8					1488.7		
$^2H_{9/2}$	3/2	1491.3					1491.6		
	1/2	1498.0					1495.0		
	1/2	1510.0					1503.7		
	1/2	1511.8					1509.2		

${}^4F_{7/2}$	3/2	1525.1					1528.7		
	1/2	1594.2					1595.0		
	3/2	1596.9					1600.4		
	1/2	1599.3					1605.1		
	1/2	1602.6					1611.8		
${}^4S_{3/2}$	3/2	1608.5					1613.9		
	1/2	1611.2					1615.6		
${}^4G_{5/2}$	1/2	1987.7	1981.8	2001.2	—	—	1983.0	1981.4	2000.9
	3/2	1998.5		2024.9	0.81	0	1994.0	2000.7	2021.9
	1/2	2022.8	2017.9		0.98	0.84	2019.2	2012.9	2041.9
${}^2G_{7/2}$	1/2	2050.4	2038.3	2053.74	—	—	2047.5	2047.5	2065.7
	3/2	2051.1	2042.6	2055.1	—	—	2051.8	2059.0	—
	1/2	2056.3		2058.9	0	1.04	2055.1	2056.0	—
	1/2	2061.5		2063.0	—	0.40	2058.6	2057.9	—





**Figure 9.6** Low temperature ( $\sim 12\text{K}$ ) PL emission spectrum in logarithmic-linear scale from the  ${}^4\text{F}_{3/2}$  to the  ${}^4\text{I}_{13/2}$ ,  ${}^4\text{I}_{11/2}$ , and  ${}^4\text{I}_{9/2}$  manifolds in GaN:Nd and AlN:Nd when optically excited at 836 nm and 837 nm, respectively. The peak emission occurs at 1106 nm and 1108 nm from GaN:Nd and AlN:Nd, respectively. (The GaN:Nd spectrum is artificially shifted up in the plot.)

Fig. 9.6 shows the PL spectra in logarithmic scale used to identify transitions from the  ${}^4\text{F}_{3/2}$  to the  ${}^4\text{I}_{9/2}$ ,  ${}^4\text{I}_{11/2}$ , and  ${}^4\text{I}_{13/2}$  manifolds between 1.30 and 1.36 eV (910–950 nm), 1.08 and 1.13 eV (1100–1150 nm), 0.84 and 0.89 eV (1400–1480 nm), respectively. The GaN:Nd and AlN:Nd materials used in Fig. 9.6 have a Nd concentration of 0.5 at% and 0.08 at%, respectively. The most intense emission peaks were observed from transitions to the  ${}^4\text{I}_{11/2}$  manifold. Due to the crystal field experienced by substitutional Nd ions at the Ga or Al sites ( $\text{C}_{3v}$  symmetry), there are a total of  $J + 1/2$  Stark sublevels in each manifold, where  $J$  is the total angular momentum. The  $\text{Nd}^{3+}$  center energy levels are the same in AlN and GaN with only small differences in the Stark shifts between the AlN and GaN host materials due to the different crystal fields. For example, the strongest PL emission line occurs at 1106 nm in GaN:Nd compared to 1108 nm in AlN:Nd. Fig. 9.7 shows resolved Stark levels in logarithmic scale with the PL peaks appearing in pairs labeled by the integer  $m$ , which corresponds to the transition from the  ${}^4\text{F}_{3/2}$  doublet to the  $m$ th Stark component of the  ${}^4\text{I}_{11/2}$  manifold of the  $\text{Nd}^{3+}$  ion. The lower (higher) energy PL peak of each pair corresponds to transitions from the ground state (first excited state) Stark level of the  ${}^4\text{F}_{3/2}$  excited state. The Stark energy levels for the  ${}^4\text{I}_{9/2}$ ,  ${}^4\text{I}_{11/2}$ , and  ${}^4\text{I}_{13/2}$  manifolds were all identified using the corresponding PL spectrum and are listed in Table 9.1. The peaks in each pair are separated by 4.1 meV (5.1 meV), indicating the splitting energy of the  ${}^4\text{F}_{3/2}$  doublet in GaN:Nd (AlN:Nd). The small size of this splitting allows thermal activation of the upper sublevel making the corresponding emission lines observable even at the lowest temperatures used in these studies. As the sample temperature was varied

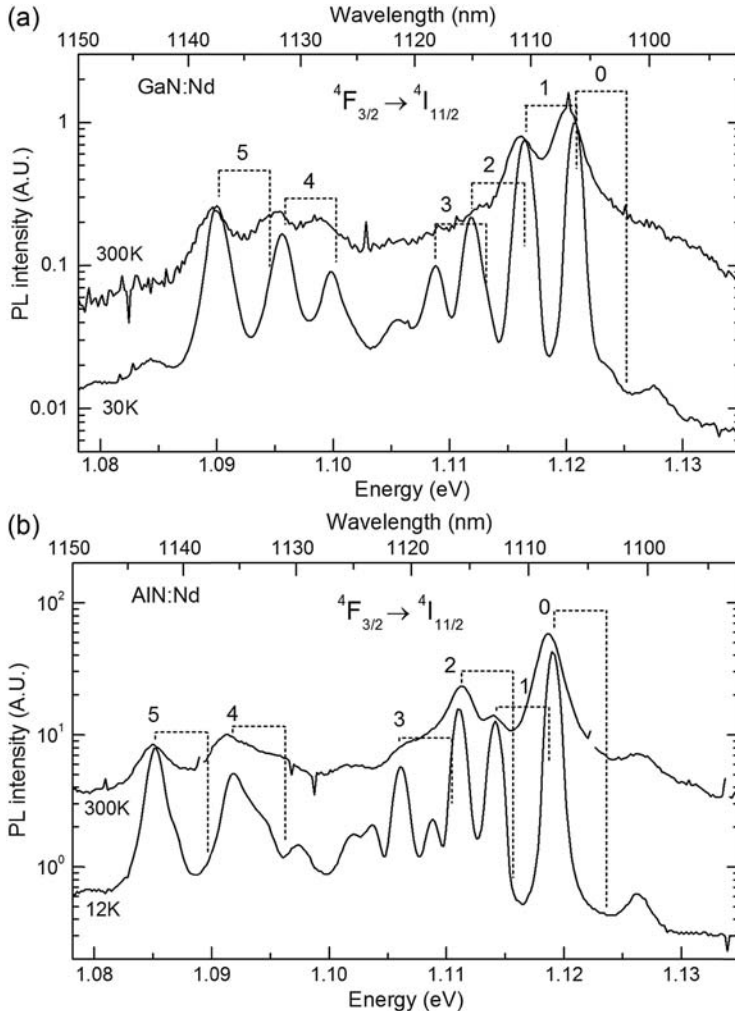


**Figure 9.7** Room-temperature and low-temperature PL emission spectrum in logarithmic scale from the  ${}^4F_{3/2}$  to the  ${}^4I_{11/2}$  transition in (a) GaN:Nd and (b) AlN:Nd showing pairing of the crystal-field split Stark levels. The GaN:Nd and AlN:Nd samples are optically excited at the resonant wavelengths 836 and 837 nm, respectively.

from  $\sim 12$  K to RT, relatively small ( $< 1$  meV) or no shifts in peak energy position occurred, consistent with the  $4f$  shell being well shielded from the host material (Metcalf et al., 2011). As seen in Fig. 9.7, strong emission is still observed at RT from transitions from the  ${}^4F_{3/2}$  level to the  ${}^4I_{9/2}$ ,  ${}^4I_{11/2}$ , and  ${}^4I_{13/2}$  manifolds.

As further optical verification of the in situ doped nitride material quality, the Nd transitions were excited indirectly by pumping the GaN matrix. Fig. 9.8 compares the PL spectra of the  ${}^4F_{3/2}$  to  ${}^4I_{11/2}$  transition in GaN:Nd when optically excited

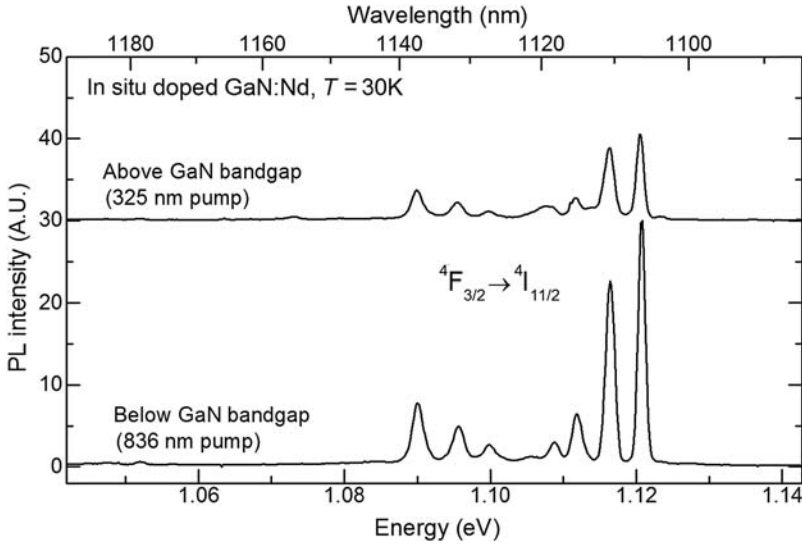


**Figure 9.8** Low temperature PL emission of the  ${}^4F_{3/2}$  to  ${}^4I_{11/2}$  transition from in situ doped GaN:Nd excited above (top) and below (bottom) the GaN bandgap. The above GaN bandgap excitation spectrum is artificially shifted up in the plot.

above (top) and below (bottom) the bandgap at 325 nm and 836 nm, respectively. The shape and relative intensity of the PL peaks from GaN:Nd excited above and below the GaN bandgap are nearly identical and consistent with one dominant incorporation site. When Nd ions occupy multiple sites within the GaN matrix, the PL for above and below bandgap excitation can reveal markedly different emission (Kim et al., 1998).

The bandedge luminescence was also measured with above-bandgap laser excitation at 266 nm. In Fig. 9.9, the PL emission at RT in the region of 360 nm is shown for Nd:GaN samples with different  $C_{Nd}$ . A significant decrease in the PL bandedge emission was observed as the  $C_{Nd}$  increased. For samples with a  $C_{Nd}$  more than  $\sim 1\%$  nearly all the bandedge luminescence was suppressed. This feature was previously reported in other studies where III-V nitride films were doped with various RE or transition metal elements. Above a certain concentration, the normal GaN bandedge luminescence was quenched.

To identify the Stark energy levels of the upper states  ${}^4F_{5/2}$ ,  ${}^2H_{9/2}$ ,  ${}^4F_{7/2}$ ,  ${}^4S_{3/2}$ ,  ${}^4G_{5/2}$ , and  ${}^2G_{7/2}$ , emission spectra were collected as a function of the excitation energy. Figs. 9.10 and 9.11 show the transitions from the  ${}^4I_{9/2}$  ground state to the upper states ( ${}^4F_{5/2}$ ,  ${}^2H_{9/2}$ ), ( ${}^4F_{7/2}$ ,  ${}^4S_{3/2}$ ), and ( ${}^2G_{7/2}$ ,  ${}^4G_{5/2}$ ) between 1.46 and 1.54 eV (805–850 nm), 1.58 and 1.62 eV (765–785 nm), and between 1.98 and 2.07 eV (600–630 nm), respectively. PLE spectra detected at different emission energies show the same peaks with similar intensity ratios. The strongest emission intensities occur at an excitation wavelength of 836 nm (837 nm) for the GaN:Nd (AlN:Nd) material. As with the PL data, the crystal-field split levels can be clearly resolved at RT and

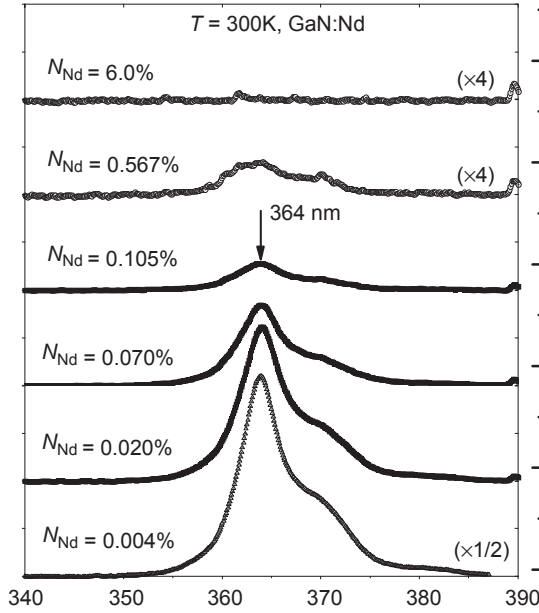


**Figure 9.9** PL bandedge emission at RT due to laser excitation at 266 nm for Nd:GaN samples prepared with different Nd concentrations. The PL intensity is plotted on a linear scale and the spectra are offset for better comparison. Concentrations have been estimated from the cell temperature during growth (see Fig. 9.1).

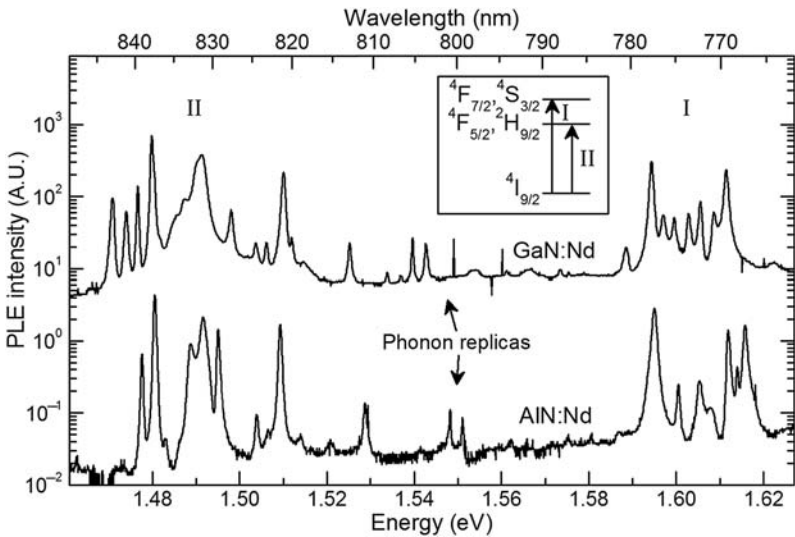


**Figure 9.10** Low temperature ( $\sim 12$  K) PLE spectrum in logarithmic scale from GaN:Nd and AlN:Nd measured at the 1106 nm and 1108 nm emission line, respectively. (The GaN:Nd spectrum is artificially shifted up in the plot.)

only slight shifts in the Stark energy levels between the GaN and AlN hosts are observed. The PLE peaks also appear in pairs but the energy difference of 5.9 meV (13.3 meV) between the pairs corresponds to the energy splitting between the lowest two Stark levels of the  $^4I_{9/2}$  ground state in GaN:Nd (AlN:Nd). This assignment is consistent with the splitting observed in the PL spectra between the  $m = 0$  and the  $m = 1$  Stark level of the  $^4I_{9/2}$  manifold. Table 9.1 summarizes the crystal-field split level energies of the  $^4F_{5/2}$ ,  $^2H_{9/2}$ ,  $^4F_{7/2}$ ,  $^4S_{3/2}$ ,  $^4G_{5/2}$ , and  $^2G_{7/2}$  manifolds of the  $Nd^{3+}$  ion in GaN and AlN.

### 9.3.3 Combined excitation-emission spectroscopy

For more details, CEES (Dierolf and Sandmann, 2007) was employed. The 3D CEES data sets for GaN and AlN shown in Fig. 9.11 not only facilitate identification of the Stark levels, but can also identify minority incorporation sites in the presence of many excitation and emission transitions. The site-selective spectroscopy studies here cover the excitation transitions to the overlapping  $^4G_{5/2}$  and  $^2G_{7/2}$  energy levels as well as the emission transitions from the  $^4F_{3/2}$  level to the  $^4I_{9/2}$  ground state. With five crystal-field levels in the  $^4I_{9/2}$  manifold and seven crystal-field levels in the  $^4G_{5/2}$  and  $^2G_{7/2}$  excited states, we expect 35 combinations of transitions for a single site in the CEES plot, in the absence of thermal activation.

Both Fig. 9.11(a) and (b) show over 100 peaks for different excitation-emission energy combinations that appear in the image maps as “mountains.” Although this number is much higher than the 35 predicted for the spectral region, this is not immediate evidence for multiple sites because thermally excited levels and electron–phonon coupled transitions are present as well. Some of them are indicated in the figure. In order to distinguish such additional peaks from an additional site, we note that for an excitation or emission energy to belong to the same site, the spectra must be identical both in spectral position and relative intensities of individual emission and excitation peaks. In fact, our data reveal that both for GaN and AlN the majority of the observed peaks are related to the single site already identified with the conventional PL and PLE data. The solid lines in Fig. 9.11 black lines indicate the 35 combinations of excitation to the seven  $^4G_{5/2}$  and  $^2G_{7/2}$  levels, and emission from the lowest level within the  $^4F_{3/2}$  excited state to the five ground state Stark sublevels.

While this main site clearly dominates the emission response under resonant excitation conditions, other defect sites can be identified through their characteristically different spectra. Fig. 9.11 shows peaks associated with two weak minority sites in each nitride host material (labeled B and C for GaN:Nd, and b and c for AlN:Nd). The intensity of their emission is orders of magnitude weaker than that of the majority site, and are much more pronounced in AlN:Nd as compared to GaN:Nd. The energies of the identified minority site transitions are included in Table 9.1. Fig. 9.11 clearly shows that the in situ doping technique leads, even for rather high doping levels, to a strongly preferential doping onto a majority site that is most likely the substitutional group III site. This conclusion is further confirmed by the observation that the above and below bandgap excitation PL spectra (Fig. 9.8) are nearly the same.

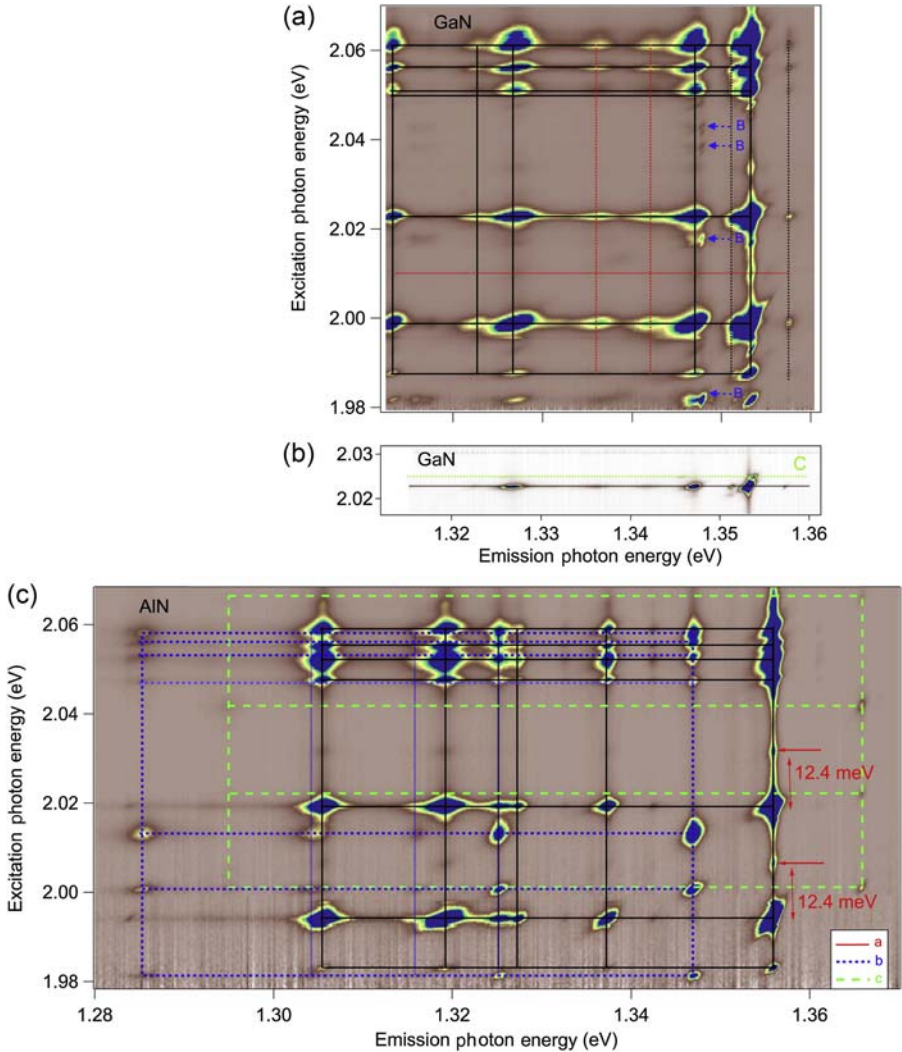


**Figure 9.11** Low temperature (4 K) CEES data of emission intensity as a function of excitation and emission energies from (a), (b) GaN:Nd, and (c) AlN:Nd. Transitions related to a main site are indicated with solid black lines. In (a) transitions originating from thermally excited levels and those related to electron–phonon coupling to a localized mode are indicated with *dotted black* and *red lines*, respectively. A phonon-assisted excitation transition is also indicated in (c) using a *red arrow*. Additional incorporation sites are highlighted in (a) and in (c) by *dotted blue* and *green lines*. In (b), and additional site is highlighted for a selected spectral area. Figure adapted from Metcalfe, G.D., Readinger, E.D., Enck, R., Shen, H., Wraback, M., Woodward, N.T., Poplawsky, J., Dierolf, V., 2011. Near-infrared photoluminescence properties of neodymium in in situ doped AlN grown using plasma-assisted molecular beam epitaxy. *Opt. Mat. Express.* 1, 84.

Such preferential doping is in contrast to the multisite incorporation found for other doping techniques and other RE dopants (Gruber et al., 2011; Dierolf et al., 2004).

As mentioned earlier, electron-phonon coupling can contribute to additional peaks observed in the CEES plots. The phonon replicas also appear in the conventional PL (PLE) spectra shown in Fig. 9.6 (Fig. 9.1) as weak peaks shifted lower (higher) in energy from the main peaks. The energy shifts are related to the longitudinal optical (LO) and transverse optical (TO) phonons (Siegle et al., 1997; Davydov et al., 1998) of the host material, as well as RE-related phonons (Metcalf et al., 2009a, 2011; Dierolf et al., 2004). In GaN:Nd (AlN:Nd), an 11 meV (12.4 meV) mode is observed due to a localized phonon related to the Nd ion. A mode of similar energy (12 meV) has been observed in the excitation-emission spectra of Eu-doped samples (Fleischman et al., 2009). From the intensity ratio of the phonon sideband peak to the relevant zero-phonon peak, an electron-phonon coupling strength is estimated to be quite weak, having a Huang-Rhys (Dierolf et al., 2004) factor  $S$  of  $<0.1$ .

## 9.4 Magnetic properties

As evidenced by the data in Section 9.3, Nd has a valence of  $3+$  when it is in the GaN or AlN host and gives rise to optical spectra characteristic of the  $\text{Nd}^{3+}$  ion. In this charge state, the  $\text{Nd}^{3+}$  ions are isovalent dopants, primarily situated on the Ga or Al sublattice, with three  $4f$  electrons shielded from the host environment by completely filled  $2s$  and  $2p$  shells. The  $4f$  electrons give rise to an effective magnetic moment of 3.6 Bohr magnetons ( $\mu_B$ ) for the  $\text{Nd}^{3+}$  ion.

### 9.4.1 Magnetization measurements of Nd:GaN samples grown by molecular beam epitaxy

The magnetic properties of the Nd:GaN samples were measured at RT using an alternating gradient magnetometer (AGM). The measurements were made with applied field strengths of  $-5$  to  $+5$  kOe for both in-plane and out-of-plane orientations. Typical magnetization curves for in-plane orientation with hysteretic behavior are shown in Fig. 9.12. The out-of-plane orientation yielded only weak magnetic signals. It can be seen that the saturation magnetization,  $M_s$ , is largest for the Nd:GaN sample with 6% Nd. However,  $M_s$  does not scale with  $C_{\text{Nd}}$  as did the PL intensities shown in Fig. 9.3. On the other hand, if  $M_s$  is normalized to an effective magnetic moment per Nd ion, then there appears to be a correlation to the PL bandedge emission intensity. Such a comparison is shown in Fig. 9.13 in which the measured  $M_s$  divided by  $C_{\text{Nd}}$  for each sample is plotted along with the associated bandedge PL intensity.

### 9.4.2 Properties of Nd:GaN samples prepared by diffusion

In a related investigation, an undoped bulk GaN sample from Kyma Technologies, Inc. was doped with Nd using solid-state diffusion. While diffusion is not a common method for introducing RE atoms into a semiconductor, Nd doping of GaN epilayers



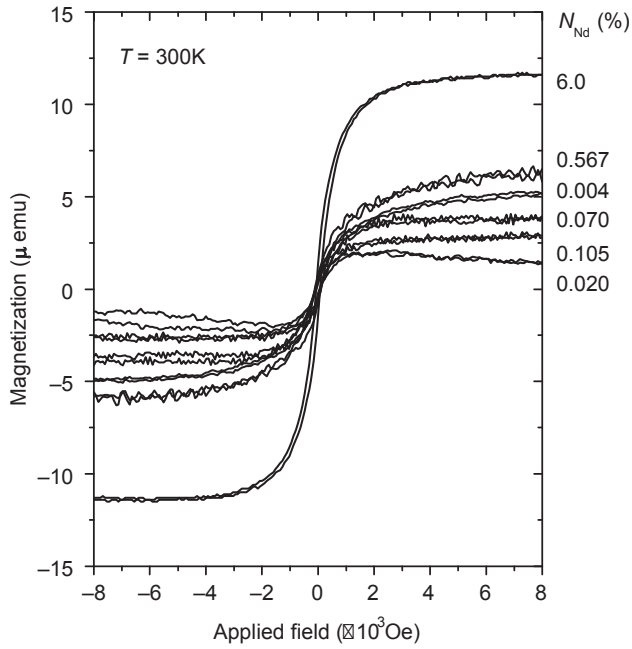


**Figure 9.12** Magnetization curves measured, in-plane orientation at RT, for Nd:GaN samples prepared with different Nd concentrations. Concentrations have been estimated from the cell temperature during growth (see Fig. 9.1).

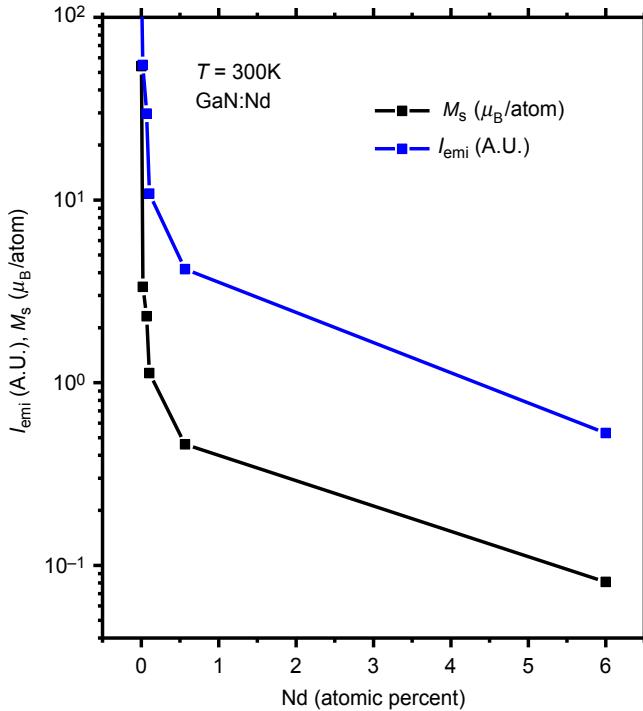


**Figure 9.13** Comparison of the normalized saturation magnetization  $M_s/C_{\text{Nd}}$  and the bandedge emission intensity  $I_{\text{emi}}$  measured at RT for Nd:GaN samples with different Nd concentrations. Concentrations have been estimated from the cell temperature during growth (see Fig. 9.1).



has been demonstrated (Luen, 2009a,b). The sample size was  $\sim 10 \times 10$  mm with a thickness of 900  $\mu\text{m}$ . The defect density was  $\sim 5 \times 10^{-6} \text{ cm}^{-2}$  and the resistivity was  $< 0.5 \text{ Ohm-cm}$ .

For the baseline of the experiment, PL measurements were performed at RT using a HeCd laser, with above-bandgap excitation at 325 nm. In Fig. 9.14 PL spectra near the bandedge are shown for the undoped bulk GaN sample (Kyma) and a typical GaN/sapphire substrate. Due to compressive strain in the GaN/sapphire substrate, its spectrum is blue-shifted by 20 meV compared to that of the bulk GaN. Magnetic measurements using the AGM did not reveal any magnetic signal prior to Nd diffusion.

The bulk GaN sample was loaded into a vacuum chamber ( $\sim 2 \times 10^{-9}$  torr) containing elemental Nd targets. A thick  $\sim 8000 \text{ \AA}$  Nd metal film was deposited on the GaN sample by pulsed laser ablation using a KrF excimer laser at 248 nm. The GaN:Nd was annealed in situ for 8 h at 800  $^{\circ}\text{C}$ . After wet etching to remove the deposited Nd-film and its oxide, SIMS analysis was made to determine the Nd distribution after diffusion. A GaN/sapphire substrate was implanted with Nd to serve as a reference standard. The resulting SIMS Nd depth profile has the typical form for diffusion from an infinite source. The profile is quite shallow and extends to only about 10  $\mu\text{m}$ .

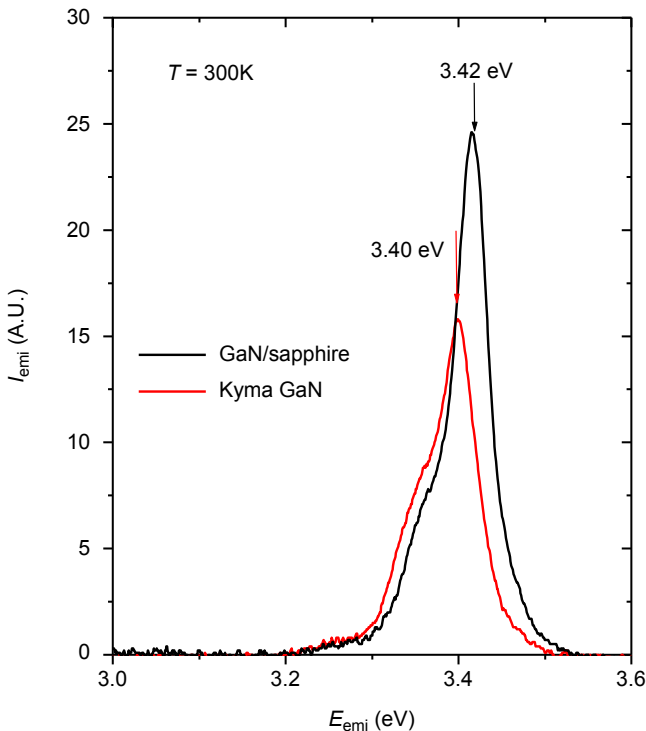


**Figure 9.14** Optical characterization of bulk GaN sample (Kyma) and a typical GaN/sapphire substrate. The bandedge emission of GaN/sapphire is blue-shifted by 20 meV due to compressive strain compared to that of bulk GaN.

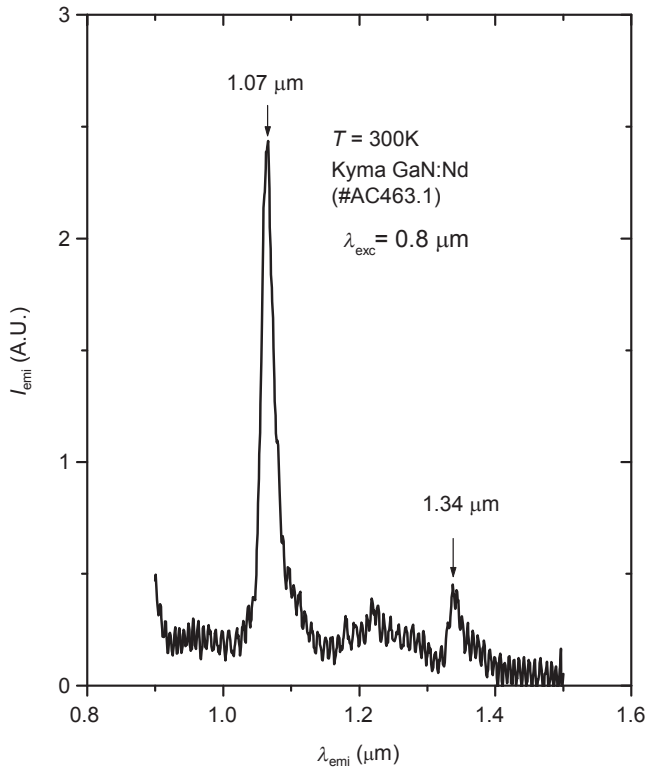


**Figure 9.15** PL emission spectrum for bulk GaN sample (Kyma) after solid-state Nd diffusion. The principal peak at  $\sim 1.07 \mu\text{m}$  corresponds to the  ${}^4\text{F}_{3/2} \rightarrow {}^4\text{I}_{11/2}$  transition of  $\text{Nd}^{3+}$ .

In addition, PL and magnetic properties were again measured at RT. In Fig. 9.15, the PL emission spectrum for the bulk GaN sample following Nd diffusion is shown. The PL spectrum contains two peaks in the near infrared region, one at  $\sim 1.07 \mu\text{m}$  corresponding to the  ${}^4\text{F}_{3/2} \rightarrow {}^4\text{I}_{11/2}$  transition of  $\text{Nd}^{3+}$ , and the other at  $\sim 1.340 \mu\text{m}$  corresponding to the  ${}^4\text{F}_{3/2} \rightarrow {}^4\text{I}_{13/2}$  transition.

AGM measurements showed hysteretic behavior for the in-plane orientation with Ms of  $\sim 2 \mu\text{emu}$ . This low value is consistent with the near surface  $C_{\text{Nd}} \sim 4 \times 10^{18} \text{ cm}^{-3}$  along with the results in Fig. 9.12. Out-of-plane AGM measurements revealed insignificant magnetization. These results provide evidence that Nd diffusion into nonmagnetic bulk GaN material leads to FM behavior for the Nd:GaN sample.

### 9.4.3 Magnetic optical measurements of Nd:GaN samples by molecular beam epitaxy

After reviewing the properties of Nd:GaN with regard to their optical and their magnetic properties in the previous sections, we turn our attention to the optical properties

under the application of a magnetic field and address the question of linkage between the observed magnetization and the spectral features of the individual Nd ions. For these studies, we focus on the sample that was grown with a cell temperature of 950 °C that exhibits well-defined optical spectra (see Fig. 9.6) and a strong remnant magnetization. Nd has an odd number of electrons in its 4*f* shell, and therefore its levels are Kramer degenerate. They can split under the application of a magnetic field into two levels. This splitting is referred to as Zeeman splitting. In our site-selective CEES measurements, this introduces a significant amount of complications. For a given excitation/emission peak, we have three levels involved. All of them split according to a level-specific *g*-factor by  $g = \Delta E / \mu_B B$ , where  $\mu_B = 5.788 \times 10^{-5}$  eV/T is the Bohr magneton. A single excitation/emission peak can then split into four excitation and four emission peaks for a total of  $4 \times 4 = 16$  excitation/emission peaks. This is schematically shown in Figs. 9.16 and 9.17. Which type of level is expected to split is determined by the symmetry of the center and can be determined by group theory. In our case of  $C_{3v}$  symmetry, levels with a crystal-field quantum number of

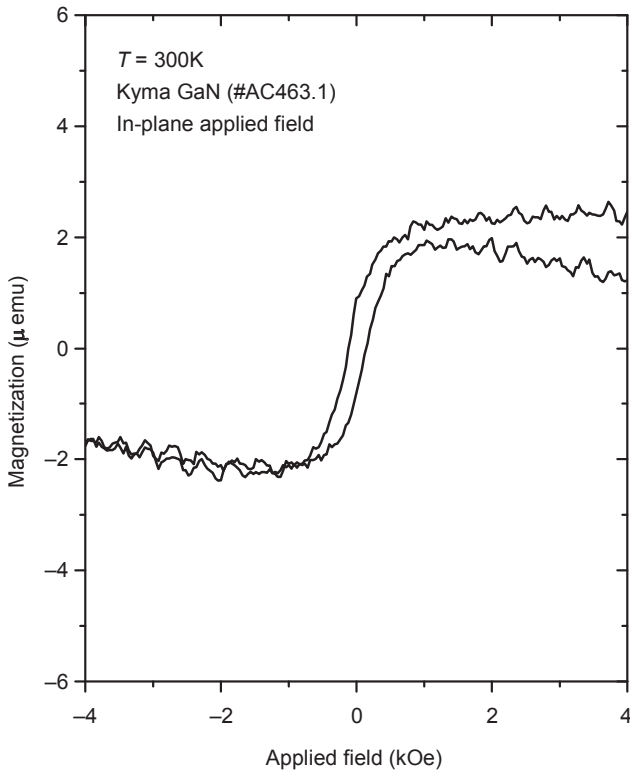


**Figure 9.16** In-plane magnetization curves measured at RT of the bulk GaN sample (Kyma) after solid-state Nd diffusion.

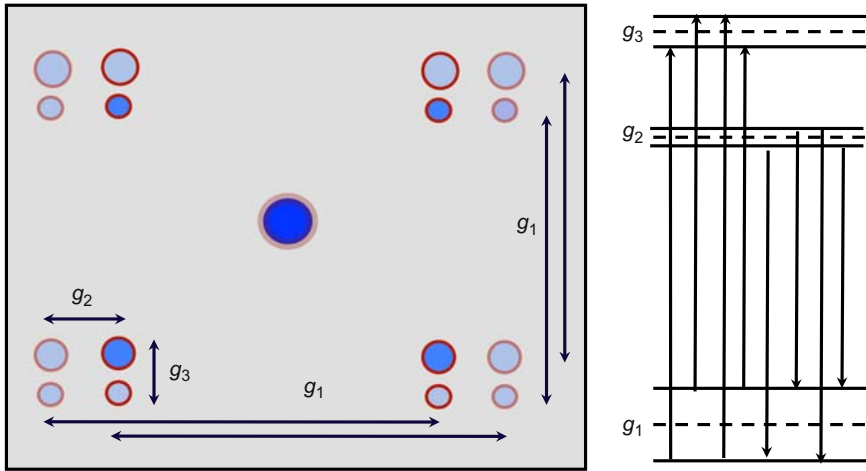


**Figure 9.17** Splitting of a single excitation/emission peak into a total of 16. The corresponding  $g$ -factors are indicated.

$\mu = 3/2$  are not expected to split for a magnetic field perpendicular to the  $c$ -axis. This corresponds to an in-plane magnetic field for our samples grown on  $c$ -sapphire substrates.

The resulting spectra contain information of many  $g$ -factors (three in the example of Fig. 9.17), and the determination can become quite cumbersome, especially if the splitting  $g$ -factors are small and similar to each other. Moreover, in many cases the peaks are not clearly separated. A systematic evaluation is required, which takes many different transitions into account in which the  $g$ -factors in question occur in different combinations. To address the issue of unresolved splitting, we have applied the method of moments for the evaluation of our spectra.

For the method of moments, consider an emission spectrum as shown in Fig. 9.18, in which a single emission peak splits into four peaks by amounts  $2b$  and  $2c$  due to the splitting of levels by  $g_1$  and  $g_2$ . The zeroth and first moment of the spectral distribution are the total emission strength and the average position. In the depicted illustration, they both are independent of the applied magnetic field. The information about the splittings is contained in the second moment that can be described as (assuming Gaussian peaks that do not change shape):

$$\langle E^2 \rangle = \frac{a}{\sqrt{\pi}} \left[ \frac{1}{4} \int_{-\infty}^{\infty} E^2 e^{-a^2(E+b)^2} dE + \frac{1}{4} \int_{-\infty}^{\infty} E^2 e^{-a^2(E-b)^2} dE \right] \\ + \frac{a}{\sqrt{\pi}} \left[ \frac{1}{4} \int_{-\infty}^{\infty} E^2 e^{-a^2(E+c)^2} dE + \frac{1}{4} \int_{-\infty}^{\infty} E^2 e^{-a^2(E-c)^2} dE \right]$$

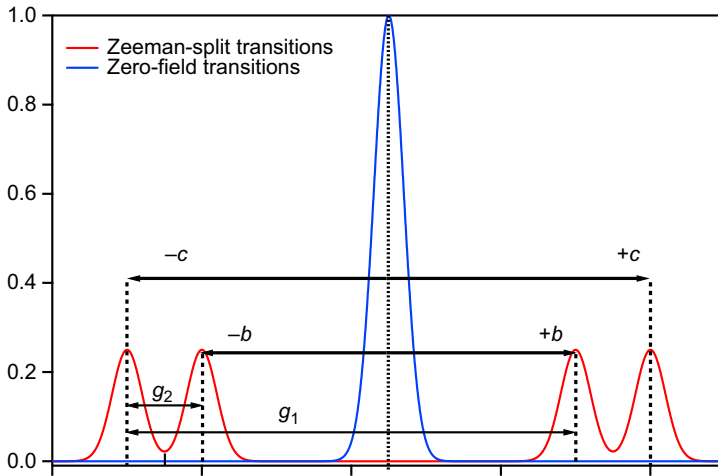


**Figure 9.18** Schematics of the splitting of a single emission line. The relationship between shifts  $b$ ,  $-b$ ,  $c$ ,  $+c$ , and the  $g$ -factors in Fig. 8.17 are indicated.

Solving the four integrals, we are left with

$$\langle E^2 \rangle = \frac{b^2}{2} + \frac{c^2}{2} + \frac{(\Delta w)^2}{2}$$

with  $w$  being the width of the emission peak, which can be determined from the emission at zero-field. In order to determine  $b$  and  $c$  separately, we need to rely on a situation in which one of the  $g$ -factors is significantly bigger than the other. Since the same  $g$ -factors play a role in the splitting of other emission peaks as well, determination of all the  $g$ -factors can be done consecutively and double-checked for overall consistency.

For all the magnetic measurements, we utilize a Faraday geometry, where the polarization of our incident laser is always perpendicular to the applied magnetic field. The setup is shown in Fig. 9.19. The excitation light is coupled into an optical fiber which is then vacuum fed into a magnetic cryostat (Janis 9 T Cryostat), which allows for applied magnetic fields up to 6.6 T utilizing a high current power supply (Oxford Spectromag SM4). Accurate control of the ramping of the current through the Helmholtz coils in the cryostat is achieved via a variable rate sweep generator. The fiber is brought down to the sample with a single mode fiber appropriate for the excitation wavelength in use (core size: 3.5–11  $\mu\text{m}$ ). The fiber is placed into an objective, which collimates and focuses the beam onto the samples. The objective is attached to three translational stages (Attocube ANP  $\times$  100), which allow for investigation of the spatial dependence of emission spectra as well as precise adjustments.

Fig. 9.20 shows the results for in-plane (perpendicular to  $c$ -axis) and out-of-plane (parallel to  $c$ -axis) magnetic fields (0–6 T) for a selected excerpt of our data. It can be seen that there are several peaks that have been split in emission and excitation,

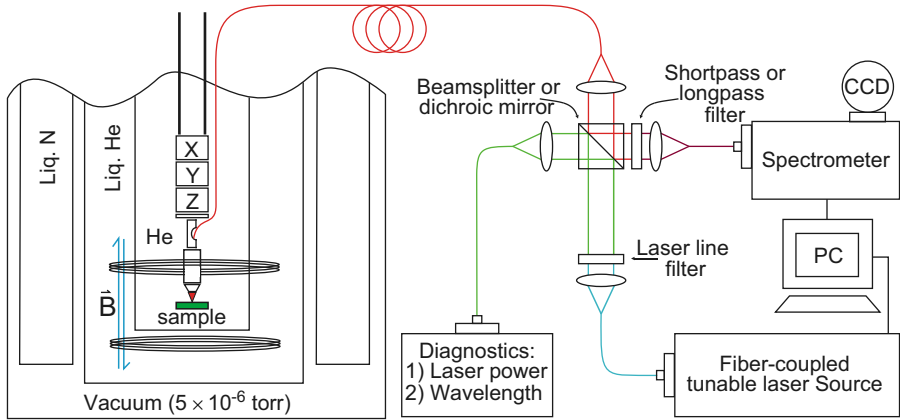


**Figure 9.19** Fiber-based confocal microscope. The sample sits in a magnetic cryostat at 4 K.

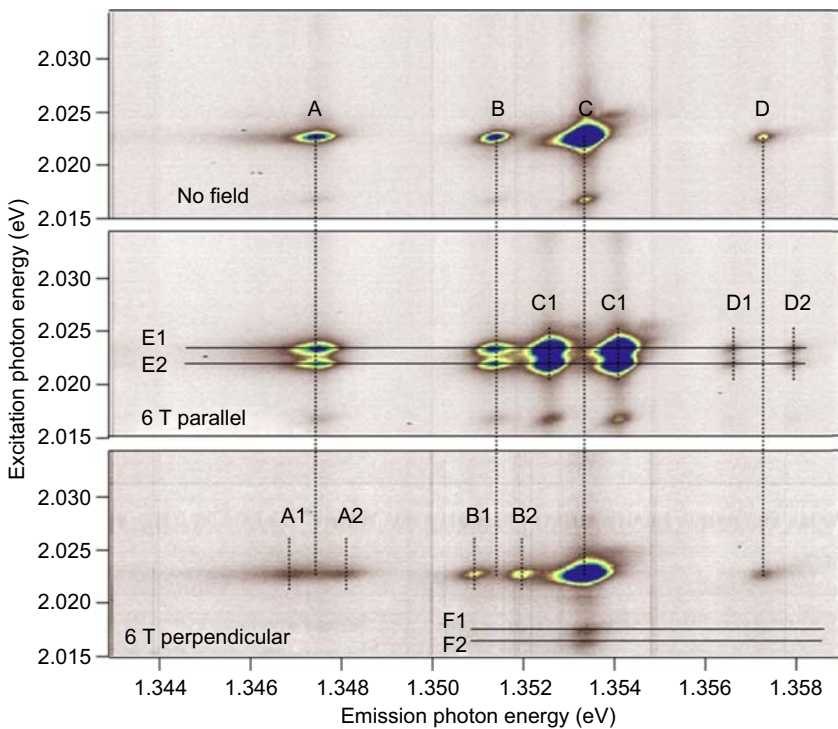


**Figure 9.20** Excerpt of CEES map for one particular excitation region. Results for no field (top); field parallel to the  $c$ -axis (center); and field perpendicular to the  $c$ -axis are shown. The different peaks in emission (A, B, C, D) as well as excitation (E, F) are labeled. See also Fig. 8.21.

allowing us to identify several  $g$ -factors in the excited and ground states of the  $\text{Nd}^{3+}$  ion. Comparing the behavior of the emission (A, B, C, D) and excitation transitions (E, F), it is apparent that the respective Zeeman splittings are clearly different for the fields applied in the two orthogonal directions. While C, D, and E split for parallel fields, the most pronounced splittings occur for A, B, and F for perpendicular fields. In order to illustrate the strategy on how the various splittings are correlated with  $g$ -factors of particular levels, we focus first on the results for out-of-plane fields and the emission to the two closely spaced lowest ground levels. In Fig. 9.21, the emission spectra obtained under field application are shown. In determining  $g$ -factors, we take advantage of the fact that several emission peaks share a common final level (see inset of Fig. 9.21). For instance, the peak labeled B is the emission line due to the upper thermally excited  ${}^4F_{3/2}$  state, which is shifted by  $\sim 4$  meV to higher energy from Peak A, which corresponds to the lower  ${}^4F_{3/2}$  level. The same is true for peaks C and D, which correspond to transitions to the lowest ground state level. For out-of-plane fields, the emission of the latter pair is clearly split while A and B are not, indicating the ground state and not the excited  ${}^4F_{3/2}$  level is the origin of the splitting of C and D. The splitting of the excited states is small seen by the fact that none of the emission peaks split into more than two peaks even with magnetic fields up to 6 T. Only for C1 and D1 a small broadening can be observed. The splitting can be converted to effective  $g$ -factors using  $g_{\text{eff}} = \Delta E / \mu_B B$ , giving an effective  $g$ -factor of the ground state of  $g = 4.03$ . Using this result, the broadening of the peaks can be exploited to calculate the splitting

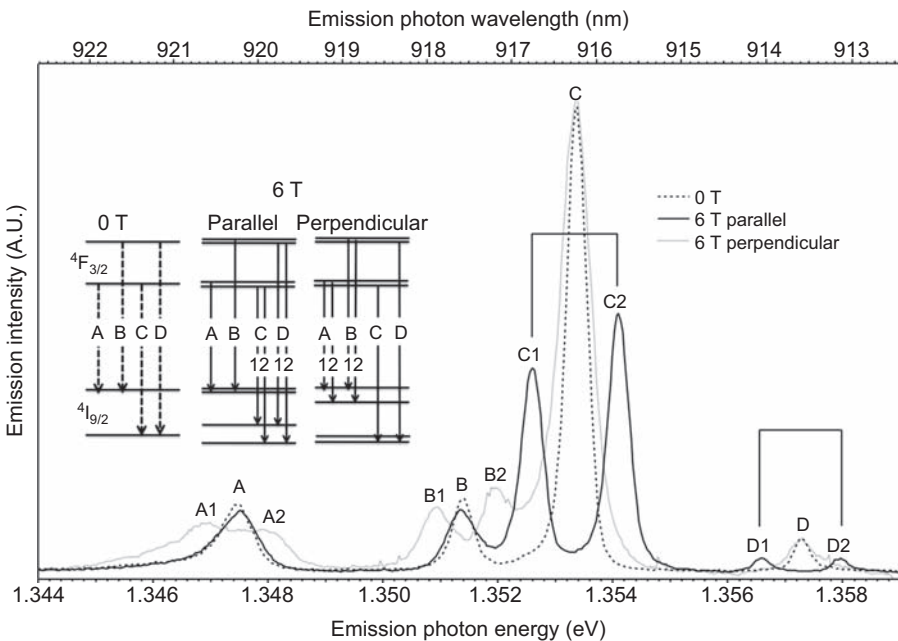


**Figure 9.21** Emission spectra without fields, and with fields applied perpendicular and parallel to the  $c$ -axis. The resulting emission transitions are labeled and illustrated in the insert.

of the excited  $^4F_{3/2}$  levels. For that, we use the method of moments described earlier and assume an unresolved splitting of the respective zero-field Gaussian-shaped peak. Under this assumption, the splitting is determined by the change in the second moment of the spectrum. Once we have the  $g$ -factors of the  $^4F_{3/2}$  levels, we can also determine the splitting for cases, in which the splitting of the final state is small. This way we are able to assign effective  $g$ -values to each of the ground state levels and the resulting values are shown in Table 9.1.

We can repeat the procedure for magnetic fields applied in-plane. For this setup, we rotated the crystal by 90 degree in the sample chamber, but for consistency maintained our excitation along the  $c$ -axis of the crystal. Thus the emission and excitation spectra at zero-field are identical. The same arguments as before can be used except that the two lowest ground state levels exchange their roles. In this case only the A and B transitions exhibit a splitting, suggesting the second lowest ground state is responsible for this splitting while the other splittings are small. The results are included in Table 9.1. As mentioned earlier levels that have splittings in fields applied perpendicular to the  $c$ -axis should be assigned to a  $\pm 1/2$  crystal-field quantum number for perfect  $C_{3v}$  symmetry. These results were used as guide for the crystal-field analysis (Gruber et al., 2011), which gave the best results assuming a slightly perturbed  $C_{3v}$  symmetry of the main Nd center.

Similar results can be obtained for Nd-doped AlN (Gruber et al., 2012). We observed the same general trends. However, we were able to clearly distinguish the two sites  $a$  and  $b$  mentioned earlier. In Fig. 9.22, the observed splitting of the ground state of  $Nd^{3+}$  is compared in the AlN and GaN host. The Zeeman spectra were obtained at 6 T and

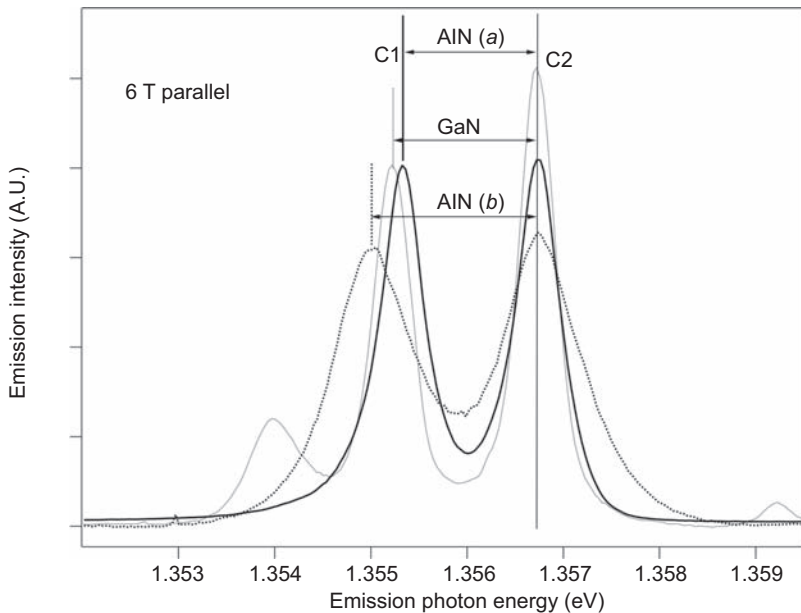


**Figure 9.22** Emission spectra under applied magnetic field for GaN and for two sites  $a$  and  $b$  for AlN.



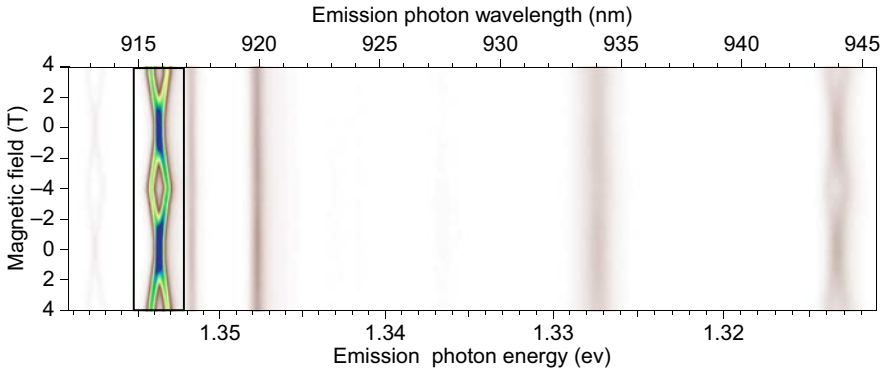


**Figure 9.23** Emission spectra as a function of magnetic field depicted as an image plot. Highest intensity is blue, followed by green, and dark brown. Light brown reflects the background.

15 K for the sample parallel to the magnetic field. The AlN site *a* or main site has a splitting of 1.3 meV, site *b* has a splitting of 1.6 meV, and the splitting in the *a* site in GaN is 1.4 meV. We note that the splitting in the *a* site is somewhat smaller in AlN than in GaN, but the splitting in the AlN *b* site is larger and the transitions involved are inhomogeneously broadened more than the transitions in the *a* sites.

One of the initial goals for the magneto-optical studies was to utilize the observed splitting as a measure for the remnant magnetization while cycling the magnetic field up and down as well as changing its direction. For out-of-plane magnetic fields (parallel to the *c*-axis) the ground state has a fairly large *g*-value while we can choose an excitation wavelength, for which the splitting is negligible. The result of such a hysteresis experiment is shown in Figs. 9.23 and 9.24. Unfortunately, evaluating the

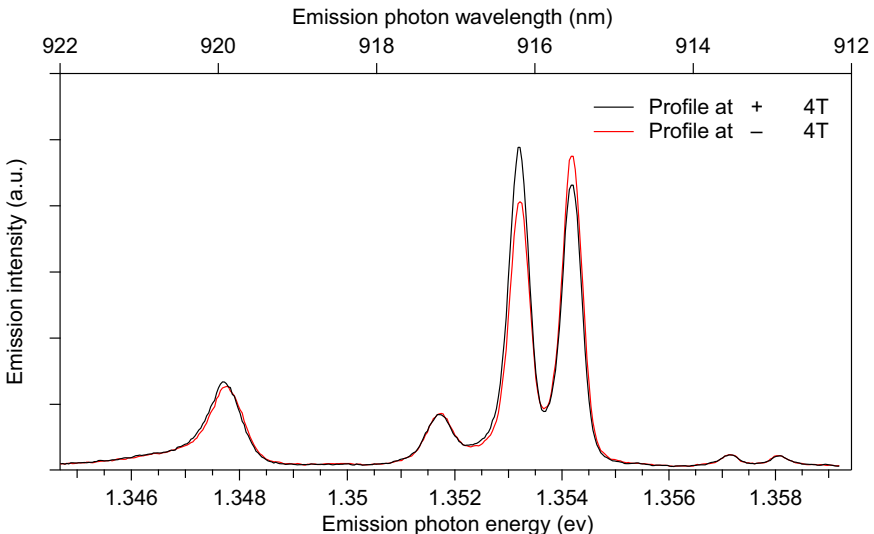


**Figure 9.24** Emission intensity for fields applied parallel and antiparallel to the *c*-axis.

splitting of the most pronounced peak using the method of moments revealed that the stability of the excitation laser was insufficient to determine a remnant field. It should be noted, however, that for none of the cycles, the curve going up followed exactly the curve going down, suggesting influence from the hysteresis effect. While this still has to be studied more carefully using a frequency-stabilized laser, another feature became quite apparent. When we compare spectra for out-of-plane fields directly upward and downward, the emission spectrum looks distinctly different. While the splitting is identical, the relative strength of these peaks has changed. This behavior is quite unexpected. It suggests a dependence of the emission intensities on the relative direction of the applied field and of epitaxial growth direction. The strength of the transitions is determined by higher order perturbation of the  $4f$  states by mixing in states with a different parity found in the outer occupied shell. These states are more sensitive to the environment and hence our observation suggests a coupling of these states with the electronic system of the host. Indirectly, this influences the properties of the  $4f$  electrons.

It can be speculated that this coupling is induced by the lattice mismatch of the epitaxial layer grown on sapphire. This mismatch induces an intrinsic electric polarization into the GaN layer. Its direction depends on the growth directions. Through multiple steps, this perturbation can be transferred and coupled to the Nd ion. Already in the absence of a magnetic field, the electronic states of the host are altered by the intrinsic polarization such that the up–down degeneracy is lifted. Under application of a magnetic field the lowest lying state has a magnetic signature, which also depends on the up or down direction of the polarization. For the influence of these states onto the emission intensity, the energy difference between the relevant states becomes critical and hence the lowest lying host states may be most relevant. Since this has both a magnetic signature and an up–down sensitivity, the up–down sensitivity could be introduced into the transition probability of the RE ion. Since the transition probability relies on high order perturbations, they are much more sensitive to the host material and details of the electronic states.  $G$ -factors, on the other hand, behave similarly to Stark shifts and are much less sensitive to the host.

## 9.5 Applications to quantum sciences

In the last decade, solids doped with RE ions have become promising new candidates for quantum memories, critical components for quantum information processing, and quantum communication (Simon et al., 2007; Tittel et al., 2010). Typically, the basic element of a quantum system uses an atom or atom-like system (such as crystal defects or color centers in diamond and quantum dots) as the quantum bit or qubit. However, these systems can be sensitive to environmental changes. Since the  $4f$  electrons in RE ions are well shielded by the outer  $5s^2$  and  $5p^6$  closed shells, the  $4f$  energy levels are unusually stable with long coherence times at cryogenic temperatures, which promises long quantum information storage times. Millisecond coherence times for optical transitions are possible in RE crystals such as  $\text{Eu}^{3+}:\text{Y}_2\text{SiO}_5$  and  $\text{Pr}^{3+}:\text{Y}_2\text{SiO}_5$  (Tittel et al., 2010). In addition, unlike color centers in solids the weak electron–phonon

interactions in RE materials result in transition intensities concentrated in the narrow zero-phonon lines without the use of resonators (Faraon et al., 2011).

Although cavities are not necessary, the ability to fabricate the host material enables resonant enhancement as well as on-chip photonic capabilities for scalable systems. Unfortunately typical crystalline hosts are difficult to fabricate and has led to the development of hybrid structures such as GaAs-based nanophotonic devices for coupling to  $\text{Nd}^{3+}:\text{Y}_2\text{SiO}_5$  (Miyazono et al., 2014). RE-doped nitride semiconductors have the added advantage of the ions being directly doped into an easily fabricated material.

## 9.6 Conclusions

As with the other elements in the lanthanide RE series, Nd is neither rare nor an earth (oxide). It constitutes nearly 38 ppm of the planet's crust and is a metal. However, due to its high reactive nature, high purity Nd has been available only since the 1930s. In spite of its relatively recent availability, Nd has found a wide range of important technological uses including strong, compact magnets as well as optoelectronics. In this chapter, the possibility of in situ doping of Nd during MBE growth has been successfully demonstrated. The availability of epitaxial layers with high optical quality, the presence of strong emission intensities, and the observed RT magnetic hysteresis suggest that this material is a candidate for new electro-optical-magnetic devices with new functionalities. However, further studies are needed to better understand the interrelation of these properties and find ways to couple most effectively.

## References

- Davydov, V.Y., Kitaev, Y.E., Goncharuk, I.N., Smirnov, A.N., Graul, J., Semchinova, O., Uffmann, D., Smirnov, M.B., Mirgorodsky, A.P., Evarestov, R.A., 1998. Phonon dispersion and Raman scattering in hexagonal GaN and AlN. *Phys. Rev. B* 58, 12899.
- Dierolf, V., Sandmann, C., Zavada, J., Chow, P., Hertog, B., 2004. Site-selective spectroscopy of Er in GaN. *J. Appl. Phys.* 95, 5464.
- Dierolf, V., Sandmann, C., 2007. Combined excitation emission spectroscopy of defects for site-selective probing of ferroelectric domain inversion in lithium niobate. *J. Lumin.* 125, 67.
- Faraon, A., Barclay, P.E., Santori, C., Fu, K.C., Beausoleil, R.G., 2011. Resonant enhancement of the zero-phonon emission from a colour centre in a diamond cavity. *Nat. Photon.* 5, 301–305.
- Favennec, P.N., Lharidon, H., Salvi, M., Moutonnet, D., Leguillou, Y., 1989. Luminescence of erbium implanted in various semiconductors: IV, III-V and II-VI materials. *Electron. Lett.* 25, 718.
- Fleischman, Z., Munasinghe, C., Steckl, A.J., Wakahara, A., Zavada, J., Dierolf, V., 2009. Excitation pathways and efficiency of Eu ions in GaN by site-selective spectroscopy. *Appl. Phys. B* 97, 607.
- Gruber, J.B., Burdick, G.W., Woodward, N.T., Dierolf, V., Chandra, S., Sardar, D.K., 2011. Crystal-field analysis and Zeeman splittings of energy levels of  $\text{Nd}^{3+}$  ( $4f^3$ ) in GaN. *J. Appl. Phys.* 110, 043109.

- Gruber, J.B., Burdick, G.W., Vetter, U., Mitchell, B., Dierolf, V., Hofsäss, H., 2012. Crystal field and Zeeman splittings for energy levels of Nd<sup>3+</sup> in hexagonal AlN. *Opt. Mater. Express* 2, 1176.
- Jadwisnienczak, W.M., Lozykowski, H.J., Berishev, I., Bensaoula, A., Brown, I.G., 2001. Visible emission from AlN doped with Eu and Tb ions. *J. Appl. Phys.* 89, 4384–4390.
- Kim, S., Rhee, S.J., Li, X., Coleman, J.J., Bishop, S.G., 1998. Photoluminescence and photoluminescence excitation spectroscopy of multiple Nd<sup>3+</sup> sites in Nd-implanted GaN. *Phys. Rev. B* 57, 14588.
- Kim, J.H., Davidson, M.R., Holloway, P.H., 2003a. *Appl. Phys. Lett.* 83, 4746.
- Kim, J.H., Shepherd, N., Davidson, M., Holloway, P.H., 2003b. *Appl. Phys. Lett.* 83, 641.
- Kim, J.H., Holloway, P.H., 2004a. Near-infrared electroluminescence at room temperature from neodymium-doped gallium nitride thin films. *Appl. Phys. Lett.* 85, 1689–1691.
- Kim, J.H., Holloway, P.H., 2004b. Room-temperature photoluminescence and electroluminescence properties of sputter-grown gallium nitride doped with europium. *J. Appl. Phys.* 95, 4787.
- Koechner, K., 1999. *Solid-State Laser Engineering*, fifth ed. Springer, Berlin, p. 37.
- Luen, M.O., 2009a. *Spintronics: Towards Room Temperature Ferromagnetic Devices via Mn and Rare Earth Doped GaN*. North Carolina State University.
- Luen, M.O., 2009b. *Erbium Doped III-nitride Semiconductors: Material Synthesizing and Applications*. North Carolina State University.
- MacKenzie, J.D., Abernathy, C.R., Pearton, S.J., Hommerich, U., Wu, X., Schwartz, R.N., Wilson, R.G., Zavada, J.M., 1996. Er doping of AlN during growth by metalorganic molecular beam epitaxy. *Appl. Phys. Lett.* 69, 2083–2085.
- Miyazono, E., Hartz, A., Zhong, T., Faraon, A., 2014. Hybrid Quantum Nanophotonic Devices for Coupling to Rare-Earth Ions. CLEO. OSA Technical Digest, paper FTu3A.5.
- Metcalfe, G.D., Readinger, E.D., Shen, H., Woodward, N.T., Dierolf, V., Wraback, M., 2009a. Crystal-field split levels of Nd<sup>3+</sup> ions in GaN measured by luminescence spectroscopy. *J. Appl. Phys.* 105, 053101.
- Metcalfe, G.D., Readinger, E.D., Shen, H., Woodward, N.T., Dierolf, V., Wraback, M., 2009b. Energy levels of Nd<sup>3+</sup> ions in GaN. *Phys. Status Solidi C* 6 (S2), S671–S674.
- Metcalfe, G.D., Readinger, E.D., Enck, R., Shen, H., Wraback, M., Woodward, N.T., Poplawsky, J., Dierolf, V., 2011. Near-infrared photoluminescence properties of neodymium in in situ doped AlN grown using plasma-assisted molecular beam epitaxy. *Opt. Mat. Express* 1, 84.
- Readinger, E.D., Metcalfe, G.D., Shen, H., Wraback, M., 2008a. GaN doped with neodymium by plasma-assisted molecular beam epitaxy. *Appl. Phys. Lett.* 92, 061108.
- Readinger, E.D., Metcalfe, G.D., Shen, P.H., Wraback, M., Jha, N., Woodward, N., Capek, P., Dierolf, V., 2008b. GaN doped with neodymium by plasma-assisted molecular beam epitaxy for potential lasing applications. *MRS Proceedings*. Vol. 1111.
- Sichel, E.K., Pankove, J.I., 1977. Thermal conductivity of GaN, 25–360 K. *J. Phys. Chem. Solids* 38, 330.
- Simon, C., de Riedmatten, H., Afzelius, M., Sangouard, N., Zbinden, H., Gisin, N., 2007. Quantum repeaters with photon pair sources and multimode memories. *Phys. Rev. Lett.* 98, 190503.
- Siegle, H., Kaczmarczyk, G., Filippidis, L., Litvinchuk, A.P., Hoffmann, A., Thomsen, C., 1997. Zone-boundary phonons in hexagonal and cubic GaN. *Phys. Rev. B* 55, 7000.
- Silkowski, E., Yeo, Y.K., Hengehold, R.L., Goldenberg, B., Pomrenke, G.S., 1996. In: *Rare Earth Doped Semiconductors II Symposium*, vol. 69.

- Slack, G.A., Tanzilli, R.A., Pohl, R.O., Vandersande, J.W., 1987. The intrinsic thermal-conductivity of AlN. *J. Phys. Chem. Solids* 48, 641–647.
- Steckl, A.J., Heikenfeld, J.C., Lee, D.S., Garter, M.J., Baker, C.C., Wang, Y.Q., Jones, R., 2002. Rare-earth-doped GaN: growth, properties, and fabrication of electroluminescent devices. *IEEE J. Sel. Top. Quantum Electron* 8, 749.
- Steckl, A.J., Birkhahn, R., 1998. Visible emission from Er-doped GaN grown by solid source molecular beam epitaxy. *Appl. Phys. Lett.* 73, 1700.
- Tittel, W., Afzelius, M., Chaneliere, T., Cone, R.L., Kroll, S., Moiseev, S.A., Sellars, M., 2010. Photon-echo quantum memory in solid state systems. *Laser Photon. Rev.* 4, 244.

## Part Three

# **Properties of magnetic semiconductors for spintronics**

This page intentionally left blank

# Transition metal and rare earth doping in GaN

10

*M.H. Kane*

Texas A&M University, Galveston, TX, United States

*S. Gupta*

Georgia Institute of Technology, Atlanta, GA, United States

*I.T. Ferguson*

Missouri University of Science and Technology, Rolla, MO, United States

## 10.1 Introduction

Wide bandgap dilute magnetic semiconductors (DMS) have been of interest in the past due to theoretical predictions of room temperature (RT) ferromagnetism in these materials. Tremendous progress has been made in doping the nitrides with transition metals (TM) or rare earth (RE) elements with the aim of obtaining RT ferromagnetism. However, the mechanism for the observed ferromagnetism in this system has been the subject of considerable debate. In this chapter, we present a synopsis of the progress made to date in nitride-based DMS. To elucidate the cause of ferromagnetism in the nitrides, the different exchange mechanisms are presented, and the various growth techniques applied along with their experimental results are summarized. This chapter explores the effects of various TM (Mn, Fe, Cr) and RE elements (Gd) to understand their impact on the optical, structural, and magnetic properties of GaN. The investigation of various TM enables the concurrent variation of a number of important parameters of interest such as the acceptor level and helps us obtain a better understanding of the observed ferromagnetic behavior.

Since the discovery of the Giant Magnetoresistance in the late 1980s by the Nobel laureates Gruenberg and Fert, significant efforts have been made in the field of spintronics (SPIN TRANSPORT electRONICS) (Wolf et al., 2006). This field exploits both the electron spin and its charge in order to introduce an additional degree of freedom to the next generation of electronic devices. Spintronic devices are of great interest since they can be designed to provide higher information storage densities, higher processing and transfer speeds, as well as lower power consumption than current electronic and optoelectronic devices. Novel functionalities such as reconfigurable logic, nonvolatile chip-based memory, and a solid state platform for quantum computing may be possible within semiconductor systems (Pearton et al., 2005). Significant efforts have been made to create heterostructures with spin injections from ferromagnetic metals into semiconductors. However, the difference in conductivities between the ferromagnetic metal and the semiconductor results in interfacial scattering and



low spin injection efficiencies rendering them impractical for device applications. An alternative method is to develop semiconductor materials that exhibit ferromagnetism at RT and can support spin transport and injection. Ferromagnetism and semiconducting properties do coexist in magnetic semiconductors such as europiums, chalcogenides, and semiconducting spinels, however these materials have not resulted in applications since it is difficult to grow high quality thin films and heterostructures. One class of materials that show promise in this regard are DMS, which are compound semiconductors doped with TM or RE elements to provide magnetic functionality (Furdyna, 1988) due to their incompletely filled *d*-shells (TMs) and *f*-shells (REs). They exhibit a net magnetic moment that is exploited in DMS-based materials and devices.

Generally, the magnetic dopants tend to substitute the cation of the host semiconductor. Since the 1980s TM-doped II-VI compounds such as CdTe and ZnS have been widely studied (Furdyna, 1988). Here the valence of the cation matches common magnetic ions such as Mn. The II-VI ferromagnetic compounds usually display paramagnetic, antiferromagnetic, or spin glass behavior. In these II-VI semiconductors giant Zeeman splitting is seen even at low temperatures and low Mn concentration. However, it is difficult to dope this material to produce either p- or n-type material, rendering it unfeasible for device applications. In the late 1990s attention was focused on making III-V semiconductors ferromagnetic by doping them with magnetic ions (Ohno, 1998). III-V semiconductors such as GaAs and GaN have found commercial applications for high speed electronic and optoelectronic devices. The introduction of magnetic ions into these established materials could pave the way for novel devices that integrate magnetic, electrical, and optical functionalities. The most widely studied III-V DMS compound is  $\text{Ga}_{1-x}\text{Mn}_x\text{As}$ , which exhibits a close coupling between carrier concentration and Curie temperature ( $T_C$ ).  $\text{Ga}_{1-x}\text{Mn}_x\text{As}$  is a p-type material based on the shallow nature of the Mn acceptor, allowing spin polarization to be observed even in the absence of an applied field. Hole carriers are thought to mediate the long-range ferromagnetic interaction between isolated Mn centers.  $\text{Ga}_{1-x}\text{Mn}_x\text{As}$  has been shown to be effective at providing a spin injection layer in optically based devices (Ohno et al., 1999). However the  $T_C$  of these systems is limited to less than 170 K, which precludes their practical use (Wang et al., 2005).

The interest in the wide bandgap diluted magnetic materials for spintronic applications was originally derived from a theoretical model by Dietl et al. (2000). This model predicted RT ferromagnetism for  $\text{Ga}_{1-x}\text{Mn}_x\text{N}$  and  $\text{Zn}_{1-x}\text{Mn}_x\text{O}$  with 5% Mn incorporation and  $3.5 \times 10^{20}$  holes/cm<sup>3</sup> (Fig. 10.1). Two primary explanations for this result were given: (1) The smaller lattice constant leads to stronger spin-dependent interaction between localized spins and holes in the valence band, which in turn leads to larger ferromagnetic coupling; and (2) the ferromagnetism in compounds with small anions, such as nitrides, is not detrimentally affected by spin-orbit interactions, which scale as  $Z^4$  (where  $Z$  is the atomic number). ZnO is a promising candidate for spintronic devices, but high quality growth of this material is an issue. It is still a challenge to obtain good quality ZnO substrates; doping this semiconductor p-type has been difficult, and the fabrication of ZnO devices is still unreliable (Liu et al., 2005). GaN-based materials are attractive as they already have a well-established technological base for

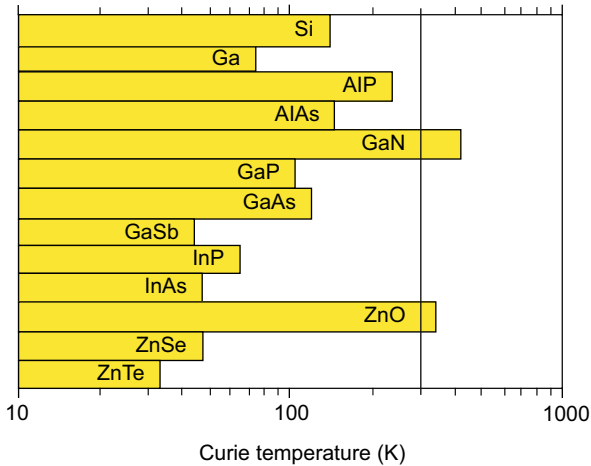


**Figure 10.1** Computed values of the Curie temperature ( $T_C$ ) for various p-type semiconductors containing 5% Mn and  $3.5 \times 10^{20}$  holes/cm<sup>3</sup>.

From Dietl, T., Ohno, H., Matsukura, F., Cibert, J., Ferrand, D., 2000. Zener model description of ferromagnetism in zinc-blende magnetic semiconductors. *Science* 287, 1019–1022.

optoelectronic devices (UV/blue light emitting diodes (LEDs) and lasers) and electronic devices (high-power field-effect transistor), into which the DMS can be incorporated to develop spintronic devices.

Gd-doped GaN (GaN:Gd) is another intriguing DMS. Although ferromagnetism above RT in Gd-doped GaN was first reported by [Asahi et al. \(2004, p. S5555\)](#), [Teraguchi et al. \(2002, p. 651\)](#), [Asahi \(2015, in this volume\)](#) it did not achieve further prominence until [Dhar et al. \(2005a, p. 037205\)](#) and [Dhar et al. \(2005b, p. 245203\)](#) reported “colossal magnetic moment,” apparently up to 4000  $\mu_B$  per Gd atom, in these films. This colossal magnetic moment was found to be even stronger in Gd-implanted samples ([Dhar et al., 2006](#); [Khaderbad et al., 2007](#)). There were reports of traces of secondary phases in GaN:Gd ([Han and Al., 2006](#), [Hejtmánek et al., 2008](#)), none of which can explain the physical origin of ferromagnetism above RT ([Ney, 2015, in this volume](#)). Paramagnetic/ferromagnetic resonance studies also found no conclusive signals that could account for the high temperature magnetism, although some evidence for either Gd or GdN clusters were reported ([Kammermeier et al., 2008](#)).

Initially the origin of this colossal magnetic moment was suggested to be the polarization of the surrounding host medium ([Sapega et al., 2005](#)). However, later studies point toward defects in the crystal lattice, since implantation led to even higher magnetization but annealing somewhat reduced it. X-ray magnetic circular dichroism studies completed on the Gd L3 edge show that the main origin of the magnetism does not appear from Gd itself ([Ney et al., 2008](#)). Several theoretical models have been proposed to explain these observations, but none of these models completely address the question of the cause of such large magnetic moment ([Lambrecht, 2015, in this volume](#)). The microscopic mechanisms in play in GaN:Gd are still subject to extensive debate, but many first-principle calculations based on density functional theory

predict that crystal defects are important contributors to the observed magnetic moments (Liu et al., 2012; Mitra and Lambrecht, 2009). In particular, interstitial oxygen ( $O_i$ ) has been predicted to have a negative formation energy in GaN:Gd and to add to the net magnetic moment of the material.

Several methods are possible for aiding in the development of these materials and ultimately understanding the true nature of the ferromagnetic ordering in these materials systems. One such method is to optimize the various growth and processing techniques, such as molecular beam epitaxy (MBE) and metalorganic chemical vapor deposition (MOCVD), and explore the nanoscale structure and atomic ordering in order to derive the true properties of the material. In order to explore the materials properties of the nitride DMS, several growth techniques have been applied to dope GaN with TMs (eg, Mn, Fe, and Cr) and RE (eg, Gd, Er, and Eu). Investigations have demonstrated that the Mn acceptor in these materials is rather deep ( $E_B \approx 1.5$  eV) (Korotkov et al., 2002), in contradiction to Dietl's assumptions, and the required hole concentration has not been achieved in either material to date. Nevertheless, tremendous progress in obtaining ferromagnetic GaTMN (TM = Mn, Fe, and Cr) was made during the 2010s. It is often unclear whether the observed ferromagnetism is due to substitutional TM or RE ions in the semiconductor lattice, unwanted precipitates, or a combination of both. In order to explore the potential of these materials, it is essential to obtain a better understanding of the exchange mechanisms that result in the observed ferromagnetism in these materials systems.

## 10.2 Classic exchange mechanisms

When semiconductors are doped with magnetic ions, exchange mechanisms exist between the magnetic ion and the host semiconductor. These exchange interactions eventually determine the overall magnetic properties. Exchange mechanisms can be divided into two main categories, direct and indirect, as described in the following paragraphs.

Direct exchange interaction occurs between neighboring magnetic atoms that have overlapping wave functions (Getzlaff, 2008). The exchange interaction ( $J$ ) between these atoms arises from the Coulombic interaction between electrons. Electrons with parallel spins are kept apart due to the Pauli exclusion principle, which leads to a decrease in Coulombic repulsion. Thus, there is a difference in the exchange energy between parallel and antiparallel couplings in the exchange energy. If  $J$  is positive then the spins are parallel and point in the same direction; however, if the exchange interaction is negative then the spins are antiparallel. Typically, the magnetic orbitals of the atoms do not possess sufficient overlap to develop ferromagnetism through direct exchange, and usually indirect exchange mechanisms are more significant in making semiconductors magnetic (Stöhr and Siegmann, 2006).

Several indirect exchange mechanisms have been developed to explain magnetism in TM- and RE-doped semiconductors. The three main classic indirect exchange mechanisms are RKKY, double exchange, and superexchange. In recent years, based

on the observations of ferromagnetism in II-VI and III-V DMS, several other indirect exchange mechanisms have been developed. This discussion begins with the explanation of the classic indirect exchange models.

RKKY is an indirect exchange mechanism named after its discoverers: Ruderman, Kittel, Kasuya, and Yosida (Ruderman and Kittel, 1954; Kasuya, 1956; Yosida, 1957). This mechanism allows for the coupling of magnetic moments through Coulomb exchanges via band electrons over relatively large distances. This theory was originally formulated to explain ferromagnetism in metals and is an efficient mechanism when a high concentration of free carriers is present (Fig. 10.2). The original RKKY studies showed that the spin polarization of the conduction electrons oscillates in sign (Friedel oscillations) as a function of the distance from localized moments. The coupling may be ferromagnetic or antiferromagnetic depending on the

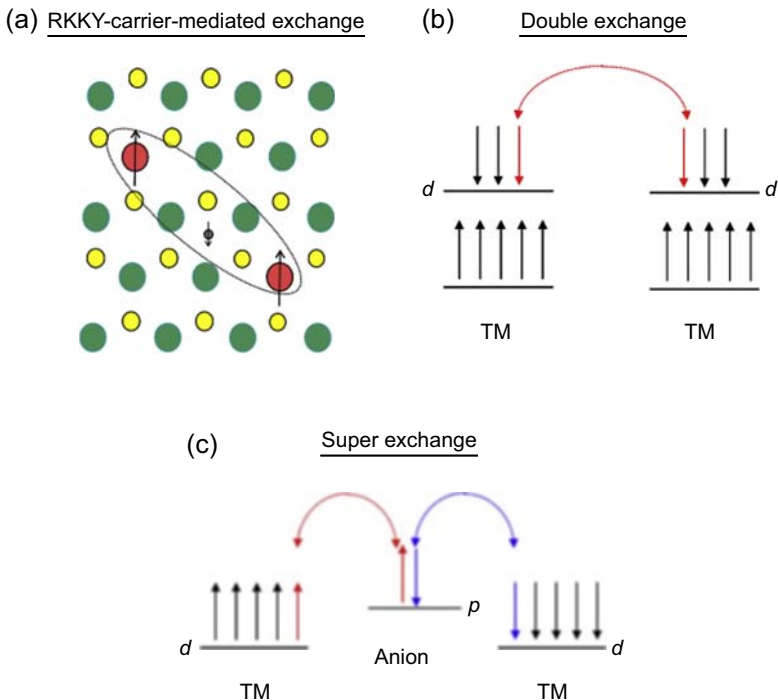


**Figure 10.2** Classic indirect exchange mechanisms: (a) carrier-mediated ferromagnetism, (b) double exchange, (c) superexchange in semiconductors.

After Kane, M.H., Asghar, A., Payne, A.M., Vestal, C.R., Strassburg, M., Senawiratne, J., Zhang, Z.J., Dietz, N., Summers, C.R., Ferguson, I.T., 2005a. Magnetic and optical properties of GaMnN grown by metalorganic chemical vapor deposition. *Semiconductor Science & Technology* 20, L5–L9; Kane, M.H., Asghar, A., Strassburg, M., Song, Q., Payne, A.M., Summers, C.J., Zhang, Z.J., Dietz, N., Ferguson, I.T., 2005b. Impact of manganese incorporation on the structural and magnetic properties of MOCVD-grown  $\text{Ga}_{1-x}\text{Mn}_x\text{N}$ . *Materials Research Society Proceedings* 831, E9.4.1.

separation of the interacting atoms. This mechanism has been used to explain the ferromagnetic mechanism for  $4f$  electrons that are localized. In  $4f$  metals, there is an indirect exchange mechanism between the outer  $5d$  electrons which partly overlap with the  $4f$  shell.

RKKY, or carrier-mediated exchange, has been found to be the ferromagnetism mechanism in  $\text{Ga}_x\text{Mn}_{1-x}\text{As}$ . This mechanism occurs because Mn is an acceptor in GaAs and introduces a hole into  $\text{Ga}_x\text{Mn}_{1-x}\text{As}$ , contributing a localized spin (Ohno et al., 1996; Ohno and Matsukura, 2001). The carrier-mediated exchange theory predicts a  $T_C$  that is dependent on the localized spin concentration as well as carrier concentration in these materials. However, the position of the TM defect levels is midgap and does not generate any free carriers to support this exchange mechanism (Mahadevan and Zunger, 2004). Overall, the carrier-mediated exchange mechanism is interesting as it allows the opportunity to alter magnetic properties by altering hole concentration. Double exchange is a term that was coined by Clarence Zener and this mechanism involves the coupling of magnetic ions in different charge states by the hopping of an electron from one ion to another through interacting with the  $p$ -orbital (Fig. 10.2) (Zener, 1951). Spin flips are not allowed in this model and it is energetically favorable if both the ions have a similar magnetic structure. This mechanism explains magnetism in spinel magnetite, manganites, and Mn perovskites. This model has been used to describe the ferromagnetism in  $\text{In}_x\text{Mn}_{1-x}\text{As}$  (Akai, 1998). In GaN, the TM  $d$  states split into a triply degenerate  $t_{2g}$  and a doubly degenerate  $e_g$  level (Fig. 10.2). In GaN the calculated levels sit at 1.44 and 0.22 eV (respectively) above the valence band maximum (VBM). The majority of  $t_{2g}$  levels have one electron in the case of Cr, two electrons in the case of Mn, and three in the case of Fe.

Another exchange interaction that is found in these materials is the coupling of nearest-neighbor TMs through a shared cation, known as superexchange (Fig. 10.2). The mechanism was first pointed out by Kramers in 1934 and then developed in detail by Anderson in 1950. It results from the virtual hopping of carriers between the completely filled  $p$ -orbitals of anions and the  $d$  orbitals of the magnetic TM cations. In order for electrons from both adjacent atoms to occupy the same  $p$ -level, they must be opposite in spin, a result of Pauli exclusion principle considerations. This leads to an antiferromagnetic coupling of nearest-neighbor cations through a shared anion. This mechanism is of importance in ionic solids such as TM oxides and fluorides, where the bonding orbitals are formed by  $3d$  electrons in the TM atoms and the  $2p$  valence electrons of the diamagnetic oxygen or fluorine atoms. Superexchange is also present in the nitrides, though the strength of the exchange integral is roughly one order of magnitude less than in the oxide-based materials (Zajac et al., 2001b).

It should be noted that there are two main spin-dependent coupling mechanisms in magnetic semiconductors that control the magneto-optical phenomenon. The first is the coupling between the conduction-band electrons ( $s$ -character) and localized spins ( $d$ -character), denoted by  $N_0\alpha$ . The other main mechanism is hole exchange coupling: coupling between the valence band holes ( $p$ -character) and localized spins ( $d$ -character), denoted by  $N_0\beta$ . This generally increases with decreasing lattice constant (Bonanni, 2007). In the tetrahedrally coordinated DMS, if the TM ( $d$  orbitals) or RE

( $d$  or  $f$  orbitals) ions substitute the host cation the resultant electronic structure will be affected by hybridization of the  $d$  or  $f$  orbitals of the magnetic ion and the  $p$  or  $s$  orbitals of the neighboring atoms. In RE ions both the  $d$  and  $f$  states can participate in spin coupling, but the  $f$  states are more localized and thus their coupling is expected to be weak.

In addition to the classic direct and indirect mechanism, additional exchange mechanisms have been proposed to explain the observation of ferromagnetism in dilute magnetic semiconductors. These additional exchange mechanisms are described in the following.

In magnetic semiconductors the magnetic moments are polarized to form sizeable magnetic moments at the vicinity of the donor/acceptor impurities. These are known as bound magnetic polarons (Fig. 10.3) (Coey et al., 2005). Decreasing temperatures result in an increase in the polaron interaction distance, leading to overlap between neighboring polarons and so allowing them to interact through the magnetic impurities, forming correlated polaron clusters. A ferromagnetic transition occurs when the size of such clusters is equal to the size of the samples. Although the direct interaction between the localized carriers is antiferromagnetic, the interaction between the bound magnetic polarons can be ferromagnetic for large concentrations of magnetic impurities. This model has been used to describe the magnetism in low carrier density systems such as electronic oxides.

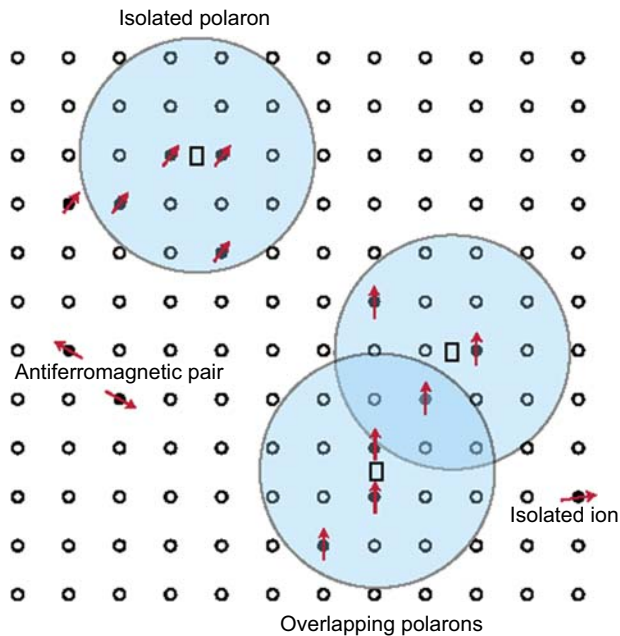


**Figure 10.3** Schematic of bound magnetic polarons interactions.

From Coey, J.M.D., Venkatesan, M., Fitzgerald, C.B., 2005. Donor impurity band exchange in dilute ferromagnetic oxides. *Nature Materials* 4, 173–179.

### 10.2.1 Donor impurity band exchange

A donor impurity band exchange model, proposed by Venkatesan et al. (2004) and Coey et al. (2005), suggests that defect centers mediate ferromagnetism and are responsible for the magnetization seen in TM-doped ZnO. Three scenarios for TM doping in ZnO were evaluated in this model (Fig. 10.4). In the first scenario of a light  $3d$  element (eg, TM = Ti), the  $3d$  spin-up states lie high in the  $2p$  (O) and  $4s$  (Zn) gap, overlapping the spin split donor impurity band. For the next element (TM = Mn) there is no overlap with the  $3d$  level and the exchange is weak, and toward the end of the series (TM = Co) the  $3d$  down states overlap with the impurity band, which then has the opposite spin-splitting for the same occupancy. High  $T_C$  is found when the unoccupied  $3d$  states overlap the impurity band. The origin of the donor impurity band has been attributed to oxygen vacancies ( $F$  centers) in ZnO and it has been proposed that this model can be used to explain ferromagnetism in GaN, which can be caused by the  $d^0$  centers. The higher magnetization that is seen in ZnO at the interfaces is due to the defects that are present in the region. Thus in order for long range magnetization to occur it is essential to have high carrier concentration and a large number of vacancies. Once the donor concentration increases significantly, the donors merge with the conduction band and then the RKKY exchange mechanism begins to dominate.

The Litvinov and Dugaev model is used to explain ferromagnetism in both degenerate and nondegenerate films. This model proposes an indirect exchange mechanism in which virtual electrons transition from the magnetic impurity acceptor level to the valence band (Litvinov and Dugaev, 2001). This model applies to semiconductors in

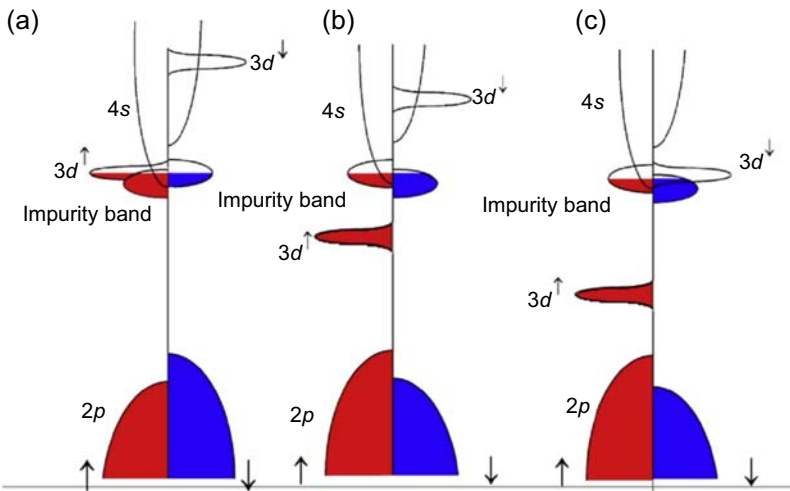


**Figure 10.4** Schematic density of states for (a) TM = Ti, (b) TM = Mn, and (c) TM = Co. The Fermi level lies in a spin split donor impurity band.

From Coey, J.M.D., Venkatesan, M., Fitzgerald, C.B., 2005. Donor impurity band exchange in dilute ferromagnetic oxides. *Nature Materials* 4, 173–179.



which there is a low concentration of magnetic ions and in which magnetic dopants do not introduce any free carriers. In this model the  $T_C$  depends on  $p$ - $d$  exchange interactions and the energy between the TM impurity level and the band electron levels. This model has been applied to explain the ferromagnetism in  $\text{Ga}_{1-x}\text{Mn}_x\text{As}$  and  $\text{Ga}_{1-x}\text{Mn}_x\text{N}$  films.

### 10.2.1.1 Theoretical models for ferromagnetism in dilute magnetic semiconductors

Based on the experimental results for the II-VI semiconductors and III-Arsenide semiconductors several theoretical models have been developed to elucidate the magnetism in these DMS, and many of these have then been extrapolated to GaN.

The Zener Mean field model has been proposed by [Dietl et al. \(2000\)](#) to determine the  $T_C$  of various zinc blende semiconductors. This model is based on the Zener and RKKY interaction models and takes into account the anisotropy associated with RKKY exchange, which is associated with the spin-orbit coupling. This model evaluates ferromagnetic interactions mediating through holes introduced by TM doping (shallow acceptors). It was found that  $T_C$  is determined by a competition between the ferromagnetic and antiferromagnetic interactions. The  $T_C$  values calculated by the mean field model for different materials were performed using [Eqs. \[10.1\] and \[10.2\]](#):

$$T_C = T_{\text{FM}} - T_{\text{AFM}} \quad [10.1]$$

$$T_C(x) = A_{\text{F}}(x_{\text{eff}}/0.05)(\beta N_0[\text{eV}])^2 \left[ \frac{N_0(\text{GaAs})}{N_0} \right] T_{\text{F}} - T_{\text{AF}}(x) \quad [10.2]$$

where AF is the Fermi liquid parameter,  $x_{\text{eff}}$  is the effective spin concentration,  $\beta$  is the  $p$ ,  $d$  exchange integral,  $N_0$  is the concentration of cation sites,  $T_{\text{F}}$  is the FM ordering temperature, and  $T_{\text{AF}}$  is the atomic force microscopy (AFM) ordering temperature. A TM concentration of 5% was used in this study along with a hole concentration of  $3.5 \times 10^{20} \text{ cm}^{-3}$ . This model agrees well with the experimental results for  $\text{p-Ga}_{1-x}\text{Mn}_x\text{As}$  and  $\text{Zn}_{1-x}\text{Mn}_x\text{Te}$  ([Ohno et al., 1996](#); [Ohno and Matsukura, 2001](#)). The  $T_C$  depends on the TM doping concentration and hole concentration and is higher for lighter elements. The spin-orbit coupling in the valence band is crucial for determining the  $T_C$  and direction of the easy axis.

Based on this model, GaN and ZnO are predicted to have a  $T_C$  higher than RT as they have smaller lattice constants and allow for greater  $p$ - $d$  hybridization and reduced spin-orbit coupling. One of the challenging theories is that the solubility limit of TM is low in GaN and so it is challenging to obtain 5% TM doping. Furthermore,  $p$ -doping in GaN is extremely challenging and hole concentrations on the order of  $10^{20} \text{ cm}^{-3}$  may not be feasible. It is this theory that has spearheaded the research in TM-doped GaN and ZnO.

[Sato et al. \(2003a\)](#) and [Katayama-Yoshida et al. \(2007\)](#) performed ab initio calculations on GaN doped with 5% of various TM. Their model shows that the  $\text{Ga}_{1-x}\text{Mn}_x\text{As}$  exhibits a spin-splitting of the density of states (DOS) in the valence



band, while GaN possess a spin-split DOS in the middle of the bandgap. Therefore, TM atom in GaN forms deep levels and does not generate free carriers (Mahadevan and Zunger, 2004). It was shown that for half-filled (or less)  $d$ -shells such as in Mn, Cr, and V the ferromagnetic state is stable in GaN. For high Mn concentration the spin glass state is favored (Fig. 10.4). Additionally, it was found that Fe, Co, and Ni doping are stable in the spin glass state in GaN. Furthermore, first-principle calculations show that TM forms an impurity band and the ferromagnetism in the nitrides is stabilized by a double exchange mechanism and broadening of the impurity band (Sato et al., 2003b; Akai, 1998). Mean field approximations predicted a high  $T_C$  of 500 and 350 K for 5% Cr and Mn-doped GaN, respectively (Sato et al., 2003b). The double exchange mechanism in this system favors short range interaction between nearest neighbors. For a high  $T_C$ , the model requires a large concentration of TM (>20%) (Bergqvist et al., 2004). Further Monte Carlo simulations revealed that the  $T_C$  of Mn-doped GaN is on the order of tens of Kelvin and so RT ferromagnetism is not feasible. This suggests that the mean field approximation overestimates the  $T_C$  significantly. It has been suggested that any RT ferromagnetism found experimentally is due to the presence of MnN clusters or secondary phases (Sato et al., 2004).

### 10.2.2 Density functional theory studies of $Ga_{1-x}Gd_xN$

$Ga_{1-x}Gd_xN$  is promising as it has the potential to be doped with donors (acceptors) with a concentration exceeding that of Gd to generate spin-polarized electrons (holes) in the conduction band (valence band), which could be applied to spintronic devices (Dhar et al., 2005a, p. 4; Dalpian and Wei, 2006). To date, there is no consistency in the mechanism proposed for the observed magnetism in  $Ga_{1-x}Gd_xN$  thin films. The first reports on ferromagnetic  $Ga_{0.94}Gd_{0.06}N$  by Asahi et al. (2004, pp. S5555–S5562) attributed the magnetism to the RKKY-type interaction via the spin-polarized valence band of GaN. Dhar et al. (2003) attributed the large magnetic moment observed to the long range spin of the GaN matrix by Gd atoms. On the other hand MBE reports by Zhou et al. predict that electrons introduced by Si doping or defects (nitrogen vacancies) help to stabilize the ferromagnetic phase in  $Ga_{1-x}Gd_xN$  films as they offer electrons that couple between the Gd  $f$  and host  $s$  states (Zhou et al., 2007).

Dalpian and Wei have performed ab initio band structure calculations and determined the DOS for zinc blende  $Ga_{1-x}Gd_xN$  for  $x = 6.25\%$  (Fig. 10.5) (Dalpian and Wei, 2006). Their calculations show that the coupling between Gd atoms in zinc blende  $Ga_{1-x}Gd_xN$  is antiferromagnetic as the spin-splitting in the ferromagnetic phase does not result in energy gain as compared to the unsplit antiferromagnetic phase. The antiferromagnetic phase is stabilized through superexchange interactions between the Gd  $4f$  and N  $p$  states. The theoretical calculations show that the addition of electrons can stabilize the ferromagnetic phase as the  $s$ - $f$  coupling results in a negative spin exchange splitting ( $\Delta E_{FM-AFM}$ ) (Dalpian and Wei, 2006). Dalpian and Wei predict that both holes and electrons will result in ferromagnetic interaction in  $Ga_{1-x}Gd_xN$  but the electrons are more efficient in stabilizing the ferromagnetic phase and should result in larger magnetic moments.

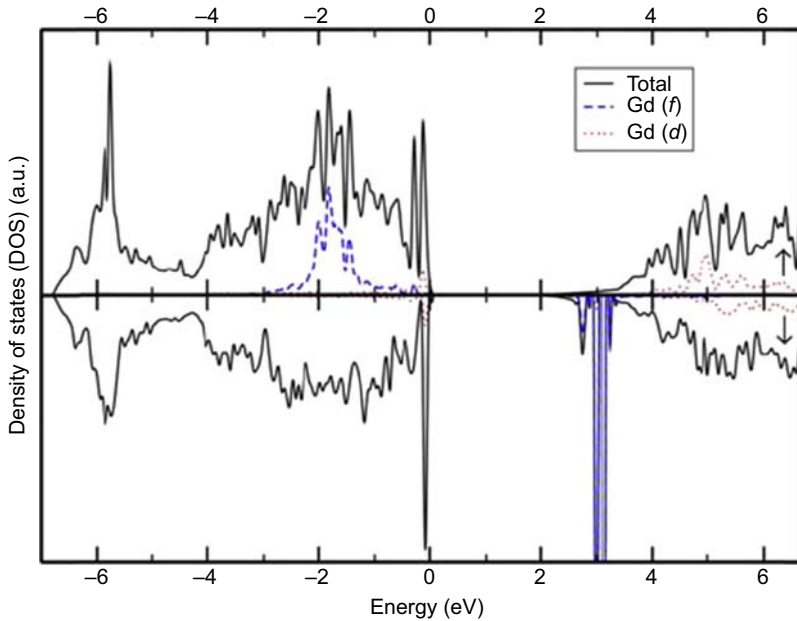


**Figure 10.5** Density of states for zinc blende  $\text{Ga}_{1-x}\text{Gd}_x\text{N}$  ( $x = 6.25\%$ ).

From Dalpian, G.M., Wei, S.H., 2006. Carrier-mediated stabilization of ferromagnetism in semiconductors: holes and electrons. *Physica Status Solidi B* 243, 2170–2187.

First-principle calculations based on spin density functional theory have resulted in the electronic structure for wurtzite  $\text{Ga}_{1-x}\text{Gd}_x\text{N}$  ( $x = 12.5\%$ ) shown in Fig. 10.6 (Hejtmánek et al., 2008; Gohda and Oshiyama, 2008). In this model, the 7.4 eV broad valence band is of  $N\ 2p$  character and the conduction band is predominantly formed by the  $4s$  Ga electrons. According to Hejtmánek et al. (2008) the  $4f$  orbitals spin-up band is positioned  $-3.5$  eV below the VBM and the spin-down states are 6 eV above the conduction band minimum (Hejtmánek et al., 2008). The substitution of Ga by Gd is isovalent and thus no electrons or holes are created. Their findings suggest that ferromagnetism in  $\text{Ga}_{1-x}\text{Gd}_x\text{N}$  is caused by the RKKY exchange mechanism and is mediated through itinerant carriers that occur due to excitation from an impurity band to the conduction band or due to an impurity band in the degenerate semiconductor (Liu et al., 2008). Unlike TM-doped GaN, which exhibits metallic or semi-metallic states, the  $\text{Ga}_{1-x}\text{Gd}_x\text{N}$  system is always a semiconductor with the bandgap gradually decreasing with an increase in Gd concentration (Zhong et al., 2008). First-principle calculations by Zhong et al. (2008) show that the Fermi level is always located at the maximum position of the valence band for different Gd concentrations ( $x$  ranging from 0.03 to 0.25).

Several theoretical analyses have been performed to determine the validity of the long-range polarization of the GaN lattice by Gd atoms (Dalpian and Wei, 2006; Liu et al., 2008; Zhong et al., 2008). These calculations show that the net spin exchange splitting in the valence band or conduction band for RE-doped GaN is

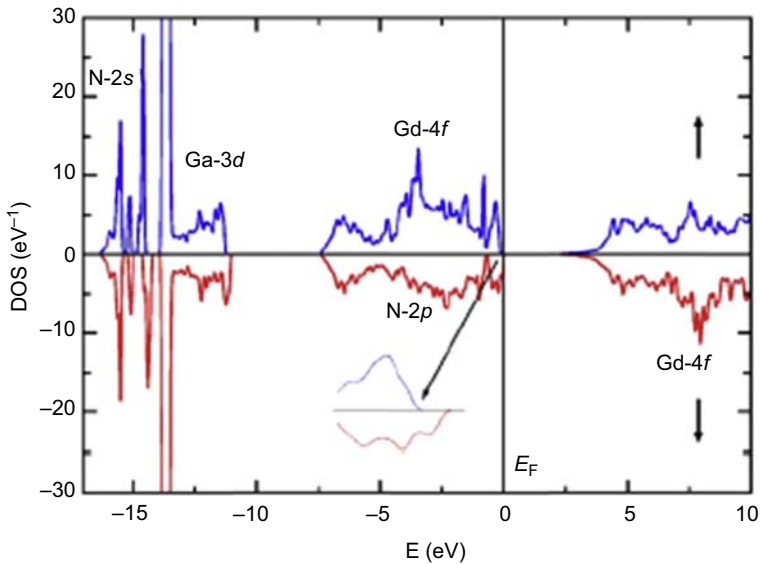


**Figure 10.6** Electronic structure of wurtzite  $\text{Ga}_{1-x}\text{Gd}_x\text{N}$  ( $x = 12.5\%$ ).

From Hejtmánek, J., Knížek, K., Maryško, M., Jiráček, Z., Sedmidubský, D., Sofer, Z., Peřina, V., Hardtdegen, H., Buchal, C., 2008. On the magnetic properties of Gd implanted GaN. *Journal of Applied Physics* 103, 07D107.

smaller than that of TM-doped. The  $f-s$ ,  $f-p$ , and  $f-d$  couplings in GaN are weaker than those of the  $d-s$ ,  $d-d$ , and  $d-p$  hybridization in  $\text{Ga}_{1-x}\text{TM}_x\text{N}$ . Thus more Gd atoms enhance the magnetic coupling through  $N$  atoms, and these  $N$  atoms are visibly polarized in the presence of Gd atoms, but this polarization is too small to result in the large magnetic moment of  $4000 \mu_B$  per Gd atom (Dhar et al., 2005a, p. 4; Zhong et al., 2008).

Unlike other DMS, Gd in GaN has both partially filled  $5d$  and  $4f$  electrons that can contribute to the magnetic moment of Gd, thus it is imperative to analyze the effect of both of these orbitals on the ferromagnetism.

Spin density functional theory calculations have been performed by Liu et al. (2008) to determine the magnetism mechanism in  $\text{Ga}_{1-x}\text{Gd}_x\text{N}$ . Their findings suggest that the  $4f$  orbitals are too far apart from the VBM and conduction band minimum, and their coupling with free carriers should be weak. Thus, they explored the impact of the Gd  $5d$  electrons. The fivefold degenerate  $5d$  orbitals of Gd are split by the tetrahedral field of the GaN lattice into two  $e_g$  and three  $t_{2g}$  states. The lowest conduction band of GaN is mainly  $s$ -like in character and has very little  $d$  character and thus the  $s-d$  coupling is expected to be weak as long as the Gd local environment has  $T_d$  symmetry. In wurtzite samples, defects and the hexagonal symmetry can result in  $s-d$  coupling. On the other hand, relatively flat Gd  $5d$  orbitals with  $t_{2g}$  symmetry occur around the  $p$ -like VBM of GaN. As the Gd  $5d$   $t_{2g}$  have the same symmetry as the GaN VBM at the zone center, the  $p-d$  hybridization is very strong as observed in Mn-doped GaAs.

The energy difference between the ferromagnetic and antiferromagnetic configurations ( $\Delta E = E_{\text{FM}} - E_{\text{AFM}}$ ) was found to be zero for the structure used in this model, suggesting that  $\text{Ga}_{1-x}\text{Gd}_x\text{N}$  should be paramagnetic unless defects exist that stabilize the ferromagnetism. Due to the larger atomic radius of Gd as compared to Ga it is expected that a large density of vacancies exist that could be responsible for the observed ferromagnetism (Larson and Satpathy, 2007; Gohda and Oshiyama, 2008).

The two possible scenarios are nitrogen vacancies and gallium vacancies. Nitrogen vacancies ( $V_{\text{N}}$ ) introduce three conduction electrons to the system and cause the Fermi level to shift well above the VBM. As the local symmetry allows  $s-d$  coupling, the lowest conduction band will contain significant  $d$ -character and thus have a significant DOS occurring at the Fermi level. The energy difference  $\Delta E$  for  $\text{Gd}_{\text{Ga}}-V_{\text{N}}$  complex is 3.9 meV/Gd atom and implies that  $s-d$  coupling is rather weak. The  $\Delta E$  for the wurtzite structure is on the order of  $-0.7$  meV/Gd atom. Liu et al. state that the  $n$ -type carriers cannot be responsible for the large magnetic moment of 4000/Gd atom observed by Dhar et al. (2005b, pp. 245203-1).

In the case of gallium vacancy ( $V_{\text{Ga}}$ ), the missing Ga atom contributes three holes, and the  $d$ -band DOS near the Fermi level shows noticeable difference between the spin-up and spin-down states (Fig. 10.7). The calculated energy difference  $\Delta E = E_{\text{FM}} - E_{\text{AFM}}$  by Liu et al. (2008) is  $-697.1$  meV/Gd atom. Their calculations show that a strong FM  $p-d$  exchange coupling exists that is 180 times stronger than  $s-d$  coupling. The  $p-d$  exchange is so strong that three unoccupied spin-down valence bands from GaN matrix are pushed above the VBM of the spin-up states, resulting in the magnetic moment of the Gd  $d$  electron being spread over the  $p$  bonding orbital. The calculated  $\Delta E_{\text{FM}} - \text{AFM}$  is  $-326.1$  meV/Gd atom for the supercell unit for a Ga vacancy. The FM  $p-d$  exchange in  $\text{Ga}_{1-x}\text{Gd}_x\text{N}$  (for both wurtzite and zinc blende) is over two orders of magnitude stronger than the  $s-d$  exchange, which implies that holes are more effective than electrons in contributing to the ferromagnetism (Liu et al., 2008).

The Gd ion in GaN introduces its own electronic states to the GaN band structure. Before taking into account coupling and hybridization effects between Gd and GaN states it is feasible to first only consider the electronic states of the isolated Gd ion in the GaN matrix. The energy schemes of Gd ions are derived from classic atom theory (Gruber et al., 2004). They differ considerably between different oxidation states. For example, the electronic structure of  $\text{Gd}^{2+}$  is strongly influenced by spin-orbit coupling, while  $\text{Gd}^{3+}$  with its exactly half-filled  $f$ -shell has an orbital momentum equal to zero and, thus, is unaffected by spin-orbit coupling. In addition, the electronic structure of Gd ions is influenced by the crystal field of GaN. This effect is about three orders of magnitude smaller than for TM ions because the partially filled  $4f$  shell is shielded by  $5s$  and  $5p$  electrons. The splitting caused by the crystal field can still be resolved in luminescence, transmission, or magneto-resonance spectra providing valuable information on the environment of the Gd ion. Carrier-mediated spin coupling is of particular significance as charge transfer transitions between Gd and the bands of the host crystal (Gd) may act as a donor or acceptor. Accordingly the energy needed to accomplish such a charge transfer process can be correlated with a position in the GaN energy band structure. Establishing this position is central for the evaluation of any DMS.

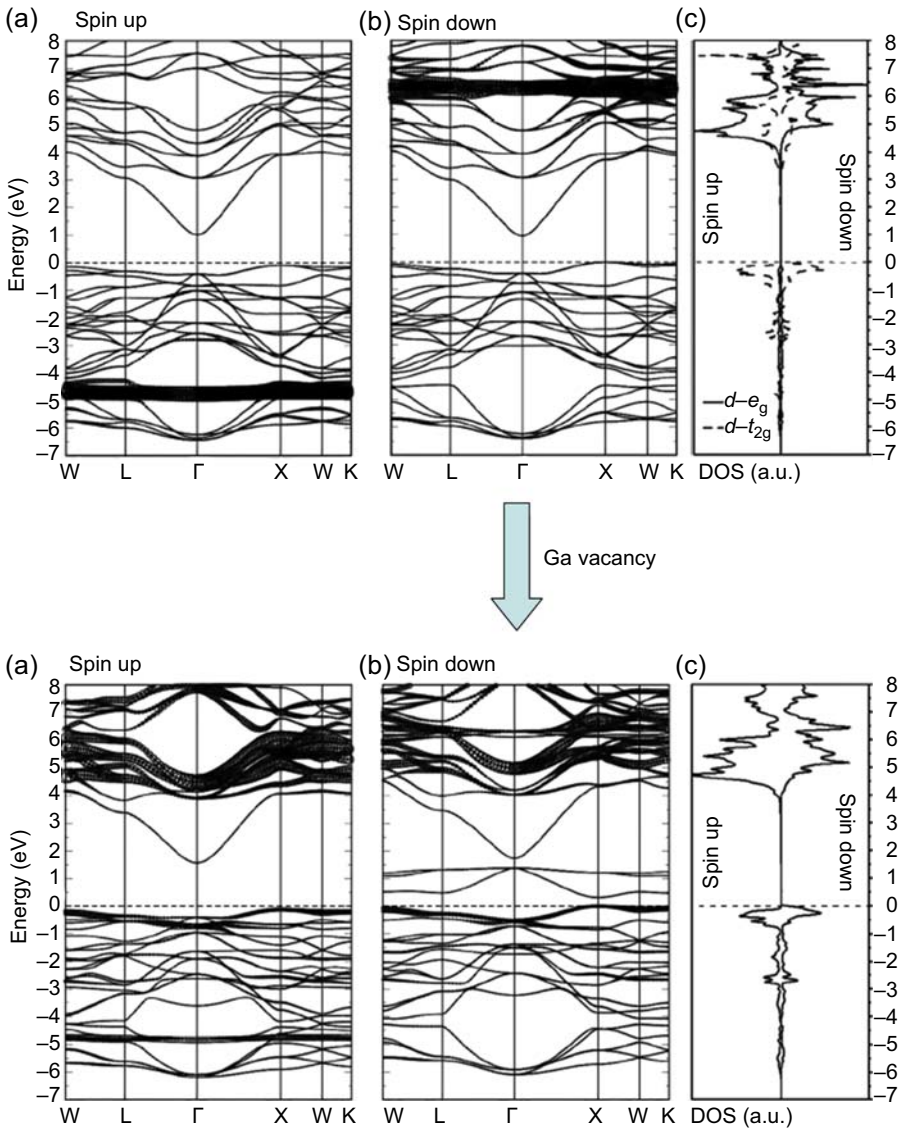


**Figure 10.7** Band structure for (a) spin up, (b) spin down, and (c)  $d$ -orbital DOS for  $\text{Ga}_{1-x}\text{Gd}_x\text{N}$  in the FM configuration. Top (without Ga vacancy) and bottom (with Ga vacancy). From Gohda, Y., Oshiyama, A., 2008. Intrinsic ferromagnetism due to cation vacancies in Gd-doped GaN: first-principles calculations. *Physical Review B* 78.

Dalpian and Wei (2006) have performed ab initio band structure calculations that show that the ferromagnetic phase in  $\text{Ga}_{1-x}\text{Gd}_x\text{N}$  can be stabilized by introducing electrons, while the coupling between Gd atoms in the alloy is antiferromagnetic. To this end Si codoping has been carried out in  $\text{Ga}_{1-x}\text{Gd}_x\text{N}$  thin films grown on sapphire

substrates by RF-plasma-assisted MBE (growth temperature  $<300^{\circ}\text{C}$ ) on sapphire substrates (Zhou et al., 2008). Si-doped  $\text{Ga}_{1-x}\text{Gd}_x\text{N}$  ( $x = 8.9\%$ ) showed a larger magnetization at RT of about  $1046 \text{ emu/cm}^3$  as compared to  $137.27 \text{ emu/cm}^3$  for the undoped GaGdN. It is considered that carriers (electrons) originating from defects such as nitrogen vacancies stabilize ferromagnetism in  $\text{Ga}_{1-x}\text{Gd}_x\text{N}$ , and Si codoping increases electron density, thereby supporting the theory of carrier-induced ferromagnetism.

We have previously studied the effects of interstitial oxygen on the ferromagnetism in Gd-doped GaN system via first-principle calculations, including both total energy and band structure calculation. In particular, the formation energies of different interstitial O atomic configurations in  $\text{Ga}_{1-x}\text{Gd}_x\text{N}$ , the resulting ferromagnetism, and its stability in n-type  $\text{Ga}_{1-x}\text{Gd}_x\text{N}$  have been studied. It was found that splitting interstitial sites O was a likely candidate for defect-induced magnetism in n-type  $\text{Ga}_{1-x}\text{Gd}_x\text{N}$  systems. Through  $p-d$  hybridization, Gd spin polarization could magnetize  $p$  state of interstitial O and in turn this hybridization renders a ferromagnetic coupling state among all Gd dopant, and a  $T_C$  above RT. It is suggested that both the  $5d$  and  $4f$  orbitals of Gd take part in the coupling to O  $2p$  orbitals. Furthermore, based on the results of formation energy of different interstitial O atomic configurations, it was found that the split-interstitial O, which could support ferromagnetism, was not the most stable site energetically. It is thought that this could be the reason why many previous experimental observations of magnetic behaviors have been contradictory.

Theoretical studies by Gohda et al. suggest that the  $5d$  electrons participate in nitrogen bonding and do not contribute to the magnetic moment. Their findings reveal that Gd incorporation causes Ga vacancies and the formation of defect complexes between Ga and Gd atoms are energetically favorable and result in ferromagnetic interactions (Fig. 10.7) (Gohda and Oshiyama, 2008). In the absence of  $V_{\text{Ga}}$ , the magnetic moment comes from the  $4f$  electrons ( $7 \mu_B$ ), and for each  $V_{\text{Ga}}$  the magnetic moment increases monotonically by  $3 \mu_B$ . Overall, this report suggests that the large magnetism observed is due to  $V_{\text{Ga}}$  that introduce holes above the VBM and implies that holes are responsible for the large magnetization.

It must be pointed out that many theoretical models reported have been developed to explain the experimental observation of the large magnetic moment of  $4000 \mu_B/\text{Gd}$  ion in the  $\text{Ga}_{1-x}\text{Gd}_x\text{N}$  films grown by Dhar et al. (2005a, p. 4). Recent theoretical predictions point to the fact that in wurtzite GaN holes result in greater exchange interactions and larger magnetization strengths as compared to electrons, but this has yet to be demonstrated experimentally (Liu et al., 2008; Gohda and Oshiyama, 2008).

Local spin density calculations have been performed by van Schilfgaarde and Mryasov (2001, pp. 233205-1) for 1–5% TM doping in III-V semiconductors. Their calculations show that the TM atoms form deep levels in the host semiconductor. Furthermore, their calculations show that there is a strong driving force that favors the clustering of the TM atoms and that whether this clustering actually occurs is ultimately decided by the growth kinetics. The model considers magnetic interactions based on number of nearest neighbors and next nearest neighbors present and the distances between them. Exchange interaction calculations show that Cr and Mn clusters are ferromagnetic and that Fe clusters result in antiferromagnetic interactions.



Thus these interactions are a function of the  $d$ -band filling. Initially increasing the TM concentration will result in an increase in the number of TM pairs and thus an increase in  $T_C$ , however, at really high concentrations the TM pairs are no longer separated and the contribution per pair starts to decrease resulting in a decrease in  $T_C$ . First-principle calculations by [Das et al. \(2006\)](#) show that TM cluster around N atoms and the TM–N interaction is AFM, while the TM–TM interaction is FM. Thus the ferromagnetic interaction in DMS is an indirect exchange mechanism mediated by N atoms. It has been suggested that the high  $T_C$  observed experimentally is due to the presence of these ferromagnetic clusters.

Furthermore, recent theoretical models by [Dietl \(2008\)](#) suggest that spinodal decomposition occurs in DMS and is responsible for the varying values of  $T_C$  reported for TM-doped GaN. Spinodal decomposition occurs when the TM doping concentration exceeds the solubility of the ion. The film then consists of regions of high and low TM concentrations, which results in magnetic nanocrystals being embedded in the semiconductor. As mentioned in the previous section, there is a strong driving force for the TM ions to cluster. The energy gained by bringing two Cr atoms together in GaN is 350 meV and for two Mn atoms is 300 meV. Spinodal decomposition does not necessarily result in a crystallographic phase and so can be hard to detect by traditional methods. These clusters may be ferromagnetic, ferrimagnetic, or antiferromagnetic. Furthermore, at this point there is no model to predict whether these clusters should be metal or insulators. However, due to the large TM concentration in the clusters, they tend to have high ordering temperatures. As mentioned earlier, the TM  $d$ -shells reside in the bandgap in the nitrides. This property has been utilized to develop semiinsulating materials as these midgap levels can trap carriers arising from impurities and defects in the materials. This trapping of carriers by the TM alters their charge state and impacts their Coulombic interactions. In materials with small carrier concentrations these interactions are not screened and so Coulombic interactions can overcompensate the lowering of the free energy arising from the nearest-neighbor bonding ([Dietl and Ohno, 2006](#)). Thus codoping of DMS with shallow acceptors or donors could provide an avenue for reducing or enhancing the TM aggregation. Furthermore, antisurfactants can be used to enhance the aggregation of TM ions if desired. Similarly, *ab initio* electronic structure calculations by the Korringa–Kohn–Rostoker coherent potential approximations (KKR-CPA) method within the local-density approximation by [Katayama-Yoshida et al. \(2007\)](#) have attributed the high  $T_C$  observed in nitrides to spinodal decomposition. For 30% Cr doping, a  $T_C$  of 100 K is formed due to a percolation network, while for 5% Cr doping a high  $T_C$  of 700 K occurs due to a 3D *Dairiseki* phase (clusters) caused by spinodal decomposition.

There are several theoretical models and exchange mechanism proposed for the ferromagnetism in DMS, with most of these models presenting conflicting arguments. These models are often revised or proven unlikely based on experimental observations. Pinning down which magnetic mechanism produces a particular experimental result is very challenging. Thorough growth and characterization studies are needed to obtain the real picture.

### 10.3 MOCVD growth of $\text{Ga}_{1-x}\text{TM}_x\text{N}$ and $\text{Ga}_{1-x}\text{RE}_x\text{N}$

There has been great confusion regarding the nature of ferromagnetism in the nitrides. This can be partly attributed to the different growth techniques used, which results in material of different quality with different structural and electronic defects within the material. MOCVD is the growth technique normally applied to achieve high quality GaN. TM doping of GaN by MOCVD has been carried out by MOCVD using a commercial rotating disk reactor with a short vertical jar configuration. The reactor has a specially modified flow flange injection system with dual injector blocks to minimize pre-reactions of the nitrogen and TM/RE precursors in the transport phase.  $\text{Ga}_{1-x}\text{Mn}_x\text{N}$  films (0.5–1  $\mu\text{m}$  thick) with Mn concentration up to  $\sim 2\%$  were grown on top of a 2  $\mu\text{m}$  GaN buffer layer, which is grown in turn on 2" sapphire (0001) substrates (Kane et al., 2005a). In this study, ammonia, trimethyl gallium (TMGa), bis-cyclopentadienyl manganese, bis-cyclopentadienyl magnesium, and silane ( $\text{SiH}_4$ ) were used as the nitrogen, gallium, manganese, p- and n-dopant sources, respectively.

Presented next are the material characterization results for these MOCVD-grown  $\text{Ga}_{1-x}\text{Mn}_x\text{N}$  films. The GaN:Gd films, typically 500 nm thick, were grown on 2  $\mu\text{m}$  thick GaN templates (GaN/sapphire). The gadolinium sources were Tris(2,2,6,6-tetramethyl-3,5-heptanedionato) gadolinium ((TMHD)<sub>3</sub>Gd), and Tris(cyclopentadienyl)gadolinium ( $\text{Cp}_3\text{Gd}$ ). The key difference between these sources is that the organic ligand in TMHD<sub>3</sub>Gd contains oxygen, while the ligand in  $\text{Cp}_3\text{Gd}$  does not. In addition, films with n-type (Si) and p-type (Mg) codoping were also grown and standard p-GaN activation steps were applied to p- $\text{Ga}_{1-x}\text{Gd}_x\text{N}$ . The in situ reflectivity data for  $\text{Ga}_{1-x}\text{TM}_x\text{N}$  thin films are shown in Fig. 10.8. It can be seen that fairly consistent oscillations were obtained indicating no significant material quality deterioration or surface roughening. Silane and Mg doping of these optimized  $\text{Ga}_{1-x}\text{TM}_x\text{N}$  films were also carried out to determine the effect of n- and p-dopants on this material system. The next section presents a detailed analysis of the material properties of the films grown.

Several growth techniques have been developed with the aim of obtaining an RT ferromagnetic semiconductor. Presented next is a synopsis of the experimental results obtained for  $\text{Ga}_{1-x}\text{TM}(\text{RE})_x\text{N}$ .

Most of the GaN growth studies have been focused on Mn, as it has the highest number of unpaired spins when it is introduced into GaN. Various growth techniques such as ammonothermal growth (Zajac et al., 2001a), ion implantation (Theodoropoulou et al., 2001b), postgrowth diffusion (Reed et al., 2001), MBE (Bimberg et al., 1999; Overberg et al., 2001), and MOCVD (Kane et al., 2005a) have been applied with the objective to develop single-phase  $\text{Ga}_{1-x}\text{Mn}_x\text{N}$  that exhibits ferromagnetism at RT.

An ammonothermal method has been used to produce microcrystalline  $\text{Ga}_{1-x}\text{Mn}_x\text{N}$  samples with Mn content up to  $x = 0.005$  (Zajac et al., 2001a). This technique resulted in the presence of nonuniform crystallites, and X-ray diffraction (XRD) showed the characteristic diffraction lines for hexagonal GaN phase mixed with a small



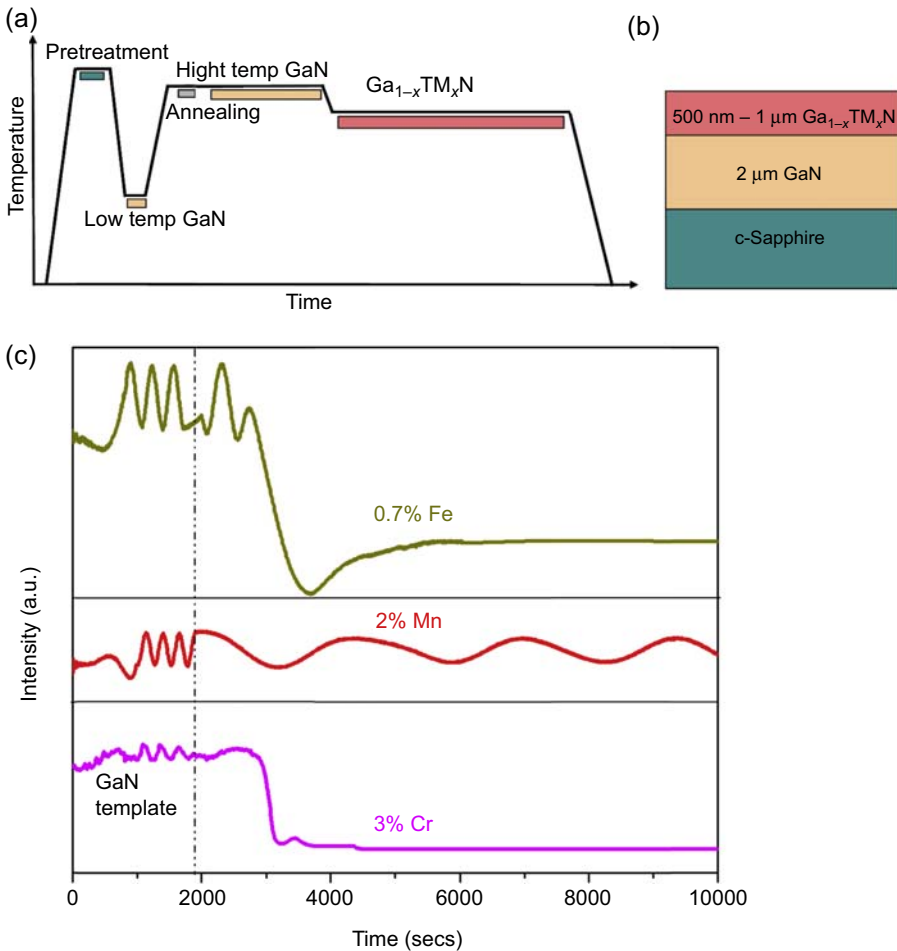


**Figure 10.8** (a) Growth profile for  $\text{Ga}_{1-x}\text{TM}_x\text{N}$  on sapphire, (b) schematic of the final structure grown, (c) in situ optical reflectometry curve for  $\text{Ga}_{1-x}\text{TM}_x\text{N}$  (after dotted line) grown on GaN templates (before dotted line).

contribution from a  $\text{Mn}_3\text{N}_2$  phase. Raman spectra exhibited peaks that could be associated with Mn-induced lattice disorder. Electron spin resonance and magnetization measurements showed that the material was paramagnetic.

$\text{Ga}_{1-x}\text{Mn}_x\text{N}$  films were later produced by ion implantation of MOCVD-grown p-GaN films with high doses ( $1 \times 10^{15} - 5 \times 10^{16} \text{ cm}^{-2}$ ) to produce Mn concentrations from 0.1% to 5% of  $\text{Mn}^+$  ions at  $\sim 350^\circ\text{C}$  and annealed at  $700-1000^\circ\text{C}$  (Theodoropoulou et al., 2001b). At low doses ( $<3\%$ ), the  $\text{Ga}_{1-x}\text{Mn}_x\text{N}$  are paramagnetic with a large number of lattice defects. At high doses ( $>3\%$ ) platelet-like structures of  $\text{Ga}_{1-x}\text{Mn}_x\text{N}$  are formed, which have been attributed to the observed ferromagnetic behavior in the samples up to  $\sim 250 \text{ K}$ .

$\text{Ga}_{1-x}\text{Mn}_x\text{N}$  has also been produced by postgrowth doping of GaN using solid state diffusion of Mn (Reed et al., 2001). This resulted in samples that had a background concentration of 1–2% Mn away from the surface where diffusion took place. Mn-doped GaN with  $T_C$  in the range of 228–370 K were obtained and structural characterization by XRD suggested that the ferromagnetic properties are not a result of secondary magnetic phases. The reported Bohr magneton number for diffusion grown  $\text{Ga}_{1-x}\text{Mn}_x\text{N}$  can exceed  $2 \mu_B/\text{Mn}$ , which is difficult to reconcile through the undetectable clustering description. These Mn-doped GaN films have ferromagnetic behavior with hysteresis curves showing a coercivity of 100–500 Oe. All these techniques produced highly nonuniform material that was difficult to measure because the data was always some average of the properties of the crystallites and the layer.

Given the low solubility limit of the TMs in GaN matrix, nonequilibrium growth techniques such as MBE and MOCVD are preferred. These techniques result in a more uniform layer and allow for easier integration of these materials into devices. A number of groups have reported the growth of  $\text{Ga}_{1-x}\text{Mn}_x\text{N}$  using various modifications of MBE with different levels of success.

One of the first reports of the thin film growth of  $\text{Ga}_{1-x}\text{Mn}_x\text{N}$  was by Overberg et al. (2001), who used gas source MBE with an N-plasma source. Auger electron spectroscopy showed that 7% Mn could be incorporated in a single phase as determined by XRD. The ferromagnetic  $\text{Ga}_{1-x}\text{Mn}_x\text{N}$  had a  $T_C$  between 10 and 25 K. A similar  $T_C$  has been reported for plasma-assisted MBE growth study (Sarianniidou et al., 2006). A low temperature (400–650°C) MBE study with 2% Mn incorporation resulted in paramagnetic films that were highly resistive (Soo et al., 2001). The most successful report of the MBE growth of  $\text{Ga}_{1-x}\text{Mn}_x\text{N}$  was by Sonoda et al. (2002), using ammonia ( $\text{NH}_3$ ). They claim to have produced wurtzite  $\text{Ga}_{1-x}\text{Mn}_x\text{N}$  films showing ferromagnetic behavior well above RT. They estimated the  $T_C$  of  $\text{Ga}_{1-x}\text{Mn}_x\text{N}$  to be 940 K, which far exceeds that measured by other groups or suggested by theoretical models.

The as-grown films  $\text{Ga}_{1-x}\text{Mn}_x\text{N}$  were specular in nature and had a reddish hue with increasing thickness and Mn incorporation. Under nonoptimal growth conditions hexagonal GaN growth temperature defects are visible via optical microscopy. Secondary ion mass spectrometry (SIMS) verified the uniform incorporation of manganese within the layers. High resolution XRD (HRXRD) scans did not show the presence of any secondary phases. Upon annealing at temperatures as low as 700°C, other phases do appear in the  $2\theta-\omega$  scans, which point to the (110) reflections of the  $\text{Mn}_3\text{GaN}$  phase. This is consistent with the report of  $\text{Mn}_3\text{GaN}$  phases as a key component in secondary phase segregation in heavily doped samples. This phase has been observed previously, though the peak position is quite close to a GaMn intermetallic phase reported to be present in overdoped MBE-grown material (Thaler et al., 2004). The  $\text{Mn}_6\text{N}_{2.58}$  and  $\text{Mn}_3\text{N}_2$  phases were not observed via XRD in the annealed MOCVD-grown samples as has been previously reported in implanted samples, though this may simply be due to the relatively small local concentrations of Mn. Note that due to the anticipated small size of the precipitates and low volume fraction used in the growth, it would be very difficult to observe precipitates through standard structural characterization techniques. High resolution cross-sectional transmission electron microscopy (TEM) also shows no indication

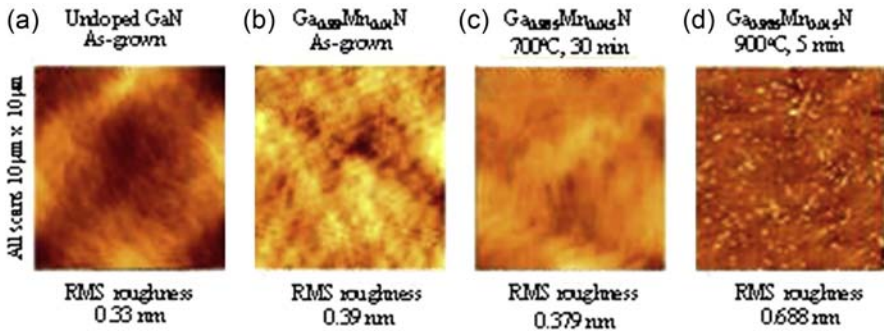


**Figure 10.9** Atomic force microscopy images of, from left to right, undoped GaN, as-grown  $\text{Ga}_{1-x}\text{Mn}_x\text{N}$  ( $x = 0.01$ ),  $\text{Ga}_{1-x}\text{Mn}_x\text{N}$  ( $x = 0.015$ ) after 30 min anneal at  $700^\circ\text{C}$ , and  $\text{Ga}_{1-x}\text{Mn}_x\text{N}$  ( $x = 0.015$ ) after 5 min anneal at  $900^\circ\text{C}$ . RMS roughnesses are, from left to right, 0.33, 0.40, 0.37, and 0.68 nm (Kane et al., 2006).

of secondary phases in the as-grown samples at low doping concentrations, though stacking faults are visible in Mn-containing buffer layers.

Surface morphology by AFM reveals clear step flow growth patterns for GaMnN films grown at low temperatures and low growth rates (Fig. 10.9). The root mean square (RMS) roughness of the Mn incorporated film is similar to that of the underlying GaN template layer ( $3.8 \text{ \AA}$  vs  $3.4 \text{ \AA}$ ). There is little change in the morphology of the layer with low temperature annealing ( $700^\circ\text{C}$ ), however there is a significant difference in the AFM images with annealing at higher temperatures. The AFM image of the uncapped sample annealed at  $900^\circ\text{C}$  shows clear areas of what is likely second phase precipitate on the surface (Fig. 10.9). XRD scans can attribute this phase to either MnN or  $\text{Mn}_3\text{GaN}$  type phases. On the other hand, the annealed capped samples show no change in surface morphology even at the elevated temperature. This suggests that one mechanism for the decay of the thermodynamically unstable  $\text{Ga}_{1-x}\text{Mn}_x\text{N}$  compound is nitrogen desorption and phase rearrangement of the surface at the  $\text{Ga}_{1-x}\text{Mn}_x\text{N}$ -to-atmosphere interface in the absence of a reactive nitrogen environment that is present during MBE or MOCVD growth.

Micro-Raman spectra were recorded at RT in a back scattering geometry for GaN epilayers varying in Mn concentration from 0.0% to 1.5%, as shown in Fig. 10.10. Most prominent in all these spectra are the  $E_2(\text{high})$  and the  $A_1(\text{LO})$  Raman modes that were detected at  $567 \text{ cm}^{-1}$  and  $734 \text{ cm}^{-1}$ , respectively. These values are in good agreement with those measured for relaxed GaN revealing that no additional strain was introduced even though a high concentration of Mn ions ( $\sim 10^{20} \text{ cm}^{-3}$ ) was incorporated in the GaN. A high carrier concentration (above  $10^{18} \text{ cm}^{-3}$ ) was ruled out since no broadening of the  $A_1(\text{LO})$  mode and no local phonon-plasmon modes were detected. The appearance of a mode at  $\sim 669 \text{ cm}^{-1}$  and a shoulder at  $664 \text{ cm}^{-1}$  were found strongly correlated to the Mn concentration. The intensity of this mode, but not the line width, increased with increasing Mn concentration. In this spectral range, a mode was found in GaN microcrystals at  $670 \text{ cm}^{-1}$ , and it was assigned to a disorder-activated vibrational mode (Gebicki et al., 2000; Limmer et al., 1998).

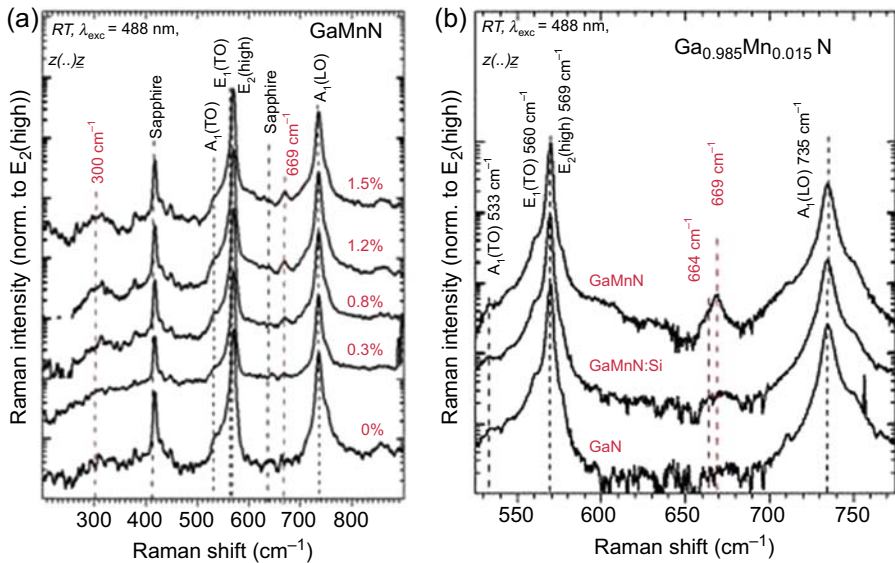


**Figure 10.10** Raman spectra of MOCVD-grown GaMnN layers. The right hand shows the sensitivity of the vacancy-induced local vibrational mode at  $669 \text{ cm}^{-1}$  on codoping in  $\text{Ga}_{0.985}\text{Mn}_{0.015}\text{N}$ .

From Kane, M.H., Strassburg, M., Asghar, A., Fenwick, W.E., Senawiratne, J., Song, Q., Summers, C.J., Zhang, Z.J., Dietz, N., Ferguson, I.T., 2006. Alloying, co-doping, and annealing effects on the magnetic and optical properties of MOCVD-grown  $\text{Ga}_{1-x}\text{Mn}_x\text{N}$ . *Materials Science and Engineering: B* 126, 230.

Whereas in a more general study [Limmer et al. \(1998\)](#) reported on such a mode caused by vacancies in ion-implanted GaN epilayers. In a more recent work based on MBE-grown  $\text{Ga}_{1-x}\text{Mn}_x\text{N}$  ([Harima, 2004](#)), this line was attributed to a local vibrational mode of the GaN host lattice caused by a vacancy. The data obtained from MOCVD-grown GaN and presented in this work appear to support the conclusions drawn by [Harima \(2004\)](#). An additional broadband around  $300 \text{ cm}^{-1}$  ([Fig. 10.10](#)) that is disorder activated ([Limmer et al., 1998](#); [Gebicki et al., 2000](#); [Zajac et al., 2001a](#)) did not show a systematic dependence on the Mn concentration but correlated more strongly with the crystalline quality determined by XRD, electron paramagnetic resonance (EPR), and AFM ([Strassburg et al., 2005](#); [Kane et al., 2005a](#)). In addition, the lower intensity of the  $669 \text{ cm}^{-1}$  mode compared to that reported elsewhere could be explained as a consequence of the MOCVD growth ([Harima, 2004](#)). Therefore, a GaN:Mn, Si sample was grown to study the role of vacancies. The Mn concentration was chosen as 1.5% and the nominal Si concentration was  $\sim 10^{20} \text{ cm}^{-3}$ . The incorporation of Si as a donor on Ga sites is known to reduce the amount of nitrogen vacancies in GaN ([Van de Walle And Neugebauer, 2004](#)). Raman spectra of the undoped and Si-doped  $\text{Ga}_{0.985}\text{Mn}_{0.015}\text{N}$  epilayers are shown in [Fig. 10.10](#). The intensity of the  $669 \text{ cm}^{-1}$  mode increases with increasing Mn concentration, though the line width does not change. Also, it is obvious that upon Si codoping the intensity of the

$669\text{ cm}^{-1}$  mode is strongly reduced. Moreover, the lack of plasmon–phonon coupled modes indicates that Mn was incorporated as an acceptor leading to the trapping of the electrons provided by the Si donors.

Local vibrational modes of Mn ions on Ga site based on the GaN  $E_2(\text{high})$  LO mode with respect to the difference in the reduced masses might be expected around  $580\text{ cm}^{-1}$ . However, no such mode was found in the  $\text{Ga}_{1-x}\text{Mn}_x\text{N}$  epilayers, and no phase separation was detected (Kane et al., 2005b). Unambiguous detection was prevented by the dominance of the GaN  $E_2(\text{high})$  LO mode and a mode near  $576\text{ cm}^{-1}$  that was also seen in the bare sapphire substrate.

van der Pauw Hall measurements were used to analyze the carrier type and concentration in these materials. The measured carrier type in all of these samples is n-type, similar to what has been reported in literature (Overberg et al., 2001). However, it is likely that this is merely a function of the template layer used to grow the samples, especially in the samples without Si codoping. To achieve high structural quality for the  $\text{Ga}_{1-x}\text{Mn}_x\text{N}$  layer, these epilayers were grown on  $1\text{ }\mu\text{m}$  thick GaN template layers; for the Si codoped samples, these layers were doped n-type. The measured Hall concentration of the as-grown, unintentionally doped  $\text{Ga}_{1-x}\text{Mn}_x\text{N}$  films was around  $n = 5 \times 10^{16}\text{ cm}^{-3}$ , which is very close to the measured background carrier concentration of the unintentionally doped template layer. Similarly increasing the Si doping within the  $\text{Ga}_{1-x}\text{Mn}_x\text{N}$  layer does not result in an increase in measured carrier concentration from  $n = 8 \times 10^{17}\text{ cm}^{-3}$ , which is similar to the measured carrier concentration of the n-type template layer on which these films were grown. Thus, all the measured n-type behavior is due to parallel conduction through the virtual template, and the observed n-type character that is often reported in these systems may be solely due to the template (Fig. 10.11). In order to clarify this point, layers were grown from

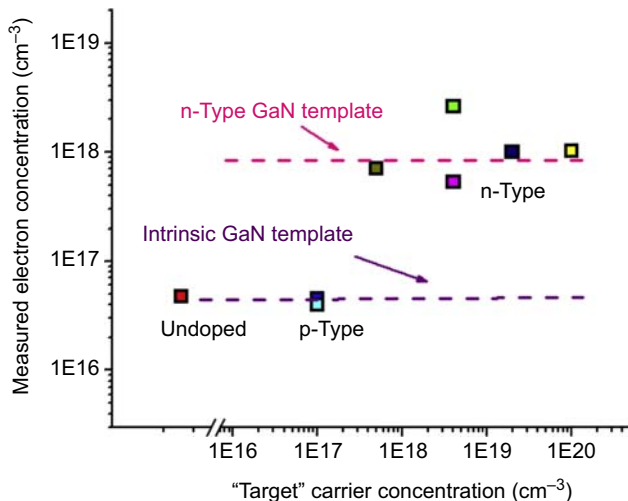


**Figure 10.11** van der Pauw Hall effect data for Mg- and Si-codoped  $\text{Ga}_{1-x}\text{Mn}_x\text{N}$ . Note that in all cases, the measured carrier concentrations fall closely along the line for the template layer doping concentrations.

the substrate with Mn in the virtual template layers. For these samples, the resistivity was too high to measure and the contact resistance increased by several orders of magnitude, consistent with predictions and other observation of Mn as a deep impurity level. It should be noted that the layers grown on the Mn-containing template have a reduced quality and do not display strong ferromagnetism even though it exhibits a strong reddish tint indicative of  $\text{Mn}^{2+}$  incorporation.

Superconducting quantum interference device (SQUID) magnetometry was performed to determine the overall magnetic behavior of the MOCVD-grown  $\text{Ga}_{1-x}\text{Mn}_x\text{N}$  films. Ferromagnetic hysteresis was recorded in the as-grown  $\text{Ga}_{1-x}\text{Mn}_x\text{N}$  films at 300 K (Fig. 10.12). There is little deviation between the magnetization data obtained at RT and 5 K, indicating the hysteresis is due to a phase with a high  $T_C$ . To check whether the magnetic behavior is due to second phases or clusters, the concentration per magnetic element was calculated. Assuming a uniform growth rate and based on the Mn concentration as measured by SIMS across the wafer, the measured saturation magnetization corresponds to a contribution of  $2.4 \mu_B/\text{Mn}$  for the 1% doped sample and  $1.2 \mu_B/\text{Mn}$  for the 1.5% doped sample. This compares favorably with the predicted contribution based on first-principle band structure calculations of  $4 \mu_B/\text{Mn}$  when the Fermi level is located in the center of the Mn impurity band. This is away from the predicted magnetic moment per  $\text{Mn}_4\text{N}$  cluster, which is  $17 \mu_B$  (Rao and Jena, 2002).

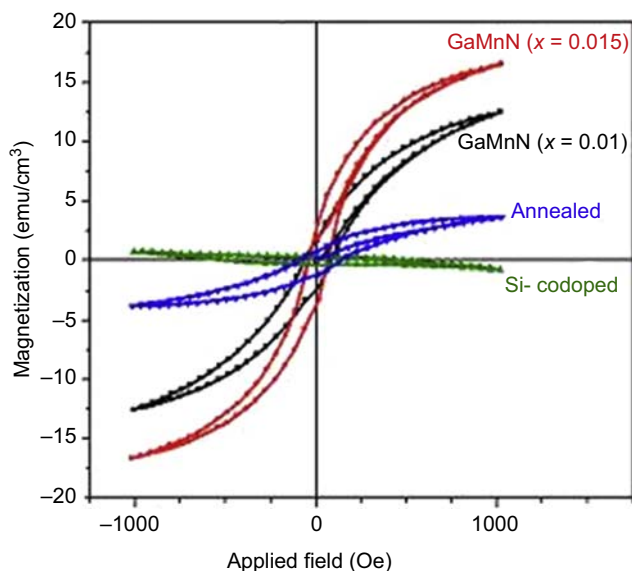


**Figure 10.12** Room temperature SQUID magnetometry measurements from various  $\text{Ga}_{1-x}\text{Mn}_x\text{N}$  films with different doping levels and processing conditions. Note the decrease in magnetization with Si-codoping or annealing of the samples.

From Kane, M.H., Strassburg, M., Asghar, A., Fenwick, W.E., Senawiratne, J., Song, Q., Summers, C.J., Zhang, Z.J., Dietz, N., Ferguson, I.T., 2006. Alloying, co-doping, and annealing effects on the magnetic and optical properties of MOCVD-grown  $\text{Ga}_{1-x}\text{Mn}_x\text{N}$ . *Materials Science and Engineering: B* 126, 230.

The strength of this magnetization depends on the thickness of the sample and film growth rate, with stronger magnetization in general being exhibited for films with slower growth rates. As seen in Fig. 10.12, upon annealing, the magnetization of the same sample drops precipitously. There is still some area remaining in the hysteresis loop observed in this sample, indicating that the ferromagnetic phase is not completely lost or there may be a small contribution from local areas of the alloy that were unaffected by the anneal or that consist of ferromagnetic second phases. A similar behavior for the magnetism is seen in the Si-doped  $\text{Ga}_{1-x}\text{Mn}_x\text{N}$  (Fig. 10.12). The magnetic moment decreases with increasing Si doping concentration and is nearly destroyed at Si concentrations greater than  $10^{19}/\text{cm}^3$ .

The large decrease in the magnetization with codoping and annealing suggests that there may be a common origin to the deterioration of the magnetic properties of  $\text{Ga}_{1-x}\text{Mn}_x\text{N}$ . EPR in the X band was used to study the incorporation and the electronic structure of the manganese ions in GaN. The typical spectra of isolated  $\text{Mn}^{2+}$  were observed in the X band, but only in annealed and Si codoped  $\text{Ga}_{1-x}\text{Mn}_x\text{N}$ .

Optical transmission measurements reveal that the incorporation of Mn into GaN layers during MOCVD growth leads to a broad absorption band, a spectrally diffuse line centered around 1.5 eV (full width half maximum (FWHM) of 150 meV), as shown in Fig. 10.13. The FWHM and intensity increased with an increase in the Mn concentration. The observed absorption band is assigned to the  $\text{Mn}^{3+}$  transitions

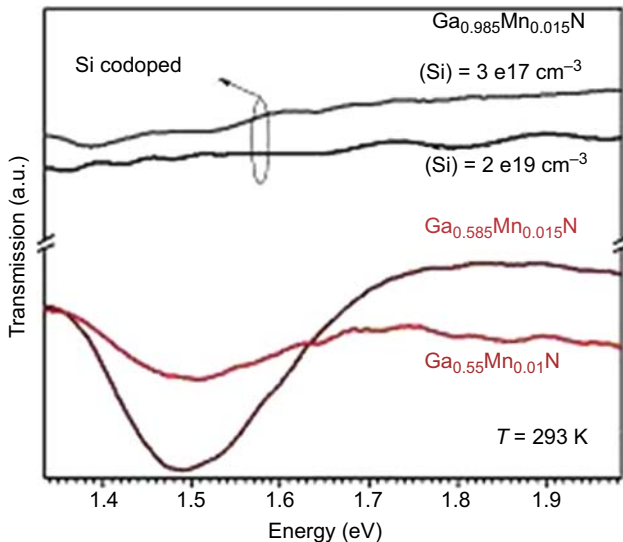


**Figure 10.13** RT optical absorption spectra from  $\text{Ga}_{1-x}\text{Mn}_x\text{N}$  with and without Si-codoping. Note the  $\text{Mn}^{3+}$  internal transition that disappears with codoping.

From Strassburg, M., Senawirante, J., Hums, C., Dietz, N., Kane, M.H., Asghar, A., Payne, A.M., Ferguson, I.T., Summers, C.J., Habocek, U., Hoffman, A., Azamat, D., Gelhoff, W., 2005. Optical and structural investigations on Mn-ion states in MOCVD-grown  $\text{Ga}_{1-x}\text{Mn}_x\text{N}$ . MRS Proceedings 831, E9.5.1.



from the E state to the partially filled  $T_2$  levels of the 5D state (Sato et al., 2003a). The absence of the absorption band around 1.5 eV in the  $\text{Ga}_{1-x}\text{Mn}_x\text{N}$  layer codoped with silicon indicates sensitivity of the E to  $T_2$  transitions to the position of the Fermi level. The Fermi level is shifted toward the conduction band because electrons are present at deep defects. No other absorption features were detected further in the infrared spectral range (down to 0.5 eV). This suggests that the location of the Fermi level in the investigated samples in the broad absorption band is around 1.8 eV above the top of the valence band, and even closer to the conduction band than for the Si codoped sample (Kane et al., 2006).

Low temperature optical transmission measurements reveal a distinct peak near 1.41 eV, which is characterized as the zero-phonon line of an internal forbidden  $d-d$  transition in  $\text{Mn}^{3+}$  ( $d_4$ ) (Graf et al., 2002). The sharpness of this peak is inconsistent with the broad impurity band-like behavior. In addition to the sharp absorption zero-phonon line, there are multiple phonon replicas at high energies; these have also been reported in MBE-grown  $\text{Ga}_{1-x}\text{Mn}_x\text{N}$ . The phonon replicas superimposed with Fabry-Perot oscillations from reflections of the film/substrate and film/air interfaces are likely responsible for the observed band-like behavior at high temperature (Yamamoto et al., 2005).

PL studies were performed in the UV and visible spectral range in order to further understand the Mn-induced midgap states of MOCVD-grown  $\text{Ga}_{1-x}\text{Mn}_x\text{N}$  epilayers. In addition to GaN peak, a blue emission band was found to dominate the PL spectrum of the samples with a Mn concentration  $>0.5\%$  resulting in two distinct peaks at 3.0 and 2.8 eV (Kane et al., 2005a). These bands are also known to appear in GaN upon compensation of acceptors by doping induced defect states as well as by the incorporation of hydrogen on interstitial sites.

Blue band emission was observed in MBE-grown  $\text{Ga}_{1-x}\text{Mn}_x\text{N}$  and ion-implanted material, and the appearance of these bands (actually a broad emission from 2.7 to 3.1 eV) was assigned to transitions from conduction-band electrons to Mn-related states and from shallow donor (eg, N vacancy) to Mn acceptor states. In comparison, a pronounced yellow band attributed to intrinsic gallium defects was observed in the lightly Mn-doped  $\text{Ga}_{1-x}\text{Mn}_x\text{N}$  samples ( $<0.5\%$ ), annealed samples, and the samples codoped with Si with almost no blue band emission. In the first case, the behavior is assigned to the lower amount of Mn ions available to substitute on lattice sites, reducing the amount of Ga vacancies. In the latter two cases, intrinsic and extrinsic shallow donor states are introduced, leading to a compensation mechanism of the  $\text{Mn}^{3+}$  acceptors. An even stronger compensation of Mn acceptors is seen for Si codoping.

To date there is great debate regarding the mechanism associated with the ferromagnetism observed in  $\text{Ga}_{1-x}\text{Mn}_x\text{N}$ . Experimental results have shown Mn is a deep acceptor in GaN and results in a semiinsulating material with localized carriers on the Mn site (Berciu and Bhatt, 2001). Despite this, ferromagnetism is still observed, contradicting the hypothesis made by the mean field Zener model. Although the double exchange mechanism does appear promising, the conflicting reports of a wide range of  $T_C$  and the presence of the sharp absorption zero-phonon line at low temperature pose a challenge to this theory. Recently, there has been a shift among



theoreticians who believe that clustering may be responsible for this observed ferromagnetism. Nanoscale clusters have been observed in some samples by TEM (Dhar et al., 2003), though only at extremely high doping levels ( $\sim 13\%$ ) and it has not been shown conclusively that this behavior will be the same at lower concentrations.

To understand the mechanism further, this chapter will proceed to investigate  $\text{Ga}_{1-x}\text{Fe}_x\text{N}$ . The investigation of various TMs enables the concurrent variation of a number of other parameters of interest in the various materials systems. In particular, the location of the acceptor level in III-V semiconductors is an important parameter, as it influences the interaction of the magnetic center and band carriers (electrons or holes) in the carrier-mediated model or polaronic radii and percolation threshold in a bound magnetic polaron model. The degenerate doping levels needed in these materials can also induce the formation of impurity bands and act as a pinning level for the Fermi energy. The location of this pinning level will also influence the materials' properties and growth behavior; in particular, the formation and nature of defects ( $V_n$  or  $\text{Ga}_i$ ) in GaN are sensitive to the position of the Fermi level within the bandgap (Van de Walle And Neugebauer, 2004). Furthermore, this method also enables verification of whether or not the magnetization is solely due to incommensurate impurities in a heterogeneous system as the relative difference in the precipitates with TM doping should point to the physical nature of these precipitates. For example,  $\text{Mn}_4\text{N}$  is ferromagnetic with a  $T_C$  of 743 K, whereas  $\text{Fe}_3\text{N}$  has a  $T_C$  of 535 K.

### 10.3.1 Experimental results for $\text{Ga}_{1-x}\text{Fe}_x\text{N}$

The use of MOCVD for the incorporation of Fe has actually been of interest for a longer period than Mn. Specifically, the use of iron in semiinsulating MOCVD-grown GaN templates for high electron mobility transistors was reported as early as 2002 (Heikman et al., 2002). Moreover, the use of MOCVD as the growth technique has a number of challenges, including memory effects and selection of suitable precursors (Heikman et al., 2002).

MOCVD-grown p-GaN ( $3 \times 10^{17} \text{ cm}^{-3}$ ) has been doped with 3% Fe by ion implantation and displayed hysteresis until 250 K with no evidence of secondary phases (Theodoropoulou et al., 2001a). A similar study showed a transition from overall paramagnetic behavior at 5% doping to RT ferromagnetic behavior at 10% doping of Fe into p-GaN by ion implantation (Shon et al., 2004). Hexagonal GaFeN microcrystals with 0.5% Fe molar concentration have been grown by the ammonothermal method. Magnetization measurements revealed the presence of both paramagnetic and ferromagnetic phases (Gosk et al., 2003). MBE have been used to dope GaN with Fe ( $10^{19} \text{ cm}^{-3}$ ) resulting in ferromagnetic properties up to 100 K. X-ray absorption fine structure data show that the Fe is substituting for Ga in GaN (Akinaga et al., 2000). X-ray absorption near edge structure spectra indicate that the observed magnetization is due to the change in Fe electronic state in response to the strong hybridization between Fe  $3d$  and N  $2p$  states (Ofuchi et al., 2001). Another MBE study with  $5 \times 10^{21} \text{ cm}^{-3}$  concentration in GaN shows superparamagnetic behavior that has been attributed to the formation of nanoscale Fe or FeN crystallites in the epilayer (Kuwabara et al., 2001). Recent efforts have focused on producing  $\text{Ga}_{1-x}\text{Fe}_x\text{N}$  at

lattice concentrations suitable for spintronics, and there have been reports of MOCVD grown material that exhibit RT ferromagnetism (Przybylinska et al., 2006, p. 222). It was determined that Fe has a 0.4% solubility in GaN. The ferromagnetic response in these films has been attributed to the presence of coherent nanocrystals (presumably Fe<sub>x</sub>N), which have been observed by TEM and energy dispersive X-ray spectroscopy (EDS) (Bonanni et al., 2007).

In order to obtain a better understanding of the properties of Ga<sub>1-x</sub>Fe<sub>x</sub>N and its performance as compared to Ga<sub>1-x</sub>Mn<sub>x</sub>N, this chapter next will discuss the results obtained by MOCVD-grown Ga<sub>1-x</sub>Fe<sub>x</sub>N (Kane et al., 2007).

We have performed MOCVD growth studies on Ga<sub>1-x</sub>Fe<sub>x</sub>N films on 2" sapphire substrates with bis-cyclopentadienyl iron (Cp<sub>2</sub>Fe) used as the Fe dopant (Kane et al., 2007). Magnetization studies resulted in a hysteresis curve at RT.

The Ga<sub>1-x</sub>Fe<sub>x</sub>N films obtained in our study were colorless, except when codoped with high levels of Si (>10<sup>19</sup> cm<sup>-3</sup>) the color of the Fe-thin films turns yellow. This coloring can be attributed to the absorptions due to the *d-d* transitions in substitutional divalent TM atoms. Similar to Ga<sub>1-x</sub>Mn<sub>x</sub>N, no secondary phases were observed in the HRXRD measurements. AFM measurements revealed step flow behavior for Ga<sub>0.999</sub>Fe<sub>0.001</sub>N films with an RMS of 0.4 nm. Increasing the concentration to 0.9% Fe doping resulted in degradation of the film quality with an increase in RMS to 28.4 nm. This degradation in film quality is observed in the reflectivity measurements during high Fe concentration growth when a sharp drop in intensity is observed.

Micro-Raman spectroscopy measurements were carried out between 525 cm<sup>-1</sup> and 750 cm<sup>-1</sup> for Ga<sub>1-x</sub>Fe<sub>x</sub>N (*x* = 0.7%). Similar to the results obtained for Ga<sub>1-x</sub>Mn<sub>x</sub>N, the most prominent features in the scans were the E<sub>2</sub>(high) and A<sub>1</sub>(LO) modes at 569 cm<sup>-1</sup> and 735 cm<sup>-1</sup>, respectively. This indicates that there is not a significant degradation in crystalline quality or strain induced with Fe doping.

Furthermore, no local phonon-plasmon coupled modes are seen in the Raman spectra near the E<sub>2</sub>(high) mode, which also points to a low carrier concentration. Similar to Ga<sub>1-x</sub>Mn<sub>x</sub>N scans, a mode is seen at 710 cm<sup>-1</sup>, which appears as a shoulder to the A<sub>1</sub>(LO). In addition to the allowed *c*-plane GaN Raman modes, in the Ga<sub>1-x</sub>Fe<sub>x</sub>N scans there appears an additional A<sub>1</sub>(TO) mode. The appearance of this mode is likely due to a relaxation of the Raman selection rules about the Fe-induced defects within the system and is consistent with the observed degradation in the structural ordering in the system (Kane et al., 2007).

Fe doping reduces the electronic concentration and results in semiinsulating GaN films. Hall measurements performed by Bonanni et al. (2007) suggest that at low Fe precursor flow rates the Hall concentration is lower than GaN, which has been attributed to the trapping of electron by Fe<sup>3+</sup> resulting in a conversion to Fe<sup>2+</sup>. Their work also shows that at high Fe concentrations (>10<sup>20</sup> cm<sup>-3</sup>), an increase in Hall concentration is observed along with a change in its temperature dependence. This has been attributed to the increase in oxygen donor density. It has also been suggested that in some cases Fe occupies the interstitial sites and Fe<sup>2+</sup> acts as a double donor.

The effects of Fe incorporation on the optical properties of GaN have also been investigated by PL. The major features in this scan are a near-band-edge luminescence

peak and a broad blue band luminescence peak centered at 2.8 eV. This peak at 2.8 eV is outside the range typically seen for intrinsic defects in GaN, which are usually located in the yellow region of the visible spectra. This is slightly different than previous results reported for Mn, where the most prominent feature is the blue emission band around 3.0 eV (Kane et al., 2005a). A transition from native defects (eg, a nitrogen vacancy) and TM-caused complexes is probably the origin of these emission bands. A finer structure near the band-edge spectra is also visible for these Fe-doped samples.

Optical measurements conducted at 20 K by Bonanni et al. reveal zero-phonon lines at 1.3 eV, which is attributed to the internal spin forbidden  $4T_1(G)-6A_1(S)$  transition. The intensity of this peak reduced with Si codoping and increased with Mg codoping. The increased electron concentration in GaN:Fe, Si as compared to GaN:Fe leads to a reduction of the carrier recombination rate at the  $Fe^{2+/3+}$  acceptor level (the opposite occurs with Mg codoping) (Bonanni et al., 2007).

We have conducted SQUID measurements to determine the ferromagnetic properties of MOCVD-grown GaFeN with 0.7% Fe doping. RT ferromagnetism is obtained for these films as shown in Fig. 10.14. Additionally, no change is observed in the magnetic signal with Si doping, unlike the case with  $Ga_{1-x}Mn_xN$ . In this case the free carrier density is too low for carrier-mediated exchange. Furthermore, the TM concentration is too low to support the double exchange mechanism. This suggests that the observed RT ferromagnetism must be attributed to another mechanism and possibly due to the presence of clusters as discussed later.

In addition to the GaN band-edge emission at 3.4 eV, the RT PL spectrum shows a broad blue band luminescence peak centered at 2.8 eV, which is likely to be due to the

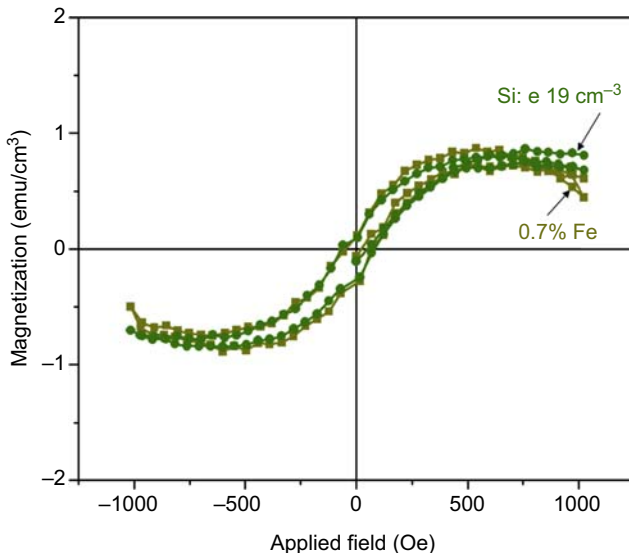


**Figure 10.14** RT magnetization results for as-grown and codoped  $Ga_{1-x}Fe_xN$ .

$\text{Fe}^{3+}/\text{Fe}^{2+}$  charge transfer level above the valence band (Malguth et al., 2006). This transition represents a hole bound to the  $\text{Fe}^{2+}$  ground state. The  $\text{Fe}^{2+}$  state is created either by optical excitation of  $\text{Fe}^{3+}$  or by the n-type carrier background of GaN that possibly converts the  $\text{Fe}^{3+}$  to  $\text{Fe}^{2+}$ , and thus both states exist in the semiconductor. Peaks are observed near the band-edge emission and probably arise from anisotropy caused by the structural degradation of the material. The transition at 2 eV has been observed in the optical transmission spectra for  $\text{Ga}_{1-x}\text{Fe}_x\text{N}$  films at temperatures of 2 K and is attributed to an internal  $\text{Fe}^{3+}$  transition between  ${}^4\text{T}_2(\text{G})$  and  ${}^6\text{A}_1\text{S}$ .

Low temperature optical measurements conducted on  $\text{Ga}_{1-x}\text{Fe}_x\text{N}$  grown by MOCVD (at 20 K) and high vapor phase epitaxy by other groups have shown the presence of zero-phonon lines at 1.299 eV, which are attributed to the internal, spin forbidden  ${}^4\text{T}_1(\text{G})\text{--}{}^6\text{A}_1(\text{S})$  transition. The intensity of this peak reduces with Si codoping and increases with Mg codoping. The increased electron concentration in GaN:Fe, Si as compared to GaN:Fe leads to a reduction of the carrier recombination rate at the  $\text{Fe}^{2+/3+}$  acceptor level and causes the drop in emission intensity (the opposite occurs with Mg doping) (Bonanni et al., 2007).

These optical studies indicate that Cr, Mn, and Fe are all deep acceptors and do not introduce free carriers in the GaN, thereby suggesting that, contrary to the theoretical predictions, carrier-mediated ferromagnetism in this system is highly unlikely and that these films should be semiinsulating.

## 10.4 Experimental studies for $\text{Ga}_{1-x}\text{Cr}_x\text{N}$

Growth studies have also been conducted on Cr-doped GaN, which is attractive since it has been stated that the background carrier concentration of the nitrides will cause the  $\text{Cr}_{\text{Al}}$  and  $\text{Cr}_{\text{Ga}}$   $t_2$  defect level which sits at  $\sim 2$  eV above the valence band to be pushed from a 1/3 filling to a 1/2 filling (Newman et al., 2006). The interatomic exchange is maximum for a 1/2 filled level as per the Zener double exchange model. First-principle calculations have shown coupling between Cr atoms in GaN to be ferromagnetic with a magnetic moment per atom of  $2.69 \mu_{\text{B}}$  in bulk GaN and  $4 \mu_{\text{B}}$  in clusters (Liu et al., 2005). Single crystals of  $\text{GaCrN}$  with a  $T_{\text{C}}$  of 280 K have been demonstrated by a sodium flux method (Park et al., 2002). In these films the carrier density in the crystal is about  $9 \times 10^{18} \text{ cm}^{-3}$  (n-type), and the mobility is about  $150 \text{ cm}^2/\text{V}$ .

(Ga,Cr)N thin films grown by MBE were deemed very encouraging. MBE has been used to grow  $\text{Ga}_{1-x}\text{Cr}_x\text{N}$  ( $x = 1.5\%$ ) on sapphire substrates with a higher  $T_{\text{C}}$  of 400 K (Hashimoto et al., 2003b). Magnetization measurements revealed that the coercivity is about 90 Oe at 300 K. The spontaneous magnetic moment per Cr atom was determined to be  $2.6 \mu_{\text{B}}$ . Optical studies conducted at 10 K on ECR-MBE grown  $\text{Ga}_{1-x}\text{Cr}_x\text{N}$  ( $x = 0.5\text{--}1.5\%$ ) show the presence of a sharp excitonic peak at 3.36 eV, a blue luminescent band centered in the range of 2.79–2.91 eV and also an increase in the yellow luminescent band. The blue luminescence is caused by Cr doping and is attributed to a donor–acceptor pair transition, where the donor is the deep-acceptor related center,  $\text{Cr}_{\text{Ga}}$ , and the acceptor is the shallow compensating vacancy complex,  $\text{Cr}_{\text{Ga}}\text{--}V_{\text{N}}$  (Subashchandran et al., 2006).

Of particular interest have been MBE reports of Cr doping of GaN (3% Cr) and AlN (7% Cr) on SiC substrates. These epitaxial films were reported to have a  $T_C$  as high as 900 K (Liu et al., 2004). The coercive field for GaCrN is 100 Oe at 325 K and decreases to 60 Oe at 800 K. On the other hand, it was reported that for 7% Cr doped AlN, the coercive field is 120 Oe at 300 K and 70 Oe at 800 K. The saturation magnetization moment for 3% Cr-doped GaN was determined to be  $1.8 \mu_B$ , implying that 60% of the Cr is magnetically active. Similarly, the maximum saturation magnetization moment for 7% Cr doped AlN was found to be  $0.6 \mu_B$ , suggesting that 20% of the Cr is magnetically active. No ferromagnetic secondary phases were seen from XRD, TEM, and electron energy loss spectrum. Trace amounts of CrN were seen in  $\text{Ga}_{1-x}\text{Cr}_x\text{N}$ , but this phase is deemed to be antiferromagnetic.

Electrical measurements of  $\text{Ga}_{1-x}\text{Cr}_x\text{N}$  grown on sapphire substrates revealed that the resistance followed the following equation:

$$R = R_0 \left[ \frac{T_0}{T} \right]^{1/2} \quad [10.3]$$

which is characteristic of variable range hopping between localized states with a Coulomb gap as per Mott's law. Theoretically and experimentally Cr is shown to form a near midgap deep level in the nitrides (Polyakov et al., 2003c; van Schilfsgaarde and Mryasov, 2001, p. 233205). The  $d$  levels are exchange split, and the crystal field causes a threefold degenerate  $t_2$  and a doubly degenerate  $e$  level, with the  $e$  level being  $\sim 1$  eV below the  $t_2$ . The majority  $t_2$  is 1/3 filled for Cr, leading to a magnetic moment of  $3 \mu_B$ . The partial filling of the  $t_2$  level accounts for the magnetism of substitutional Cr in GaN and AlN. The observed conduction is due to the variable range hopping of spin-polarized electrons in the Cr impurity band and concludes that ferromagnetism in Cr-doped GaN and AlN can be attributed to the double exchange mechanism within the partially filled Cr  $t_2$  band (Newman et al., 2006). The electron carrier density and Hall mobility at 300 K for  $\text{Ga}_{1-x}\text{Cr}_x\text{N}$  were measured to be  $1.4 \times 10^{20} \text{ cm}^{-3}$  and  $0.06 \text{ cm}^2/\text{V s}$  for magnetic fields up to 5 T. The extremely low mobility is related to the observed hopping conductivity. The Cr-AlN (grown on sapphire substrates) samples were found to be quite resistive, with a resistivity greater than  $10^3 \Omega \text{ cm}$  (Liu et al., 2004).

MOCVD-grown GaCrN has been reported, which shows a hysteresis curve at a low temperatures of 5 K (Cho et al., 2007).

Early experimental results to date point to double exchange being the mechanism for ferromagnetism in  $\text{Ga}_{1-x}\text{Cr}_x\text{N}$  and this magnetization is expected to be enhanced by Si doping as an extra electron is added to the  $t_2$  level. Based on the AFM images and the in situ reflectometry curves, it is apparent that the solubility of the TM ions in the GaN host lattice is fairly low. The solubility limit of Mn is higher than for Cr and Fe as it is possible to obtain smooth surfaces for 2% Mn doping, whereas the GaN films doped with Cr and Fe are limited to 0.7% Cr and 0.3% Fe doping, respectively. The low solubility limit presents a challenge for obtaining a uniform DMS, as cluster formation is more favorable under these conditions.

Raman spectroscopy studies were performed to examine the effect of TM incorporation on the vibrational modes of the GaN lattice. These studies were recorded at RT in back scattering geometry. Fig. 10.15 shows the Raman spectra for an as-grown GaN epilayer along with GaN doped with 3% Cr, 1.5% Mn, and 0.7% Fe. The most prominent feature in all of these scans is the  $E_2(\text{high})$  and  $A_1(\text{LO})$  modes at  $569\text{ cm}^{-1}$  and  $735\text{ cm}^{-1}$ , respectively. These observations indicate that there is no significant strain introduced by TM doping since no shift is observed in the dominant peaks. Furthermore, the high intensity of the  $E_2(\text{high})$  peak indicates that there is no significant degradation of the crystalline quality. Furthermore, the presence of the  $A_1(\text{LO})$  mode (which is similar to GaN in both intensity and FWHM) indicates that there are no free carriers introduced by TM doping, providing further confirmation that carrier-induced ferromagnetism is unlikely in these materials.

Furthermore, for both the Mn and Fe samples there is an additional mode at  $710\text{ cm}^{-1}$  which appears as a shoulder to the  $A_1(\text{LO})$  mode. With increasing doping concentration of the TM, this mode increases in intensity. This mode has previously

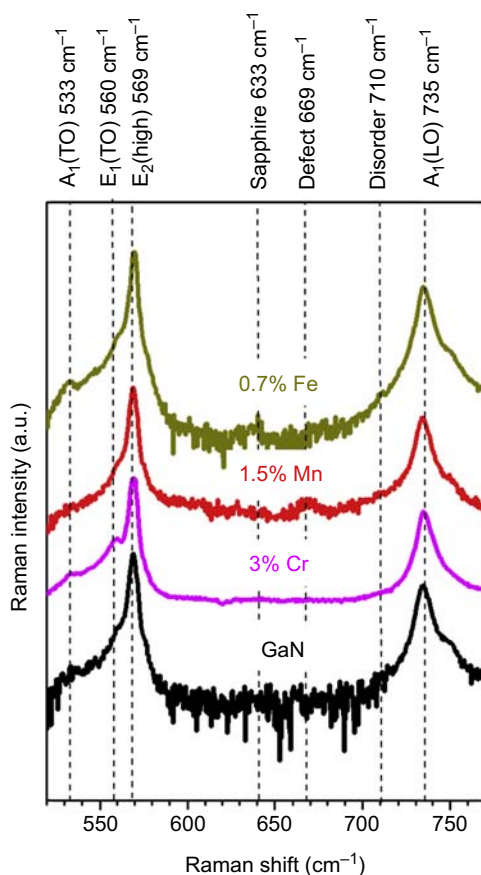


**Figure 10.15** Raman spectrum for TM-doped GaN reveals strain-free films.

been reported in other Raman studies of TM-doped GaN and due to its insensitivity to the nature of the dopant, has been best attributed to a structurally induced disorder mode (Shanthi et al., 2005). In addition to the allowed c-plane GaN Raman modes, in the Cr- and Fe-doped sample scans there appears an additional  $A_1(\text{TO})$  mode. The appearance of this mode is likely to be due to a relaxation of the Raman selection rules about the Cr- and Fe-induced defects within the system and is consistent with the observed degradation in the structural ordering of the system (Harima, 2004).

A zoomed-in Raman spectrum (conducted with a 532 nm sources) showing the effect of Cr concentration and Si doping is presented in Fig. 10.15. It can be seen that as the Cr or Si concentration increases, the intensity of the  $E_1(\text{TO})$  mode at  $560\text{ cm}^{-1}$  reduces (Fig. 10.15). Additionally a blue shift is observed in the  $E_2(\text{high})$  upon increased Si doping, indicating the possibility of strain. With regard to the  $A_1(\text{LO})$  mode, upon Si doping a blue shift is observed and the intensity of this mode decreases and broadens, which is to be expected as free carriers are introduced. This may be promising since with Si-doped Cr has the same electronic configuration as  $\text{Mn}^{3+}$ .

RT PL studies reveal that Cr doping dampens the band-edge emission, with the emission completely disappearing when codoped with 3% Cr. PL measurements for Si and Mg-doped  $\text{Ga}_{0.995}\text{Cr}_{0.005}\text{N}$  films revealed similar features to codoped GaN, which is not surprising when the low Cr concentration used in the codoped films is considered.

To obtain an in-depth understanding synchrotron radiation deep UV (150–300 nm) excitation PL measurements were conducted on GaN doped with 0.5% Cr over a temperature range of 20–300 K (Fig. 10.16). The GaN excitation recombination peak at 365 nm is observed along with a series of peaks at 379, 389, 400, and 416 nm, respectively. These shoulder peaks become more prominent at temperatures below 77 K (Subashchandran et al., 2006). For Si-doped samples, the GaN exciton line at 365 nm became weaker and broader, indicating that the crystalline perfection became poorer. In addition, the neighboring peaks are shifted and the peaks that appear at 380.0, 390.6, 403.3, and 419.9 nm are shifted upon Si doping to 379.0, 389.0, 400.8, and 415.9 nm, respectively. These shoulder peaks are characteristic of donor–acceptor pair (DAP) transitions that have also been observed in MBE-grown  $\text{Ga}_{0.985}\text{Cr}_{0.015}\text{N}$  films (Subashchandran et al., 2006). These DAP peaks are attributed to a transition between nitrogen vacancy and chromium.

The effects of Cr concentration on the magnetization at RT were analyzed by SQUID measurements, the results of which are shown in Fig. 10.17. The magnetization strength increases from approximately  $3\text{ emu/cm}^3$  for the 0.5% Cr to  $4\text{ emu/cm}^3$  for 0.7% Cr and then to  $7\text{ emu/cm}^3$  for 3% Cr. Low temperature SQUID measurements were performed at 5 K on these films, but there is no significant difference in the magnetization data. These results are similar to the magnetization results reported for MBE-grown films, which attribute the observed ferromagnetism to a double exchange mechanism (Newman et al., 2006).

Based on the double exchange mechanism, codoping Cr with Si should cause an extra electron to be added to the  $t_2$  level of Cr and enhance the magnetic moment of each Cr atom. Codoping studies with Si and Mg were carried out on the GaN films



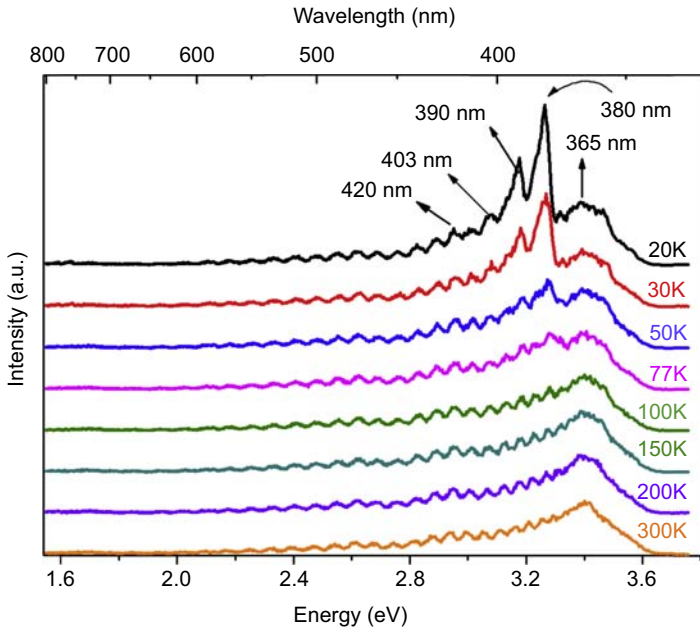


**Figure 10.16** Synchrotron radiation measurements on  $\text{Ga}_{0.995}\text{Cr}_{0.005}\text{N}$  as a function of temperature.

doped with 0.5% Cr. The RT magnetization results are presented in Fig. 10.17. Contrary to expectations, it is seen that Si doping causes a reduction in the magnetization and makes the film diamagnetic.

Furthermore, it would be expected that with Mg doping the magnetization would reduce as the  $t_2$  band will be empty, but this does not occur; rather, the magnetization is further increased. Carrier-mediated magnetization is unlikely as Cr is a deep acceptor (impurity level of 2 eV) and no free carriers exist. In addition, the double exchange seems unlikely. Based both on these experimental results and on theoretical calculations it is proposed that a percolation limit of 20% is necessary to facilitate nearest-neighbor interactions (Katayama-Yoshida et al., 2007). The origins of these magnetic properties are explored in the next section.

RT magnetic hysteresis is observed in both the Mn- and Fe-doped samples, even at relatively dilute alloying concentrations. These doping levels are far less than the percolation threshold needed in either a double exchange or impurity band-mediated (Coey et al., 2005) model for ferromagnetism in the systems. Hysteresis curves for both the Fe- and Mn-alloyed samples show a distinct parallelogram-like shape instead of the more square-shaped hysteresis loop shapes typically observed in  $\text{Ga}_{1-x}\text{Mn}_x\text{As}$ ; this has been attributed to nonuniform cluster distributions in the  $\text{Ga}_{1-x}\text{Mn}_x\text{As}$  samples. With increasing silicon doping, the strength of the measured magnetization decreases considerably in the Mn-doped samples; there is roughly no change in the magnetization of the Fe-doped samples and a hysteretic magnetic signal persists in all the measured curves. SIMS has confirmed that there is no systematic variation in



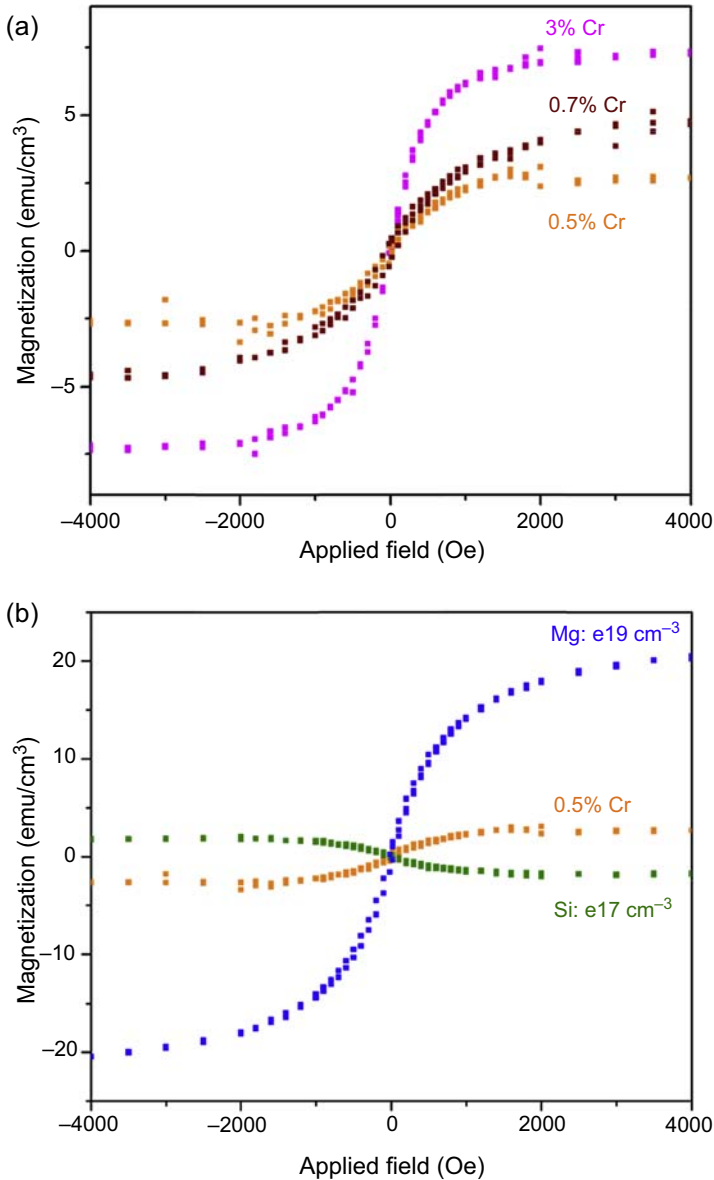


**Figure 10.17** RT magnetization data from SQUID for Ga<sub>1-x</sub>Cr<sub>x</sub>N (a) effect of varying Cr concentration, (b) effect of codopants on magnetization.

the overall incorporation of Mn, save for some local lateral fluctuations across the wafer described in more detail later. The zero field cooled (ZFC) and field cooled (FC) magnetization curves from as-grown films show no indication of a classic superparamagnetic cusp (Fig. 10.18(a)). Three contributions exist to the overall measured

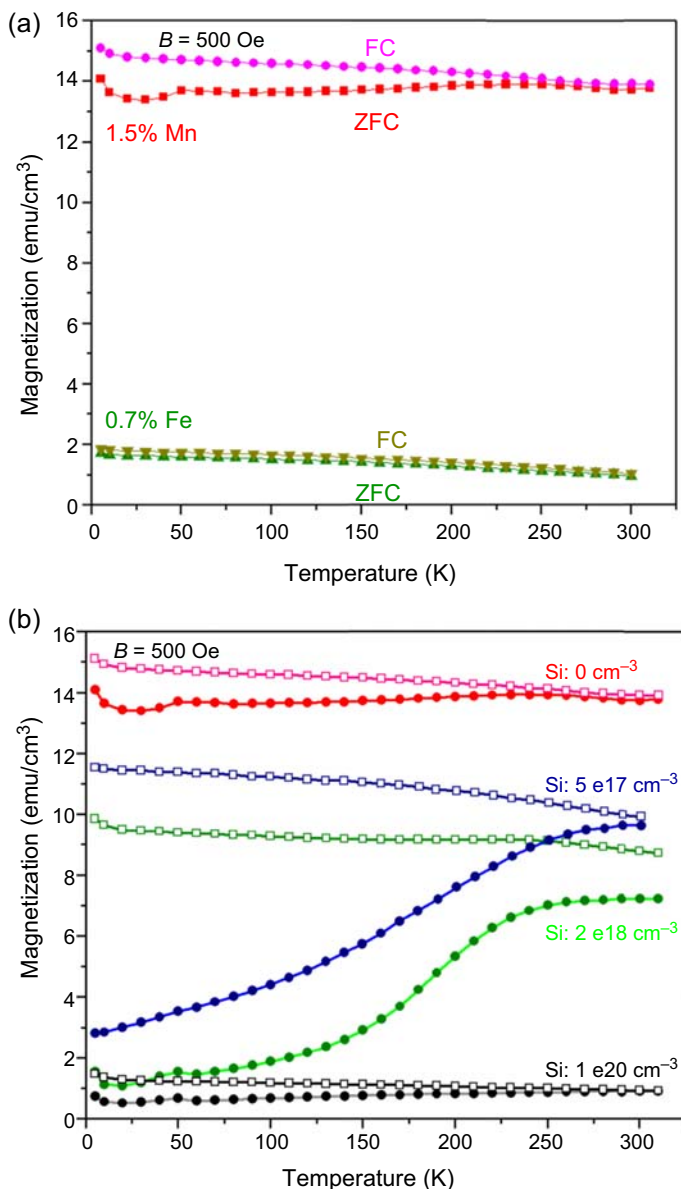


**Figure 10.18** (a) ZFC and FC measurements for as-grown and codoped Ga<sub>1-x</sub>Mn<sub>x</sub>N and as-grown Ga<sub>1-x</sub>Fe<sub>x</sub>N, (b) effect of different Si doping levels on the magnetic properties of Ga<sub>1-x</sub>Mn<sub>x</sub>N ( $x = 1.5\%$ ).

magnetization—a Pauli paramagnetic contribution from the  $d^5$  ions (Mn<sup>2+</sup>/Fe<sup>3+</sup>), a temperature independent Van Vleck paramagnetic contribution from the  $d^4/d^6$  (Mn<sup>3+</sup>/Fe<sup>2+</sup>) ions, and an above-RT ferromagnetic contribution from an as-yet unidentified Mn-rich phase. Van Vleck paramagnetism has been previously reported

from  $\text{Cr}^{2+}$  ( $d^4$ ) and  $\text{Fe}^{2+}$  ( $d^6$ ) ions in II-VI semiconductors (Karthouser et al., 1993, p. 14127); more recently, it has been suggested to be the source of the temperature independent contribution in  $\text{Ga}_{1-x}\text{Fe}_x\text{N}$  films (Przybylinska et al., 2006, p. 222). The relative strengths of the temperature independent portions of the ZFC/FC curves are consistent with this assignment, as the trivalent state of the  $\text{Mn}^{3+}$  ion has an even number of electrons, which is more conducive to Van Vleck paramagnetic behavior than the odd-numbered  $\text{Fe}^{3+}$  or  $\text{Mn}^{2+}$  (postcodoping) ions.

An interesting behavior is observed in the films with increasing Si codoping (Fig. 10.18(b)). A pronounced superparamagnetic splitting reminiscent of distributed sizes of magnetic nanoparticles can be observed in the ZFC/FC curves with increasing Si molar flow rate. This observation can be understood by looking at the role of silane on both the charge state of the manganese ions and the expected behavior of a group of magnetic nanoparticles of distributed size. The equation for the blocking temperature ( $T_b$ ) of a magnetic cluster is given by:

$$T_b = \frac{KV}{k_B \ln\left(\tau_{\text{exp}}/\tau_0\right)} \quad [10.4]$$

where  $V$  is particle volume,  $K$  is the anisotropy constant,  $\tau_{\text{exp}}$  is the measurement time, and  $\tau_0$  is the lifetime due to the natural gyromagnetic frequency of the particles. The two parameters of particular importance in the  $T_b$  of the  $\text{Ga}_{1-x}\text{Mn}_x\text{N}$  films are the magnetic anisotropy term and the volumetric term, since the blocking temperature scales linearly with each. The magnetic anisotropy term can be particularly high for the embedded  $\text{Ga}_x\text{Mn}_y\text{N}_z$  particles, due to the highly anisotropic nature of the polar wurtzite GaN films and 2D surface diffusion during the growth. Combined with the volume of the particles, this could lead to blocking temperatures well above RT, and an observed magnetic hysteresis in the films below the blocking temperature.

Silicon has two effects on the growth of MOCVD-grown films that could affect these samples. One effect is the aforementioned reduction of the Mn valence state, which could result in an effective decrease in the order parameter and the inhibition of Mn–Mn interactions, which would result in spinodal decomposition. The second effect of silicon is that of an antisurfactant, and it has been used as a nucleation center for the high temperature MOCVD growth of quantum dots (QDs) (Tanaka et al., 2000). Silicon on the GaN growth surface increases the local surface energy, and acts as a nucleation site for islands, which lowers the effective diffusion length of these atoms, and hence lowers the number of Mn–Mn interactions necessary for the formation of the Mn-rich phase. This results in an overall decrease in the volume of the nanoparticles, which in turn leads to a greater fraction of this assembly with lower  $T_b$ , and hence a more pronounced splitting in the ZFC/FC magnetization curves.

It might be expected that the Fe codoped samples should also exhibit a similar decrease in the magnetization strength based on interaction of charged impurities. However, it should be noted that the absence of such a behavior is not surprising in light of the growth processes and relative concentrations of the Mn and Fe used. The growth rate for the Mn-doped films in these studies was  $0.4 \mu\text{m/h}$  as monitored

by in situ reflectivity during the growth process; for the Fe-doped films, a higher growth rate of 0.9  $\mu\text{m}/\text{h}$  was employed. This allows for shorter diffusion distances and fewer Fe–Fe interactions. The lower precursor ratios, which lead to fewer TM ions on the surface, increase the surface diffusion path necessary to reach additional TM atoms on the surface, thus reducing the rate at which spinodal decomposition occurs. Moreover, since the rates of bulk diffusion in GaN at typical MOCVD growth temperatures are considerably smaller than the surface diffusion lengths, 2D surface diffusion is the dominant effect that results in Mn–Mn interactions and Mn-rich phase formation. As a result, the expected shape of the embedded nanoparticles is not spherical, but disc-like. As the major axis of these embedded nanoparticles would be perpendicular to the growth direction, their observation in cross-sectional TEM would be almost impossible.

The low alloy concentrations of Mn used in this study likely preclude the observation of the theoretically proposed columnar Konbu-phase (Fukushima et al., 2006). The Fe films also have increased surface roughness, which is consistent with lower overall surface diffusion lengths and more 3D growth. Conditions that promote longer diffusion lengths and smoother surfaces would also tend to promote Mn–Mn interactions and phase decomposition. The concurrent observation of the appearance of the superparamagnetic phase and the optical observation of the conversion of  $\text{Mn}^{3+}$  ions to  $\text{Mn}^{2+}$  is consistent with predictions (Dietl, 2006) of charged controlled phase separation in these semiconductor alloys. Similarly, magnetization reports by Bonanni et al. (2007) also suggest the RT ferromagnetism observed in their GaFeN samples is due to the presence of Fe-rich nanocrystals formed by spinodal decomposition.

Three contributions exist to the overall measured magnetization—a Pauli paramagnetic contribution from the  $d^5$  ions ( $\text{Mn}^{2+}/\text{Fe}^{3+}$ ), a temperature independent Van Vleck paramagnetic contribution from the  $d^4/d^6$  ( $\text{Mn}^{3+}/\text{Fe}^{2+}$ ) ions, and an above-RT ferromagnetic contribution from an as-of-yet unidentified Mn-rich phase. Van Vleck paramagnetism has been previously reported from  $\text{Cr}^{2+}$  ( $d^4$ ) and  $\text{Fe}^{2+}$  ( $d^6$ ) ions in II–VI semiconductors (Kartheuser et al., 1993, p. 14127); more recently, it has been suggested to be the source of the temperature independent contribution in  $\text{Ga}_{1-x}\text{Fe}_x\text{N}$  films (Przybylinska et al., 2006, pp. 222–5). The relative strengths of the temperature independent portions of the ZFC/FC curves are consistent with this assignment, as the trivalent state of the  $\text{Mn}^{3+}$  ion has an even number of electrons, which is more conducive to Van Vleck paramagnetic behavior than the odd-numbered  $\text{Fe}^{3+}$  or  $\text{Mn}^{2+}$  (postcodoping) ions.

ZFC and FC measurements were conducted to enable a better understanding of the ferromagnetism mechanism in  $\text{Ga}_{1-x}\text{Cr}_x\text{N}$  as well. The ZFC and FC measurements were performed in the presence of an applied field of 200 Oe for  $\text{Ga}_{1-x}\text{Cr}_x\text{N}$  at several different Cr concentrations. The results are shown in Fig. 10.19, and reveal a pronounced splitting for all tested concentrations of Cr in GaN. From the ZFC and FC plots, it is apparent that the Si- $\text{Ga}_{1-x}\text{Cr}_x\text{N}$  is magnetically inactive. Si codoping of  $\text{Ga}_{1-x}\text{Cr}_x\text{N}$  converts the  $\text{Cr}^{3+}$  to the  $\text{Cr}^{2+}$ , which has been associated with Van-Vleck-type paramagnetism (magnetization that does not vary with temperature) in II–VI semiconductors (Kartheuser et al., 1993, pp. 14127–14134). On the other hand the Mg-doped films show a pronounced splitting (larger than the  $\text{Ga}_{1-x}\text{Cr}_x\text{N}$

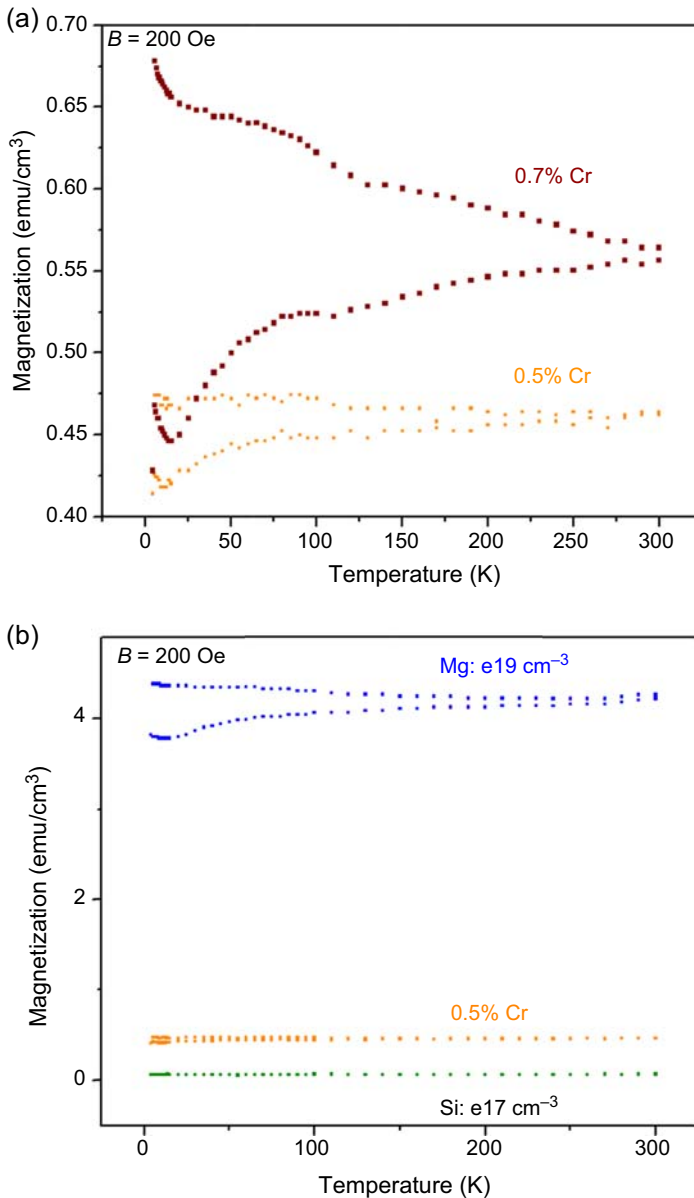


**Figure 10.19** ZFC and FC measurements for (a) as-grown, and (b) n- and p-doped Ga<sub>0.995</sub>Cr<sub>0.005</sub>N under an applied field of 200 Oe.

films), indicating that magnetic clusters exist in the material and are enhanced by Mg doping. These measurements point toward the fact that the enhanced magnetization is due to magnetic clusters that are occurring in the material rather than the formation of a DMS. As mentioned this is consistent with unoptimized

p-Ga<sub>1-x</sub>Mn<sub>x</sub>N films in which Mg facilitates the increase in Mn concentration and thereby enhances the magnetization by as much as four times (Reed et al., 2005).

This markedly different behavior, namely the increasing ZFC/FC difference on lowering temperature, indicates the presence of clusters state whose response is determined by thermally activated processes across some energy barriers. This behavior is characteristic of anisotropic magnetic clusters below its blocking temperature. Thus, the Cr doping in GaN undergoes spinodal decomposition (ie, segregates into regions of varying TM concentration) above the solubility limit to create magnetic clusters. The size distribution of these clusters results in a distribution of  $T_b$  and thus the  $T_b$  recorded is a mean value for all the magnetic clusters present. Energy density calculations show that Cr distribution in GaN is not random or homogeneous but that it is energetically favorable for the Cr atoms to be embedded as clusters, and it is likely that the clusters formed will be of varying sizes and configurations (Cui et al., 2005). The cluster formation is enhanced both by increasing the TM concentration and also by high growth temperatures. These allow for enhanced TM cluster interactions and for enhanced TM mobility, respectively. Density function calculations have shown that Cr atoms may cluster around N to form Cr<sub>2</sub>N and Cr<sub>3</sub>N nanoclusters, which have been found to be ferromagnetic with magnetic moments of 9 and 13  $\mu_B$ , respectively (Wang et al., 2003). The p-doping causes an increase in magnetization and a pronounced splitting in the ZFC and FC measurements are consistent with the theoretical studies that state that doping with shallow acceptors enhances carrier screening and leads to nanocrystal aggregation (Dietl, 2008).

Spinodal decomposition is limited in Ga<sub>1-x</sub>Mn<sub>x</sub>As since it is grown at low temperatures and phase segregation is kinetically limited. Furthermore, Mn is a shallow acceptor and, due to its large Bohr radius, the holes reside in the valence band, which in turn makes the Mn negatively charged, reducing the clustering and making it possible to deposit homogeneous films beyond the solubility limit (Dietl, 2008; van Schilfgaarde and Myrasov, 2001, p. 233205). Overall, the experimental results in this study along with theoretical predictions support the fact that ferromagnetism in Ga<sub>1-x</sub>TM<sub>x</sub>N is mediated through magnetic clusters that are promoted through spinodal decomposition and Coulombic interactions rather than the double exchange mechanism previously reported.

#### 10.4.1 Rare earth doping of GaN

RE elements are promising alternatives to TMs for use in developing a DMS for spintronic applications. RE elements have unpaired electrons in the 4f orbitals and thus have a higher net magnetic moment as compared to TM ions. The 4f orbitals are localized and the direct coupling between the 4f ions is weak (Zhong et al., 2008). There have been several attempts of using RE elements for optoelectronic applications, as their various internal f-shell electronic transitions vary in energy from infrared to visible (Steckl et al., 2001, 2002).

RE elements have also been used as dopants for spintronic applications. Instead of relying on the d-shells of the TMs as the magnetic element, the f electrons from the RE

elements are used. There have been several reports of using RE elements for optoelectronic applications, as it is possible to cover the entire spectrum from the infrared to the visible range due to the different internal  $f$ -shell electronic transitions (Steckl et al., 2002). However, the low solid solubility of RE elements in the GaN lattice results in reduced efficiency of these electronic devices. There exists a chemical driving force away from solubility on the lattice site, and differences in ion sizes provide a hindrance for the lattice solubility of RE in GaN. Such challenges will be magnified for the development of RE compounds for spintronic applications, as they will need, in general, to exhibit much larger concentrations of RE ions in order to promote magnetic interactions based on most of the existing theories.

In spite of these challenges, there have been explorations and reports on the use of  $\text{Ga}_{1-x}\text{Gd}_x\text{N}$  and  $\text{Ga}_{1-x}\text{Eu}_x\text{N}$  and their magnetic properties, though the data are still not well understood (Hashimoto et al., 2003a; Dhar et al., 2005a, pp. 037205-4). The first reports on epitaxial  $\text{Ga}_{1-x}\text{Gd}_x\text{N}$  layers were made by Teraguchi et al. (2002, pp. 651–653) who used RF-plasma-assisted MBE to grow the epitaxial layers on (0001) Si-face of SiC substrate. They grew  $\text{Ga}_{0.94}\text{Gd}_{0.06}\text{N}$ , which displayed ferromagnetic behavior with  $T_C$  higher than 400 K.

Their optical characterization at RT yielded an emission peak at 370 nm and slightly longer than that of GaN (363 nm), which means that the bandgap shrinks when Gd atoms are incorporated. An emission peak centered around 645 nm was also observed and is believed to be related to  $\text{Gd}^{3+}$  according to the analogy of Eu-doped GaN (Teraguchi et al., 2002, pp. 651–653). Another study on GaN bulk crystals doped with Gd shows that Gd doping introduces some new features. Low temperature PL measurements performed at 4.2 K reveal that in addition to the GaN bandgap, luminescent peaks have been observed at 3.3 eV and have been attributed to a transition from  $\text{Gd}^{3+}(4f^7)$  excited level  ${}^6\text{P}_{7/2}$  to its ground state  ${}^8\text{S}_{7/2}$ . Additional peaks are also seen at 1.6–1.8 eV and have been attributed to  $\text{Gd}^{3+}$ . These are believed to be a transition between  ${}^6\text{G}_{7/2}$  to  ${}^6\text{P}_J$  ( $J = 7/2, 5/2, 3/2$ ) states (Lipinska et al., 2006).

Lightly doped ( $<10^{16} \text{ cm}^{-3}$ )  $\text{Ga}_{1-x}\text{Gd}_x\text{N}$  were grown by reactive molecular beam on SiC substrates. This epitaxial film appeared to be a single phase material and exhibited a very large ferromagnetic moment ( $\sim 4000 \mu_B/\text{Gd}$  as opposed to its atomic moment of  $8 \mu_B/\text{Gd}$ ) (Dhar et al., 2005b, pp. 245203-9). Based on the convergence of the FC and ZFC curves, the  $T_C$  was reported to be 360 K. As of yet, there is not a robust theory to explain the giant magnetic moment observed in these materials, but a phenomenological model has been proposed that suggests that the long-range spin polarization of the GaN matrix is caused by the strain field induced by the introduction of the Gd atom (Dhar et al., 2005b, pp. 245203-9). It has been suggested that because Gd has a larger atomic size than Ga, it is possible that Gd substitution of Ga in GaN produces a large strain field around it. Due to the large piezoelectric coefficient of GaN along the  $c$ -axis, it is quite plausible that the strain field generates a potential dip around each Gd atom. These potential minima can trap carriers locally. If there is a spin-splitting in the band structure, the localized carriers will be spin polarized.  $\text{Ga}_{1-x}\text{Gd}_x\text{N}$  thin films with Gd concentration as high as 12.5% were obtained by RF-plasma-assisted MBE (growth temperature  $<300^\circ\text{C}$ ) on sapphire substrates

(Zhou et al., 2008). X-ray diffraction results showed no obvious secondary phase and yielded films that displayed RT ferromagnetism. Extended X-ray absorption fine structure measurement show that the Gd atoms were mainly incorporated into Ga sites.

Ga<sub>1-x</sub>Eu<sub>x</sub>N films grown by MBE have also been studied for their magnetic properties (Hite et al., 2006). Under certain conditions, RT ferromagnetic hysteresis can also be observed in these films. It was concluded that this must also be the function of a DMS alloy, because there are known unitary or binary Eu alloys and compounds with above-RT ferromagnetic ordering. Other possibilities include TM impurities, interfacial effects, oxygen-induced valence band splitting, or the formation of nonequilibrium magnetic phases.

GaGdN is promising, since it has the potential to be doped with donors (acceptors) with a concentration exceeding that of Gd to generate spin-polarized electrons (holes) in the conduction band (valence band), which could be applied to spintronic devices (Wolf et al., 2001; Dhar et al., 2005a, pp. 037205-4).

GaN:Gd thin films have been successfully grown by MOCVD to date (Gupta et al., 2011), which is the standard commercial growth technique for producing device-quality compound semiconductor thin films. These films were found to be ferromagnetic at RT and electrically conducting although the mechanism for the ferromagnetism was not well understood (Jamil et al., 2011). We have completed a more systematic investigation of the interrelationship of chemical, magnetic, and electrical properties of GaN:Gd. First-principle calculations based on density functional theory have shown that the ferromagnetism was likely mediated by interstitial oxygen as described earlier. This was confirmed, in part, because ferromagnetism was only observed in GaN:Gd thin films grown using TMHD<sub>3</sub>Gd, an oxygen-containing metalorganic Gd precursor. It was found that the GaN:Gd was residually n-type (mid 10<sup>17</sup> cm<sup>-3</sup>) rather than the highly resistive material grown using TMs and could be effectively n-type (Si) or p-type (Mg) doped without losing their ferromagnetic properties. These Si and Mg codoped GaN:Gd films could then be used for spin injection into spin LEDs and other spintronic devices.

A series of GaN:Gd films were grown by MOCVD using two different Gd sources to study the role of oxygen in the observation of ferromagnetism in these materials. In this instance, Tris(2,2,6,6-tetramethyl-3,5-heptanedionato)-gadolinium (TMHD<sub>3</sub>Gd) and Tris(cyclopentadienyl)-gadolinium (Cp<sub>3</sub>Gd) were used as the Gd sources. The key difference between these sources is that the organic ligand in TMHD<sub>3</sub>Gd contains oxygen, while the ligand in Cp<sub>3</sub>Gd does not. This means that one series of samples grown using TMHD<sub>3</sub>Gd should potentially have oxygen incorporated in them, depending on the growth conditions, and the other series of samples grown with Cp<sub>3</sub>Gd should not. Table 10.1 shows the atomic composition of GaN:Gd films produced with varying flow rates of the two precursors. Flow rates are given here because of the difficulty of measuring the actual Gd composition. The samples produced with the TMHD<sub>3</sub>Gd precursor all showed the presence of both gadolinium and oxygen in the films, however varying the flow rate of this precursor did not appear to systematically change the observed Gd density measured by EDS. The films produced using the Cp<sub>3</sub>Gd source all showed much higher Gd content than the TMHD<sub>3</sub>Gd films, but contained no oxygen.



**Table 10.1 EDS data for MOCVD-grown GaN:Gd samples**

Precursor, flow	Ga%	N%	Gd%	O%
TMHD <sub>3</sub> Gd, 10 sccm	44.46	44.41	0.06	1.18
TMHD <sub>3</sub> Gd, 40 sccm	49.07	48.46	0.01	0.88
TMHD <sub>3</sub> Gd, 80 sccm	47.74	48.61	0.01	1.55
Cp <sub>3</sub> Gd, 10 sccm	46.51	47.03	0.35	0.00
Cp <sub>3</sub> Gd, 80 sccm	46.33	46.37	0.34	0.00
Cp <sub>3</sub> Gd, 160 sccm	47.48	46.34	0.53	0.00

XRD measurements of the films showed no discreet evidence of macroscopic secondary phases of Gd<sub>2</sub>O<sub>3</sub>, GdN, or Gd metal; only a peak around GaN 002 was observed. The TMHD<sub>3</sub>Gd samples showed a systematic shift of the GaN 002 peak to higher diffraction angles with increasing precursor flow. This is likely due to the incorporation of oxygen, as oxygen typically substitutes for nitrogen in GaN, and oxygen has a smaller covalent radius than nitrogen, leading to a slight decrease in lattice size. The Cp<sub>3</sub>Gd films did not show this trend, which supports the theory that the shift is likely due to oxygen incorporation.

The magnetic properties of films produced with both precursors were studied using vibrating sample magnetometry (VSM). Fig. 10.20 shows magnetization curves for (a) TMHD<sub>3</sub>Gd films and (b) Cp<sub>3</sub>Gd films. The GaN:Gd films produced with TMHD<sub>3</sub>Gd exhibited smooth, well-defined S-curves, with saturation magnetic moments of approximately 40 emu/cm<sup>3</sup>. The films produced with Cp<sub>3</sub>Gd showed much lower magnetic moments. The film produced with 80 sccm appeared to be diamagnetic, similar to the undoped GaN reference, while the film with 160 sccm precursor flow exhibited very weak ferromagnetism with a saturation magnetization of ~5 emu/cm<sup>3</sup>. These results supported the theory that oxygen incorporation in GaN:Gd enhances the ferromagnetic behavior of the material although the actual incorporation of the oxygen and the type of interstitial, if it exists, has not yet been investigated.

GaN:Gd films grown by MOCVD showed residual n-type conductivity, typically mid 10<sup>17</sup> cm<sup>-3</sup>, which opens the possibility to control the conductivity of these films with codoping without destroying the ferromagnetism. A series of n-type (Si) and p-type (Mg) GaN:Gd films were grown with expected Gd concentrations between 0.5% and 4% in the gas phase. Typical p-GaN activation steps were applied to p-GaN:Gd. GaN:Gd films with an apparent Gd incorporation from 10<sup>12</sup> cm<sup>-3</sup>–10% appeared possible in this growth system, at least in the gas phase. However, it should be understood that there are always tremendous difficulties in accurately calibrating new material compositions. XRD and Raman spectroscopy revealed good structural quality with no significant deterioration or strain induced through the Gd incorporation even though Gd is a large atom. XRD measurements of the samples did not detect any secondary phases or precipitates. In addition,

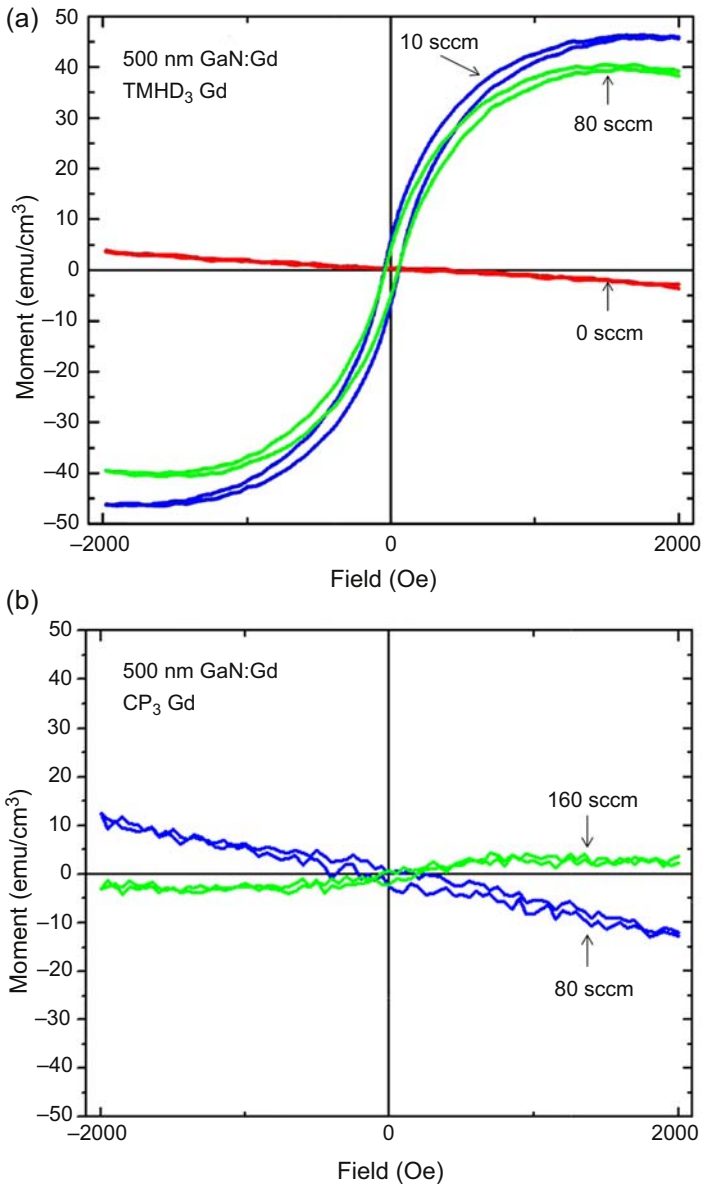


**Figure 10.20** VSM curves for (a) TMHD<sub>3</sub>Gd films, and (b) Cp<sub>3</sub>Gd films with Gd precursor flows. Gd precursor flows indicated for each curve. From Gupta, S., Zaidi, T., Melton, A., Malguth, E., Yu, H., Liu, Z., Liu, X., Schwartz, J., Ferguson, I.T., 2011. Electrical and magnetic properties of Ga<sub>1-x</sub>Gd<sub>x</sub>N grown by metal organic chemical vapor deposition. *Journal of Applied Physics* 110, 083920.

AFM studies revealed smooth sample surfaces with no apparent surface precipitations. RT magnetization data for GaN:Gd have been obtained by VSM (Fig. 10.20). It was observed that as the Gd flow rate is increased, a transition from diamagnetism to ferromagnetism occurs; the magnetization strength observed was  $20 \text{ emu/cm}^3$  for 4% Gd flow for undoped material. Additionally, the GaN:Gd could be systematically codoped with Si or Mg and the saturation magnetization was found to be enhanced by this n-type or p-type codoping (Fig. 10.20). A maximum magnetization of  $\sim 500 \text{ emu/cm}^3$  was obtained for p-type  $\text{Ga}_{1-x}\text{Gd}_x\text{N}$  with ( $x = 4\%$ ) following annealing to activate the dopant. This is the first report of observed RT ferromagnetism in p-type GaN:Gd or successful codoping of GaN:Gd with Mg. At this time, the underlying mechanism for the observed magnetism remains unknown but this will be further investigated by Anomalous Hall Effect and Circular Magnetic Dichroism measurements since, unlike TM-doped GaN, these Gd-doped GaN layers were found to be conducting.

RT and low temperature PL measurements performed on the epitaxial  $\text{Ga}_{1-x}\text{Gd}_x\text{N}$  ( $x = 4\%$ ) layers show the presence of peaks in the range of 3.1–3.3 eV in addition to the GaN emission. In the literature these peaks have been attributed to the internal transition associated with  $\text{Gd}^{3+}$  and other deep levels (Kenyon, 2002) and this could be used in optimizing the material properties.

## 10.5 LEDs containing nitride dilute magnetic semiconductors

The development of a spintronic device that functions at RT has been a quest for a decade now. In this regard, RT spin LEDs are interesting to pursue as they are comparatively easy to fabricate. The analysis of the polarization of the light emission from these LEDs can provide insight into the spin injection efficiency, transport, and spin lifetimes.

Ion implantation of p-GaN with Mn have been carried out to develop a spin LED (Polyakov et al., 2003b). Such a device should allow the modulation of the polarization of the light emitted by the spin LED by the application of an external magnetic field. However, it was found that the high resistance of the implanted region and high density of deep recombination centers significantly decrease the electroluminescence (EL) efficiency, and increase the forward voltage ( $V_f$ ) from  $\sim 4$  to  $\sim 8$  V. No reports on the polarization analysis were made in this study.

MBE-growth of  $\text{Ga}_{1-x}\text{Mn}_x\text{N}$  ( $x = 3\%$ ) films that show RT ferromagnetism has been reported by several groups (Thaler et al., 2004). Due to the n-type conductivity of these layers it was necessary to grow inverted LED structures with an n-type contact layer (Polyakov et al., 2003a; Buyanova et al., 2004). However, such a structure is difficult to fabricate and has a higher series resistance due to the lower lateral conductivity of p-GaN compared to n-GaN. It has also been shown that it is more difficult to attain a high quality of the GaN/InGaN multiple quantum well (MQW) active region when growing on a very heavily Mg-doped p-GaN layer. Further,  $\text{Ga}_{1-x}\text{Mn}_x\text{N}$  is

highly resistive and results in poor ohmic contact formation. It is essential to ensure that the annealing temperature of the ferromagnetic layers does not destroy the ferromagnetism.

### 10.5.1 GaMnN-based light emitting diodes

Through the use of MOCVD, LED structures were grown with the aim of using the  $\text{Ga}_{1-x}\text{Mn}_x\text{N}$  as a spin aligner layer. In this device unpolarized holes are made to pass through the ferromagnetic  $\text{Ga}_{1-x}\text{Mn}_x\text{N}$  layer with the aim of aligning the holes to make them spin polarized. These spin-polarized holes should then recombine with the unpolarized electrons to produce circularly polarized light. The polarization of this light will provide insight into the spin injection efficiency of this LED structure.

To this end, a thin 100 nm  $\text{Ga}_{0.985}\text{Mn}_{0.015}\text{N}$  layer was inserted into a regular LED structure right before the p-GaN layer was grown (Fig. 10.21). The active structure consisted of five MQW structures consisting of  $\text{In}_x\text{Ga}_{1-x}\text{N}$  wells (with  $x = \sim 12\%$ ) and GaN barriers. Magnetization measurements were conducted on this device, showing that the  $\text{Ga}_{0.985}\text{Mn}_{0.015}\text{N}$  retains its magnetization despite its reduced thickness in the device structure. However, upon annealing to activate the p-type carriers, the magnetization is significantly reduced, but is still ferromagnetic. A reference LED was grown, which is basically a regular GaN-based LED without the ferromagnetic  $\text{Ga}_{1-x}\text{Mn}_x\text{N}$  layer.

I-V measurements were conducted on both the spin LED outlined earlier and on a reference LED. It was found that the spin LED had a higher turn on voltage ( $V_f$ ) of 6.5 V, compared with 3.5 V for the reference LED when both were biased at 20 mA (Fig. 10.21). This increase in turn on voltage is not surprising as Mn is a deep acceptor in GaN and increases the resistivity of the ferromagnetic film and thus of the overall device.

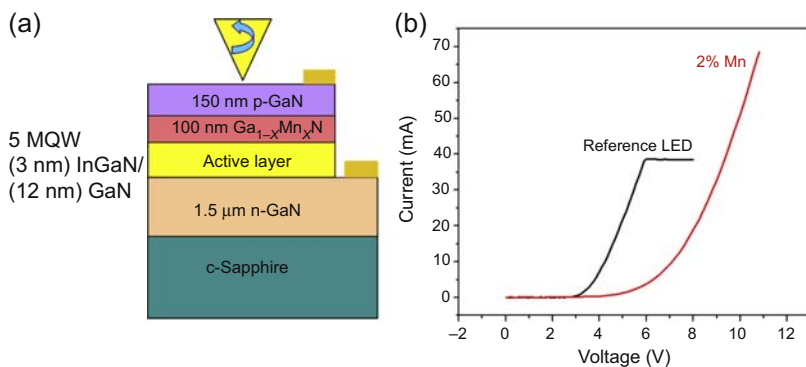


**Figure 10.21** (a) Schematic of the spin LED structure using a spin aligner layer, (b) turn on voltage for the spin LED in comparison to a reference LED.

EL measurements showed a broad peak with maxima at 448 and 456 nm. The two peaks result from fluctuations in the indium composition, which in turn arise from the spinodal decomposition of indium in the nitrides. This is caused by strain-induced piezoelectric effects resulting from the growth conditions. RT EL measurements were performed in the presence of a magnetic field, but no difference was found in the light emissions at polarizations of both left and right polarization of the light as the magnetic field strength was increased (Fig. 10.22).

Very similar results to those found here have been reported in the literature: both Polyakov et al. and Buyanova et al. report EL peaking at 450 nm with a  $V_f$  of 15 V (Buyanova et al., 2004; Polyakov et al., 2003a). No polarization of light emission at RT was observed in applied magnetic fields ranging from 0 to 5 T in either of their EL and PL measurements. It was determined that, independent of the spin polarization of the  $\text{Ga}_{1-x}\text{Mn}_x\text{N}$  ( $x = 3\%$ ) layer, the fast spin relaxation in the  $\text{In}_{1-x}\text{Ga}_x\text{N}$  ( $x = 40\%$ ) MQW will itself destroy any spin polarization of injected carriers leading to the vanishing spin injection efficiency of the spin LED. It was stated that the observed fast spin relaxation in the  $\text{In}_{1-x}\text{Ga}_x\text{N}$  MQW is likely to be caused by breaking of symmetry and the resultant mixing of the spin states. This in turn is caused by strong compositional nonuniformity, strain, and a built-in electric field in  $\text{In}_{1-x}\text{Ga}_x\text{N}$ , as well as strong spin scattering by defects.

Thus, an effective spin detector that will be sensitive to injected spin polarization (eg, by increasing the hh–lh energy separation), or looking at alternate recombination schemes, is needed. It has been suggested that it is difficult to create polarized carriers with high indium composition due to large Stokes shift (up to 200 meV) in the MQWs (Julier et al., 1999). However another study has suggested that high indium composition results in phase separation causing the formation of QDs (Nagahara et al., 2005). The carrier localization in these QDs suppresses the scattering process, which

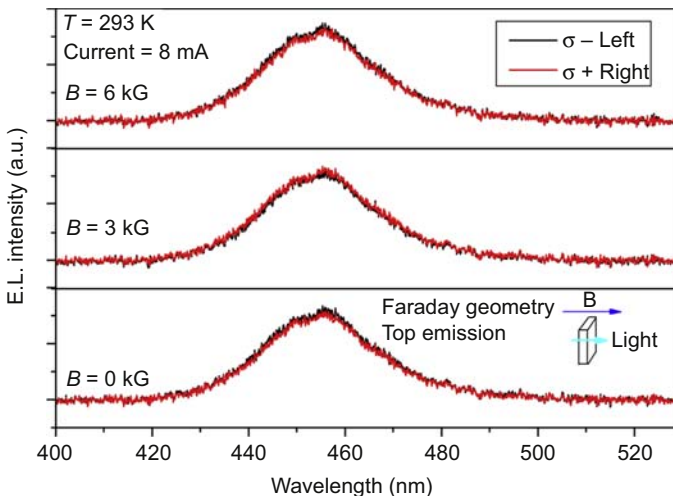


**Figure 10.22** RT EL for a spin LED for varying magnetic fields.

decreases the spin flip rate, thereby increasing the spin lifetime. At this time, the effect of indium composition in the InGaN MQW on spin relaxation time is unclear and further study is needed to clarify this.

A great challenge to the use of TM-doped GaN in spintronic devices is the reduction in magnetization upon annealing (a crucial step in LED processing). Moreover, as the ferromagnetism is caused by cluster formation it will be essential to exercise control over their magnetic properties through the use of growth and codoping methods to ensure their utility in device structures.

### 10.5.2 GaN:Gd spin light emitting diodes

Even though the precise mechanism for the ferromagnetism in the codoped GaN:Gd is not well understood this does not stop the development of devices using this material as a potential spin injector. In addition, if these devices work they provide additional insight into the physical mechanism for the ferromagnetism. A series of consecutive LED structures were grown with and without the GaN:Gd spin injector layer. Both n-type and p-type spin injection layers were used in these devices. Simplified schematics of the GaN-based reference LED structure and the GaN:Gd-based spin-polarized LEDs are shown in Fig. 10.23 (Jamil et al., 2011). These device structures consisted of a 500 nm n-type layer, followed by GaN/InGaN MQW active region, and finally a p-type region. The n- and p-type regions in the spin LED were GaN:Gd layers, based on the layers discussed previously, and have the same physical properties. The I-V curves for the two LEDs are shown in Fig. 10.23 and it can be seen that the GaN:Gd LED has a larger series resistance and a slightly higher turn on voltage. The larger series is most likely due to the slightly higher resistance of the p-type GaN:Gd compared to the p-type GaN grown under the same conditions.

The GaN:Gd LED and the reference GaN LEDs were both mounted on a nonmagnetic DIP package for functional testing under magnetic field. This testing was performed in a Faraday configuration, in which the LED is placed inside the poles of an electromagnet capable of generating up to 5000 Gauss magnetic field. Current is passed through the devices, and the resulting EL is collected and focused through a quarter wave plate. As expected, no response was seen for the reference GaN LED with magnetic field for either right circularly polarized (RCP) or left circularly

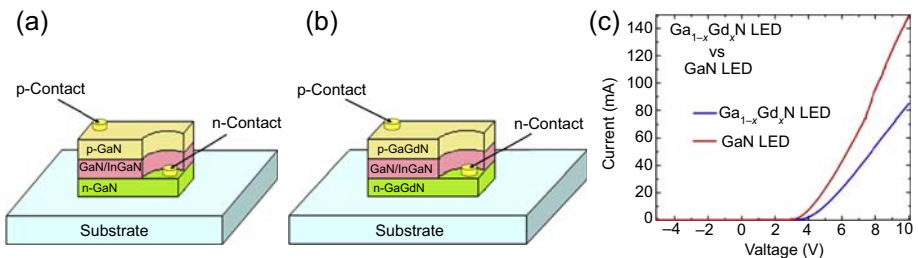


**Figure 10.23** Schematic of LED device structures of (a) reference LED, (b) Ga<sub>1-x</sub>Gd<sub>x</sub>N LED, and (c) I-V curves for both structures.

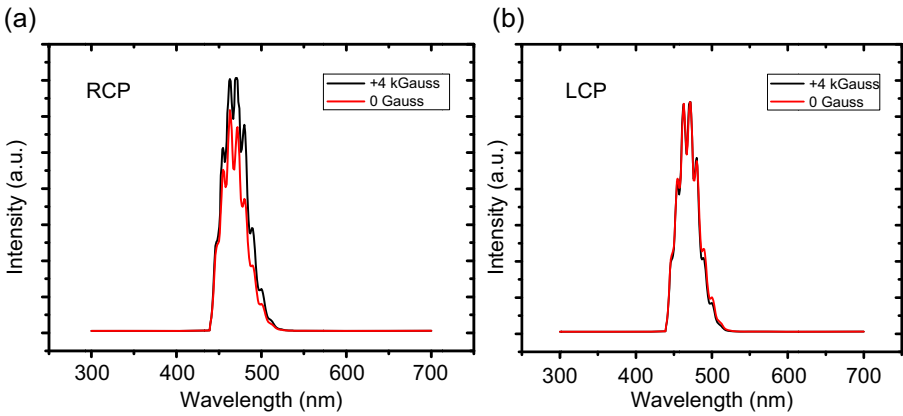


**Figure 10.24** (a) Right and (b) left circularly polarized EL from reference GaN-based LED. From Jamil, M., Zaidi, T., Melton, A., Xu, T., Ferguson, I.T., 2011. Ga<sub>1-x</sub>Gd<sub>x</sub>N-based spin polarized light emitting diode. In: MRS Proceedings, 2011, Cambridge Univ Press, mrsf10-1290-i02-05.

polarized (LCP) EL from these devices (Fig. 10.24). This was not the case for the GaN:Gd LED, which showed a systematic variation of the RCP and LCP emission with magnetic field (Fig. 10.25). The primary figure of merit for a spin LED is the degree of polarization,  $P_{\text{spin}}$ , which is defined as the difference between the left and the right circularly polarized light intensities divided by their sum. A maximum EL polarization of 14.6% was observed at an applied field of 5000 Gauss at RT shown evidence for

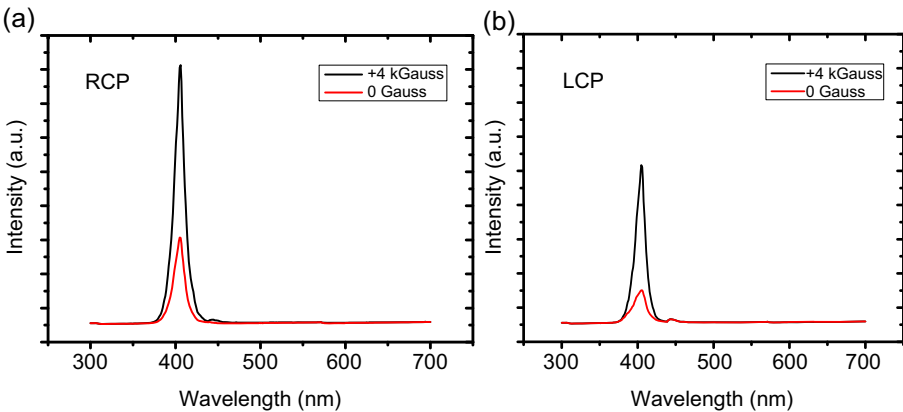


**Figure 10.25** (a) Right and (b) left circularly polarized EL from GaN:Gd-based spin LED (plotted on same scale). Both right and left circularly polarized light are significantly increased by a 4 kGauss applied field.

From Jamil, M., Zaidi, T., Melton, A., Xu, T., Ferguson, I.T., 2011. Ga<sub>1-x</sub>Gd<sub>x</sub>N-based spin polarized light emitting diode. In: MRS Proceedings, 2011, Cambridge Univ Press, mrsf10-1290-i02-05.

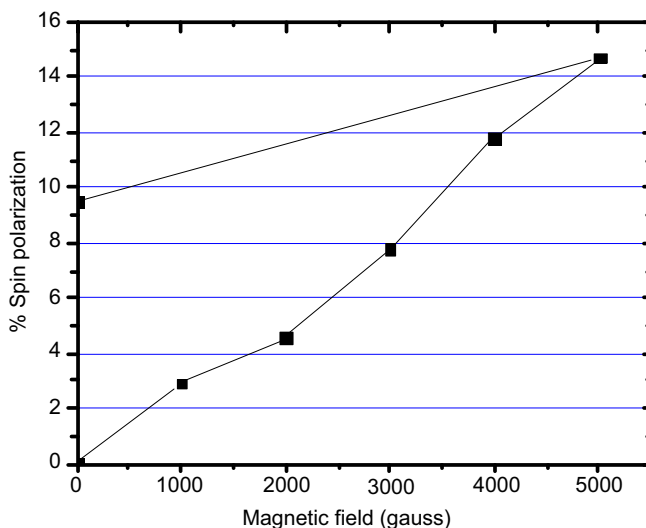


**Figure 10.26** Degree of polarization of EL from  $\text{Ga}_{1-x}\text{Gd}_x\text{N}$ -based LED at sequentially applied magnetic fields (RT).

From Jamil, M., Zaidi, T., Melton, A., Xu, T., Ferguson, I.T., 2011.  $\text{Ga}_{1-x}\text{Gd}_x\text{N}$ -based spin polarized light emitting diode. In: MRS Proceedings, 2011, Cambridge Univ Press, mrsf10-1290-i02-05.

spin injection at RT. This is comparable to the 22.1% polarization at 10,000 Gauss and 10 K reported for a  $\text{Ga}_{1-x}\text{Mn}_x\text{As}$  LED (Kohda et al., 2006).

Fig. 10.26 shows the normalized values of  $P_{\text{spin}}$  for the GaN:Gd LED at sequentially applied magnetic fields. These values form one quadrant of a hysteresis curve starting at 0 Gauss, sweeping up to 5000 Gauss, then back to 0 Gauss. The EL polarization of 14.6% was highest observed in this study at an applied field of 5000 Gauss; however, the EL polarization did not appear to have saturated at this value of field. The final measurement shows a persistent EL polarization of 9.3% after removal of the applied magnetic field, at 0 Gauss. It was found that the sign of the applied magnetic field did not change the sign of the EL spin polarization for this device. Additional studies are needed to fully understand this behavior and to investigate the performance of alternate GaN:Gd-based device structures.

## 10.6 Conclusions

Tremendous progress has been made in the growth of TM- and RE-doped GaN, despite the constraints posed by the solubility limits of these dopants. Based on several theoretical and experimental results it is apparent that the TMs are located deep in the GaN bandgap, making these materials unsuitable for spin injection. Significant effort has been applied to grow  $\text{Ga}_{1-x}\text{Mn}_x\text{N}$  thin films. RT ferromagnetism was obtained for this material and it was shown that the magnetization can be controlled by TM



concentration, Si codoping, and annealing. Further studies have now shown that spinodal decomposition occurs during the growth of transition and RE-doped GaN and nanoclusters (which are difficult to detect with the current characterization) are responsible for the observed magnetization. Furthermore, interesting results were obtained on Gd doping in the nitrides. In MOCVD-grown samples, the magnetization is strongly dependent on the precursor and oxygen contamination is the likely origin of the ferromagnetic signal. Preliminary spin-polarized GaN:Gd-based LEDs were produced, which had a maximum spin polarization of 14.6% at 5000 Gauss and exhibited magnetic hysteresis at RT. The ultimate key to the future utilization of DMS for spintronic applications will be to determine the mechanism behind the observed ferromagnetism and to be able to use the growth techniques to control their properties in a systematic and consistent manner.

## References

- Akai, H., 1998. Ferromagnetism and its stability in the diluted magnetic semiconductor (In,Mn)As. *Physical Review Letters* 81, 3002–3005.
- Akinaga, H., Nemeth, S., De Boeck, J., Nistor, L., Bender, H., Borghs, G., Ofuchi, H., Oshima, M., 2000. Growth and characterization of low-temperature grown GaN with high Fe doping. *Applied Physics Letters* 77, 4377–4379.
- Anderson, P.W., 1950. Antiferromagnetism — theory of superexchange interaction. *Physical Review* 79, 350–356.
- Asahi, H., Zhou, Y.K., Hashimoto, M., Kim, M.S., Li, X.J., Emura, S., Hasegawa, S., 2004. GaN-based magnetic semiconductors for nanospintronics. *Journal of Physics: Condensed Matter* 16.
- Asahi, H., Zhou, Y.K., Emura, S., Hasegawa, S., 2015. Gadolinium-doped III-nitride diluted magnetic semiconductors for spintronics applications (Chapter 11, in this volume).
- Berciu, M., Bhatt, R.N., 2001. Effects of disorder on ferromagnetism in diluted magnetic semiconductors. *Physical Review Letters* 87, 107203.
- Bergqvist, L., Eriksson, O., Kudrnovsky, J., Drchal, V., Korzhavyi, P., Turek, I., 2004. Magnetic percolation in diluted magnetic semiconductors. *Physical Review Letters* 93, 4.
- Bonanni, A., 2007. Ferromagnetic nitride-based semiconductors doped with transition metals and rare earths. *Semiconductor Science and Technology* 22, R41–R56.
- Bonanni, A., Kiecana, M., Simbrunner, C., Li, T., Sawicki, M., Wegscheider, M., Quast, M., Przybylinska, H., Navarro-Quezada, A., Jakiela, R., Wolos, A., Jantsch, W., Dietl, T., 2007. Paramagnetic GaN:Fe and ferromagnetic (Ga,Fe)N: the relationship between structural, electronic, and magnetic properties. *Physical Review B (Condensed Matter and Materials Physics)* 75, 125210–125218.
- Buyanova, I.A., Izadifard, M., Chen, W.M., Kim, J., Ren, F., Thaler, G., Abernathy, C.R., Pearton, S.J., Pan, C.C., Chen, G.T., Chyi, J.I., Zavada, J.M., 2004. On the origin of spin loss in GaMnN/InGaN light-emitting diodes. *Applied Physics Letters* 84, 2599–2601.
- Bimberg, D., Grundmann, M., Ledentsov, N.N., 1999. *Quantum Dot Heterostructures*. John Wiley & Sons, England.
- Cho, Y.S., Kaluza, N., Guzenko, V., Schapers, T., Hardtdegen, H., Bochem, H.P., Breuer, U., Ghadimi, M.R., Fecioru-Morariu, M., Beschoten, B., Luth, H., 2007. The growth of Cr-doped GaN by MOVPE towards spintronic applications. *Physica Status Solidi A Applications and Materials* 204, 72–77.

- Coey, J.M.D., Venkatesan, M., Fitzgerald, C.B., 2005. Donor impurity band exchange in dilute ferromagnetic oxides. *Nature Materials* 4, 173–179.
- Cui, X.Y., Medvedeva, J.E., Delley, B., Freeman, A.J., Newman, N., Stampfl, C., 2005. Role of embedded clustering in dilute magnetic semiconductors: Cr doped GaN. *Physical Review Letters* 95.
- Dalpian, G.M., Wei, S.H., 2006. Carrier-mediated stabilization of ferromagnetism in semiconductors: holes and electrons. *Physica Status Solidi B-Basic Solid State Physics* 243, 2170–2187.
- Dhar, S., Brandt, O., Ramsteiner, M., Sapaga, V.F., Ploog, K.H., 2005a. Colossal magnetic moment of Gd in GaN. *Physical Review Letters* 94.
- Dhar, S., Brandt, O., Trampert, A., Daweritz, L., Friedland, K.J., Ploog, K.H., Keller, J., Beschoten, B., Guntherodt, G., 2003. Origin of high-temperature ferromagnetism in (Ga,Mn)N layers grown on 4H-SiC(0001) by reactive molecular-beam epitaxy. *Applied Physics Letters* 82, 2077–2079.
- Dhar, S., Kammermeier, T., Ney, A., Pérez, L., Ploog, K.H., Melnikov, A., Wieck, A.D., 2006. Ferromagnetism and colossal magnetic moment in Gd-focused ion-beam-implanted GaN. *Applied Physics Letters* 89, 062503.
- Dhar, S., Perez, L., Brandt, O., Trampert, A., Ploog, K.H., Keller, J., Beschoten, B., 2005b. Gd-doped GaN: a very dilute ferromagnetic semiconductor with a Curie temperature above 300 K. *Physical Review B (Condensed Matter and Materials Physics)* 72.
- Dietl, T., 2006. Self-organized growth controlled by charge states of magnetic impurities. *Nature Materials* 9, 673.
- Dietl, T., 2008. Origin and control of ferromagnetism in dilute magnetic semiconductors and oxides (invited). *Journal of Applied Physics* 103, 07D111-1–07D111-6.
- Dietl, T., Ohno, H., 2006. Engineering magnetism in semiconductors. *Materials Today* 9, 18–26.
- Dietl, T., Ohno, H., Matsukura, F., Cibert, J., Ferrand, D., 2000. Zener model description of ferromagnetism in zinc-blende magnetic semiconductors. *Science* 287, 1019–1022.
- Das, G.P., Rao, B.K., Jena, P., Kawazoe, Y., 2006. Dilute Magnetic III-V Semiconductor Spintronics Materials: A First-Principles Approach. Elsevier Science Bv, pp. 84–90.
- Fukushima, T., Sato, K., Katayama-Yoshida, H., Dederichs, P.H., 2006. Spinodal decomposition under layer by layer growth condition and high Curie temperature quasi-one-dimensional nano-structure in dilute magnetic semiconductors. *Japanese Journal of Applied Physics, Part 2: Letters* 45, 416–418.
- Furdyna, J.K., 1988. Dilute magnetic semiconductors. *Journal of Applied Physics* 64, R29–R64.
- Gebicki, W., Strzeszewski, J., Kamler, G., Szyszko, T., Podsiadlo, S., 2000. Raman scattering study of  $\text{Ga}_{1-x}\text{Mn}_x\text{N}$  crystals. *Applied Physics Letters* 76, 3870–3872.
- Getzlaff, M., 2008. *Fundamentals of Magnetism*. Springer, Berlin.
- Gohda, Y., Oshiyama, A., 2008. Intrinsic ferromagnetism due to cation vacancies in Gd-doped GaN: first-principles calculations. *Physical Review B* 78.
- Gosk, J., Zajac, M., Byszewski, M., Kaminska, M., Szczytko, J., Twardowski, A., Strojek, B., Podsiadlo, S., 2003. Magnetic properties of (Ga,Fe)N. *Journal of Superconductivity* 16, 79–82.
- Graf, T., Gjukic, M., Brandt, M.S., Stutzmann, M., Ambacher, O., 2002. The  $\text{Mn}^{3+/2+}$  acceptor level in group III nitrides. *Applied Physics Letters* 81, 5159–5161.
- Gruber, J.B., Vetter, U., Hofsäss, H., Zandi, B., Reid, M.F., 2004. Spectra and energy levels of  $\text{Gd}^{3+}(4f^7)$  in AlN. *Physical Review B* 69, 195202.

- Gupta, S., Zaidi, T., Melton, A., Malguth, E., Yu, H., Liu, Z., Liu, X., Schwartz, J., Ferguson, I.T., 2011. Electrical and magnetic properties of  $\text{Ga}_{1-x}\text{Gd}_x\text{N}$  grown by metal organic chemical vapor deposition. *Journal of Applied Physics* 110, 083920.
- Han, S.Y., Al, E., 2006. Effect of Gd implantation on the structural and magnetic properties of GaN and AlN. *Applied Physics Letters* 88, 042102.
- Harima, H., 2004. Raman studies on spintronics materials based on wide bandgap semiconductors. *Journal of Physics: Condensed Matter* 16, S5653–S5660.
- Hashimoto, M., Yanase, A., Asano, R., Tanaka, H., Bang, H.J., Akimoto, K., Asahi, H., 2003a. Magnetic properties of Eu-doped GaN grown by molecular beam epitaxy. *Japanese Journal of Applied Physics, Part 2: Letters* 42, L1112–L1115.
- Hashimoto, M., Zhou, Y.K., Kanamura, M., Katayama-Yoshida, H., Asahi, H., 2003b. MBE growth and properties of GaCrN. *Journal of Crystal Growth* 251, 327–330.
- Heikman, S., Keller, S., Denbaars, S.P., Mishra, U.K., 2002. Growth of Fe doped semi-insulating GaN by metalorganic chemical vapor deposition. *Applied Physics Letters* 81, 439–441.
- Hejtmánek, J., Knížek, K., Maryško, M., Jiráček, Z., Sedmidubský, D., Sofer, Z., Peřina, V., Hardtdegen, H., Buchal, C., 2008. On the magnetic properties of Gd implanted GaN. *Journal of Applied Physics* 103, 07D107.
- Hite, J., Thaler, G.T., Khanna, R., Abernathy, C.R., Pearton, S.J., Park, J.H., Steckl, A.J., Zavada, J.M., 2006. Optical and magnetic properties of Eu-doped GaN. *Applied Physics Letters* 89, 132119.
- Jamil, M., Zaidi, T., Melton, A., Xu, T., Ferguson, I.T., 2011.  $\text{Ga}_{1-x}\text{Gd}_x\text{N}$ -based spin polarized light emitting diode. In: *MRS Proceedings*, 2011. Cambridge Univ Press mrsf10-1290-i02-05.
- Julier, M., Vinattieri, A., Colocci, M., Lefebvre, P., Gil, B., Scalbert, D., Tran Jr., C.A., K., R.F., Lascaray, J.P., 1999. Slow spin relaxation observed in InGaN/GaN multiple quantum wells. *Physica Status Solidi (B)* 216, 341–345.
- Kammermeier, T., Dhar, S., Ney, V., Manuel, E., Ney, A., Ploog, K.H., Lo, F.-Y., Melnikov, A., Wieck, A.D., 2008. Paramagnetic and ferromagnetic resonance studies on dilute magnetic semiconductors based on GaN. *Physica Status Solidi (A)* 205, 1872–1875.
- Kane, M.H., Asghar, A., Payne, A.M., Vestal, C.R., Strassburg, M., Senawiratne, J., Zhang, Z.J., Dietz, N., Summers, C.R., Ferguson, I.T., 2005a. Magnetic and optical properties of GaMnN grown by metalorganic chemical vapor deposition. *Semiconductor Science & Technology* 20, L5–L9.
- Kane, M.H., Asghar, A., Strassburg, M., Song, Q., Payne, A.M., Summers, C.J., Zhang, Z.J., Dietz, N., Ferguson, I.T., 2005b. Impact of manganese incorporation on the structural and magnetic properties of MOCVD-grown  $\text{Ga}_{1-x}\text{Mn}_x\text{N}$ . *Materials Research Society Proceedings* 831, E9.4.1.
- Kane, M.H., Gupta, S., Fenwick, W.E., Li, N., Park, E.H., Strassburg, M., Ferguson, I.T., 2007. Comparative study of Mn and Fe incorporation into GaN by metalorganic chemical vapor deposition. *Physica Status Solidi A-Applications and Materials Science* 204, 61–71.
- Kane, M.H., Strassburg, M., Asghar, A., Fenwick, W.E., Senawiratne, J., Song, Q., Summers, C.J., Zhang, Z.J., Dietz, N., Ferguson, I.T., 2006. Alloying, co-doping, and annealing effects on the magnetic and optical properties of MOCVD-grown  $\text{Ga}_{1-x}\text{Mn}_x\text{N}$ . *Materials Science and Engineering: B* 126, 230.
- Kartheuser, E., Rodriguez, S., Villeret, M., 1993. Van Vleck paramagnetism of chromium-doped and iron-doped-II-VI semiconductors. *Physical Review B* 48, 14127.
- Kasuya, T., 1956. A theory of metallic ferromagnetism and antiferromagnetism on Zeners model. *Progress of Theoretical Physics* 16, 45–57.
- Katayama-Yoshida, H., Sato, K., Toyoda, M., Kizaki, H., Dinh, V.A., Dederichs, P.H., 2007. *Theory of Ferromagnetic Semiconductors*. Wiley-VCH Verlag GmbH, pp. 15–32.

- Kenyon, A.J., 2002. Recent developments in rare-earth doped materials for optoelectronics. *Progress in Quantum Electronics* 26, 225–284.
- Khaderbad, M.A., Dhar, S., Pérez, L., Ploog, K.H., Melnikov, A., Wieck, A.D., 2007. Effect of annealing on the magnetic properties of Gd focused ion beam implanted GaN. *Applied Physics Letters* 91, 072514.
- Kohda, M., Ohno, Y., Matsukura, F., Ohno, H., 2006. Effect of  $n^+$ -GaAs thickness and doping density on spin injection of GaMnAs/ $n^+$ -GaAs Esaki tunnel junction. *Physica E: Low-Dimensional Systems and Nanostructures* 32, 438–441.
- Korotkov, R.Y., Gregie, J.M., Wessels, B.W., 2002. Optical properties of the deep Mn acceptor in GaN:Mn. *Applied Physics Letters* 80, 1731–1733.
- Kramers, H.A., 1934. L'interaction Entre les Atomes Magnétogènes dans un Cristal Paramagnétique. *Physica* 1, 182–192.
- Kuwabara, S., Ishii, K., Haneda, S., Kondo, T., Munekata, H., 2001. Preparation of wurtzite GaN-based magnetic alloy semiconductors by molecular beam epitaxy. *Physica E: Low-Dimensional Systems and Nanostructures* 10, 233–236.
- Lambrecht, W.R.L., 2015. Electronic structure of magnetic impurities and defects in semiconductors: a guide to the theoretical models (Chapter 2, in this volume).
- Larson, P., Satpathy, S., 2007. Effect of vacancies on ferromagnetism in GaN:Mn dilute magnetic semiconductors from first-principles. *Physical Review B* 76, 8.
- Limmer, W., Ritter, W., Sauer, R., Mensching, B., Liu, C., Rauschenbach, R., 1998. Raman scattering in ion-implanted GaN. *Applied Physics Letters* 72, 2589–2591.
- Lipinska, Z., Pawlowski, M., Zolnierowicz, H., Wysmolek, A., Palczewska, M., Kaminska, M., Twardowski, A., Bockowski, M., Grzegory, I., 2006. Photoluminescence and electron paramagnetic resonance studies of bulk GaN doped with gadolinium. *Acta Physica Polonica A* 110, 243–248.
- Litvinov, V., Dugaev, V., 2001. Ferromagnetism in magnetically doped III-V semiconductors. *Physical Review Letters* 86, 5593–5596.
- Liu, C., Yun, F., Morkoc, H., 2005. Ferromagnetism of ZnO and GaN: a review. *Journal of Materials Science: Materials in Electronics* 16, 555–597.
- Liu, H.X., Wu, S.Y., Singh, R.K., Lin, G., Smith, D.J., Newman, N., Dilley, N.R., Montes, L., Simmonds, M.B., 2004. Observation of ferromagnetism above 900 K in Cr—GaN and Cr—AlN. *Applied Physics Letters* 85, 4076–4078.
- Liu, L., Yu, P.Y., Ma, Z., Mao, S.S., 2008. Ferromagnetism in GaN:Gd: a density functional theory study. *Physical Review Letters* 100, 127203.
- Liu, Z., Yi, X., Wang, J., Kang, J., Melton, A.G., Shi, Y., Lu, N., Wang, J., Li, J., Ferguson, I., 2012. Ferromagnetism and its stability in n-type Gd-doped GaN: first-principles calculation. *Applied Physics Letters* 100, 232408.
- Mahadevan, P., Zunger, A., 2004. Trends in ferromagnetism, hole localization, and acceptor level depth for Mn substitution in GaN, GaP, GaAs, and GaSb. *Applied Physics Letters* 85, 2860–2862.
- Malguth, E., Hoffmann, A., Gehlhoff, W., Gelhausen, O., Phillips, M.R., Xu, X., 2006. Structural and electronic properties of  $Fe^{3+}$  and  $Fe^{2+}$  centers in GaN from optical and EPR experiments. *Physical Review B* 74.
- Mitra, C., Lambrecht, W.R., 2009. Interstitial-nitrogen- and oxygen-induced magnetism in Gd-doped GaN. *Physical Review B* 80, 081202.
- Nagahara, S., Arita, M., Arakawa, Y., 2005. Long-lived electron spins in  $In_xGa_{1-x}N$  multiquantum well. *Applied Physics Letters* 86, 242103–242111.
- Newman, N., Wu, S.Y., Liu, H.X., Medvedeva, J., Gu, L., Singh, R.K., Yu, Z.G., Krainsky, I.L., Krishnamurthy, S., Smith, D.J., Freeman, A.J., van Schilfhaarde, M., 2006. Recent

- progress towards the development of ferromagnetic nitride semiconductors for spintronic applications. *Physica Status Solidi A-Applications and Materials Science* 203, 2729–2737.
- Ney, A., 2015. Gadolinium-doped gallium-nitride (GaN:Gd): synthesis routes, structure and magnetism (Chapter 6, in this volume).
- Ney, A., Kammermeier, T., Ney, V., Ye, S., Ollefs, K., Manuel, E., Dhar, S., Ploog, K.H., Arenholz, E., Wilhelm, F., 2008. Element specific magnetic properties of Gd-doped GaN: very small polarization of Ga and paramagnetism of Gd. *Physical Review B* 77, 233308.
- Ofuchi, H., Oshima, M., Tabuchi, M., Takeda, Y., Akinaga, H., Nemeth, S., De Boeck, J., Borghs, G., 2001. Fluorescence X-ray absorption fine structure study on local structures around Fe atoms heavily doped in GaN by low-temperature molecular-beam epitaxy. *Applied Physics Letters* 78, 2470–2472.
- Ohno, H., 1998. Making nonmagnetic semiconductors ferromagnetic. *Science* 281, 951–956.
- Ohno, H., Matsukura, F., 2001. A ferromagnetic III-V semiconductor: (Ga,Mn)As. *Solid State Communications* 117, 179–186.
- Ohno, H., Shen, A., Matsukura, F., Oiwa, A., Endo, A., Katsumoto, S., Iye, Y., 1996. (Ga,Mn)As: a new diluted magnetic semiconductor based GaAs. *Applied Physics Letters* 69, 363–365.
- Ohno, Y., Young, D.K., Beschoten, B., Matsukura, F., Ohno, H., Awschalom, D.D., 1999. Electrical spin injection in a ferromagnetic semiconductor heterostructure. *Nature* 402, 790–792.
- Overberg, M.E., Abernathy, C.R., Pearton, S.J., Theodoropoulou, N.A., McCarthy, K.T., Hebard, A.F., 2001. Indication of ferromagnetism in molecular-beam-epitaxy-derived n-type GaMnN. *Applied Physics Letters* 79, 1312–1314.
- Park, S.E., Lee, H.-J., Cho, Y.C., Jeong, S.-Y., Cho, C.R., Cho, S., 2002. Room-temperature ferromagnetism in Cr-doped GaN single crystals. *Applied Physics Letters* 80, 4187.
- Pearton, S.J., Norton, D.P., Frazier, R., Han, S.Y., Abernathy, C.R., Zavada, J.M., 2005. Spintronics device concepts. *IEE Proceedings-Circuits, Devices and Systems* 152, 312–322.
- Polyakov, A.Y., Smirnov, N.B., Govorkov, A.V., Jihyun, K., Ren, F., Thaler, G.T., Overberg, M.E., Frazier, R., Abernathy, C.R., Pearton, S.J., Lee, C.M., Chyi, J.I., Wilson, R.G., Zavada, J.M., 2003a. Comparison of the electrical and luminescent properties of p-layer-up and n-layer-up GaN/InGaN light emitting diodes and the effects of Mn doping of the upper n-layer. *Solid-State Electronics* 47, 981–987.
- Polyakov, A.Y., Smirnov, N.B., Govorkov, A.V., Kim, J., Ren, F., Overberg, M.E., Thaler, G., Abernathy, C.R., Pearton, S.J., Lee, C.-M., Chyi, J.-I., Wilson, R.G., Zavada, J.M., 2003b. Electrical and electroluminescent properties of GaN light emitting diodes with the contact layer implanted with Mn. *Solid State Electronics* 47, 963–968.
- Polyakov, A.Y., Smirnov, N.B., Govorkov, A.V., Pashkova, N.V., Shlensky, A.A., Pearton, S.J., Overberg, M.E., Abernathy, C.R., Zavada, J.M., Wilson, R.G., 2003c. Electrical and optical properties of Cr and Fe implanted n-GaN. *Journal of Applied Physics* 93, 5388–5396.
- Przybylinska, H., Bonanni, A., Wolos, A., Kiecana, M., Sawicki, M., Dietl, T., Malissa, H., Simbrunner, C., Wegscheider, M., Sitter, H., 2006. Magnetic properties of a new spintronic material—GaN:Fe. *Materials Science and Engineering: B* 126.
- Rao, B.K., Jena, P., 2002. Giant magnetic moments of nitrogen-doped Mn clusters and their relevance to ferromagnetism in Mn-doped GaN. *Physical Review Letters* 89, 185504.
- Reed, M.J., Arkun, F.E., Berkman, E.A., Elmasry, N.A., Zavada, J., Luen, M.O., Reed, M.L., Bedair, S.M., 2005. Effect of doping on the magnetic properties of GaMnN: Fermi level engineering. *Applied Physics Letters* 86, 102504.

- Reed, M.L., El-Masry, N.A., Stadelmaier, H.H., Ritums, M.K., Reed, M.J., Parker, C.A., Roberts, J.C., Bedair, S.M., 2001. Room temperature ferromagnetic properties of (Ga, Mn)N. *Applied Physics Letters* 79, 3473–3475.
- Ruderman, M.A., Kittel, C., 1954. Indirect exchange coupling of nuclear magnetic moments by conduction electrons. *Physical Review* 96, 99–102.
- Stöhr, J., Siegmann, H.C., 2006. *Magnetism: From Fundamentals to Nanoscale Dynamics*. Springer, Berlin.
- Sapega, V.F., Ramsteiner, M., Dhar, S., Brandt, O., Ploog, K.H., 2005. Large spin splitting of GaN electronic states induced by Gd doping. *Journal of Physics: Condensed Matter* 0509198.
- Sarigiannidou, E., Wilhelm, F., Monroy, E., Galera, R.M., Bellet-Amalric, E., Rogalev, A., Goulon, J., Cibert, J., Mariette, H., 2006. Intrinsic ferromagnetism in wurtzite (Ga,Mn)N semiconductor. *Physical Review B (Condensed Matter and Materials Physics)* 74, 041306.
- Sato, K., Dederichs, P.H., Katayama-Yoshida, H., Kudrnovsky, J., 2003a. Magnetic impurities and materials design for semiconductor spintronics. *Physica B* 340–342, 863–869.
- Sato, K., Katayama-Yoshida, H., Dederichs, P.H., 2003b. Curie Temperatures of III-V Diluted Magnetic Semiconductors Calculated from First-Principles in Mean Field Approximation. Kluwer Academic/Plenum Publishers, pp. 31–35.
- Sato, K., Schweika, W., Dederichs, P.H., Katayama-Yoshida, H., 2004. Low-temperature ferromagnetism in (Ga, Mn)N: ab initio calculations. *Physical Review B* 70, 4.
- Shanthi, S., Hashimoto, M., Zhou, Y.K., Kimura, S., Kim, M.S., Emura, S., Hasuike, N., Harima, H., Hasegawa, S., Ishimaru, M., Hirotsu, Y., Asahi, H., 2005. Polymorphism in the ferromagnetic GaCrN-diluted magnetic semiconductor: luminescence and structural investigations. *Journal of Applied Physics* 98, 013526.
- Shon, Y., Kwon, Y.H., Park, Y.S., Yuldashev, S.U., Lee, S.J., Park, C.S., Chung, K.J., Yoon, S.J., Kim, H.J., Lee, W.C., Fu, D.J., Kang, T.W., Fan, X.J., Park, Y.J., Oh, H.T., 2004. Ferromagnetic behavior of p-type GaN epilayer implanted with Fe<sup>+</sup> ions. *Journal of Applied Physics* 95, 761–763.
- Sonoda, S., Hori, H., Yamamoto, Y., Sasaki, T., Sato, M., Shimizu, S., Suga, K.-I., Kindo, K., 2002. Properties of ferromagnetic Ga<sub>1-x</sub>Mn<sub>x</sub>N films grown by ammonia-MBE. *Magnetics, IEEE Transactions on* 38, 2859–2862.
- Soo, Y.L., Kioseoglou, G., Kim, S., Huang, S., Kao, Y.H., Kuwabara, S., Owa, S., Kondo, T., Munekata, H., 2001. Local structure and chemical valency of Mn impurities in wide-band-gap III–V magnetic alloy semiconductors Ga<sub>1-x</sub>Mn<sub>x</sub>N. *Applied Physics Letters* 79, 3926–3928.
- Steckl, A.J., Heikenfeld, J., Lee, D.S., Garter, M., 2001. Multiple color capability from rare earth-doped gallium nitride. *Materials Science and Engineering B* 81, 97–101.
- Steckl, A.J., Heikenfeld, J.C., Lee, D.S., Garter, M.J., Baker, C.C., Wang, Y.Q., Jones, R., 2002. Rare-earth-doped GaN: growth, properties, and fabrication of electroluminescent devices. *IEEE Journal of Selected Topics in Quantum Electronics* 8, 749–766.
- Strassburg, M., Senawirante, J., Hums, C., Dietz, N., Kane, M.H., Asghar, A., Payne, A.M., Ferguson, I.T., Summers, C.J., Haboeck, U., Hoffman, A., Azamat, D., Gelhoff, W., 2005. Optical and structural investigations on Mn-ion states in MOCVD-grown Ga<sub>1-x</sub>Mn<sub>x</sub>N. *MRS Proceedings* 831, E9.5.1.
- Subashchandran, S., Kimura, S., Kim, M.S., Kobayashi, S., Zhou, Y.K., Hasegawa, S., Asahi, H., 2006. Nature of deep-level defects in GaCrN diluted magnetic semiconductor. *Japanese Journal of Applied Physics Part 1-Regular Papers Brief Communications & Review Papers* 45, 3522–3525.

- van Schilfgaarde, M., Mryasov, O.N., 2001. Anomalous exchange interactions in III-V dilute magnetic semiconductors. *Physical Review B* 63, 233205.
- Tanaka, S., Takeuchi, M., Aoyagi, Y., 2000. Anti-surfactant in III-nitride epitaxy – quantum dot formation and dislocation termination. *Japanese Journal of Applied Physics, Part 2: Letters* 39, 831–834.
- Teraguchi, N., Suzuki, A., Nanishi, Y., Zhou, Y.-K., Hashimoto, M., Asahi, H., 2002. Room-temperature observation of ferromagnetism in diluted magnetic semiconductor GaGdN grown by RF-molecular beam epitaxy. *Solid State Communications* 122.
- Thaler, G.T., Frazier, R.M., Stapleton, J., Abernathy, C.R., Pearton, S.J., Kelly, J., Rairigh, R., Hebard, A.F., Zavada, J.M., 2004. Properties of GaMnN with and without detectable second phases. *Electrochemical and Solid-State Letters* 7, G34–G36.
- Theodoropoulou, N., Hebard, A.F., Chu, S.N.G., Overberg, M.E., Abernathy, C.R., Pearton, S.J., Wilson, R.G., Zavada, J.M., 2001a. Characterization of high dose Fe implantation into p-GaN. *Applied Physics Letters* 79, 3452–3454.
- Theodoropoulou, N., Hebard, A.F., Overberg, M.E., Abernathy, C.R., Pearton, S.J., Chu, S.N.G., Wilson, R.G., 2001b. Magnetic and structural properties of Mn-implanted GaN. *Applied Physics Letters* 78, 3475–3477.
- Van de Walle, C.G., Neugebauer, J., 2004. First-principles calculations for defects and impurities: applications to III-nitrides. *Journal of Applied Physics* 95, 3851–3879.
- Venkatesan, M., Fitzgerald, C.B., Lunney, J.G., Coey, J.M.D., 2004. Anisotropic ferromagnetism in substituted zinc oxide. *Physical Review Letters* 93, 177206.
- Wang, K.Y., Champion, R.P., Edmonds, K.W., Sawicki, M., Dietl, T., Foxon, C.T., Gallagher, B.L., 2005. Magnetism in (Ga,Mn)As Thin Films with TC up to 173 K. USA AIP, Flagstaff, AZ, pp. 333–334.
- Wang, Q., Sun, Q., Rao, B.K., Jena, P., Kawazoe, Y., 2003. Nitrogen-induced magnetic transition in small chromium clusters. *Journal of Chemical Physics* 119, 7124–7130.
- Wolf, S.A., Awschalom, D.D., Buhrman, R.A., Daughton, J.M., Von Molnar, S., Roukes, M.L., Chtchelkanova, A.Y., Treger, D., 2001. Spintronics, a spin-based electronics vision for the future. *Science* 294, 1488–1495.
- Wolf, S.A., Chtchelkanova, A.Y., Treger, D.M., 2006. Spintronics- a retrospective and perspective. *IBM Journal of Research and Development* 50, 101–110.
- Yamamoto, T., Marcet, S., Gheeraert, E., Kuroda, S., Mariette, H., Ferrand, D., Cibert, J., 2005. *Journal of Crystal Growth* 275, e2233.
- Yosida, K., 1957. Magnetic properties of Cu-Mn alloys. *Physical Review* 1, 893–898.
- Zajac, M., Doradzinski, R., Gosk, J., Szczytko, J., Lefeld-Sosnowska, M., Kaminska, M., Twardowski, A., Palczewska, M., Grzanka, E., Gebicki, W., 2001a. Magnetic and optical properties of GaMnN magnetic semiconductor. *Applied Physics Letters* 78, 1276–1278.
- Zajac, M., Gosk, J., Kaminska, M., Twardowski, A., Szyszko, T., Podsiadlo, S., 2001b. Paramagnetism and antiferromagnetic d–d coupling in GaMnN magnetic semiconductor. *Applied Physics Letters* 79, 2432–2434.
- Zener, C., 1951. Interaction between the d shells in transition metals. II. Ferromagnetic compounds of manganese with Perovskite structure. *Physical Review* 82, 403–405.
- Zhong, G.H., Lwang, J., Zeng, Z., 2008. Electronic and magnetic structures of 4f in  $\text{Ga}_{1-x}\text{Gd}_x\text{N}$ . *Journal of Physics-Condensed Matter* 20, 295221–295227.
- Zhou, Y.K., Choi, S.W., Emura, S., Hasegawa, S., Asahi, H., 2008. Large magnetization in high Gd concentration GaGdN and Si-doped GaGdN grown at low temperatures. *Applied Physics Letters* 92.
- Zhou, Y.K., Choi, S.W., Kimura, S., Emura, S., Hasegawa, S., Asahi, H., 2007. High Gd concentration GaGdN grown at low temperatures. *Journal of Superconductivity and Novel Magnetism* 429–432.

# Gadolinium-doped III-nitride diluted magnetic semiconductors for spintronics applications

11

H. Asahi, Y.K. Zhou, S. Emura, S. Hasegawa  
Osaka University, Osaka, Japan

## 11.1 Introduction

Diluted magnetic semiconductors (DMSs) have been gathering much interest from the industrial viewpoint because of their potentiality as a new functional material, which will open a way to fabricate novel functional semiconductor devices. For the device application, it is very important that the Curie temperature ( $T_C$ ) of DMSs should be higher than room temperature (RT). GaMnAs is a well-investigated and well-established DMS [1]. However, the  $T_C$  for the GaMnAs is still  $\sim 160$  K [2] and is much lower than RT.

Theoretical calculations suggested that the transition metal-doped GaN will exhibit RT ferromagnetism [3,4]. Mn-doped GaN was grown by molecular beam epitaxy (MBE) and observed high-temperature ferromagnetic (FM) characteristics with  $T_C$  as high as 940 K [5]. Cr-doped GaN was also grown by MBE and observed high-temperature ( $>400$  K) FM characteristics [6] as well as the photoluminescence (PL) emission [7]. The observation of PL emission at RT is important to fabricate practical spintronic devices that control charges, photons, and spins; this is in contrast to GaMnAs, where no PL emission was observed. High-temperature FM characteristics were also reported by many other groups [8,9]. The observation of FM characteristics was attributed to double exchange interaction by ab initio computations. However, the first principles Monte Carlo simulations suggested that the magnetic exchange interactions in wide bandgap DMSs are effectively short range and the calculated  $T_C$  should be low for the low concentrations of magnetic ions and in the absence of delocalized or weakly localized carriers [10]. Considering the spinodal decomposition into one-dimensional high concentration of magnetic ions (*Konbu* phase), high-temperature FM characteristics were simulated [11].

Rare earth (RE)-doped semiconductors are widely studied for the application to photonic devices. However, the first observation of high-temperature FM characteristics was reported for the MBE-grown Gd (gadolinium)-doped GaN with  $T_C > 400$  K, similar to GaCrN [12]. Since then, extensive studies have been conducted theoretically [13–17] and experimentally on the magnetic semiconductor GaGdN prepared by various techniques, which include MBE [18–21], metal organic vapor phase epitaxy (MOVPE) [22], as well as via Gd ion implantation into GaN [23,24]. In addition, ferromagnetism with incredibly high values of  $T_C$  ( $T_C \sim 700$  K) was reported in GaGdN



films [25]. The enhancement of magnetization by Si codoping was reported [24,26]. On the other hand, Dhar et al. reported the colossal magnetic moment in the low Gd concentration ( $10^{16}$ – $10^{18}$  cm $^{-3}$ ) of GaGdN grown by MBE and explained within the framework of the phenomenological model [27]. They also reported the colossal magnetic moment in the low Gd concentration ( $10^{16}$ – $10^{18}$  cm $^{-3}$ ) of the Gd-implanted GaGdN [28]. The origin of the FM order was attributed to the polarization of the surrounding host medium, interstitial nitrogen, and oxygen-induced or electron-mediated ferromagnetism [14,29].

Examples of the semiconductor spintronic devices are tunnel magnetoresistance (TMR) devices, circular-polarized laser diodes (CP-LDs), and spin field effect transistors. CP-LDs are one of important devices to realize the optical communication systems that are resistant to wiretapping. CP-LDs can be fabricated by using the DMS as an active layer or a cladding layer. CP-LDs are also important devices to construct the information processing systems by the combination of circular-polarized light-controlled TMR devices. Bhattacharya et al. [30] reported the fabrication of CP-LDs by using vertical-cavity surface-emitting laser structure with GaMnAs DMS layer as spin-polarized carrier (hole) supplying layer and the observation of circular-polarized light at a low temperature (LT) of 80 K because of low  $T_C$  of GaMnAs. To fabricate practical CP-LDs, RT FM DMS is requisite. The Gd- and dysprosium (Dy)-doped III-nitride DMS exhibited the RT FM characteristics as well as PL emission and conducting characteristics. Therefore we can expect to fabricate the spintronic devices operating at RT.

In this chapter, we will describe the experimental results for the Gd- and Dy-doped III-nitride DMSs so far reported until now.

## 11.2 Growth and structural properties of Gd-doped III-nitride semiconductors

RE-doped III-nitride semiconductors and their superlattice (SL) structures were grown on sapphire (0001) substrates and MOVPE-grown GaN (0001) templates after the growth of GaN buffer layer by plasma-assisted MBE. Elemental Ga, In, Gd, and Dy, and plasma-enhanced N $_2$  were used as sources. Growth temperature was 600–700°C for most samples, while the LT growth was also conducted to increase the RE atom concentration. Si codoping into (In)GaGdN layers and GaN barrier layers of SL structures were also carried out.

X-ray diffraction (XRD) curves for the GaGdN layers with Gd concentration of 0–7.8% are shown in Fig. 11.1(a) [31]. No diffraction peaks from secondary phases are observed for the samples with 0–6% Gd concentrations. Only 7.8% sample exhibits additional peaks assigned as NaCl-type GdN (111) and GdN (222). Expanded XRD curves near GaGdN (0004) diffraction are shown in Fig. 11.1(b). The peak position for the GaGdN shifts to lower angle as Gd concentration increases up to 5.8%, indicating that the lattice constant  $c$  in the  $c$ -direction increases with the increase of GdN content  $x$ , as can be seen in Fig. 11.1(c). This tendency agrees with the larger atomic diameter of

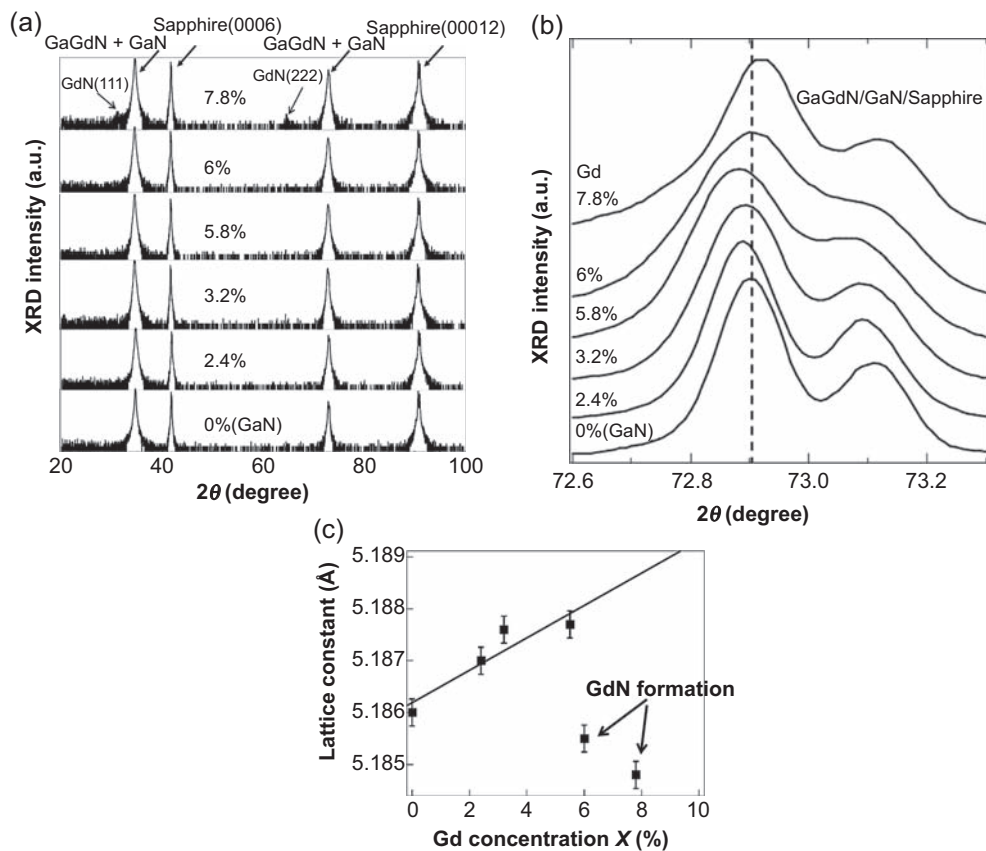


**Figure 11.1** (a) XRD curves for GaGdN layers with Gd concentration of 0–7.8%, (b) expanded XRD curves near GaGdN (0004) diffraction, (c) lattice constant  $c$  as a function of Gd concentration.

After Asahi H, Hasegawa S, Zhou YK, Emura S. Proceedings of 2010 fall MRS meeting; 2010. p. 110205e.

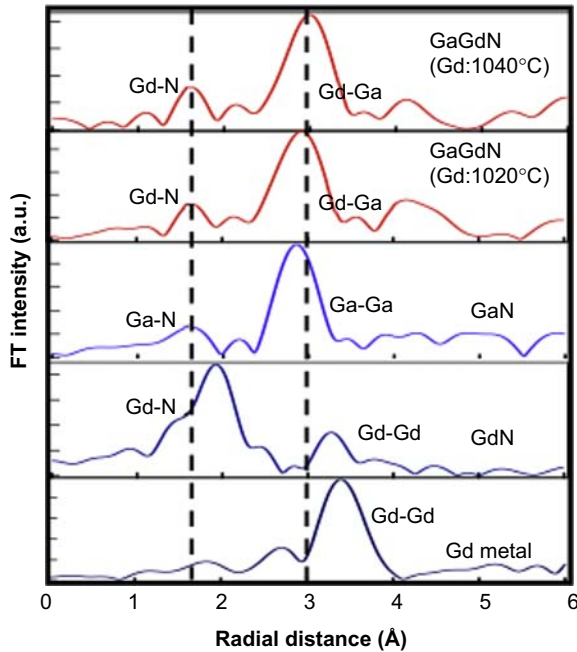


**Figure 11.2** Radical distribution functions for GaGdN samples calculated with the XAFS data. For comparison, those of GaN, NaCl-type GdN, and metal Gd are also shown. After Asahi H, Hasegawa S, Zhou YK, Emura S. Proceedings of 2010 fall MRS meeting; 2010. p. 110205e.

Gd than that of Ga. Fig. 11.1(b) and (c) show that for the Gd concentration higher than 6% the diffraction peak and lattice constant again approach those of GaN. This indicates that the lattice relaxation occurred for these Gd concentrations.

X-ray absorption fine structure (XAFS) measurements were conducted to study the Gd atom substitution of Ga site in GaGdN samples [31]. Radical distribution functions for GaGdN samples calculated with the XAFS data are shown in Fig. 11.2. The first nearest (N) and second nearest (Ga) atom peaks from the Gd atom agree well with those of GaN (*middle curve*) and are clearly different from those of NaCl-type GaN and Gd metal (*lower two curves*). This clearly indicates that the most of Gd atoms substitute the Ga sites. The substitutional incorporation of Gd atoms into InGaGdN layer was also confirmed by XAFS [32].

## 11.3 Properties of Gd-doped III-nitride semiconductors

### 11.3.1 Magnetic and optical properties of single layers

Magnetization versus magnetic field ( $M$ - $H$ ) curves for the GaGdN sample at 7 and 300 K are shown in Fig. 11.3(a) [12]. The magnetic field is parallel to the sample

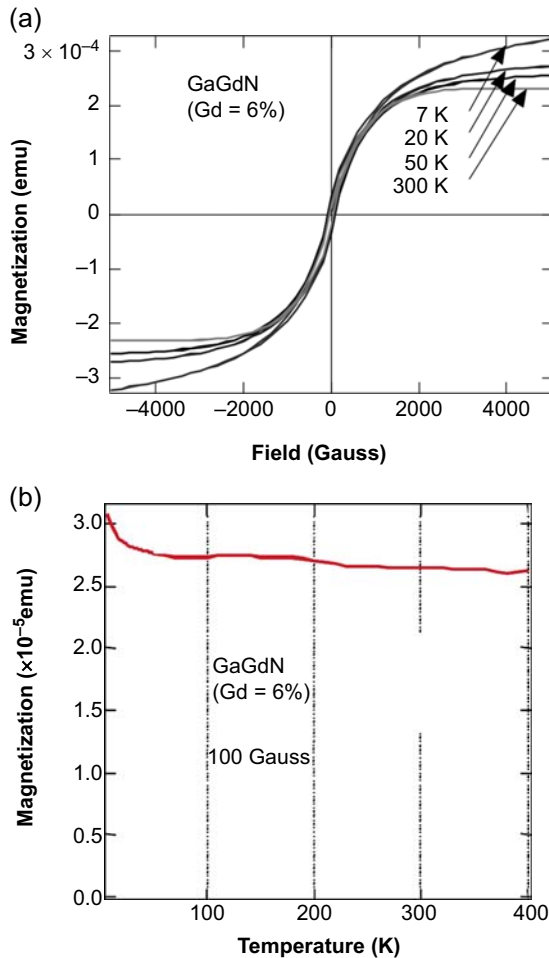


**Figure 11.3** (a)  $M$ - $H$  curves for the GaGdN sample at 7–300 K. (b) Temperature dependence of magnetization for the GaGdN sample at applied magnetic field of 100 G. After Teraguchi N, Suzuki A, Nanishi Y, Zhou YK, Hashimoto M, Asahi H. *Solid State Commun* 2002;122:651.

plane. Hysteresis curves are observed at both temperatures. This indicates that the GaGdN is FM at both temperatures. The saturation field was about 2 T and the coercivity  $H_c$  was about 0.07 T (70 Oe) at 300 K.

Temperature dependence of magnetization at applied magnetic field of 100 G is shown in Fig. 11.3(b) [12]. The magnetization decreases slowly with increasing temperature and remains even at 400 K and there was no discontinuous change in the curve. This indicates that  $T_C$  of GaGdN is higher than 400 K.

To fabricate the long wavelength spin-controlled photonic devices, InGaGdN layers were also grown on MOVPE-grown GaN (0001) template substrates at

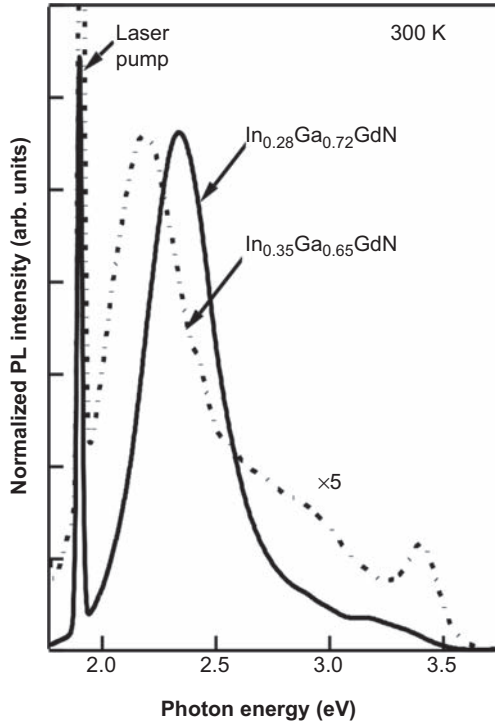


**Figure 11.4** RT PL spectra taken for the InGaGdN layers of different InN molar fractions (InN molar fraction of 35%, *broken line*; and InN molar fraction of 28%, *solid line*). After Asahi H, Hasegawa S, Zhou YK, Emura S. *J Lumin* 2012;132:3136.

400°C [32]. Fig. 11.4 shows RT PL spectra for the InGaGdN layers with different In compositions [33]. Both samples contain about  $\sim 1\%$  of Gd concentrations. For the samples with the In composition of 28% and 35%, the emission peaks are observed at 2.38 and 2.19 eV, respectively. The peak energy is red-shifted according to their InN molar fractions.

PL spectra for the InGaGdN (In: 23%, Gd:  $\sim 1\%$ ) sample as a function of temperature are shown in Fig. 11.5 [33]. PL emission is clearly observed at all measuring temperatures (10–300 K). The temperature variation of PL peak energy exhibits S-shaped behavior (redshift—blueshift—redshift) with increasing temperature, which is attributed to localized excitonic emission due to inhomogeneity and carrier localization in InGaGdN alloys with the consideration of the band-tail approach [33]. This temperature variation is similar to those for the InGaN layers without Gd doping.

*M-H* curves for the InGaGdN single-layer samples with different Gd concentrations exhibit clear hysteresis and saturation magnetization ( $M_S$ ) at RT, as shown in Fig. 11.6 [34]. Even clear hysteresis can be further observed from the expanded curve of both samples as shown in the inset of Fig. 11.6. It shows that the saturation magnetization increases with the increase in Gd concentration. With the increase of magnetic Gd atoms, the FM interaction is increased.

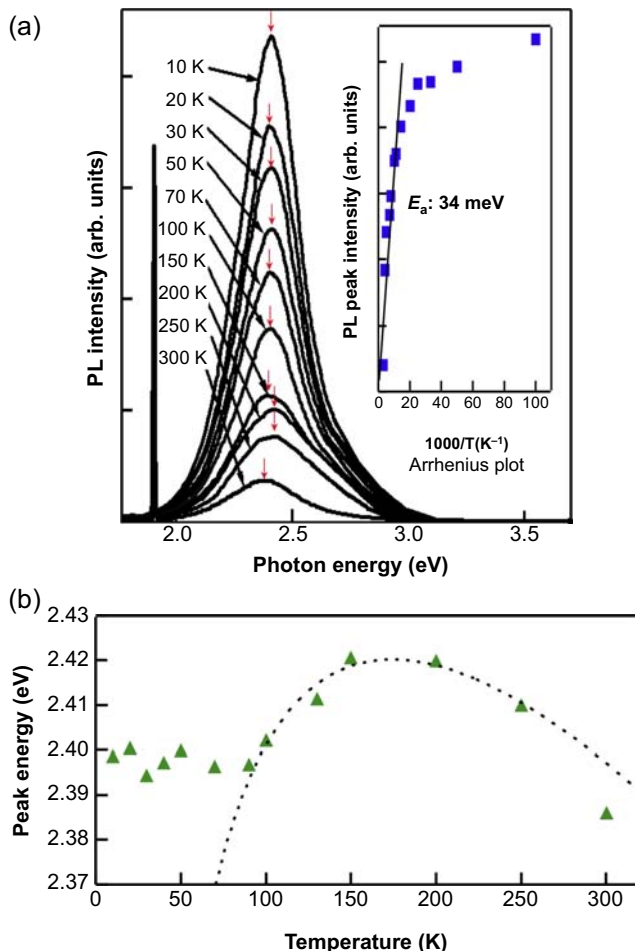
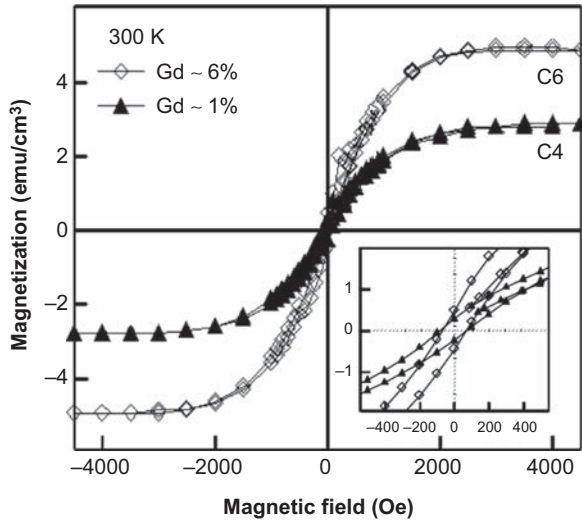


**Figure 11.5** (a) PL spectra for the InGaGdN sample (In: 28%, Gd:  $\sim 1\%$ ) as a function of temperature. (b) Temperature variation of PL peak energy.

After Asahi H, Hasegawa S, Zhou YK, Emura S. *J Lumin* 2012;132:3136.

### 11.3.2 Effect of low-temperature growth

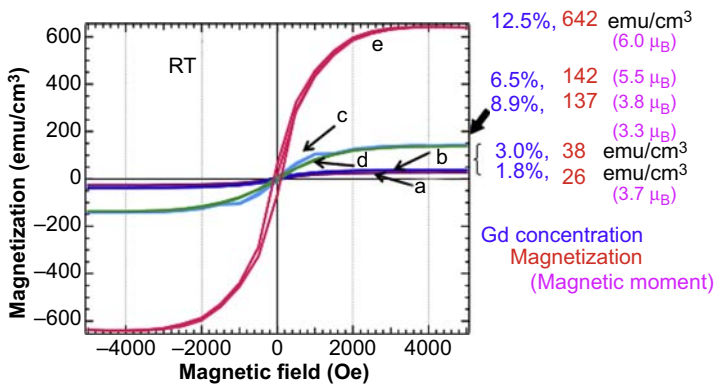
To increase the incorporated Gd concentration without secondary phase formation and to enhance the magnetization, GaGdN layers were grown at LT of  $300^{\circ}\text{C}$  on sapphire (0001) substrates [26]. XRD  $\theta-2\theta$  scan curves for the LT-grown GaGdN samples showed diffraction peaks from sapphire and GaGdN, but no obvious secondary phase such as GdN was detected. XRD peak from the GaGdN layer showed single crystalline characteristics, though the full width at half maximum is about twice of GaGdN layer grown at  $700^{\circ}\text{C}$  [26]. By LT-growth, GaGdN layers with Gd concentration as high as 12.5% and no secondary phases were obtained. When the growth was conducted at  $700^{\circ}\text{C}$ , the highest Gd concentration is about 5.8%. Radical distribution function



**Figure 11.6** RT  $M$ - $H$  curves for the InGaGdN films with 1% and 6% Gd concentration. (After Tawil SNM, Krishnamurthy D, Kakimi R, Emura S, Hasegawa S, Asahi H. *J Cryst Growth* 2011;323:351.) Inset shows the expanded  $M$ - $H$  curves in the low magnetic field region.

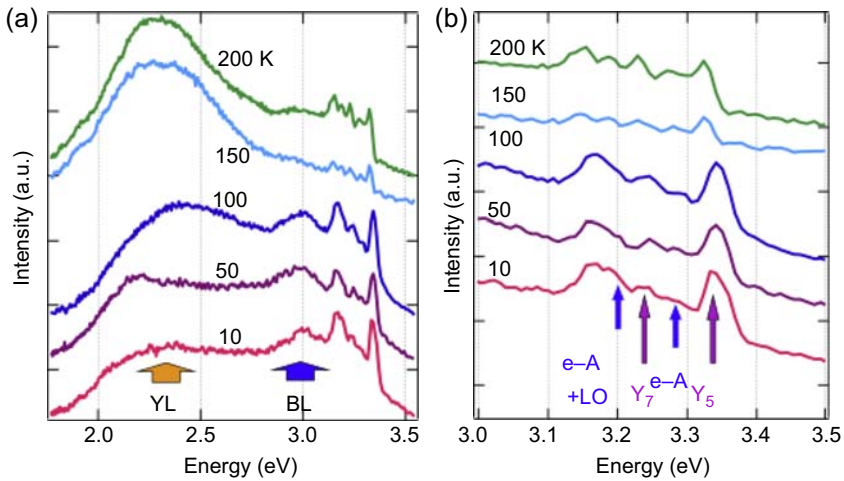
obtained by the XAFS measurement clearly showed that the Gd atoms substitute the Ga sites [26].

Fig. 11.7 shows the RT  $M$ - $H$  curves for the GaGdN layers grown at 300°C with different Gd concentrations [26]. With increasing Gd concentration, magnetization per unit volume is increased. Theoretical calculations [13,14] showed that the spinglass state is stable for the GaGdN without carriers, but electron doping into



**Figure 11.7**  $M$ - $H$  curves at RT for the LT (300°C)-grown GaGdN samples with different Gd concentrations. Samples a–e are GaGdN with Gd concentrations of 1.8%, 3.0%, 6.5%, 8.9%, and 12.5%, respectively.

After Zhou YK, Choi SW, Emura S, Hasegawa S, Asahi H. *Appl Phys Lett* 2008;92:062505.



**Figure 11.8** PL spectra for the LT (300°C) grown GaGdN layer as a function of temperature. (After Asahi H, Hasegawa S, Zhou YK, Emura S. *Proceedings of 2010 fall MRS meeting; 2010. p. 110205e.*) (a) PL spectra in the wide photon energy range (1.8–3.6 eV), (b) those in the narrow range (3.0–3.5 eV).

GaGdN enhances the FM interaction in GaGdN. It is possible that the carriers (electrons) coming from some types of defects such as nitrogen vacancies enhance the ferromagnetism in GaGdN layers.

From LT-grown GaGdN samples, PL emission was observed in the photon energy range of 2–3.5 eV as shown in Fig. 11.8 [31]. Most emission peaks are related to defects. Yellow and blue broad luminescence peaks are observed at 2.28 and 3.0 eV, respectively, in Fig. 11.8(a). In the expanded energy figure (Fig. 11.8(b)),  $Y_5$  and  $Y_7$  exciton bound to structural defect emissions as well as e-A related emissions are also observed at 3.34, 3.23, and 3.28 eV, respectively.

### 11.3.3 Effect of superlattice structures on magnetic properties

GaGdN/GaN SLs having various GaGdN and GaN layer thicknesses were grown on sapphire (0001) substrates [19,21].  $M$ - $H$  measurements for the 230-nm-thick GaGdN bulk layer and the GaGdN/GaN SL samples having nearly the same total thickness of GaGdN (Gd concentration: 1.2%) showed the clear hysteresis and saturation (FM characteristics). The magnetization for the SL samples is larger than that for bulk sample [19]. Furthermore, the thinner each GaGdN QW layer thickness is or the thicker each GaN barrier layer thickness is, a larger magnetic moment per Gd atom was observed as shown in Fig. 11.9 [21]. In Fig. 11.9(a), the GaN layer thickness is kept constant at 3.8 nm and the GaGdN thickness is varied from 1.1 to 2.9 nm. With decreasing the GaGdN layer thickness, the magnetic moment per Gd atom is increased. In Fig. 11.9(b), the GaGdN layer thickness is kept constant at 1.3 nm and the GaN thickness is varied from 2.2 to 10.8 nm. With increasing the GaN layer thickness, the magnetic moment per Gd atom is increased.



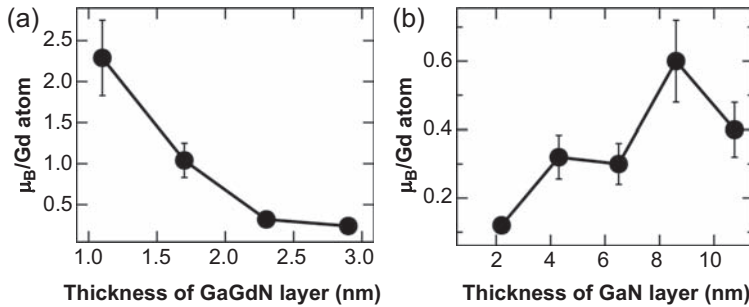


**Figure 11.9** Magnetic moment per Gd atom at RT for the GaGdN/GaN SLs as a function of (a) GaGdN and (b) GaN layer thickness with constant thickness of (a) GaN and (b) GaGdN layer, respectively.

After Zhou YK, Choi SW, Kimura S, Emura S, Hasegawa S, Asahi H. Thin Solid Films 2010; 518:5659.

It is expected that electron carriers in GaN layers flow into and accumulate in the narrower bandgap GaGdN layers resulting in higher electron concentration ( $>10^{18} \text{ cm}^{-3}$ ) in the thinner GaGdN layers. Especially, the distribution of Gd atoms is inhomogeneous in the layer [26], so that local areas having higher Gd concentration would have very high electron concentration in the GaGdN layers. The stronger interaction between Gd spins through the electron spins is expected in the thinner GaGdN layer. Therefore the observed enhanced magnetic moment can be understood with the carrier-mediated ferromagnetism.

Similar enhanced magnetization was also observed on the InGaGdN/GaN SL samples compared with that for the InGaGdN single-layer (thickness: 100 nm), as shown in Fig. 11.10 [33]. Both samples were grown under similar growth conditions except for the sample structure. The magnetic properties of these samples show clear saturation magnetization at about 16 and 7 emu/cm<sup>3</sup> for the SL sample and single-layer sample, respectively. In the SLs, electron carriers can flow into narrow bandgap InGaGdN well layers from the wider bandgap GaN layers. These increased carrier concentrations improve the magnetization.

However, in the InGaN/GaGdN SL structures the magnetization was decreased. Such observation is indicated in the *M-H* curves in Fig. 11.11, between the InGaGdN/GaN SL and InGaN/GaGdN SL set of samples measured at RT [33]. In the InGaN/GaGdN SL structure, carriers (electrons) flow out of the Gd-containing GaGdN layers and into the narrow bandgap InGaN layers. So the carrier concentrations in the GaGdN layers are decreased, resulting in the suppression of the carrier-mediated magnetization.

### 11.3.4 Si codoping effect on magnetic and electric properties

Si-codoped GaGdN layers were grown at 300°C. Fig. 11.12 shows the RT *M-H* curves for the Si-doped and undoped GaGdN samples with Gd concentration of 8.9% [26]. Clear hysteresis was observed for both samples. The saturation magnetization of Si-doped GaGdN, about 1046 emu/cm<sup>3</sup>, is seven times as large as that of undoped

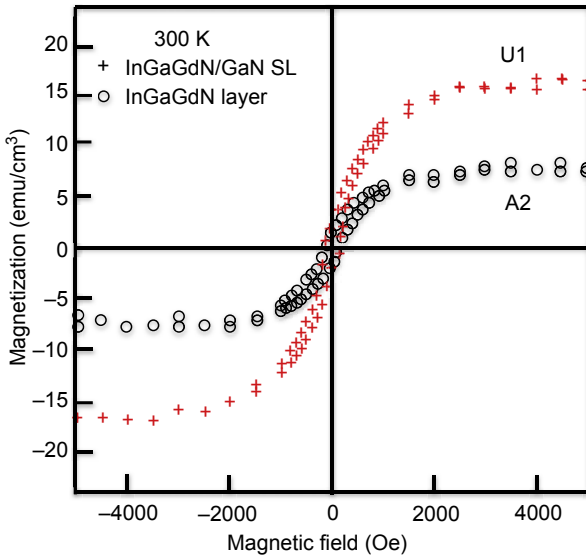


**Figure 11.10** *M-H* curves measured in-plane at 300 K for InGaGdN single layer (A2) and InGaGdN/GaN SL (U1) samples. In the InGaGdN/GaN SL structure, electrons flow into InGaGdN layer from GaN layer and enhanced magnetization is observed.

After Asahi H, Hasegawa S, Zhou YK, Emura S. *J Lumin* 2012;132:3136.

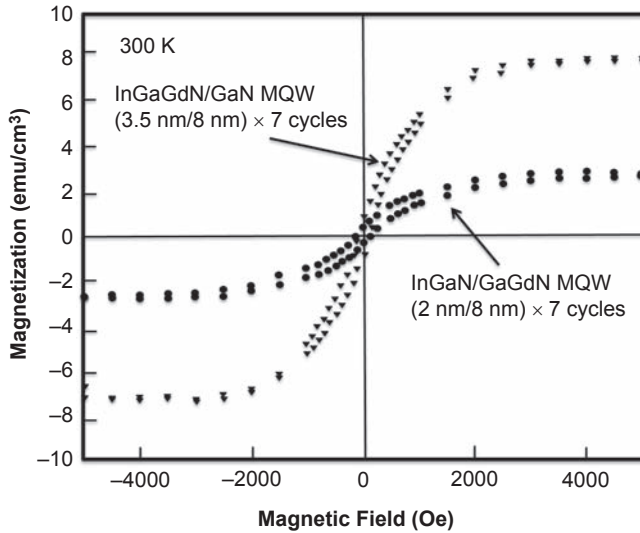


**Figure 11.11** *M-H* curves measured in-plane at 300 K for InGaGdN/GaN SL and InGaN/GaGdN SL. In the InGaN/GaGdN SL, electrons flow out from GaGdN layer into InGaN layer and reduced magnetization is observed.

After Asahi H, Hasegawa S, Zhou YK, Emura S. *J Lumin* 2012;132:3136.

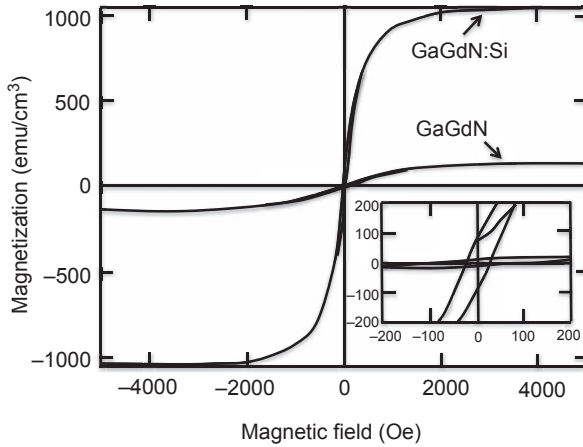


**Figure 11.12** RT  $M$ - $H$  curves for the Si-doped and undoped GaGdN samples grown at  $300^{\circ}\text{C}$  with Gd concentration of 8.9%. Inset shows the expanded curves. Clear hysteresis and saturation are observed for both samples and enhancement of magnetization is obtained by Si codoping. After Zhou YK, Choi SW, Emura S, Hasegawa S, Asahi H. Appl Phys Lett 2008;92:062505.

GaGdN. Codoping with Gd and Si is expected to increase the shallow donor concentration and to enhance the FM interaction. The enhancement of magnetization by Si codoping suggests the carrier-mediated ferromagnetism.

A similar effect was also observed for the InGaGdN samples [35]. Fig. 11.13 shows the  $M$ - $H$  curves of the InGaGdN sample and Si-codoped InGaGdN sample. Both samples show clear hysteresis and saturation characteristics measured at 300 K. With the increase of Si cell temperature (that is the increase of Si concentration), the increase of the saturation magnetization was observed [35]. Electrical properties are listed in Table 11.1. The increase in magnetization for the Si-codoped sample is closely related to carrier-mediated ferromagnetism; that is, the Si codoping increases the electron concentrations in InGaGdN layers as also inferred in the Si-codoped GaGdN samples and GaGdN/GaN SL samples.

Moreover, Si doping into wide bandgap GaN barrier layers in the InGaGdN/GaN SL structures was found to increase the magnetization as clearly observed from the RT  $M$ - $H$  curves shown in Fig. 11.14 [33]. One reason that could induce the enhancement of magnetization is also the carrier-mediated ferromagnetism.

### 11.3.5 Properties of nanorod structures

GaGdN nanorod structures were grown on Si(001) substrates with native  $\text{SiO}_2$  layer by radio-frequency plasma-enhanced MBE (RF-MBE) under nitrogen-rich conditions [36]. After thermal cleaning of Si substrates at  $870^{\circ}\text{C}$  for 15 min, LT GaN buffer layers were grown at  $450^{\circ}\text{C}$  for 60 s. Then annealing was performed at  $850^{\circ}\text{C}$  for 10 min in the plasma-activated nitrogen atmosphere followed by the growth of GaN nanorods at  $800^{\circ}\text{C}$  for 15 min. Then GaGdN nanorods were grown. Finally GaN layers were deposited to prevent the oxidation of GaGdN nanorods' surface.

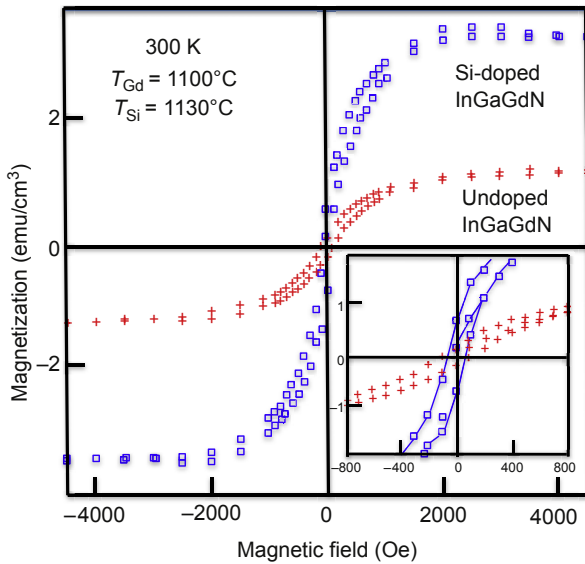


**Figure 11.13**  $M$ - $H$  curves measured in-plane at 300 K for Si-doped InGaGdN and undoped InGaGdN layers. Inset indicates the expanded view of the  $M$ - $H$  curves.

After Tawil SNM, Krishnamurthy D, Kakimi R, Ishimaru M, Emura S, Hasegawa S, et al. Phys Status Solidi C 2011;8:491.

**Table 11.1** Magnetic and electrical properties obtained at room temperature for the undoped and Si-doped InGaGdN samples shown in Fig. 11.13

Sample	Gd (%)	$M_s$ (emu/cm <sup>-3</sup> )	$H_c$ (Oe)	Electron concentration (cm <sup>-3</sup> )	Resistivity (ohm cm)
Undoped InGaGdN	3.7	1.8	120	$1.1 \times 10^{17}$	0.01
Si-doped InGaGdN	3.0	4.0	60	$4.7 \times 10^{18}$	0.003

After Tawil SNM, Krishnamurthy D, Kakimi R, Ishimaru M, Emura S, Hasegawa S, et al. Phys Status Solidi C 2011;8:491.

When GaGdN nanorods were grown at high substrate temperatures, for example at 850°C, the nanorod diameter is kept constant independent of nanorod length [36]. However, when grown at LTs, for example at 550°C, to increase the incorporated Gd concentration, the use of high Gd flux gradually increased the diameter of GaGdN nanorods with the progress of growth and the crystalline quality of nanorods degraded [37]. To solve this problem, the GaGdN/GaN SL structure nanorods were grown, as shown in Fig. 11.15(a) [38].

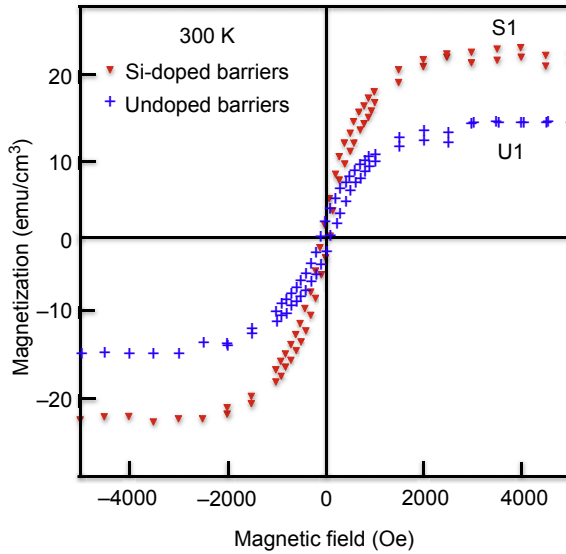


**Figure 11.14** *M-H* curves measured in-plane at 300 K for the InGaGdN/GaN SLs with and without Si doping into wide bandgap GaN layers.

After Asahi H, Hasegawa S, Zhou YK, Emura S. *J Lumin* 2012;132:3136.

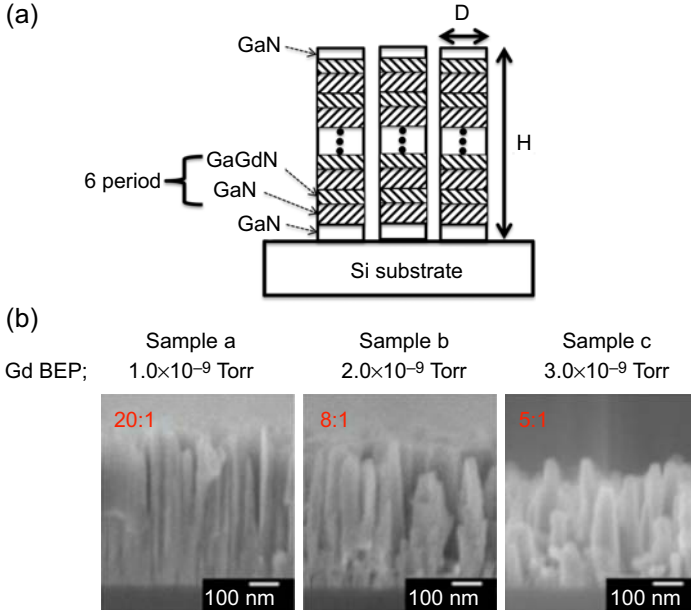


**Figure 11.15** (a) Schematic view of grown GaGdN/GaN SL nanorod structures.

(b) Cross-sectional SEM images for GaGdN/GaN SL nanorod structures as a function of Gd beam equivalent pressure (BEP).

After Uenaka M, Kimura M, Hasegawa S, Asahi H. Abstracts of the 59th Japan Society of Applied Physics Spring Meeting, #17a-F12-9 (Tokyo, Japan); 2012.

**Table 11.2 Residual magnetization ( $M_r$ ) ratio for the GaGdN nanorod structures as a function of nanorod aspect ratio (height/diameter)**

	Ga flux (Torr)	Gd (%)	Aspect ratio (H/D)	$M_r$ ratio ( $(M_r/M_s)_\perp/(M_r/M_s)_\parallel$ )
A	$1 \times 10^{-9}$	1.2	20	0.97
B	$2 \times 10^{-9}$	2.2	8	0.94
C	$3 \times 10^{-9}$	8.7	5	0.28

$M_s$  is saturation magnetization.

After Uenaka M, Kimura M, Hasegawa S, Asahi H. Abstracts of the 59th Japan Society of Applied Physics Spring Meeting, #17a-F12-9 (Tokyo, Japan); 2012.

Cross-sectional scanning electron microscopy (SEM) photographs for these GaGdN/GaN SL structure nanorods with different nanorod aspect ratio (height-to-diameter ratio) are shown in Fig. 11.15(b) [38]. On these GaGdN nanorods, clear hysteresis and saturation were observed in the  $M$ - $H$  curves at RT. Furthermore, by changing the nanorod aspect ratio, the vertical magnetization was improved as shown in Table 11.2 [38]. To realize the CP-LDs, vertically magnetized DMS layers are essentially required.

## 11.4 Properties of Dy-doped GaN

RE Dy-doped GaN is considered to be a very attractive material. As a trivalent metallic RE element, Dy ion has the highest magnetic moment ( $10.6 \mu_B$ ) of all naturally occurring elements and possesses other unusual magnetic properties [39]. It is expected that GaDyN will have the largest magnetic moment of any RE-doped GaN with the same concentration of the RE element.

GaDyN layers were grown on c-plane sapphire substrates at  $300^\circ\text{C}$  and  $700^\circ\text{C}$  by RF-MBE with various Dy concentrations. Elemental Ga (purity: 7N) and Dy (purity: 3N) and RF plasma-enhanced  $\text{N}_2$  were used as sources [39]. XRD measurements on the GaDyN samples grown at 300 and  $700^\circ\text{C}$  showed two diffraction peaks at around  $42^\circ$  from sapphire (0006) and  $35^\circ$  from GaDyN (0002), respectively. No obvious secondary phase, such as DyN, was detected [39].

### 11.4.1 Magnetic and optical properties

Hysteresis and saturation characteristics were observed in the  $M$ - $H$  curves at RT (Fig. 11.16) [40]. This indicates that GaDyN is FM.

PL spectra for the  $700^\circ\text{C}$ -grown GaDyN at various measuring temperatures are shown in Fig. 11.17(a) [40,41]. Broadbands are originated from crystal defects. Sharp lines are assigned to those within a framework of intra- $4f$  transitions, because these peaks are sharp, the peak energies are independent of temperature, and the lifetime of

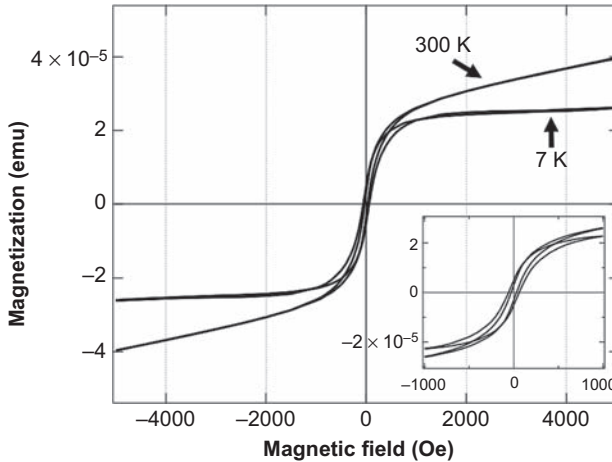


**Figure 11.16** *M-H* curves for the GaDyN layer at 7 and 300 K. Inset shows the expanded curves. (After Zhou YK, Takahashi M, Emura S, Hasegawa S, Asahi H. *J Supercond Nov Magn* 2010;23:103.) Inset shows the expanded *M-H* curves in the low magnetic field region.

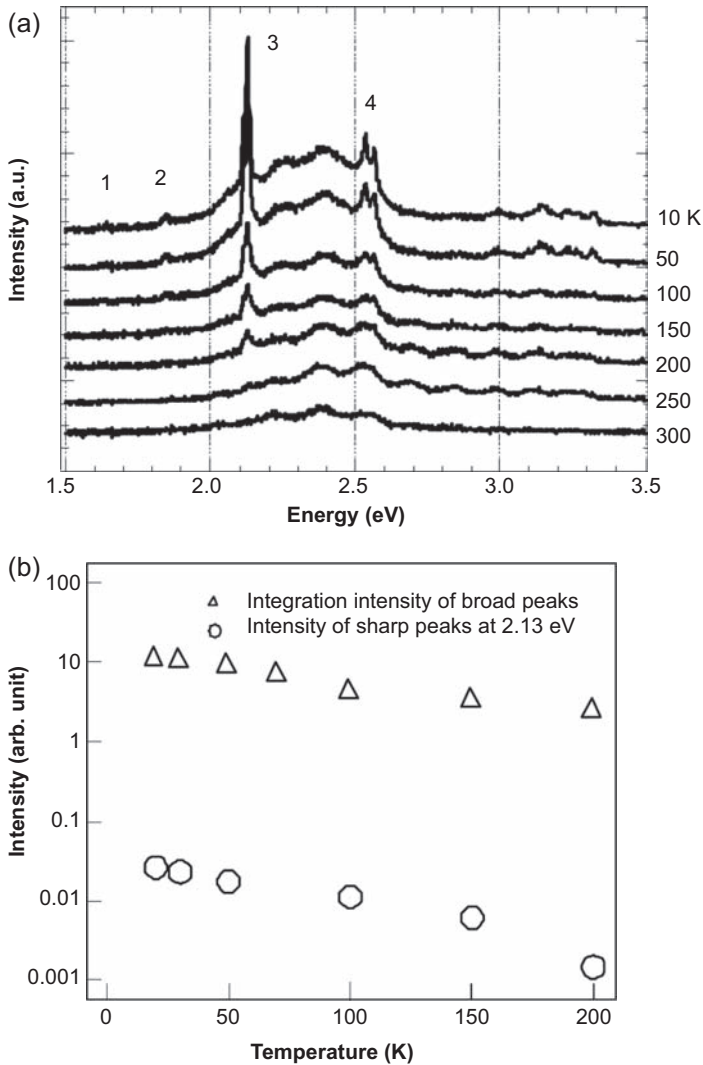
these emissions was 87  $\mu\text{s}$  at 13 K. These sharp peaks, labeled 1 through 4, are assigned to the following intra- $4f$  orbital transitions:  ${}^4F_{9/2} - {}^6H_{9/2}$ ,  ${}^4F_{9/2} - {}^6H_{15/2}$ ,  ${}^4F_{9/2} - {}^6H_{13/2}$ , and  ${}^4F_{9/2} - {}^6H_{15/2}$  transitions, respectively [42,43].

Fig. 11.17(b) shows the temperature variations of the integrated PL intensities of the broad peak from about 2.0 to 2.6 eV (*open triangles*) and the sharp line at 2.13 eV (*open circles*) [40]. The PL intensity of the 2.13-eV sharp peak decreases with increasing temperature in proportion to that of broad peak. In general, the intra- $4f$  orbital transition is independent of the thermal effects of the crystal. Therefore these sharp intra- $4f$  orbital transition peaks are related to the broad peak luminescence. That is, the Dy ion absorbs luminescence photons from the defects. This excites the Dy ion to a higher level of  $4f$  multiplets. Through the adequate paths, the excited electron relaxes to the initial state  ${}^4F_{9/2}$  and produces the observed sharp luminescence.

### 11.4.2 Magnetic circular dichroism

GaDyN exhibited significant enhancement of magnetic circular dichroism (MCD) signals compared with GaN, which suggests that the observed magnetic properties originate from the interaction between host semiconductor and doped magnetic ions [39]. Fig. 11.18 shows the MCD spectra at 10 K for the 300°C-grown GaN and GaDyN at the magnetic field of 1, 0, and  $-1$  T. Large Zeeman splitting is observed at around bandgap energy of GaDyN. Compared with GaN, the maximum MCD signal value from the GaDyN layer is nine times larger than that from GaN.

The MCD signal from GaDyN grown at 700°C was smaller than that grown at 300°C (Fig. 11.19) [39]. This is because the reevaporation of Ga and Dy atoms are larger than that at lower growth temperature and the GaDyN grown at 700°C has lower Dy concentration. LT growth technique can obtain higher RE element concentration



**Figure 11.17** (a) PL spectra of 700°C-grown GaDyN with a Dy concentration of 3% at various temperatures. (b) Temperature variations of the integrated PL intensities of the two peaks from the GaDyN sample.

After Zhou YK, Takahashi M, Emura S, Hasegawa S, Asahi H. J Supercond Nov Magn 2010; 23:103.

without secondary phase separation [41]. The MCD spectra for GaDyN with different Dy concentration also supported this result.

The MCD signal as a function of magnetic field for GaDyN grown at 300°C shows very clear hysteresis as shown in Fig. 11.20, where the measurements were conducted at 10 K and the wavelength was fixed at 363 nm [39]. This curve is not like the  $M$ - $H$



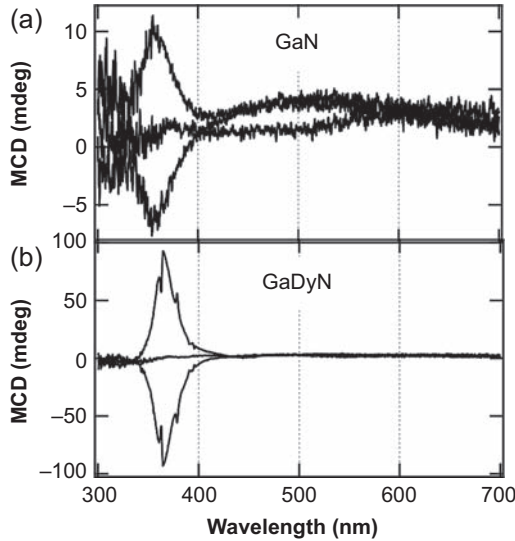


**Figure 11.18** MCD spectra at 10 K for the 300°C-grown (a) GaN and (b) GaDyN samples. After Zhou YK, Emura S, Hasegawa S, Asahi H. *Phys Status Solidi C* 2011;8:2173.

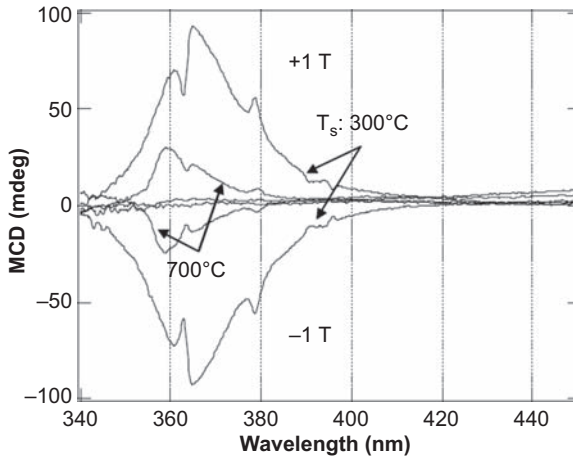


**Figure 11.19** MCD spectra at 10 K for the GaDyN samples grown at 300°C and 700°C. After Zhou YK, Emura S, Hasegawa S, Asahi H. *Phys Status Solidi C* 2011;8:2173.

curve measured by the superconducting quantum interference device magnetometer, which shows clear saturation magnetization for GaDyN. In the GaN, A-band, and B-band, free excitons exist near to the  $\Gamma$  point, and their energy separation is about 10 meV. Because A-band and B-band excitons have almost the same energy, cancellation of optical polarization for equal population at A and B state results in no-spin polarization [44,45]. However, in low-temperature grown GaDyN, many types of

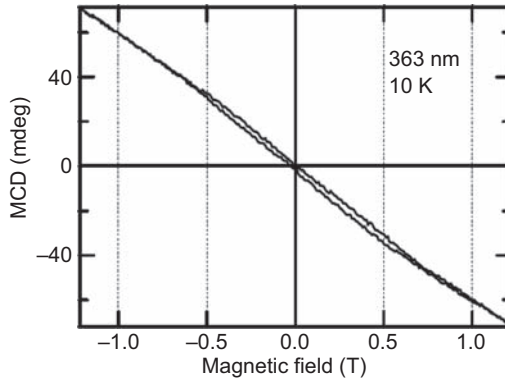


**Figure 11.20** MCD signal versus magnetic field at 363 nm measured at 10 K. After Zhou YK, Emura S, Hasegawa S, Asahi H. *Phys Status Solidi C* 2011;8:2173.

defects were included, and they cause the incomplete cancellation of optical polarization. On the other hand, high-concentration magnetic Dy ions enhanced Zeeman splitting of A and B bands because of  $s$ - $f$  exchange coupling. The observation of hysteresis loop implies the  $s$ - $f$  exchange coupling in FM coupling.

## 11.5 Spintronic device application

In this section, examples of the target spintronic devices and then the present status for the preparation of such devices are described.

Fig. 11.21(a) shows the schematic illustration of the CP-LD, where the cladding layer or active layer of the LD is replaced with the DMS layer. As shown in Fig. 11.21(b), when the spin-polarized electrons are recombined with holes, circular-polarized light is emitted and circular-polarized laser operation is realized. Fig. 11.22 shows the schematic illustration of the TMR device consisting of DMS layers and a tunnel barrier layer. This device acts as circular-polarized light-controlled TMR device. When the circular-polarized light is incident, the spin direction of the DMS layer is changed according to the direction of the circular-polarized light. This process is the inverse of Fig. 11.21(b). The combination of these two devices acts as an information processing system.

CP-LED (spin-LED) was fabricated by using MOVPE-grown Gd-doped GaN [46]. InGaN/GaN multiple quantum well (MQW) active layer was sandwiched with Si and Mg-codoped GaGdN cladding layers (inset of Fig. 11.23(a)). The fabricated light-emitting diode (LED) exhibited RT spin-polarized electroluminescence, controllable through an applied magnetic field in the Faraday configuration (Fig. 11.23(a)). Additionally, polarization hysteresis was observed, with the spin-LED retaining 9.3% spin polarization at zero-applied field after being exposed to the magnetic field of 5 kG (Fig. 11.23(b)).

With the interesting magnetic and optical properties observed on the Gd-doped InGaN-based DMS layers, InGaN-based DMS material will enable the fabrication

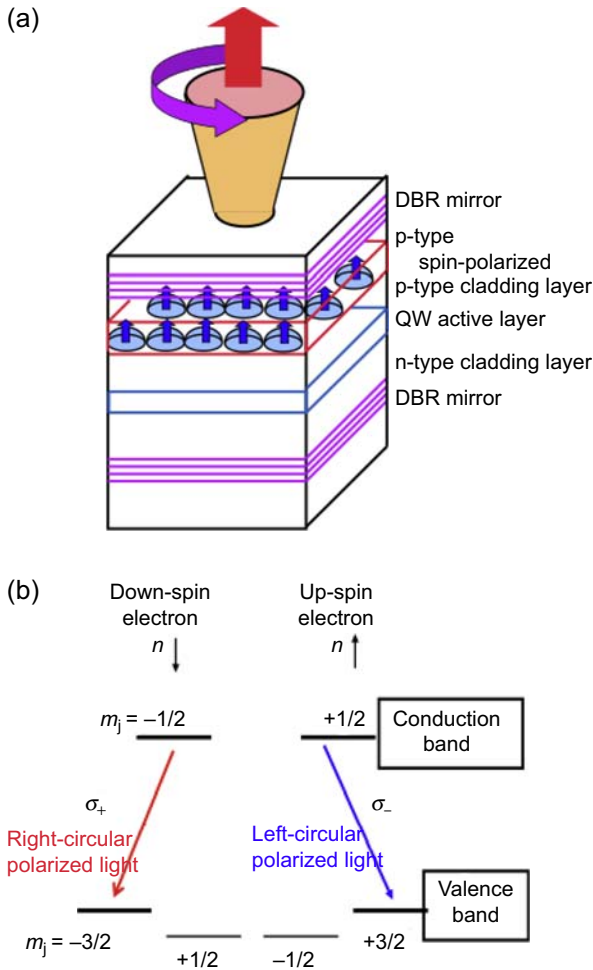


**Figure 11.21** (a) Schematic illustration of the CP-LD. (b) Recombination process of the spin-polarized carriers leading to circular-polarized light emission.

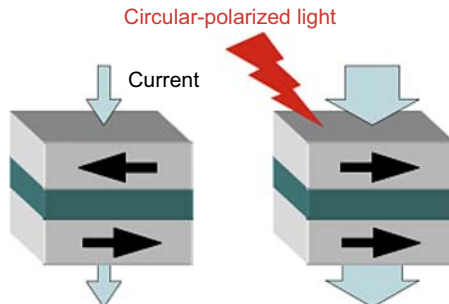


**Figure 11.22** Schematic illustration of the circular-polarized light-controlled TMR device.

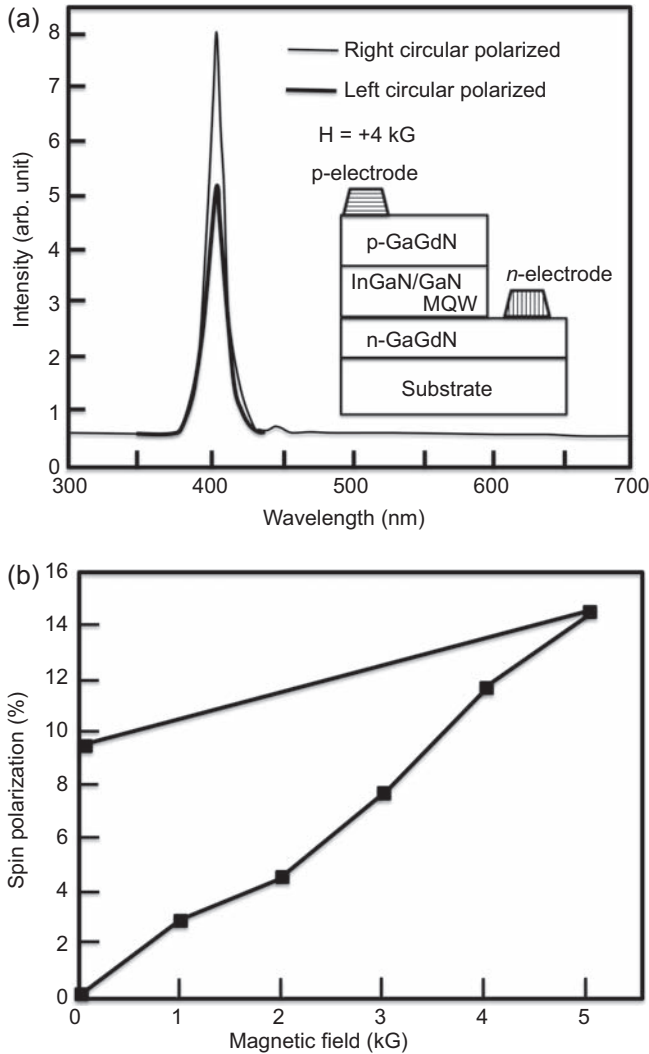


**Figure 11.23** (a) EL spectra with left- and right-circular polarized emissions. Inset shows the spin-LED structure. (b) Hysteresis of spin-polarized EL in GaGdN LED.

After Melton AG, Zaidi T, Jamil M, Xu T, Ferguson IT. Abstracts of the 9th International Conference on Nitride Semiconductors, #E4-3 (Glasgow, UK); 2011.

of longer wavelength spin-based electronic (spintronic) devices such as CP-LEDs and CP-LDs. MQW LED structures, 3 nm-InGaGdN (In:  $\sim 3.9\%$  and  $\sim 6\%$ , Gd:  $\sim 1\%$ )/9 nm-GaN, sandwiched between Si-doped n-type and Mg-doped p-type GaN layers, were grown on n-type GaN templates [33]. From these MQW LED structure samples, PL emission from the InGaGdN/GaN MQW layer was observed at around 400–500 nm at RT as shown in Fig. 11.24. Emission from GaN layers and defect-related broadband emission are also observed. To realize the current

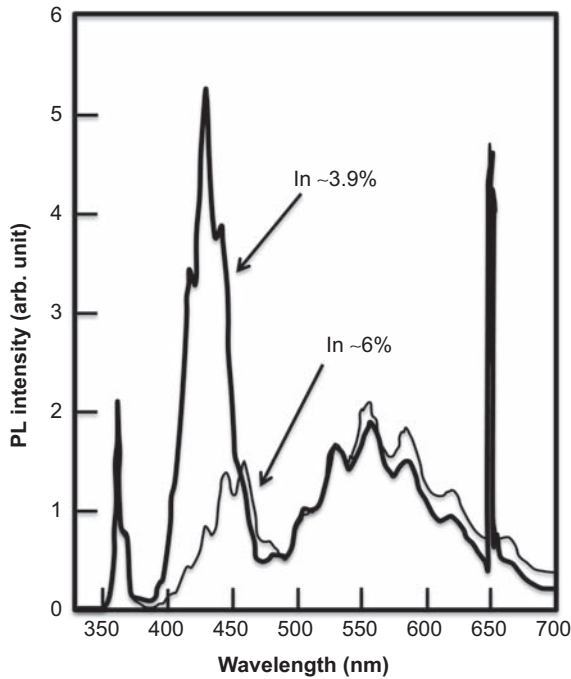


**Figure 11.24** RT PL spectra from the 3 nm-InGaGdN (In:  $\sim 3.9\%$  and  $\sim 6\%$ , Gd:  $\sim 1\%$ )/ 9 nm-GaN MQW LED structures.

After Asahi H, Hasegawa S, Zhou YK, Emura S. *J Lumin* 2012;132:3136.

injection CP-LEDs and CP-LDs by using MBE-grown GaGdN or GaDyN layers as an active layer or cladding layer, further studies are needed.

## 11.6 Summary

In this chapter, the present status of the Gd- and Dy-doped III-nitride semiconductor layers grown by plasma-assisted MBE was described. XRD measurements indicated no phase separation and the Gd incorporation was verified with the XAFS measurement. PL emission was also observed and the PL peak energy for the InGaGdN was red-shifted according to the InN molar fraction. Clear hysteresis and saturation were observed in the  $M$ - $H$  curves at RT. Si codoping into (In)GaGdN layers enhanced the magnetization. In the InGaGdN/GaN SL samples, enhanced magnetization was also observed. Si doping into wide bandgap GaN layers in these SL structures further increased the magnetization. Such results can be understood with the carrier-mediated ferromagnetism. Results for the LT growth and the growth of the nanorod structures were also described. Finally, examples of the spintronic devices, where the relation between the spin-polarized carriers and the circular-polarized light is used, and the present status to realize such devices were described.

## References

- [1] Ohno H, Shen A, Matsukura F, Oiwa A, Endo A, Katsumoto S, et al. *Appl Phys Lett* 1996;69:363.
- [2] Chiba D, Takamura K, Matsukura F, Ohno H. *Appl Phys Lett* 2003;82:3020.
- [3] Dietl T, Ohno H, Matsukura F, Cibert J, Ferrand D. *Science* 2000;287:1019.
- [4] Sato K, Katayama-Yoshida H. *Semicond Sci Technol* 2002;17:377.
- [5] Sonoda S, Shimizu S, Sasaki T, Yamamoto Y, Hori H. *J Cryst Growth* 2002;237:1358.
- [6] Hashimoto M, Zhou YK, Kanamura M, Asahi H. *Solid State Commun* 2002;122:37.
- [7] Hashimoto M, Tanaka H, Asano R, Hasegawa S, Asahi H. *Appl Phys Lett* 2004;84:4191.
- [8] Park M, Kuh K, Myoung J, Lee J, Chang J, Lee K, et al. *Solid State Commun* 2002;124:11.
- [9] Liu H, Wu S, Singh R, Gu L, Smith D, Newman N, et al. *Appl Phys Lett* 2004;85:4076.
- [10] Sato K, Schweika W, Dederichs PH, Katayama-Yoshida H. *Phys Rev B* 2004;70:201202.
- [11] Katayama-Yoshida H, Sato K, Fukushima T, Toyoda M, Kizaki H, Dinh VA, et al. *J Mag Mat* 2007;310:2070.
- [12] Teraguchi N, Suzuki A, Nanishi Y, Zhou YK, Hashimoto M, Asahi H. *Solid State Commun* 2002;122:651.
- [13] Hashimoto M, Araki K, Sato K, Asahi H, Katayama-Yoshida H. In: *Extended abstracts of the 8th symposium on the physics and application of spin-related phenomena in semiconductors*, Sendai, Japan; 2002. p. 165–8.
- [14] Dalpian GM, Wei SH. *Phys Rev B* 2005;72:115201.
- [15] Gohda Y, Oshiyama A. *Phys Rev B* 2008;78:161201.
- [16] Liu L, Yu PY, Ma Z, Mao SS. *Phys Rev Lett* 2008;100:127203.
- [17] Litvinov VI, Dugaev VK. *Appl Phys Lett* 2009;94:212506.
- [18] Dhar S, Perez L, Brandt O, Trampert A, Ploog KH, Keller J, et al. *Phys Rev B* 2005;72:245203.
- [19] Choi SW, Zhou YK, Kim MS, Kimura S, Emura S, Hasegawa S, et al. *Phys Status Solidi A* 2006;203:2774.
- [20] Hite JK, Frazier RM, Davies R, Thaler GT, Abernathy CR, Pearton SJ. *Appl Phys Lett* 2006;89:092119.
- [21] Zhou YK, Choi SW, Kimura S, Emura S, Hasegawa S, Asahi H. *Thin Solid Films* 2010;518:5659.
- [22] Hung IH, Lai YH, Feng ZC, Gupta S, Zaidi T, Ferguson I, et al. *Proc SPIE* 2010;7784:77840H.
- [23] Han SY, Hite JK, Thaler GT, Frazier RM, Abernathy CR, Pearton SJ, et al. *Appl Phys Lett* 2006;88:042102.
- [24] Hite JK, Frazier RM, Davies RP, Thaler GT, Abernathy CR, Pearton SJ, et al. *J Electron Mater* 2007;36:391.
- [25] Hejtmanek J, Knížek K, Maryško M, Jirak Z, Sedmidubský D, Sofer Z, et al. *J Appl Phys* 2008;103:07D107.
- [26] Zhou YK, Choi SW, Emura S, Hasegawa S, Asahi H. *Appl Phys Lett* 2008;92:062505.
- [27] Dhar S, Brandt O, Ramsteiner M, Sapega VF, Ploog KH. *Phys Rev Lett* 2005;94:037205.
- [28] Dhar S, Kammermeier T, Ney A, Perez L, Ploog K, Melnikov A, et al. *Appl Phys Lett* 2006;89:062503.
- [29] Mitra C, Lambrecht WRL. *Phys Rev B* 2009;80:081202(R).
- [30] Holub M, Shin J, Chakrabarti S, Bhattacharya P. *Appl Phys Lett* 2005;87:091108.

- 
- [31] Asahi H, Hasegawa S, Zhou YK, Emura S. In: Proceedings of 2010 fall MRS meeting; 2010. p. 110205e.
- [32] Tawil SNM, Kakimi R, Krishnamurthy D, Ishimaru M, Emura S, Tambo H, et al. *Phys Status Solidi Rap Res Lett* 2010;4:308.
- [33] Asahi H, Hasegawa S, Zhou YK, Emura S. *J Lumin* 2012;132:3136.
- [34] Tawil SNM, Krishnamurthy D, Kakimi R, Emura S, Hasegawa S, Asahi H. *J Cryst Growth* 2011;323:351.
- [35] Tawil SNM, Krishnamurthy D, Kakimi R, Ishimaru M, Emura S, Hasegawa S, et al. *Phys Status Solidi C* 2011;8:491.
- [36] Tambo H, Hasegawa S, Higashi K, Kakimi R, Tawil SNM, Zhou YK, et al. *Phys Status Solidi C* 2011;8:494.
- [37] Tambo H, Hasegawa S, Kameoka H, Zhou YK, Emura S, Asahi H. *J Cryst Growth* 2011; 323:323.
- [38] Uenaka M, Kimura M, Hasegawa S, Asahi H. In: Abstracts of the 59th Japan Society of Applied Physics Spring Meeting; 2012. #17a-F12-9 (Tokyo, Japan).
- [39] Zhou YK, Emura S, Hasegawa S, Asahi H. *Phys Status Solidi C* 2011;8:2173.
- [40] Zhou YK, Takahashi M, Emura S, Hasegawa S, Asahi H. *J Supercond Nov Magn* 2010; 23:103.
- [41] Zhou YK, Kim MS, Li XJ, Kimura S, Kaneta A, Kawakami Y, et al. *J Phys Condens Matter* 2004;16:S5743.
- [42] Teraguchi N, Suzuki A, Saito Y, Yamaguchi T, Araki T, Nanishi Y. *J Cryst Growth* 2001; 230:392.
- [43] Lozykowski HJ, Jadwisienczak WM, Brown I. *Appl Phys Lett* 1999;74:1129.
- [44] Skromme BJ. *Mater Sci Eng B* 1997;50:117.
- [45] Kuroda T, Yabushita T, Kosuge T, Tackeuchi A, Taniguchi K, Chinone T, et al. *Appl Phys Lett* 2004;85:3116.
- [46] Melton AG, Zaidi T, Jamil M, Xu T, Ferguson IT. In: Abstracts of the 9th International Conference on Nitride Semiconductors; 2011. #E4-3 (Glasgow, UK).

# Ferromagnetic behavior in transition metal-doped III-N semiconductors

12

*N.A. El-Masry*

North Carolina State University, Raleigh, NC, United States

*J.M. Zavada*

NYU Tandon School of Engineering, Brooklyn, NY, United States

*N. Nepal*

U.S. Naval Research Laboratory, Washington, DC, United States

*S.M. Bedair*

North Carolina State University, Raleigh, NC, United States

## 12.1 Introduction

Semiconductors can be classified into two categories: nonmagnetic or magnetic. Among the nonmagnetic semiconductors, silicon (Si) is the most technologically important and forms the basis for modern electronics. Other nonmagnetic semiconductors include the III-V compounds, such as GaAs, InP, and GaN, which have a direct bandgap and are the basis for optoelectronic light emission applications. On the other hand, magnetic semiconductors provide an additional level of functionality that offers the potential for on-chip integration of electronic, optical, and magnetic capabilities.

Typically, magnetic semiconductors are formed by introducing magnetic ions, such as transition metal (TM) or rare-earth (RE) atoms, into a semiconductor host material. Many magnetic semiconductors, including spinels and Eu chalcogenides, are alloys in which the magnetic ions constitute a large percentage of the overall material. On the other hand, dilute magnetic semiconductors (DMS) are semiconductor materials in which only a small fraction of the host atoms are replaced by TM or RE atoms. The synthesis of these materials is relatively easy compared to the magnetic semiconductor alloys, and methods for device fabrication are already in place. Mn-doped III-V compounds are among the most widely studied DMS materials and carrier-mediated ferromagnetic (FM) ordering has been well documented.

Since the discovery of FM behavior in Mn:GaAs and Mn:InAs, there has been widespread research activity to optimize such materials for potential applications that involve both information processing and data storage (Ohno *et al.*, 1996; Munekata *et al.*, 1989). In Mn-doped III-V arsenide semiconductors, Mn substitutes for the cation, providing a p-type dopant and inducing a magnetic moment. DMS



materials that function at room temperature (RT) would have a tremendous technological impact especially in the field of spin transfer electronics, where the spin of the electron is manipulated in addition to its charge transport. Among the potential spintronic devices is a new class of magnetic random access memories, with nonvolatility, low power consumption, and ultra-high storage density. The efficient injection, transport, and detection at RT of spin-polarized electrons in a semiconductor material are essential requirements. However, in spite of numerous efforts, the FM properties of Mn:GaAs and Mn:InAs materials have a Curie temperature ( $T_C$ ) limited to  $\sim 160$  K, which is a major disadvantage for device development (Chen et al., 2011; Reed et al., 2000; Parker et al., 1999a,b).

Several different models have been proposed to explain the magnetic properties of DMS materials based on doping with TM elements. In these materials, TM atoms lose their outermost electrons and the remaining  $3d$  shell electrons give rise to magnetic effects. In the Zener mean field theory model, FM ordering occurs through correlation of the spins of the localized magnetic ions (Zener, 1951). Based on Hund's rule of maximum multiplicity, if two or more electron orbitals of equal energy are available, the  $3d$  electrons will occupy them singly before filling them in pairs. In addition, the lowest energy state for the atom occurs when all the spins of unpaired electrons are aligned in the same direction. Since each electron carries a magnetic moment of one Bohr magneton  $\mu_B$ , the overall atom will then have a net effective magnetic moment  $\mu_{\text{eff}}$ . Table 12.1 lists the spin orientation of the electrons in the  $3d$  shells for selected TM elements, showing the occupancy order, the number of electrons present per shell, and the magnetic moment. The magnetic interaction between the  $3d$  shell electrons of adjacent atoms leads to an antiferromagnetic (AFM) coupling. However, since the spin

**Table 12.1 Spin orientation of  $3d$  shell electrons for transition metal elements**

Transition metal ions	Spin of $3d$ orbitals					Magnetic moment ( $\mu_B$ )
Ti <sup>3+</sup> , V <sup>4+</sup>	↑					1
Ti <sup>2+</sup> , V <sup>3+</sup>	↑	↑				2
V <sup>2+</sup> , Cr <sup>3+</sup> , Mn <sup>4+</sup>	↑	↑	↑			3
Cr <sup>2+</sup> , Mn <sup>3+</sup>	↑	↑	↑	↑		4
Mn <sup>2+</sup> , Fe <sup>3+</sup>	↑	↑	↑	↑	↑	5
Fe <sup>2+</sup> , Co <sup>3+</sup>	↑↓	↑	↑	↑	↑	4
Co <sup>2+</sup>	↑↓	↑↓	↑	↑	↑	3
Ni <sup>2+</sup>	↑↓	↑↓	↑↓	↑	↑	2
Cu <sup>2+</sup>	↑↓	↑↓	↑↓	↑↓	↑	1
Zn <sup>2+</sup> , Cu <sup>+</sup>	↑↓	↑↓	↑↓	↑↓	↑↓	0

of an incomplete  $3d$  shell is strongly coupled to the conduction electrons, this coupling tends to align the spins in an FM manner. The competition between these two mechanisms determines the magnetic state of the material. Without conduction electrons, magnetic ordering is not possible. The  $T_C$  is determined through a competition between the AFM and FM interactions. The Zener model has been able to successfully predict the  $T_C$  of Mn:GaN and Mn:InAs.

Another model, the double exchange mechanism, was proposed to explain ferromagnetism in TM-doped ZnO, a wide bandgap II-VI semiconductor (Sato and Katayama-Yoshida, 2000). In this model magnetic ions in different valence states couple with each other by a virtual hopping of the “extra” electron from one ion to another. If the magnetic moments of neighboring TM metal ions are aligned, the  $3d$  energy band is widened by the hybridization between the spin-up states. The band energy in the FM configuration is lowered by introducing carriers in the  $3d$  band. In this case, the partially filled  $3d$  bands of the TM ions facilitate hopping of carriers from one ion’s orbital to another, provided that the spins of the hopping electrons are in the same direction (see Lambrecht, 2015, this volume, for further details). Consequently, the electrons lower their kinetic energy by hopping in the FM state. This model has also been successfully used to explain FM behavior in Mn:InAs (Akai, 1998; Akai and Dederichs, 1993).

The Zener mean field theory model has been extended to treat magnetic behavior in zinc-blende Mn-doped III-V and II-VI semiconductors (Dietl et al., 2000). This study predicted that the wide bandgap semiconductors, such as GaN and ZnO, would exhibit FM behavior with a  $T_C > 300$  K provided that the semiconductors had a Mn concentration  $>5$  at.% and a hole concentration  $>3.5 \times 10^{20}/\text{cm}^3$ . This prediction resulted in a flurry of research activity focused on TM-doped wide bandgap semiconductors, especially Mn-doped GaN (Mn:GaN). Several research groups have reported FM behavior at RT in Mn:GaN specimens even though the TM concentrations and the hole concentrations, required by the model, were not achieved (Reed et al., 2001a,b). In addition, the experimental results from these different groups are not in good agreement, indicating that the synthesis and processing conditions have a major effect on the resultant magnetic properties.

Various synthesis methods have been used to incorporate TM in III-V nitride semiconductors and to examine the magnetic behavior. The principal ones include solid state diffusion, ion implantation, and epitaxial growth, such as metal organic chemical vapor deposition (MOCVD) and molecular beam epitaxy (MBE). Each of these methods possesses certain advantages and disadvantages. Solid state diffusion is a rather simple method that can be used for different TMs. This was one of the first methods to successfully dope GaN with Mn with evidence of FM behavior having a  $T_C$  as high as 380 K (Reed et al., 2001a,b). However, diffusion is limited by solubility constraints and only shallow doped regions, with a nonuniform dopant distribution, are produced. Ion implantation is a nonequilibrium method that can be used to incorporate a wide range of elements into a given host material. However, ion implantation creates significant lattice damage and post-implantation annealing is needed. In addition, the implanted ions have a nonuniform distribution and are limited to shallow surface regions (Hebard et al., 2002). In situ doping during epitaxial growth has been shown

to produce GaN layers having uniform Mn concentrations. Even though the III-V nitrides lack a natural substrate, this approach has been shown to produce thick Mn-doped GaN (Mn:GaN) films with high Mn concentrations. However, these films typically suffer from a large density of dislocations that adversely affect conductivity properties. Nevertheless, each of these methods has been shown to produce Mn:GaN films with FM properties at RT even though the conductivity and Mn concentrations do not correspond to the necessary conditions of the theoretical model.

The experimental data presented in this chapter are aimed at clarifying the origin of FM ordering in TM-doped III-V nitride semiconductors and determination of the synthesis and processing conditions needed to optimize the observed magnetization. In [Section 12.2](#) we describe results pertaining to Mn-doping of GaN and InGaN films through solid state diffusion. Structural characterization and magnetic measurements of RT-FM behavior are presented. Related experiments concerning Fe-doping of GaN films by diffusion are also given. In [Section 12.3](#), we summarize results of in situ Mn-doping of GaN films using MOCVD. In [Section 12.4](#), we describe our efforts to enhance the magnetic behavior of Mn:GaN epilayers by modifying the Fermi level in heterostructures. In [Section 12.5](#), we present results concerning a prototype spin device in which the FM effects can be turned on and off by means of an applied electric field.

## 12.2 Transition metal-doping of III-V nitride films by diffusion

A two-step process was used to diffuse Mn into GaN and InGaN films. First III-V nitride templates were prepared by atmospheric MOCVD on *c*-plane sapphire substrates. Initial growth of a GaN buffer layer, 40–100 nm thick, grown at 500°C was followed by recrystallization of the layer by high temperature annealing. Subsequently, an epitaxial GaN was grown at ~1010°C, with film thickness of ~1.3 μm. For certain GaN templates this layer was codoped with either Mg or Si to produce p-type or n-type conductivity, respectively. For  $\text{In}_x\text{Ga}_{1-x}\text{N}$  templates the temperature was lowered to ~750–830°C for growth of films with an In content (*x*) less than 0.20. Following MOCVD growth the GaN and  $\text{In}_x\text{Ga}_{1-x}\text{N}$  templates were cleaned and loaded into an ultra-high vacuum-pulsed laser deposition (PLD) chamber for deposition of a thin layer of Mn, ~10–100 nm thick. A Lambda Physik KrF Excimer Laser with emission wavelength of 248 nm was used as the laser source for the PLD. Samples were then annealed at temperatures ranging from 250 to 800°C for times up to 24 h to permit solid state diffusion of Mn into the GaN and InGaN films. The post-deposition annealing was carried out at the deposition temperature. In situ reflective high-energy electron diffraction (RHEED) patterns were recorded during this process to monitor changes in crystalline quality and lattice parameters of the films. After diffusion the specimens were unloaded and etched in 30%  $\text{H}_2\text{O}_2$  solution for up to 10 min to remove the remaining Mn metal from the surface.

### 12.2.1 Structural and magnetic characterization of Mn-doped GaN films

In Fig. 12.1 RHEED patterns for GaN along the  $[1\bar{1}20]$  azimuth prior to Mn deposition and after Mn deposition and diffusion are shown. These RHEED patterns are typical for samples grown and annealed at substrate temperatures ranging from 550–600°C. The streaky pattern in Fig. 12.1(b) indicates 2D growth of single crystalline GaN material with wurtzite structure. These results are similar to RHEED patterns reported for 2D growth of Mn:GaN by MBE (Kuwabara et al., 2001; Kondo et al., 2002; Sonoda et al., 2002).

The RHEED pattern in Fig. 12.1(b) for Mn:GaN shows an increase in the streak separation as compared to the as-grown GaN film in Fig. 12.1(a). An increase in the streak pattern represents a decrease in the distance between the atoms in the lattice; that is, the diffusion of Mn causes the GaN lattice to contract.

Secondary ion mass spectrometry (SIMS) analysis verified that the diffusion process was successful for Mn doping of GaN (Reed et al., 2001a,b). The Mn diffusion

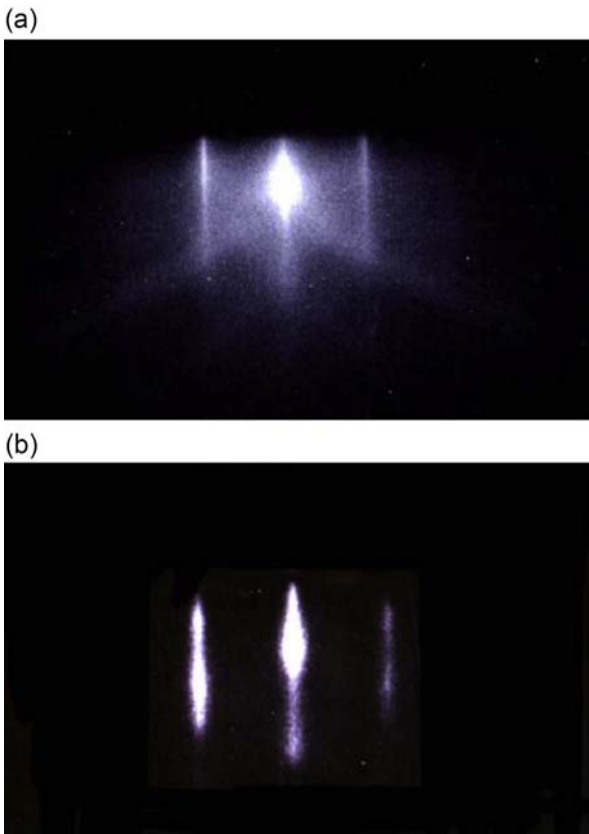


**Figure 12.1** RHEED pattern for (a) GaN along the  $[1\bar{1}20]$  direction prior to Mn deposition and (b) epitaxial Mn:GaN after diffusion. Addition of Mn causes the GaN lattice to contract.

profiles, shown in Fig. 12.2, indicate that the diffusion rate of Mn in n-type GaN samples occurs more rapidly than for undoped GaN. The units for these SIMS measurements are given as counts per second as a function of sputtering rate, and the thickness (depth) was determined by measuring the crater depth after the analysis.

In Table 12.2, the samples used in this study are listed along with the Mn deposition temperatures ( $T_D$ ) and annealing times. The table also lists the magnetic response (FM = ferromagnetic, PM = paramagnetic, and DM = diamagnetic), and  $T_C$  of Mn:GaN films.

The crystalline quality of Mn:GaN films was determined by X-ray diffraction (XRD) measurements that were calibrated using the (0006) diffraction peak from the  $Al_2O_3$  substrate. The binary Mn–Ga phases and cubic perovskite  $Mn_3GaN$  phase are known to be structurally compatible with the wurtzite structure of GaN. The  $Mn_3GaN$  phase can be formed by the direct reaction of Mn with GaN where Mn replaces Ga in the lattice (Bouchaud, 1968). These phases are ferrimagnetic and can form epitaxially either as clusters or platelets within a GaN film. We have observed formation of  $Mn_3GaN$  in some samples that were processed at high temperatures and annealed for times in excess of 24 h. An XRD pattern showing the presence of the (111) reflection peak from secondary  $Mn_3GaN$  phase is shown in Fig. 12.3. Since the Neel temperature for  $Mn_3GaN$  is  $\sim 20$  K, it would not result in a magnetic moment at RT.

Superconducting quantum interference device (SQUID) measurements were performed at RT to determine the magnetic properties of the Mn:GaN samples. The

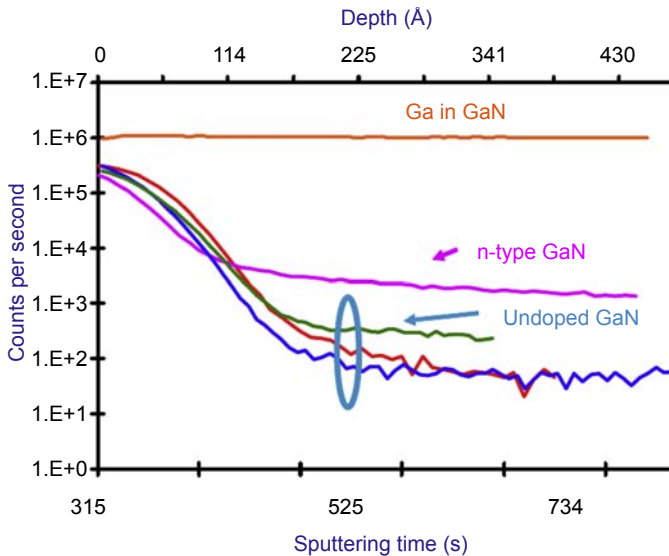


**Figure 12.2** SIMS depth profiles showing the general trend for the diffusion of Mn into n-type and undoped GaN substrates. The Mn profile is shown as counts per second versus sputtering time and depth.

**Table 12.2 Samples studied in these diffusion experiments (the data clearly indicate that Mn incorporation, and resulting magnetic properties, depend on the processing conditions)**

Sample ID	$T$ (°C) (Mn-doping)	Annealing $T$ (°C)	Annealing Time (min)	Magnetic response	$T_C$ (°K)
Mn-037	280	700	123	PM	—
Mn-051	320	350	360	PM	—
Mn-049	460	N/A	N/A	PM	—
Mn-050-01	460	430	60	PM	—
Mn-059	500	N/A	N/A	DM	—
Mn-054	500	500	60	DM	—
Mn-053	500	500	77	PM	—
Mn-062	550–600	550–600	60	PM	—
Mn-067	550–600	550–600	60	FM	298
Mn-068	550–600	550–600	60	PM	—
Mn-077	550–600	550–600	60	FM	264
Mn-079	550–600	550–600	60	FM	>380
Mn-080	550–600	550–600	60	FM	264
Mn-082	550–600	550–600	60	FM	>363
Mn-087	550–600	550–600	60	PM	—
Mn-088	550–600	550–600	60	FM	>363
Mn-095	550–600	550–600	60	FM	330
Mn-044	550–600	550–600	60	FM	357
Mn-048	550–600	550–600	60	FM	247
Mn-105	550–600	550–600	80	PM	—
Mn-102	550–600	550–600	100	PM	—
Mn-098	550–600	550–600	145	PM	350
Mn-052	550–600	550–600	180	PM	—
Mn-034	680	680	174	FM	>300

applied field ( $H_a$ ) was applied in both parallel and perpendicular directions to the plane of the film and the resulting magnetization ( $M$ ) recorded. Estimates of  $T_C$  were obtained by measuring the saturation magnetization ( $M_s$ ) as a function of temperature ( $T$ ), which was varied from 5 to 400 K. Determination of the precise origin of the FM

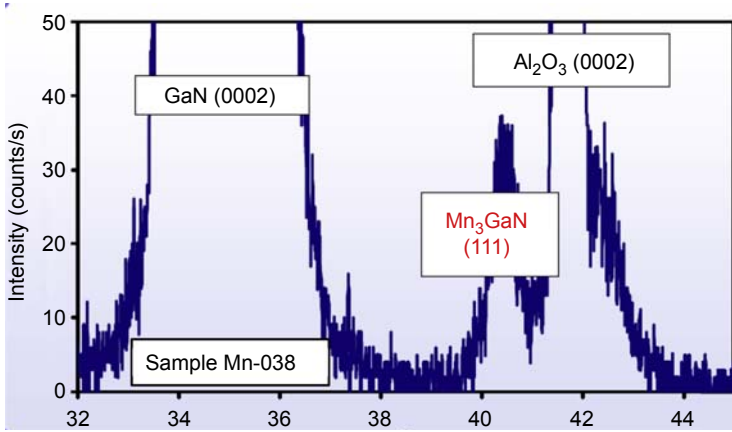


**Figure 12.3** XRD ( $\theta$ - $2\theta$ ) pattern for sample Mn-038 showing the (111)  $\text{Mn}_3\text{GaN}$  reflection peak. Diffusion was done at a high temperature,  $680^\circ\text{C}$ , and for a time in excess of 24 h.  $\text{Mn}_3\text{GaN}$  is a ferrimagnetic phase with a Neel temperature of 20 K.

properties is extremely important since phase separated precipitates, or clusters with small volumes, can exhibit superparamagnetic behavior. Criteria for the existence of superparamagnetism are (1) magnetization curves measured at different temperatures ( $M_s$  as a function of  $H_a/T$ ) overlap and (2) no hysteresis is found; that is, the coercive field ( $H_C$ ) and residual magnetization ( $M_r$ ) are zero.

To confirm that the Mn layer was completely removed from the surface prior to magnetic measurements, energy dispersive X-ray spectroscopy (EDX) analysis was performed. The absence of a Mn peak in the EDX spectrum indicated that no Mn atoms remained on the surface. RT SQUID measurements with the  $H_a$  perpendicular to the plane of the film are shown in Fig. 12.4. The magnetic curves indicate FM behavior with a coercivity  $\sim 100$  Oe and  $M_s = 20\text{--}25$  emu/cm<sup>3</sup>. Based on the estimated Mn concentration [Mn]  $\sim 2\%$ , the effective magnetization was determined to be  $2.8 \mu_B/\text{Mn}$  atom.

### 12.2.2 Electrical characterization of Mn:GaN films

Electrical transport measurements as a function of temperature and applied field provided detailed information regarding the magnetic ordering in the Mn:GaN samples. In particular, extraordinary Hall Effect (EHE) measurements were performed using the van der Pauw setup for magnetic characterization of these films. The Hall resistance ( $R_{\text{Hall}}$ ) in FM materials can be expressed by (Ohno, 1999):

$$R_{\text{Hall}} = \frac{R_0 B}{d} + \frac{R_s M}{d} \quad [12.1]$$

where  $R_0$  is the ordinary Hall coefficient,  $R_s$  is the anomalous Hall coefficient,  $d$  is the sample thickness, and  $M$  is the magnetization.

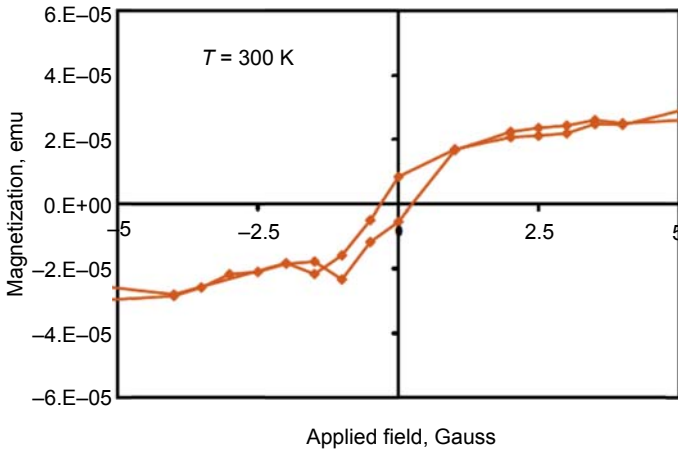


**Figure 12.4** SQUID measurement at 300 K for Mn:GaN sample Mn-79 showing FM behavior. The effective magnetization was estimated to be  $2.8 \mu_B/\text{Mn}$  atom.

In Fig. 12.5(a) hysteresis curves measured by EHE at RT for Mn:GaN sample Mn-079 are shown. The coercive field of this sample was  $\sim 500$  Oe, which is consistent with results measured by SQUID. The EHE results for an un-doped GaN sample, shown in Fig. 12.5(b), indicates that this sample was diamagnetic (DM).

EHE measurements were made at different temperatures to study the transition from PM to FM behavior of the GaMnN samples. The effects of temperature on the shape of the magnetization curves for two samples, Mn-048 and Mn-079, are shown in Fig. 12.6. The magnetization curves undergo a transition from a linear behavior to a typical S-shape curve at lower temperatures. This approach provides a method for determining the magnetic ordering temperature, which was found to be  $\sim 247$  K for sample Mn-048. The  $T_C$  for Mn-079 could not be determined as it was above the maximum achievable temperature for the EHE setup.

Little information exists for superparamagnetic behavior in Mn particles since close coupling between Mn atoms results in AFM alignment of the spins. However, superparamagnetic behavior may result from small size secondary phases within the film. Substantial effort has been made to identify the presence of any secondary phases within the film but no experimental evidence of their presence was found at low Mn concentrations ( $< 1\%$  Mn). Several authors have claimed that secondary phases, or precipitates, can exist within the material even though they cannot be detected by high resolution characterization techniques such as high-resolution transmission electron microscopy (HRTEM) (Overberg et al., 2001; Kuwabara et al., 2001; Sonoda et al., 2002). In order to rule out superparamagnetic M behavior in the Mn:GaN samples prepared by solid state diffusion, temperature-dependent Hall measurements were performed. Results of these measurements are shown in Fig. 12.7 where  $R_{\text{Hall}}$  versus  $H_a/T$  curves are plotted for a typical sample. However, no evidence of superparamagnetic was observed and the FM properties reported for the Mn:GaN samples are due to a solid solution of Mn atoms in the GaN film.



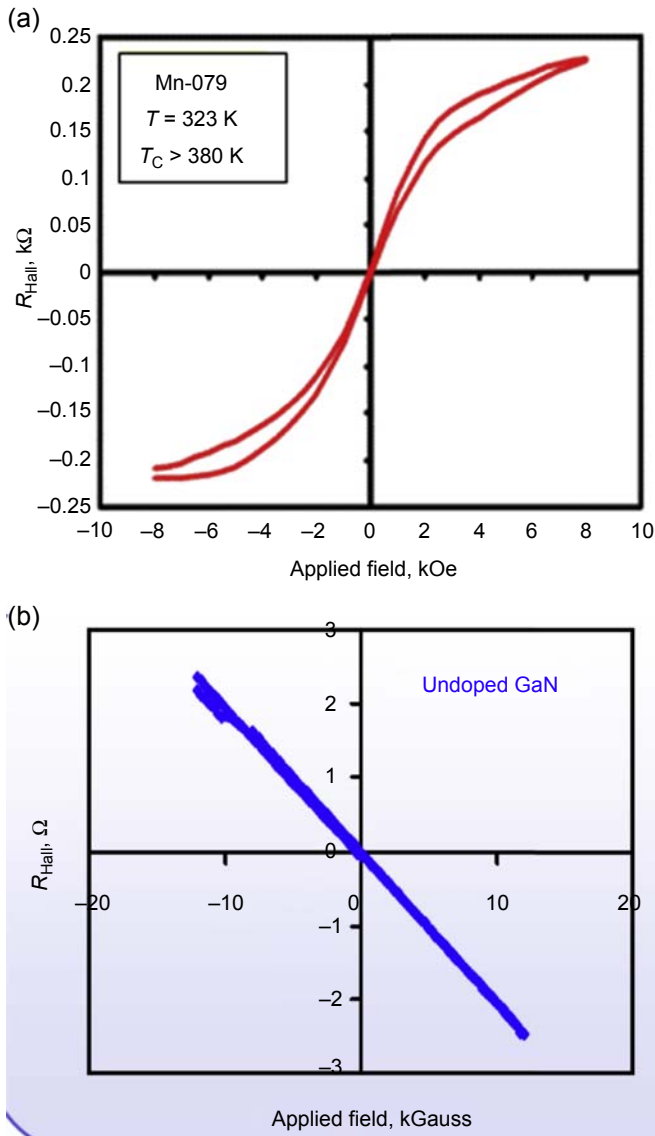


**Figure 12.5** (a) EHE measurements for sample Mn-079 at  $T = 323$  K showing FM behavior with  $T_C > 380$  K; (b) typical response for a GaN without Mn doping.

We have observed that the magnetic properties of the Mn:GaN samples depend upon the electrical properties of the substrate. In general, DM behavior was observed using Si-doped (n-type) substrates; PM behavior using Mg-doped (p-type) substrates; and FM behavior using nonintentionally doped (u-GaN) substrates. After

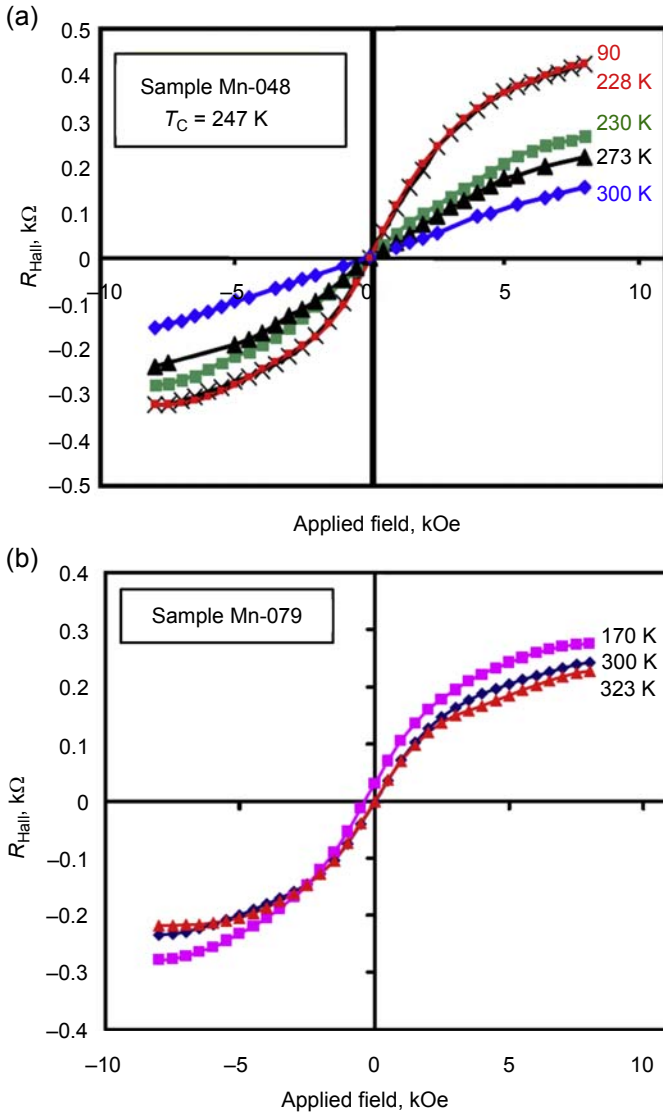


**Figure 12.6** Temperature dependence of the EHE data for Mn:GaN samples (a) Mn-48, and (b) Mn-079. The  $T_C$  for sample Mn-048 was  $\sim 247$  K, for Mn-079 it was estimated to be  $>380$  K.

Mn diffusion most of the films became very resistive, making it difficult to measure the carrier type and concentration. This change in electrical behavior is due to a deep-level acceptor at 1.4 eV above the valence band in Mn-doped GaN films (Korotkov et al., 2001).

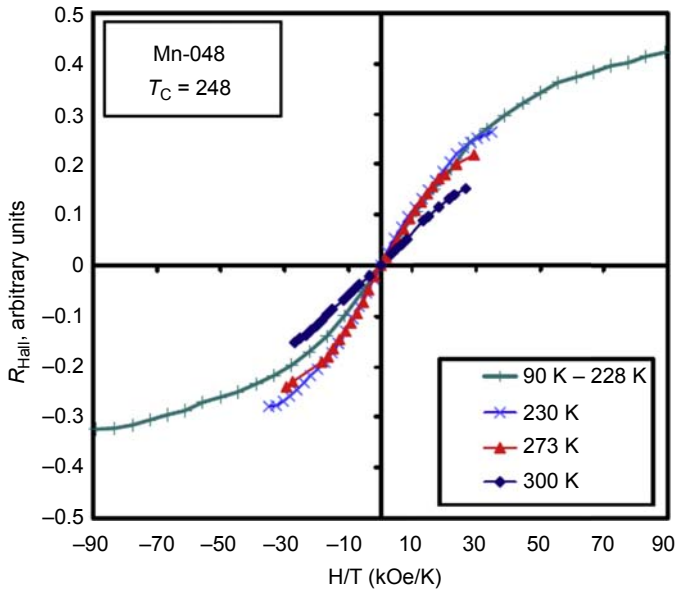


**Figure 12.7**  $R_{\text{Hall}}$  plotted as a function of  $H_a/T$  for Mn:GaN sample Mn-048. The absence of hysteresis clearly eliminates superparamagnetic behavior;  $R_{\text{Hall}}$  is directly proportional to the magnetization.

### 12.2.3 Structural and magnetic characterization of Mn-doped InGaN films

$\text{In}_x\text{Ga}_{1-x}\text{N}$  has been a key material system in the development of blue-green light emitting diodes and lasers. These devices rely on GaN/InGaN double heterostructures and quantum wells (QWs), where the  $\text{In}_x\text{Ga}_{1-x}\text{N}$  is under compressive strain due to its lattice mismatch with GaN. The compressive strain in these films greatly affects their electrical and optical properties. Achieving FM properties in ternary compounds, such as  $\text{In}_x\text{Ga}_{1-x}\text{N}$ , allows the investigation of the effect of strain on the spin polarization properties and the role of spin-polarized carriers in the QWs where electron–hole recombination process takes place.

The  $\text{In}_x\text{Ga}_{1-x}\text{N}$  films were grown on III-nitride templates using MOCVD and Mn diffusion was performed as described earlier. The In content was limited to  $<20\%$  to avoid any complications due to ordering, spinoidal decomposition, and/or phase separation (El-Masry et al., 1998; Behbehani et al., 1999) that have been observed for values of  $x > 0.2$ . The resulting films exhibited FM properties, with  $T_C$  exceeding RT and the magnetic orientation was determined by the strain state of the as-grown  $\text{In}_x\text{Ga}_{1-x}\text{N}$  film. The In content of relaxed  $\text{In}_x\text{Ga}_{1-x}\text{N}$  films, with thickness  $t > 0.3 \mu\text{m}$ , was determined using XRD ( $\theta$ - $2\theta$  scans) of the (0002) and (0004) reflection peaks. The thicker  $\text{In}_x\text{Ga}_{1-x}\text{N}$  films were determined to be unstrained since the measured lattice spacings ( $a$  and  $c$ ) were independent of film thickness, and  $a(\text{InGaN})$  was larger than that of  $a(\text{GaN})$ . The (0004) reflection peak was used to calculate values

**Table 12.3 Summary of the results for the magnetic properties for Mn:InGaN samples studied in this work**

Sample ID	$x$	Stress state	Thickness (InGaN, nm)	In plane Hs (Oe)	Out of plane Hs (Oe)
In-122	0.154	Strained	35	None	None
In-03	0.154	Transitional	105	2700	3200
In-125	0.154	Relaxed	420	None	2000
In124	0.154	Relaxed	630	None	5100
In-123	0.154	Relaxed	840	None	None
In-01	0.051	Strained	157	3750	None
In-02	0.063	Transitional	175	1000	2190
In-06	0.048	Relaxed	315	None	2700

of  $x$  for thick  $\text{In}_x\text{Ga}_{1-x}\text{N}$  films in accordance with Vegard's law. Thinner films grown under identical growth conditions as the thick films were assumed to have the same In content. Table 12.3 lists the In content and strain state of the  $\text{In}_x\text{Ga}_{1-x}\text{N}$  films used for these experiments.

XRD was used to determine the crystalline quality of the Mn: $\text{In}_x\text{Ga}_{1-x}\text{N}$  films and to establish whether any secondary phases were present. In Fig. 12.8 XRD spectra for sample In-124,  $\text{In}_{0.154}\text{Ga}_{0.845}\text{N}$ , are shown for both the as-grown film and after Mn diffusion. No change in In-concentration was found for this sample or for any film as a result of Mn diffusion. In addition, the XRD spectra did not show any change in the lattice constant of the film, keeping in mind that the XRD peaks are fairly broad due to the high density of defects in this material system.

Therefore, within the accuracy of our measurements, no additional strain results from the diffusion process and no secondary magnetic phases, such as MnGa or  $\text{Mn}_4\text{N}$ , or  $\text{Mn}_3\text{GaN}$ , were present. In Fig. 12.9 the electron diffraction pattern (EDP) is shown for sample In-02, Mn: $\text{In}_{0.06}\text{Ga}_{0.94}\text{N}$ , which exhibited FM behavior at RT. The absence of extra diffraction spots in the EDP indicates the absence of secondary phases in the film.

The Mn concentration profiles in the Mn: $\text{In}_x\text{Ga}_{1-x}\text{N}$  samples were measured using SIMS based on a Mn ion implanted GaN standard. In Fig. 12.10 the Mn, In, and Ga depth profiles for sample In-02 are shown. The Mn concentration is reported in atoms/ $\text{cm}^3$ , whereas the Ga and the In-concentrations are reported in counts per second. The thickness of the  $\text{In}_{0.06}\text{Ga}_{0.94}\text{N}$  film was estimated to be  $\sim 180$  nm, after which the In content drops off rapidly, as indicated by the arrows in the figure. Although not uniform, the average Mn concentration in the  $\text{In}_{0.06}\text{Ga}_{0.94}\text{N}$  layer is  $\sim 3.7 \times 10^{21}$  atoms/ $\text{cm}^3$ , which corresponds to  $\sim 8-9$  at.%. Such a large Mn incorporation might be expected to lead to a change in the lattice parameters of the film. However, the shift may be embedded in the broad XRD spectrum of the  $\text{In}_x\text{Ga}_{1-x}\text{N}$  layer shown in Fig. 12.8.

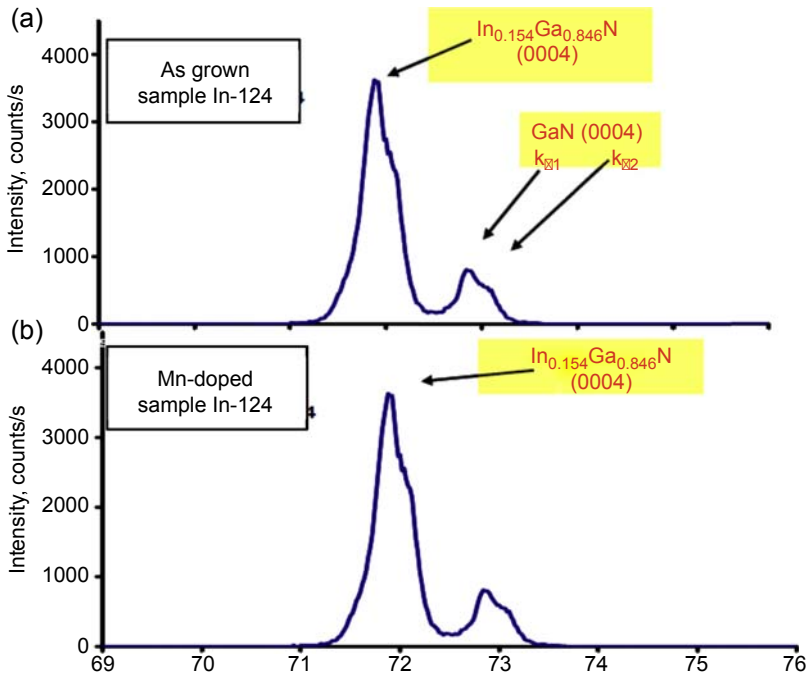


**Figure 12.8** XRD spectra for sample In-124,  $\text{In}_{0.154}\text{Ga}_{0.845}\text{N}$ , showing the (0004) peak for the (a) as grown and (b) the Mn-doped film. No secondary magnetic phases were observed.

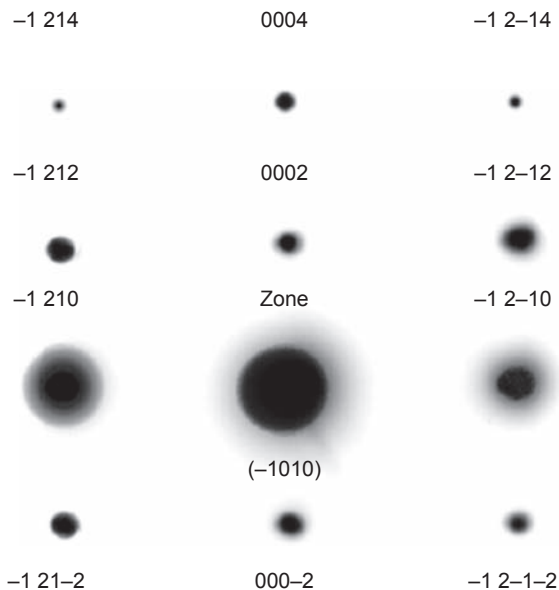


**Figure 12.9** Electron diffraction pattern of sample In-02,  $\text{Mn}:\text{In}_{0.06}\text{Ga}_{0.94}\text{N}$ , showing the  $(0\ 1\ \bar{1}\ 0)$  zone axis. The absence of extra spots, or streaks in the film, indicates that the film is single crystal.

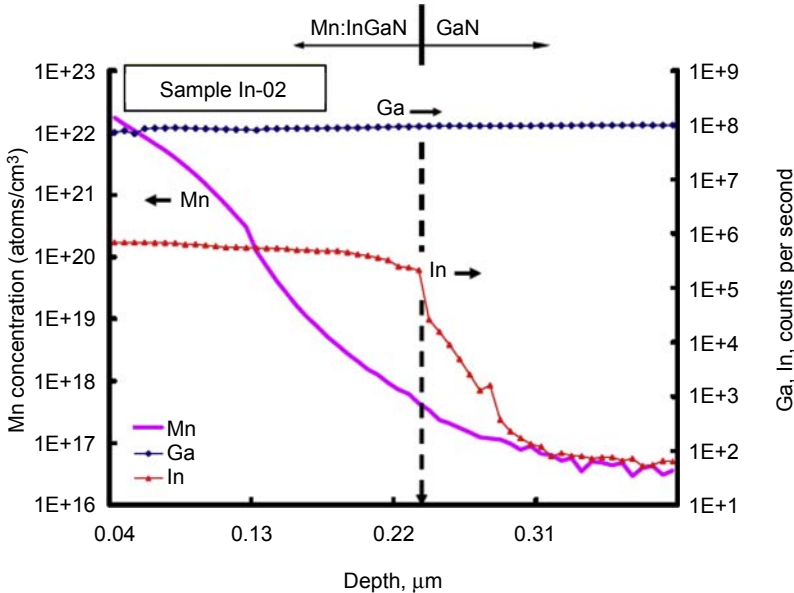


**Figure 12.10** SIMS depth profiles of Mn, Ga, and In in the 180-nm-thick  $\text{In}_{0.06}\text{Ga}_{0.94}\text{N}$  layer of sample In-02. Average Mn concentration was  $\sim 8\%$  over the thickness of this film. The InGaN/GaN interface is denoted by arrows.

Vibrating sample magnetometry (VSM) measurements were performed at RT to characterize the magnetic properties of the  $\text{Mn}:\text{In}_x\text{Ga}_{1-x}\text{N}$  samples. The data indicate that the easy axis is either in-plane or out-of-plane, depending on the stress state of the  $\text{In}_x\text{Ga}_{1-x}\text{N}$  film. The RT VSM curves for sample In-01 are presented in Fig. 12.11. The  $\text{In}_{0.051}\text{Ga}_{0.949}\text{N}$  layer was 157 nm thick and is determined under compressive strain. The easy axis for this sample is in-plane with coercive field  $H_C = 420$  Oe.

Some samples showed hysteresis behavior both for in-plane and out-of-plane applied field orientations. This behavior can be seen in Fig. 12.12, for sample In-03, with  $x = 0.15$  and a thickness of 154 nm. The as-grown  $\text{In}_{0.15}\text{Ga}_{0.85}\text{N}$  layer was in a transitional state of stress.

In Fig. 12.13 the hysteresis curves for a relaxed sample, In-125, are shown. The as-grown  $\text{In}_{0.154}\text{Ga}_{0.846}\text{N}$  layer was 154 nm thick. The easy axis for this film was out-of-plane with  $H_C = 60$  Oe.

Our data provide evidence that the stress state of the  $\text{Mn}:\text{In}_x\text{Ga}_{1-x}\text{N}$  films affects the magnetic properties of these films. The effect of strain on the magnetic properties may be due to the magnetoelastic effect as was reported for Mn:GaAs and Mn:InGaAs compounds (Yun et al., 2002; Matsuhura et al., 1998, 1999). In those studies the easy axis of magnetization was in-plane when the film was under compression and out-of-plane when it was under tension.

Similarly, our findings for  $\text{Mn}:\text{In}_x\text{Ga}_{1-x}\text{N}$  films can be explained in terms of the magnetoelastic effect. In general, the magnetic anisotropy depends on the crystal symmetry of the host material. Its effect is determined by the interaction between

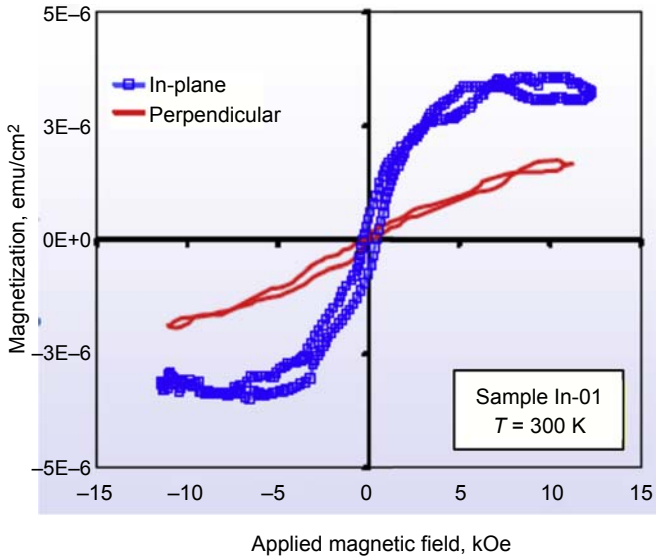


**Figure 12.11** RT VSM curves for sample In-01,  $\text{Mn}:\text{In}_{0.051}\text{Ga}_{0.949}\text{N}$ . The film is under compressive strain and the easy axis is in-plane.

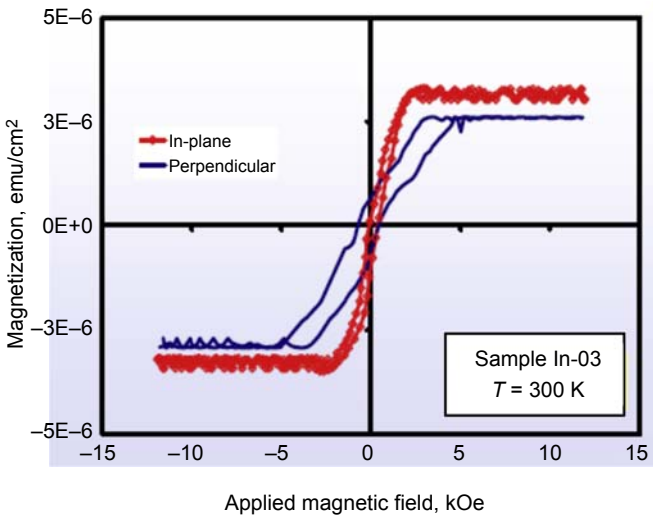


**Figure 12.12** RT VSM curves for sample In-03,  $\text{Mn}:\text{In}_{0.15}\text{Ga}_{0.85}\text{N}$ , showing isotropic magnetic properties. The as-grown  $\text{In}_{0.15}\text{Ga}_{0.85}\text{N}$  layer was 154 nm thick and was in a transitional state of stress.

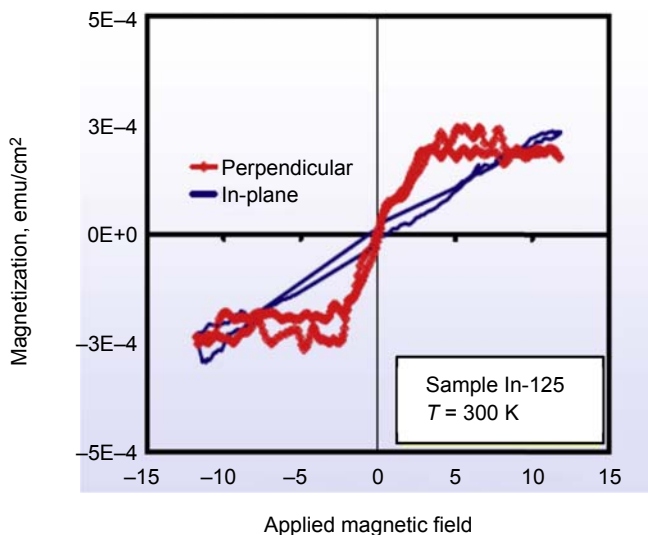


**Figure 12.13** RT VSM curves for sample In-125,  $\text{Mn}:\text{In}_{0.154}\text{Ga}_{0.846}\text{N}$ , with an out-of-plane easy axis. The as-grown  $\text{In}_{0.154}\text{Ga}_{0.846}\text{N}$  layer was 154 nm thick and the film was in the relaxed state.

the orbital state of the magnetic ion and the surrounding crystalline field, which can be altered by the amount of strain present in the film. The  $\text{In}_x\text{Ga}_{1-x}\text{N}$  films, grown on a GaN template, are under a compressive strain for thicknesses below the critical layer thickness (CLT) for a given In content. Therefore, the spin–orbit coupling along the  $a$ -axis will be strong when the films are under compressive strain. Upon relaxation, this will change and the easy axis will be along the  $c$ -axis of the films, which is typical for hexagonal crystals.

Previously, we studied the relaxation process for wurtzite  $\text{In}_x\text{Ga}_{1-x}\text{N}$  films as a function of film thickness. We reported that the transition from the strained to the relaxed state does not occur abruptly as in the case of zinc-blende As-based films such GaAs (Reed et al., 2000; Parker et al., 1999a,b). For  $\text{In}_x\text{Ga}_{1-x}\text{N}$  films this transition occurs gradually as the strained films undergo partial relaxation as the film thickness begins to exceed the CLT. A possible explanation for this occurrence is that the misfit dislocations, which are required to relieve the lattice mismatch, are more difficult to form in III-V nitride compounds than in zinc-blende III-V arsenide compounds.

Samples In-02 and In-03 were determined to be in a transitional state of stress, and as a result, these films exhibited both in-plane and out-of-plane FM behavior. These samples displayed similar magnetization curves at RT even though the Mn concentration was  $3.7 \times 10^{21}$  atoms/cm<sup>3</sup> for In-02 and only  $9.64 \times 10^{20}$  atoms/cm<sup>3</sup>, for In-03. The effective magnetic moment  $\mu_{\text{eff}}$  of In-02 was only  $0.392 \mu_{\text{B}}/\text{Mn}$  atom, versus  $3.43 \mu_{\text{B}}/\text{Mn}$  atom for In-03. The lower  $\mu_{\text{eff}}$  in the film with higher Mn concentration may be due to AFM coupling that results from a closer separation between Mn atoms.



### 12.2.4 Structural and magnetic characterization of Fe-doped GaN films

Here we report on our findings concerning solid state diffusion of Fe into GaN films and the resulting FM behavior. The undoped GaN films were grown by MOCVD on III-V nitride templates as described in Section 12.2. Fe doping was achieved by PLD deposition and annealing at temperatures ranging from 400 to 600°C. The post-deposition annealing time was varied between 45 and 180 min and was carried out at the deposition temperature. Following annealing, the Fe:GaN samples were etched in a solution of (3:1) HCl:H<sub>2</sub>O for 10 min to remove residual Fe on the sample surface.

Atomic depth profiles of Fe in the Fe:GaN samples were measured by SIMS. A typical profile is shown in Fig. 12.14 for sample Fe-51, in which the Fe concentration ( $N_{\text{Fe}}$ ) forms a gradient profile ranging from  $\sim 3 \times 10^{21}$  Fe/cm<sup>3</sup> at the surface to  $\sim 2 \times 10^{17}$  Fe/cm<sup>3</sup> at a depth of 0.38  $\mu\text{m}$ . Relative to the Ga sublattice,  $N_{\text{Fe}}$  was estimated to be  $\sim 7.6\%$ , at the top of the film. An estimate of the average  $N_{\text{Fe}}$  in the top 0.2  $\mu\text{m}$  of the doped region is  $\sim 2.3 \times 10^{20}$  atoms/cm<sup>3</sup>. The SIMS data also indicate that no Fe atoms remain on the surface of the etched sample.

The crystalline quality of the Fe:GaN films, which were etched samples and found to be magnetic, was examined by XRD. No peaks were found corresponding to secondary magnetic phases such as Fe<sub>x</sub>N, or stable oxides such as Fe<sub>3</sub>O<sub>4</sub>, Fe<sub>2</sub>O<sub>3</sub>, FeO. Some of the diffraction patterns did show a very weak peak at  $\theta \approx 17.9^\circ$  that corresponds to the forbidden (0001) GaN peak and is likely due to double diffraction or stacking faults in the films (Reed et al., 2001a).

To investigate whether secondary phases, such as nanoscale Fe or Fe<sub>x</sub>N precipitates, had been formed in the Fe:GaN films, EDX (STEM mode) measurements were made covering the film thickness at 1 nm steps. The EDX spectra showed no Fe peaks indicating the absence of precipitates larger than 1 nm, which is the STEM

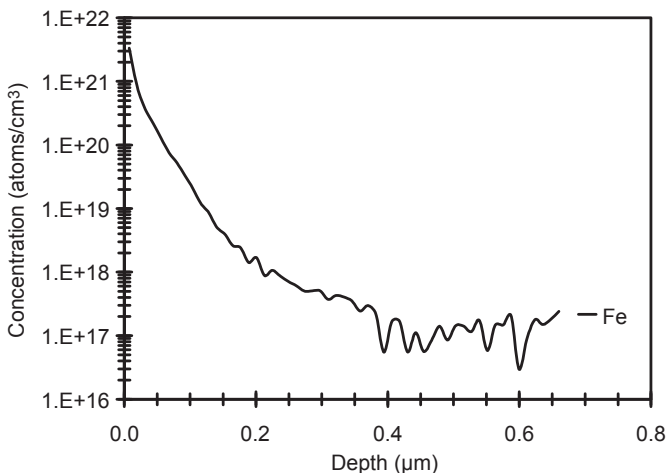
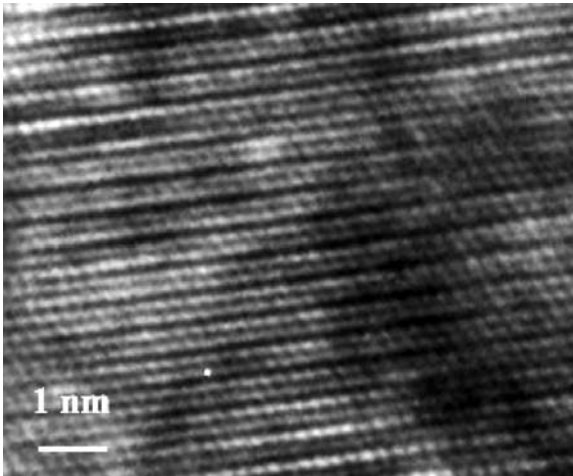


Figure 12.14 SIMS measurement of the Fe depth profile in Fe:GaN sample Fe-51.



**Figure 12.15** HRTEM image of the Fe:GaN sample Fe-51; no coherent or incoherent precipitates are observed in all the images taken for the film.

resolution limit. Special attention was given to the top of the GaN film and at locations such as at dislocation lines or stacking fault boundaries, where faster diffusion might be expected. However, no Fe peaks were detected.

The HRTEM image in Fig. 12.15 is an image of a Fe:GaN film, Fe-51, in which no Moiré fringes or irregularities in the lattice spacing are present, indicating that the sample contains no Fe rich precipitates, or particles larger than 1 nm.

Another approach to verify that any magnetic behavior found in the Fe:GaN films is not due to Fe crystallites or clusters is to calculate the mean distance between two possible Fe clusters that would lead to FM behavior. The mean distance between clusters, assuming them to be 1.7 nm in diameter and containing  $\sim 1.77 \times 10^{17}$  Fe atoms, in the top 0.2  $\mu\text{m}$  is  $\sim 38$  nm. Considering the field of the transmission electron microscopy (TEM), which is  $\sim 200$  nm, it should have been possible to identify such crystallites, if they were present in the film. However, no clusters were observed.

The possibility of clusters smaller than 1 nm being superparamagnetic needs to be addressed. The transition between FM and superparamagnetic behavior depends on both temperature and clusters size, with lower temperatures and larger sizes supporting FM behavior. The transition, or blocking, temperature ( $T_B$ ), below which the clusters are FM, can be estimated for spherical shapes from the expression:

$$\kappa V_p / kT_B = 25 \quad [12.2]$$

where  $V_p$  is the cluster volume,  $k$  is Boltzmann's constant ( $1.38 \times 10^{-16}$  erg/K), and  $\kappa$  is the anisotropy constant for Fe ( $4.8 \times 10^5$  erg/cm<sup>3</sup>) (Cullity, 1972). Clusters with diameters less than the TEM detection limit of 1 nm would have  $T_B < 1$  K and could be superparamagnetic. However, an additional criterion for superparamagnetic behavior is that magnetization curves measured at different temperatures ( $M$  vs  $H_d/T$ )

must superimpose on a common curve. A corollary is that the low-field magnetic susceptibility must follow a Curie law; that is, be proportional to  $1/T$ .

SQUID measurements were made at 5, 200, and 300 K with  $H_a$  parallel to the sample plane. Data for an etched Fe:GaN sample, Fe-47, are shown in Fig. 12.16(a), where the DM background from the GaN substrate was subtracted. There is a magnetic saturation at all temperatures and a decrease in  $M_S$  from  $1.2 \times 10^{-4}$  emu at 5 K to  $8.9 \times 10^{-5}$  emu at 300 K. The low-field susceptibility did not vary over this wide temperature range, a trend that is not compatible with superparamagnetic behavior. In addition, when  $M$  is plotted as a function of  $H_a/T$ , as seen in Fig. 12.16(b), the data do not superimpose on a universal curve. In Fig. 12.16(c)  $M_S$  is plotted as a function of  $T$ , with  $H_a = 3500$  Oe for temperatures from 5 to 400 K. The observed FM behavior indicates that the ordering temperature of Fe:GaN exceeds 400 K.

VSM data for etched Fe:GaN samples Fe-47 and Fe-45 are shown in Fig. 12.17. Sample Fe-47 displayed FM behavior while Fe-45 exhibited DM behavior, even though both samples were prepared on the same GaN substrate. However, Fe-47 was annealed at 500°C for 135 min whereas sample Fe-45 was annealed at 410°C for 210 min. The difference in magnetic behavior can be attributed to the higher concentration of magnetically active Fe atoms in sample Fe-47 as a result of higher diffusion temperature (Table 12.4).

## 12.3 Mn doping of GaN films by MOCVD

Initial experiments regarding the in situ Mn-doping GaN during MOCVD growth were focused on establishing the basic properties of the films and the relationship to the growth conditions. The samples were grown in an in-house custom-built MOCVD reactor. The films were extensively characterized both magnetically and structurally in order to gain a good understanding of the growth parameters. The first set of experiments focused on determining the concentration of Mn ( $C_{Mn}$ ) in the films based on the precursor flow rate (PFR) of ethyl bisethyl cyclopentadienyl-Mn [(EtCp)<sub>2</sub>Mn] during growth.

Samples were grown with (EtCp)<sub>2</sub>Mn PFRs of 50, 100, or 200 sccm and analyzed by SIMS. A Mn-implanted GaN standard was used for calibration and to quantify the  $C_{Mn}$  data. The SIMS data established that Mn was incorporated into the GaN film and the average  $C_{Mn}$  was  $2.3 \times 10^{19}$ ,  $4.7 \times 10^{19}$ , and  $1.1 \times 10^{20}$  Mn/cm<sup>3</sup> for PFR of 50, 100, and 200 sccm, respectively. Fig. 12.18 illustrates the SIMS depth profiles for Mn and Ga obtained from GaMnN sample N133-03 grown at a 200 sccm PFR. SIMS data for Mn are given in Mn/cm<sup>3</sup> and in counts/sec for Ga.

In Fig. 12.19 the average  $C_{Mn}$  is plotted as a function of PFR at the growth temperature of 1021°C; another data point at 993°C is also presented. The data suggest that lower growth temperatures result in higher  $C_{Mn}$  in the final film for the same flow rate.

A wide range of flow rates, up to 500 sccm, was studied to determine the onset of secondary phase formation and ensure the growth of single crystal films. The experiments led to a phase diagram, shown in Fig. 12.20, indicating regions where

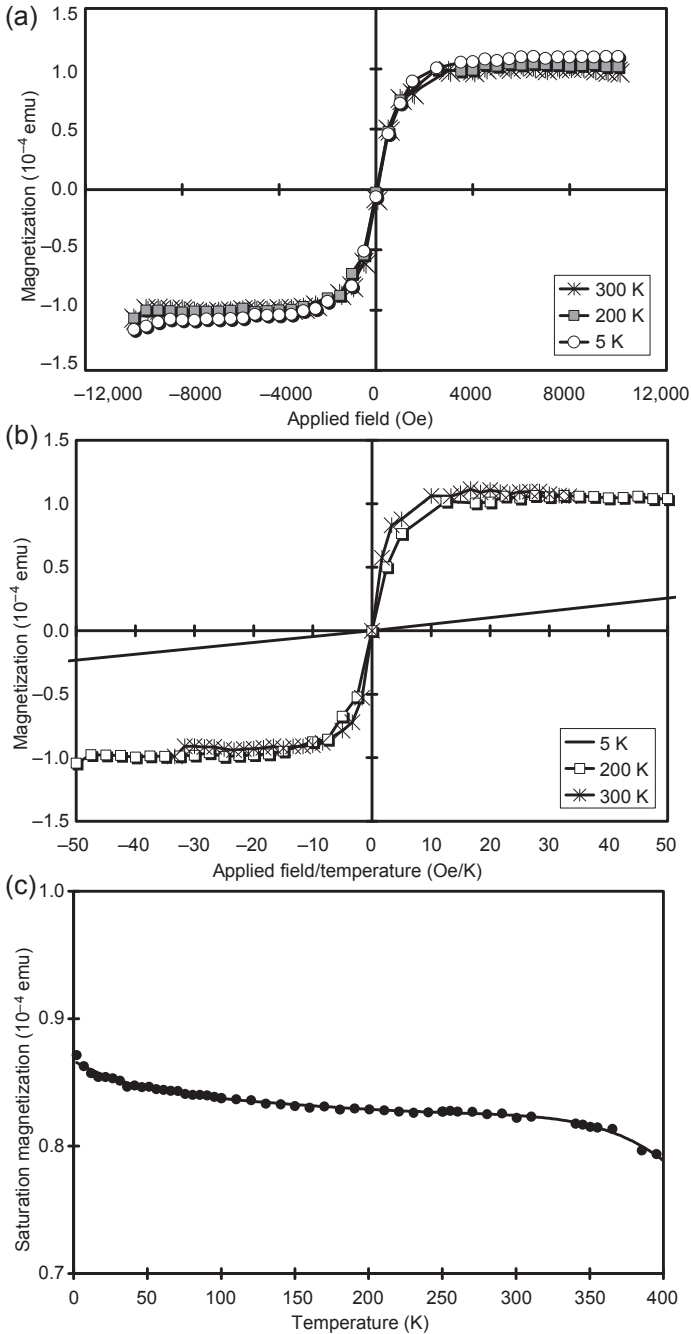


**Figure 12.16** (a) Temperature dependence of the magnetization curves for etched sample Fe-47 showing the decrease in  $M_s$  with increasing temperature. (b) Magnetization curves plotted versus  $H_a/T$  showing that the curves do not superimpose as required by superparamagnetic behavior. (c) The temperature dependence of  $M_s$  with  $H_a = 3500$  Oe applied parallel to the film. FM behavior is still present at 400 K, which is the operating limit of the equipment.

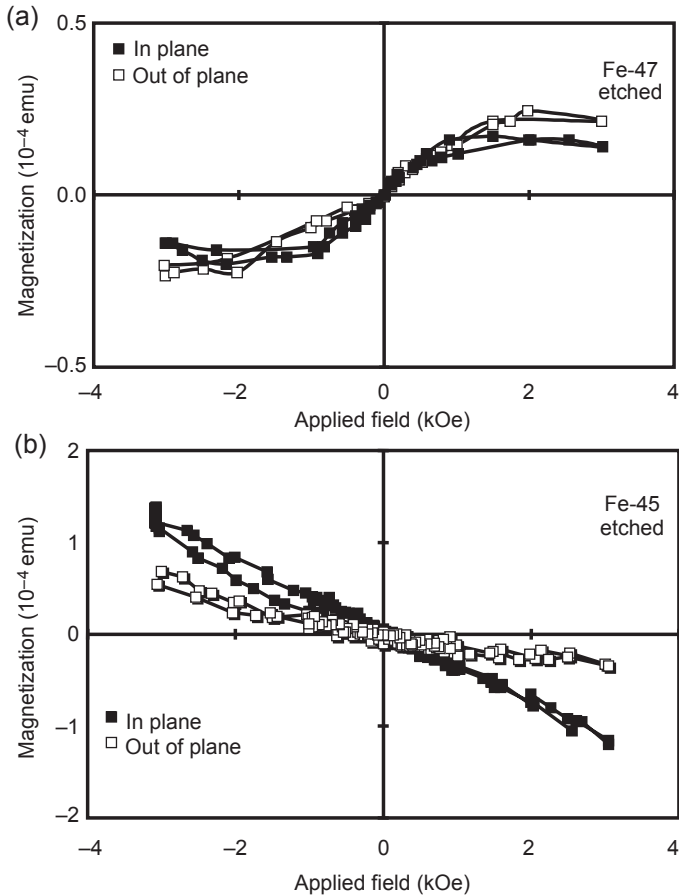


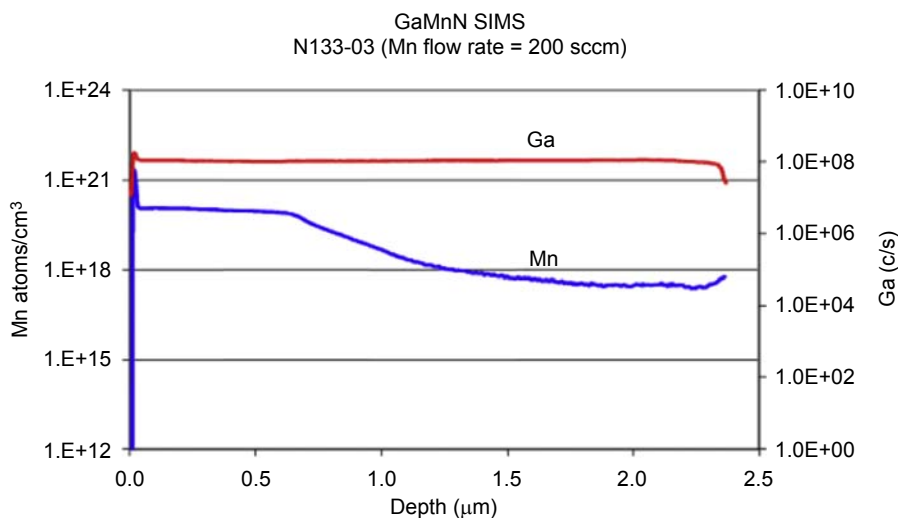
**Figure 12.17** VSM magnetization curves at RT for etched Fe:GaN samples (a) Fe-47 showing FM behavior and (b) Fe-45 showing DM behavior.

single crystal films are free of secondary phases and other regions where secondary and polycrystalline phases are obtained. The solid red circles represent GaMnN films with secondary phases that had magnetic behavior, whereas open red circles indicate those with nonmagnetic behavior. The solid blue circles represent GaMnN films with no secondary phases that had magnetic behavior, whereas open blue circles indicate those with nonmagnetic behavior.

In these experiments higher flow rates and higher growth temperatures led to films with rough surfaces, polycrystalline GaN phases, and eventually to secondary phases. The optimum PFR and temperature for a smooth surface were determined to be 100 sccm and 1020°C. To examine the presence of secondary phases, XRD scans of all samples were made. A typical XRD scan for GaMnN sample N131-03 is shown in Fig. 12.21. No peaks from secondary phases were found, only those from GaN and the sapphire substrate.

**Table 12.4 List of annealing conditions and magnetic behavior, after etching, of Fe:GaN samples using two different GaN substrates**

Sample name	$T_{\text{Anneal}}$ (°C)	Time (growth + anneal) (min)	Magnetic behavior after etching
Fe-43	560	210	Ferromagnetic
Fe-51	500	270	Ferromagnetic
Fe-47	500	135	Ferromagnetic
Fe-45	410	210	Diamagnetic
Fe-40	560	165	Diamagnetic
Fe-42	560	210	Diamagnetic
Fe-50	500	270	Ferromagnetic
Fe-46	500	135	Diamagnetic

**Figure 12.18** SIMS depth profiles for Mn and Ga for GaMnN sample N133-03 grown at 1021°C with a PFR of 200 sccm.

A SQUID magnetometer was used to measure the magnetization of the GaMnN films grown by MOCVD. Fig. 12.22 shows results of a SQUID measurement at RT for GaMnN sample N129-03 indicating the FM hysteresis behavior with finite remnance and coercivity.

TEM measurements indicated that the MOCVD grown GaMnN material is single crystal and free of secondary phases. Some twin boundaries, stacking faults, and dislocation loops were observed.

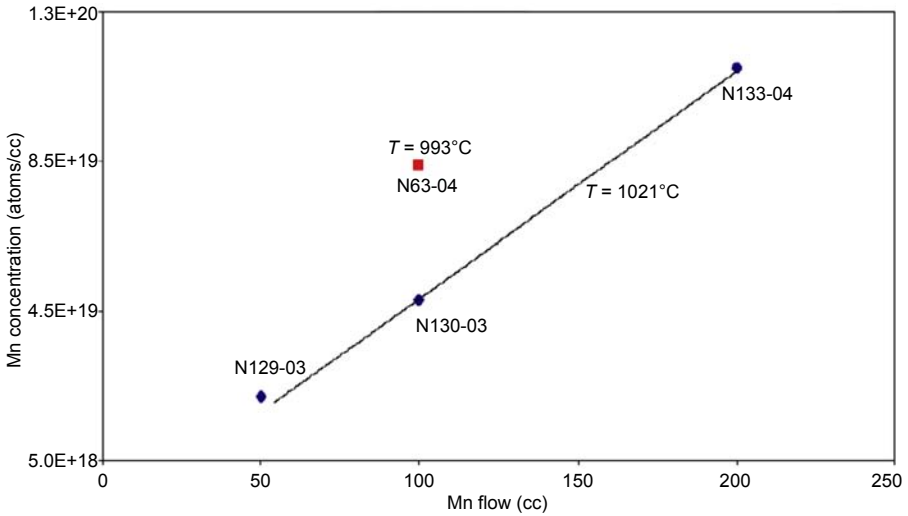


**Figure 12.19** The average Mn concentration in GaMnN films as a function of the PFR. The solid line is the best fit for samples grown at 1021°C.

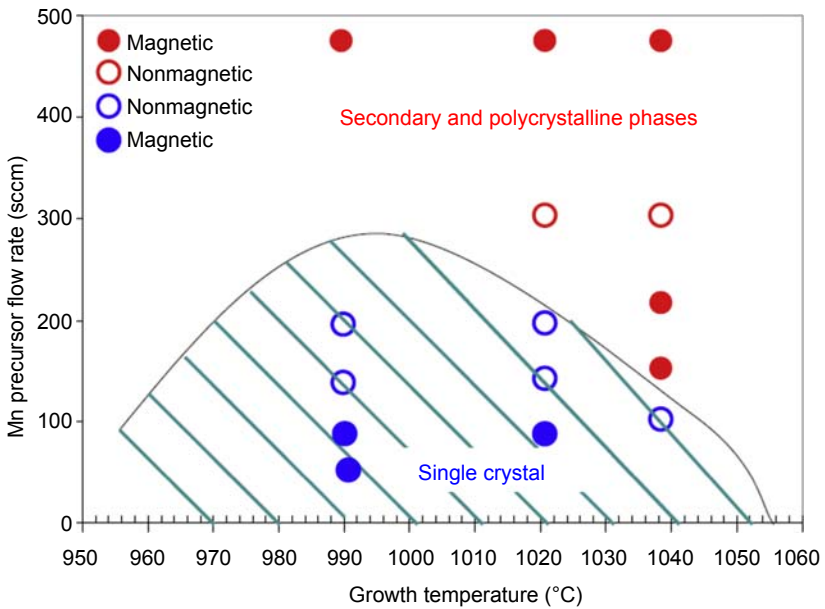


**Figure 12.20** Phase fields for GaMnN films grown by MOCVD indicating single phase regions and secondary and polycrystalline phase regions. Results of magnetic measurements are also indicated.

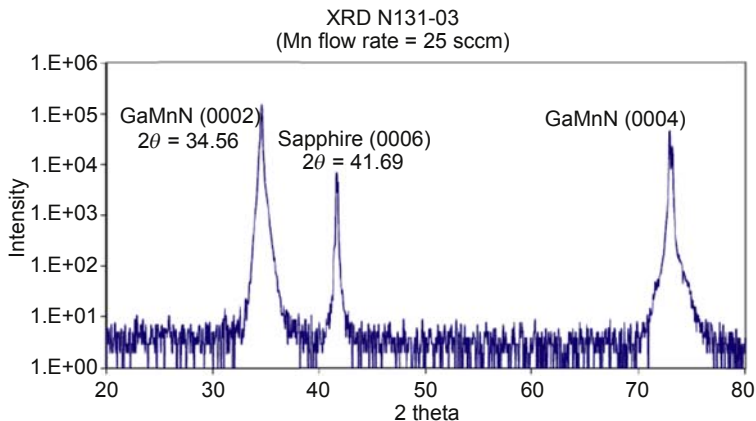


**Figure 12.21** XRD scan of GaMnN sample N131-03 indicating the absence of secondary phases. The observed peaks are from GaN and the sapphire substrate.

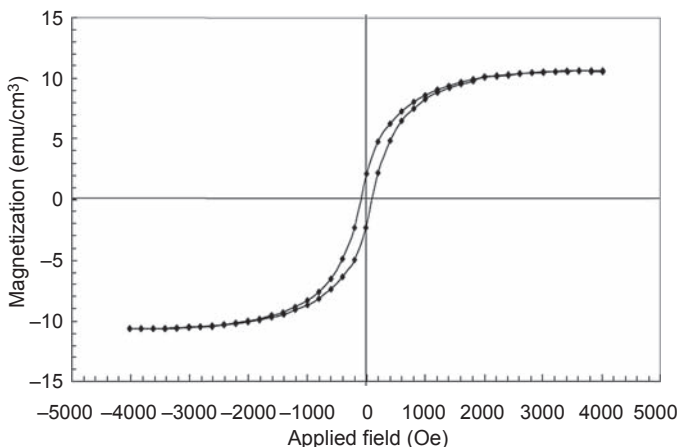


**Figure 12.22** Hysteresis data for GaMnN sample N129-03 at 300 K indicating FM behavior.

The SQUID measurements at RT showed that the  $M_S$  of the films scaled with  $C_{Mn}$  up to a maximum at  $\sim 5\%$ . Further increases in  $C_{Mn}$  caused the magnetization to decrease to the background value. In Fig. 12.23, the dependence of  $M_S$  on  $C_{Mn}$  is illustrated for films grown at 1021°C. Two data points for films grown at 903°C are also shown. The reduction in  $M_S$  with  $C_{Mn} > \sim 5\%$  may be due to AFM coupling between the Mn ions at higher concentrations.

There have been conjectures that secondary phases, spin-glass behavior, or superparamagnetic clusters are responsible for the FM behavior in wide bandgap semiconductor materials. In order to rule out the possibility that spin-glass behavior occurs, remnant magnetization ( $M_R$ ) measurements were performed as a function of time. In FM materials, the value of  $M_R$  should be constant for extended periods of



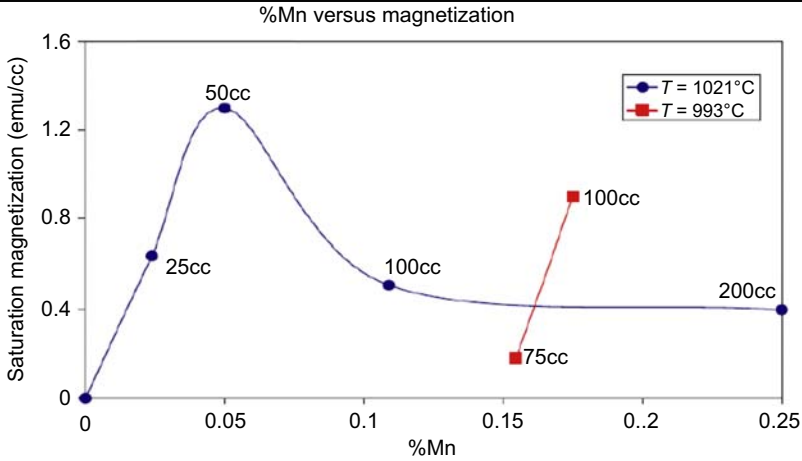


**Figure 12.23** Saturation magnetization as a function of the Mn concentration in GaMnN films grown by MOCVD.

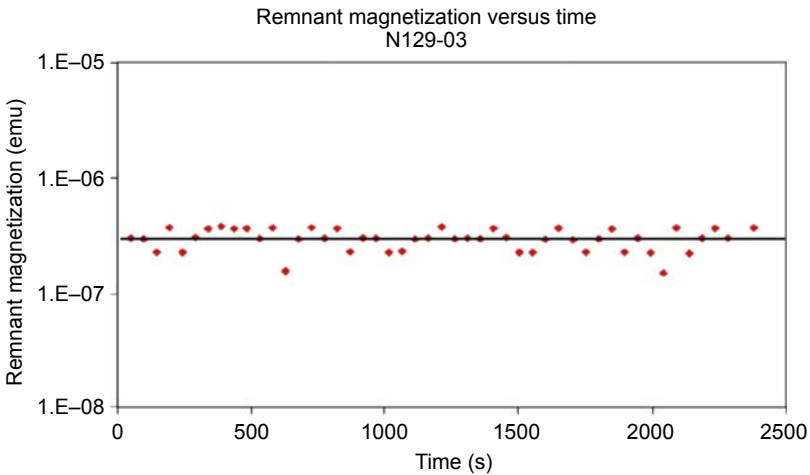


**Figure 12.24** Time dependence of  $M_R$  for GaMnN sample N129-03 recorded at 20 K with a zero applied field.

time,  $\geq 30$  min, below the critical temperature. Fig. 12.24 shows the results of such a measurement for GaMnN sample N129-03, which was cooled to 20 K and saturated with a field of 1 T. There was little change in  $M_R$  for over 8 h, which is the behavior of an FM material.

In superparamagnetic materials,  $M_R$  is negligible and plots of magnetization ( $M$ ) versus  $H_d/T$  should overlap. Data from such measurements for GaMnN sample N131-03 are shown in Fig. 12.25. Clearly the hysteresis curves at different temperatures have different slopes and are not overlapping, excluding superparamagnetic behavior in the MOCVD GaMnN grown films.

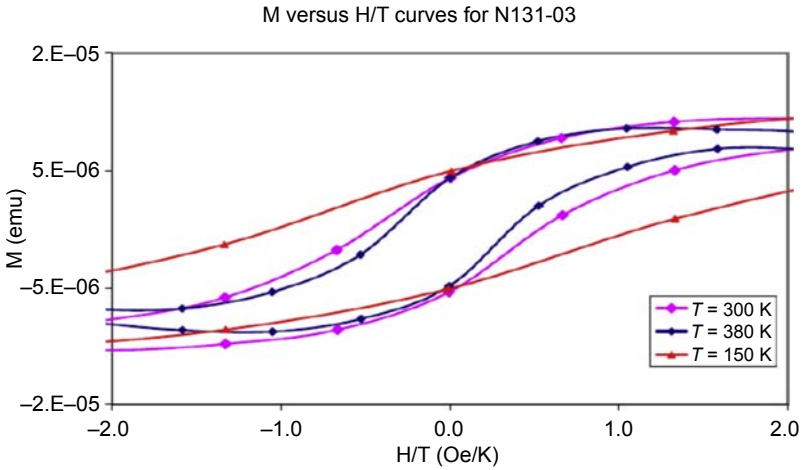


**Figure 12.25** M versus  $H_a/T$  measurements for sample GaMnN N131-03 excluding the possibility of superparamagnetic behavior.

## 12.4 Fermi level engineering of magnetic behavior of GaMnN

As described in [Section 12.2](#), the Zener theory of FM behavior in semiconductor materials is based on the interaction between the delocalized carriers and localized spins of the magnetic impurities. This theory works well to explain the FM properties of GaMnAs and InMnAs semiconductors. In these materials Mn assumes a 2+ valency that results in formation of an acceptor level band near the valence band ( $E_{VB}$ ) of GaAs or InAs. This impurity band also hybridizes with  $E_{VB}$  provided that a sufficient Mn concentration is reached. An abundance of holes in p-type GaMnAs mediates the magnetic interaction and leads to FM behavior. However, for GaMnN materials the situation is quite different; Mn forms a deep impurity level approximately 1.4 eV above the  $E_{VB}$  of GaN. This deep band, whose width depends on the Mn concentration ([Korotkov et al., 2001](#); [Kronik et al., 2002](#)), does not supply holes to hybridize with  $E_{VB}$  and hence the resulting crystal is electrically insulating. Consequently, carrier-mediated ferromagnetism in GaMnN does not occur in the same manner as with GaMnAs. Since we have observed FM properties (see [Sections 12.2 and 12.3](#)) and have precluded the existence of secondary phases or spin-glass behavior, a different mechanism must be at work to produce magnetic ordering in the GaMnN films.

Based on our experimental data, we have proposed that FM properties in GaMnN are a function of the position of the Fermi level ( $E_F$ ) within the crystal ([Reed et al., 2005a,b](#)). More specifically, long-range magnetic ordering occurs when  $E_F$  coincides with the Mn-induced impurity band ( $E_{\{Mn\}}$ ). Once this band is partially filled, carriers (holes) are rendered mobile and can polarize the spins of the Mn ions resulting in FM order. When  $E_F$  is below  $E_{\{Mn\}}$ , this band is devoid of carriers and minimal interaction between the Mn ions occurs. Conversely, if  $E_F$  is located above  $E_{\{Mn\}}$ , then the band is

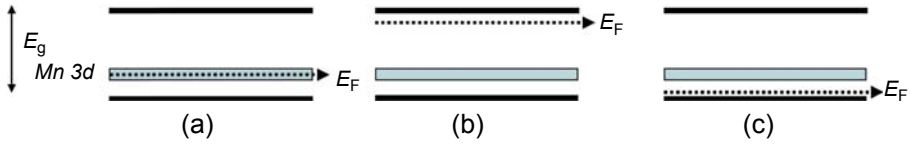


**Figure 12.26** Illustration of the GaMnN band structure with the location of the Mn impurity band and three possible positions for the Fermi level: (a)  $E_F$  coincides with the Mn band, (b)  $E_F$  lies above the Mn band, and (c)  $E_F$  is below the Mn band. Magnetic ordering occurs only in case (a).

completely filled with electrons, and again FM ordering is prohibited. The three cases are illustrated in Fig. 12.26.

### 12.4.1 Codoping of GaMnN with either silicon or magnesium

Several experiments were undertaken to alter the position of the Fermi level in the GaMnN crystal and to monitor the change in the magnetic properties. The first approach was in situ codoping of GaMnN during MOCVD growth with either Si or Mg, which are n-type and p-type dopants, respectively.

MOCVD growth conditions were selected to produce FM properties in the undoped films. The silane was added as a Si codopant at different flow rates during the growth. The addition of silane was expected to raise the position of the  $E_F$  level in the bandgap of GaMnN material. After growth, the films were examined using alternating gradient magnetometry (AGM) for magnetic properties. In Fig. 12.27 magnetization versus applied field  $H_a$  curves are shown, indicating that the addition of silane during growth lowers the saturation magnetization.

SIMS measurements were performed on these samples to determine the change in Si concentration due to the silane flow rate. SIMS atomic depth profiles are shown in

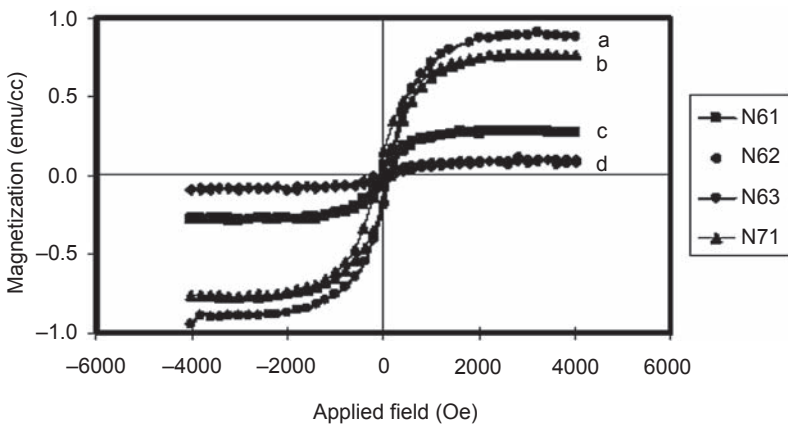


**Figure 12.27** Magnetization versus applied field curves at RT for GaMnN films grown: (a) without silane, and under different silane flow rates; (b) 2.0 nmol/min; (c) 6.78 nmol/min; and (d) 84 nmol/min.

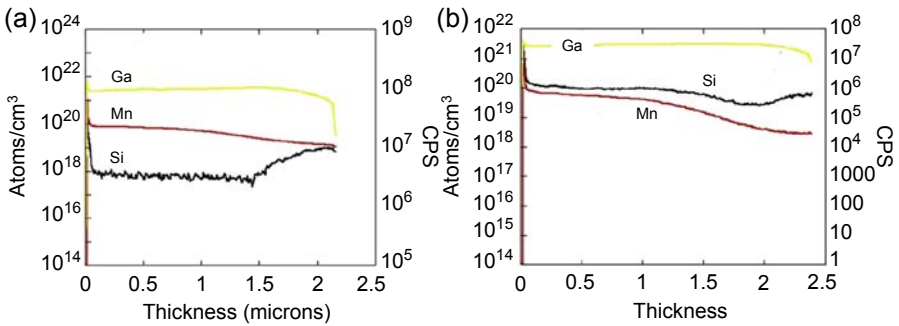


**Figure 12.28** SIMS depth profiles for Si, Ga, and Mn in GaMnN films grown under different silane flow rates: (a) low flow rate and (b) high flow rate.

Fig. 12.28 for two of the GaMnN samples. The Si concentration is  $\sim 10^{18}/\text{cm}^3$  for a low flow rate and  $\sim 10^{20}/\text{cm}^3$  for a high flow rate. Depth profiles for Ga and Mn are also shown indicating only small changes due to Si codoping. The  $E_F$  rises toward the conduction band ( $E_{CB}$ ) under high flow rate conditions and the film becomes paramagnetic (PM).

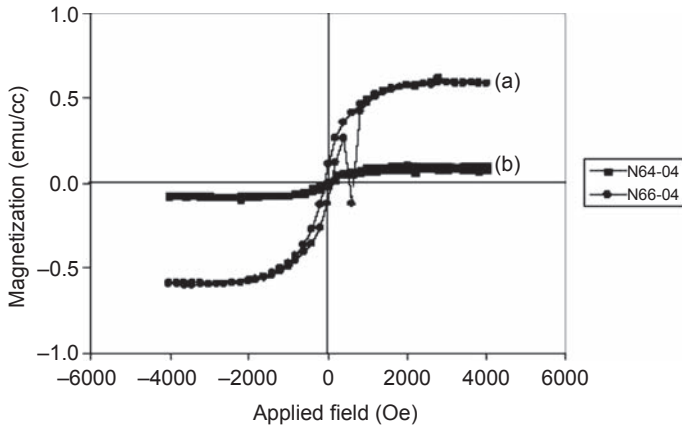
Next, the effect of Mg codoping on the magnetic properties of the GaMnN films was studied using bicycle penta-dienylmagnesium ( $\text{Cp}_2\text{Mg}$ ) as the Mg source during MOCVD growth. It has been well established that Mg-doping of GaN leads to a deep acceptor level located about 0.15 eV above the  $E_{VB}$ . At RT, the Mg acceptor level in GaN:Mg is barely activated and for a Mg concentration of  $\sim 5 \times 10^{19}/\text{cm}^3$ , the hole concentration is only  $\sim 10^{17}/\text{cm}^3$ . For Mg-doped GaMnN films, carriers are thermalized into the acceptor level and as the Mg increases the  $E_F$  is lowered below  $E_{\{\text{Mn}\}}$ . This depletes carriers in the  $E_{\{\text{Mn}\}}$  band and reduces the magnetic moment of these films. Fig. 12.29 illustrates the effect of Mg codoping on the magnetic properties of GaMnN films. Magnetization curve (a) represents an undoped GaMnN film grown under ideal growth conditions for FM behavior. Curve (b) is the magnetic response of a GaMnN film grown under identical conditions except for Mg codoping, which essentially eliminates the hysteresis.

Fig. 12.30 summarizes the effect of codoping GaMnN films with either Mg (red lines) or Si (black lines). Codoping moves the  $E_F$  away from the  $E_{\{\text{Mn}\}}$  and reduces the availability of carriers to mediate magnetic ordering. Consequently, the magnetization decreases.

### 12.4.2 Charge transfer through heterojunction interfaces

In order to further clarify these effects another set of experiments was conducted in which the GaMnN layer remained undoped but was grown adjacent to a Mg-doped or Si-doped GaN layer. Results of these experiments show that the FM properties of the GaMnN layer can be altered by carrier transfer across heterojunction interfaces.

In the first case GaMnN films were grown under conditions that are *outside* the range for producing FM behavior in the GaMnN films. The Mn concentration in these



**Figure 12.29** Magnetization versus applied field curves measured at RT for (a) undoped and (b) Mg codoped GaMnN films.

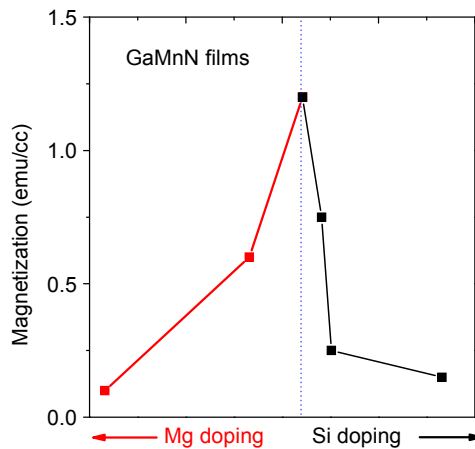


**Figure 12.30** Magnetization saturation values measured at RT for GaMnN films and plotted as a function of Mg codoping (red lines) or Si codoping (black lines). In either case, the  $E_F$  moves away from the Mn impurity band and the magnetization decreases.

films was  $10^{20}/\text{cm}^3$ , as measured by SIMS, and magnetization curves indicated very weak FM or PM behavior. Essentially,  $E_F$  was above the  $E_{\{\text{Mn}\}}$  band and holes were not available to mediate magnetic ordering. However, the magnetic behavior could be altered by growing a GaN:Mg/GaMnN single heterostructure (SHS) shown schematically in the inset to Fig. 12.31. In this set of samples the GaMnN layer thickness was kept constant at  $0.375 \mu\text{m}$  and the GaN:Mg layer thickness varied from  $0.15$  to  $0.75 \mu\text{m}$ . Initially, there was only weak FM response of the SHS for a GaN:Mg thickness of  $0.15 \mu\text{m}$ . However, by increasing the GaN:Mg layer thicknesses, the

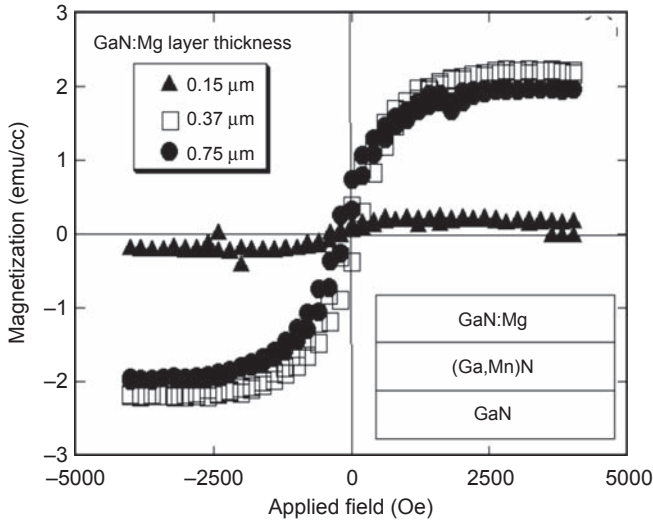


**Figure 12.31** Magnetization versus applied field curves measured at RT for GaMnN/GaN:Mg single heterostructures with different thickness of the top GaN:Mg layer.

magnetization response increased. Sufficient holes from GaN:Mg layer entered the GaMnN film and the  $E_F$  was moved within the  $E_{\{Mn\}}$  band.

Another set of samples consisted of GaN:Mg/AlGaN/GaMnN/AlGaN/GaN:Mg multilayer heterostructures with the AlGaN layers serving as a wide bandgap barriers for the carriers (see inset in Fig. 12.32). Based on the data presented in Fig. 12.31, the GaMnN films were grown under conditions that are *outside* the range for producing FM behavior. The thicknesses of the GaN:Mg (0.75  $\mu\text{m}$ ) and GaMnN (0.38  $\mu\text{m}$ ) layers were held constant whereas the thickness ( $t_b$ ) of the AlGaN barriers, with Al

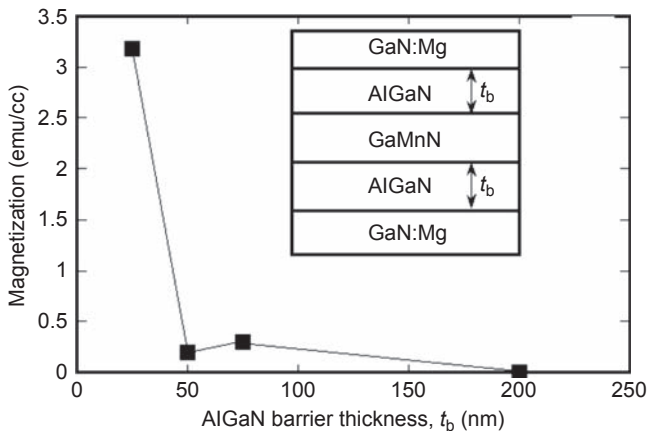


**Figure 12.32** Magnetization versus applied field curves measured at RT for GaN:Mg/Al<sub>0.3</sub>Ga<sub>0.7</sub>N/GaMnN/Al<sub>0.3</sub>Ga<sub>0.7</sub>N/GaN:Mg heterostructures. The thickness  $t_b$  of the Al<sub>0.3</sub>Ga<sub>0.7</sub>N barrier layers varied from 25 to 200 nm.

concentration of 30%, varied from 25 to 200 nm. The magnetization versus applied field curves of these multilayer structures are shown in Fig. 12.32. For the structure with barrier thickness  $t_b \sim 25$  nm, curve (a), magnetic behavior was nearly the same as for films having no AlGaIn barriers (see Fig. 12.31). Charge transfer across the GaN:Mg/GaMnN interfaces took place by tunneling, or thermionic emission, and magnetic ordering occurred. However, as the barrier thickness was increased  $t_b > 50$  nm (see curves (b) and (c)), the AlGaIn barrier layers impeded carrier transfer from the GaN:Mg layers and the films did not exhibit any magnetization (hysteresis or  $M_s$ ). The magnetic response for these samples was practically paramagnetic, as shown in Fig. 12.32.

A third set of samples was grown to study the effect of adjacent layers with Si-doping. In this case, the GaMnN layer was grown between GaN:Si layers to form a double heterostructure (DHS) GaN:Si/GaMnN/GaN:Si, shown in the inset in Fig. 12.33. The GaMnN layer was grown under conditions that led to FM behavior, (ie,  $E_F$  was within  $E_{(Mn)}$ ). Magnetization versus applied field curves measured at RT are shown in Fig. 12.33 for the GaMnN film, having Mn concentration of 0.3%, and for the two DHS samples. The magnetic response for the single film, curve (a), displays hysteresis and  $M_s > 0$ . When such a layer is grown between GaN:Si layers, the magnetic response was reduced (see curves (b) and (c)). For sample (b), the Si-doping concentration was  $\sim 5 \times 10^{18}/\text{cm}^3$  and the magnetic response still showed hysteresis, but with a reduced  $M_s$ . In sample (c), the Si-doping concentration was  $\sim 10^{20}/\text{cm}^3$  and no indication of FM behavior was found. Since Si is a shallow donor in GaN with an energy level 5–10 meV below the conduction band ( $E_{CB}$ ), electrons from the GaN:Si layers were able to transfer to the GaMnN layer. For sample

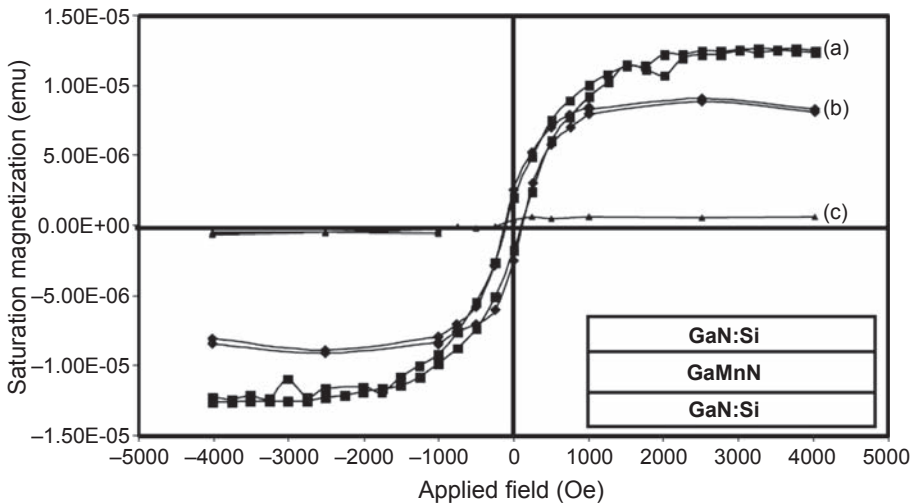


**Figure 12.33** Magnetization versus applied field curves measured at RT for a GaMnN single layer (a); and, for GaN:Si/GaMnN/GaN:Si double heterostructures. The Si-doping concentration was  $\sim 5 \times 10^{18}/\text{cm}^3$  for (b), and  $\sim 10^{20}/\text{cm}^3$  for (c).

(b) the Si doping was much less than the Mn content and the carrier transfer from the GaN:Si layer to GaMnN layer was not sufficient to quench the FM behavior properties. However for sample (c), the higher Si doping was sufficient to reduce  $E_F$  below  $E_{\{Mn\}}$  to eliminate FM behavior.

These results provide compelling evidence that FM behavior depends upon the Fermi level in MOCVD grown GaMnN. When  $E_F$  was within the Mn  $3d$  band  $E_{\{Mn\}}$ , FM behavior was observed. However, when  $E_F$  is either above or below  $E_{\{Mn\}}$ , magnetic ordering did not occur. Furthermore, FM behavior of a GaMnN film could be altered by growing multilayer heterostructures with either GaN:Mg or GaN:Si layers. Transfer of carriers from such adjacent layers can change  $E_F$  in GaMnN and the availability of carriers in the  $E_{\{Mn\}}$  band that are necessary to produce FM behavior.

## 12.5 Room-temperature spintronic device based on GaMnN

There have been previous reports of electric field control of the FM properties in structures based on GaMnAs magnetic films. However, due to the low  $T_C$  of these materials, such devices function only at temperatures less than  $\sim 110$  K (Matsukura et al., 2015). In this section we present a novel GaMnN structure that enables electric field control of the FM behavior at RT. Such devices could utilize both the charge and spin of electrons to process and store data, with higher speeds and lower power consumption, than conventional Si-based devices (Bedair et al., 2010).

In Section 12.4 we demonstrated that the location of  $E_F$  in the GaMnN film determines the magnetic interaction between Mn ions leading to FM behavior ordering (Arkun et al., 2004). We also showed that the  $E_F$  in the GaMnN film can be altered by adjacent Mg or Si-doped GaN layers. In addition, since Mn forms a deep acceptor band in GaMnN, the resulting films are highly insulating (Arkun et al., 2004; Mahros et al., 2007; Schubert et al., 1996). Based on these results, several p-GaN:Mg/GaMnN/n-GaN:Si (p-i-n) structures were grown by MOCVD and processed into prototype devices. However, electric field control of FM behavior was not observed. Two main issues appeared: high Mn concentrations in p-GaN:Mg led to poor crystal quality, and electrical p-type conductivity in this layer was still too low for device demonstration. In order to overcome these issues, p-type ( $Al_{0.2}Ga_{0.8}N$ /GaN:Mg) strained-layer superlattice (SLS) multilayers, with a period of  $\sim 16.6$   $\mu m$ , were grown to replace the p-GaN:Mg layer (Wojtowicz et al., 2003). The p-GaN-SLS structures had higher hole concentrations than the single p-GaN:Mg layers due to strain-induced polarization effects and band-bending at the interfaces. Furthermore, the GaMnN was grown on top of the p-GaN-SLS to form an i-p-n device structure to improve electrical control of carriers (holes) necessary for magnetic ordering (Schubert et al., 1996; Wojtowicz et al., 2003).

Fig. 12.34 shows a schematic of the multilayer GaMnN/p-GaN-SLS/n-GaN structure grown on the c-plane GaN/sapphire substrate. The GaMnN layer had a thickness of  $0.5$   $\mu m$  and Mn concentration  $\sim 10^{20}$   $cm^{-3}$  as determined by SIMS measurements.



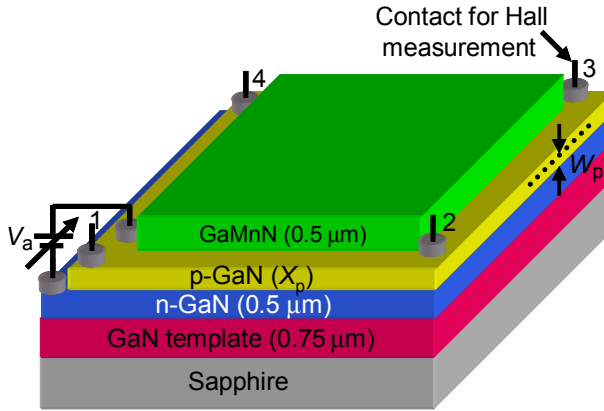


**Figure 12.34** Schematic diagram of the fabricated GaMnN i-p-n device structure where  $X_p$  is the p-GaN-SLS thickness,  $W_p$  the depletion width, and  $V_a$  the applied voltage. Under reverse bias,  $W_p$  at the p-n interface increases and the hole concentration, mediating FM behavior, decreases. Also shown are the four point contacts used to perform Hall measurements.

Device structures with different p-GaN-SLS layer thickness ( $X_p$ ) were fabricated using photolithography and inductively coupled plasma dry etching. The size of each device was about  $2 \times 2$  mm. Contacts were deposited on the p-GaN-SLS and n-GaN layers forming a rectifying junction. Under reverse bias, the depletion width ( $W_p$ ) increased at the p-n interface and the available carriers (hole) required for mediating FM ordering decreased.

The GaMnN layer was grown under conditions that would lead to PM behavior. Magnetic properties of fabricated device structures were examined using AGM measurements at RT. Similar to the results shown in Fig. 12.31, the magnetic response of the i-p-n device structure had a strong dependence on the thickness of the p-GaN-SLS layer (Reed et al., 2005b). For thin layers,  $X_p \leq 0.066 \mu\text{m}$ , the GaMnN structure is PM as a result of insufficient mediating holes due to carrier depletion at the p-n junction. As the thickness  $X_p$  increases, the magnetic response of the structure begins to show FM behavior and reaches a maximum for  $X_p \geq 0.25 \mu\text{m}$ . Since  $M_s$  depends on the interaction between itinerant holes from p-GaN-SLS and the localized Mn ions, magnetic ordering is limited by the penetration of the hole wave function into the GaMnN layer. Previously, the magnetic properties of modulation-doped GaMnAs/AlGaAs:Be heterostructures have been reported (Wojtowicz et al., 2003; Bougrov et al., 2001). That study indicated that the source of holes had to be less than 3 nm away from the GaMnAs layer for coupling to occur between holes and Mn ions.

The next step in demonstrating a functional device for control of FM behavior was to provide an applied voltage ( $V_a$ ) to the GaN p-n junction. AGM measurements of the magnetization versus applied field were made at RT for the GaMnN i-p-n device structure under different values of  $V_a$  (Nepal et al., 2009). Results of these measurements clearly show FM behavior as a function of the reverse bias voltage (see Fig. 12.35). For forward bias and reverse bias voltages down to  $-3$  V, hysteresis curves with a

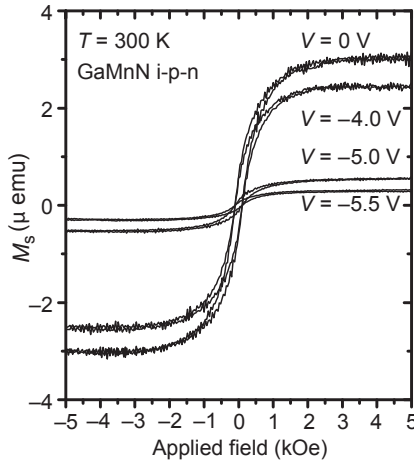


**Figure 12.35** Magnetization versus applied field curves at RT for the GaMnN i-p-n device under different values of reverse bias voltage.

constant  $M_s$  were measured. With increased reverse bias, the  $M_s$  decreased at  $V_a \sim -4$  V and at  $\sim -5$  V the magnetic response was nearly PM. The data provide evidence that ferromagnetism can be modulated by an applied voltage to a  $p$ - $n$  junction adjacent to the GaMnN layer.

The results of these measurements can be explained in terms of the electronic properties of the semiconductor multilayer structure. The GaMnN i-p-n device had a p-GaN-SLS with thickness  $X_p = 0.25$   $\mu\text{m}$ . At zero bias the depletion width  $W_p$  was  $\sim 161$  nm due to built-in potential between the  $p$ - $n$  regions. With increasing bias voltage  $W_p$  also increased and was  $\sim 0.221$   $\mu\text{m}$  at  $-3$  V. This still left  $\sim 30$  nm of the p-GaN-SLS region next to GaMnN layer for holes to mediate magnetic ordering. Since the penetration depth for the hole wave function into the GaMnN layer is  $\sim 30$  nm, the hysteresis curves and the value of  $M_s$  was constant for  $V_a > -3$  V.

However, with further increases in the bias voltage the hysteresis curves changed and the value of  $M_s$  decreased due to the reduction of holes at the p-GaN-SLS/GaMnN interface. For  $V_a \sim -5$  V the depletion width  $W_p$  was  $\sim 25$   $\mu\text{m}$  and the GaMnN layer became mostly PM. There were almost no itinerant holes remaining to mediate magnetic ordering in the GaMnN layer. Consequently, the bias voltage changed the depletion width at the  $p$ - $n$  junction and decreased the holes available at the junction to interact with the localized Mn ions to produce FM behavior. Several fabricated devices were found to repeat these results and confirm the hole-mediated FM properties.

As further illustration of this mechanism, two different i-p-n devices were etched to investigate dependence of magnetic behavior upon the thickness of the p-GaN-SLS layer and that of GaMnN. In one structure the thickness of the p-GaN-SLS was 0.17 and 0.25  $\mu\text{m}$  in the other. In both samples the initial thickness of the top GaMnN layer was 0.5  $\mu\text{m}$ . After etching of the GaMnN layer, to reduce its thickness, AGM magnetic measurements at zero bias voltage were performed. Results of these measurements at RT are shown in Fig. 12.36. For the i-p-n device with p-GaN-SLS

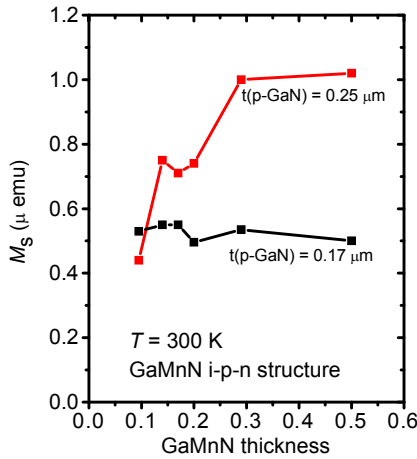


**Figure 12.36** Results of AGM measurements at RT and zero bias voltage for two i-p-n devices before and after etching of the top GaMnN later. The  $M_s$  data points in black correspond to the device having p-GaN-SLS thickness  $X_p = 0.17 \mu\text{m}$  and indicate no FM behavior. The points in red are for the device with  $X_p = 0.25 \mu\text{m}$  and show that  $M_s$  decreases if the thickness of GaMnN layer becomes  $< \sim 0.3 \mu\text{m}$ .

thickness  $X_p = 0.17 \mu\text{m}$ , no hysteresis was observed either initially or after etching. The built-in potential at the  $p$ - $n$  junction depletes carriers in the p-GaN-SLS layer and magnetic ordering cannot occur. For the i-p-n device with p-GaN-SLS thickness  $X_p = 0.25 \mu\text{m}$ , there is no change in the FM behavior until the GaMnN layer is etched to a thickness less than  $\sim 0.03 \mu\text{m}$ . At this stage, the limited penetration of the hole wave function into the GaMnN layer starts to take effect. While there are sufficient holes for magnetic ordering, there are less Mn ions available for FM behavior. This result emphasizes that the magnetic properties found in the i-p-n device, and in the structures discussed in Section 12.4, are due to FM ordering of Mn ions only near the GaMnN/p-layer interface.

Magnetic ordering in the GaMnN i-p-n devices was also studied by Hall resistance measurements using the four point contacts on the p-GaN-SLS layer, shown in Fig. 12.37. The Hall measurements indicated that the n-GaN and p-GaN-SLS layers had carrier concentrations of  $1.5 \times 10^{18} \text{cm}^{-3}$  and  $1.2 \times 10^{17} \text{cm}^{-3}$ , respectively. In Fig. 12.37(a) results of measurements made at RT using the measurements made of the magnetoresistance ( $\Delta R_{\text{Hall}}$ ) data for these layers are displayed. For these layers  $R_{\text{Hall}}$  is a linear function of the applied magnetic field, indicating an ordinary Hall Effect (OHE). Similar measurements for the GaMnN i-p-n devices at different values of applied voltage resulted in much different behavior as shown in Fig. 12.37(b). For  $V_a = 0$  the  $\Delta R_{\text{Hall}}$  has a steep initial slope followed by a plateau for higher magnetic fields typical of the anomalous Hall Effect (AHE). The negative modest slope of AHE curve for zero bias indicates that the carriers in the film are p-type. The AHE dominates at low fields and  $R_{\text{Hall}}$  saturates once magnetization reaches higher levels (Nepal et al., 2009). With applied reverse voltage, holes in the

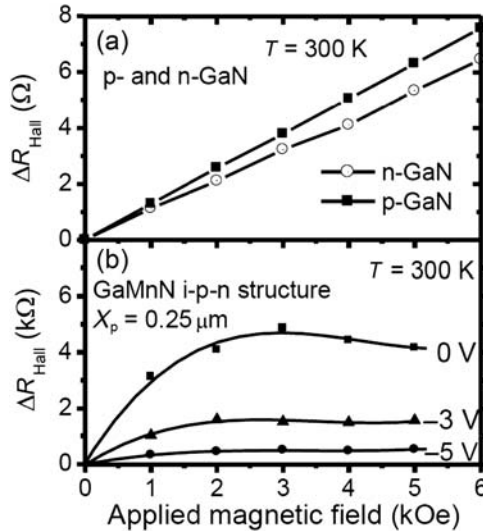


**Figure 12.37** Magnetoresistance Hall measurements at RT of (a) n-GaN and p-GaN-SLS films showing the linear response due to the OHE, and (b) GaMnN i-p-n device with p-GaN<sup>SLS</sup> thickness 0.25  $\mu\text{m}$  as a function of applied magnetic field and reverse bias voltage.

p-GaN-SLS layer are depleted and the induced magnetic ordering in the GaMnN layer is reduced. Consequently, the AHE behavior is less pronounced. For  $V_a \sim -5\text{ V}$ , in close agreement with the AGM measurements, the Hall measurements show OHE behavior indicating full depletion of the p-layer and elimination of magnetic ordering. These results provide evidence that the magnetoresistance in the device structure can be controlled by applying reverse bias voltage to the *p-n* junction.

The measurements show the AHE with a steep initial response to the applied field followed by a plateau. Under an applied reverse voltage p-GaN-SLS becomes depleted and a linear response is observed at  $-5\text{ V}$ .

## 12.6 Summary and concluding remarks

We have conducted multiple experiments demonstrating that GaN can be doped with Mn by several techniques: (1) diffusion of Mn in GaN thin-film single crystal, and (2) MOCVD doping of GaN thin films. The FM behavior of GaMnN layers can be controlled by the hole concentration in a GaMnN/*p*-GaN heterostructure. Furthermore, the holes can be modulated by applying a reverse bias to the GaMnN/*p*-GaN/*n*-GaN structure, producing a transition from PM to FM behavior. We have demonstrated that this electric current control of the FM can be achieved at RT and that the AHE depends on the holes of the *p*-GaN layer and the applied reverse bias. Such current-controlled FM GaMnN i-p-n devices would have important applications at RT, especially in nonvolatile memory storage systems.

## Acknowledgments

The authors of this chapter would like to acknowledge the Army Research Office, NSF (Grant # ECCS-1307004) and DARPA (DMS) for funding this work.

N.E. would like to thank all her graduate students whose research contributions led to this chapter.

## References

- Akai, H., Dederichs, P.H., 1993. Local moment disorder in ferromagnetic-alloys. *Physical Review B* 47 (14), 8739–8747.
- Akai, H., 1998. Ferromagnetism and its stability in the diluted magnetic semiconductor (In,Mn)As. *Physical Review Letters* 81 (14), 3002–3005.
- Arkun, F.E., Reed, M.J., Berkman, E.A., El-Masry, N.A., Zavada, J.M., Reed, M.L., Bedair, S.M., 2004. Dependence of ferromagnetic properties on carrier transfer at GaMnN/GaN: Mg interface. *Applied Physics Letters* 85 (25), 3809–3811.
- Bedair, S.M., Zavada, J.M., El-Masry, N., 2010. A Spin to Remember. *IEEE Spectrum* 47 (11), 44–49.
- Behbehani, M., Liu, S.X., El-Masry, N.A., Bedair, S.M., 1999. *Applied Physics Letters* 75, 2202–2204.
- Bouchaud, J.P., 1968. *Annales de Chimie Series* 14 (3), 81.
- Bougrov, V., Levinshtein, M.E., Rumyantsev, S.L., Zubrilov, A., 2001. *Properties of Advanced Semiconductor Materials GaN, AlN, InN, BN, SiC, SiGe*. Wiley, New York.
- Chen, L., Yang, X., Yang, F., Zhao, J., Misuraca, J., Xiong, P., von Molnár, S., 2011. *Nano Letters* 11 (2584). <http://dx.doi.org/10.1021/nl201187m>.
- Cullity, B.D., 1972. *Introduction to Magnetic Materials*. Addison-Wesley Publishing Company, Reading, Massachusetts.
- Dietl, T., Ohno, H., Matsukura, F., Cibert, J., Ferrand, D., 2000. Zener model description of ferromagnetism in zinc-blende magnetic semiconductors. *Science* 287 (5455), 1019–1022.
- El-Masry, N.A., Piner, E.L., Liu, S.X., Bedair, S.M., 1998. *Applied Physics Letters* 72, 40–43.
- Hebard, A.F., Chu, S.N.G., Overberg, M.E., Abernathy, C.R., Pearton, S.J., Wilson, R.G., Zavada, J.M., 2002. Use of ion implantation to facilitate the discovery and characterization of ferromagnetic semiconductors. *Journal of Applied Physics* 91, 7499.
- Kondo, T., Kuwabara, S., Owa, H., Munekata, H., 2002. *Journal of Crystal Growth* 237, 1353–1357.
- Korotkov, R.Y., Gregie, J.M., Wessels, B.W., 2001. Electrical properties of p-type GaN: Mg codoped with oxygen. *Applied Physics Letters* 78 (2), 222–224.
- Kronik, L., Jain, M., Chelikowsky, J.R., 2002. Electronic structure and spin polarization of  $\text{Mn}_x\text{Ga}_{1-x}\text{N}$ . *Physical Review B* 66 (4), 0412031–0412034.
- Kuwabara, S., Ishii, K., Haneda, S., Kondo, T., Munekata, H., 2001. *Physica E* 10, 233–236.
- Lambrecht, W.R.L., 2015. *Electronic Structure of Magnetic Impurities and Defects in Semiconductors: A Guide to the Theoretical Models*. This Volume.
- Mahros, A.M., Luen, M.O., Emara, A., Bedair, S.M., Berkman, E.A., El-Masry, N.A., Zavada, J.M., 2007. Magnetotransport properties of (AlGaIn/GaN)/(GaMnN) heterostructures at room. *Applied Physics Letters* 90 (25), 252503–252505.
- Matsukura, F., Shen, A., Sugawara, Y., Omiya, T., Ohno, Y., Ohno, H., 1999. *Compound Semiconductors* 1998, 547–552.

- Matsukura, F., Ohno, H., Shen, A., Sugawara, Y., 1998. *Physical Review B* 57 (14), R2037–R2040.
- Matsukura, F., Tokura, Y., Ohno, H., 2015. Control of magnetism by electric fields. *Nature Nanotechnology Focus Review Article NNANO* (22), 209–220.
- Munekata, H., Ohno, H., von Molnar, S., Segmuller, A., Chang, L.L., Esaki, L., 1989. *Physical Review Letters* 63, 1849.
- Nepal, N., Oliver Luen, M., Zavada, J.M., Bedair, S.M., Frajtag, P., El-Masry, N.A., 2009. Electric field control of room temperature ferromagnetism in III-N dilute magnetic semiconductor films. *Applied Physics Letters* 94, 132505.
- Ohno, H., 1999. *Journal of Magnetic Materials* 200, 110.
- Ohno, H., Shen, A., Matsukura, F., Oiwa, A., Endo, A., Katsumoto, S., Iye, Y., 1996. *Applied Physics Letters* 69, 363–365.
- Overberg, M.E., Abernathy, C.R., Pearton, S.J., Theodoropoulou, N.A., McCarthy, K.T., Hebard, A.F., 2001. *Applied Physics Letters* 79, 1312–1314.
- Parker, C.A., Roberts, J.C., Bedair, S.M., Reed, M.J., Liu, S.X., El-Masry, N.A., Robins, L.H., 1999a. *Applied Physics Letters* 75, 2566–2568.
- Parker, C.A., Roberts, J.C., Bedair, S.M., Reed, M.J., Liu, S.X., El-Masry, N.A., 1999b. *Applied Physics Letters* 75, 2776–2778.
- Reed, M.J., El-Masry, N.A., Parker, C.A., Roberts, J.C., Bedair, S.M., 2000. *Applied Physics Letters* 77, 4121–4123.
- Reed, M.L., Reed, M.J., Luen, M.O., Berkman, E.A., Arkun, F.E., Medair, S.M., Zavada, J.M., El-Masry, N.A., 2005a. Magnetic properties of Mn-doped GaN and p-i-n junctions. *Physica Status Solidi C* 1–4.
- Reed, M.J., Arkun, F.E., Berkman, E.A., El-Masry, N.A., Zavada, J.M., Luen, M.O., Reed, M.L., Bedair, S.M., 2005b. Effect of doping on the magnetic properties of GaMnN: fermi level engineering. *Applied Physics Letters* 86, 1–3.
- Reed, M.L., Ritums, M.K., Stadelmaier, H.H., Reed, M.J., Parker, C.A., Bedair, S.M., El-Masry, N.A., 2001a. *Materials Letters* 51, 500–503.
- Reed, M.L., El-Masry, N.A., Stadelmaier, H.H., Ritums, M.K., Reed, M.J., Parker, C.A., Roberts, J.C., Bedair, S.M., 2001b. Room temperature ferromagnetic properties of (GaMn) N. *Applied Physics Letters* 79 (21), 3473–3475.
- Sato, K., Katayama-Yoshida, H., 2000. Material design for transparent ferromagnets with ZnO-based magnetic semiconductors. *Japanese Journal of Applied Physics Part 2-Letters* 39 (6B), L555–L558.
- Schubert, E.F., Grieshaber, W., Goepfert, I.D., 1996. *Applied Physics Letters* 69, 3737–3739.
- Sonoda, S., Shimizu, S., Sasaki, T., Yamamoto, Y., Hori, H., 2002. *Journal of Crystal Growth* 237, 1358–1362.
- Wojtowicz, T., Lim, W.L., Liu, X., Dobrowolska, M., Furdyna, J.K., Yu, K.M., Walukiewicz, W., 2003. *Applied Physics Letters* 83, 4220–4222.
- Yun, F., Reshchikov, M.A., He, L., Morkoc, H., Inoki, C.K., Kuan, T.S., 2002. *Applied Physics Letters* 81, 4142–4144.
- Zener, C., 1951. Interaction between the D-Shell in the transition metals. *Physical Review* 81 (3), 440–444.

This page intentionally left blank

# Bipolar magnetic junction transistors for logic applications

13

*B.W. Wessels*

Northwestern University, Evanston, IL, United States

## 13.1 Introduction

With the discovery of III-V dilute magnetic semiconductors (DMSs), there has been widespread interest in developing these materials for logic and memory devices [1]. Of particular interest are bipolar magnetic junction diodes and transistors. These devices show large changes in their current transport with magnetic field. Much of the theory of bipolar magnetic semiconductor junction devices has centered on the effect of magnetic field on the band structure of the junction. Upon application of a magnetic field the conduction and valence band offsets in the heterojunction are predicted to be altered as a result of the giant Zeeman effect, leading to a large junction magnetoresistance [2–5]. Other magnetic field junction effects have been proposed including spin-selective scattering of carriers that leads to magnetoresistance. Early on it was noted that the magnetoresistance of the magnetic semiconductor junctions had a complex dependence on magnetic field [6]. For InMnAs epitaxial layers the magnetoresistance is negative at low temperature (<15K) whereas at higher temperature the magnetoresistance is positive [7]. This behavior can't be simply explained by the giant Zeeman effect on band structure alone as originally proposed; other magnetotransport factors must be considered. Here we present a two-band model to describe magnetoconduction in a DMS diode and transistor for fields up to 18 T. The carrier transport can be expressed as a parallel circuit consisting of two resistors that represent the minority and majority spin channels. As the magnetic field increases, the spin polarization increases. The spin-polarized conduction leads to the giant magnetoresistance observed in the diodes and the negative magnetoamplification in the bipolar magnetic junction transistors (MJTs).

## 13.2 Spin diodes

Using the magnetoresistance effect spin diodes can be constructed. The spin diode is a two-layer structure consisting of a magnetic semiconductor and a nonmagnetic semiconductor [2]. For the case of a III-V host such as InAs or GaAs addition of the magnetic ion Mn leads to p-type conduction. For low Mn concentration the layers are paramagnetic while for high concentration the layers are ferromagnetic. The Mn ion concentration also determines the conductivity and magnetoresistance of the layers.



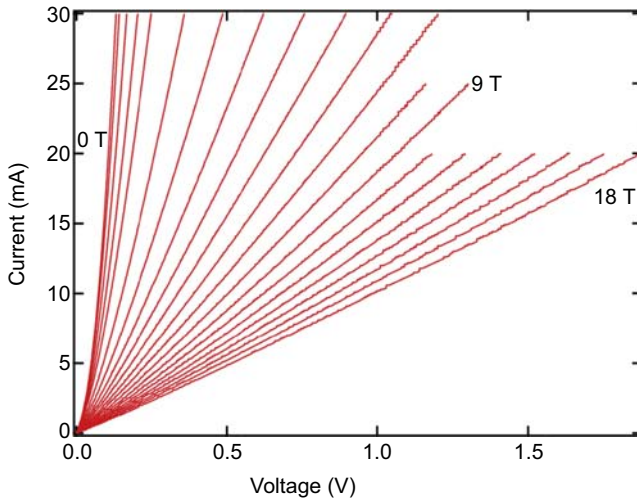


**Figure 13.1** Current versus voltage characteristic for a p-n InMnAs/InAs heterojunction at room temperature. An external magnetic field up to 18 T parallel to the current and electric field was applied.

From Rangaraju N, Li P, Wessels BW. Phys Rev B 2009;79:205209.

The narrow gap semiconductor InMnAs has shown either positive or negative magnetoresistance depending on the temperature [8]. A large positive magnetoresistance in junctions was first observed in InMnAs/InAs heterojunction diodes by May and Wessels in 2005 [9]. Subsequently a giant magnetoresistance was observed for these diodes at high fields. Fig. 13.1 shows the current–voltage characteristics of the heterojunction in magnetic fields up to 18 T [10]. As can be seen there is a large increase in the junction resistance with magnetic field.

To describe the magnetic behavior of the junction characteristics a semiempirical equation given by the Shockley diode equation was utilized where there is an additional series resistance due to the junction magnetoresistance. The current  $I$  for a bias  $V$  is given by:

$$I = I_0 \left( \exp \left( \frac{qV - IR(H)}{kT} \right) - 1 \right) \quad [13.1]$$

where  $I_0$  is a prefactor that depends on band structure and  $R(H)$  is the series resistance that depends on the junction magnetoresistance that depends on magnetic field  $H$ . The term  $k$  is the Boltzmann constant and  $T$  is the absolute temperature. Note that  $R(H)$  can be either positive or negative depending on the spin-scattering mechanism, as will be discussed. For the case of a positive magnetoresistance the junction conductance will decrease with increasing magnetic field, whereas for a negative magnetoresistance it will increase with field.

To explain the origin of the magnetoresistance, a two-band model for conduction in a magnetic semiconductor diode was developed based on the Mott model applied to

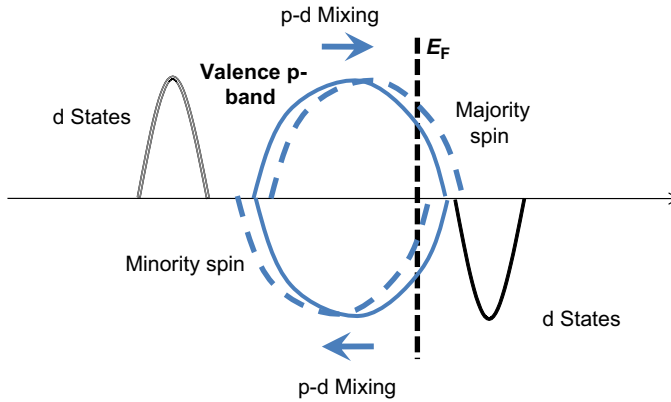


**Figure 13.2** Density of states for ferromagnetic InMnAs. The Fermi level is resonant with the spin-split valence band.

From Rangaraju N, Li P, Wessels BW. Phys Rev B 2009;79:205209.

conduction in ferromagnetic metals [11]. In this model the valence band of the magnetic semiconductor is split into two spin-polarized bands as a result of the giant Zeeman effect [10]. This can be seen in Fig. 13.2. Conduction can occur via both the minority and majority spin bands, however the bands will have different effective masses depending whether the band is more p-like or d-like. The p-like bands will have a higher conductance than the d-like bands due to differences in mobility. Furthermore the populations of the two bands will differ. The respective carrier populations will depend on both temperature and magnetic field strength. The carrier transport thus occurs via two channels that are parallel. The conduction can be expressed by a parallel circuit consisting of two resistances that represent the minority and majority spin channels. To describe the magnetoconduction, the conductance and its magnetic field dependence is given by the expression [10]

$$G = \frac{1}{2\cosh\left(\frac{\mu_B g H}{k_B T}\right)} \left( G_1 \exp\left(\frac{-\mu_B g H}{k_B T}\right) + G_2 \exp\left(\frac{\mu_B g H}{k_B T}\right) \right) \quad [13.2]$$

where  $G_1$  and  $G_2$  are the conductances of channel 1 and channel 2, and  $G$  is the total conductance of the junction. The term  $\mu_B$  is the Bohr magneton,  $g$  is the effective Lande factor, and  $H$  is the magnetic field.

As the magnetic field increases the relative carrier population of the two bands will change. The resulting current through the device will be spin polarized. The effective spin polarization  $P$  depends on the channel conductances  $G_1$  and  $G_2$  and is given by:

$$P = \frac{G_1 - G_2}{G_1 + G_2} \quad [13.3]$$

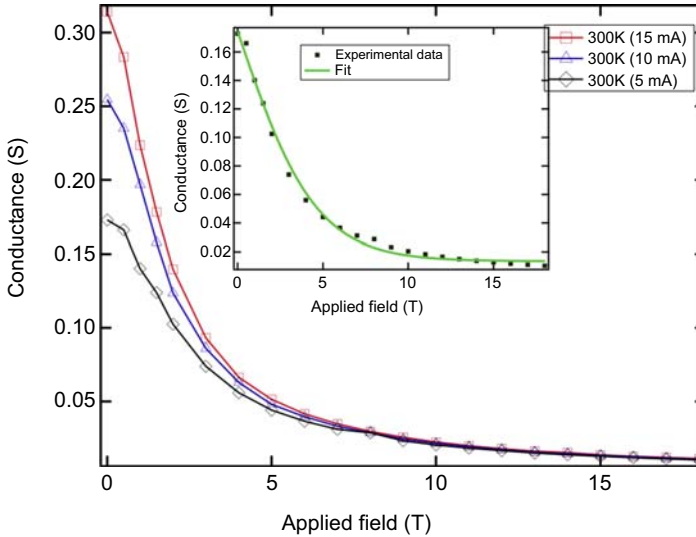


**Figure 13.3** Conductance versus applied field for an InMnAs/InAs heterojunction diode. The inset shows fit using a two-band model.

From Rangaraju N, Li P, Wessels BW. Phys Rev B 2009;79:205209.

This spin-polarized conduction leads to the giant magnetoresistance. Fig. 13.3 shows the conductance characteristic of an InMnAs/InAs p-n heterojunction as a function of applied field up to fields of 18 T at 300K. The solid lines are the theoretical curves given by Eq. [13.2]. As can be seen, the conductance decreases rapidly with external magnetic field.

### 13.3 Bipolar magnetic junction transistor

The heterojunction diode forms the basis of the bipolar MJT [12]. In principle, the transistor contains two or more magnetic semiconductor layers to take advantage of the parallel and antiparallel magnetization configurations that lead to different output currents. Nevertheless transistors with only one magnetic semiconductor layer and two nonmagnetic semiconductor layers have also been proposed and demonstrated. In this case the magnetic layer can be either the emitter or the collector and the base is the nonmagnetic semiconductor. When the emitter is a magnetic semiconductor, under forward bias the emitter-base current will be a strong function of magnetic field due to the positive junction magnetoresistance. Changes in the current transfer ratio  $\alpha$  ( $\alpha = I_c/I_e$ ) will be observed with a magnetic field. Similarly the collector can be a magnetic semiconductor and the other two layers can be nonmagnetic semiconductors, both configurations leading to a dependence of  $\alpha$  on  $H$ .

Using fabrication techniques developed for a p-n heterojunction, spin transistors were fabricated and their characteristics demonstrated [12]. A schematic of the bipolar

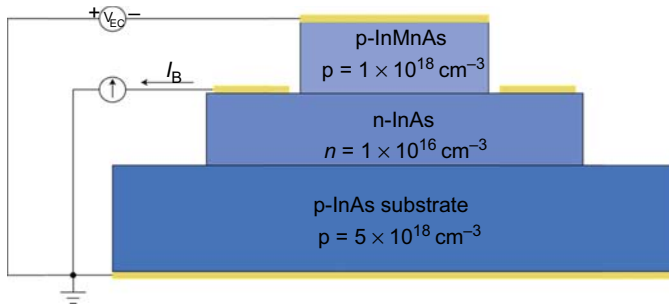


**Figure 13.4** Schematic of a p-n-p InMnAs/InAs/InAs heterojunction transistor. From Rangaraju N, Peters JA, Wessels BW. Phys Rev Lett 2010;105:117202.

magnetic junction transistor is shown in Fig. 13.4. The transistor consists of three active regions p-InMnAs/n-InAs/p-InAs. The heterojunctions were fabricated by first depositing a 150 nm layer of InAs ( $n = 1 \times 10^{16} \text{ cm}^{-3}$ ) on a p-type InAs substrate by metalorganic vapor phase epitaxy. Subsequently a p-type InMnAs layer was deposited forming a p-n-p transistor structure.

The transistor current gain  $\beta_{dc}$  was measured as a function of the collector current  $I_c$ . The gain is given by:

$$\beta_{dc} = \frac{I_c(I_B) - I_c(0)}{I_B} \quad [13.4]$$

where  $I_B$  is the base current. Fig. 13.5(a) shows the  $\beta_{dc}$  versus  $I_c$  characteristics for different values of the base current. The highest amplification that was observed for this series of transistors is 20 at 298K and zero magnetic field. At low values of  $I_c$  the value of  $\beta_{dc}$  is limited due to generation-recombination current. At higher collector currents there is a narrow region where the transistor characteristic approaches ideal behavior.

The transistor current gain was measured in a magnetic field. The gain for different values of the magnetic field and collector current is shown in Fig. 13.5(b). The gain of the transistor changes in a magnetic field, resulting in a magnetoamplification (MA) factor given by:

$$MA = \frac{\beta_{dc}(B) - \beta_{dc}(0)}{\beta_{dc}(0)} \quad [13.5]$$

It should be noted that the value of  $MA$  can be either negative or positive. When  $\beta_{dc}(0)$  is greater than  $\beta_{dc}(B)$ , a negative magnetoamplification results. The experimentally observed negative magnetoamplification is consistent with a positive junction magnetoresistance as observed for the heterodiodes.

The behavior is well described by an Ebers-Moll model for a transistor that includes a series magnetoresistance [12,13]. In this case the equivalent circuit for the device

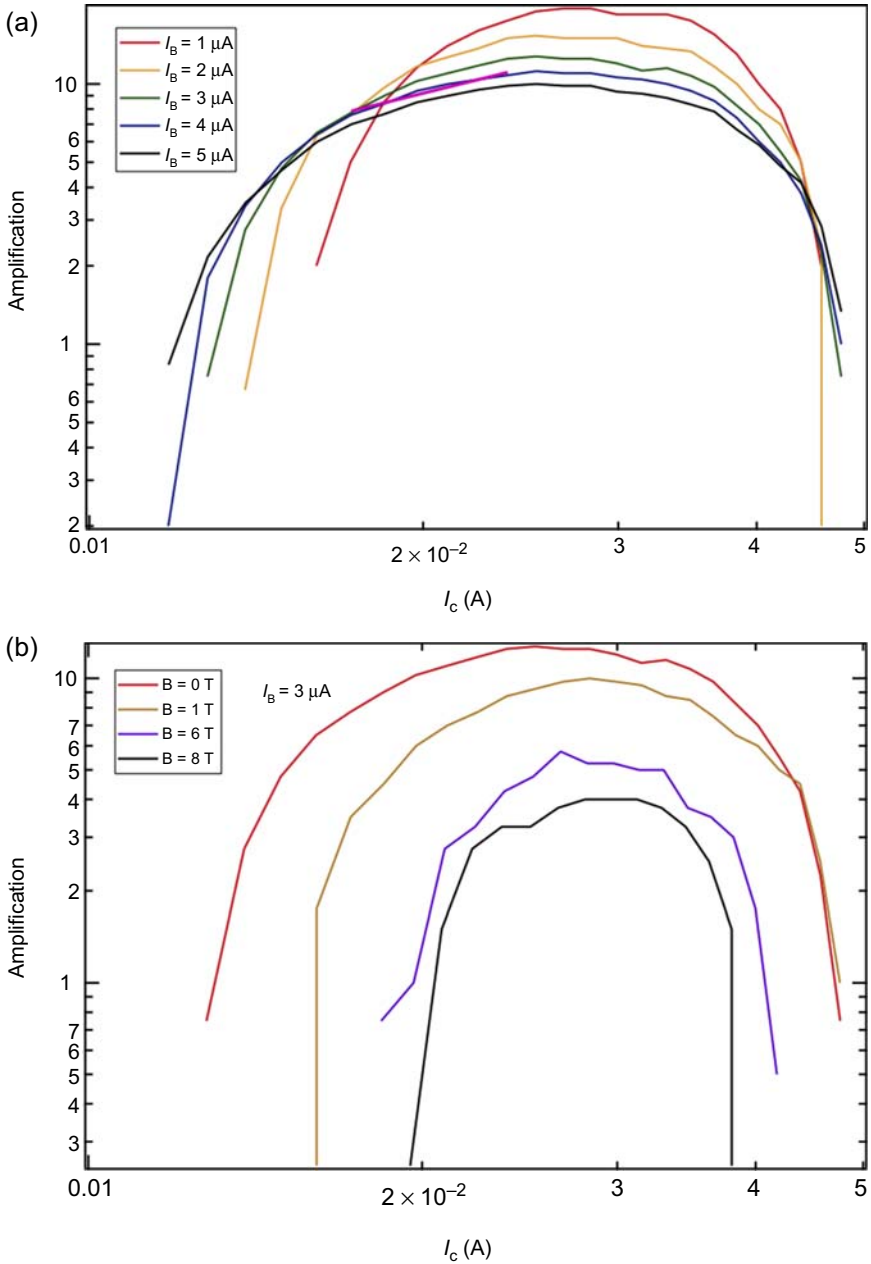


**Figure 13.5** Amplification versus collector current (a) for base current of 1–5  $\mu\text{A}$  (b) for external fields of 0–8 T. The base current is kept constant at 3  $\mu\text{A}$ .

From Rangaraju N, Peters JA, Wessels BW. Phys Rev Lett 2010;105:117202.

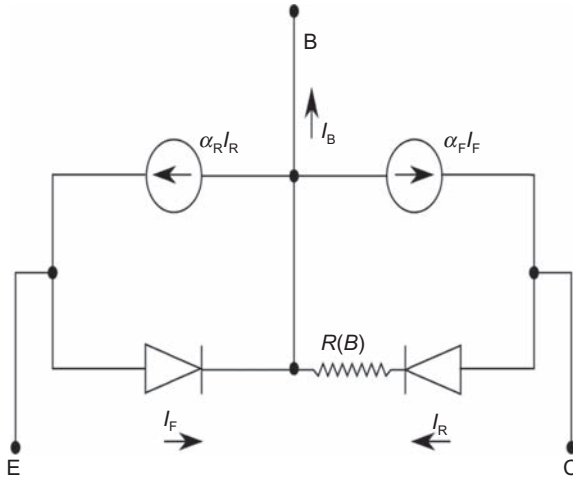


**Figure 13.6** Ebers-Moll model for an MJT. The magnetoresistance is labeled by  $R(B)$ . From Rangaraju N, Peters JA, Wessels BW. Phys Rev Lett 2010;105:117202.

consists of two coupled diodes and a magnetic field-dependent resistance  $R(B)$  in series with a reverse biased collector–base junction as shown in Fig. 13.6. This resistance accounts for the magnetoresistance of the transistor. When a magnetic field is applied perpendicular to the junction of the transistor, spin-selective transport in the reverse bias junction leads to an increase in  $R(B)$ .

While the modified Ebers-Moll model describes the behavior of the bipolar MJT, the atomic origin of the junction magnetoresistance is not well understood. It is of interest to examine the magnetoresistance of the semiconductor thin films for potential insight into the junction properties. As shown in Fig. 13.7 the magnetoresistance of the InMnAs layers is a function of field and temperature. As is evident in Fig. 13.7 negative magnetoresistance is observed at low temperatures only [8]. For temperatures above 15K the magnetoresistance is positive. This positive magnetoresistance is similar to the behavior observed for the heterojunction diodes. Thus it is presumed that the same mechanisms are responsible for the magnetoresistance of the thin films, diodes, and transistors. That is, the magnetoresistance is attributed to spin-selective scattering of spin-polarized holes. Here it is presumed that the magnetoresistance  $R(H) = f(M)$ , where  $M$  is the magnetization of the magnetic semiconductor [14]. The magnetization in turn is a function of magnetic ion concentration, temperature, and magnetic field. For a DMS the magnetization  $M$  is given by:

$$M = M_0 B_0(x) \quad [13.6]$$

where  $M_0$  is the low temperature magnetization,  $x = gN_B\mu_B H/kT$ ,  $B_0(x)$  is the Brillouin function, where  $x$  depends on the effective  $g$  factor and the temperature  $T$ .  $N_B$  is the transition metal concentration. At high fields and low temperatures the term  $M(H)$  saturates, whereas at low fields and high temperature  $M(H)$  is linear in field.

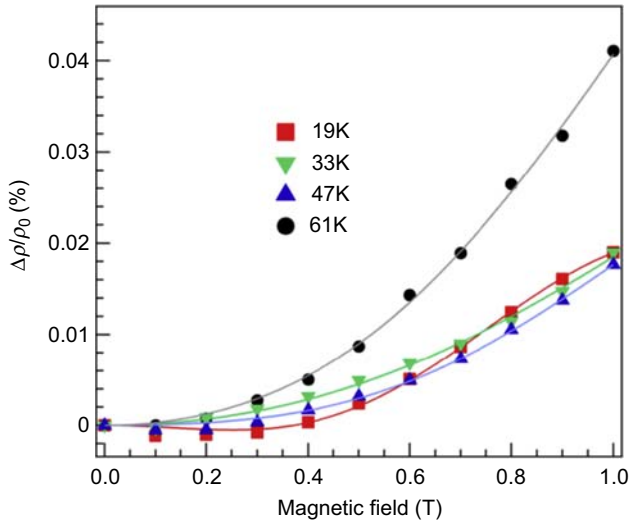


**Figure 13.7** Magnetoresistance of InMnAs epitaxial thin film.  
From Peters J, Wessels BW. Phys E 2010;42:1447.

If  $M$  is taken to be a linear function of  $H$ , then the magnetoresistance would be quadratic in magnetic field at low fields. At higher fields the magnetoresistance would be expected to saturate as is the case for  $M$  in Eq. [13.6]. This saturation is indeed what is observed for InMnAs and InMnSb heterodiodes and is consistent with the conductance behavior of the junction described by Eq. [13.2] [10,15].

For practical device applications in logic and magnetosensing, small external fields are required. As can be seen in Fig. 13.3, a field of the order of 5 T is needed to reduce the diode conductance by an order of magnitude. To increase the junction magnetoresistance, increases in the magnetic ion concentration or low temperature are needed. However, for these semiconductors the solubility of magnetic ions is limited, so the magnetization of the single phase alloys is limited. Nevertheless there is the possibility of increasing the magnetization by considering two phase alloys consisting of a III-V host and a magnetic compound. One material example is GaAs:MnAs, which has been widely investigated [16].

Another factor that comes into play in determining the junction magnetoresistance is the effective  $g$  factor. This term depends on the semiconductor band structure and the exchange energy, so it is host specific. Experimental  $g$  values of the order of 100 have been measured for InMnAs/InAs and InMnSb/InSb p-n junction heterodiodes [10,15]. The  $g$  factor has been found to be temperature dependent. Furthermore since  $g$  is in the argument of an exponential function, as in Eq. [13.2], a strong temperature dependence of the magnetoconductance properties should be observed. In Eq. [13.2] for the junction conductance the term  $g\mu_B H/kT$  is the argument of the exponential, thus large junction magnetoresistance effects are expected at low temperature. There should be an advantage of operating these transistors at low temperatures. Much lower fields will then be required to change the operating characteristic, including magnetoamplification.

While the magnetoresistance is limited due to the limited solubility of magnetic ions, an alternative approach to obtain a large magnetoamplification is to use a high gain structure. Consider a p-n-p MJT structure with a base width of  $W$ . For a bipolar transistor the gain is given by:

$$\beta_{dc} = \frac{\gamma\alpha_T}{1 - \gamma\alpha_T} \quad [13.7]$$

where  $\gamma$  is the emitter injection efficiency and  $\alpha_T$  is the base transport factor given by:

$$\alpha_T = 1 - \frac{W^2}{2L_p^2} \quad [13.8]$$

$L_p$  is the minority carrier diffusion length. From the minority carrier lifetime measurements, the length is calculated to be 9  $\mu\text{m}$ . For a base width of 150 nm, a base transfer ratio of 0.9998 is calculated. Thus for a gain of 20,  $\gamma$  is 0.95. Since the magnetoamplification is proportional to  $\beta_{dc}$ , large values of the magnetoamplification are predicted. It is expected that for large gain, magnetoamplification will increase, thus requiring small fields to change the logic state. This should enable emitter-coupled spin-transistor logic (ECSTL) to operate at lower fields, thus simplifying logic devices and logic circuits. However this needs to be experimentally demonstrated.

## 13.4 Applications

As for the potential applications of the magnetic diodes and transistors, they have been proposed for new integrated circuit architectures. For example, they can be used in reconfigurable logic circuits. One such logic that has been recently proposed is diode logic, where in this case a magnetic heterodiode is used as the principal logic device [17]. This logic family also enables constructing an intriguing and simple set-reset (S-R) latch, shown in Fig. 13.8. As seen in the diagram, each latch NOR gate output is routed to the other's input, forcing the propagation of opposite values. When one of the diodes propagates a high current, the current is suppressed in the second diode, which allows the first diode to propagate a high current, thereby maintaining a self-consistent state. To set the value stored in the latch, an external current is passed through one of the diodes. To set a 1, a current is passed through NOR1, and to set a 0, a current is sent through NOR2. This circuit is a bistable inverter chain, and can be used to create stable memory storage.

Furthermore a logic circuit that can be potentially envisioned is an ECSTL, where the elements are bipolar MJTs [18,19]. By replacing traditional transistors with bipolar MJTs, a new logic family is created that results in additional functionality without adding transistors. By routing a wire whose current depends on the logical state it is possible to realize more complex logical functions without adding additional circuitry. It has been proposed that ECSTL will have lower power dissipation at higher



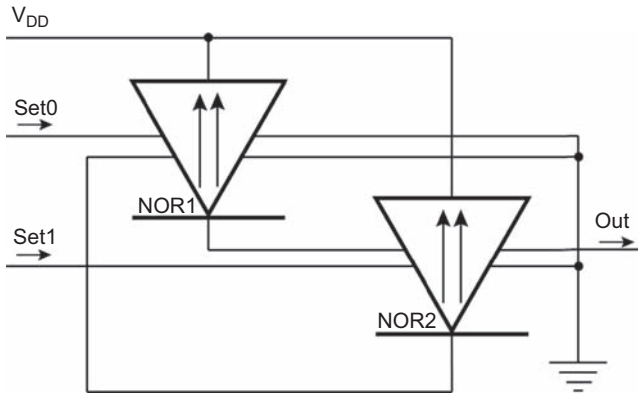


**Figure 13.8** Diode logic circuit using a magnetic junction diode.

From Friedman J, Rangaraju N, Ismail Y, Memik G, Wessels BW. *IEEE Trans Nanotechnol* 2012;11:1026.

frequencies than that of CMOS logic circuits, making it attractive for high-speed applications. For this new logic family there is a speed-up of three to five times and a 70% decrease of power consumption, resulting in a decrease in the power-delay product of 10–25.

Another potential application is in information storage [20]. Since both InMnAs and InMnSb alloys are ferromagnetic for Mn concentrations of several percent, the devices made from these alloys can show nonvolatility. Thus both nonvolatile logic and reconfigurable logic could be realized, with the spin transistors making it promising for semiconductor spintronic integrated circuits.

## Acknowledgments

This work is supported by the National Science Foundation (NSF) under grant #DMR-0804479 and DMR1305666. Extensive use of the facilities of the Materials Research Center at Northwestern University supported by the NSF (No. DMR 0076097) is acknowledged. Use of the Center for Nanoscale Materials at Argonne National Laboratory was supported by the US Department of Energy, Office of Science, Office of Basic Energy Sciences, under Contract No. DE-AC02-06CH11357.

## References

- [1] Munekata H, Ohno H, von Molnar S, Segmuller A, Chang LL, Esaki L. *Phys Rev Lett* 1989;63:1849.
- [2] Zutic I, Fabian J, Das Sarma S. *Phys Rev Lett* 2002;88:066603.
- [3] Fabian J, Zutic I, Das Sarma S. *Appl Phys Lett* 2004;84:85.
- [4] Zutic I, Fabian J, Das Sarma S. *Rev Mod Phys* 2004;76:323.

- 
- [5] Lebedeva N, Kuivalainen P. *J Appl Phys* 2003;93:9845.
  - [6] May SJ, Wessels BW. *Appl Phys Lett* 2006;88:072105.
  - [7] Peters J, Wessels BW. *Phys E* 2010;42:1447.
  - [8] May S, Blattner A, Wessels BW. *Phys Rev B* 2004;70:073303.
  - [9] May S, Wessels BW. *JVST B* 2005;23:1769.
  - [10] Rangaraju N, Li P, Wessels BW. *Phys Rev B* 2009;79:205209.
  - [11] Mott N. *Proc R Soc London* 1936;153:699.
  - [12] Rangaraju N, Peters JA, Wessels BW. *Phys Rev Lett* 2010;105:117202.
  - [13] Fabian J, Zutic I. *Appl Phys Lett* 2005;86:133506.
  - [14] Khosla RP, Fischer JR. *Phys Rev B* 1970;2:4084.
  - [15] Peters JA, Rangaraju N, Feeser C, Wessels BW. *Appl Phys Lett* 2011;98:193506.
  - [16] Hai PN, Takahashi K, Yokoyama M. *J Magn Magn Mater* 2007;310:1932.
  - [17] Friedman J, Rangaraju N, Ismail Y, Memik G, Wessels BW. *IEEE Trans Nanotechnol* 2012;11:1026.
  - [18] Friedman JS, Ismail YI, Memik G, Sahakian AV, Wessels BW. In: *Proceedings of IEEE/ACM International Symposium on Nanoscale Architectures*; July 2012. p. 139–45.
  - [19] Friedman JS, Peters JA, Memik G, Wessels BW, Sahakian AV. *J Parallel Distrib Comput* 2014;74:2461.
  - [20] Wolf S, Liu J, Stan MR, Chen E, Treger D. *Proc IEEE* 2010;98:2155.

This page intentionally left blank

# Index

*Note:* ‘Page numbers followed by “f” indicate figures and “t” indicate tables.’

## A

- Alternating gradient magnetometer (AGM),  
241–242, 244–245, 298,  
300, 422
- Anomalous Hall Effect (AHE), 430–431
- Antiferromagnetic (AFM) coupling, 60–64,  
396–397
- Antiferromagnetic magnetic alloys, 152t
- Antiferromagnetic rare-earth compounds,  
spintronic possibilities with,  
156–158, 158f
- Atomic force microscopy (AFM), 229, 230f

## B

- Bandedge luminescence, 294
- Bethe–Salpeter equation, 57–58
- Bipolar magnetic junction transistors  
applications, 443–444, 444f  
defined, 438–443, 439f–442f  
spin diodes, 435–438, 436f–438f
- Bound magnetic polarons, 321, 321f

## C

- Circular-polarized laser diodes (CP-LDs),  
372
- Classic exchange mechanisms, 318–330
- Clustering  
discussion, 89–90  
experimental evidence and defects,  
87–89, 88f
- Codoping method, 12–14, 13f
- Combined excitation emission spectroscopy  
(CEES), 241–243, 246–247,  
247f–248f, 268, 296f, 297–298
- Computational materials design (CMD),  
31–32
- Computational methods  
density functional theory, failures of,  
50–52

- dynamic mean field theory, 58–59
- GW method, 55–58
- Hubbard  $U$  correction, 52–54
- hybrid functionals, 54–55
- Computational Nano-Materials Design  
(CMD<sup>®</sup>) system, 4, 5f, 7
- Conduction, 436–437
- Conduction band (CB), 108–109
- Conduction band minimum (CBM), 27–28
- Core-shell nanoparticles, 115–116
- Critical layer thickness (CLT), 409–411
- Crystal-field resonance (CFR), 47

## D

- Dangling-bond hybrid (DBH), 47
- Death Valley, 4, 6f
- Deformation energy, 112–113
- Density functional theory (DFT), 50–51  
failures of, 50–52
- Density of states (DOS), 9
- Diethylzinc (DEZn), 172–173
- Digital alloys, 147–149, 148f–149f
- Dilute magnetic semiconductors (DMS),  
315, 317, 395  
antiferromagnetic rare-earth compounds,  
spintronic possibilities with,  
156–158, 158f
- GaN, Gd in  
clustering, growth simulations of,  
86–90  
exchange interactions analysis, 79–81,  
80f–81f  
experimental literature, 71–75, 72f  
fermi-level pinning near clusters,  
85–86  
Ga vacancies, 77  
Ga vacancy clusters, 81–83, 82f–83f  
influence model, sphere of, 75  
interstitials, 78–79

- Dilute magnetic semiconductors (DMS)  
 (*Continued*)  
 percolation theory, results of, 83–84,  
 84f–85f  
 s–f coupling model, 75–76  
 vacancy model, critique of, 77–78  
 inhomogeneous/mixed-phase magnetic  
 rare-earth systems, 142–146,  
 144f–145f  
 magnetic rare-earth compounds,  
 heterostructures of, 146–151  
 complex rock-salt/zinc-blende  
 composites, 150f, 151  
 digital alloys, 147–149, 148f–149f  
 superlattice and multilayer  
 semiconductor/rare-earth  
 combinations, 144f–145f, 146–147,  
 147f  
 magnetism  
 critical temperatures calculating, 67–68  
 disordered local moments theory, 64  
 $d^0$  magnetism, 70  
 electronic structure methods, 66–67,  
 66f  
 Heisenberg model, total energy  
 differences on, 62–63  
 Liechtenstein's linear response theory,  
 63–64  
 magnetic moments/ferromagnetic and  
 antiferromagnetic coupling, 60–64  
 magnetic moments, spatial fluctuations  
 of, 64–65, 65f  
 model exchange mechanisms, 70–71  
 percolation theory, 66  
 spinodal decomposition, 68–69, 69f  
 objectives, 129–132, 130t, 131f  
 organization, 133  
 rare-earth-based layered chalcogenides  
 and pnictides/mixed anion, 151–156,  
 152t  
 layered rare-earth-based pnictides/  
 chalcogenides and oxide systems, 156  
 122 structure, 152–154, 153f  
 1111 structure, 154–156, 155f  
 rare-earth ions, properties of, 132  
 single-phase magnetic semiconductor alloys  
 heterovalent rare-earth incorporation,  
 homogeneous magnetic alloys based  
 on, 141–142  
 isovalent rare-earth incorporation,  
 magnetic semiconductors with,  
 133–140  
 transition-metal and rare-earth elements,  
 electronic structure of  
 basic energy level scheme, 45–48  
 f electrons multiplet splittings and  
 Hund's rules, 49–50  
 Diode logic circuit  
 using magnetic junction diode, 443, 444f  
 Disordered dilute magnetic semiconductors,  
 8–14  
 p-d exchange and double exchange  
 mechanisms, 8–10, 9f–10f  
 reliable calculation of  $T_c$ , 10–12, 11f  
 toward high  $T_c$ , 12–14  
 Disordered local moments theory, 64  
 $d^0$  magnetism, 70  
 Donor impurity band exchange, 322–324,  
 322f  
 ferromagnetism, 323–324  
 Double exchange mechanism, 397  
 Double heterostructure (DHS), 426–427  
 Dy-doped GaN, properties of  
 magnetic and optical properties, 385–386,  
 386f–387f  
 magnetic circular dichroism, 386–389,  
 388f–389f  
 Dynamic mean field theory (DMFT), 50,  
 58–59
- E**  
 Ebers-Moll model, 439–441  
 Electron diffraction pattern (EDP), 407  
 Electronic structure methods, 66–67, 66f  
 Electron paramagnetic resonance (EPR),  
 60  
 Electron spin resonance (ESR)  
 A, B, and C electron spin resonance centers,  
 origin of, 188–189  
 defined, 170  
 Er concentration dependence, 180–188  
 GaAs:Er,O with charge carriers,  
 183–188, 186f–187f  
 GaAs:Er,O without charge carrier,  
 180–183, 183f  
 Er pair model, 189–190  
 extended X-ray absorption fine structure  
 (EXAFS), 169–170

- GaAs:Er,O  
 fundamental properties of, 175–178  
 temperature dependences in, 177  
 growth conditions, Er-related PL spectra  
 on, 173–174  
 measurements, temperature dependences  
 in, 177  
 OMVPE growth systems, 172–173  
 organometallic vapor-phase epitaxy  
 (OMVPE), 169–170  
 sample preparations, 172–174  
 trap level, proposed model for, 190–192,  
 190f, 192f  
 Zn codoping (hole carriers) effect,  
 177f, 178–180
- Emitter-coupled spin-transistor logic  
 (ECSTL), 443–444
- Empty cage isomer, 120–121
- Energy dispersive X-ray spectroscopy,  
 340–341, 402
- Eu-doping  
 chemical structure and physical properties,  
 263t  
 LED structure, 263  
 OMVPE, 261–263, 262f  
 photoluminescence (PL) measurements,  
 263  
 structural/optical and magneto-optical  
 properties, 268–278  
 evaluation of, 272–278, 273t,  
 274f–277f  
 majority center/sites and local  
 defect assignment of, 268–272,  
 269f  
 X-ray absorption fine structure (EXAFS),  
 265, 265f
- Exchange interactions analysis, 79–81,  
 80f–81f
- Extraordinary Hall Effect (EHE)  
 measurements, 402, 404f
- F**
- Fabrication techniques, 438–439
- Face-centered cubic (FCC), 19–21
- Faraday geometry, 304–305
- Fermi-level pinning near clusters, 85–86
- Ferromagnetic coupling, 60–64
- Full width half maximum (FWHM),  
 338–339
- G**
- Gallium arsenide (GaAs), 103
- Gallium nitride (GaN)  
 bound magnetic polarons, 321, 321f  
 classic exchange mechanisms, 318–330  
 dilute magnetic semiconductors (DMS),  
 315, 317  
 donor impurity band exchange, 322–324,  
 322f  
 Ga<sub>1-x</sub>Cr<sub>x</sub>N, experimental studies for,  
 343–358, 345f, 347f–349f, 352f,  
 356t, 357f  
 Ga<sub>1-x</sub>Gd<sub>x</sub>N, density functional theory  
 studies of, 324–330, 325f–326f,  
 328f
- Gd in  
 clustering, growth simulations of,  
 86–90  
 exchange interactions analysis, 79–81,  
 80f–81f  
 experimental literature, 71–75, 72f  
 fermi-level pinning near clusters,  
 85–86  
 Ga vacancies, 77  
 Ga vacancy clusters, 81–83, 82f–83f  
 influence model, sphere of, 75  
 interstitials, 78–79  
 percolation theory, results of, 83–84,  
 84f–85f  
 s–f coupling model, 75–76  
 vacancy model, critique of,  
 77–78
- MOCVD, 331–343, 332f, 334f–338f,  
 342f
- nitride dilute magnetic semiconductors,  
 LEDs containing, 358–363  
 GaMnN-based light emitting diodes,  
 359–363, 359f, 361f–363f
- rare-earth impurities in, 25–31  
 circularly polarized luminescence,  
 30–31, 30f  
 high-density doping, 26–28, 28f  
 high-efficiency light emission,  
 25–26, 26f  
 Zener's p–f exchange interaction,  
 29–30, 29f
- RKKY, 319–320
- X-ray magnetic circular dichroism,  
 317–318

- Gallium-nitride:gadolinium-doped (GaN:Gd)  
 colossal magnetic moments  
 Gd ion-implanted wurtzite molecular beam epitaxy, 205–207, 206f  
 MBE-grown wurtzite SiC(0001) substrates, 203–205, 203f, 205f  
 dilutemagnetic semiconductor (DMS), 195–196  
 general considerations and experimental methods  
 magnetic properties, 197–198  
 SQUID magnetometry, 198–201, 200f  
 XAS-based techniques, 201–202  
 ion implantation, 207–213  
 Gd-implanted GaN samples, magnetic properties of, 212–213  
 wurtzite molecular beam epitaxy grown GaN/AlGaN-based HEMT on Si(111), 211–212, 212f  
 wurtzite molecular beam epitaxy grown GaN/Si(111), 209–211  
 zincblende MBE-grown GaN/SiC(001), 208–209, 208f  
 metal organic chemical vapor deposition (MOCVD), 204, 205f  
 molecular beam epitaxy (MBE), 196–197  
 Al<sub>2</sub>O<sub>3</sub>(0001), PAMBE and MOCVD on, 217–220, 218f–219f  
 SiC(0001), 214–217, 214f–217f  
 synchrotron-based investigations on, 213–220  
 overview, 196–197  
 plasma-assisted MBE (PAMBE), 204  
 GaMnN, 421–427, 422f  
 codoping, 422–423, 422f–424f  
 heterojunction interfaces, charge transfer through, 423–427, 424f–426f  
 room-temperature spintronic device, 427–431, 428f–431f  
 GaMnN-based light emitting diodes, 359–363, 359f, 361f–363f  
 GaN nanoparticles  
 doping, 111–115  
 Eu atoms, 111–113, 112f–113f  
 Gd and Nd atoms, 121, 121f  
 rare earths, 115–121  
 Si and Eu, codoping of, 113–115, 118f–119f  
 generalized gradient approximation (GGA), 109  
 metal organic chemical vapor deposition (MOCVD), 104–105  
 methods of calculation, 109–111, 110f  
 Si, Eu and codoping with, 116–121  
 spin-polarized density, 111–112  
 valence band (VB), 111  
 Gd-doped III-nitride magnetic semiconductors  
 circular-polarized laser diodes (CP-LDs), 372  
 Dy-doped GaN, properties of  
 magnetic and optical properties, 385–386, 386f–387f  
 magnetic circular dichroism, 386–389, 388f–389f  
 growth and structural properties, 372–374, 373f–374f  
 metal organic vapor phase epitaxy (MOVPE), 371–372  
 properties  
 low-temperature growth effect, 377–380, 378f–381f  
 magnetic and electric properties, Si codoping effect on, 380–382, 382f  
 nanorod structures, 382–385, 383f, 383t, 384f, 385t  
 single layers, magnetic and optical properties of, 374–376, 375f–377f  
 spintronic device application, 389–392, 390f–392f  
 tunnel magnetoresistance (TMR) devices, 372  
 Generalized gradient approximation (GGA), 51–52, 109  
 Generalized perturbation method (GPM), 17–18
- H**  
 Hall resistance ( $R_{\text{Hall}}$ ), 430–431  
 Hartree–Fock theory’s exchange, 52–53, 55–56  
 Heisenberg model, total energy differences on, 62–63  
 Heterojunction diode forms, 438  
 Heterovalent rare-earth incorporation  
 homogeneous magnetic alloys based on, 141–142

- Heterovalent rare-earth incorporation,  
homogeneous magnetic alloys  
based on  
final comment, 142  
II-VI semiconductor lattice, 141–142  
III-V semiconductor lattice, 141
- High-angle annular dark-field (HAADF),  
143–144
- High electron mobility transistor (HEMT),  
211–212
- High-resolution transmission electron  
microscopy (HRTEM), 403, 413
- High resolution XRD (HRXRD),  
333–334
- Hubbard  $U$  correction, 52–54
- Hund's rule, 396–397
- I**
- III-V nitride (III-N), 104
- Influence model, sphere of, 75
- InGaN alloys, 109–111
- Inhomogeneous/mixed-phase magnetic rare-  
earth systems, 142–146, 144f–145f
- InMnAs epitaxial layers, 435
- Isovalent rare-earth incorporation, magnetic  
semiconductors with, 133–140  
advanced tetrahedrally bonded structures,  
137–139, 138f–139f  
III-V and group-IV semiconductor lattice,  
136–137, 137f  
IV-VI semiconductor lattice, alloys based  
on, 139–140, 140f  
II-VI semiconductor lattice, rare-earth  
alloys based on, 133–136, 134f–135f
- K**
- Kohn–Sham scheme methods, 55
- Korringa-Kohn-Rostoker coherent potential  
approximations (KKR-CPA)  
method, 330
- Korringa–Kohn–Rostoker (KKR) theory,  
54
- L**
- Layered ferromagnetic magnetic alloys,  
152t
- Liechtenstein's formula, 32–33
- Light emitting diodes (LEDs), 7
- Linearized muffin-tin orbital (LMTO), 54
- Line shape analyses, 182–183
- Litvinov and Dugaev model, 322–323
- Local density approximation (LDA), 50–51
- Local spin density functional approach  
(LSDA), 52–53
- Low-temperature growth effect, 377–380,  
378f–381f
- Low temperature optical measurements,  
343
- M**
- Magnetic junction diode  
diode logic circuit using, 443, 444f
- Magnetic moments coupling, 60–64
- Magnetic properties, 298–309  
diffusion, samples prepared by, 298–300,  
299f–300f  
magnetic optical measurements, 300–309,  
301f–309f  
magnetization measurements, 298
- Magnetic rare-earth compounds,  
heterostructures of, 146–151  
complex rock-salt/zinc-blende composites,  
150f, 151  
digital alloys, 147–149, 148f–149f  
superlattice and multilayer semiconductor/  
rare-earth combinations, 144f–145f,  
146–147, 147f
- Magnetic semiconductors, 321
- Magnetism  
critical temperatures calculating,  
67–68  
disordered local moments theory, 64  
 $d^0$  magnetism, 70  
electronic structure methods,  
66–67, 66f  
Heisenberg model, total energy differences  
on, 62–63  
Liechtenstein's linear response theory,  
63–64  
magnetic moments  
ferromagnetic and antiferromagnetic  
coupling, 60–64  
spatial fluctuations of, 64–65, 65f  
model exchange mechanisms, 70–71  
percolation theory, 66  
spinodal decomposition, 68–69, 69f  
Magnetization, temperature dependence  
of, 382



- Magnetoconduction, 436–437  
 Magnetoresistance, 436–437  
 Matsubara frequencies, 58  
 Metal-insulator-semiconductor (MIS), 259–261  
 Metal organic chemical vapor deposition (MOCVD), 104–105, 204, 205f, 331–343, 332f, 334f–338f, 342f, 397–398, 414–420, 417f, 417t, 418f–421f  
   Er-doped III-N films, 226–234, 227f  
     alternative substrates, III-N:Er growth on, 233–234, 233f  
     GaN:Er films, 228–230, 229f–230f  
     InGaN:Er films, 231–232, 232f  
   III-N:Er thin films, magnetic properties of, 241–254, 242f  
     GaN:Er, 243–251, 243f–244f  
     influence of light on, 252–254, 253f  
     InGaN:Er, 251–252, 251f  
     strain-induced effects, 244–251, 245f–249f, 249t, 250f  
   optical properties  
     electroluminescent devices, 238–240, 239f–241f  
     photoluminescence characterization, 234–238, 235f–238f  
 Metal organic vapor phase epitaxy (MOVPE), 371–372  
 Metropolis algorithm, 22–23  
 Micro-Raman spectroscopy measurements, 334, 341  
 Microscopic mechanisms, 317–318  
 Mn-doped GaN (Mn:GaN) films, 397–398  
 Model exchange mechanisms, 70–71  
 Molecular beam epitaxy (MBE), 28, 104, 228–229, 397–398  
   background, 282–283  
   defined, 283–284  
   material characterization, 284–286, 285f–287f  
 Monomethylsilane (MMSi), 261–263  
 Monte Carlo simulation (MCS), 7  
 Multiple quantum well (MQW), 389  
 Multiple scattering theory, 10–11
- N**
- Nanoparticle surfaces, 120–121  
 Nanoscale clusters, 339  
 Nanospintronics materials  
   Computational Nano-Materials Design (CMD<sup>®</sup>) system, 4, 5f, 7  
   disordered dilute magnetic semiconductors, 8–14  
     p-d exchange and double exchange mechanisms, 8–10, 9f–10f  
     reliable calculation of  $T_c$ , 10–12, 11f  
     toward high  $T_c$ , 12–14  
   gallium nitride, rare-earth impurities in, 25–31  
     circularly polarized luminescence, 30–31, 30f  
     high-density doping, 26–28, 28f  
     high-efficiency light emission, 25–26, 26f  
     Zener's p-f exchange interaction, 29–30, 29f  
   MgO-based high- $T_c$  nanospintronics, 31–37, 32f–36f  
   spinodal nanodecomposition and high blocking temperature, 15–23  
     chemical pair interaction, 17–18  
     Dairiseki phase, 19–21, 20f–21f  
     Konbu phase, 21–22  
     mixing energy, 15–17, 17f  
     simulation, 18–22  
     superparamagnetic blocking phenomena, 22–23, 24f  
 Nitride dilute magnetic semiconductors, 358–363  
 III-V Nitride films by diffusion, transition metal-doping of, 398–414  
   Fe-doped GaN films, structural and magnetic characterization, 412–414, 412f–413f  
   Mn-doped GaN films, structural and magnetic characterization of, 399–402, 399f  
   Mn-doped InGaN films, structural and magnetic characterization of, 406–411, 407t, 408f–411f  
   Mn:GaN films, electrical characterization of, 402–405, 403f–406f  
 III-Nitride semiconductors  
   magnetic properties, 298–309  
     diffusion, samples prepared by, 298–300, 299f–300f  
     magnetic optical measurements, 300–309, 301f–309f  
     magnetization measurements, 298

- molecular beam epitaxy growth
  - background, 282–283
  - defined, 283–284
  - material characterization, 284–286, 285f–287f
- optical characterization
  - background, 287–288, 288f
  - combined excitation-emission spectroscopy (CEES), 296f, 297–298
  - conventional photoluminescence studies, 288–297, 289t–291t, 292f–295f
  - quantum sciences applications, 310
- O**
- Optical characterization
  - background, 287–288, 288f
  - combined excitation-emission spectroscopy (CEES), 296f, 297–298
  - conventional photoluminescence studies, 288–297, 289t–291t, 292f–295f
- Ordered vacancy compounds (OVCs), 138–139, 139f
- Ordinary Hall Effect (OHE), 430–431
- Organometallic vapor-phase epitaxy (OMVPE), 169–170, 172–173
- P**
- Percolation theory, 66
- Phonon-assisted transitions, 270
- Photoluminescence (PL), 136, 137f
  - intensity, 294, 295f
  - measurements, 104, 263
- Plasma assisted molecular beam epitaxy (PAMBE), 204, 217–220, 218f, 282
- Polaron-induced magnetism, 137–138
- Precursor flow rate (PFR), 414
- Q**
- Quantum wells (QWs), 406
- R**
- Radio-frequency plasma-enhanced MBE (RF-MBE), 382
- Raman spectroscopy, 345
- Random phase approximation (RPA), 56
- Rare-earth-based layered chalcogenides and pnictides/mixed anion, 151–156, 152t
  - layered rare-earth-based pnictides/chalcogenides and oxide systems, 56
  - 122 structure, 152–154, 153f
  - 1111 structure, 154–156, 155f
- Rare-earth ions, properties of, 132
- RE-doped compound semiconductor nanoparticles, 115–116
- Reflective high-energy electron diffraction (RHEED), 283–284, 398
- RKKY, 319–320
- Root mean square (RMS), 334
- Rutherford backscattering/channeling (RBS/C) measurements, 265
- S**
- Secondary ion mass spectrometry (SIMS), 108, 203, 228–229, 230f, 333–334, 399–400
- Selective area growth (SAG), 233
- Self-interaction correction approach (SIC), 54
- s-f coupling model, 75–76
- Si-CMOS technology, 6
- Simple set-reset (S-R) latch, 443
- Single heterostructure (SHS), 423–425
- Single-phase magnetic semiconductor alloys
  - heterovalent rare-earth incorporation, homogeneous magnetic alloys based on, 141–142
  - isovalent rare-earth incorporation, magnetic semiconductors with, 133–140
- Spin density functional theory, 326–327
- Spinodal decomposition, 68–69, 69f, 330, 353
- Spinodal nanodecomposition and high blocking temperature, 15–23
  - chemical pair interaction, 17–18
  - Dairiseki phase, 19–21, 20f–21f
  - Konbu phase, 21–22
  - mixing energy, 15–17, 17f
  - simulation, 18–22
  - superparamagnetic blocking phenomena, 22–23, 24f
- Spin-polarized conduction, 438
- Spin-polarized density, 29–30, 111–112
- Spin–spin interactions, 142–143
- Spintronic device application, 389–392, 390f–392f
- Strained-layer superlattice (SLS) multilayers, 427

Superconducting quantum interference device (SQUID), 195–196, 198–201, 200f, 337, 337f, 400–402, 414, 417, 419

Superparamagnetic (SPM), 198  
blocking phenomena, 14  
materials, 420

Surface morphology, 334

## T

Tetrahedron, 47

Transition metal (TM), 6–7

Transition metal-doped III-N  
semiconductors

3d shell electrons for, 396–397, 396t

GaMnN, 421–427, 422f

codoping, 422–423, 422f–424f

heterojunction interfaces, charge transfer  
through, 423–427, 424f–426f

room-temperature spintronic device,  
427–431, 428f–431f

MOCVD, 414–420, 417f, 417t, 418f–421f

III-V nitride films by diffusion, transition  
metal-doping of, 398–414

Fe-doped GaN films, structural and  
magnetic characterization, 412–414,  
412f–413f

Mn-doped GaN films, structural and  
magnetic characterization of,  
399–402, 399f

Mn-doped InGaN films, structural and  
magnetic characterization of,  
406–411, 407t, 408f–411f

Mn:GaN films, electrical characterization  
of, 402–405, 403f–406f

Transmission electron microscopy (TEM),  
333–334, 413

Trimethylgallium (TMGa), 261–263

Tris(2,2,6,6-tetramethyl-3,5-heptanedionato)  
gadolinium ((TMHD)3Gd), 331

Tris(cyclopentadienyl) gadolinium  
(Cp3Gd), 331

Tunnel magnetic resistance (TMR), 35–36,  
372

## V

Vacancy model, critique of, 77–78

Valence band (VB), 45–46, 111

van der Pauw Hall measurements,  
336–337

Vibrating sample magnetometry (VSM),  
356, 357f, 409, 410f–411f, 414

## W

Wide bandgap semiconductor (WBGs),  
236–237

## X

X-ray absorption fine structure (EXAFS),  
169–170, 265, 265f

X-ray absorption spectra (XAS), 59  
techniques, 201–202

X-ray diffraction (XRD), 284, 285f, 400

X-ray emission spectra (XES), 59

X-ray linear dichroism (XLD), 201–202,  
211–213

X-ray magnetic circular dichroism,  
317–318

X-ray photoemission spectroscopy (XPS),  
59

## Z

Zeeman splitting analysis, 136, 276, 278,  
300–302

Zener Mean field model, 323, 397

Zener theory, 421

Zero field cooled (ZFC), 198, 347–350

Traditional semiconductor devices are based on control of the electron's electric charge. In addition to the charge, the electron has a spin. The energy needed for switching the spin orientation from up to down and vice versa, is much smaller than the charging energy, so the problematic heat generation in today's semiconductor devices could be overcome. The use of the electron spin in semiconductor devices has recently become a rapidly growing research field, known as semiconductor spintronics. Spintronics refers to technologies that take advantage of the inherent spin in electrons and their related magnetic momentum. With spintronics, the aim is to produce smaller, faster and more power-efficient computers and other devices. This book looks at the semiconductor materials used for spintronics, focusing on wide band-gap semiconductors doped with transition metals and rare earths.

The book opens with a section covering the theory of magnetism in III-V semiconductors. Part Two moves on to review magnetic semiconductors based on rare earth/transition metals. Chapters analyze aspects such as gadolinium-doped gallium-nitride (GaN:Gd) and MOCVD growth and magnetic-optical characterization of Er-doped III-N films. Part Three details the properties of magnetic semiconductors for spintronics, including magnetotransport and magnetization dynamic measurements in semiconductor materials. The final section to the volume covers prototype spintronic devices, such as bipolar magnetic junction transistors for logic applications.

*Rare Earth and Transition Metal Doping of Semiconductor Materials* is a key reference for post-graduate students, scientists, applied researchers and production engineers working in the fabrication, design, testing, characterization and analysis of new semiconductor materials for spintronics applications.

Professor Volkmar Dierolf is Distinguished University Professor of Physics and Materials Science & Engineering. Professor Ian Ferguson is Vice Provost and Dean of Engineering and Computing at Missouri University of Science and Technology. Dr. John Zavada is a former Program Director at the National Science Foundation and currently Research Professor at NYU Polytechnic School of Engineering.



**WP**  
WOODHEAD  
PUBLISHING

An imprint of Elsevier • [store.elsevier.com](http://store.elsevier.com)

ISBN 978-0-08-100041-0



9 780081 000410